



*The Abdus Salam*  
**International Centre for Theoretical Physics**



**SMR 1829 - 10**

## **Winter College on Fibre Optics, Fibre Lasers and Sensors**

12 - 23 February 2007

### **Spectroscopy of Rare Earth Doped Glasses**

(articles used in the lectures)

**Anderson S. L. Gomes**

Department of Physics  
Universidade Federal de Pernambuco  
Recife, PE, Brazil

## Frequency upconversion of orange light into blue light in $\text{Pr}^{3+}$ -doped fluoroindate glasses

Luís E. E. de Araújo, A. S. L. Gomes, and Cid B. de Araújo

*Departamento de Física, Universidade Federal de Pernambuco, 50670-901 Recife, Pernambuco, Brazil*

Y. Messaddeq, A. Florez, and M. A. Aegerter

*Instituto de Física e Química de São Carlos, Universidade de São Paulo, 13560-970 São Carlos, São Paulo, Brazil*

(Received 19 July 1994)

Excitation of the transition  ${}^3H_4 \rightarrow {}^1D_2$  in a  $\text{Pr}^{3+}$ -doped fluoroindate glass at  $\sim 588$  nm results in efficient blue emission at  $\sim 480$  nm which is ascribed to the  ${}^3P_0 \rightarrow {}^3H_4$ . The upconversion process is due to an energy transfer involving a pair of  $\text{Pr}^{3+}$  ions. The dynamical behavior of the anti-Stokes emission is described using a rate-equation model which allows one to obtain the energy-transfer rates involving the pair states which contribute to the upconversion process.

### I. INTRODUCTION

Laser spectroscopic studies of energy transfer involving rare-earth (RE) ions in solids have helped to establish a broad understanding of these processes. Among the several phenomena already investigated, the cooperative energy transfer between ions in pairs or larger aggregates has been demonstrated in a large number of compounds.<sup>1</sup> This is a multipolar interaction through which a number of ions de-excite simultaneously and transfer the released energy to a nearby ion which is promoted to an excited state of high energy. Subsequent emission from that higher excited state produces photons with higher energy than the energy of the absorbed photons (anti-Stokes emission). This effect, known as a frequency upconversion, is attracting a great interest because of the possibility of fluoride-crystal-based upconversion lasers.<sup>2</sup> Recently, fluoride glasses became available with large upconversion efficiencies and fluorozirconate fiber lasers have been reported.<sup>3</sup>

Fluoroindate glasses are now emerging as a promising group of halide glasses for optical amplifiers and also for fibers lasers.<sup>4-6</sup> These glasses present higher transparency in the mid-infrared range (up to  $8 \mu\text{m}$ ) compared to fluorozirconate glasses and are more stable against atmospheric moisture. Studies of their optical properties in the visible region have also attracted attention since rare-earth ions can be easily incorporated in these compounds. It is now well established that the nonradiative relaxation rates of dopant ions levels in fluoroindate glasses are small due to their smaller phonon energies in comparison with other fluoride-based glasses.<sup>7-11</sup>

In this paper we report frequency upconversion studies in fluoroindate glasses doped with  $\text{Pr}^{3+}$ . The generation of anti-Stokes fluorescence ( ${}^3P_0 \rightarrow {}^3H_4$ ) excited via the  ${}^3H_4 \rightarrow {}^1D_2$  transition is studied. The phenomenon, which corresponds to a two-ion cooperative energy-transfer process involving  $\text{Pr}^{3+}$  ions, is described by  ${}^1D_2 + {}^1D_2 \rightarrow {}^3P_0 + {}^1G_4 + \text{phonons} \rightarrow {}^3P_0 + {}^3H_4 + \text{phonons}$ .

The energy transfer is followed by blue emission corresponding to the transition from level  ${}^3P_0$  to the ground

state. The observation of this kind of process in  $\text{LaF}_3:\text{Pr}^{3+}$  was due to Zalucha, Wright, Fong;<sup>12</sup> afterwards it was extensively studied by other groups in a variety of crystalline systems.<sup>13-18</sup> The effect was also investigated in borate glasses<sup>19</sup> and more recently in silica-based fibers doped with  $\text{Pr}^{3+}$ .<sup>20</sup>

Here we exploit the upconversion effect as a spectroscopical probe to investigate some characteristics of  $\text{Pr}^{3+}$ -doped in the fluoroindate matrix. In particular, the dynamics of the upconverted fluorescence is studied to evaluate upconversion transfer rates.

### II. EXPERIMENTAL

The glass samples studied have the following compositions: (mol. %)  $(39-x)\text{InF}_3-20 \text{ ZnF}_3-16\text{BaF}_2-20\text{SrF}_2-2\text{GdF}_3-2\text{NaF}-1\text{GaF}_3-x\text{PrF}_3$  ( $x=0.05; 0.1; 0.2; 1; 2$ ).

$\text{InF}_3$  was obtained by fluorination of  $\text{In}_2\text{O}_3$  at  $400^\circ\text{C}$  with  $\text{NH}_4\text{F}$  and  $\text{HF}$  in a platinum crucible. Then, all the fluoride components were mixed and heated in a dry box under argon atmosphere at  $700^\circ\text{C}$  for melting and  $800^\circ\text{C}$  for fining. After the fining process the melt was poured and cooled into a preheated brass mold. The obtained samples have a good optical quality and are nonhygroscopic. Previous studies with this material have been reported recently.<sup>4,7,9-11</sup>

The excitation within the  ${}^1D_2$  band of  $\text{Pr}^{3+}$  was achieved with a Nd:YAG pumped dye laser which produces 8-ns pulses of  $\sim 20$  kW (linewidth of  $\sim 0.5 \text{ cm}^{-1}$ ).

The linearly polarized excitation beam was focused into the sample with a 15-cm focal length lens and the emitted fluorescence was collected along a direction perpendicular to the incident beam. The signal was analyzed in a 0.5-m spectrometer equipped with a photomultiplier tube.

Optical-absorption measurements were made with a double-beam spectrophotometer. For all measurements the spectra resolution was much greater than the observed linewidths. All the data was taken at room temperature.

### III. RESULTS AND DISCUSSION

Figure 1 shows the absorption spectrum in the visible range, obtained with the  $x=0.2$  sample. The broad features of several Angstroms bandwidth can be easily identified with transitions from the ground state ( $^3H_4$ ) to the excited states of the  $\text{Pr}^{3+}$  ion. The bands positions and the relative intensities observed agree with previous reports on  $\text{Pr}^{3+}$  ions in other fluoride hosts.<sup>21,22</sup> The large bandwidths result from the site-to-site variation of the crystalline-field strength. The spectra obtained for the other studied samples are similar, except for the bands intensities and their linewidths which are dependent on the  $\text{Pr}^{3+}$  concentration. No changes in the wavelengths of maxima were observed. This is because the absorption bands are due to electronic transitions within the  $4f$  shell which is not very sensitive to the crystalline field.

Figure 2 shows the upconverted fluorescence spectrum obtained for one of the samples. The band peaking at  $\sim 480$  nm (transition  $^3P_0 \rightarrow ^3H_4$ ) was obtained by exciting the  $^3H_4 \rightarrow ^1D_2$  transition at 588 nm. The small feature centered around 468-nm corresponds to transition ( $^3P_1, ^1I_6$ )  $\rightarrow ^3H_4$ . Similar spectra was observed when exciting with the laser wavelength tuned from 586 to 590 nm.

The intensity of the upconverted fluorescence exhibits a quadratic dependence with the  $\text{Pr}^{3+}$  concentration and with the laser intensity. This behavior indicates that two  $\text{Pr}^{3+}$  ions and two incident photons participate in the process which generates each photon of the upconverted fluorescence signal. The results are explained according to the following process: A pair of neighboring  $\text{Pr}^{3+}$  ions are both excited to the  $^1D_2$  state by the laser pulse. Then cross relaxation takes place and the energy stored in the two ions is redistributed inside the pair in such way that one of the ions is promoted to the  $^3P_2$  state; afterwards a blue fluorescence is observed to arise from the  $^3P_0$

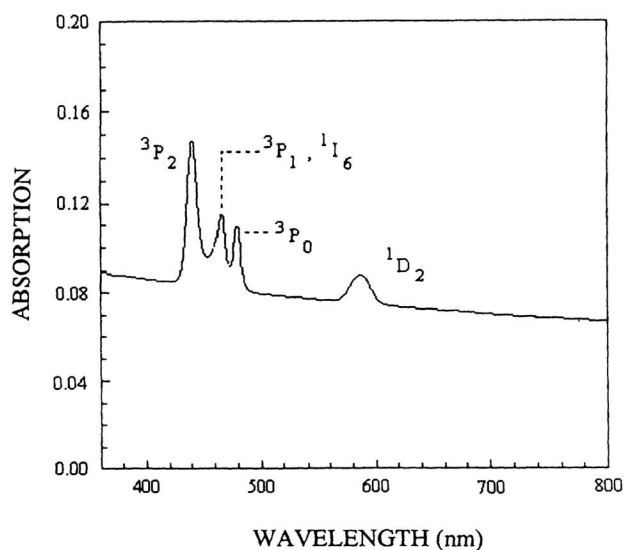


FIG. 1. Absorption spectrum of  $\text{Pr}^{3+}$  in fluoroindate glass at room temperature (sample with  $x=0.2$ ).

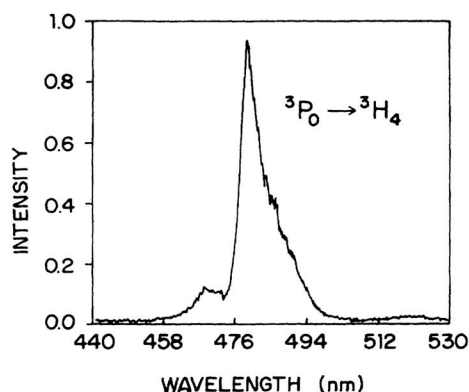


FIG. 2. Fluorescence spectrum corresponds to the transition  $^3P_0 \rightarrow ^3H_4$ . The excitation wavelength was in resonance with the transition  $^3H_4 \rightarrow ^1D_2$ . (Sample with  $x=0.2$ ).

state.<sup>13-18</sup> A fraction of the energy stored in the pair is dissipated by emission of phonons.

The temporal evolution of the blue emission is illustrated in Fig. 3 for the studied samples. As can be seen a similar behavior is observed for all samples, with rise and decay times which are  $\text{Pr}^{3+}$  concentration dependent. The solid lines represent the fitting to the expression ( $e^{-t/\tau_d} - e^{-t/\tau_r}$ ) for each sample where  $\tau_r$  and  $\tau_d$  represent the rise and decay times of the upconverted fluorescence, respectively. The values obtained for  $\tau_r$  and  $\tau_d$  are shown in Table I. Their dependence with the  $\text{Pr}^{3+}$  concentration is due to energy transfer among the excited ions and their neighbors.<sup>23</sup>

The dynamical behavior of the anti-Stokes intensity signal can be derived from rate equations for the populations of the pair states involved in the process. The temporal evolution after excitation of the populations of the initial state of the pair (that is, the pair state directly pumped by the laser) and of its final fluorescent state (one ion in the  $^3P_0$  state and another ion in the ground state) can be described by

$$\dot{n}_1 = -[W_{12}(x) + \gamma_1(x)]n_1, \quad (1)$$

$$\dot{n}_2 = -\gamma_2(x)n_2 + W_{12}(x)n_1, \quad (2)$$

when  $n_1$  and  $n_2$  are the populations of the pair states  $|1\rangle = |^1D_2, ^1D_2\rangle$  and  $|2\rangle = |^3P_0, ^3H_4\rangle$ , respectively.  $\gamma_1(x)$  represents the relaxation of state  $|1\rangle$  due to all possible mechanisms except the transfer to state  $|2\rangle$ .  $W_{12}(x)$  is the energy-transfer rate from state  $|1\rangle$  to state  $|2\rangle$ , and  $\gamma_2(x)$  is the total radiative relaxation rate from the state

TABLE I. Observed rise and decay times of the blue fluorescence  $^3P_0 \rightarrow ^3H_4$  for all studied samples.

| $x$  | $\tau_r$ ( $\mu\text{s}$ ) | $\tau_d$ ( $\mu\text{s}$ ) |
|------|----------------------------|----------------------------|
| 0.05 | 17                         | 224                        |
| 0.1  | 17                         | 193                        |
| 0.2  | 16                         | 126                        |
| 1.0  | 4                          | 50                         |
| 2.0  | 1                          | 22                         |

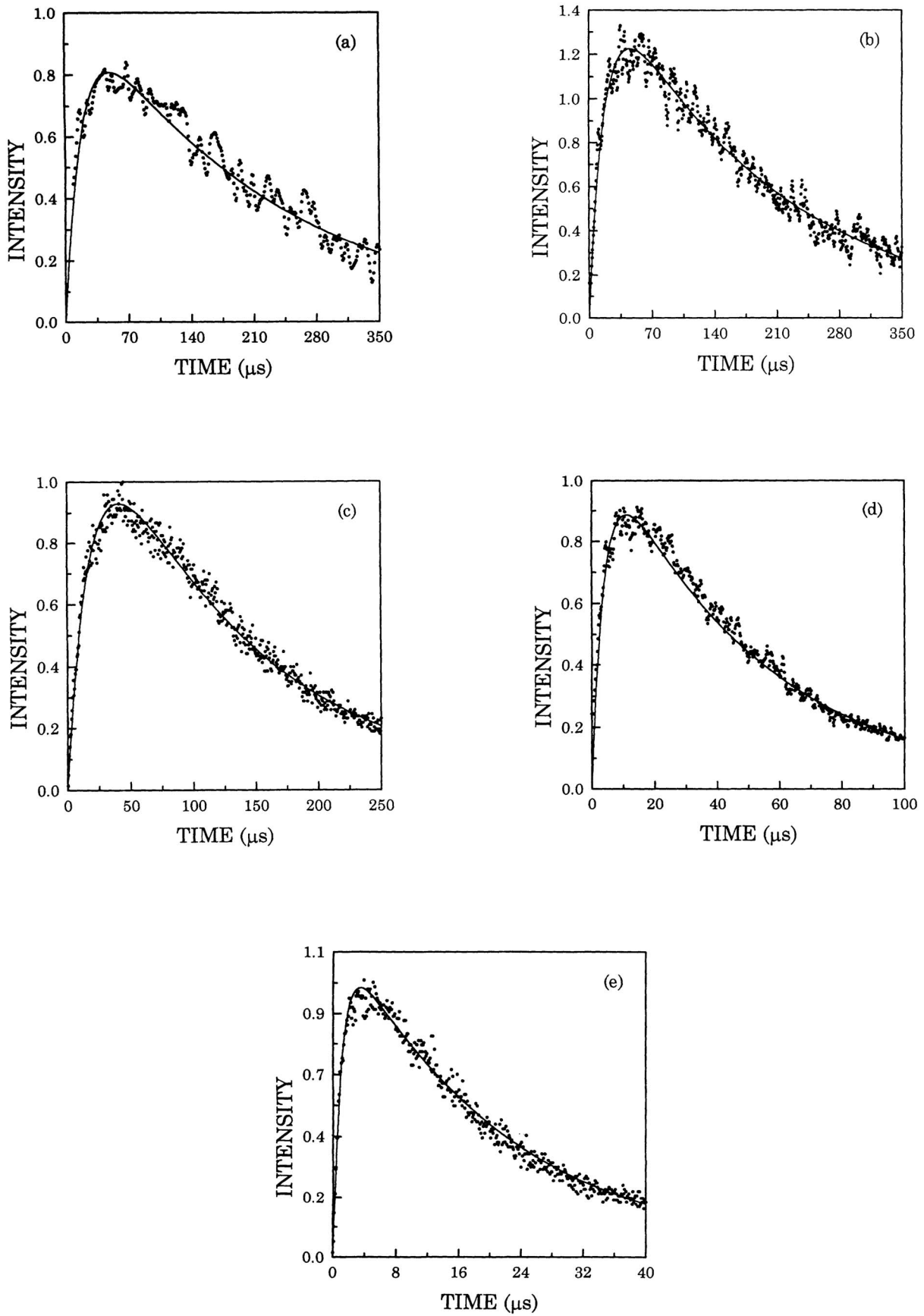


FIG. 3. Time evolution of the upconverted fluorescence: (a)  $x=0.05$ ; (b)  $x=0.1$ ; (c)  $x=0.2$ ; (d)  $x=1$ ; (e)  $x=2$ .

|2⟩. The solutions for these equations are

$$n_1(t) = n_1(0)e^{-(W_{12} + \gamma_1)t}, \quad (3)$$

$$n_2(t) = \frac{n_1(0)W_{12}}{W_{12} + \gamma_1 - \gamma_2} (e^{-\gamma_2 t} - e^{-(W_{12} + \gamma_1)t}). \quad (4)$$

To compare with the measured rise and decay time we first note that  $\tau_r^{-1}$  is the larger of the two rates ( $\gamma_1 + W_{12}$ ) and  $\gamma_2$ ;  $\tau_d^{-1}$  corresponds to the smaller rate.

Therefore, for long times, the fluorescence signal decays with an exponential decay time equal to  $\tau_d$  and we have observed decay times which are about one order of magnitude longer than the lifetime of the  $^3P_0$  state. Consequently,  $\tau_d^{-1}$  must be identified with  $(W_{12} + \gamma_1)$  and  $\tau_r^{-1}$  is equal to  $\gamma_2$ . It is interesting to note that  $(W_{12} + \gamma_1)$  is higher than  $2\tau_D^{-1}$  [ $\tau_D$  is the lifetime of state  $^1D_2$  determined by resonance fluorescence measurements for isolated ions,  $\tau_D = 460 \mu\text{s}$  (Ref. 23)]. This is a reasonable result since the decay rate of a pair state  $|m\rangle = |i, j\rangle$  is determined by the relation  $\gamma_m = \gamma_i + \gamma_j + W_T(i, j)$ , where  $\gamma_i$  and  $\gamma_j$  are the ions relaxation rates and  $W_T(i, j)$  is the total probability of transfer between the ions in the states  $i$  and  $j$ . The determination of  $W_T(i, j)$  is only possible when  $W_T(i, g)$  and  $W_T(j, g)$  ( $g$  designates the ground state) are negligible compared to  $\gamma_i$ ,  $\gamma_j$  and  $W_T(i, j)$ .<sup>18</sup> For example, in the specific case of state  $|^1D_2, ^1D_2\rangle$  resonant fluorescence measurements cannot provide reliable values to derive  $W_{12}$  and  $\gamma_1$  because the  $\tau_D$  value obtained in those experiments corresponds to isolated atoms. Moreover, the value of  $W_T(^1D_2, ^3H_4)$  may be affected by the excitation power density.

It is important to emphasize that we do not expect that multiphonon processes give an important contribution to the lifetime of levels  $^1D_2$  and  $^3P_0$ . As has been shown before<sup>21,24</sup> multiphonon decay rates exhibit an exponential dependence on the energy gap. In the present case, the

energy difference between the centers of the  $^3P_0$  and  $^1D_2$  is  $\Delta E \sim 3800 \text{ cm}^{-1}$ , while for the bands  $^1D_2$  and  $^1G_4$  we have  $\Delta E \approx 6800 \text{ cm}^{-1}$ . Those energy gaps correspond to a large number of high-energy phonons and the corresponding decay rates are negligible in comparison with the values calculated from Table I.

Finally, it is worthwhile to note that the large efficiency observed for upconversion generation in the fluoroindate glasses deserves further investigation which is beyond the scope of the present work. In fact, considering a density of  $5 \text{ g/cm}^3$  (Ref. 8) results in a distance of  $\sim 39 \text{ \AA}$  between  $\text{Pr}^{3+}$  ions for a sample with 0.2 mol. %. On the other hand, the Forster's critical transfer distance<sup>25</sup> for two rare-earth ions is  $\approx 20 \text{ \AA}$ . Therefore the large efficiency observed suggests clustering of the RE ions as proposed in Ref. 26 for other fluoride glasses. However more investigations are necessary to elucidate this point.

#### IV. CONCLUSION

Efficient blue upconversion was observed under excitation with an orange laser beam resonant with the  $^3H_4 \rightarrow ^1D_2$  transition of  $\text{Pr}^{3+}$ . Fluorescence transients were investigated and their rise and decay times were fitted by a model which considers the energy transfer inside a pair of  $\text{Pr}^{3+}$  ions as the dominant mechanism for generation of the upconverted signal. The present results show the large potential of fluoroindate glasses to be used as efficient hosts for upconversion generation.

#### ACKNOWLEDGMENTS

This work was supported in part by the Brazilian Agencies Conselho Nacional de Desenvolvimento Científico e Tecnológico (CNPq) and Financiadora Nacional de Estudos e Projetos (FINEP).

<sup>1</sup>For references on the subject, see, *Spectroscopy of Solids Containing Rare Earth Ions*, edited by A. A. Kaplyanski and R. M. Macfarlane (North-Holland, New York, 1987).

<sup>2</sup>A. Silversmith, W. Lenth, and R. M. Macfarlane, *Appl. Phys. Lett.* **45**, 1977 (1987).

<sup>3</sup>J. Y. Allain, M. Monerie, and H. Poignant, *Electron. Lett.* **26**, 166 (1990).

<sup>4</sup>Y. Messaddeq and M. Poulain, *Mater. Sci. Forum* **67/68**, 161 (1991).

<sup>5</sup>M. C. Brierley and C. A. Millar, *Electron. Lett.* **24**, 438 (1988).

<sup>6</sup>T. Sugana, Y. Miyasima, and T. Komuki, *Electron. Lett.* **26**, 2042 (1990).

<sup>7</sup>R. M. Almeida, J. C. Pereira, Y. Messaddeq, and M. A. Aegerter, *J. Non-Cryst. Solids* **161**, 105 (1993).

<sup>8</sup>Y. Messaddeq, A. Delben, M. A. Aegerter, A. Soufiane, and M. Poulain, *J. Mater. Res.* **8**, 885 (1993).

<sup>9</sup>R. Reiche, L. A. O. Nunes, C. C. Carvalho, Y. Messaddeq, and M. A. Aegerter, *Solid State Commun.* **85**, 773 (1993).

<sup>10</sup>S. J. L. Ribeiro, R. E. O. Diniz, Y. Messaddeq, L. A. Nunes, and M. A. Aegerter, *Chem. Phys. Lett.* **220**, 214 (1994).

<sup>11</sup>For a recent review of fluoride glasses, their synthesis and

properties, see for example, M. Poulain, A. Soufiane, Y. Messaddeq, and M. A. Aegerter, *Braz. J. Phys.* **22**, 205 (1992).

<sup>12</sup>D. J. Zalucha, J. C. Wright, and F. K. Fong, *J. Chem. Phys.* **59**, 997 (1973).

<sup>13</sup>J. C. Vial, R. Buisson, F. Madeore, and M. Poirier, *J. Phys. (Paris)* **40**, 913 (1979); R. Buisson and J. C. Vial, *ibid.* **42**, L115 (1981).

<sup>14</sup>A. Lezama, M. S. Oriá, and Cid B. de Araújo, *Phys. Rev. B* **33**, 4493 (1986).

<sup>15</sup>O. L. Malta, E. Antic-Fidancev, M. Lemaitre-Blaise, M. Dexpert-Ghys, and B. Piriou, *Chem. Phys. Lett.* **129**, 557 (1986).

<sup>16</sup>Y. L. Khong, G. D. Jones, and R. W. G. Syme, *Phys. Rev. B* **48**, 672 (1993).

<sup>17</sup>M. Mujaji, G. D. Jones, and R. W. G. Syme, *Phys. Rev. B* **48**, 710 (1993).

<sup>18</sup>F. Pelle and Ph. Glodner, *Phys. Rev. B* **48**, 9995 (1993).

<sup>19</sup>E. M. Pacheco and Cid B. de Araújo, *Chem. Phys. Lett.* **148**, 334 (1988).

<sup>20</sup>E. S. Moraes, M. M. Opalinska, A. S. L. Gomes, and Cid B. de Araújo, *Opt. Commun.* **84**, 2799 (1991).

- <sup>21</sup>J. L. Adam and W. A. Sibley, *J. Non-Cryst. Solids* **76**, 267 (1985).
- <sup>22</sup>J. L. Adam, W. A. Sibley, and D. R. Gabbe, *J. Lumin.* **33**, 391 (1985).
- <sup>23</sup>L. E. E. de Araújo, M.S. thesis, Universidade Federal de Pernambuco, 1994. [We have studied the temporal decay of the fluorescence following the direct excitation of levels  $^1D_2$  and  $^3P_0$ . For the samples with  $x=0.05$ , 0.1, and 0.2, we have obtained a nonexponential behavior which indicates the occurrence of energy transfer to nearest acceptors for short times ( $t < 50 \mu s$ ). For longer times the behavior is dominated by nearly isolated donors. For the samples with higher concentrations ( $x=1.0$  and 2.0) we have observed a fast exponential decay which indicates an energy migration process. Although these results express a behavior associated to the majority of the ions, they give us a qualitative understanding for the behavior of the ions which participate in the pair-upconversion process.]
- <sup>24</sup>C. B. Layne, W. H. Lowdermilk, and M. J. Weber, *Opt. Commun.* **18**, 173 (1976).
- <sup>25</sup>R. K. Watts, in *Optical Properties of Ions in Solids*, edited by B. DiBartolo (Plenum, New York, 1975), p. 317.
- <sup>26</sup>J. Y. Allain, M. Monerie, and H. Poignant, *Electron. Lett.* **27**, 445 (1991).

## Scanning thermal imaging of microelectronic circuits with a fluorescent nanoprobe

Lionel Aigouy<sup>a)</sup> and Gilles Tessier

Laboratoire "Spectroscopie en Lumière Polarisée," UPR A0005 du CNRS, ESPCI, 10 rue Vauquelin, 75231 Paris Cedex 5, France

Michel Mortier

Laboratoire de Chimie Appliquée de l'Etat Solide, UMR 7574 du CNRS, ENSCP 11 rue Pierre et Marie Curie, 75231 Paris Cedex 5, France

Benoît Charlot

TIMA, 46 avenue Félix Viallet, 38031 Grenoble, France

(Received 7 June 2005; accepted 8 September 2005; published online 26 October 2005)

We have developed a scanning thermal imaging method that uses a fluorescent particle as a temperature sensor. The particle, which contains rare-earth ions, is glued at the end of an atomic force microscope tip and allows the determination of the temperature of its surrounding medium. The measurement is performed by comparing the relative integrated intensity of two fluorescence lines that have a well-defined temperature dependence. As an example of application, we show the temperature map on an operating complementary metal-oxide-semiconductor integrated circuit.

© 2005 American Institute of Physics. [DOI: 10.1063/1.2123384]

An important development of scanning probe microscopy is the thermal microscope that allows to study local thermal effects at the surface of materials.<sup>1</sup> The applications of this technique concern the determination of the temperature of a sample surface, like an operating device<sup>2,3</sup> and the thermal conductivity of materials with a high lateral resolution.<sup>4,5</sup> For these applications, two main types of scanning probes have been implemented. The first one is a thermocouple junction situated at the extremity of the tip of a scanning tunneling or an atomic force microscope.<sup>6-8</sup> The temperature measurement is performed by monitoring the voltage between the two metals that constitute the thermocouple. The second probe is a resistive wire, bent at its extremity in order to form a sharp tip.<sup>5,9,10</sup> The temperature of the sample is determined by measuring the variation of electrical resistance of the wire.

One parameter that can limit the resolution of the probes is the size of the sensor. Even if the contact zone with the surface is as small as a few nanometers, the measurement can be perturbed by heat convection in air or by radiative energy transfer between the surface and the higher parts of the sensor. This can for instance, be the case of some resistive probes that have active zones extended over several microns above the sample surface. In this letter, we present a method to perform scanning thermal microscopy that uses a small fluorescent particle settled at the extremity of an atomic force microscope tip as a temperature sensor. Since fluorescence is a strongly temperature-dependent effect, its measurement can allow to perform a temperature map of a surface. In this technique, the size of the sensor can be reduced down to a few hundreds or even a few tens of nanometers, thus reducing strongly the zone from which the measurement is performed. We will first describe how the temperature can be extracted from a fluorescence signal. Then we will present an example showing the temperature

increase at the surface of an integrated circuit.

Different kinds of fluorescent particles have already been proposed as temperature sensors. Among them, CdSe quantum dots are good candidates<sup>11</sup> because their fluorescence intensity strongly varies with temperature. Rare-earth doped nanocrystals have also been suggested recently.<sup>12</sup> For practical applications, fluorescent europium-based molecules have been spin coated on the surface of a device to visualize its temperature distribution<sup>13,14</sup> but the problem of spin coating is that the particles remain on the structure after the measurement. By positioning the particle at the extremity of an atomic force microscope tip, we can perform a contact, but nondestructive measurement.

The fluorescent particles we have used are made from an erbium/ytterbium codoped fluoride glass. They were excited by a nonlinear mechanism called up-conversion: a laser diode ( $\lambda=980$  nm) illuminates the material and two photons are absorbed by ytterbium ions. The excitation is then resonantly transmitted to an adjacent erbium ion which radiatively relaxes to its ground level.<sup>15</sup> A fluorescence spectrum of the material at 300 K is given in Fig. 1(a). We are interested in the two peaks located around 527 and 550 nm. They correspond to transitions between the excited energy levels  $^2H_{11/2}$  and  $^4S_{3/2}$ , respectively, and the ground level  $^4I_{15/2}$ . These levels are in thermal equilibrium<sup>12</sup> and their population is ruled by a Boltzmann law of the form

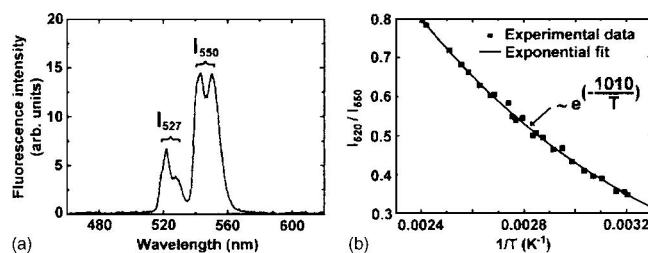


FIG. 1. (a) Photoluminescence spectrum of a micron-size particle; (b) dependence of the fluorescence ratio  $I_{527}/I_{550}$  with the inverse temperature.

<sup>a)</sup>Author to whom correspondence should be addressed; electronic mail: aigouy@optique.espci.fr

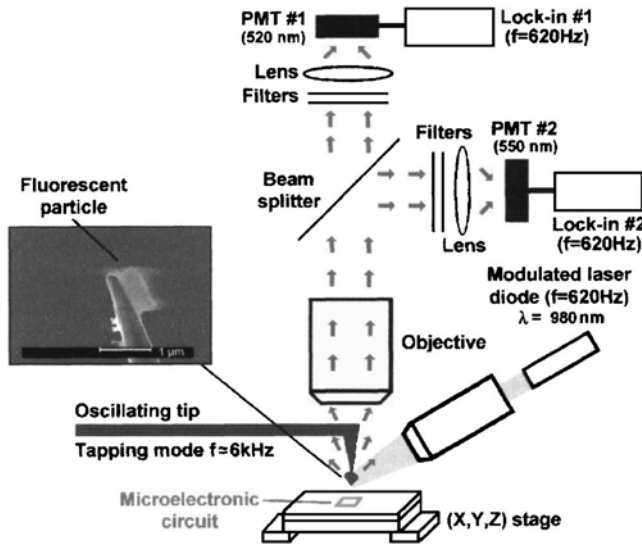


FIG. 2. Sketch of the experimental setup. The inset shows a scanning electron micrograph of a particle settled at the extremity of a tip.

$$\frac{I_{527}}{I_{550}} \propto \exp\left(-\frac{\Delta E}{kT}\right), \quad (1)$$

where  $I_{527}$  and  $I_{550}$  are the integrated intensity of the peaks,  $\Delta E$  is the energy separation of the levels, and  $k$  is the Boltzmann constant. Therefore, the ratio of the peaks area allows to determine the temperature  $T$ .<sup>12</sup> We have calibrated the ratio  $I_{527}/I_{550}$  by measuring the fluorescence spectra of a particle deposited on a heated substrate whose temperature is known. More precisely, we have integrated the two peaks in 10 nm bandwidth zones: [515–525] for the lower peak and [545–555] for the higher one because for the imaging experiments that will be described later, the fluorescence intensities will be detected in these spectral zones. A plot of the ratio as a function of the inverse temperature is given on Fig. 1(b) with an exponential fit that shows a dependence similar to the one predicted by Eq. (1). The fitting coefficient in front of the temperature is equal to  $1010 \pm 90$  K, a value which is very close to the parameter  $\Delta E/k$  ( $\sim 1180$  K) calculated with Eq. (1). We have performed a similar study on several particles that have different sizes (from around 1 to  $10 \mu\text{m}$ ) and have observed a similar dependence. In the case of particles whose diameter is smaller than  $100$  nm, size effects might occur and different temperature dependence could be observed.

In order to develop a scanning probe, a particle is stuck at the extremity of an atomic force microscope tip by a procedure described in Ref. 15. As represented in Fig. 2, the light is collected by a microscope objective and split towards two photomultiplier tubes (PMT). Two interferential filters centered at 520 and at 550 nm (bandwidth  $\sim 10$  nm) are placed in front of the PMTs. After a scan, we obtain two optical images that represent the fluorescence emitted at 520 and 550 nm, respectively. The thermal contrast is visualized by dividing the image at 520 nm by the image at 550 nm. The topography is also measured simultaneously in the tapping mode with an oscillation amplitude of 10 nm at a 6 kHz frequency. To allow a good thermalization of the particle, the scan speed was very slow (ten points per second). The sample studied is a polysilicon resistor stripe implemented on a standard  $0.8 \mu\text{m}$  complementary metal-oxide-

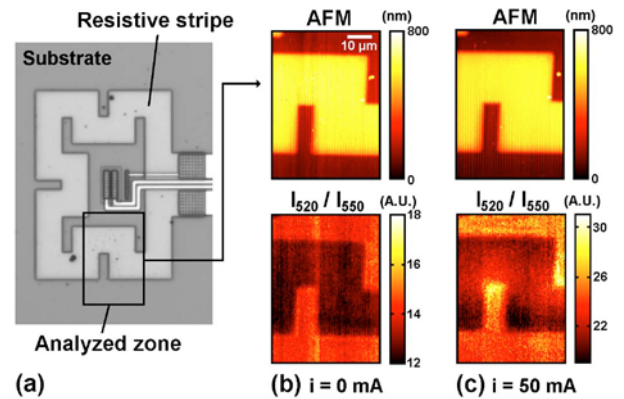


FIG. 3. (Color online) (a) Optical micrograph of the microelectronic circuit; (b) topography and fluorescence ratio images of the structure when no current is passing through the stripe; (c) topography and fluorescence ratio images when a current of  $\sim 50$  mA is passing through the structure. The bright (hot) zones are clearly visible on the stripe. The image size is  $45 \times 60 \mu\text{m}^2$ .

semiconductor process. The  $20 \mu\text{m}$  width polysilicon resistor is placed on top of the isolation oxide and is covered by silicon dioxide and silicon nitride layers. A micrograph of the chip is given in Fig. 3(a).

The topography and the ratio of the fluorescence images ( $I_{520}/I_{550}$ ) when no current is passing-through the resistor are displayed on Fig. 3(b). For this experiment, the temperature ( $\sim 30^\circ\text{C}$ ) is the same everywhere. However, by dividing the two optical images, an optical contrast is visible between the stripe and the substrate. To explain this difference, we must understand that the fluorescence emitted by the particle can reach the detector either directly, or indirectly after reflection or scattering by the sample surface. Therefore, since the sample is made of materials with different dielectric constants, a contrast is visible between the different zones. In general, dividing the two images at 520 and 550 nm does not fully cancel the difference because the ratio of the reflection coefficients at 520 and 550 nm is not the same for both materials. The units on the scale bar of Fig. 3(b) are arbitrary and depend on the gain of the PMTs. Nevertheless, they are directly linked to the temperature. The average values on the substrate and on the stripe are, respectively, 14.3 and 12.6.

The images of Fig. 3(c) represent the topography and the ratio of the fluorescence images when a current of 50 mA is passing through the resistor stripe. One can see that the scalebar values are twice higher than on the measurement performed without current. This means that the temperature of the whole structure has strongly increased. The electrical current induces a Joule heating of the stripe and heat diffuses in the structure. In addition to the global temperature augmentation, we can also see that the temperature is not uniform on the resistor. A hot curved zone is visible all along the middle of the stripe which corresponds to a locally higher electron density. This behavior has also been observed on the same sample by thermoreflectance.<sup>16</sup>

The optical image of Fig. 3(c) clearly shows a contrast related to the temperature of the surface. We have tried to analyze it quantitatively and to link it to the real value of the temperature. This can be done by comparing this image with the one obtained without current. For this purpose, we have normalized the image of Fig. 3(c) by the average value of the contrast at room temperature (14.3 for the substrate and 12.6

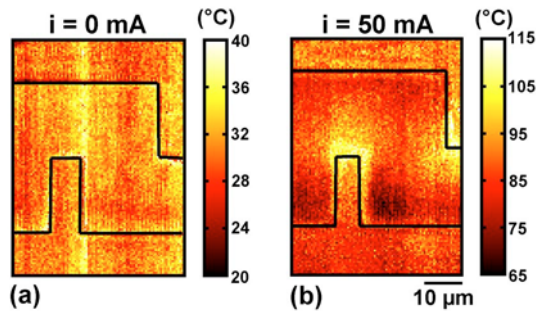


FIG. 4. (Color online) Reconstruction of the temperature map when (a) no current is passing through the structure and (b) a current of  $\sim 50$  mA is circulating in the stripe. The contour of the stripe has been drawn in black for clarity. The image size is  $45 \times 60 \mu\text{m}^2$ .

for the resistor, respectively). We obtain two images with different scalebars: one is valid for the substrate and the other one is valid for the stripe. These scalebars can then be converted to temperature by using a law derived from Eq. (1). Once the conversion has been performed, we can adjust each image with an identical intensity scale, and superpose them by only keeping the valid regions (the substrate for one and the stripe for the other). This manual combination allows to visualize the temperature distribution of the whole device.

The temperature maps obtained with and without an electrical current are displayed in Fig. 4. For both images, a noise of around  $5^\circ\text{C}$  is visible. For the image acquired with a current of 50 mA, the temperature distribution clearly shows the hot zone in the resistor and the substrate. The difference in temperature is approximately equal to  $30^\circ\text{C}$  between the hot zones of the stripe (near the angles) and its cold zones. Note that we have a temperature discontinuity of around  $5^\circ\text{C}$  at the frontier of the stripe and the substrate. We do not exactly know the origin of this discontinuity and particularly if it really has a physical meaning. It can be related to a thermal drift of the collection optics. Another possible explanation is that the temperature dependence of the fluorescence is slightly different on the resistor and the substrate. The thermal transfer mechanisms between the surface and the particle might not be the same on different materials. All these effects still have to be studied in detail.

In conclusion, we have developed a scanning thermal microscope that utilizes a fluorescent particle as a probe. The particle used had a diameter of around  $1 \mu\text{m}$ , a size small enough for the device studied for which the heat is diffusing over several dozens of micrometers. Reducing the particle size down to 100 nm is perfectly possible in order to study smaller devices for which heat diffuses over smaller distances. A theoretical study of the heat transfer mechanisms between the particle and a surface would also permit to determine the limits of the method, and for instance to calculate the time it takes for the particle to thermalize to the surface temperature, a parameter that can be important for the scanning speed of the measurements.

The authors thank D. Fournier for stimulating discussions. This work has been performed thanks to the financial support of the Centre National de la Recherche Scientifique (CNRS).

<sup>1</sup>H. M. Pollock and A. Hammiche, *J. Phys. D* **34**, R23 (2001).

<sup>2</sup>A. Majumdar, J. Lai, M. Chandrachood, O. Nakabeppu, Y. Wu, and Z. Shi, *Rev. Sci. Instrum.* **66**, 3584 (1995).

<sup>3</sup>Y. Zhang, Y. Zhang, J. Blaser, T. S. Sriram, A. Enver, and R. B. Marcus, *Rev. Sci. Instrum.* **69**, 2081 (1998).

<sup>4</sup>A. Hammiche, H. M. Pollock, M. Song, and D. J. Hourston, *Meas. Sci. Technol.* **7**, 142 (1996).

<sup>5</sup>S. Lefèvre and S. Volz, *Rev. Sci. Instrum.* **76**, 033701 (2005).

<sup>6</sup>C. C. Williams and H. K. Wickramasinghe, *Appl. Phys. Lett.* **49**, 1587 (1986).

<sup>7</sup>A. Majumdar, J. P. Carrejo, and J. Lai, *Appl. Phys. Lett.* **62**, 2501 (1993).

<sup>8</sup>G. Mills, H. Zhou, A. Midha, L. Donaldson, and J. M. R. Weaver, *Appl. Phys. Lett.* **72**, 2900 (1998).

<sup>9</sup>A. Hammiche, R. Reading, H. M. Pollock, M. Song, and D. J. Hourston, *Rev. Sci. Instrum.* **67**, 4268 (1996).

<sup>10</sup>P. G. Royall, V. L. Kett, C. S. Andrews, and D. Q. M. Gray, *J. Phys. Chem. B* **105**, 7021 (2001).

<sup>11</sup>G. W. Walker, V. C. Sundar, C. M. Rudzinski, A. W. Wun, M. G. Bawendi, and D. G. Nocera, *Appl. Phys. Lett.* **83**, 3555 (2003).

<sup>12</sup>M. A. R. C. Alencar, G. S. Maciel, C. C. B. de Araujo, and A. Patra, *Appl. Phys. Lett.* **84**, 4753 (2004).

<sup>13</sup>P. Kolodner and J. A. Tyson, *Appl. Phys. Lett.* **40**, 782 (1982).

<sup>14</sup>E. Van Keuren, M. Cheng, O. Albertini, C. Luo, J. Currie, and M. Paranjape, *Sens. Mater.* **17**, 1 (2005).

<sup>15</sup>L. Aigouy, Y. De Wilde, M. Mortier, J. Giérak, and E. Bourhis, *Appl. Opt.* **43**, 3829 (2004).

<sup>16</sup>B. Charlot, K. Torki, G. Tessier, C. Filloy, and D. Fournier, *Proceedings of the 10th International Workshop on Thermal investigations of ICs and Systems*, 2004, p. 261.

# Upconversion and Anti-Stokes Processes with f and d Ions in Solids

François Auzel

GOTR, UMR 7574-CNRS, 1, Place A-Briand, 92195 Meudon Cedex, France

Received February 25, 2003

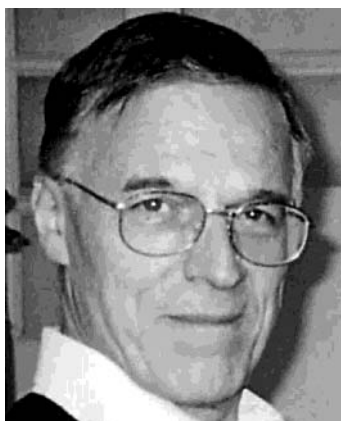
## Contents

|  |     |   |     |
|--|-----|---|-----|
| 1. Introduction and Historical Background  | 139 | 5. Cross-Relaxation and the Photon Avalanche Effect                                   | 161 |
| 2. Energy Transfers between RE Ions: Role of Energy Diffusion in Up- and Downconversion  | 141 | 5.1. Avalanche Process as a Positive Feedback System                                  | 161 |
| 2.1. Recall of Basics of Energy Transfer with Activator in Its Ground State  | 141 | 5.2. Conditions in Order To Observe an Avalanche Threshold                            | 162 |
| 2.2. Upconversion Processes by Sequential Energy Transfers (APTE or ETU Process): Comparison with ESA and Typical Examples   | 145 | 5.3. $\text{Er}^{3+}$ - $\text{LiYF}_4$ as an Avalanche Model Experiment              | 163 |
| 3. Upconversion in a Single-Ion Level Description for APTE (ETU) or ESA and in a Pair-Level One (Cooperative Effects): Theoretical and Experimental Discrimination | 146 | 5.4. Photon Avalanche in $\text{Er}^{3+}$ -Fluoride Glasses in Fiber and Bulk Shape   | 165 |
| 3.1. Three Different Kinds of Pair States  | 146 | 5.5. Avalanche in Codoped Systems   | 166 |
| 3.2. Fundamental Difference for Transitions between Single-Ion States, Dynamical and Static Pair States, and Cooperative Pair States                               | 147 | 5.6. Upconversion Laser with Multiphonon-Assisted Pumping Scheme and Photon Avalanche | 167 |
| 3.3. Application of Cooperative Luminescence; Theory, and Examples   | 150 | 6. Perspectives and Future Advances   | 167 |
| 4. Experimental Results and Their Implications in Various Fields   | 151 | 6.1. Upconversion UV-Tunable Lasers   | 167 |
| 4.1. Recent Upconversion Studies in Lanthanide (4f) and Actinide (5f) Ion-Doped Solids with APTE (ETU) and ESA Processes   | 151 | 6.2. New Materials for Low-Intensity IR Imaging                                       | 168 |
| 4.1.1. $\text{Pr}^{3+}$ (4f <sup>2</sup> ) Ion   | 151 | 6.3. Upconversion Material Intrinsic Bistability                                      | 168 |
| 4.1.2. $\text{Nd}^{3+}$ (4f <sup>3</sup> ) Ion   | 151 | 6.4. Hot Emission and Avalanche Like Co-Doped Systems                                 | 169 |
| 4.1.3. $\text{Gd}^{3+}$ (4f <sup>7</sup> ) Ion   | 152 | 6.5. Biological Applications  | 169 |
| 4.1.4. $\text{Dy}^{3+}$ (4f <sup>9</sup> ) Ion   | 152 | 7. Conclusion   | 170 |
| 4.1.5. $\text{Ho}^{3+}$ (4f <sup>10</sup> ) Ion  | 152 | 8. Acknowledgments  | 170 |
| 4.1.6. $\text{Er}^{3+}$ (4f <sup>11</sup> ) Ion  | 152 | 9. References   | 170 |
| 4.1.7. $\text{Tm}^{3+}$ (4f <sup>12</sup> ) Ion  | 153 |   |     |
| 4.1.8. $\text{Tm}^{2+}$ (4f <sup>13</sup> ) Ion  | 154 |   |     |
| 4.1.9. $\text{U}^{4+}$ (5f <sup>2</sup> ) Ion  | 154 |   |     |
| 4.1.10. $\text{U}^{3+}$ (5f <sup>5</sup> ) Ion   | 154 |   |     |
| 4.2. Recent Upconversion Studies in Transition-Metal (3d, 4d, 5d) Ion-Doped Solids with APTE (ETU), ESA, or Cooperative Processes                                  | 155 |   |     |
| 4.2.1. $\text{Ti}^{2+}$ (3d <sup>2</sup> ) Ion   | 155 |   |     |
| 4.2.2. $\text{Cr}^{3+}$ (3d <sup>3</sup> ) Ion   | 155 |   |     |
| 4.2.3. $\text{Ni}^{2+}$ (3d <sup>8</sup> ) and $\text{Mn}^{2+}$ (3d <sup>5</sup> ) Ions  | 155 |   |     |
| 4.2.4. $\text{Mo}^{3+}$ (4d <sup>3</sup> ) Ion   | 156 |   |     |
| 4.2.5. $\text{Re}^{4+}$ (5d <sup>3</sup> ) Ion   | 156 |   |     |
| 4.2.6. $\text{Os}^{4+}$ (5d <sup>4</sup> ) Ion   | 156 |   |     |
| 4.3. APTE (ETU) for Display and IR Detection Applications  | 156 |   |     |
| 4.4. General Negative Roles Brought up by Undesired APTE (ETU) Effects   | 158 |   |     |
| 4.5. APTE (ETU) and ESA Pumped Lasers  | 159 |   |     |

## 1. Introduction and Historical Background

Before the 1960s, all anti-Stokes emissions, which were known to exist, involved emission energies in excess of excitation energies by only a few kT. They were linked to thermal population of energy states above excitation states by such an energy amount. It was the well-known case of anti-Stokes emission for the so-called thermal bands or in the Raman effect for the well-known anti-Stokes sidebands. Thermoluminescence, where traps are emptied by excitation energies of the order of kT, also constituted a field of anti-Stokes emission of its own. Superexcitation, i.e., raising an already excited electron to an even higher level by excited-state absorption (ESA), was also known but with very weak emissions. These types of well-known anti-Stokes processes have been reviewed in classical textbooks on luminescence.<sup>1</sup>

All fluorescence light emitters usually follow the well-known principle of the Stokes law which simply states that excitation photons are at a higher energy than emitted ones or, in other words, that output photon energy is weaker than input photon energy. This, in a sense, is an indirect statement that efficiency cannot be larger than 1. This principle is



Francois Auzel, born July 5, 1938 in Roanne (France), graduated as both an engineer from ISEP (Institut Supereur d'Electronique, de Paris) in 1961 and a "Licencié-es Sciences Physique" in 1962 from the University of Paris. He was with France-Telecom Research Center (CNET) from 1961 to 1999. There, in 1961, he started working on Nd-doped phosphate glasses. In 1968, he received his Ph.D. degree from the University of Paris on "Erbium doped glasses for laser" under the guidance of Professor Otto Deutschbein and with Professor Alfred Kastler as adviser; as an outcome of this work, he proposed rare-earth-doped fluorophosphate glasses as laser materials with weak OH interactions. During his thesis work he demonstrated the possibility of upgoing sequential energy transfers (ETU) giving rise to upconversion of infrared to visible light, using Yb-Er (green emission) and Yb-Tm (blue emission) couples. In 1973, he received the Foucault prize from the "Société Française de Physique" for his discovery of upconversion processes by energy transfers (APTE effect)(1965–1966). In 1989, the French Academy of Science granted him the "Prix Winter-Klein" for his pioneer work on the spectroscopy of erbium-doped glasses (1965–1968). Other advances have been the experimental demonstration of the existence of Stokes and anti-Stokes multiphonon sidebands for trivalent lanthanides (1976), the proposal of a scalar crystal field parameter proportional to the maximum splitting of a J term (1979), the first observation of superradiance emission of a lanthanide (Er ions at 2.7  $\mu\text{m}$  at 10 K in weakly doped YLF crystals) (1986), the room-temperature avalanche effect of Er-doped glasses and crystals (1993), and the saturation effect of multiphonon decays in glasses (1996). He has been a part-time Professor at Ecole Centrale des Arts et Manufactures (1971–99) and at Orsay University (DEA Ecole Polytechnique-Lab. Aime Cotton) (1990–99). He created and headed the "Groupe d'Optique des Terres Rares", a team belonging to both CNRS and CNET, until his retirement from CNET in 1999. He is currently a voluntary researcher at CNRS and a consultant for active optical materials.

valid, of course, only when one excited ion system is considered.

In this review we will discuss anti-Stokes emissions or upconversion processes for which emission is found to exceed excitation energies by 10–100 times  $kT$ , which is violating Stokes law in its basic statement.

It will be shown that coupled lanthanide and uranide f ions and transition-metal d ions, when embedded in solids, may deviate rather easily from the above principle, producing upconversion emissions of the anti-Stokes types under moderate to strong excitation density.

A number of different mechanisms have been recognized to be involved in upconversion either alone or in combination.

Besides multistep excitation due to classical excited-state absorption (ESA), there is the very efficient process of upconversion by sequential energy transfers which has been named by Auzel APTE effect (for addition de photon par transferts d'énergie;<sup>2</sup> this effect was also later termed ETU for energy transfer upconversion.<sup>3</sup> This last phenomenon has to be

distinguished from a third process, namely, cooperative upconversion either between two ions or between a pair of ions and a third one. Though some aspects of its theoretical behavior are rather analogous with upconversion by energy transfers, its efficiency is usually much weaker. This is because it involves quasi-virtual pair levels between which transitions have to be described in a higher order of perturbation due to their double-operator nature.

A fourth process will also be considered: the photon avalanche effect, also based on sequential energy transfers but of the downconversion type (usually called cross-relaxation), whereas the upconversion step itself is due to ESA.

The various experimental techniques, which allow distinctions between the behaviors of these various processes, will be analyzed taking examples from the literature.

With the advent of high energy density laser sources, these processes have been observed in various types of ion-doped solids such as crystals and glasses in bulk, fiber, or waveguide form; the recent advances will be encompassed and described thereafter.

The whole field of upconversion in ion-doped systems can be traced back to an idea of Bloembergen in 1959,<sup>4</sup> proposing that infrared (IR) photons could be detected and counted through sequential absorption (ESA) within the levels of a given ion in a solid, that is using superexcitation as a detector. This was a short proposal for a detector called an infrared quantum counter (IRQC). In fact, because there was little chance with incoherent pumping that the same single doping ion would receive two photons in sequence at its given position during the first excited-state lifetime, the experimental demonstration of this effect had to wait for laser excitations and fiber local confinement. Some of the first experiments<sup>5</sup> have been proved later to be due to energy diffusion through energy transfers between identical ions.<sup>6</sup>

The role of energy transfers in upconversion processes was not recognized until 1966, when it was suggested by Auzel that energy transfers between RE ions could take place between two ions, both of them being in an excited state at the energy transfer initial step.<sup>7</sup> Until then, all energy transfers were assumed to take place from a first ion in an excited state to a second one in its ground state.<sup>8</sup> Because upconversion by sequential energy transfers or APTE effect is so efficient, it could initially be obtained through black-body excitation or spontaneous diode emission even before laser sources became commonly available.<sup>2</sup>

Principles and applications of such upconversion phosphors have already been presented in several reviews up to the 1970s by Auzel,<sup>2</sup> Mita and Nagazawa,<sup>9</sup> Garlick,<sup>10</sup> and Wright.<sup>3</sup> Since then, laser excitation in the IR and/or the use of fibers have become so easy that upconversion has become a pervading effect in all RE-doped materials under high-density IR excitation. Also, another type of upconversion, namely, the photon avalanche process,<sup>11,12</sup> has been widely investigated in recent years.

Limited aspects of recent progress have partially been reviewed through the 1980s and 1990s,<sup>13–18</sup> but

the general field has recently evolved from the rare-earth (4f) consideration toward the use of actinide (5f) and transition-metal (3d, 4d, 5d) ions with a systematic use of laser excitation at precisely defined wavelengths.

This evolution justifies the present review.

Because it appears that the language in the upconversion field is still not completely fixed, possibly inducing misinterpretation, the basic processes of energy transfers, cooperative processes, and their application to upconversion together with their more recent evolutions and selected examples of applications will be presented in reference to the accepted vocabulary proposed by the pioneers. Some of the original papers in this field were reprinted in 1998 in a collective edition.<sup>19</sup>

## 2. Energy Transfers between RE Ions: Role of Energy Diffusion in Up- and Downconversion

In the following, the mutual interactions between ions are the key feature.

When the concentration of active ions is increased, long before the appearance of new lines due to pairs or modifications in radiative transition probabilities, a migration of energy between the centers is found. We are going to study this now, assuming that multiphonon decays and the radiative transitions remain one-center processes.

As single f and d ions properties are supposed to be known, multiion processes, namely, energy transfers, are now dealt with. Energy transfer occurs in a system where absorption and emission do not take place within the same center. It may occur without any charge transport. Then one may distinguish between radiative and nonradiative, resonant, and phonon-assisted energy transfer. Theoretical approaches start from a microscopic point of view with a macroscopic result averaged over all the centers in the sample. In fact, an energy transfer between two given ions cannot by itself increase efficiency; it can only provide a new excitation wavelength range with a reduced efficiency since it consists of the product of two processes with intrinsic efficiency less than or equal to 1. Overall efficiency improvement by energy transfers is gained only from the spatial averaging due to the macroscopic process of diffusion.

### 2.1. Recall of Basics of Energy Transfer with Activator in Its Ground State<sup>20,21</sup>

In a schematic way, the different microscopic energy transfer processes between two ions can be presented as in Figure 1. Following the traditional vocabulary of the phosphor field, the ion being first directly excited is called a sensitizer (S); some people would call it a donor, but because f and d ions may also be imbedded in semiconductors, such vocabulary leads to confusion and is not retained here. The ion to which energy is transferred and which emits the output photon is called an activator; in a synonymous manner, it is some times termed an acceptor. To avoid any ambiguity with the semiconductor field, this vocabulary is not retained in the following.

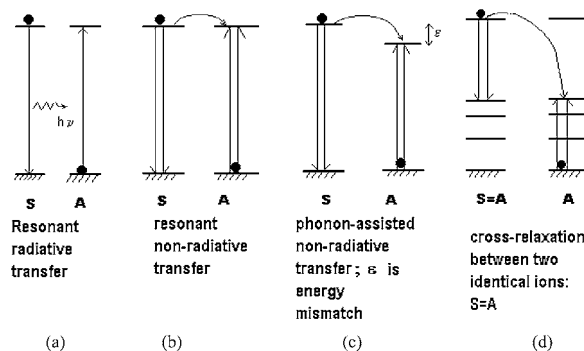


**Figure 1.** Various basic energy transfer processes between two ions considered before 1966: note that activator ion (A) receiving the energy from the sensitizer (S) is initially in its ground state. Cross-relaxation is the special case where S is identical to A. Doubled arrows symbolize the Coulombic interaction: (a) radiative resonant transfer; (b) resonant nonradiative transfer; (c) phonon-assisted non-radiative transfer;  $\epsilon$  is energy mismatch; (d) cross-relaxation special case of nonradiative transfer.

One usually distinguishes radiative transfer (Figure 1a), nonradiative energy transfer (Figure 1b), and multiphonon-assisted energy transfer (Figure 1c). S and A may also be identical ions, and nonradiative transfer may give rise to self-quenching by cross-relaxation (Figure 1d).

When energy transfer is radiative (Figure 1a), real photons are emitted by the sensitizer ions (S) and are then absorbed by any activator ions (A) within a photon travel distance. As a consequence, such transfer depends on the shape of the sample.

Moreover, according to the degree of overlap between the emission spectrum of the sensitizer (S) and the absorption spectrum of the activator (A), the structure of the emission spectrum of the sensitizer will change with activator concentration. Since photons are emitted anyway, the sensitizer lifetime is independent of the activator concentration. These three facts are the criteria used to distinguish between radiative and nonradiative resonant energy transfer.

Probability for such transfer between two ions at a sufficiently large distance  $R$  is found to be<sup>20</sup>

$$P_{SA}(R) = \frac{\sigma_A}{4\pi R^2 \tau_S} \int g_S(\nu) g_A(\nu) d\nu \quad (1)$$

where  $\tau_S$  is the sensitizer lifetime and  $\sigma_A$  the absorption-integrated cross section. The integral represents the spectral overlap between A and S. It should be noted that the distance dependence goes as  $R^{-2}$ . Such resonant radiative transfer may permit long-range energy diffusion between identical ions and gives rise to photon-trapping effects of the same type as the ones observed a long time ago in gases.<sup>22</sup> Trapping effects increase the apparent experimental lifetime, and  $\tau_S$  has to be measured on thin and lightly doped samples. These effects are particularly strong in  $\text{Cr}^{3+}$  and  $\text{Yb}^{3+}$ .<sup>23–25</sup>

Let us consider the simple case of two ions, each with one excitable electronic state separated from its electronic ground state by nearly equal energy; it is the case described in Figure 1b. With suitable

interaction between the two electronic systems, which is the case for nonradiative energy transfer, the excitation will jump from one ion to the other before one is able to emit a quantum of fluorescence. The mutual interactions are Coulomb interactions of the van der Waals type between the two ions. Förster,<sup>26</sup> who first treated such a case theoretically by quantum-mechanical theory, considered the dipole–dipole interaction. He assumed that the interaction is strongest if for both transitions electric–dipole transitions are allowed.<sup>26</sup> The interaction energy is then proportional to the inverse of the third power of the interionic distance and the transfer probability is given by

$$p_{SA} = \frac{2\pi}{h} |\langle S^* A^0 | H_{SA} | S^0 A^* \rangle|^2 \rho_E \quad (2)$$

$H_{SA}$  = electric dipole–dipole interaction Hamiltonian, proportional to the inverse third power of ion separation,

$\rho_E$  = density of states provided by the vibrational motion contributing to the line broadening of the transition,

$p_{SA}$  is proportional to the inverse sixth power of the ion separation. The wave functions to be considered for the matrix element describe an initial state of the system with the sensitizer in its excited state and the activator in its ground state, the final state having the sensitizer in its ground state and the activator in its excited state.

Therefore, the transfer probability can be written as

$$p_{SA} = \frac{1}{\tau_S} \left( \frac{R_0}{R} \right)^6 \quad (3)$$

where  $\tau_S$  is the actual lifetime of the sensitizer excited state, including multiphonon radiative decay, and  $R_0$  is the critical transfer distance for which excitation transfer and spontaneous deactivation of the sensitizer have equal probability.

However, Dexter pointed out<sup>27</sup> that this theory should be extended to include higher multipole and exchange interactions. In fact, for an isolated atom, one can consider the transition probability as decreasing as  $(a_0/\lambda)^{2n}$ , where  $a_0$  is the Bohr radius,  $\lambda$  the wavelength, and  $n$  an integer. However, in an energy transfer process with a dependence on near-zone interactions, the transition probabilities drop off as  $(a_0/\rho)^{2n}$ , where  $\rho$  is the separation of the interacting ions.  $\rho$  can be as much as 3 orders of magnitude smaller than  $\lambda$ , so that the energy transfer effect tends to be more pronounced in systems with forbidden transitions.<sup>27</sup> This holds true for ions for which transitions to first order are forbidden, such as transition-metal and lanthanide ions.

The energy transfer probability for electric multipolar interactions can be more generally written as<sup>27</sup>

$$p_{SA} = \frac{(R_0/R)^s}{\tau_S} \quad (4)$$

where  $s$  is a positive integer taking the following values:

- $s = 6$  for dipole–dipole interactions,
- $s = 8$  for dipole–quadrupole interactions,
- $s = 10$  for quadrupole–quadrupole interactions.

It should be noted that for dipole–dipole interactions, the difference between radiative and nonradiative resonant transfer lies essentially in the fact that for radiative transfer there is no critical  $R_0$  depending only upon concentration. The variation goes as  $R^{-2}$  instead of  $R^{-6}$ , and the sensitizer lifetime does not depend on the distance  $R$ .

Now, to be able to calculate effectively  $p_{SA}(R)$ , eq 4 is not very useful because  $R_0$  cannot be easily obtained theoretically. Applying Racah's tensorial methods at the beginning of the calculation of Dexter, eq 2, allows development of calculations analogous to Judd's theory for radiative transitions. The case of the multipolar interactions was treated in this way by Kushida<sup>28</sup> and extended by Pouradier and Auzel<sup>29</sup> to magnetostatic and exchange interactions, showing that a single general formula could be used for all types of energy transfers.

The general form obtained is then

$$p_{SA}(R) = \frac{2\pi}{h} \frac{I}{g_S \cdot g_{A^0}} \sum_{l_1 l_2} |C_{l_1 l_2} \langle S^* || U^{(l_1)} || S^0 \rangle \times \langle A^0 || U^{(l_2)} || A^* \rangle|^2 \quad (5)$$

with

$$I = \int \gamma_S(E) \Gamma_A(E) dE \quad (6)$$

where  $g_S \cdot g_{A^0}$  is the degeneracy of the  $S^*(A^0)$  level,  $\gamma_S(E) \Gamma_A(E)$  is the normalized line shape function of emission (absorption) spectrum,  $U^{(l)}$  are the tensorial operators already seen for Judd's theory.  $|C_{l_1 l_2}|^2$  can be considered as a parameter analogous to Judd  $T_i$  ( $\Omega_i$ ) for oscillator strength.

This expression of the transfer probability has the following advantages.

- (1) Radial and orbital parts have been separated.
- (2) Only a few reduced matrix elements need be calculated. They are the same for the three interactions we consider (for any interaction leaving spins unchanged).

(3) Comparison between two different interactions can be made through comparison of  $C_{l_1 l_2}$  coefficients. They are independent of the states involved in the transfer, and we call them  $E_{l_1 l_2}$ ,  $M_{l_1 l_2}$ , and  $X_{l_1 l_2}$  for electrostatic, magnetostatic, and exchange interactions, respectively.

(4) Forced electric–dipole transitions, as calculated by Judd's method, can be included in eq 5.

(5) This expression also gives a single mathematical form regardless of the interaction, which is a convenient result. The somewhat complicated expressions for the different  $C_{l_1 l_2}$  of 4f electrons are given in ref 29. However, we can note the following.

(a) For electrostatic interaction  $E_{l_1 l_2}$ , the  $l_1 = 1$  and  $l_2 = 1$  term, corresponding to dipolar–dipolar interaction, is zero in first order, which makes the introduction of Judd's  $T_i$  parameters necessary. The  $E_{l_1 l_2}$  values are typically between  $E_{22} \approx 30 \text{ cm}^{-1}$  for

quadrupole–quadrupole intensities and  $E_{66} \approx 3 \times 10^{-1} \text{ cm}^{-1}$ , but all contain some dipole–dipole part due to the  $T_{\lambda}$ .

(b) For magnetostatic interactions ( $M_{l_i l_b}$ ), only terms with  $l_i = 1, 3$ , and  $5$  are nonzero. They have the order of magnitude  $M_{11} \approx 1 \text{ cm}^{-1}$  and  $M_{55} \approx 2 \times 10^{-7} \text{ cm}^{-1}$ .

(c) For exchange interactions ( $X_{l_i l_b}$ ), we have  $1 \leq l_i \leq 6$ , giving estimates of  $1\text{--}10^{-1} \text{ cm}^{-1}$  for the coefficients.

These results show that exchange or magnetostatic interactions can be found in cases of small dipole–dipole and quadrupole electrostatic interactions if the matrix elements allow them.

If now we consider two ions with excited states of different energies (Figure 1c), the probability for energy transfer should drop to zero when the overlap integral  $\int g_S(\nu)g_A(\nu) d\nu$  vanishes. However, it has been experimentally found that energy transfer can take place without phonon-broadened electronic overlap provided that the overall energy conservation is maintained by production or annihilation of phonons with energies approaching  $k\Theta_d$ , where  $\Theta_d$  is the Debye temperature of the host matrix.<sup>30</sup> Then for small energy mismatches ( $100 \text{ cm}^{-1}$ ), energy transfer assisted by one or two phonons can take place.<sup>31</sup> However, for energy transfers between rare earths, energy mismatches as high as several thousand reciprocal centimeters are encountered. This is much higher than the Debye cutoff frequency found in normally encountered hosts, so multiphonon phenomena have to be considered here.

Miyakawa and Dexter<sup>32</sup> showed that it is still legitimate to write the probability of energy transfer in the form of eq 2, where  $\rho(E)$  is taken as  $S_{SA}$ , the overlap of the line shape functions for emission by ion S and absorption by ion A, including the phonon sidebands in the line shape. It is necessary to consider each partial overlap between the  $m$ -phonon emission line shape of ion S and the  $n$ -phonon absorption line shape of ion A. A physical meaning to this mathematical assumption, criticized in ref 31, has been given by Auzel's experimental demonstration<sup>33</sup> of the existence of multiphonon sidebands for trivalent rare-earth ions. Their existence could be revealed by laser excitation spectroscopy even though they had not been seen by usual absorption spectroscopy because of their very small electron–phonon coupling.

Along the same lines as for vibronic sideband studies,  $S_{SA}$  can be expressed as follows

$$S_{SA} = \sum_N e^{-(S_{OS} + S_{OA})} \frac{(S_{OS} + S_{OA})^N}{N!} \times \sigma_{SA}(0,0;E)\delta(N,\Delta E/\hbar\omega) \quad (7)$$

where  $S_{OS}$  and  $S_{OA}$  are the respective lattice coupling constants for the ions S and A,  $N$  is the order of the multiphonon process with  $N = \Delta E/\hbar\omega_m$ ,  $\Delta E$  is the energy mismatch between both ions, and  $\hbar\omega_m$  is the phonon cutoff frequency.  $\sigma_{SA}(0,0;E)$  is the zero-

phonon overlap integral between S and A. Equation 7 contains a Pekar function of the Poisson type.<sup>20</sup>

The expression for  $S_{SA}$  with an energy mismatch of  $\Delta E$  for small  $S_0$  constants and for an occupation number  $\bar{n} = (\exp(\hbar\omega/kT) - 1)^{-1}$ , not exceeding 1 at the operating temperature, can be approximated with Stirling's formula by

$$S_{SA}(\Delta E) = S_{SA}(0)e^{-\beta\Delta E} \quad (8)$$

where  $S_{SA}(0)$  is the zero-phonon overlap between S and A in the case where there is no energy mismatch between the two ions.  $\beta$  is given by

$$\begin{aligned} \beta &= (\hbar\omega)^{-1} \log N/S_0(\bar{n} + 1) - \log \left( 1 + \frac{S_{OA}}{S_{OS}} \right) \\ &\cong \alpha_S - \gamma \approx \alpha_S - \log 2 \end{aligned} \quad (9)$$

involving  $\alpha_S$  the nonradiative decay parameters and assuming identical electron–phonon coupling for ions A and S. This exponential dependence on energy mismatch is well substantiated by experiments.<sup>34</sup>

Up to this point we have been dealing with the microscopic case of two ions interacting with one another. To discuss the case of real macroscopic samples with many ions and to obtain a link with experimental facts, a statistical analysis of the energy transfer is necessary.

We have then to think about the overlap integrals that arise in all transfers between two ions as already seen. In the microscopic case we are sure that the involved line shapes can be only due to some homogeneous broadening even for transfer between two identical ions in different lattices sites.

In the macroscopic case, we can measure absorption and emission spectra taking into account all broadening processes averaged over the whole sample; for instance, the inhomogeneous broadening process due to emission and absorption at centers in different lattice sites. Then the overlap integral measured experimentally from the usual spectra is a measure in excess of the real overlap since we take into account emission and absorption of centers at any distances, even those which cannot interact. The error is the largest for the processes occurring at shortest interacting distances (exchange) and a contrario is certainly negligible for radiative transfer, since photons can travel a much larger distance than the spread of the spatial disorder. The error is also smaller for systems with small inhomogeneous broadening and having centers in only one type of lattice site, that is, without disorder.

Fluorescence line-narrowing techniques (FLN) could give some idea about the homogeneous part of an emission line, but the statistical analysis for the whole sample should still be performed. Supposing only a sensitizer–activator interaction, an averaged transfer efficiency can be calculated.<sup>27</sup> This has been studied in some detail by Inokuti and Hirayama.<sup>35</sup> They considered the number of activators located at random in a sphere around a sensitizer in such a way that the activator concentration is constant when the volume of the sphere and the number of activator ions considered goes to infinity. Then the averaged prob-

ability for transfer from one sensitizer to any acceptor is

$$W_{SA} = N_A \int_{R_{\min}}^{\infty} p_{SA}(R) 4\pi R^2 dR \quad (10)$$

Introducing eq 1 into the expression for the intensity emitted by all sensitizers, each with different activator neighborhood, they obtained the following relation for the intensity decay of the emission of the sensitizer surrounded by many activators

$$I(t) = \exp\left(-\frac{t}{\tau_{SO}} - \Gamma\left(1 - \frac{3}{S}\right) \frac{C}{C_0} \left(\frac{t}{\tau_{SO}}\right)^{3/S}\right) 3/S \quad (11)$$

where  $\tau_{SO}$  is the decay constant of the sensitizer in the absence of activators;  $C$  is the activator concentration;  $C_0$  is the critical activator concentration, and  $s$  is the parameter of the multipolar interaction. The comparison between experimental decay and this theoretical expression has been widely used to determine the index of the multipolar interaction involved. However, because it is difficult to avoid diffusion between sensitizers, fits of experimental results using eq 11 have to be taken with great care. For example, values of  $s$  larger than 10 have been found and it has been shown that for large  $s$  values the multipolar result has the same limit as the exponential behavior of an exchange process.<sup>24</sup> Yet, one cannot infer, as is sometimes done, that exchange coupling<sup>36</sup> is more likely than multipolar coupling. In fact, eq 11 is valid only at the microscopic level when there is neither sensitizer-to-sensitizer transfer nor activator-to-activator transfer. This formulation, therefore, has to be modified for high concentrations of sensitizers and activators. Then, due to the perfect resonance conditions in such cases, rapid energy migration between sensitizers or between activators is possible. The general result is complicated,<sup>37</sup> but Weber has shown that for large  $t$ ,  $I(t)$  decays exponentially<sup>38</sup>

$$I(t) = \exp\left(-\frac{t}{\tau_S} - \frac{t}{\tau_D}\right) \quad (12)$$

Then, two cases can be distinguished.

(i) In one case, spontaneous decay of excited sensitizers, diffusion among sensitizers, and energy transfer between sensitizers and activators are of about the same order of magnitude.

For sufficiently long times and dipole–dipole interactions one has<sup>38</sup>

$$\tau_D^{-1} = VN_S N_A \quad (13)$$

where  $V = 8\pi C^{1/4} C_{SS}^{3/4}$ ,  $N_S$  is the sensitizer concentration,  $N_A$  is the activator concentration,  $C$  is the sensitizer–activator energy transfer constant, such that  $C = (R_0)^5/R$ , and  $C_{SS}$  is the sensitizer–sensitizer transfer constant.

(ii) For high sensitizer concentration, the diffusion rate can be faster than spontaneous sensitizer decay or sensitizer–activator energy transfer. The limiting step is no longer diffusion, and  $D$  appears to saturate with increased donor concentration; each activator

experiences the same excited sensitizer neighborhood.  $R$  is taken as the minimum distance between sensitizers as permitted by the lattice ( $R = R_{\min}$ ). One has

$$\tau_D^{-1} = UN_A \quad (14)$$

with  $U$  being a constant depending on the type of interaction as discussed earlier in this section through eq 5.

Another approach to the macroscopic case is the use of the well-known rate equations that deal with the population of ions in a given state. This was used as a phenomenological approach in studies of lasers. The applicability of those equations in relation to the Inokuti and Hirayama statistics has been discussed by Grant.<sup>39</sup> The basic result of Grant is that the energy transfer probability is proportional to the activator concentration

$$W_t = UN_A \quad (15)$$

This result is the same as that obtained in fast-diffusion studies (eq 14). The practical interest in considering diffusion is that the decays are again exponential, as when ions are not interacting. This validates the use of rate equations.

Cross-relaxation terminology usually refers to all types of downconversion energy transfers occurring between identical ions. In such a case the same kind of ion is both sensitizer and activator.

As shown in Figure 1d, cross-relaxation may give rise to the diffusion process already considered between sensitizers when the involved levels are identical or self-quenching when they are different. In the first case there is no loss of energy, whereas in the second case there is a loss or a change in the energy of the emitted photons.

Theoretically, the same treatment is valid as in the more general case of energy transfer. However, it may be more difficult experimentally to distinguish between sensitizers and activators. Thus, any of the microscopic processes discussed above may happen with a maximum overlap when an identical couple of levels are involved. From the macroscopic point of view, the diffusion-limited case predicts from eq 13

$$\tau_D^{-1} = VN^2 \quad (16)$$

for  $N_S = N_A = N$ , and in the fast-diffusion case

$$\tau_D^{-1} = UN \quad (17)$$

A typical illustration of this is found for the self-quenching behavior of  $\text{Nd}^{3+}({}^4\text{F}_{3/2})$ . In weak quenching materials, such as  $\text{La}_{1-x}\text{Nd}_x\text{P}_5\text{O}_{14}$ , self-quenching is found to behave linearly with ion concentration, whereas for strong quenching ones, such as YAG, a quadratic behavior is obtained. This, respectively, reflects the fast diffusion before the quenching step in the first type of materials and the limited diffusion before quenching in the second type of materials.<sup>20,40</sup>

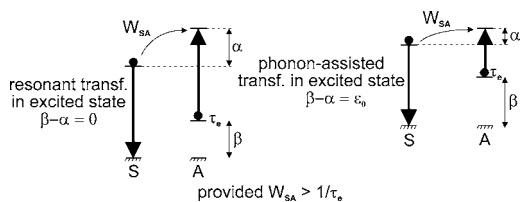


**Figure 2.** APTE basic step: energy transfer toward an ion already in an excited state. Nonradiative energy transfer is either resonant or phonon-assisted with energy mismatch  $\epsilon_0 \neq 0$ .

## 2.2. Upconversion Processes by Sequential Energy Transfers (APTE or ETU Process): Comparison with ESA and Typical Examples

As said in the Introduction, up to 1966 all identified energy transfers between rare-earth ions were of the types summarized in Figure 1, that is the activator ion receiving the energy from a nearby sensitizer (S) was in its *ground state*. Then Auzel proposed to consider cases where activators (A) were already in an *excited state*<sup>7</sup> as shown in Figure 2. Because activator ions usually have several ( $n$ ) excited states but a single ground state, one can understand why  $n$ -photons may be summed up through this new consideration. This becomes obvious when one realizes that only energy differences and not absolute energy can be exchanged between ions.

The reason for proposing such upgoing transfer was to point out that energy transfers then used<sup>41</sup> to improve the laser action of  $\text{Er}^{3+}$  by pumping  $\text{Yb}^{3+}$  in a glass matrix could also have the detrimental effect of increasing reabsorption.<sup>7,24</sup> The simple proof of such an effect was to look for an upconverted green emission (from  $^4\text{S}_{3/2}$  of  $\text{Er}^{3+}$ ) while pumping  $\text{Yb}^{3+}$  ( $^2\text{F}_{7/2} - ^2\text{F}_{5/2}$ ) transition, which was effectively observed.<sup>7,42</sup> Of course, the situation in Figure 2 could repeat itself several times at the activator. This meant that  $n$ -photon upconversion by energy transfer was possible as demonstrated by the three-photon upconversion of  $0.97 \mu\text{m}$  into blue light ( $0.475 \mu\text{m}$ ) in the  $\text{Yb}^{3+}-\text{Tm}^{3+}$  couple.<sup>7</sup> Independently this IR to blue upconversion was interpreted by Ovsyankin and Feofilov<sup>43</sup> as a two-photon effect connected with two excited  $\text{Yb}^{3+}$  ions and a cooperative sensitization of  $\text{Tm}^{3+}$  initially in its ground state. This interpretation originated from the law for output versus excitation, which was quadratic instead of cubic as found in ref 7 and because energy transfers between excited states were only being recognized independently at the time.<sup>7</sup> The experimental discrepancy aroused probably from a saturation in an intermediate step in the APTE process.<sup>44</sup>

Recently a systematic analysis of the power law governing the APTE (or ETU) process has been performed by Pollnau,<sup>45</sup> generalizing by rate equations what had been discussed for the  $\text{Yb}-\text{Tm}$  couple:<sup>2</sup> a  $P^n$  law can be found for an  $n$ -photon process when  $W_{\text{APTE}}$ , the APTE (ETU) upconversion probability, is weak, whereas a  $P^1$  law can be asymptotically obtained when  $W_{\text{APTE}}$  is large in front of other processes depopulating the metastable state.

To make the terminology clearer, a schematic comparison between the APTE (ETU) effect and other

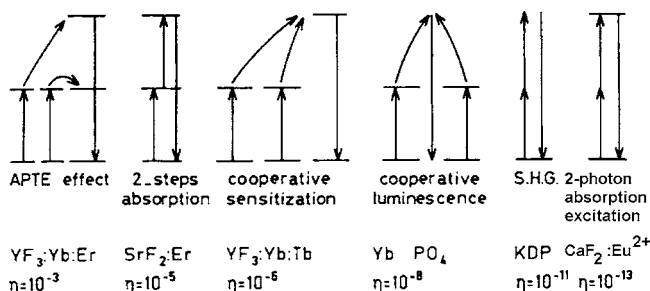


**Figure 3.** Various two-photon upconversion processes with their relative efficiency in considered materials.

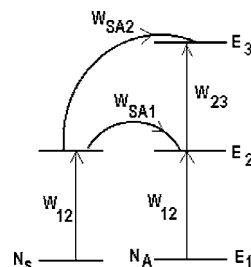


**Figure 4.** Simplified energy level scheme and symbols used in eqs 18–22.

two-photon upconversion processes, namely, two-step absorption, cooperative sensitization, cooperative luminescence, second-harmonic generation (SHG), and two-photon absorption excitation, is presented in Figure 3 together with their respective typical efficiency.

Since we are dealing with nonlinear processes, usual efficiency, as defined in percent, has no meaning because it depends linearly on excitation intensity. Values are then normalized for incident flux and given in  $\text{cm}^2/\text{W}$  units for a two-photon process. More generally, for an  $n$ -photon process it should be in  $(\text{cm}^2/\text{W})^{n-1}$ .

A simple review of the energy schemes shows that they differ at first sight by the resonances involved for in- and outgoing photons: for highest efficiency, photons have to interact with the medium a longer time, which is practically obtained by the existence of resonances. As shown, the APTE (ETU) effect is the most efficient because it is closest to the full resonance case.

However, reality is sometimes not so simple, and different upconversion processes may exist simultaneously or their effects can be tentatively made to reinforce each other. For instance, a combination of two-photon absorption and cooperative absorption has been theoretically investigated.<sup>46</sup> Also, SHG and cooperative luminescence have been considered simultaneously in order to increase SHG by the partial resonance of cooperative luminescence.<sup>47,48</sup>

Let us consider now the role of macroscopic energy diffusion in both APTE (ETU) and ESA upconversion second-order processes.

The probability for ESA in a two-step absorption ( $W_{13}$ ) connecting a state  $E_1$  to  $E_3$  by the intermediate state  $E_2$  is just given by the product of the probabilities for each step (Figure 4)

$$W_{13} = W_{12} \cdot W_{23} \quad (18)$$

To obtain the same result by an APTE effect, we also have to consider the product of two energy transfer probabilities and calculate the equivalent rate for populating  $E_3$  by APTE (ETU); we get (Figure 4)

$$N_A W_{13} \equiv (N_A N_S^* W_{SA1}) N_S^* W_{SA2} \quad (19)$$

or

$$W_{13} \equiv N_S^* W_{SA1} W_{SA2} \quad (20)$$

where  $W_{SA}$  are the energy transfers probabilities for each step and  $N_S^*$  is the concentration of excited sensitizers which is given by

$$N_S^* = N_S W_{12}$$

Assuming all  $W_{ij}$  have the same magnitude and all  $W_{SA}$  also, as is typical for rare-earth ions, we have to compare

$$W_{13} \approx W_{12}^2 \quad \text{for single-ion ESA} \quad (21)$$

with

$$W_{13} \approx N_S^{*2} W_{SA}^2 = N_S^2 W_{12}^2 W_{SA}^2 \quad \text{for two-ion APTE} \quad (22)$$

Clearly, the APTE (ETU) gain over one ion ESA comes from the product  $N_S^2 W_{SA}^2$ , which has to be as large as possible. However, this simple quadratic behavior with sensitizer concentration for a two-photon upconversion though observed in the past<sup>2</sup> can be questioned in some practical case as recently shown by Mita;<sup>49</sup> for Yb–Tm:BaY<sub>2</sub>F<sub>8</sub>, a quadratic behavior is first observed for a three-photon case and then a linear one (probability is constant) at Yb concentration above about 10%.

In any case, this points to an increase in sensitizer concentration ( $N_S$ ) which leads to fast diffusion<sup>38</sup> and allows the use of rate equations in such multiion systems.<sup>39</sup> This validates a posteriori the implicate use of the rate equation for establishing eqs 18–22. Now the behavior is different for certain hosts where ions are clustered into pairs even at low average concentration. This has been shown by Pellé and Goldner<sup>50</sup> for CsCdBr<sub>3</sub>:Yb, Er for which an Yb optimum concentration of 1% has been demonstrated, a significant difference with the usual 15% for other materials.<sup>51</sup>

Besides nonradiative diffusion at the sensitizer level, it has been observed that radiative diffusion plays also a role in APTE (ETU) upconversion. The measured time constants for the Er<sup>3+</sup> or Tm<sup>3+</sup> emission have been observed to be correlatively lengthened by the photon-trapping lengthening of the Yb<sup>3+</sup> lifetime, reflecting the radiative diffusion at the sensitizer level.<sup>52</sup> Also, reducing single crystals doped with Yb–Er or Tm to powder form usually produces an intensity reduction when the grain size is less than 100  $\mu\text{m}$ . This shows that the effective radiative diffusion length is of this order of magnitude in this experiment. Recently, studies on nanometric size upconversion phosphors with crystallites of Y<sub>2</sub>O<sub>3</sub>:Yb,-

Er, ranging from 75 to 200 nm in grains between 600 and 800 nm have shown that the maximum intensity for the blue and green emission under 632.8 nm excitation is obtained for the maximum size of 800 nm.<sup>53,54</sup> This effect is also most probably in connection with diffusion within Yb ions which, though not being directly excited, plays a role in an intermediate relay step of the APTE (ETU) process.

Many times in the literature, when ESA is not advocated, upconversion involving coupled ions is referred to as cooperative effects or cooperative energy transfers without proof when in fact APTE (ETU) effects are involved as can be guessed from their relative efficiencies and from the provided description. The fact that the APTE (ETU) effect and cooperative ones are often mistaken is due to a number of common properties.<sup>2</sup> For instance, for two-photon upconversion, both processes show quadratic increases on excitation and on absorber concentrations; both show an emission lifetime equal to one-half the absorber lifetime. However, they show different rise times; cooperative rise time is instantaneous as for ESA or any absorption, whereas APTE (ETU) rise time reflects the population accumulation at the sensitizer excited state. However, as shown below, the difference is more basic, though sometimes difficult to establish experimentally except in special cases where single-ion resonances clearly do not exist or where diffusion between ions is prohibited by a too small concentration with still an interaction as in clusters.

The basic distinction between both upconversion processes (ETU or ESA) within a single-ion state description and cooperative pair states is the purpose of the next section.

### 3. Upconversion in a Single-Ion Level Description for APTE (ETU) or ESA and in a Pair-Level One (Cooperative Effects): Theoretical and Experimental Discrimination

Because in the field of upconversion pair states or more recently dimer states are advocated to explain some of the observed processes, it is felt appropriate here to precisely define the vocabulary, which is done in the next subsection.

#### 3.1. Three Different Kinds of Pair States

In fact, when active ion concentration is increased, besides the occurrence, at first, of changes in probabilities for lower concentration as already pointed above, its value may reach a point where clusters may be formed and new levels may be experimentally observed. We think it is useful to distinguish between three types of pair levels, according to their different origin and shift from their parent single-ion level. When two resonant systems are coupled, it is a basic physical phenomenon that their degeneracy is removed. This may be called a dynamic shift, and for rare-earth ions it is typically 0.5  $\text{cm}^{-1}$ <sup>55</sup> up to a maximum of a few  $\text{cm}^{-1}$ ; it is 2.7  $\text{cm}^{-1}$  for Nd<sup>3+</sup> in CdF<sub>2</sub><sup>56</sup> and 3  $\text{cm}^{-1}$  in the stoichiometric compound Cs<sub>2</sub>Yb<sub>2</sub>Br<sub>9</sub> with built-in pairs with a distance of 3.9 Å.<sup>57</sup> In a stoichiometric material this would give rise

to a Frenkel excitonic band, though for rare-earth ions it has been shown to be rather limited by the weakness of the interaction.<sup>58</sup> Now in divalent materials or even in trivalent hosts,<sup>59</sup> when the active trivalent ion concentration is increased, one may understand that the local static crystal field is modified by the replacement of a divalent cation with a trivalent one or even by the ion size modification. This gives rise to a spectral shift on the considered single-ion levels when its concentration is increased. Such a shift may reach up to 10 cm<sup>-1</sup>. Though still often called a pair level,<sup>59</sup> this new single-ion level is of completely different origin from the previous one; it is sometimes also called a new site or a static pair state due to the active ion concentration increase.<sup>59</sup> It must be stressed here that one-center operators just as for transitions between single-ion states govern any transitions between such pair states.

Now, the third type of pair levels coming from what are called cooperative processes are very different from the two previous types because, as we are going to see, they involve two-center operators and are second order with respect to the transitions between pair levels of the two previous types. As we will see, the shift from the single parent states is the sum of the energy of the parent states; it is several hundreds or thousands of cm<sup>-1</sup>,<sup>60</sup> which does not represent the interaction strength inside the pair. The cooperative pair levels will be dealt with in more detail below (sections 3.2 and 3.3).

### 3.2. Fundamental Difference for Transitions between Single-Ion States, Dynamical and Static Pair States, and Cooperative Pair States

When active ions are situated at sufficiently short distances for interactions between them to take place, two types of upconversion processes may occur: summation of photon energy through energy transfers<sup>2</sup> (APTE (ETU) effect) and/or cooperative effects either by sensitization<sup>43</sup> or emission as found by Nakazawa and Shionoya.<sup>61</sup> Both APTE (ETU) effects and cooperative ones are often mistaken for the one another because both present several similarities and may simultaneously occur in a given system for a given excitation. In particular, both processes reflect the n-photon order versus excitation density and sensitizer concentration in the same manner.

As seen in the Introduction, upconversion by energy transfer is a generalization of Dexter's energy transfer<sup>27</sup> to the case where the activator is in a metastable state instead of being in its ground state; this requires the interaction between S and A ( $H_{SA}$ ) to be smaller than the vibronic interaction of S and A, so that both ions can be described by single-ion levels coupled to the lattice. It is generally the case since for fully concentrated rare-earth crystals or for clusters, pair level splitting is of the order of 0.5 cm<sup>-1</sup>;<sup>55,62</sup> in host with smaller concentrations, this interaction can be even weaker, whereas one-phonon or multiphonon sidebands may modulate the level positions by several hundreds of cm<sup>-1</sup>. Further, upconversion requires the transfer probability for the second step ( $W_{SA}$ ) to be faster than radiative and nonradiative decay from the metastable level, that

is  $W_{SA} > \tau^{-1}$  with  $\tau$  measured intermediate state lifetime for ion A.  $W_{SA}$  is obtained from

$$W_{SA} = \frac{2\pi}{\hbar} |\langle \Psi_S^e \Psi_A^0 | H_{SA} | \Psi_S^0 \Psi_A^e \rangle|^2 \rho(E) \quad (23)$$

where the wave functions are simple products of single-ion wave functions;  $\rho(E)$  describes the dissipative density of states due to the coupling with the lattice.  $H_{SA}$  is the interaction Hamiltonian, the origin of which may be multipolar or exchange interactions as discussed above in section 2.1.

All cooperative processes, including the simple cooperative absorption in PrCl<sub>3</sub> first observed by Varsanyi and Dieke<sup>63</sup> and the cooperative Stokes emission as observed by Van der Ziel and Van Uitert in EuAlO<sub>3</sub>:Cr<sup>3+</sup><sup>64</sup> from pair states and called exciton-(Eu) sidebands of localized excitons (Cr) or cooperative upconversion emission,<sup>61</sup> have to be considered as two-operator transitions between pair levels for both ions as a whole. A one-center dipolar electric transition would be strictly forbidden for a two-center transition, and as a difference with energy transfers for which plain product wave functions are used, one needs product wave functions corrected to first order to account for interaction between electrons of different centers<sup>65</sup>

$$\Psi_{\text{pair}} = \Psi^0(S)\Psi^0(A) - \sum_{s'' \neq 0} \sum_{a'' \neq 0} \frac{\langle s'' a'' | H_{SA} | 00 \rangle}{\delta_{s''} - 0 + \epsilon_{a''} - 0} \Psi_{s''}(S) \Psi_{a''}(A) \quad (24)$$

as given, for example, for the ground state;  $s''$ ,  $a''$  denote intermediate states for S and A and  $\delta_s, \epsilon_a$  denote their corresponding energies. Then any one-photon transition in the cooperative description involves already four terms in the matrix element, which cannot be reduced to eq 5 that contains only single-ion wave functions and not pair wave functions as in eq 24:

APTE (ETU) upconversion or ESA, even between static or dynamic pair levels, corresponds to a lower order of perturbation than cooperative processes, which involve cooperative pair states; the latter have to be considered practically only when the first type cannot take place.

Such is the case when real single-ion levels do not exist to allow energy transfer; it is the case for Yb<sup>3+</sup>-Tb<sup>3+</sup> upconversion<sup>55,66,67</sup> or when the concentration is too small to allow efficient transfer by energy diffusion between sensitizers. Then cooperative upconversion is likely within clusters.<sup>59,68</sup> One may also look for crystal structures where the pair clustering is built-in.<sup>57,62,69</sup>

Because cooperative transitions are of second order with respect to transitions between other pair states or single-ion states, they are very weak, about 3–4 orders of magnitude less than one-center transitions, and consequently they can usually be observed on small samples only in excitation and emission spectra. For example, a direct absorption spectra for a cooperative process between Yb and an allowed OH transition has only been observed on very long samples of about 5 cm and high Yb concentration

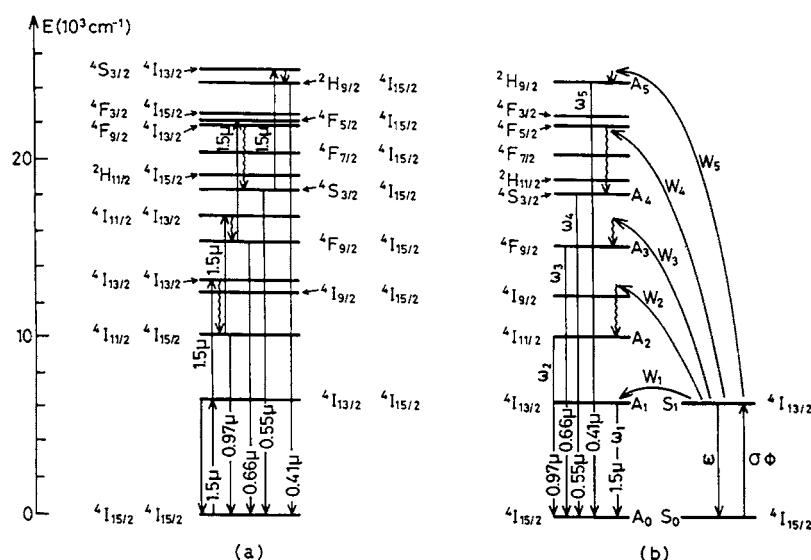


Figure 5. Cooperative (a) and APTE (b) energy scheme for  $n$ -photon ( $n = 1-5$ ) upconversion in  $\text{Er}^{3+}$ -doped hosts.

(from  $1.6 \times 10^{22}$  to  $4.3 \times 10^{23} \text{ cm}^{-3}$ )<sup>60</sup> with an intensity ratio to single-ion transition of about  $10^{-3}$ . Very recently similar results have been obtained for cooperative Yb–Yb pairs on 1–12 cm long Yb-doped laser crystals.<sup>70</sup> The intensity was found to be  $1.3 \times 10^{-5}$  of the single-ion one for a 1 cm long crystal of  $\text{Y}_2\text{O}_3:\text{Yb}(10\%)$ , that is with a concentration of  $2.8 \times 10^{21} \text{ cm}^{-3}$ . Such very weak ratios demonstrate the role of the double-operator nature of the transition. The 2 orders of magnitude difference, in both ratios given above, reflect in part the fact that Yb–Yb pairs are forbidden–forbidden pairs whereas Yb–OH are forbidden–allowed pairs.

Generally, experimental discrimination between APTE (ETU) and cooperative processes is not straightforward apart from the trivial cases where no real intermediate energy level exists for the APTE (ETU) effect to take place, even from unwanted impurities. The weak ion concentration level alone is not a good argument to eliminate APTE (ETU) upconversion, knowing that RE ion clusters may exist, for instance, in glasses, even at a doping level as low as 70 ppm.<sup>71</sup>

To illustrate the experimental difference between APTE (ETU) and cooperative upconversion, we will discuss an example of excitation line-narrowing effect in  $n$ -photon summation as a mean to distinguish between both processes.<sup>72,73</sup> Irradiating  $\text{Er}^{3+}$ -doped samples with IR radiation at  $1.5 \mu\text{m}$  leads to various visible emissions.

Room-temperature IR F-center laser excitation between 1.4 and  $1.6 \mu\text{m}$  of 10%  $\text{Er}^{3+}$ -doped vitrocera-mics and of  $\text{YF}_3:\text{Er}$  leads to emission bands from the near-IR to the UV. Such emission may be ascribed to multiphoton excitation, respectively, of order 1 to 5, either of the APTE (ETU) or of the cooperative type as depicted, respectively, with energy levels of single-ion (APTE) or cooperative pair levels (Figure 5).<sup>72,73</sup>

Successive absorptions in Figure 5a involve a combination of several J states. APTE (ETU) effect, because of self-matching by multiphoton processes, involves (Figure 5b) only  $J = 15/2$  and  $13/2$  states.<sup>72</sup>

Excitation spectra in Figure 6 show a striking behavior: each spectrum presents the same spectral

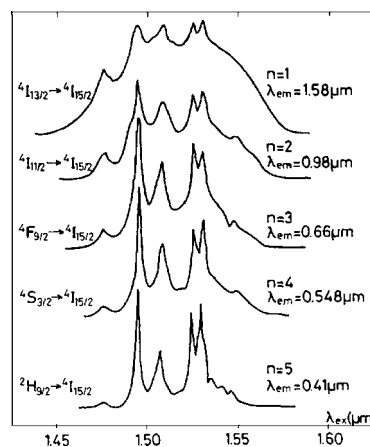


Figure 6. Excitation spectra for  $n$ -photon ( $n = 1-5$ ) upconversion in Er-doped  $\text{YF}_3$ .

structure with clearly an increasing narrowing with process order. The structure reproduces the Stark structure of the  ${}^4\text{I}_{15/2} - {}^4\text{I}_{13/2}$  first excited terms as can be obtained by a diffuse reflectance spectrum.

The spectral narrowing can be understood by a rate equation treatment where higher excited populations are neglected in front of the lower ones in order to obtain a tractable development (weak excitation assumption).

The emitted power from an  $n$ -photon summation is then given by

$$P_n(\lambda) = \frac{W_n \dots W_2}{(\omega_{(n-1)} \dots \omega_2)} P_1^n(\lambda) \quad (25)$$

with symbols of Figure 5b and  $P_1(\lambda)$  the line shape of  ${}^4\text{I}_{15/2} - {}^4\text{I}_{13/2}$  absorption.<sup>72</sup>

The obtained excitation spectra are direct proof of the validity of the APTE (ETU) explanation, since a cooperative effect should show the convolution of all J states involved in the multiple absorption between pair levels.<sup>72</sup>

Until the 1980s, few unquestionable experimental examples of cooperative upconversion were demonstrated besides the Yb–Tb cooperative sensitization

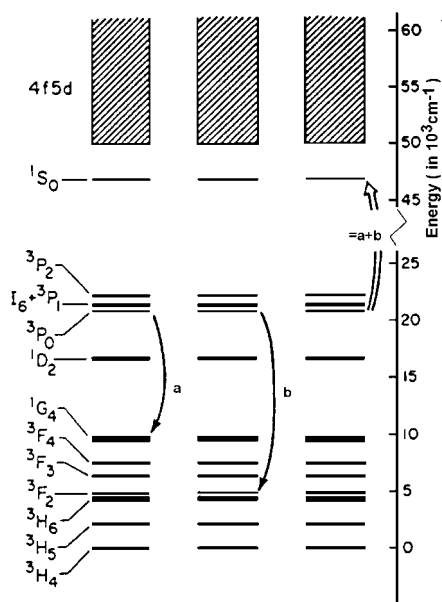


Figure 7. Cooperative luminescence and APTE (activator ion already in an excited state) cooperative sensitization in  $\text{LaF}_3:\text{Pr}^{3+}$  system. (Reprinted with permission from ref 75. Copyright 1984 American Physical Society.)

quoted above and the cooperative luminescence in  $\text{Yb}^{3+}$  described in detail below.<sup>61</sup> Since then, many more cases have been described:

The cooperative luminescence in the UV (from 405 to 270 nm) comes from two ( $^2\text{P}_0$ ) $\text{Pr}^{3+}$  excited ions in  $\text{PrF}_3$ <sup>74</sup> and  $\text{LaF}_3:\text{Pr}^{3+}$ ; the APTE (ETU) cooperative sensitization of the  $^1\text{S}_0$  state of one  $\text{Pr}^{3+}$  ion is already in its excited state ( $^3\text{P}_0$ ) from the energy annihilation of two other  $\text{Pr}^{3+}$  ions also in their  $^2\text{P}_0$  excited state as for the cooperative luminescence case.<sup>75</sup> Overall, this is a three-ion, three-photon effect which, from 477 nm blue excitation, gives an upconversion in the UV region (400–250 nm). Figure 7 describes the energy schemes and mechanisms for both processes. However, for some unknown reason, the cubic law which should be present for emission intensity versus

excitation is not observed for the  $^1\text{S}_0$  level emission<sup>74</sup> and a quadratic law is obtained as for the cooperative luminescence case. The cooperative effects were clearly discriminated from other processes through excitation spectra investigations.

Very recently, Valiente et al. obtained upconversion from near-IR  $\text{Yb}^{3+}$  excitation with visible emission from  $\text{Mn}^{2+}$  ions in stoichiometric materials,  $\text{CsMnCl}_3$ ,  $\text{RbMnCl}_3$ ,  $\text{CsMnBr}_3$ , and  $\text{Rb}_2\text{MnCl}_4$ , respectively at 690, 630, 680, and 625 nm.<sup>76–79</sup> Explanations were based on sequential absorption between dimer states built from  $\text{Yb}$  and  $\text{Mn}$  single-ion states which are in fact the cooperative pair states discussed above and shown, for instance, for  $\text{Er}^{3+}$  in Figure 6a in a cooperative hypothesis. This explanation is coming from the fact that emission of  $\text{Mn}^{2+}$  is instantaneous, as it would be for ESA between the dimer states, which have to be considered since both ions are involved. Along the same lines, the  $\text{Yb}-\text{Tb}$  case has been reconsidered in  $\text{SrCl}_2$  and  $\text{Cs}_2\text{Tb}_2\text{Br}_9:\text{Yb}(1\%)$ ,<sup>80,81</sup> and the cooperative effect is found to be ESA between cooperative pairs states and  $\text{Yb}$  cooperative luminescence with  $10^{-6}$  efficiency<sup>81</sup> (at 5.6  $\text{kW}/\text{cm}^2$  excitation) for  $T < 100$  K instead of the usual cooperative sensitization as in ref 66 found at larger  $T$ . As rarely given, efficiency for the cooperative sensitization process has been determined to be  $10^{-4}$  under 2.4  $10^4$   $\text{W}/\text{cm}^2$  at 300 K for  $\text{SrCl}_2$ ,<sup>80</sup> that is  $4.2 \times 10^{-9}$  at a normalized excitation level of 1  $\text{W}/\text{cm}^2$  for comparison, see Figure 3 and Table 1, with the values for cooperative sensitization of  $10^{-6}$  in  $\text{Yb},\text{Tb}:\text{YF}_3$  and of  $10^{-8}$  for cooperative luminescence in  $\text{YbPO}_4$ .

The  $\text{Yb}-\text{Tb}$  cooperative effect has also been revisited by Streck's group in  $\text{KYb}(\text{WO}_4)_2:\text{Tb}$ .<sup>82</sup> Besides the cooperative upconversion process itself, the interesting feature of a lifetime depending on the excitation level has been observed. It has been attributed to the inverse of cooperative sensitization, first predicted a long time ago by Dexter<sup>83</sup> and only recently identified experimentally for the first time by Basiev et al.<sup>84</sup> in  $\text{La}_{1-x}\text{Ce}_x\text{F}_3$ . This is different from quantum cutting,

Table 1. Available Measured Normalized Absolute Efficiencies for Various Upconversion Processes

| matrix  | ions                            | process            | order n | temp (K) | efficiency ( $\text{cm}^2/\text{W}$ ) <sup>n-1</sup> | ref   |
|---|---------------------------------|--------------------|---------|----------|--|-------|
| $\text{YF}_3$                                       | $\text{Yb}^{3+}-\text{Er}^{3+}$ | APTE (ETU)         | 2       | 300      | $\approx 10^{-3}$                                    | 2     |
| $\text{SrF}_2$                                      | $\text{Er}^{3+}$                | ESA                | 2       | 300      | $\approx 10^{-5}$                                    | 2     |
| $\text{YF}_3$                                       | $\text{Yb}^{3+}-\text{Tb}^{3+}$ | coop. sensitiz.    | 2       | 300      | $\approx 10^{-6}$                                    | 2     |
| $\text{YbPO}_4$                                     | $\text{Yb}^{3+}$                | coop. lumin.       | 2       | 300      | $\approx 10^{-8}$                                    | 13,61 |
| KDP   |                                 | SHG                | 2       | 300      | $\approx 10^{-11}$                                   | 2     |
| $\text{CaF}_2$                                      | $\text{Eu}^{2+}$                | two-phot. absorpt. | 2       | 300      | $\approx 10^{-13}$                                   | 2     |
| $\text{YF}_3$                                       | $\text{Yb}^{3+}-\text{Er}^{3+}$ | APTE (ETU)         | 2       | 300      | $2.8 \times 10^{-1}$                                 | 201   |
| vitroceramics                                       | $\text{Yb}^{3+}-\text{Er}^{3+}$ | APTE (ETU)         | 2       | 300      | $2.8 \times 10^{-1}$                                 | 51    |
| $\text{NaYF}_4$                                     | $\text{Yb}^{3+}-\text{Tm}^{3+}$ | APTE (ETU)         | 3       | 300      | $3.4 \times 10^{-2}$                                 | 158   |
| $\text{YF}_3$                                       | $\text{Yb}^{3+}-\text{Tm}^{3+}$ | APTE (ETU)         | 3       | 300      | $4.25 \times 10^{-2}$                                | 158   |
| vitroceramics                                       | $\text{Yb}^{3+}-\text{Tm}^{3+}$ | APTE (ETU)         | 3       | 300      | $8.5 \times 10^{-2}$                                 | 158   |
| $\text{NaYF}_4, \text{Na}_2\text{Y}_3\text{F}_{11}$ | $\text{Yb}^{3+}-\text{Er}^{3+}$ | APTE (ETU)         | 2       | 300      | $10^{-2}$ to $2 \times 10^{-4}$                      | 191   |
| $\text{NaYF}_4$                                     | $\text{Yb}^{3+}-\text{Er}^{3+}$ | APTE (ETU)         | 2       | 300      | $2.5 \times 10^{-4}$                                 | 16    |
| $\text{NaYF}_4$                                     | $\text{Yb}^{3+}-\text{Tm}^{3+}$ | APTE (ETU)         | 3       | 300      | $5.5 \times 10^{-2}$                                 | 191   |
| $\text{NaYF}_4$                                     | $\text{Yb}^{3+}-\text{Tm}^{3+}$ | APTE (ETU)         | 3       | 300      | $3 \times 10^{-7}$                                   | 16    |
| fluorohafnate glass                                 | $\text{Yb}^{3+}-\text{Tm}^{3+}$ | APTE (ETU)         | 2       | 300      | $6.4 \times 10^{-3}$                                 | 129   |
| fluorohafnate glass                                 | $\text{Yb}^{3+}-\text{Ho}^{3+}$ | APTE (ETU)         | 2       | 300      | $8.4 \times 10^{-4}$                                 | 129   |
| vitroceramics                                       | $\text{Yb}^{3+}-\text{Tm}^{3+}$ | APTE (ETU)         | 2       | 300      | $3.5 \times 10^{-1}$                                 | 157   |
| vitroceramics                                       | $\text{Yb}^{3+}-\text{Tm}^{3+}$ | APTE (ETU)         | 3       | 300      | $3.6 \times 10^{-3}$                                 | 157   |
| $\text{ThBr}_4$                                     | $\text{U}^{4+}$                 | ESA                | 2       | 300      | $2 \times 10^{-6}$                                   | 161   |
| $\text{SrCl}_2$                                     | $\text{Yb}^{3+}-\text{Yb}^{3+}$ | coop. lumin.       | 2       | 100      | $1.7 \times 10^{-10}$                                | 80    |
| $\text{SrCl}_2$                                     | $\text{Yb}^{3+}-\text{Tb}^{3+}$ | coop. sensitiz.    | 2       | 300      | $8 \times 10^{-8}$                                   | 80    |
| $\text{SrCl}_2$                                     | $\text{Yb}^{3+}-\text{Tb}^{3+}$ | coop. sensitiz.    | 2       | 100      | $1.8 \times 10^{-8}$                                 | 80    |

considered by Wegh et al.,<sup>85–89</sup> which is just the reverse of the APTE effect. Both quantum cutting and cooperative quenching can produce quantum efficiency larger than 1 but not with the same energy efficiency.

Along analogous lines, cooperative upconversion and downconversion processes mixed with multiphonon processes have been investigated in KYb(WO<sub>4</sub>)<sub>2</sub>:Eu,Tb<sup>90</sup> and in KYb<sub>0.8</sub>Eu<sub>0.2</sub>(WO<sub>4</sub>)<sub>2</sub>.<sup>91</sup>

A more complicated case of cooperative explanation has been given by Orlovskii et al.<sup>56,92</sup> for Nd<sup>3+</sup> in CaF<sub>2</sub>, CdF<sub>2</sub>, and SrF<sub>2</sub> at 4.2 K. There the three kinds of pair states discussed in section 3.1 are simultaneously involved in a qualitative description through both APTE (ETU) and ESA processes. Unfortunately no quantitative analysis with respect to the mixing of first-order and second-order transitions has been given.

### 3.3. Application of Cooperative Luminescence; Theory, and Examples

Because cooperative processes are less effective than APTE (ETU) ones by 4–5 orders of magnitude, very few applications of such processes exist except, as we will see, the detection of RE ion clusters. We proposed that the simplest cooperative process, the cooperative luminescence of Yb<sup>3+</sup>,<sup>61</sup> be used as a probe of the existence of Yb<sup>3+</sup> ions clusters in glasses.<sup>68</sup>

Cooperative luminescence (or its opposite cooperative absorption) is the simplest cooperative phenomenon, and the corresponding two-center matrix element is

$$\langle \Psi_{\text{pair}}^g | D_1^{(1)} + D_2^{(1)} | \Psi_{\text{pair}}^e \rangle \quad (26)$$

where the operator is the sum of the electric dipole operators for ion 1 and ion 2. The wave functions for both ions in their excited state  $\Psi_{\text{pair}}^e$  and in their ground state  $\Psi_{\text{pair}}^g$  are derived from expressions given by eq 24. The calculation of eq 26 gives four terms that are represented in Figure 8; terms III and IV provide the cooperative emission at twice the energy of the single-ion excited state.

Since along the RE series nearest neighbor ions have analogous chemical properties, we assumed that Yb<sup>3+</sup> would chemically behave for the clustering process ion the same way as for Er<sup>3+</sup>, the ion generally used in optical amplifiers. Because Yb<sup>3+</sup> ions have only two spin-orbit states, they are good examples of the simple situation schematized in Figure 8. This is one of the reasons for its use as a cluster probe. The other reason is as follows:

In optical amplifier applications, the basic limitation linked with the existence of the so-called clustering of RE ions was addressed. Clusters of RE dopant, as found in the literature from direct fiber amplification experiments,<sup>71,93,94</sup> are related to what could be called interaction clusters which are much larger than chemical clusters. Because of spatial diffusion as shown in section 2.1, such interaction clusters could have a spatial extension of more than 20–100 Å for nonradiative interaction clusters and up to 100 μm for radiative ones. Clearly, such clusters have

The 4 terms in  $\langle \Psi_{\text{pair}}^g | D_1^{(1)} + D_2^{(1)} | \Psi_{\text{pair}}^e \rangle$ :

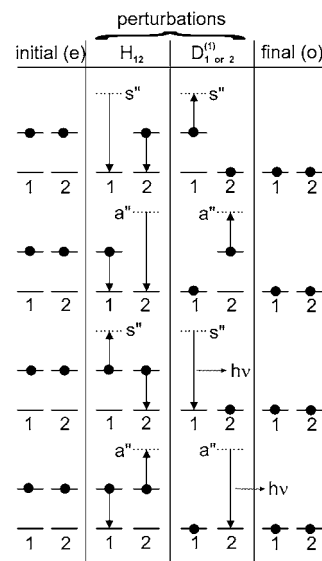


Figure 8. Four terms for cooperative luminescence in a two-level ion system (the Yb<sup>3+</sup> case).

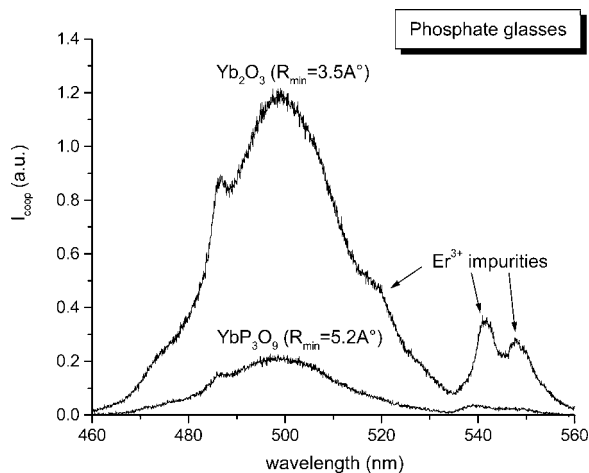


Figure 9. Normalized cooperative emission spectra for Yb<sup>3+</sup> in a phosphate glass for two doping precursors with different Yb–Yb shortest distance  $R_{\text{min}}$ .

nothing to do with chemical clusters, which depend only on the chemical processes of the glass preparation. The existence of chemical clusters of spatial extension of a few Angstroms would increase tremendously ion–ion interactions of any kind. One need to obtain a signature of such clusters that is the only one that chemistry could eventually modify. Cooperative luminescence of Yb<sup>3+</sup> has been proposed as a signature of the existence of chemical clusters in glasses.<sup>68</sup>

Cooperative luminescence<sup>68,95–97</sup> is a phenomenon which, requiring very close proximity of interacting RE ions in order to be seen in experiments, is a very good signature of clusters constituted by ions at distances of less than about 5 Å. Such distances, or shorter ones, between interacting ions are also the order of magnitude of the size of chemical clusters. Figure 9 presents the cooperative luminescence of Yb<sup>3+</sup> in a phosphate glass doped with Yb<sup>3+</sup> introduced through various precursors with different Yb–Yb shortest distances.<sup>98</sup> It has been shown that the normalized cooperative intensities depend on such

distances. Also, it can be noted that unwanted impurities ( $\text{Er}^{3+}$ ,  $\text{Tm}^{3+}$ ) introduced with  $\text{Yb}^{3+}$  oxide are revealed at ppm level by the much more efficient APTE (ETU) effect.<sup>99</sup>

#### 4. Experimental Results and Their Implications in Various Fields

##### 4.1. Recent Upconversion Studies in Lanthanide (4f) and Actinide (5f) Ion-Doped Solids with APTE (ETU) and ESA Processes

(Cooperative processes have been discussed in sections 3.2 and 3.3 above.)

Most of the more recent published results on upconversion under various laser pumpings have aimed, besides cooperative effects already discussed, at distinguishing the processes involved and mainly at separating APTE (ETU) from plain ESA. Most of the examples treat cases of upconversion in the now classical 4f ion-doped solids and few in the 5f ones.

###### 4.1.1. $\text{Pr}^{3+}$ ( $4f^2$ ) Ion

When doping fluoride glasses of the ZBLAN type in either fiber or bulk form,  $\text{Pr}^{3+}$  shows blue upconversion both of the ESA (two photon) and APTE (ETU) (three photon) types from the  $^3\text{P}_0$  state when pumping into the  $^1\text{G}_4(^1\text{D}_2)$  state.<sup>100</sup> Analogous results are obtained for  $\text{LiKY}_{1-x}\text{Pr}_x\text{F}_5$  crystals,<sup>101</sup> but the process is mainly APTE (ETU). Identifying the process is based on the presence of an excitation delay.

Germanate of general formula  $60\text{GeO}_2 \cdot 25\text{PbO} \cdot 15\text{NbO}_5$  as well as chalcogenide glasses of general formula  $50\text{GeS}_2 \cdot 25\text{Ga}_2\text{S}_3 \cdot 25\text{CsX}$  with  $\text{X} = \text{Cl}, \text{Br}$ , and  $\text{I}$ ,<sup>102</sup> doped with  $\text{Pr}^{3+}$  have been investigated. IR to blue upconversion is obtained under both ESA and APTE (ETU) processes as revealed by the absence or the presence of an excitation delay. The excitation sequence is  $^3\text{H}_4$  to  $^1\text{G}_4$  then  $^1\text{G}_4$  to  $^3\text{P}_0$  (ESA) or/and  $^1\text{D}_2$  (ETU).  $^3\text{P}_0$  gives the blue emission and  $^1\text{D}_2$  the orange one. In  $\text{Bi}_4\text{Ge}_3\text{O}_{12}:\text{Pr}^{3+}$  crystal red, green, and blue upconversion is obtained with mainly ESA and a less important APTE (ETU) process.<sup>103</sup> From a dynamic study of a  $\text{Pr}^{3+}$ -doped tellurite glass, ESA is proposed to explain the  $^3\text{H}_4$  to  $^1\text{D}_2$  followed by a multiphonon process connected to a  $^3\text{H}_6$  to  $^3\text{P}_1$  sequence.<sup>104</sup> An analogous process is proposed for  $\text{LiYF}_4:\text{Pr}^{3+}$ ,<sup>105</sup> whereas a two-photon absorption is proposed for an IR to blue upconversion in a  $60\text{ZrF}_4 \cdot 33\text{BaF}_3 \cdot 7\text{LaF}_3$  glass doped with  $\text{Pr}^{3+}$ ,<sup>106</sup> however, because a two-photon process is likely to be less probable than a sideband absorption,<sup>33</sup> this explanation may be questioned.<sup>105</sup>

In  $\text{KYb}(\text{WO}_4)_2:\text{Pr}(0.42\%)$ ,<sup>107</sup> blue upconversion under red and IR excitation is obtained along now classical APTE (ETU) schemes.

###### 4.1.2. $\text{Nd}^{3+}$ ( $4f^3$ ) Ion

Probably due to the availability of  $\text{Nd}^{3+}$ -doped materials for laser research, many investigations in Fernandez's group with  $\text{Nd}^{3+}$  in various kinds of hosts have been recently performed. In germanate

glasses of composition  $60\text{GeO}_2 \cdot 25\text{PbO} \cdot 15\text{NbO}_5$  doped with  $\text{Nd}^{3+}$ ,<sup>108</sup> the APTE (ETU) process has been observed under CW IR excitation in the  $^4\text{I}_{9/2}$  to  $^4\text{F}_{5/2}$  absorption. Green, red, orange emissions have been detected from  $^4\text{G}_{7/2}$  due to the following upconversion energy transfer ( $^4\text{F}_{3/2}, ^4\text{F}_{3/2}$  gives  $^4\text{G}_{7/2}, ^4\text{I}_{13/2}$ ). ESA has also been observed with the sequence  $^4\text{I}_{9/2}$  to  $^4\text{F}_{5/2}$ , nonradiative decay to  $^4\text{F}_{3/2}$ , followed by ESA to  $^2\text{P}_{1/2}$  decaying to  $^4\text{G}_{7/2}$ . In a fluoride glass of composition  $25\text{CdF}_2 \cdot 13.5\text{CdCl}_2 \cdot 30\text{NaF} \cdot 20\text{BaF}_2 \cdot 1.5\text{BaCl}_2$  doped with  $0.5\%\text{Nd}^{3+}$ ,<sup>109</sup> mostly APTE (ETU) is observed as revealed by the delay in the emission wavelengths ranging from red to UV and the analogy between the absorption and their excitation spectra. The output slope for  $\text{P}^n$  with  $n = 1.7$  indicates a two-photon process.

In fluoroarsenate,<sup>110</sup> fluoroindate,<sup>111</sup> and in chalcogenide glasses,<sup>112</sup> upconversion by  $\text{Nd}^{3+}$  ions has been studied too, taking advantage of the weak energy phonons of such glasses. It is mostly APTE (ETU), with some ESA for the  $^4\text{G}_{7/2}$  emission, that have been observed from  $^2\text{P}_{1/2}$  as shown by the similar spectral features in the excitation and absorption spectra for two-photon processes.

In  $\text{Pb}_5\text{Al}_3\text{F}_{19}:\text{Nd}^{3+}$  crystals,<sup>113</sup> at 300 and 4.2 K, APTE (ETU) is observed for visible (from  $^4\text{G}_{7/2}$ , with  $n = 1.5$ ) and UV emission (from  $^2\text{P}_{3/2}$ , with  $n = 2.2$ ) as indicated by similar excitation and absorption spectra.

In the stoichiometric laser material  $\text{K}_5\text{Nd}(\text{MO}_4)_4$ , IR to visible, blue (from  $^4\text{G}_{7/2}$  with  $n = 1.6$ ), and UV (from  $^2\text{P}_{3/2}$  with  $n = 2.4$ ) emissions have been studied with the very high Nd concentration of  $2.37 \times 10^{21} \text{ cm}^{-3}$ .<sup>114</sup> The studies, conducted in or outside the IR lasing phases, show that the laser metastable state is depopulated during the lasing phase as shown by the stronger blue and orange emission. Again, upconversion is essentially of the APTE (ETU) type as shown by comparing excitation and absorption spectra.

In  $\text{LiYF}_4:\text{Nd}(0.1-3\%)$ ,<sup>115</sup> upconversion is found to be due to ESA, the first step being a one-phonon sideband absorption situated at  $16563-15919 = 644 \text{ cm}^{-1}$  above the  $^2\text{H}_{11/2}$  state followed by the ESA step populating  $^4\text{D}_{3/2}$ . In the same type of fluoride crystal as well as in YAG, the following APTE (ETU) steps have been observed: ( $^4\text{F}_{3/2}, ^4\text{F}_{3/2}$ ) giving ( $^4\text{I}_{15/2}, ^4\text{G}_{5/2}$ ); ( $^4\text{F}_{3/2}, ^4\text{F}_{3/2}$ ) giving ( $^4\text{I}_{13/2}, ^4\text{G}_{7/2}$ ), and ( $^4\text{F}_{3/2}, ^4\text{F}_{3/2}$ ) giving ( $^4\text{I}_{11/2}, ^2\text{G}_{9/2}$ )<sup>116,117</sup> to some extent similar with the high-intensity quenching of the  $^4\text{F}_{3/2}$  state.<sup>118</sup>  $\text{BaLu}_2\text{F}_8:\text{Nd}^{3+}(0.6\%)$  crystals have also been studied.<sup>119</sup> Yellow to blue and green upconversion has been observed due to ESA, whereas under IR excitation, green upconversion is due to APTE (ETU) when site selection is involved at low temperature. Also,  $\text{KLiYF}_5:\text{Nd}^{3+}$  has been investigated, and upconversion through ESA from  $^4\text{F}_{3/2}$  has been observed.<sup>120</sup> With  $\text{CaF}_2$  thin films on  $\text{LaF}_3$  crystalline sample in waveguide form, three-photon APTE upconversion ( $n = 2.9$ ) can be easily observed through pumping confinement.<sup>121</sup> Very interestingly, emission at 381 nm in the UV from  $^4\text{D}_{3/2}$  ends on  $^4\text{I}_{11/2}$ , thus providing good hope for a UV four-level scheme laser.

#### 4.1.3. Gd<sup>3+</sup> (4f<sup>7</sup>) Ion

Due to the fact that its lowest excited state (<sup>6</sup>P<sub>7/2</sub>) is at very high energy (32 000 cm<sup>-1</sup>), this ion is mainly considered for downconversion studies and is involved in fewer upconversion studies than the two previous ones. However, upconversion has been considered in the stoichiometric material with centrosymmetric sites Cs<sub>2</sub>NaGdCl<sub>6</sub>.<sup>122</sup> ESA has been advocated (maybe with some direct two-photon allowed absorption) for the emissions between excited states from the 5d to <sup>6</sup>I<sub>J</sub> and <sup>6</sup>P<sub>J</sub> bands at 578 and 755 nm under excimer laser excitation into the <sup>6</sup>P<sub>J</sub> lines. Another stoichiometric material, K<sub>2</sub>GdF<sub>3</sub>, has also been investigated in upconversion.<sup>123</sup> Pumping is into the <sup>6</sup>P<sub>1/2</sub> state at 312 nm. Three anti-Stokes emissions attributed to <sup>6</sup>G<sub>7/2</sub> and <sup>6</sup>I<sub>7/2</sub> down to the ground state <sup>8</sup>S<sub>7/2</sub> at 204.7, 242.0, and 2798 nm have been observed and attributed to an APTE (ETU) process.

#### 4.1.4. Dy<sup>3+</sup> (4f<sup>9</sup>) Ion

This ion had the reputation of being a poisonous center even at trace levels for APTE (ETU) in usual Yb–Er and Yb–Tm or Ho upconversion matrices.<sup>2</sup> For this reason it was banished from the laboratory. This could explain why so few studies exist about the upconversion properties of this ion. It is probably also because the proximity of the lower excited states requires low-energy phonon matrices. The level structure is also somewhat analogous to the situation for Eu and Tb for which essentially cooperative upconversions have been observed (see section 3.2). Yet recently CsCdBr<sub>3</sub>:Dy<sup>3+</sup> (0.2%) has been studied in upconversion.<sup>124</sup> Both APTE (ETU) and ESA processes have been observed at 10 K. Near-IR excitation is by absorption into <sup>6</sup>F<sub>5/2</sub> at 12 338 cm<sup>-1</sup> and into <sup>6</sup>F<sub>3/2</sub> at 13 200 cm<sup>-1</sup>. Emission is from <sup>4</sup>F<sub>9/2</sub> to <sup>6</sup>H<sub>13/2</sub> at 17 341 cm<sup>-1</sup>. Two APTE (ETU) schemes are likely, the more probable being (<sup>6</sup>F<sub>5/2</sub>, <sup>6</sup>F<sub>5/2</sub>) giving (<sup>4</sup>F<sub>9/2</sub>, <sup>6</sup>H<sub>13/2</sub>). At higher temperature (295 K) and large concentration, ESA is operative from <sup>6</sup>F<sub>9/2</sub> to <sup>4</sup>F<sub>9/2</sub>. At lower concentration, ESA appears to be from <sup>6</sup>F<sub>5/2</sub> to <sup>4</sup>I<sub>13/2</sub>.

#### 4.1.5. Ho<sup>3+</sup> (4f<sup>10</sup>) Ion

Though this ion is among the first studied in upconversion<sup>2</sup> with Yb codoping, it has later been studied alone. First, some years ago,<sup>125</sup> red to blue upconversion was observed as well as a red (He–Ne laser) pumped IRQC for 2 μm detection at 300 K was demonstrated in Ho<sub>x</sub>Y<sub>1-x</sub>F<sub>3</sub> (x from 0.005% to 1). An APTE (ETU) process, (<sup>5</sup>F<sub>5</sub>, <sup>5</sup>I<sub>7</sub>) giving (<sup>5</sup>F<sub>3</sub>, <sup>5</sup>I<sub>8</sub>), provides the <sup>5</sup>F<sub>3</sub> emission at 485 nm. Much more recently, CsCdBr<sub>3</sub>:Ho<sup>3+</sup> (0.035% and 2.25%)<sup>126</sup> has been studied, this host differing from the previous one by its lower phonon maximum energy (163 versus 560 cm<sup>-1</sup>) and its pair building ability. A two-photon process has also been found for the blue emission from <sup>5</sup>F<sub>3</sub> with slope n = 1.8. ESA is advocated at a higher temperature (T > 100K), whereas APTE (ETU) is found at T < 100K. Comparison of excitation spectra with absorption and delay in the emission help to separate the processes. Ho<sup>3+</sup> has also been

excited in the red at 647 nm from a gas Kr laser in LiTaO<sub>3</sub>:Ho(0.3%).<sup>127</sup> At 15 K, a green emission with n = 2 is observed; it is attributed to the <sup>5</sup>S<sub>2</sub> to <sup>5</sup>I<sub>8</sub> transition excited by an ESA process. In a more classical experiment, Ho is excited via Yb in YVO<sub>4</sub>:Yb,Ho.<sup>128</sup> The near-IR excitation at 1 μm provides both a red emission from <sup>5</sup>F<sub>5</sub> by an ESA process (n = 1.6) and a faint green one from <sup>5</sup>S<sub>2</sub> (n = 1.6) attributed to an APTE (ETU) process. Interestingly and along the same lines in Yb, Ho-doped fluorohafnate glasses,<sup>129</sup> APTE (ETU) IR to green upconversion has been measured to give an absolute efficiency of 8.4 × 10<sup>-4</sup> cm<sup>2</sup>/W, a value directly comparable to the one of Figure 3 and Table 1, with 10<sup>-3</sup> cm<sup>2</sup>/W for YF<sub>3</sub>:Yb,Er.

#### 4.1.6. Er<sup>3+</sup> (4f<sup>11</sup>) Ion

(See also section 4.2.)

Er<sup>3+</sup> was the first ion showing upconversion,<sup>2</sup> and it seems that the numerous previous studies have not exhausted its upconversion properties. It still appears as the most studied ion in recent times, as will be shown in the following.

With the availability, in the 1980s, of efficient laser diodes (LD) and tunable Ti–sapphire lasers in the 800–1100 nm range, the field of upconversion studies with Er<sup>3+</sup> has been renewed. In particular, Er<sup>3+</sup> has demonstrated its capacity as a laser ion just as Nd<sup>3+</sup> did a long time ago, and consequently, all kinds of upconversion emissions have been observed and studied. The role of upconversion on the CW functioning of the LiYF<sub>4</sub>:Er and ZBLAN fiber lasers at 2.7 μm<sup>130–132</sup> has recently been confirmed,<sup>133</sup> and a cascade laser at 1.72 and 2.7 μm laser have been optimized, in particular, in a ZBLAN glass doped with Er(0.25–8.75%) alone or with Pr(0.25–1.65%)–Er<sup>134</sup> using the APTE (ETU) process for optimizing the <sup>4</sup>I<sub>11/2</sub> and <sup>4</sup>I<sub>13/2</sub> lifetimes. Even classical laser hosts have been investigated: YAG:Er,<sup>135</sup> YSGG:Er,<sup>136</sup> and YAlO<sub>3</sub><sup>137</sup> for which either ESA or APTE (ETU) have been observed.

In a more fundamental approach, Cs<sub>3</sub>Lu<sub>2</sub>Cl<sub>9</sub>, Cs<sub>3</sub>Lu<sub>2</sub>Br<sub>9</sub>, and Cs<sub>2</sub>Lu<sub>2</sub>I<sub>9</sub> doped with Er<sup>3+</sup> (1%) as well as the stoichiometric material Cs<sub>3</sub>Er<sub>2</sub>X<sub>9</sub> (X = Cl, Br, I) have been investigated<sup>138,139</sup> under 1.5 μm excitation. As in ref 72, an APTE (ETU) process describes the observed four-photon upconversion process at higher Er concentration, though the process is called cooperative energy transfer.<sup>139</sup>

In BaLu<sub>2</sub>F<sub>8</sub>:Er(1%; 4.5%), IR (0.97 μm) to green upconversion from <sup>4</sup>S<sub>3/2</sub> is observed.<sup>140</sup> Both APTE (at all temperature) and ESA at lower temperature from <sup>4</sup>I<sub>11/2</sub> and <sup>4</sup>I<sub>9/2</sub> are identified by the transients of the upconversion emission. Ba<sub>2</sub>YCl<sub>7</sub>:Er (1–100%) has been studied<sup>141</sup> under 800 nm excitation of the <sup>4</sup>I<sub>9/2</sub> state. Depending on excitation energy and concentration, both APTE (ETU) (for Ba<sub>2</sub>ErCl<sub>7</sub>) and ESA are observed. In RbGd<sub>2</sub>Br<sub>7</sub>:Er (1%),<sup>142</sup> under 980 nm excitation of <sup>4</sup>I<sub>11/2</sub>, both APTE (ETU) and ESA, discriminated by the excitation transients, are observed with a ratio depending on excitation energy and temperature. Besides the above studies, the Güdel's group in a systematic manner also studied BaY<sub>2</sub>F<sub>8</sub>:Er and Cs<sub>3</sub>Er<sub>2</sub>Br<sub>9</sub><sup>143</sup> in order to compare the

upconversion properties from near-IR to green in two hosts differing by their highest phonon energy, respectively, 415 and 190  $\text{cm}^{-1}$ . In  $\text{Cs}_3\text{Lu}_2\text{Br}_9\text{:Er}$  (1%),<sup>144</sup> a lattice with built-in pair structure, both ESA and APTE (ETU) processes are observed but mostly ESA when exact matching between levels and laser excitation is obtained. Energy migration is noted even at the relatively low 1% doping.

Similar studies have been performed in  $\text{Ca}_3\text{Al}_2\text{-Ge}_3\text{O}_{12}\text{:Er}$ , where both ESA and APTE are observed depending on the excitation wavelength.<sup>143</sup> In  $\text{LiYF}_4\text{:Er}$  (3%),  $\text{Yb}$  (20%),<sup>146</sup> five-photon near-IR to UV has been observed with APTE (ETU) processes similarly to<sup>72</sup> for Er alone.

A rather original and interesting result in a classical  $\text{Yb}$  (0.5%)– $\text{Er}$  (0.1%) system is the optical amplification in an upconversion-pumped chalcogenide glass ( $70\text{Ga}_2\text{S}_3\text{-}30\text{La}_2\text{O}_3$ ).<sup>147</sup> Pumping is at 1.06  $\mu\text{m}$  in an anti-Stokes two-phonon sideband at 2 times 425  $\text{cm}^{-1}$  from the  $\text{YAG:Nd}$  laser photon energy. Amplification, which is maximum at 165 °C is at 555 nm with a gain factor of 10. This corresponds to an amplification efficiency of 0.012 dB/mW in the bulk glass sample without optical confinement. Also, in the same aim of amplification in the green spectral region with near-IR pumping,  $\text{LiYF}_4\text{:Er}$  has been studied in detail under an  $\text{InGaAs}$  LD pumping.<sup>148</sup>  $\text{LiNbO}_3\text{:Ti-Er}$  waveguides<sup>149</sup> have been studied for upconversion-pumped laser either at 550 nm or 2.7  $\mu\text{m}$ . Both APTE (ETU) and ESA are observed. For a 550 nm laser, APTE (ETU) is necessary and can be obtained essentially in Er clusters which have to be increased at  $\text{Li}^+$  and  $\text{Nb}^{5+}$  sites. Here Er clusters are looked for, in contrast to the situation in Er-doped optical fibers for 1.55  $\mu\text{m}$  amplification, see section 3.3.  $\text{LiNbO}_3\text{:Er}$  waveguides, carefully pumped in a site-selective manner<sup>150</sup> have shown ESA and APTE (ETU) upconversion according to the pumping photon energy. When weaker than 12450  $\text{cm}^{-1}$ , ESA is observed; otherwise APTE (ETU) is obtained. A two-photon process exists in both cases as shown by the observed  $n = 1.92$  value. Pumping is into  $^4\text{I}_{9/2}$  at 800 nm, and emission is from  $^4\text{S}_{3/2}$ . ESA is from  $^4\text{I}_{13/2}$  to  $^2\text{H}_{11/2}$  with some involved nonradiative decays. For APTE (ETU), after a nonradiative decay to  $^4\text{I}_{11/2}$ , the following takes place: ( $^4\text{I}_{9/2}$ ,  $^4\text{I}_{11/2}$ ) gives ( $^4\text{I}_{15/2}$ ,  $^4\text{F}_{3/2}$ ) providing the  $^4\text{S}_{3/2}$  excitation reached by a nonradiative decay from  $^4\text{F}_{3/2}$ . In the same kind of waveguide, traces of avalanche (see section 4) have been identified.<sup>151</sup>

#### 4.1.7. $\text{Tm}^{3+}$ ( $4f^{12}$ ) Ion

$\text{Tm}^{3+}$  is known to be one of the first ions having shown upconversion either alone or with the help of  $\text{Yb}^{3+}$ .<sup>2</sup> As for other ions, the advent of lasers has renewed its interest. Also, research of upconversion-pumped lasers has also been an impulse to the research.  $\text{LiYF}_4\text{:Tm}$  has been studied from its spectroscopic parameter point of view for laser applications<sup>123</sup> with codoping with  $\text{Pr}^{3+}$  as well.<sup>152</sup> After a  $^3\text{H}_6$  to  $^3\text{H}_4$  excitation at 12 643  $\text{cm}^{-1}$  (791 nm) in the  $\text{Tm}^{3+}$  ion, a double excitation,  $^3\text{H}_6$  to  $^1\text{G}_4$  then to  $^3\text{P}_2$  by an APTE (ETU) process in the  $\text{Pr}^{3+}$  ion, as revealed by a delay in the built-up transient, allows

emission from  $^3\text{P}_0$  to  $^3\text{H}_6$  (600 nm) and  $^3\text{H}_4$  (490 nm) in the  $\text{Pr}^{3+}$  ion.

Upconversion has been studied in the stoichiometric crystal  $\text{TmP}_5\text{O}_{14}$  as well as in the amorphous  $\text{Tm}_{0.1}\text{La}_{0.9}\text{P}_5\text{O}_{14}$ .<sup>153</sup> Under red pumping, UV and blue emission are observed from  $^1\text{D}_2$  with  $n = 2$ , respectively, to  $^3\text{H}_6$  (360 nm) and  $^3\text{F}_4$  (450 nm).  $^1\text{G}_4$  emission at 480 nm is quenched at a concentration of 100% down to 10%. Comparing excitation spectra, stepwise APTE (ETU) and ESA are conjectured. The amorphous sample provides the largest intensity at 450 nm. An emission at 347 nm from  $^5\text{I}_6$  to  $^3\text{F}_4$  can be observed with  $n = 2.5$ .

In garnets  $\text{Y}_3\text{Sc}_2\text{Ga}_3\text{O}_{12}$ ,  $\text{Gd}_3\text{Ga}_5\text{O}_{12}$  and in  $\text{GdAlO}_3$  doped with  $\text{Yb}$  (10%) and  $\text{Tm}$  (0.1%),<sup>154</sup> upconversion to 460–500 nm can be observed under Ti-sapphire excitation at 790 nm corresponding to the  $^3\text{H}_6$  to  $^3\text{H}_4$  transition in  $\text{Tm}^{3+}$ . Then a back transfer to  $\text{Yb}$  allows the  $^2\text{F}_{5/2}$   $\text{Yb}^{3+}$  population and the subsequent APTE (ETU) process from  $^3\text{H}_4$  to  $^1\text{G}_4$ . This behavior is different from the classical  $\text{Yb-Tm}$  case under a first  $\text{Yb}$  excitation.

In  $\text{Cs}_3\text{Yb}_2\text{Cl}_9\text{:Tm}$ , a matrix with low-energy phonons ( $<280 \text{cm}^{-1}$ ), up to five-photon APTE (ETU) process is observed with a scheme analogous to the one of Figure 6b, however, with a nonradiative step replaced by an internal APTE (ETU) step within the  $\text{Tm}^{3+}$  itself.<sup>155</sup> The slopes, respectively, observed are  $n = 1.4, 2.0, 2.6,$  and  $3.4$  for emissions from  $^3\text{H}_4, ^3\text{F}_3, ^1\text{G}_4,$  and  $^1\text{D}_2$ . The respective excitation spectra are the  $\text{Yb}$  absorption narrowed by the power law as shown in Figure 7 for the Er case, also proving the APTE (ETU) process. The difference here is that because of the internal APTE (ETU) process in  $\text{Tm}^{3+}$ , the power law to be considered for  $^1\text{G}_4$  and  $^1\text{D}_2$  are here, respectively,  $3/2$  and  $4/2$ , as already explained for the  $n = 3/2$  slope mentioned in one of the red upconversion processes of  $\text{Yb-Er}^2$ .

Fluorohafnate glasses doped classically with  $\text{Yb}$  and  $\text{Tm}$  have been investigated,<sup>129</sup> and absolute efficiency has been shown to be  $6.4 \times 10^{-3} \text{cm}^2/\text{W}$  for the 804 nm emission. This two-photon upconversion efficiency is similar to the one given for  $\text{Yb-Er}$ , see Figure 3 and Table 1.

In a silica fiber 3.5 m in length doped with  $\text{Tm}$  alone, visible and UV upconversions at 650, 470, and 366 nm all with a slope of  $n = 3$  have been analyzed.<sup>156</sup> Absorption is at 8300  $\text{cm}^{-1}$  in the  $^3\text{H}_6$  to  $^3\text{H}_5$  transition. Upconversion is thought to be enhanced by the first and second Raman transitions observed at 1120 and 1180 nm. Above a threshold at 10 mW, line narrowing is observed and is considered as an indication of superluminescence.

Along the same directions as in ref 51, lead germanate vitroceraamics doped with  $\text{Yb}$  (15%)– $\text{Tm}$  (0.1%) have shown APTE (ETU) upconversion with a two-photon process at 779 and 698 nm, a three-photon process at 478 nm ( $^1\text{G}_4$ ), and a four-photon one at 363 nm ( $^1\text{D}_2$ ).<sup>157</sup> Measured absolute efficiencies were  $5.8 \times 10^{-3}$  at 779 nm and  $10^{-6}$  at 478 nm under a 16.5 mW/ $\text{cm}^2$  excitation. In normalized units it gives respectively for the two-photon and the three-photon processes  $3.5 \times 10^{-1} \text{cm}^2/\text{W}$  and  $3.6 \times 10^{-3} (\text{cm}^2/\text{W})^2$ .

Interestingly this IR to IR two-photon process is much more efficient than the IR to green process in Yb–Er. On the other hand, the IR to blue transition is about 20 times less efficient than the efficiency obtained in the first Yb–Tm-doped vitroceraamics ( $8.5 \times 10^{-2} \text{ (cm}^2/\text{W)}^2$ ,<sup>158</sup> see Table 1). In the fluoride glass BiGaZyBTzr:Tm<sup>3+</sup>,<sup>159</sup> a crossover from cooperative sensitization to APTE (ETU) is concluded from the time behavior changes with pulse excitation length.

#### 4.1.8. Tm<sup>2+</sup> (4f<sup>13</sup>) Ion

This ion is considered for the first time in upconversion. It is isoelectronic with Yb<sup>3+</sup> and as such has the same level structure: two spin–orbit states <sup>2</sup>F<sub>7/2</sub> and <sup>2</sup>F<sub>5/2</sub> separated by about 8840 cm<sup>-1</sup> and parity-allowed 4f–5d bands above 15 000cm<sup>-1</sup>. The presence of Tm<sup>2+</sup> is not common due to its propensity to oxidation, but here due to the considered SrCl<sub>2</sub> divalent host, 2% of Tm<sup>2+</sup> has been successfully introduced<sup>160</sup> without the presence of any Tm<sup>3+</sup>. The level structure is such that the 4f–5d bands are at about twice the energy of the first <sup>2</sup>F<sub>5/2</sub> excited state and has prompted Güdel's group to investigate this new ion for upconversion at 15 K under a filtered 80 W lamp excitation at 8840 cm<sup>-1</sup> and with a pulsed Nd:YAG laser for the transient study. The absence of delay in the upconversion signal indicates an ESA process.

#### 4.1.9. U<sup>4+</sup> (5f<sup>2</sup>) Ion

This is the first 5f ion in which upconversion has been observed<sup>161</sup> in ThCl<sub>4</sub> and ThBr<sub>4</sub>:U<sup>4+</sup> (0.05%). The first observation was fortuitously found at CNET on a supposedly undoped ThBr<sub>4</sub> sample. Under a Nd:YAG pulsed excitation, a green SHG signal at 532 nm was looked for in order to detect the crystal eventual noncentrosymmetry. In fact, instead of the green spectrally narrow signal at 532 nm, we essentially observed a broad red one at a luminescence emission wavelength known for U<sup>4+</sup>. This observation indicated that upconversion was active in U<sup>4+</sup> at very weak concentration levels. A derived conclusion was that the oscillator strengths were very large and probably the energy transfers were too. This induced the first determination of U<sup>4+</sup> oscillator strengths that showed values of  $\approx 10^{-4}$ <sup>162</sup> about 2 orders of magnitude larger than for Ln<sup>3+</sup> and one order larger than then known values for U<sup>3+</sup>. Recent results for U<sup>3+</sup>, introduced for the first time by a pure chemical way in a ZnCl<sub>2</sub>-based glass, indicate values of  $\approx 10^{-6}$  which is about the same as that for Ln<sup>3+</sup><sup>163</sup> and 2 orders of magnitude less than that for U<sup>4+</sup>.

With the 1 KW tungsten iode filtered lamp experiment already used for the first Yb–Er and Yb–Tm investigations (see Figure 17 in section 4.2), several emission lines in the red and green have been attributed to ESA either for excitation at 950 and 1170 nm separately or for excitation at 950 plus 1170 nm.<sup>161</sup> The involved levels are connected by absorption from the ground-state <sup>3</sup>H<sub>4</sub> to <sup>3</sup>H<sub>6</sub>, <sup>3</sup>F<sub>3</sub>, and <sup>3</sup>H<sub>5</sub> and then ESA from these states to <sup>3</sup>P<sub>0</sub>, <sup>3</sup>P<sub>1</sub>, and <sup>1</sup>I<sub>6</sub>, see Figure 10. The linear behavior with concentration showed that upconversions were not due to APTE

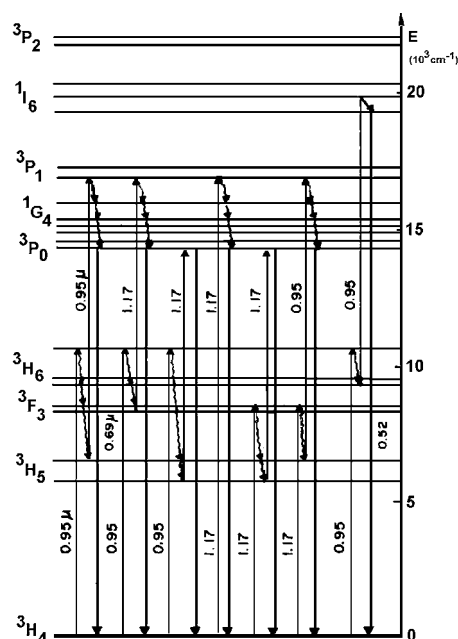


Figure 10. Energy scheme for various ESA upconversions involved in ThBr<sub>4</sub>:U<sup>4+</sup>.

(ETU) processes. On the other hand, as shown for Yb–Er and Yb–Tm,<sup>51</sup> photon trapping was present as indicated by the grain size effect on lifetimes and on the upconversion efficiencies. It shows that radiative diffusion plays an important role also in ESA upconversion. Normalized efficiency is found to be  $2 \times 10^{-6} \text{ cm}^2/\text{W}$ , see Table 1, for ThBr<sub>4</sub> grains doped with 0.05% U<sup>4+</sup> and of 0.2–0.3 mm optimized size.<sup>161</sup>

#### 4.1.10. U<sup>3+</sup> (5f<sup>5</sup>) Ion

Though there has been one publication on the upconversion properties in trihalide-doped Cm<sup>3+</sup>,<sup>164</sup> most of the upconversion studies with trivalent actinides are with U<sup>3+</sup> from Streck's group. In LaCl<sub>3</sub>:U<sup>3+</sup> and LaCl<sub>3</sub>:U<sup>3+</sup>, Pr<sup>3+</sup>,<sup>165</sup> under Nd:YAG laser excitation, ESA is found to give the <sup>2</sup>K<sub>15/2</sub> to <sup>4</sup>I<sub>9/2</sub> green emission in U<sup>3+</sup> alone. When coupled to Pr<sup>3+</sup>, a cross-relaxation process allows a second ESA within the Pr<sup>3+</sup> ion giving its <sup>3</sup>P<sub>0</sub> excitation. A refined study indicates a more complex upconversion process with back transfer to U<sup>3+</sup> and APTE (ETU) process within U<sup>3+</sup>.<sup>166</sup> Under red laser pumping in the <sup>4</sup>I<sub>9/2</sub> to <sup>2</sup>K<sub>13/2</sub> transition, green emission from <sup>2</sup>K<sub>15/2</sub> to <sup>4</sup>I<sub>9/2</sub> can be observed. This upconversion is attributed to two processes:<sup>167</sup> (i) a sequential absorption within one U<sup>3+</sup> ion where the second photon populates the 5f<sup>5</sup>-6d bands and thus the energy is transferred to the <sup>2</sup>K<sub>15/2</sub> emitting state and (ii) an APTE (ETU) process within an U<sup>3+</sup> pair of ions following the sequence (<sup>4</sup>F<sub>9/2</sub>, <sup>4</sup>F<sub>9/2</sub>) ⇒ (<sup>2</sup>H<sub>9/2</sub>, <sup>2</sup>H<sub>11/2</sub>) –35 cm<sup>-1</sup> (a weak phonon energy). Other paths for excitation have also been investigated in LaCl<sub>3</sub>:U<sup>3+</sup>,<sup>168</sup> and green and red emissions have been obtained with slopes, respectively, equal to n = 1.97–2.5 and 1.7–1.85, according to the precise excitation wavelength.

In centrosymmetric elpasolites Cs<sub>2</sub>NaYBr<sub>6</sub> and in Cs<sub>2</sub>NaYCl<sub>6</sub> doped with U<sup>3+</sup>,<sup>169</sup> due to multiphonon quenching, ESA upconversion has been observed only in the bromide type.

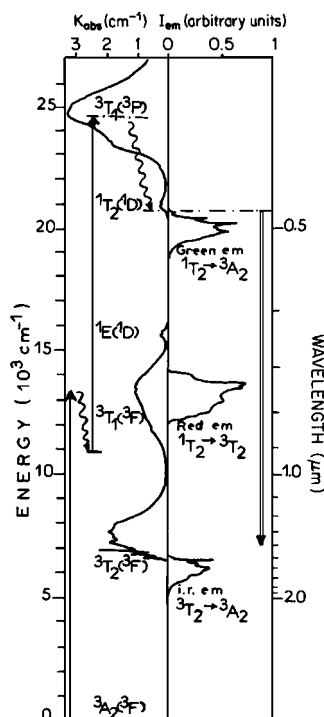


Figure 11. Energy scheme for ESA upconversion in  $\text{MgF}_2:\text{Ni}^{2+}$ .

#### 4.2. Recent Upconversion Studies in Transition-Metal (3d, 4d, 5d) Ion-Doped Solids with APTE (ETU), ESA, or Cooperative Processes

The first consideration of d ions in upconversion can be found in the work of Cresswell et al.<sup>170</sup> in 1978, where in  $\text{Cs}_2\text{NaYCl}_6$  they considered  $\text{Re}^{4+}$ , a  $5d^3$  ion, as a replacement for Yb in the IR to blue upconversion in Yb–Tm systems, with the idea of having an APTE (ETU) two-photon process instead of a three-photon one. This was supposed to improve overall efficiency in diode-pumped anti-Stokes visible light sources. Unfortunately this system proved itself to be surprisingly inefficient. The second example was obtained in Auzel's group at CNET in the tunable laser material  $\text{MgF}_2:\text{Ni}^{2+}$ .<sup>171</sup> Due to the strong Stokes shift experienced by d ions in solids caused by a medium crystal field strength inducing itself medium electron–phonon couplings, resonant diffusion is not as effective as in lanthanides. Under a krypton gas laser excitation at 752.5 nm, green upconversion at 80 K was observed at 500 nm coming from the  $^1\text{T}_2$  ( $^1\text{D}$ ) to  $^3\text{A}_2$  ( $^3\text{F}$ ) transition, see Figure 11. It was attributed to the  $^3\text{T}_1$  ( $^3\text{F}$ ) to  $^3\text{T}_1$  ( $^3\text{P}$ ) ESA transition. A cross-relaxation, ( $^1\text{T}_2$ ,  $^3\text{A}_2$ ) giving ( $^3\text{T}_2$ ,  $^3\text{T}_1$ ), was observed to self-quench the green emission. The determined microparameter values for this energy transfer were consistent with an exchange interaction. This upconversion was not studied in order to improve upconversion itself but because it was seen as a drawback to be reduced in the IR laser functioning of  $\text{Ni}^{2+}$ .

Following these two pioneering works one can say that the field of upconversion in d ion-doped solids has been developed by the systematic work of Güdel's group in recent years. Presentation of this field is the subject of the following paragraphs.

##### 4.2.1. $\text{Ti}^{2+}$ ( $3d^2$ ) Ion

In NaCl- and  $\text{MgCl}_2$ -doped (0.1–0.2%)  $\text{Ti}^{2+}$  crystals, the near-IR (9400  $\text{cm}^{-1}$ ) to visible upconversion is analyzed at 15 K in these two hosts.<sup>172</sup> Spectral analysis of these two crystals reveals that NaCl and  $\text{MgCl}_2$  have crystal field strength on both sides of the spin crossover point for the first excited metastable state. For NaCl it is  $^3\text{T}_2$  with the same spin as the ground-state  $^3\text{T}_1$ , whereas for  $\text{MgCl}_2$  it is  $^1\text{T}_2$ , i.e., it gives a spin-forbidden transition to the ground state. This dramatically changes the metastable state radiative lifetime from, respectively, 1.4 to 109 ms and consequently the relative efficiencies of the ESA processes observed in both crystals.

##### 4.2.2. $\text{Cr}^{3+}$ ( $3d^3$ ) Ion

In YAG<sup>173</sup> and YGG ( $\text{Y}_3\text{Ga}_5\text{O}_{12}$ )<sup>174,175</sup> codoped with (2%)  $\text{Cr}^{3+}$  and (1%)  $\text{Yb}^{3+}$ , upconversion of  $\text{Cr}^{3+}$  through a near-IR pumping of  $\text{Yb}^{3+}$  is observed at 10 K with an efficiency of 6% under 150 mW of excitation<sup>173–175</sup> but at undefined energy density. The presence of a delay in the transient of the emitted signal indicates the presence of an energy transfer. Because there is no metastable level below the  $^2\text{E}$   $\text{Cr}^{3+}$  emitting state, a cooperative sensitization process can only explain the whole process. Further, the cooperative luminescence of  $\text{Yb}^{3+}$  is simultaneously observed. The role of the efficient diffusion of energy among the  $\text{Yb}^{3+}$  ions is stressed as is generally the case with this ion.

Even three ion systems have been studied one of them being  $\text{Cr}^{3+}$  in YAG: (5.76%)  $\text{Tm}^{3+}$ , (0.36%)  $\text{Ho}^{3+}$ , and (1%)  $\text{Cr}^{3+}$ ,<sup>176</sup> a well-known 2.1  $\mu\text{m}$  laser material. Under near-IR (720–790 nm) and red excitation (610–660 nm), a blue emission from  $^1\text{G}_4$  (Tm) at 486 nm and from  $^5\text{F}_3$  (Ho) at 486, 489, and 497 nm can be seen; an upconverted emission is obtained also from the  $^2\text{E}$  ( $\text{Cr}^{3+}$ ) level at 688.7 and 687.6 nm, the  $\text{R}_1$  and  $\text{R}_2$  lines. All such emissions are losses for the laser process. They come from cross energy transfers between the three ions and ESA excitation.

##### 4.2.3. $\text{Ni}^{2+}$ ( $3d^8$ ) and $\text{Mn}^{2+}$ ( $3d^5$ ) Ions

Besides  $\text{Ni}^{2+}$  in  $\text{MgF}_2$ ,<sup>171</sup> already mentioned,  $\text{Ni}^{2+}$  (0.1–10%) has been investigated as an upconversion ion either alone in  $\text{RbCdCl}_3$ ,<sup>177</sup>  $\text{CsCdCl}_3$ ,<sup>178</sup> and  $\text{Rb}_2\text{-CdCl}_4$ ,<sup>179</sup> or coupled with  $\text{Mn}^{2+}$  in  $\text{RbMnCl}_3$ ,<sup>180</sup>  $\text{CsMnCl}_3$ , and  $\text{RbMnCl}_3$ ,<sup>178</sup> and in  $\text{Rb}_2\text{MnCl}_4$ .<sup>179</sup>

Under near-IR excitation at 15 K,  $\text{Ni}^{2+}$  alone is found to produce a green upconversion by an ESA process as explained above for  $\text{MgF}_2:\text{Ni}^{2+}$ <sup>171</sup> but with different level attributions, maybe due to the fact that crystal field strengths are different and that zero-phonon lines have not been considered. Here, the ground-state absorption is from  $^3\text{A}_2$  to  $^1\text{E}$  and ESA from  $^3\text{T}_2$  to  $^1\text{T}_2$ ; emission is the same transition  $^1\text{T}_2$  to  $^3\text{A}_2$ . In  $\text{RbCdCl}_3$ , a pressure study modifying the crystal field strength shows an increase in upconversion due an increase in the spectral overlap between ground-state absorption and ESA.

With the  $\text{Mn}^{2+}$  presence, a strong increase in upconversion is observed, though  $\text{Mn}^{2+}$  has no metastable level below  $^1\text{T}_2$  ( $\text{Ni}^{2+}$ ). On the contrary, the metastable state  $^4\text{T}_1$  of  $\text{Mn}^{2+}$  is in resonance with  $^1\text{T}_2$

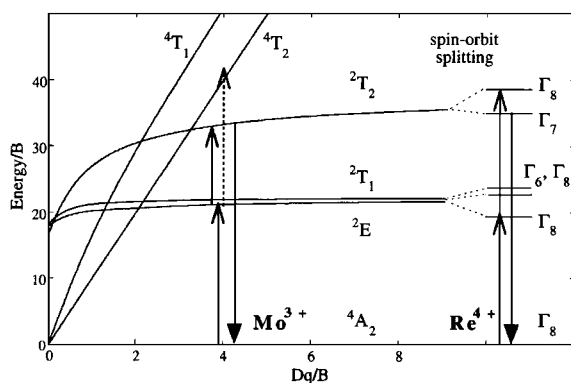


Figure 12. Tanabe and Sugano diagram for the  $d^3$  configuration of  $\text{Cr}^{3+}$  and corresponding energy schemes involved in upconversion by ESA processes for  $\text{Mo}^{3+}$  and  $\text{Re}^{4+}$ . (Reprinted with permission from ref 181. Copyright 1998 American Chemical Society.)

( $\text{Ni}^{2+}$ ) and in  $\text{CsMnCl}_3$  is found to emit slightly at the expense of  ${}^1\text{T}_2$ , which is then slightly quenched. An explanation is given by a strong enhancement of the  ${}^1\text{E}$  absorption intensity due to a stronger spin-orbit interaction linked to the proximity of the  ${}^3\text{T}_1$  and  ${}^1\text{E}$  state. The upconversion enhancement also found in  $\text{RbMnCl}_3$  cannot be of this type because this proximity does not exist. It is attributed to a strong exchange coupling<sup>178</sup> between  $\text{Ni}^{2+}$  and  $\text{Mn}^{2+}$ , removing the spin selection rule for the  ${}^3\text{A}_2$  to  ${}^1\text{E}$  absorption from  $\Delta S = 1$  to 0, and coming from the mixing of both  $\text{Ni}^{2+}$  considered states with the  $\text{Mn}^{2+}$   ${}^6\text{A}_1$  ground state.

#### 4.2.4. $\text{Mo}^{3+}$ ( $4d^3$ ) Ion

This ion has been studied in  $\text{Cs}_2\text{NaYCl}_6$  and  $\text{Cs}_2\text{-NaYBr}_6$ <sup>181,182</sup> at 2% doping concentration. Under near-IR excitation from a Ti-sapphire laser, red upconversion is observed from 10 to 150 K. Under one-wavelength excitation, both ESA and APTE are observed. Under two-wavelength excitation, essentially ESA provides upconversion with a better efficiency. ESA upconversion implies a  ${}^2\text{T}_1/{}^2\text{E}$  to  ${}^4\text{T}_2$  absorption preceded by a  ${}^4\text{A}_2$  to  ${}^2\text{T}_1/{}^2\text{E}$  from the ground state, see Figure 12. APTE is provided by the ( ${}^2\text{T}_1/{}^2\text{E}$ ,  ${}^2\text{T}_1/{}^2\text{E}$ ) to ( ${}^4\text{A}_2$ ,  ${}^4\text{T}_2$ ) energy transfer, giving the emission from  ${}^4\text{T}_2$ . In the chloride host, the ratios for upconversion processes are estimated to be APTE (15%) and ESA (85%). For the bromide, it is, respectively, 35% and 65%. This ion is characterized by a very long lifetime of 67.5 ms coming from the relatively weak oscillator strengths; it can be noted that electron-phonon parameters are weak ( $S = 0.05$ ) for the intermediate states  ${}^2\text{E}/{}^2\text{T}_1$  and strong ( $S = 4.5\text{--}5.7$ ) for the final excited state very near the emitting state ( $S = 0.05$ ). This explains the necessity of the low temperature for the upconversion emission.

#### 4.2.5. $\text{Re}^{4+}$ ( $5d^3$ ) Ion

This ion, also being a  $d^3$  configuration ion, has roughly the same Tanabe and Sugano energy diagram<sup>183</sup> as other better known transition metals (TM) such as  $\text{Cr}^{3+}$  and  $\text{Mo}^{3+}$ . It has been studied in  $\text{Cs}_2\text{-ZrCl}_6$ <sup>181,184</sup> and  $\text{Cs}_2\text{GeF}_6$ .<sup>185</sup> Though  $\text{Re}^{4+}$  has the same level structure as  $\text{Cr}^{3+}$  and  $\text{Mo}^{3+}$ , as shown in Figure

12, it has been the first TM ion to show upconversion at room temperature.<sup>181,184</sup> Contrary to other TM ions,  $\text{Re}^{4+}$  shows an efficient APTE (ETU) process because selection rules on spin are relaxed by a larger spin-orbit coupling. The main difference with  $\text{Mo}^{3+}$  can be traced back to the larger oscillator strength for the  ${}^4\text{A}_2(\Gamma_8)$  to  ${}^2\text{T}_1(\Gamma_8)$  by a factor  $10^2$  with respect to  ${}^4\text{A}_2$  to  ${}^2\text{T}_1/{}^2\text{E}$  in  $\text{Mo}^{3+}$ . The upconversion energy transfer involved being ( ${}^2\text{E}/{}^2\text{T}_1(\Gamma_8)$ ,  ${}^2\text{E}/{}^2\text{T}_1(\Gamma_8)$ ) gives ( ${}^4\text{A}_2(\Gamma_8)$ ,  ${}^2\text{T}_2(\Gamma_8)$ ). Thus, excitation into  ${}^2\text{T}_1(\Gamma_8)$  at about  $1.1\ \mu\text{m}$  (Nd:LiYF<sub>4</sub> laser at  $1.047\ \mu\text{m}$ ) provides a red emission at about 725 nm.

In a solution-grown  $\text{Cs}_2\text{GeF}_6:(2\%)\text{Re}^{4+}$  crystal,<sup>185</sup> the upconversion luminescence decreases down to 2% when temperature is increased from 15 to 300 K. This is explained only partially by the larger maximum phonon energy, 600 versus  $350\ \text{cm}^{-1}$  in chlorides and  $220\ \text{cm}^{-1}$  in bromides, which increases nonradiative transitions, and mainly by a decreasing absorption cross section at the laser excitation wavelength. Upconversion is here also mainly an APTE (ETU) process as shown by the time transient measurements.

#### 4.2.6. $\text{Os}^{4+}$ ( $5d^4$ ) Ion

This 5d TM ion has been found to have also the right sequence of levels to show upconversion, see Figure 12. An APTE (ETU) effect is observed in  $\text{Cs}_2\text{-ZrCl}_6:\text{Os}^{4+}$  (1%)<sup>186,187</sup> below 80 K; in  $\text{Cs}_2\text{ZrBr}_6:\text{Os}^{4+}$  two ESA processes lead to upconversion;<sup>187</sup> and in  $\text{Cs}_2\text{-GeF}_6:\text{Os}^{4+}$ , no upconversion is detected.<sup>187</sup> Such differences are traced back, in the fluoride host, to the strong nonradiative decay from the  ${}^1\text{A}_1(\Gamma_1)$  state, which would emit the visible light at about twice the excitation energy. In the bromide<sup>188</sup> and chloride<sup>189</sup> the level sequences allow both resonant and out of resonance ground-state absorption, which contribute to APTE (ETU), ESA, and avalanche upconversion (see section 4).

In the double-doped  $\text{Cs}_2\text{NaYCl}_6:\text{Os}^{4+}$ ,  $\text{Er}^{3+}$ ,<sup>190</sup> upconversion is observed under a scheme similar to the pioneer work<sup>170</sup> involving a TM ion for absorption and a lanthanide for emission. The green emission from  ${}^4\text{S}_{3/2}(\text{Er}^{3+})$  has been found to be both of the APTE (ETU) and ESA types (though called cooperative) with some back-transfer from  $\text{Er}^{3+}$  to  $\text{Os}^{4+}$ .

### 4.3. APTE (ETU) for Display and IR Detection Applications

In display technology the light-emitting material is always in powder form, traditionally called a phosphor. Because of various inclinations of the crystallite external surfaces reducing total internal reflection, more light output is extracted in a wider view angle from crystallites than from the equivalent single crystal. The upconversion phosphor field has recently been reinvestigated<sup>191–195</sup> for the now well-known two-photon and three-photon phosphors based, respectively, on Er–Yb and Tm–Yb codoped materials. Beyond the older light-emitting incoherent sources,<sup>2</sup> the renewed interest stems from potential applications ranging from simple handheld devices used to find IR laser beams<sup>196–198</sup> to visible enhanced detection of IR emissions, X-rays reusable memory plates,<sup>199</sup> and 3-D display technologies.<sup>200</sup>

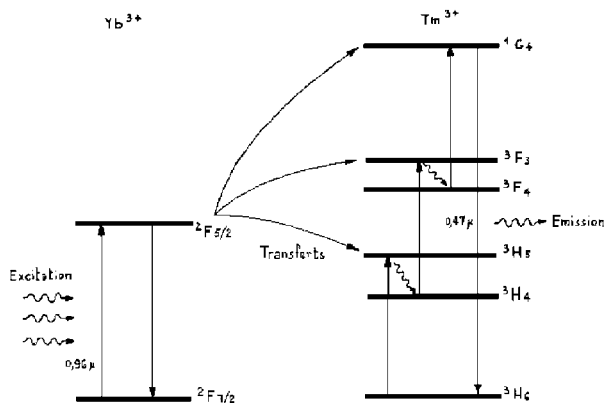


Figure 13. Three-photon APTE upconversion energy scheme in  $\text{Yb}^{3+}$ – $\text{Tm}^{3+}$  couples.

In particular, with now available tunable lasers and fiber beam homogenizers, the various efficiencies have been recently revisited in Krupke's group<sup>191</sup> with more refined experiments than pioneering ones.<sup>158,201,202</sup> Results essentially confirm the previously measured efficiencies below saturation; normalized efficiencies of  $10^{-2}$  and  $2 \times 10^{-4} \text{ cm}^2/\text{W}$ , for two photons, have been obtained, respectively, for the fluoride hosts  $\text{NaYF}_4$  and  $\text{Na}_2\text{Y}_3\text{F}_{11}$ , instead of  $10^{-3} \text{ cm}^2/\text{W}$  as shown in Figure 3 and in Table 1 for  $\text{YF}_3$ . In the case of the  $\text{Yb}$ – $\text{Tm}$  couple, the initial energy level diagram depicting the involved processes, as shown in Figure 13,<sup>7</sup> is confirmed<sup>191</sup> against the cooperative sensitization scheme<sup>43</sup> of Figure 3. In  $\text{NaYF}_4$ , efficiency as high as 2% is reached under pump excitation of  $6 \text{ W}/\text{cm}^2$  at  $960 \text{ nm}$ , though a saturation density of  $4 \text{ W}/\text{cm}^2$  is estimated for the first intermediate step ( $^4\text{H}_4$ ). In the  $\text{Yb}$ – $\text{Er}$  case, the saturation is found at about  $100 \text{ W}/\text{cm}^2$  for fluoride hosts  $\text{NaYF}_4$  and  $\text{Na}_2\text{Y}_3\text{F}_{11}$ ;<sup>191</sup> observed saturation is explained by an excitation trapping into the long lifetime  $^4\text{I}_{13/2}$  state. These more recently obtained results actually confirm the theoretical prediction<sup>73,159</sup> that fluorides should be the ideal hosts for green and blue emissions with the  $\text{Yb}$ – $\text{Er}$  and  $\text{Yb}$ – $\text{Tm}$  couples, see Figure 14.

In this respect, Quimby et al. studied heavy-metal fluoride glasses<sup>203</sup> and Auzel et al.<sup>51</sup> proposed and studied particularly efficient composite APTE (ETU) upconversion materials in which the RE ions were substituted into a crystalline matrix ( $\text{PbF}_2$ ) itself embedded into an oxygen-based glass material. By such means, the multiphonon processes were optimized in the fluoride crystals whereas the overall sample was obtained through classical oxygen glass techniques. Silver nanometric particles have been shown to couple to lanthanide in glasses,<sup>204</sup> and such coupling has been used in  $\text{Er}$ – $\text{Yb}$ -doped vitrocera-mics as a way to study this coupling inside a scattering medium.<sup>205</sup> As expected, it shows a quenching of the APTE process. The vitrocera-mic pioneering work has recently been extended to transparent glass ceramics by Ohwaki's group.<sup>206</sup> Transparency was obtained by reducing the crystallite ( $\text{Pb}_{0.5}\text{Cd}_{0.5}\text{F}_2$ ) size down to about  $20 \text{ nm}$ .

The same group also recently investigated  $\text{Er}^{3+}$ -doped  $\text{BaCl}_2$  and  $\text{ErX}_3$  ( $\text{X} = \text{Br}, \text{I}$ )<sup>207</sup> polycrystalline phosphors for  $1.5 \mu\text{m}$  detection cards,<sup>198</sup> which follow

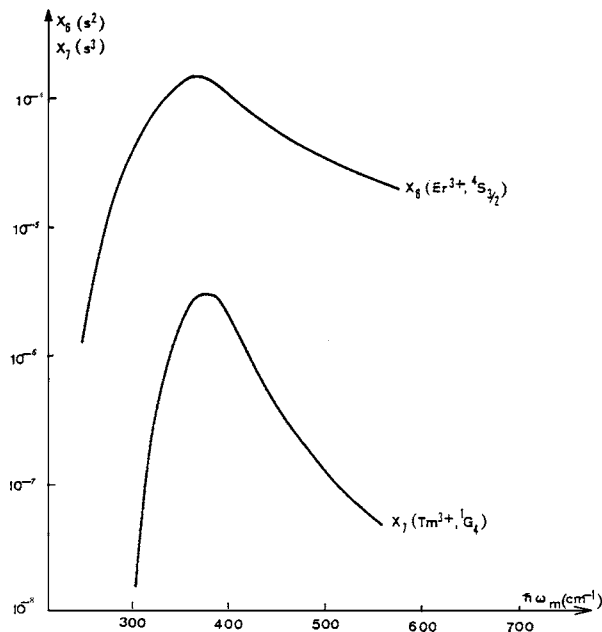


Figure 14. Theoretical effective phonon energy optimization for  $\text{Yb}$ – $\text{Er}$  (green upconversion) and  $\text{Yb}$ – $\text{Tm}$  (blue upconversion).

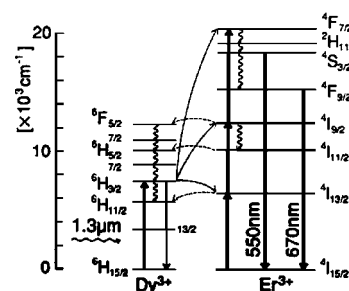


Figure 15. APTE scheme for  $1.3 \mu\text{m}$  to visible upconversion in  $\text{Dy}^{3+}$ – $\text{Er}^{3+}$ -doped  $\text{BaCl}_2$ . (Reprinted with permission from ref 208. Copyright 1994 American Physical Society.)

the upconversion processes described in Figure 5b. More recently, they demonstrated<sup>208</sup> a  $1.3 \mu\text{m}$  to visible detection in a  $\text{Dy}^{3+}$ – $\text{Er}^{3+}$  codoped  $\text{BaCl}_2$  phosphor. The involved APTE (ETU) scheme is given in Figure 15. As can be seen,  $\text{Dy}^{3+}$  is the sensitizer while  $\text{Er}^{3+}$  is the activator. It should be noted that some back transfer from  $\text{Er}$  to  $\text{Dy}$  is taking place and will be a basic limitation as it has been known for years that  $\text{Dy}^{3+}$  is a quencher for the  $\text{Er}^{3+}$  emissions.<sup>2</sup>

Besides equal energy photon summation as just seen, different energy photons may be summed up by APTE (ETU), so producing an effective IRQC with visible-enhanced IR detection.<sup>209</sup> Again, with the  $\text{Yb}$ – $\text{Er}$  couple, embedded in vitrocera-mics of general composition,  $\text{PbF}_2$ – $\text{GeO}_2$ – $\text{YbF}_3$ – $\text{ErF}_3$ , an IRQC has been obtained for  $1.5 \mu\text{m}$ , using an additive pump flux at  $0.96 \mu\text{m}$ . Final detection at  $0.66 \mu\text{m}$  is obtained by summation as shown in Figure 16a. The experimental test scheme is presented in Figure 16b; the pump flux is produced by an IR  $\text{GaAs}:\text{Si}$  light-emitting diode (Mullard GAL-10); the signal is produced by a filtered tungsten lamp; a  $\text{GaAs}$  photocathode photo-multiplier provides the final detection at  $0.66 \mu\text{m}$ . A noise equivalent power of  $10^{-11} \text{ WHz}^{-1/2}$  has been obtained for  $3 \text{ mW}$  of pumping at  $0.96 \mu\text{m}$  and useful

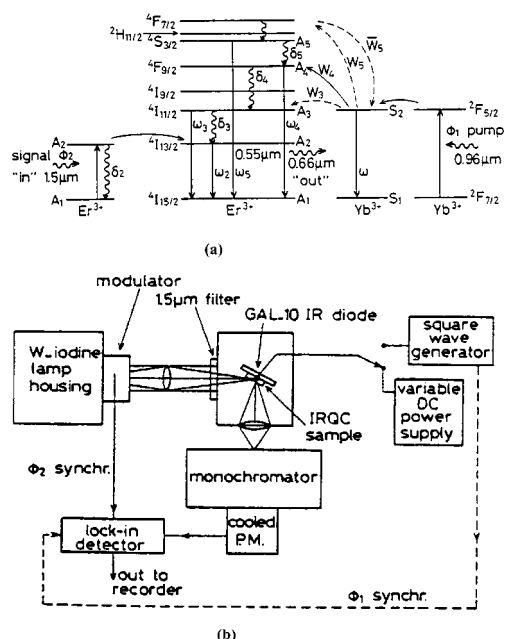


Figure 16. Experimental scheme for a  $0.96 \mu\text{m}$  diode-pumped IRQC at  $1.55 \mu\text{m}$  with energy transfers (a); experimental setup for IRQC detection at  $1.55 \mu\text{m}$  (b).

concentration of  $10\%(\text{Yb}^{3+})$  and  $5\%(\text{Er}^{3+})$ . As always in APTE (ETU) effects, it can be noted that the sensitizer concentration is larger than the activator one, as predicted by eq 22. Of course, if instead of a photomultiplier the detection is made through an electronic image intensifier, an imaging IRQC can be obtained for IR visualization purposes. This approach has recently been systematically considered in Smirnov's group<sup>210</sup> in order to make an IR image converter at wavelengths beyond the usual S1 or GaAs photocathode limits. Here, IR( $1.5\text{--}1.6 \mu\text{m}$ ) to -IR( $0.8\text{--}0.9 \mu\text{m}$ ) upconversion phosphors have been developed with the addition of microchannel image intensifiers. On the basis of  $\text{Y}_{0.85}\text{Er}_{0.15}\text{O}_2\text{S}$  phosphors and an image intensifier with a GaAs photocathode, an IR sensitivity of  $10^{-11} \text{ W/cm}^2$  is anticipated for an image converter screen illuminance of  $0.1 \text{ cd/m}^2$ .<sup>211</sup>

In another direction, reusable X-ray memory detection plates have been made from screens based on the same type of vitroceraics as mentioned above. X-rays are then the source of defect centers, which reduce the Yb lifetime, which in turn reduces the APTE upconversion efficiency. After an X-ray irradiation through the object to be investigated, the X-ray latent image is revealed in the visible spectrum by an IR irradiation at  $0.96 \mu\text{m}$ , the  $\text{Yb}^{3+}$  excitation wavelength. The sensitivity is increased with the higher order upconversion processes. An image so produced in the blue spectrum is shown in Figure 17 for a three-photon APTE (ETU) process in a Yb-Tm-doped vitroceraic screen revealed under IR after a 90 KV, 5 mA, 1 min 45 s X-ray irradiation.<sup>199</sup> The screen may be reused after a heating procedure, which bleaches the defect centers.

The inherent nonlinearity of the APTE (ETU) process had been considered as an incoherent optical amplifier since the first days of APTE.<sup>7</sup> Its principle, given in Figure 18, is based on a two-beam scheme; one of them, the pump beam, is at broad band and



Figure 17. Latent X-ray image of a tooth in a Yb-Tm-doped vitroceraic, revealed by the blue emission under an IR irradiation at  $960 \text{ nm}$ .

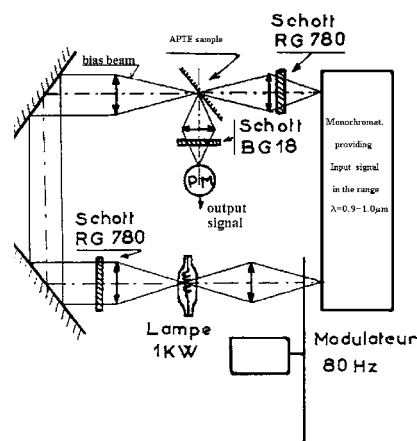


Figure 18. Incoherent amplifier scheme with an APTE sample.

CW; it fixes the bias point of the sample. The other beam (narrow band and modulated) is the signal beam which is tuned through the excitation band to be investigated. Practical gain of a few factors of 10 can be so obtained. This procedure has been effectively used to obtain the excitation spectra for upconversion both in 4f systems<sup>7</sup> and 5f systems ( $\text{U}^{4+}$  in  $\text{ThBr}_4$  and  $\text{ThCl}_4$ ),<sup>161</sup> in the absence, at the time, of synchronous electronic amplifiers.

The first proposed use of APTE (ETU) phosphors has been the handheld laser mode visualization screen<sup>196</sup> since then proposed again for visualization of both  $0.96$  and  $1.5 \mu\text{m}$  spectral regions.<sup>197,198</sup>

In ending this section, it may be useful from an applied point of view to summarize in Table 1 the various values for measured normalized efficiencies as they have appeared in the literature. As it may have been noticed, such values are rarely given but are important in showing the relative practical interest of the various proposed upconversion schemes.

#### 4.4. General Negative Roles Brought up by Undesired APTE (ETU) Effects

APTE (ETU) being an anti-Stokes process does induce reabsorption from excited states. Because it is so efficient when concentration and excitation



obtained in  $\text{LiYF}_4$  under laser diode pumping at  $0.791 \mu\text{m}$  at 40 K,<sup>220</sup> this was followed by obtaining the laser blue emission at  $0.470 \mu\text{m}$  with a 10 mW threshold under the same conditions.<sup>221</sup>

Upconversion, attributed to the ESA type, has even provided violet emission at  $0.380 \mu\text{m}$  in  $\text{LaF}_3:\text{Nd}^{3+}$  by summing an IR and a yellow laser pump or two yellow dye laser pumps,<sup>222</sup> however, only at low temperature (at 90 K). Low temperature has been a general drawback for CW upconversion lasers. In solids, a three-level scheme at room temperature generally becomes a quasi-four-level scheme at lower temperature. This explains why the first upconversion lasers were working in a pulsed mode at room temperature and continuous operation could only be obtained at lower temperature. This drawback has recently been overcome by using glass fibers or/and higher density laser pumping, so providing ground-state quasi-saturation. In particular, the versatile tunable Ti-sapphire laser has helped a lot in this matter.

In recent years, Huber's group in Hamburg has obtained many new upconversion laser results. After an initial pulsed laser operation in  $\text{KYF}_4:\text{Er}$  at  $0.551 \mu\text{m}$  at room temperature,<sup>223</sup> the CW functioning has been reached,<sup>224</sup> in both cases with an attributed ESA upconversion pumping by a Ti-sapphire laser; for CW operation, the laser threshold has, however, the large value of 2.2–2.4 W. On the other hand, a very efficient CW laser effect has recently been achieved in a 3 mm long single crystal of  $\text{LiYF}_4:\text{Yb}(3\%)-\text{Er}(1\%)$ ; the pumping at  $0.966 \mu\text{m}$  at a level of 1.6 W was provided by a Ti-sapphire. An upconversion laser threshold of 418 mW was obtained, and the nature of the pumping was proved to be of the APTE type both by the laser excitation spectrum analysis replicating the Yb absorption spectrum and by a nonlinear narrowing as described in section 3.2. The laser useful output at  $0.551 \mu\text{m}$  is 40 mW with 5% output coupling.<sup>225</sup>

Research on upconversion-pumped laser materials continues to be active, and groups of laboratories have considered  $\text{GdAlO}_3$ ,  $\text{LiGd}(\text{MoO}_4)_2$ ,  $\text{Y}_3\text{Sc}_2\text{Ga}_3\text{O}_{12}$ , and  $\text{Gd}_3\text{Ga}_5\text{O}_{12}$ , doped with Yb, Tm, not in the usual scheme with Yb pumping, but with Tm excitation by the  $^3\text{H}_6$  to  $^3\text{H}_4$  absorption with forth and back transfer with Yb.<sup>154</sup> The conclusion is that for  $^1\text{G}_4$  ( $\text{Tm}^{3+}$ ) emission at 480 nm, the  $\text{Y}_3\text{Sc}_2\text{Ga}_3\text{O}_{12}$  host would be better than the  $\text{LiYF}_4$  one.

Because of their inherent small core diameter, glass fibers easily allow one to obtain high pumping density over long lengths. Such high densities over long lengths cannot be provided by any lens focusing system. Ground-state depletion of any doped fiber can be easily reached with less than 100 mW pumping.<sup>227</sup> In particular, fluoride fibers favor anti-Stokes lasers for three reasons:

- (i) the existence of long-lived metastable states linked with the low-energy phonons of the fluoride matrix;
- (ii) ground-state saturation allowing a CW laser functioning even in a three-level laser energy scheme;

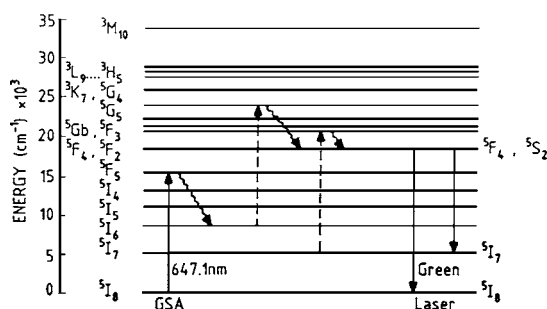


Figure 22. Energy scheme for the first visible CW upconversion Ho-doped fiber laser. (Reprinted with permission from ref 230. Copyright 1991 Institute of Electrical and Electronic Engineers.)

(iii) the advantage of a nonlinear pumping linked again with the optical confinement of the fiber medium.

Since the first demonstration in 1986<sup>228</sup> of the feasibility of CW room-temperature three-level lasers in the  $\text{Er}^{3+}$ -doped glass fibers, one could think that an upconversion-pumped three-level scheme could also be used in CW operation at room temperature for  $\text{Er}^{3+}$  emission at 540 nm.<sup>132</sup> After preliminary results, obtained first at 77 K with  $\text{Tm}^{3+}$ -doped fluorozirconate fiber, lasing at 455 and 480 nm,<sup>229</sup> the very first CW, room-temperature upconversion laser was demonstrated at CNET by Allain et al.<sup>230</sup> in a three-level scheme of the  $\text{Ho}^{3+}$ -doped fluoride fiber laser (Figure 22). Because of the weak  $\text{Ho}^{3+}$  concentration (1200 ppm), it was believed that within the single-ion level system ESA was taking place. However, since clustering with subsequent APTE (ETU) effect may sometimes occur at much lower concentration (70 ppm in ref 71), some doubt is cast about the effective pumping process, as in many of the subsequent upconversion-pumped fiber lasers.

$\text{Er}^{3+}$ -doped glass fibers have also shown CW room-temperature three-level laser emission at 540 nm when pumped at 801 nm.<sup>231</sup> Because the pumping wavelength is in the diode laser range, there was some hope that a compact fiber laser could be obtained.

Besides these two-photon upconversion-pumped lasers, a three-photon pumped one has been demonstrated in a  $\text{Tm}^{3+}$ -doped ZBLAN fiber:<sup>232</sup> pumping at  $1.12 \mu\text{m}$ , a room-temperature CW laser emitting at 480 nm, with a differential efficiency of 18%, has been obtained with the rather low threshold of 30 mW.

$\text{Pr}^{3+}$ -doped fluoride fibers, because of their low phonon energy with respect to  $\text{Pr}^{3+}$ -emitting level energy differences, have allowed CW room-temperature anti-Stokes lasers at blue, green, and red wavelengths in a single fiber.<sup>233</sup> More detailed results on such upconversion laser recent evolution may be found in ref 234.

However, before closing this section, it is worth mentioning the possibility of upconversion laser with multiphonon pumping in the electronic rare-earth ion sideband transitions mentioned in section 3. It presents the advantage of the self-adaptation of the ESA absorption to a single pump wavelength. Upconversion pumping is successful through multiphonon sideband pumping with energy mismatches as large

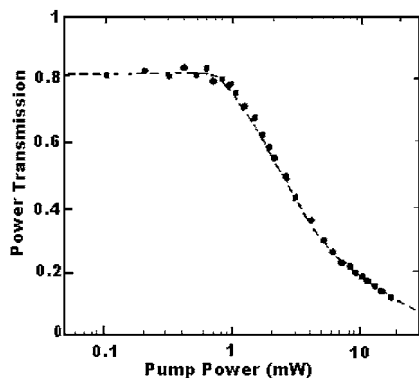


Figure 23. Decrease of transmission in a  $\text{Pr}^{3+}:\text{LaCl}_3$  sample under  ${}^3\text{H}_5\text{--}{}^3\text{P}_1$  pumping. (Reprinted with permission from ref 12. Copyright 1990 Elsevier.)

as  $1000\text{ cm}^{-1}$ . This is the case for the  $\text{Tm}^{3+}$  fluoride fiber laser pumped at  $1.06\text{ }\mu\text{m}$  in a three-photon ESA process and lasing at  $1.47\text{ }\mu\text{m}$ .<sup>235</sup> This provides an efficient four-level scheme laser that allows CW oscillation with a differential efficiency of 27% at room temperature. On the other hand, this opens the door to long (kilometer) distributed amplifiers where the losses per unit length would be compensated at each point by the gain; the transmission line would then be turned into a lossless line.

Multiphonon pumping is also one of the processes involved in the avalanche upconversion process described in the next section.

## 5. Cross-Relaxation and the Photon Avalanche Effect

The most recently discovered upconversion process is the photon avalanche effect.<sup>11</sup> Since it has not been considered in the review of 1973,<sup>2</sup> more detailed attention will be paid to it here.

While looking for two-step absorption (ESA) in  $\text{Pr}^{3+}$ -doped  $\text{LaCl}_3$  and  $\text{LaBr}_3$  at low temperature ( $<40\text{ K}$ ) as a means to detect an IR photon by its energy summation with a more energetic photon (IRQC) so performing excited-state absorption (ESA), it was found that the higher energy photon alone could, in the same time, give rise to upconversion and reduce the transmission of the sample above a given intensity threshold;<sup>11</sup> see Figure 23. The effect was attributed to an increase of population of an excited state resulting from a cross-relaxation process. The starting process was initially not completely determined. In the  $\text{Pr}^{3+}$  case, the  ${}^3\text{H}_5\text{--}{}^3\text{P}_1$  absorption is initially very weak at low temperature because  ${}^3\text{H}_5$  is about  $2000\text{ cm}^{-1}$  above the ground state (see Figure 24); however, above about 1 mW of excitation, this transition is increased; the cross-relaxation process ( ${}^3\text{H}_6, {}^3\text{H}_4$ ) ( ${}^3\text{H}_5, {}^3\text{H}_5$ ) increases the  ${}^3\text{H}_5$  population which in turn reduces the transparency of the sample at the ( ${}^3\text{P}_1\text{--}{}^3\text{H}_5$ ) energy. Since the more the ( ${}^3\text{P}_1\text{--}{}^3\text{H}_5$ ) energy is absorbed the more the  ${}^3\text{H}_5$  population is increased, the process was termed photon avalanche.<sup>11</sup> It is clearly a way to increase ESA in a sample.

Afterward, similar effects have been observed in  $\text{Sm}^{3+}$ -,  $\text{Nd}^{3+}$ -,  $\text{Ni}^{2+}$ -, and  $\text{Tm}^{3+}$ -doped halide crystals.<sup>236–239</sup> Recently the photon avalanche effect has

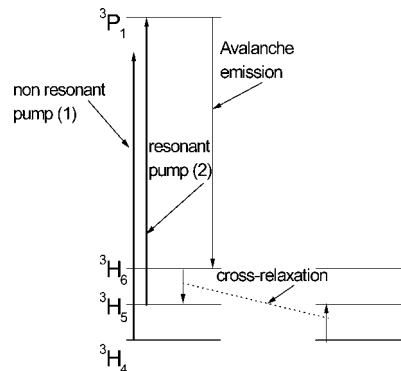


Figure 24. Simplified  $\text{LaCl}_3:\text{Pr}^{3+}$  energy scheme for the avalanche mechanism.

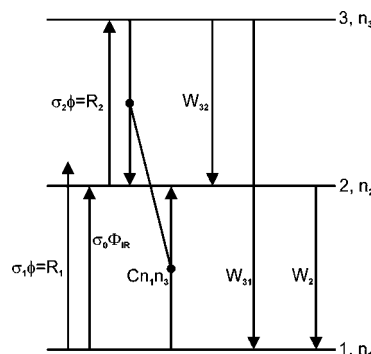


Figure 25. Avalanche simplified three-level scheme;  $C$  is the cross-relaxation coefficient;  $W_{ij}$  are the spontaneous emission terms.

been obtained at room temperature for the  $\text{Er}^{3+}$  ion in a ZBLAN glass both in bulk and in fiber form<sup>240–243</sup> and in a  $\text{LiYF}_4$  crystal.<sup>244</sup>

The photon avalanche process is characterized by three distinct nonlinear behaviors:

(i) transmission, (ii) emission, and (iii) rise time on the pump power intensity with generally the existence of a critical pump threshold.

Particularly long rise times, from seconds to minutes,<sup>244,245</sup> have been observed.

At this point it is worth discussing the notion of threshold for avalanche. Because of the complexity of the phenomenon, it has been usually modeled by a simplified three-level system.<sup>246–248</sup>

### 5.1. Avalanche Process as a Positive Feedback System<sup>244</sup>

Using the three-level simplified model of ref 246 or 247 and adding to the initial ground-state absorption ( $\sigma_1\Phi = R_1$ ) an auxiliary direct feeding into the metastable state ( $\sigma_0\Phi_{\text{IR}}$ ) we may write the following set of equations (see Figure 25 for explanation of symbols which except for the trigger  $\sigma_0\Phi_{\text{IR}}$  are the same as in ref 246).

Being interested in the steady-state initial step of avalanche, we assume

$$(i) \frac{dn_1}{dt} = \frac{dn_2}{dt} = \frac{dn_3}{dt} = 0$$

$$(ii) n_1 = 1 - n_2 - n_3 \approx 1$$

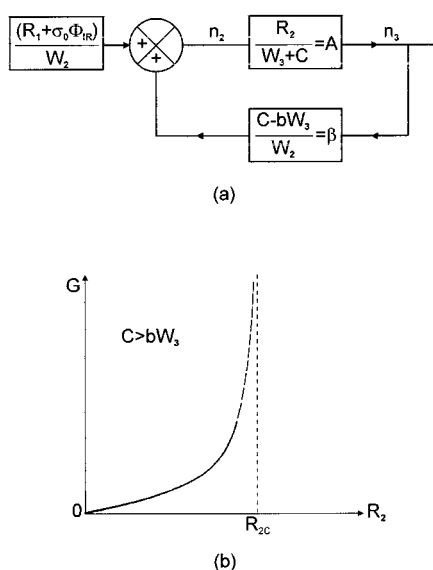


Figure 26. (a) Positive feedback model for avalanche. (b) Gain behavior of the model versus  $R_2$ ; positive feedback condition is  $b > CW_3$ ; the asymptote  $R_{2c}$  corresponds to the avalanche threshold.

Then the rate equations are simplified to

$$0 = -R_1 - \sigma_0 \Phi_{IR} + bW_3 n_3 + W_2 n_2 - Cn_3 \quad (27)$$

$$0 = (1 - b)W_3 n_3 - W_2 n_2 + 2Cn_3 + R_1 + \sigma_0 \Phi_{IR} - R_2 n_2 \quad (28)$$

$$0 = R_2 n_2 - W_3 n_3 - Cn_3 \quad (29)$$

with  $C$  being the cross-relaxation parameter and  $b$  the branching ratio, the following relationships exist between the transition probabilities

$$(1 - b)W_3 = W_{32}; bW_3 = W_{31}; W_3 = W_{32} + W_{31}$$

Equation 29 can be written as

$$n_2 \frac{R_2}{W_3 + C} = n_3 \quad (30)$$

Considering amplitude and using the symbolic representation for feedback systems, eq 30 gives block  $A$  of Figure 26a.

In the same way, eq 27 is written

$$n_2 = \frac{R_1 + \sigma_0 \Phi_{IR}}{W_2} + \frac{C - bW_3}{W_2} n_3 \quad (31)$$

which can be symbolized in Figure 26a by block  $\beta$  and an adder with input source

$$(R_1 + \sigma_0 \Phi_{IR})/W_2$$

Combining eqs 31 and 30 gives the classical feedback systems scheme of Figure 26a.

Such a system is known to be unstable for  $A\beta = 1$ . One can define a gain of the closed loop feedback system,  $G$ , by the ratio between the green output to a pump related input signal ( $R_1$ ) plus an eventual

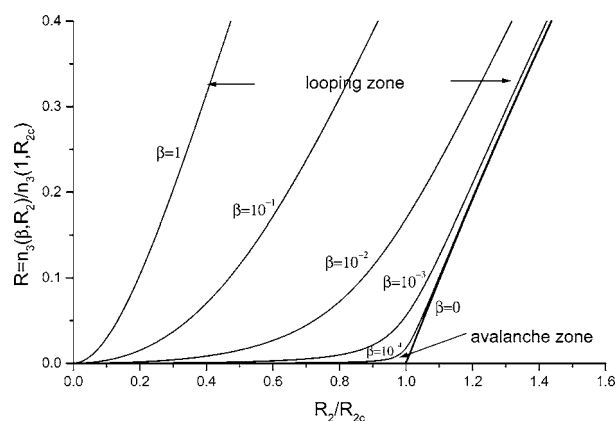


Figure 27. Third-level normalized population,  $R = n_3(\beta, R_2)/n_3(\beta = 1, R_2 = R_{2c})$ , versus pumping term ( $R_2$ ) with  $\beta$  as a parameter. (Reprinted with permission from ref 248. Copyright 1995 Elsevier.)

external trigger ( $\Phi_{IR}$ )

$$G = \frac{n_3}{(R_1 + \sigma_0 \Phi_{IR})/W_2} \quad (32)$$

It is well-known that in terms of the  $A$  and  $\beta$  of Figure 26a, one has

$$G = \frac{A}{1 - A\beta} \quad (33)$$

The stability condition is then written as

$$\frac{R_2}{W_3 + C} \frac{C - bW_3}{W_2} < 1 \quad (34)$$

Its limit is just the threshold condition given by Joubert et al.<sup>246</sup> obtained here in a simplified way as

$$R_{2c} = \frac{W_2(W_3 + C)}{C - bW_3} \quad (35)$$

with  $C > bW_3$  for a positive feedback.

The behavior of our feedback system below threshold can be described by the behavior of  $G(R_2)$ , Figure 26b.

The feedback black box approach has also been considered in studying the dynamics of the above three-level system.<sup>249</sup> It is based on the fact that the general feedback linear theory may solve algebraically time variable differential equation systems by using the Laplace transform of the time-dependent functions.

## 5.2. Conditions in Order To Observe an Avalanche Threshold<sup>248,250</sup>

Neglecting the first nonresonant absorption step ( $R_1$ ) and taking into account only the second resonant absorption step ( $R_2$ ) when calculating the population of the third level ( $n_3$ ) versus  $R_2$  (the pumping excitation) leads to a well-defined nonlinearity in  $n_3$  for the asymptotic curve ( $R_1/R_2 = 0$ ), as shown in Figure 27.

When the first step ( $R_1$ ) is explicitly taken into account,<sup>248</sup> the threshold nonlinearity is progressively smoothed out while increasing the ratio  $R_1/R_2$  as

shown in Figure 24. This corresponds to a progressively more resonant first step. As shown by Goldner and Pellé,<sup>248</sup> practically a clear avalanche threshold can be expected only for  $R_1/R_2 \leq 10^{-4}$

Some of the features of the avalanche effect have been observed at room temperature in  $\text{Tm}^{3+}:\text{YAlO}_3$ <sup>239</sup> and in  $\text{Pr}^{3+}$  in silica glass fibers.<sup>251</sup> The lack of a clear threshold in these two systems can certainly be related to the above prediction.

The region in Figure 24, where  $10^{-4} < R_1/R_2 < 1$ , corresponds to cases for which the losses in the feedback loop may exceed the loop gain for  $R_2$  values below  $R_{2C}$ , so that after a number of loopings of the excited population between level 3 and the metastable level 2, the system would neither diverge nor maintain  $n_3$  independently of  $R_1$ . Such cases have been called a looping mechanism.<sup>252</sup> We believe that some of the reported cases of quasi-zero threshold avalanche cases in the literature<sup>251,253</sup> belong to large  $10^{-3} < R_1/R_2 < 1$  cases for which, as shown in Figure 24, it is very difficult to distinguish between avalanche and sequential two-photon absorption (ESA) which occurs strictly for  $\beta = 1$ . Sometimes such cases have been termed quasi-avalanche.<sup>248</sup> This intermediate behavior has been well studied in  $\text{YAlO}_3:\text{Er}^{3+}$  under 790–810 nm excitation.<sup>254</sup> The three kinds of upconversion, ESA, APTE(ETU), and quasi-avalanche, are simultaneously found to exist according to the precise excitation wavelength. For a 796 nm excitation, the blue-green upconversion is attributed for 23% to ESA and for 77% to the looping effect (quasi-avalanche).

$\text{Er}^{3+}$ , with  $(R_1/R_2) \cong 10^{-6}$ , has shown at room temperature all three characteristic features of avalanche when doping a  $\text{LiYF}_4$  crystal or a ZBLAN fluoride glass both in bulk and in a fiber shape (see sections 5.3 and 5.4); even a long delay of several seconds to a minute was observed.<sup>242–244</sup> For comparison, the following values for the critical parameter ( $\beta = R_1/R_2$ ) have been found for  $\text{Nd}^{3+}-\text{LiYF}_4$ ,  $(R_1/R_2) = 1.7 \times 10^{-4}$  for avalanche at  $T = 40$  K,<sup>237,246</sup> for  $\text{Tm}^{3+}-\text{Ho}^{3+}-\text{Gd}_2\text{Ga}_5\text{O}_{12}$ ,  $(R_1/R_2) = 3.6 \times 10^{-2}$  for the two-ion looping process;<sup>255</sup> for a  $\text{Tm}^{3+}-\text{BiGaZrZr}$  glass,  $(R_1/R_2) = 1.2 \times 10^{-2}$ <sup>256</sup> for what was claimed to be avalanche at 100 K.<sup>257</sup> In this last case since the delay reaches only 16 times the metastable state lifetime ( $W_2^{-1}$ ), it looks more like a looping process case. In  $\text{Er}^{3+}$ , as can be seen from sections 5.3 and 5.4, the avalanche delay reaches  $6 \times 10^2$  to  $10^4$  times  $W_2^{-1}$ , respectively, for Er-doped fluoride glass and crystal.

For  $\text{Tm}^{3+}$  ions, in divalent fluorides,  $\text{SrF}_2$ ,  $\text{CaF}_2$ ,  $\text{BaF}_2$ , and  $\text{CdF}_2$ , avalanche has been studied<sup>258</sup> in a red to blue upconversion scheme. Avalanche is characterized by the slow build-up of the signal and the spatial spreading. In  $\text{Y}_2\text{SiO}_5:\text{Tm}^{3+}$ ,<sup>259</sup> avalanche, as shown by a kick in the output slope,  $n$ , for 100 mW excitation, is believed to explain  $^1\text{G}_4$  emission, whereas upconversion from  $^1\text{D}_4$  is attributed to ESA and APTE (ETU).

In a ZBLAN glass, doped either with (0.1–5%) $\text{Ho}^{3+}$  alone or with  $\text{Ho}^{3+}$  and (3%) $\text{Tm}^{3+}$ ,<sup>260</sup> clear avalanche threshold is obtained at about 140  $\text{W}/\text{cm}^2$  of 585 nm laser excitation for the codoped sample, at both 77

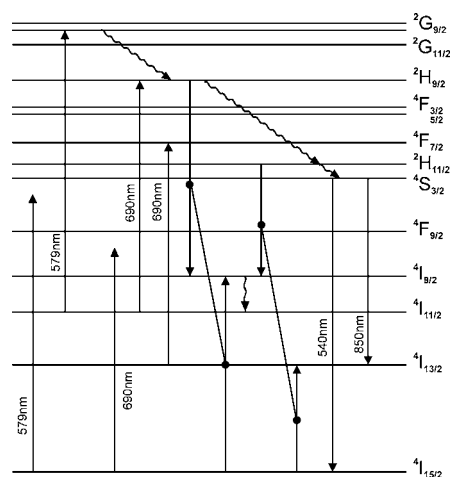


Figure 28. Energy scheme of  $\text{Er}^{3+}$ , and principal mechanisms responsible for photon avalanche cycles under excitation at 579 and 690 nm.

and 300 K. Establishing times, which are the signatures for avalanche, are, respectively, 250 and 30 ms. Upconverted emission from  $\text{Ho}^{3+}$  is at 545 nm from  $^5\text{S}_2/{}^3\text{F}_4$ . The nonresonant first step is in a multiphonon sideband and for the second resonant step in static pair levels induced on  $\text{Ho}^{3+}$  by  $\text{Tm}^{3+}$  as revealed by the excitation spectrum.

As for other types of upconversion, the advent of research with d ion-doped crystal has shown that avalanche could also be obtained with such ions.  $\text{Cs}_2\text{-ZrBr}_6:\text{Os}^{4+}$ <sup>187,188, 261</sup> has shown clear signs of an avalanche process: slowing of the upconversion establishment from a few milliseconds up to 1.5 s at a threshold of 3.8 mW and nonlinearity (higher slope) in the slope 2 line of the two-photon upconversion process when excited aside the resonant ground-state absorption. From the information given, one can estimate the  $R_1/R_2$  ratio to be in that case  $5 \times 10^{-3}$ . This is weak in principle to show a marked threshold, yet one can compute that the number of feedback loops is about  $1.2/1.6 \times 10^{-3} = 750$ , which is as large as in an Er-doped ZBLAN glass (see above). In  $\text{Cs}_2\text{-ZrCl}_6:(1\%)\text{Os}^{4+}$ ,<sup>189</sup> signs of avalanche with a weak threshold of 2.6 mW have also been found from 15 to 50 K. The fitted  $R_1/R_2$  ratio is given to be  $3.3 \times 10^{-3}$ , which also is weak for a marked threshold. Here the number of looping cycles is only about  $0.5/20 \times 10^{-3} = 25$ . This is a quasi-avalanche or looping effect.

### 5.3. $\text{Er}^{3+}-\text{LiYF}_4$ as an Avalanche Model Experiment

In the case of  $\text{Er}^{3+}$ , the first step for photon avalanche has been clearly identified and attributed to anti-Stokes multiphonon sideband absorption<sup>240,241</sup> (see Figure 28). Calculating the  $R_1/R_2$  ratio from multiphonon absorption allows one to estimate a value of  $5 \times 10^{-6}$ ,<sup>243,244</sup> as shown in Figure 29, which displays the multiphonon sideband absorption in the avalanche excitation region. As observed, this experimental situation provides a marked threshold behavior in the erbium case.<sup>240</sup>

The simple theory of section 5.1 has been verified by experimentally measuring  $G(R_2)$ . This was done using the following method (see the experimental

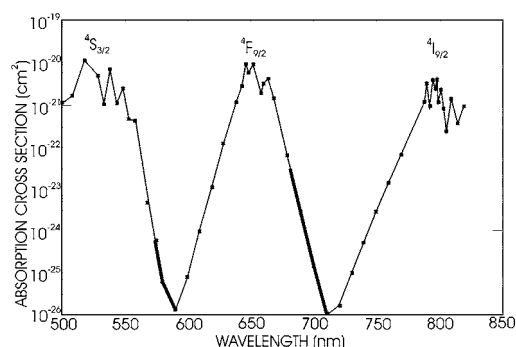


Figure 29. Absorption cross section for  $\text{Er}^{3+}\text{-LiYF}_4$  taking into account the multiphonon contribution; the heavier lines show the anti-Stokes zones which contribute to  $W_1$  for the avalanche processes in erbium.

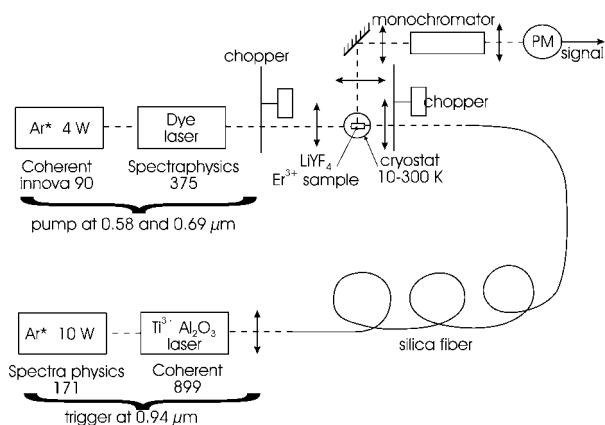


Figure 30. Experimental scheme for measuring the positive feedback gain and for an external triggering.

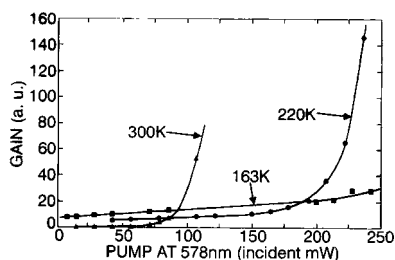


Figure 31. Experimental  $G(R_2)$  for three temperatures: 30, 220, and 163 K; residual signal near  $R_2 = 0$  comes from direct upconversion under  $0.94 \mu\text{m}$  excitation.

setup in Figure 30): having obtained a given green output for a pump  $R_2$  with  $\Phi_{\text{IR}} = 0$ ,  $R_2$  is reduced while increasing  $\Phi_{\text{IR}}$  in order to maintain a constant green output.  $\Phi_{\text{IR}}$  is an infrared signal at  $0.94 \mu\text{m}$  in resonance with the metastable state 2 (here  $^4I_{11/2}$ ) absorbing with a cross-section  $\sigma_0$ .

Each point is obtained after waiting for a steady state. Because of the large ratio for  $\sigma_0/\sigma_1$ , this experiment provides a good description of  $G(R_2)$ , as shown by the results in Figure 31 for three temperatures. One can define an  $R_{2C}$  asymptote only at 300 and 220 K, respectively, 120 and 240 mw. At 163 K one cannot reach an asymptote (threshold) in that experiment at the maximum available power of 250 mw. Thus, the effect of lowering temperature is essentially to increase  $R_{2C}$ .

The part in  $R_{2C}$  which is most sensitive to temperature is  $C$  because it is related to the phonon energy of only  $100 \text{ cm}^{-1}$ , whereas  $W_2$  and  $W_3$  are related to

phonons covering the energy gap below levels 3 and 2, that is energies  $> 2000 \text{ cm}^{-1}$ . However, this requires  $C$  to be of the same order as  $W_3$  or  $bW_3$ ; otherwise, as long as  $C \gg W_3$ ,  $bW_3$ , one has  $R_{2C} \cong W_2$  and its temperature dependence is just the same as  $W_2$ .

Comparing the theoretical threshold as given by eq 35 with experimental conditions, one can verify the simple feedback model.

Assuming level 1 to be  $^4I_{15/2}$ , level 2 to be  $^4I_{11/2}$ , and level 3 to be the aggregation of levels between  $^2G_{9/2}$  and  $^4S_{3/2}$  with the emission properties of  $^4S_{3/2}$  (see Figure 28) and taking the room-temperature data given by ref 256 and 257, the following parameters are found:  $W_3 = 2500 \text{ s}^{-1}$ ;  $b = 0.5$ ;  $C = 0.5 \times 10^6 \text{ s}^{-1}$ ;  $W_2 = 140 \text{ s}^{-1}$ , because corresponding oscillator strengths are about equal ( $0.4 \times 10^{-6}$ ),<sup>262</sup> one can also assume  $\sigma_2 = \sigma_0 = 4 \times 10^{-21} \text{ cm}^2$ .

Using reduced population units (pure number), it becomes  $R_{2C} = 140(2500 + 510^5)/(510^5 - 1250) = 141 \text{ s}^{-1} \cong W_2$  (at room temperature) from which it can be estimated

$$\Phi_{\text{threshold}} = 141/4 \times 10^{-21} = 3.5 \times 10^{22} \text{ s}^{-1} \text{ cm}^{-2}$$

At  $0.578 \mu\text{m}$  it gives, for a  $50 \mu\text{m}$  diameter spot, a threshold power of  $P_{\text{th}} = 222 \text{ mW}$ ; this value is of the same order as threshold values observed for  $0.578 \mu\text{m}$  pumping.

$G(R_2)$  shows (Figure 26b) that the  $\text{Er}^{3+}$ -doped solid constitutes a marginally stable positive feedback system: even below the  $R_{2C}$  asymptote, it is known from feedback theory that a strong input signal can drive a system that is otherwise stable into its instability state (existence of a gain stability margin).

To experimentally verify this behavior, a pulsed trigger of amplitude  $\sigma_0 \Phi_{\text{IR}}/W_2$  is added to the input signal  $R_1/W_2$  given by the pump; the experimental setup is again the same as that presented in Figure 30.

The results at room temperature are given in Figure 32a–c. In the absence of a trigger, with  $P_p = 114 \text{ mW}$  at  $578 \text{ nm}$  incident on sample, the threshold is reached after a very long time ( $> 50 \text{ s}$ ) (Figure 32a). With the same pump intensity ( $P_p = 114 \text{ mW}$ ) and with a short trigger of  $0.6 \text{ s}$ , the avalanche state is obtained quickly and maintained after trigger extinction (Figure 32b). With the same trigger but with a reduced pump ( $P_p = 99 \text{ mW}$ ), the avalanche state cannot be reached. This behavior, as depicted in Figure 32a–c, is obtained down to 180 K.

Below 180 K, the observed threshold increases as shown in Figure 31. However, due to the temperature scan cycles relatively short time constant ( $3 \text{ s/K}$  from 10 to 50 K, then  $21 \text{ s/K}$  from 50 to 150 K), it is not sure whether or not the threshold could be reached for an avalanche delay time  $> 50 \text{ s}$ .

From this experiment, it is understood that measuring an avalanche threshold depends on the time one is ready to wait before its observation. This time depends not only on the excited-state pumping but also on the ground-state absorption conditions. In any

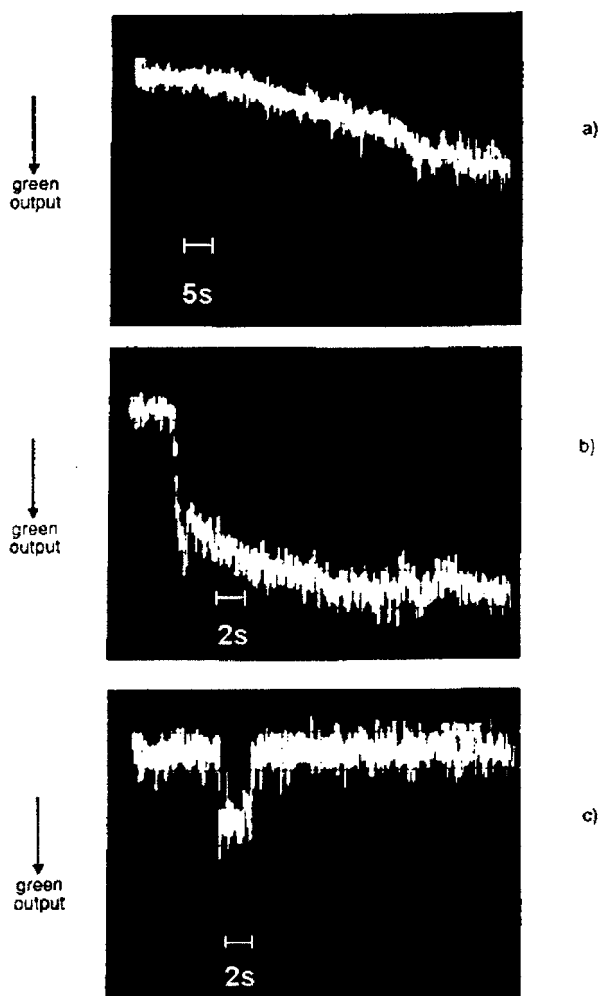


Figure 32. Avalanche behavior just below threshold without (a) and with (b) a trigger feeding the metastable state and (c) much below threshold.

case, below 180 K, being then limited by the pump laser at a much lower power than the threshold, the result of Figure 32c is obtained. This triggering effect constitutes an optical analogue of a thyatron providing an intrinsic material-based optical bistability.

The time delay behavior of the avalanche process has been studied theoretically quite recently within the general model of Landau for phase transition.<sup>256</sup> The time delay at threshold, in fact a critical slowing time,  $t_c$ , proved itself to be the most sensitive experimental data when looping or avalanche takes place. It has been shown to be given by<sup>256,263</sup>

$$t_c = K\sqrt{\sigma_2/\sigma_1} \quad (36)$$

where  $K$  depends on other spectroscopic parameters. Equation 36 is rather well verified in the above experiments for which avalanche delay times have been determined for two different excitation wavelengths of known multiphonon anti-Stokes cross sections: at  $\lambda = 688$  nm, with  $\sigma_1 = 10^{-24}$  cm<sup>2</sup>, delay is found to be 0.4 s; whereas at  $\lambda = 579$  nm, with  $\sigma_1 = 2 \times 10^{-26}$  cm<sup>2</sup>, the observed delay is 4 s. Assuming for  $\sigma_2$  the same value in both cases of excitation, the ratio of the delays is 0.1, which is in agreement with the value of 0.14 as given by eq 36.

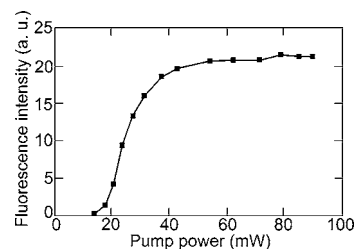


Figure 33. Upconversion emission at 550 nm showing the existence of the avalanche threshold in a ZBLAN:Er<sup>3+</sup> fiber observed from its extremity.

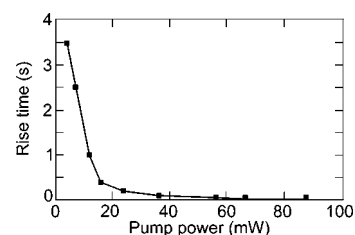


Figure 34. Time delay for the avalanche establishment versus incident pump power at 579 nm in a ZBLAN:Er<sup>3+</sup> fiber.

Above the threshold, the delay for avalanche has been given by ref 264 as

$$t_c = kW_2^{-1}/(\Phi/\Phi_c - 1) \quad (37)$$

with  $k = W_3^{-1}/(1 + b)(2C + W_3)$  and where  $\Phi_c = R_c/2$  is the pumping flux at threshold and  $\Phi$  the effective pumping flux.

#### 5.4. Photon Avalanche in Er<sup>3+</sup>-Fluoride Glasses in Fiber and Bulk Shape

Recently, the photon avalanche effect has been observed at room temperature in a Pr<sup>3+</sup>-doped silica fiber<sup>251</sup> and in an Er<sup>3+</sup>-doped fluoride glass fiber.<sup>241,243</sup> In the first case, only a nonlinearity of the transmission is observed and not the upconversion emission threshold. It was believed that the threshold was so low that it could not be observed. We think that this is explained by the too large nonresonant to resonant absorption ratio as mentioned in section 5.2. On the other hand, in the second case, clear thresholds at 5 and 4 mW of incident power at, respectively, 579 and 690 nm<sup>243</sup> are observed because in these last two cases the first step is a weak anti-Stokes multiphonon absorption giving again a  $R_1/R_2$  ratio of about  $10^{-6}$ , much below the critical value of  $10^{-4}$ . The involved energy scheme for both excitations is essentially the same as that in Figure 28; it shows both pumping routes and the two types of involved cross-relaxations. In Figure 33, the typical threshold behavior for the avalanche upconversion emission is presented. The long delay behavior is displayed in Figure 34, showing, near threshold, the very long time (3.5 s), widely in excess of any of the lifetimes of the metastable states of erbium. The observed delay follows rather well the behavior predicted by eq 37.

As for glass fibers, the same results can be obtained in bulk samples.<sup>240,241</sup> Because the first absorption step, being of a multiphonon nature, is featureless, the excitation spectrum for avalanche directly pro-

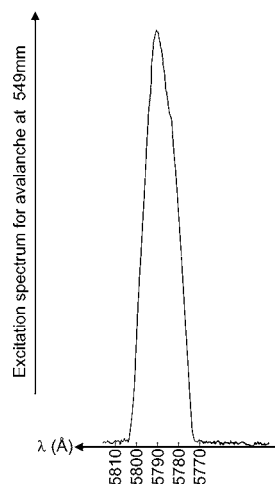


Figure 35. Excitation spectrum for the avalanche emission at 549 nm in a ZBLAN:Er<sup>3+</sup> glass showing the spectrum for the  $^4I_{11/2} \rightarrow ^2G_{9/2}$  ESA transition.

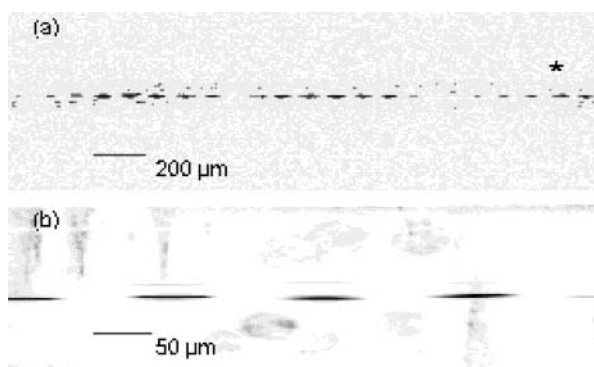


Figure 36. Spatial domains observed along the fiber above the photon avalanche threshold: (a) dot separation about 1 mm. (b) Microscope view of a 1 mm avalanche dot. The scale is 100  $\mu\text{m}$  per division.

vides the ESA spectrum of the resonant second absorption with a single excitation beam as shown in Figure 35 for the  $^4I_{11/2} \rightarrow ^2G_{9/2}$  transition of Er<sup>3+</sup>; this gives a new method<sup>242</sup> to reach ESA spectra otherwise difficult to obtain without a double-beam excitation.

The main difference with a bulk sample is that in the fluoride fiber case upconversion spatial domains appear with periodic structures with periods ranging from a few centimeters to millimeters themselves containing substructures with a period of about 100  $\mu\text{m}$ ,<sup>241,243</sup> as shown in Figure 36. This behavior has been explained by the high contrast provided by the avalanche effect; it then optically reveals the internal electric field mode structure of the fiber waveguide.<sup>241,265</sup>

### 5.5. Avalanche in Codoped Systems

Up to this point, avalanche has been described within a single type of ions. As far as energy transfers in general are considered, the sensitizers and the acceptors may be either of the same or of a different nature. Thus, in the avalanche process, instead of having two ions of the same nature participating in the cross-relaxation step, as described to date, the cross relaxation has also been considered between two ions of a different type. This was the case of the first study by Brenier et al. of the avalanche involving

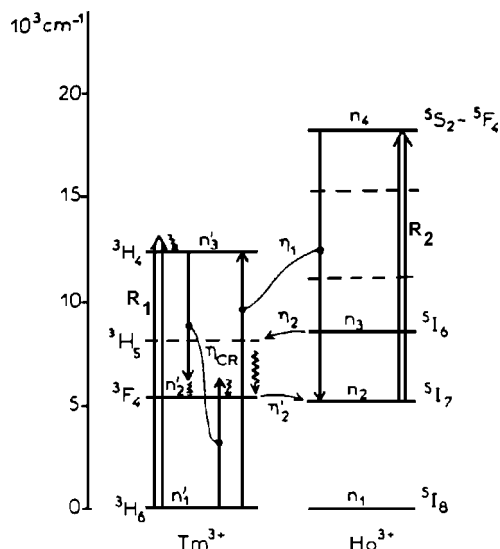


Figure 37. Energy scheme and mechanism for looping effect in the Ho<sup>3+</sup>–Tm<sup>3+</sup> codoped system. (Reprinted with permission from ref 255. Copyright 1994 Elsevier.)

Tm<sup>3+</sup>–Ho<sup>3+</sup>.<sup>255</sup> A complex process of cross-relaxation within two Tm<sup>3+</sup> ions together with a back transfer from Ho<sup>3+</sup> to Tm<sup>3+</sup> has been proposed. The first excitation step is out of resonance with the  $^3H_6 \rightarrow ^3H_4$  absorption of Tm<sup>3+</sup>; it is followed by a cross-relaxation within two Tm<sup>3+</sup> ions; which populates the  $^3F_4(\text{Tm}^{3+})$  state, itself transferring its energy to the  $^5I_7(\text{Ho}^{3+})$  state from which the resonant second step of excitation toward  $^5S_2(\text{Ho}^{3+})$  takes place. Then another cross-relaxation (energy back-transfer) between Ho<sup>3+</sup> and Tm<sup>3+</sup> of the type  $^3H_6(\text{Tm}^{3+}) + ^5S_2(\text{Ho}^{3+}) \Rightarrow ^3H_4(\text{Tm}^{3+}) + ^5I_7(\text{Ho}^{3+})$  provides the feedback loop, see Figure 37. However, the avalanche threshold is not reached, and calculating the  $R_1/R_2$  ratio from the data in ref 255, the critical parameter

$$\beta = 6.16 \times 10^{-22} / 1.73 \times 10^{-20} = 3.6 \times 10^{-2}$$

is determined. This clearly confirms, what the authors have found, that the behavior of this system is in the looping region of Figure 27. The looping process is different from avalanche in the sense that it has a reversible character that real avalanche does not have. In the case of the codoped Yb–Pr system, real avalanche has been reached.<sup>266</sup> In this system, see Figure 38, the first nonresonant excitation step is in the Yb<sup>3+</sup> ion, which transfers to the metastable state  $^1G_4(\text{Pr}^{3+})$  from which the resonant second step up to  $^3P_0(\text{Pr}^{3+})$  takes place. The cross-relaxation step within two Pr<sup>3+</sup> ions feeds the metastable state  $^1G_4(\text{Pr}^{3+})$  and the back transfer to Yb<sup>3+</sup> again feeds the  $^1G_4(\text{Pr}^{3+})$  metastable state. The ratio  $\beta$  from the nonresonant to resonant pumping was estimated to be from  $10^{-6}$  to  $10^{-8}$ <sup>266</sup>, well within the condition to observe a real avalanche threshold.

In YAlO<sub>3</sub>:(10%)Yb, (1%)Ho,<sup>267</sup> a green emission from  $^5S_2(\text{Ho})$  is obtained under 750 and 840 nm excitation. Yb plays a role in the back transfer which helps to populate the metastable state  $^5I_6(\text{Ho})$ . A slight nonlinearity found in the output signal slope is an indication of a looping mechanism.

The Ho–Tm codoped ZBLAN glass system<sup>260</sup> observed in section 5.2 does not seem to enter into the

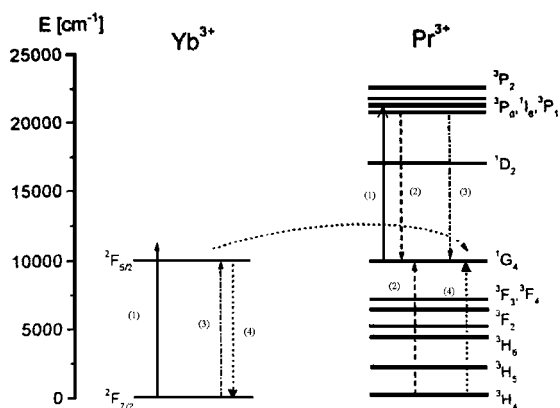


Figure 38. Energy scheme and mechanisms for the codoped  $\text{Yb}^{3+}$ - $\text{Pr}^{3+}$  avalanche system: pumping at  $0.85 \mu\text{m}$  into  $\text{Yb}^{3+}$  sideband and in resonance by ESA into  $\text{Pr}^{3+}$ ; cross-relaxation within  $\text{Pr}^{3+}$ ;  $\text{Yb}^{3+}$ - $\text{Pr}^{3+}$  cross-relaxation;  $\text{Pr}^{3+}$ - $\text{Yb}^{3+}$  back-transfer. (Reprinted with permission from ref 266. Copyright 2000 Elsevier.)

avalanche codoped category since the Tm ion does not seem to play a role in the feedback loop but only in the  $R_2$  excitation term.

In analogy with the previous case, avalanche in  $\text{La}_{1-x}\text{Ce}_x\text{Cl}_3:\text{Nd}^{3+}$ <sup>268</sup> shows that for  $x > 0.1$ , Ce plays a role in increasing the avalanche output signal. This effect is attributed to the presence of undefined pair states in clusters.

Other systems with codoping with 4f and 5f ions have been investigated: In  $\text{LaCl}_3:(1\%)\text{Pr}^{3+}$ ,  $(0.1\%)\text{U}^{3+}$ <sup>269</sup> under a dye laser excitation between 615 and 617 nm, the blue emission from  ${}^3\text{P}_0$  to  ${}^3\text{H}_4$  in  $\text{Pr}^{3+}$  is observed at the very low level of 2 mW and is ascribed to a double excitation: the first one from the ground state in  $\text{U}^{3+}$  and the second one between excited states in  $\text{Pr}^{3+}$ ; cross relaxation between  $\text{U}^{3+}$  and  $\text{Pr}^{3+}$  provides the population of the metastable level  ${}^3\text{H}_6$ -( $\text{Pr}^{3+}$ ) from which takes place the resonant ESA to  ${}^3\text{P}_0$ ( $\text{Pr}^{3+}$ ). However, because the matching is probably too good between excitation and ground-state absorption, no real threshold is observed and a looping mechanism is advocated to explain that the presence of  $\text{U}^{3+}$  increases the blue output of  $\text{Pr}^{3+}$  by 3 orders of magnitude.

## 5.6. Upconversion Laser with Multiphonon-Assisted Pumping Scheme and Photon Avalanche

Besides pumping in the electronic RE ions transitions, we have also seen that upconversion laser pumping could be attempted in multiphonon sidebands with energy mismatch as large as  $1000 \text{ cm}^{-1}$ <sup>235</sup>; see section 4.5.

Of course, most of the avalanche-pumped lasers also enter this category because of the required weak first step absorption. It is worth mentioning the first avalanche laser in  $\text{LaCl}_3:\text{Pr}^{3+}$ <sup>270</sup> A CW emission in a four-level scheme was obtained at  $0.644 \mu\text{m}$  through an upconversion avalanche process under  $0.677 \mu\text{m}$  pumping which corresponds to an ESA pumping for the second step and probably to multiphonon absorption for the first step, as recently observed for amplified spontaneous emission at  $0.850 \mu\text{m}$  in a

ZBLAN: $\text{Er}^{3+}$  fiber in an avalanche-pumped regime.<sup>271</sup> Powerful avalanche-pumped upconversion lasers have been obtained in a CW regime, first at low temperature (7 K) in  $\text{YAlO}_3:\text{Er}^{3+}$ <sup>272,273</sup> 33 mW of output at  $0.549 \mu\text{m}$  has been reached with an optical efficiency of 3.5%. Interestingly, the same crystal system may provide laser under APTE (ETU) upconversion pumping simply by tuning-in the first excitation step ( $0.8069 \mu\text{m}$ ). The laser threshold is then lowered ( $\sim 100 \text{ mW}$ ) in comparison with the avalanche regime ( $\sim 380 \text{ mW}$  at  $0.7913 \mu\text{m}$ ); the output law is quadratic versus pumping in the APTE (ETU) regime, while for the avalanche regime it has a much higher power law above threshold saturating toward a square law at about 1 W of incident pump power. In the APTE (ETU) regime, the laser output is 166 mW with an optical conversion efficiency of 17%.

As already mentioned in section 4.5, fiber optical confinement may allow one to obtain CW three-level lasers even at room temperature. This has also been the case for avalanche-pumped lasers. A high-power upconversion laser has been demonstrated in a ZBLAN: $\text{Pr},\text{Yb}$  double-clad fiber under avalanche pumping.<sup>274</sup> The energy scheme and avalanche processes, which are involved, are the ones described in the previous subsection for the avalanche process with  $\text{Yb}$ - $\text{Pr}$  codoping.<sup>266</sup> Laser emission is from the  ${}^3\text{P}_0$ - ${}^3\text{F}_2$  transition of  $\text{Pr}^{3+}$  at  $0.635 \mu\text{m}$  with a record output of 1020 mW. The pumping is from two Ti-sapphire lasers providing 5.51 W at  $0.850 \mu\text{m}$ . This last wavelength, being detuned from the maximum  $\text{Yb}^{3+}$  absorption at  $0.96 \mu\text{m}$  but tuned with the  ${}^1\text{G}_4$ - ${}^1\text{I}_6$   $\text{Pr}^{3+}$  absorption, provides the condition for the avalanche regime of a weak  $\beta$  ( $10^{-6}$  to  $10^{-8}$ ) as seen above.

## 6. Perspectives and Future Advances

From the most recent studies and their respective aims as described in the above sections and from some emerging new research, one can try to derive some future trends and perspectives to better understand some of the observed features. In the following they will be divided into the five main directions that can be anticipated:

- (i) upconversion pumped lasers;
- (ii) new materials for low-level IR visualization;
- (iii) intrinsic material optical bistability;
- (iv) hot emission and avalanche-like codoped system; and
- (v) biological applications.

### 6.1. Upconversion UV-Tunable Lasers

Because optically pumped lasers are originally based on a Stokes pumping process, one basic problem is to obtain a high-density pumping source at a shorter wavelength than their emitting wavelength. With the tendency to go all solid state, there will be a continuous race between the shortest wavelength of the pumping semiconductor-based source and the shortest solid-state laser-emitting wavelength.

Few years ago the anticipated pumping diode emitted only in the near-IR; now that blue semiconductor lasers have begun to appear, one can theoreti-

cally anticipate that, sometimes, blue diodes could pump visible solid-state lasers. However, because powerful red semiconductor lasers do not exist yet that could be used for solid-state laser pumping, one can also anticipate that for many years to come no UV CW semiconductor or even frequency-multiplied semiconductor laser will not exist that will be powerful enough to usefully pump tunable a CW UV solid-state laser.

Clearly, upconversion pumping of a tunable UV solid-state laser has a role to play. So much the better that presently available gas UV laser are not tunable. Recent results give hints for that. As already shown in section 4.5, UV emission has been obtained from  $\text{LaF}_3:\text{Nd}^{3+}$  at 380 nm through a somewhat complicated anti-Stokes pumping scheme.<sup>223</sup> On the other hand, a very efficient tunable UV laser from  $\text{LiLuF}_4:\text{Ce}^{3+}$  has recently been obtained from 305 to 333 nm under Stokes pumping provided by a frequency-doubled copper vapor laser;<sup>275</sup> the slope efficiency was 51%. This particular result has to be connected to other recent results<sup>276</sup> on upconversion and energy transfers from  $\text{Pr}^{3+}$  (4f–5d) to  $\text{Ce}^{3+}$  (5d) to see that a tunable UV laser by anti-Stokes pumping can be imagined. The recently issued collection of selected papers on upconversion lasers<sup>232</sup> certainly comforts this trend.

## 6.2. New Materials for Low-Intensity IR Imaging

As pointed out in section 4.3, an interesting point of view is the IR–IR upconversion for low-intensity IR viewing. Though it is basically the old IRQC concept to upconvert IR out of the photocathode range to the photocathode detection range (GaAs and S1, from 760 to 1200 nm), little research has used the more recent understanding of RE-doped materials for this application. It has been recently proposed to use low-phonon energy glasses such as chalcogenide glasses ( $\text{GeS}_2\text{--Ga}_3\text{S}_3$ ) as 1500–1000 nm converters, with most of the upconverted energy at the latter wavelength.<sup>277</sup> Of course, other low-phonon energy materials such as the stable  $\text{CsCdBr}_3$  which is well-known in this respect together with strong RE–RE pair coupling could be designed for still farther IR ranges.

## 6.3. Upconversion Material Intrinsic Bistability

This is certainly the most recent fundamental subject in the upconversion field. A few years ago it was found in Güdel's group<sup>278,57</sup> that the cooperative luminescence (see section 3) of  $\text{Yb}^{3+}:\text{Cs}_3\text{Y}_2\text{Br}_9$  and  $\text{Cs}_3\text{Yb}_2\text{Br}_9$  in the visible as well as the usual Stokes emission in the IR clearly displayed an hysteresis loop under variable excitation density and fixed temperature between 11 and 31 K. Correlatively a hysteresis loop was also observed when excitation was kept constant and the temperature was varied as shown in Figure 39. The physical explanation was given in the framework of the optical coherent field coupling between two ions in a solid that had been theoretically proposed<sup>279,280</sup> by Heber. The problem with this model is to what extent it can describe a

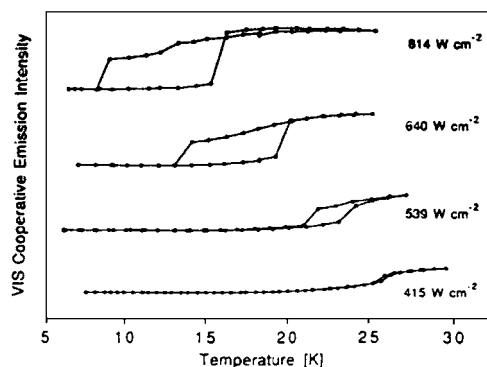


Figure 39. Thermal hysteresis loop for cooperative luminescence in  $\text{Cs}_3\text{Y}_2\text{Br}_9:\text{Yb}^{3+}$ . (Reprinted with permission from ref 284. Copyright 1996 American Institute of Physics.)

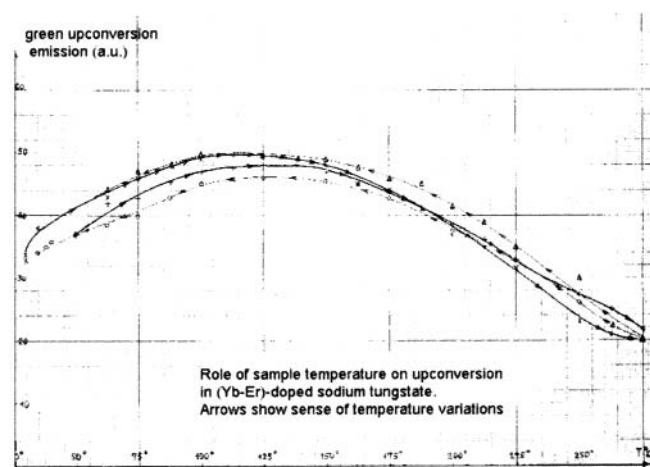


Figure 40. First observation (from 1967 unpublished original document) of a thermal hysteresis loop for APTE upconversion in  $\text{WO}_4\text{Na}_{0.5}\text{Yb}_{0.5}:2\%\text{Er}^{3+}$ . Arrows show direction of the temperature variations for two sets of experiments.

RE-doped system physical reality. This can be questioned.

It has been recognized for a long time now that optical bistability within a cavity could originate from optical cooperative coupling between cavity modes and the atomic system in a way similar to the optical cooperative coupling between atomic systems giving rise to superfluorescence.<sup>281</sup> However, superfluorescence in RE-doped systems is very difficult to observe because it requires long dephasing times ( $T_2$ ) which are impossible to obtain in a solid at high doping concentration due to ion–ion and ion–phonon dephasing. Observation of superfluorescence in  $\text{LiYF}_4:\text{Er}$  requires both low  $T$  ( $<30$  K) and very weak concentration ( $<0.3\%$ )<sup>282</sup> and a threshold of  $842$   $\text{W cm}^{-2}$ . The rather high concentration used here in the  $\text{Yb}^{3+}$  experiment certainly imposes that the Rabi frequency be less than the ion line width at the considered excitation density of  $800$   $\text{W cm}^{-2}$ , which is also about the threshold for the observed hysteresis loop.<sup>278</sup> This forbids any sizable coherent field coupling.

Interestingly, in the very first experiment on APTE upconversion, thermal hysteresis loops were observed at high temperature,<sup>283</sup> see Figure 40. Clearly, at such high temperatures it has nothing to do with coherent field coupling. Also, the bistability observed

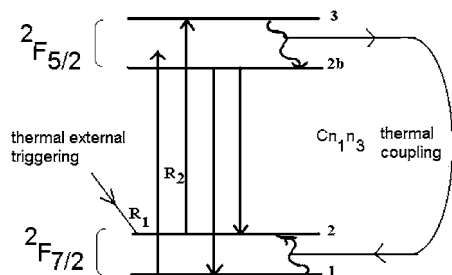


Figure 41. Yb<sup>3+</sup> simplified energy scheme according to the simplified three-level energy scheme of Figure 25 for avalanche with a thermal cross-relaxation process explaining the thermal hysteresis loop of 285. The external triggering term corresponds to the temperature variable of the experiment.

in avalanche systems (see section 5.3) has been described within the framework of population rate equations. Then it appears more in accordance with physical reality not to consider coherent field coupling as the root of observed bistability. This is implicitly recognized for Cs<sub>3</sub>Y<sub>2</sub>Br<sub>9</sub>:Yb in a later paper<sup>284</sup> pointing out the analogy with avalanche bistability and describing the effect through population rate equations. As the temperature changes, so do the overlap integrals ruling the RE–RE energy transfers, which provide the necessary nonlinear feedback effect. Clearly, it can also be the only explanation for the high-temperature (430 K) hysteresis loops that had been initially observed in WO<sub>4</sub>Na<sub>0.5</sub>Yb<sub>0.5</sub>:2%Er.<sup>283</sup> From this result and the fact that the hysteresis behavior is produced at the Yb<sup>3+</sup> ion, it can be predicted that all upconversion systems with Yb as a sensitizer could show thermal hysteresis. For the last 2 years, the thermal explanation has clearly been retained as explained by Gamelin et al.<sup>285</sup> and said to be due to the variable thermal absorption properties of Yb<sup>3+</sup>. It is described as a thermal avalanche with a thermal cross-relaxation in analogy with the photon avalanche described above in section 5.1. According to Figure 41, the equivalent of  $R_1$ , the weak ground-state absorption, is a nonresonant absorption between  $2F_{7/2}$  to  $2F_{5/2}$ . The resonant absorption term  $R_2$  is from a Stark level of  $2F_{7/2}$  to a Stark level of  $2F_{5/2}$ ; the cross-relaxation term,  $C_{n_1 n_3}$  of Figure 25, is produced by the heat released within the Stark levels of  $2F_{5/2}$  by the phonon emission, which in turn, by absorption of phonons, populates a higher Stark excited state of  $2F_{7/2}$ . This is the loop of this thermal avalanche. An external thermal triggering term, equivalent to  $\sigma_0 \Phi_{IR}$  of Figure 25, is provided by the external temperature variable  $T$  of the experiment.

As seen in section 5.1, one can predict that the threshold and the hysteresis will be steeper and the time constant longer for weaker  $R_1/R_2$  ratios. Consequently, we can propose here that a large crystal field should be better for higher temperature observations and that it should be the case for hard oxides and YAG in particular.<sup>286</sup>

At any rate, the thermal avalanche convincing explanation certainly describes in a correct way the published observations including the one of 1967,<sup>283</sup> which was thought to be due to the thermal behavior of the overlap integral between coupled Yb–Er ions and had been unexplained until now!

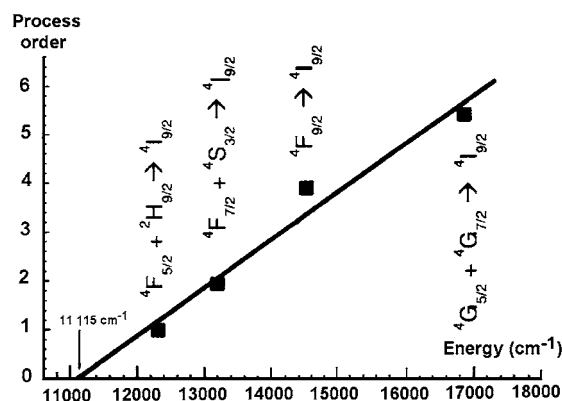


Figure 42. Upconversion power law indexes versus energy gap between emitting states and  $4F_{3/2}$  (Nd<sup>3+</sup>) in Yb,Nd:YAG. (Reprinted with permission from ref 287. Copyright 2002 Institute of Physics Publishing.)

#### 6.4. Hot Emission and Avalanche Like Co-Doped Systems

Here, it is interesting to discuss a not yet completely elucidated new phenomena recently observed by Bednarkiewicz and Streck<sup>287</sup> in an upconversion study of Nd<sup>3+</sup>–Yb<sup>3+</sup> codoped YAG nanocrystallite ceramics. Under laser diode pumping at 976 nm into the Yb absorption, visible orange antiStokes emission is observed at 300 K with broadened features at 579 nm from  $4G_{5/2} - 4G_{7/2}$ , 690 nm from  $4F_{9/2}$ , 757 nm from  $4F_{7/2} - 4S_{3/2}$ , and 813 nm from  $4F_{5/2} - 2H_{9/2}$ , all transitions to the Nd<sup>3+</sup>  $4I_{9/2}$  ground state. These emissions decrease with decreasing temperature. Those visible emissions are described by a,  $P^n$ , law for output versus excitation with,  $n$  linearly depending on the energy gap above  $4F_{3/2}$  as shown in Figure 42 There is also an establishing time constant increasing with the order parameter,  $n$ , reaching 1.5 s for  $n = 4$ . It was recognized that because the metastable character of  $4F_{3/2}$  is reduced by back transfer to Yb, the multiphonon process shown which could have explained the result of Figure 42 cannot be retained; moreover, dividing the energy gap between  $4F_{3/2}$  and emitting states by  $n$  provides virtual phonon energies not existing in YAG.

No real explanation is presented in ref 287, and this result is still a question. Though not mentioned by the authors, we think, however, that the long time transient is the clear signature of avalanche processes which have yet to be analyzed in detail.

#### 6.5. Biological Applications

Very recently upconversion applications of the APTE (ETU) systems Yb–Er and Yb–Tm have been devised by Zilmans et al.<sup>288</sup> for detection of cell and tissue surface antigens as luminescent bioassays. Submicrometer-sized phosphor crystals (200–400 nm) of the usual oxysulfide, fluoride, gallate, and silicate types doped with Yb–Er and Yb–Tm couples are considered. The main advantage is that IR-upconverting phosphors are excited by wavelengths that cannot excite the natural biological materials, so providing a better detection contrast with respect to autofluorescence than the more usual luminescent bioassays working in the Stokes emission mode. The

upconversion method overcomes many of the limitations of the common reporters used in immunocytochemical applications.

A still more recent result that could be connected to previous application is the dissolution of nanoparticles (6–8 nm) of Yb–Er- and Yb–Tm-doped LuPO<sub>4</sub> as colloids in chloroform solutions.<sup>289</sup> Because of the inherent high efficiency of the APTE (ETU) effect, such colloids can show green, red, and blue upconversion in the liquid phase for the first time.

## 7. Conclusion

The general principles of upconversion have been presented in a self-contained way together with typical examples. Because these effects are now so generally observed with the general use of laser excitations, it was thought to be important to distinguish them in precise ways in order for future researchers to start from well-established definitions and to speak a common language.

Besides a didactical approach, I tried to present most of all the recent important results if not in an exhaustive way at least in a complete way for all important turning points.

If there was some general philosophy to derive from this review, it would be that upconversion is an endless field and that some features are becoming as common as plain Stokes luminescence. Some aspects of this reviewed field though not really exploited at some time may become important with more refined experiments and availability of new technologies. Also, the implied processes may help understand other aspects of optical processes in RE-doped solids.

An example could be the presently considered photon-cutting effect,<sup>84–88</sup> just the opposite of APTE (ETU) upconversion, which may open the way to new efficient lighting systems. The opposite of cooperative luminescence, cooperative quenching, recently discovered, may explain some of the yet not understood features of concentration quenching.<sup>83</sup>

From an applied point of view, it is observed that with the general use of lasers and the easiness in observing visible to the naked eye upconversion, too few people have found it necessary to measure efficiencies in order to be able to compare quantitatively the various proposed upconversion systems. This should be done to push upconversion beyond the qualitative approach that still too often characterizes it. Most of the recently proposed systems can be observed only at low temperature and no efficiency values are provided. One can also verify through this review that, as is often in science, the most efficient systems are the ones discovered at first, here the Yb–Er and the Yb–Tm systems.<sup>7</sup>

## 8. Acknowledgments

It is a pleasure to acknowledge a number of researchers who have kindly sent me their reprints and have so helped me in writing this review. I would like to mentioned particularly Dr. Junichi Owaki (NTT), Pr. Günter Huber (Hambourg University), Pr. Johann Heber (Darmstadt University of Technology),

Drs. Valery Smirnov and Alina Man'shina (Russian Center for Laser Physics), Pr. Georges Boulon and Dr. Marie-France Joubert (Université de Lyon), Pr. Hans Güdel (Bern University), Dr. Markus Pollnau (Lausanne University), Pr. Wieslaw Srek (Low Temperature Physic Institute, Wrawclaw), and Pr. Joaquim Fernandez (Universidad del Pais Vasco, Bilbao). I would like to thank also Dr. Marco Bettinelli (University di Verona, Italy) for kindly pointing to me the bioassay application and Pascal Gerner (Bern University) for providing me with the very recent last reference. Many thanks also for my good friend Peter Lewis for reading over the whole text. Last but not least, thanks are due to my wife, Odile, for having accepted that I divert a lot of leisure time for that work.

## 9. References

- (1) Leverenz, H. W. *Introduction to Luminescence of Solids*; Dover Publications: New York, 1968.
- (2) Auzel, F. *Proc. IEEE* 1973, 61, 758.
- (3) Wright, J. Up-conversion and excited-state energy transfer in rare-earth doped materials. In *Radiationless Processes in Molecules and Condensed Phases*; Fong, F. K., Ed.; Topics in Applied Physics; Springer: New York, 1976; Volume 15, p 239.
- (4) Bloembergen, N. *Phys. Rev. Lett.* 1959, 2, 84.
- (5) Brown, M. R.; Thomas, H.; Williams, J. M.; Woodwards, R. J. *J. Chem. Phys.* 1969, 51, 3321.
- (6) Auzel, F. *J. Lumin.* 1984, 31/32, 759.
- (7) Auzel, F. *C. R. Acad. Sci. (Paris)* 1966, 262, 1016. Auzel, F. *C. R. Acad. Sci. (Paris)* 1966, 263, 819.
- (8) Van Uitert, L. G.; Johnson, L. F. *J. Chem. Phys.* 1966, 44, 3514.
- (9) Mita, Y.; Nagasawa, E. *NEC Res. Dev.* 1974, 33, 61.
- (10) Garlick, G. F. *J. Contemp. Phys.* 1976, 17, 127.
- (11) Chivian, J. S.; Case W. E.; Eden, D. D. *Appl. Phys. Lett.* 1979, 35, 124.
- (12) Case, W. E.; Koch, M. E.; Kueny, A. W. *J. Lumin.* 1990, 45, 351.
- (13) Auzel, F. *Semiconductor Optoelectronics*; Wiley and PWN: New York and Warszawa, 1980; Chapter 10, p 233. Auzel, F. *J. Lumin.* 1990, 45, 341. Auzel, F. In *Luminescence: Phenomena, Materials and Devices*; Rao, R. P., Ed.; Nova Science Pub.: New York, 1992; p 33. Auzel, F. In *Nonlinear Spectroscopy of Solids; Advances and Applications*; DiBartolo, B., Bowlby, B., Eds.; Plenum Press: New York, 1994; p 531.
- (14) Huber, G.; Heumann, E.; Sandrok, T.; Petermann, K. *J. Lumin.* 1997, 72/74, 1.
- (15) Gamelin, D. R.; Güdel, H. U. *Acc. Chem. Res.* 2000, 33, 235.
- (16) Hehlen, M. P.; Phillips, M. L. F.; Cockroft, N. J.; Güdel, H. U. *Encyclopedia of Materials: Science and Technology*; Elsevier Science Ltd.: New York, 2001; p 9956.
- (17) Gamelin, D. R.; Güdel, H. U. *Top. Curr. Chem.* 2001, 214, 1.
- (18) Auzel, F. *SPIE* 2001, 4766, 179. Auzel, F. In *Spectroscopic properties of rare-earths in optical materials*; Liu, G. K., Jacquier, B., Eds.; Springer-Verlag: New York, 2003; Chapter 5.
- (19) *Selected papers on Photoluminescence of Inorganic Solids*; Weber, M., Ed.; SPIE Milestone Series, Vol. MS150; SPIE: Bellingham, WA, 1998.
- (20) Auzel, F. Multiphonon processes, cross-relaxation and upconversion in ion activated solids, exemplified by minilaser materials. In *Radiationless Processes*; DiBartolo, B., Goldberg, V., Eds.; Plenum Publishing Co.: New York, 1980; p 213.
- (21) Henderson, B.; Imbusch, G. F. *Optical Spectroscopy of Inorganic Solids*; Clarendon Press: Oxford, 1989; p 445.
- (22) Milne, E. A. *J. London Math. Soc.* 1926, 1, 1.
- (23) Varsanyi, F.; Wood, D. L.; Schawlow, A. L. *Phys. Rev. Lett.* 1959, 3, 544.
- (24) Auzel, F. *Ann. Telecom. (France)* 1969, 24, 363.
- (25) Auzel, F.; Bonfigli, F.; Gagliari, S.; Baldacchini, G. *J. Lumin.* 2001, 94/95, 293.
- (26) Förster, T. *Ann. Phys.* 1948, 2, 55.
- (27) Dexter, D. L. *J. Chem. Phys.* 1953, 21, 836.
- (28) Kushida, T. *J. Phys. Soc. Jpn.* 1973, 34, 1318.
- (29) Pouradier, J. F.; Auzel, F. *J. Phys. (France)* 1978, 39, 825.
- (30) Axe, J. D.; Weller, P. F. *J. Chem. Phys.* 1964, 40, 3066.
- (31) Orbach, R. *Optical Properties of Ions in Solids*; DiBartolo, B., Ed.; Plenum Press: New York, 1975; p 445.
- (32) Miyakawa, T.; Dexter, D. L. *Phys. Rev.* 1971, B1, 70.
- (33) Auzel, F. *Phys. Rev.* 1976, B13, 2809.
- (34) Yamada, N.; Shionoya, S.; Kushida, T. *J. Phys. Soc. Jpn.* 1972, 32, 1577.
- (35) Inokuti, M.; Hirayama, F. *J. Chem. Phys.* 1965, 43, 1978.

- (36) Barthem, R. B.; Buisson, R.; Vial, J. C. *J. Phys.* 1985, 46, C7–483.
- (37) Yokota, M.; Tanimoto, O. *J. Phys. Soc. Jpn.* 1967, 22, 779.
- (38) Weber, M. J. *Phys. Rev.* 1971, B4, 2932.
- (39) Grant, W. J. C. *Phys. Rev.* 1958, 109, 648.
- (40) Auzel, F. *Mater. Res. Bull.* 1979, 14, 223.
- (41) Snitzer, E.; Woocock, R. *Appl. Phys. Lett.* 1965, 6, 5.
- (42) Auzel, F.; Deuschlein, O. *Z. Naturforsch.* 1969, 24a, 1562.
- (43) Ovsyankin, V. V.; Feofilov, P. P. *Sov. Phys. JETP Lett.* 1966, 4, 317.
- (44) Hewes, R. A.; Sarver, J. F. *Phys. Rev.* 1969, 182, 427.
- (45) Pollnau, M.; Gamelin, D. R.; Lüthi, S. R.; Güdel, M. *Phys. Rev.* 2000, B61, 3337.
- (46) Rios Leite, J. R.; de Araujo, C. B. *Chem. Phys. Lett.* 1980, 73, 71.
- (47) Bonneville, R.; Auzel, F. *Opt. Commun.* 1976, 18, 51.
- (48) Ovsyankin, V. V.; Fedorov, A. A. *Opt. Spectrosc.* 1981, 50, 565.
- (49) Mita, Y.; Ide, T.; Katase, T.; Yamamoto, H. *J. Lumin.* 1997, 72/74, 959.
- (50) Goldner, P.; Pellé, F. *J. Lumin.* 1994, 60/61, 651.
- (51) Auzel, F.; Pecile, D.; Morin, D. *J. Electrochem. Soc.* 1975, 122, 101.
- (52) Auzel, F.; Pecile, D. *C. R. Acad. Sci. Paris* 1973, 277B, 155.
- (53) Silver, J.; Martinez-Rubio, M. I.; Ireland, T.G.; Fern, G. R.; Withnall, R. J. *Phys. Chem.* 2001, B105, 948.
- (54) Silver, J.; Martinez-Rubio, M. I.; Ireland, G. R.; Withnall, R. J. *Phys. Chem.* 2001, B105, 7200.
- (55) Ovsyankin, V. V. *Spectroscopy of Solids Containing Rare-Earth Ions*; Kaplyanski, A. A., MacFarlane, R. M., Eds.; North-Holland: Amsterdam, 1987; p 405.
- (56) Orlovskii, Y. U.; Basiev, T. T.; Papashvili, A. G.; Voroev, I. N.; Alimov, O. K.; Osiko, V. V.; Heber, J. *SPIE* 2001, 4766, 204.
- (57) Gamelin, D. R.; Lüthi, S. R.; Güdel, H. U. *J. Phys. Chem.* 2000, B104, 11045. Lüthi, S. R.; Hehlen, M. P.; Riedener, T.; Güdel, H. U. *J. Lumin.* 1998, 76/77, 447.
- (58) Auzel, F.; Dexpert-Ghys, J.; Gauthier, C. *J. Lumin.* 1982, 27, 1.
- (59) Vial, J. C.; Buisson, R.; Madeore, F.; Poirier, M. *J. Phys. (France)* 1979, 40, 913.
- (60) Dexpert-Ghys, J.; Auzel, F. *J. Chem. Phys.* 1984, 80, 4003.
- (61) Nakazawa, E.; Shionoya, S. *Phys. Rev. Lett.* 1970, 25, 1710.
- (62) Cockroft, N. J.; Jones, G. D.; Syme, R. W. *G. J. Lumin.* 1989, 43, 275.
- (63) Varsanyi, F.; Dieke, G. H. *Phys. Rev. Lett.* 1961, 7, 442.
- (64) Van der Ziel, J. P.; Van Uitert, L. G. *Phys. Rev.* 1969, 180, 343.
- (65) Stavola, M.; Dexter, D. L. *Phys. Rev.* 1979, B20, 1867.
- (66) Livanova, L. D.; Saitkulov, I. G.; Stolov, A. L. *Sov. Phys. Solid State* 1969, 11, 750.
- (67) Ostermayer, F. W., Jr.; Van Uitert, L. G. *Phys. Rev.* 1970, B1, 4208.
- (68) Auzel, F.; Meichenin, D.; Pellé, F.; Goldner, P. *Opt. Mater.* 1994, 4, 35.
- (69) Heber, J.; Nikitin, S. I.; Demirbilek, R.; Papashvili, A. G.; Vorobeve, I. N.; Alimov, O. K.; Orlovskii, Y. V.; Orlovskaya, E. O. *SPIE* 2001, 4766, 218. Schäfer, U.; Neukum, J.; Bodenschatz, N.; Heber, J. *J. Lumin.* 1994, 60/61, 633.
- (70) Noginov, M. A.; Loutts, G. B.; Steward, C. S.; Lucas, B. D.; Fider, D.; Peters, V.; Mix, E.; Huber, G. *J. Lumin.* 2002, 96, 129.
- (71) Blixt, P.; Nilsson, J.; Carlknäs, J.; Jaskorzynska, B. *IEEE Trans. Photon Techn.* 1991, 3, 996.
- (72) Auzel, F. *J. Lumin.* 1984, 31/32, 759.
- (73) Auzel, F. In *Rare-Earth Spectroscopy*; Trzebiatowska, B., Legendziewicz, J., Streck, W., Eds.; World Scientific: Singapore, 1985; p 502.
- (74) Rand, S. C.; Lee, L. S.; Schawlow, A. L. *Opt. Commun.* 1982, 42, 179.
- (75) Lee, L. S.; Rand, S. C.; Schawlow, A. L. *Phys. Rev.* 1984, B29, 6901.
- (76) Valiente, R.; Wenger, O.; Güdel, H. *Chem. Phys. Lett.* 2000, 320, 639.
- (77) Valiente, R.; Wenger, O.; Güdel, H. *Phys. Rev.* 2001, B63, 165102–1.
- (78) Gerner, P.; Wenger, O.; Valiente, R.; Güdel, H. *Inorg. Chem.* 2001, 40, 4534.
- (79) Valiente, R.; Wenger, O.; Güdel, H. *J. Chem. Phys.* 2002, 116, 5196.
- (80) Salley, G. M.; Valiente, R.; Güdel, H. *J. Lumin.* 2001, 94/95, 305.
- (81) Salley, G. M.; Valiente, R.; Güdel, H. *J. Phys.: Condens. Matter* 2002, 14, 5461.
- (82) Streck, W.; Bednarkiewicz, A.; Deren, P. *J. Lumin.* 2001, 92, 229.
- (83) Dexter, D. L. *Phys. Rev.* 1957, 108, 630. Dexter, D. L. *Phys. Rev.* 1962, 126, 1962.
- (84) Basiev, T.T.; Dorochenko, M. E.; Osiko, V. V. *JETP Lett.* 2000, 71, 8.
- (85) Vegh, R. T.; Donker, H.; van Loef, E. V. D.; Oskam, K. D.; Meijerink, A. *J. Lumin.* 2000, 87/89, 1017.
- (86) Wegh, T. T.; Donker, H.; Meijerink, A.; Lamminmäki, R. J.; Hölsa, J. *Phys. Rev.* 1997, B56, 13841.
- (87) Wegh, R. T.; Donker, H.; Oskam, K. D.; Meijerink, A. *J. Lumin.* 1999, 82, 93.
- (88) Wegh, R. T.; Meijerink, A. *Acta Phys. Pol.* 1996, A90, 333.
- (89) Weegh, R. T.; Donker, H.; Oskam, K. D.; Meijerink, A. *Science* 1999, 283, 663.
- (90) Streck, W.; Deren, P.; Bednarkiewicz, A. *J. Lumin.* 2000, 87/89, 999.
- (91) Streck, W.; Deren, P. J.; Bednarkiewicz, A.; Kalisky, Y.; Boulangier, P. *J. Alloys Compd.* 2000, 300/301, 180.
- (92) Orlovskii, Y. V.; Basiev, T. T.; Papashvili, A. G.; Vorobeve, I. N.; Alimov, O. K.; Osiko, V. V.; Heber, J. *J. Lumin.* 2002, 99, 223.
- (93) Delevaque, E.; Georges, T.; Monerie, M.; Lamouler, P.; Bayon, J. F. *IEEE Photon Techn. Lett.* 1993, 5, 73.
- (94) Maurice, E.; Monnom, G.; Dussardier, B.; Ostrowsky, D. B. *Opt. Lett.* 1995, 20, 2487.
- (95) Auzel, F. *J. Lumin.* 1990, 45, 341.
- (96) Goldner, P.; Pellé, F.; Meichenin, D.; Auzel, F. *J. Lumin.* 1997, 71, 137.
- (97) Goldner, P.; Pellé, F.; Auzel, F. *J. Lumin.* 1997, 72/74, 901.
- (98) Auzel, F.; Goldner, P. *Opt. Mater.* 2001, 16, 93.
- (99) Schaudel, B.; Goldner, P.; Prassas, M.; Auzel, F. *J. Alloys Compd.* 2000, 300/301, 443.
- (100) Remillieux, A.; Jacquier, B. *J. Lumin.* 1996, 68, 279.
- (101) Balda, R.; Fernandez, J.; Saez de Ocariz, I.; Voda, M.; Garcia, A. *J. Phys. Rev.* 1999, B59, 9972.
- (102) Fernandez, J.; Balda, R.; Mendorioz, A.; Garcia-Adeva, A. *J. Phys. Condens. Matter* 2001, 13, 10347. Balda, R.; Saez de Ocariz, I.; Fernandez, J.; Fdez-Navarro, J. M.; Arriandaga, M. A. *J. Phys. Condens. Matter* 2000, 12, 10623.
- (103) Ju, J. J.; Ro, J. H.; Cha, M. *J. Lumin.* 2000, 87/89, 1045.
- (104) Kim, S. I.; Yun, S. I. *J. Lumin.* 1994, 60/61, 233.
- (105) Malinowski, M.; Joubert, M. F.; Jacquier, B. *J. Lumin.* 1994, 60/61, 179.
- (106) Hirao, K.; Higuchi, M.; Soga, N. *J. Lumin.* 1994, 60/61, 115.
- (107) Deren, P. J.; Mahiou, R.; Streck, W.; Bednarkiewicz, A.; Bertrand, G. *Opt. Mater.* 2002, 19, 145.
- (108) Balda, R.; Sanz, M.; Fernandez, J.; Fdez-Navarro, J. M. *J. Opt. Soc. Am.* 2000, B17, 1671.
- (109) Fernandez, J.; Balda, R.; Mendorioz, A.; Sanz, M.; Adam, J. L. *J. Non-Cryst. Solids* 2001, 287, 437.
- (110) Fernandez, J.; Balda, R.; Sanz, M.; Lacha, L. M.; Oleaga, A.; Adam, J. L. *J. Lumin.* 2001, 94/95, 325.
- (111) Acioli, L. H.; Guo, J. T.; de Araujo, C. B.; Messaddeq, T.; Aegerter, M. A. *J. Lumin.* 1997, 72/74, 68.
- (112) Balda, R.; Sanz, M.; Mendorioz, A.; Fernandez, J.; Griscom, L. S.; Adam, J. L. *Phys. Rev.* 2001, B64, 144101.
- (113) Fernandez, J.; Sanz, M.; Mendorioz, A.; Balda, R.; Chaminade, J. P.; Ravez, J.; Lacha, L. M.; Voda, M.; Arriandaga, M. A. *J. Alloys Compd.* 2001, 323/324, 267.
- (114) Iparraguirra, I.; Al-Saleh, M.; Balda, R.; Voda, M.; Fernandez, J. *J. Opt. Soc. Am.* 2002, B19, 1.
- (115) Malinowski, M.; Jacquier, B.; Bouazaoui, M.; Joubert, M. F.; Linares, C. *Phys. Rev.* 1990, B41, 31.
- (116) Pollnau, M.; Hardman, P. J.; Kern, M. A.; Clarkson, W. A.; Hanna, D. C. *Phys. Rev.* 1998, B58, 16070.
- (117) Pollnau, M.; Hardman, P. J.; Clarkson, W. A.; Hanna, D. C. *Opt. Commun.* 1998, 147, 203.
- (118) Blätte, M.; Danielmeyer, H. G.; Verich, R. *Appl. Phys. (Germany)* 1973, 1, 275.
- (119) Wenger, O. S.; Gamelin, D. R.; Güdel, H. U. *Phys. Rev.* 2000, B61, 16530.
- (120) Holliday, K.; Russell, D. L.; Henderson, B. *J. Lumin.* 1997, 72/74, 927.
- (121) Zhang, X.; Daran, E.; Serrano, C.; Lahoz, F. *J. Lumin.* 2000, 87/89, 1011.
- (122) Deren, P. J.; Streck, W.; Krupa, J. C. *Chem. Phys. Lett.* 1998, 298, 217.
- (123) Mahiou, R.; Metin, J.; Cousseins, J. C. *J. Lumin.* 1990, 45, 363.
- (124) Wermuth, M.; Riedener, T.; Güdel, H. U. *Phys. Rev.* 1998, B57, 4369.
- (125) Pouradier, J. F.; Auzel, F. *J. Phys.* 1976, 37, 421.
- (126) Müller, P.; Wermuth, M.; Güdel, H. *Chem. Phys. Lett.* 1998, 290, 105.
- (127) Ryba-Romanovski, W.; Deren, P. J.; Golab, S.; Dominiak-Dzik, G. *J. Appl. Phys.* 2000, 88, 6078.
- (128) Ryba-Romanovski, W.; Golab, S.; Dominiak-Dzik, G.; Solarz, P. *Appl. Phys. Lett.* 2001, 79, 3026.
- (129) Chamarro, M. A.; Cases, R. *J. Lumin.* 1988, 42, 267.
- (130) Auzel, F.; Hubert, S.; Meichenin, D. *Appl. Phys. Lett.* 1989, 54, 681.
- (131) Ronac'h, D.; Guibert, M.; Auzel, F.; Meichenin, D.; Allain, J. Y.; Poignant, H. *Electron. Lett.* 1991, 27, 511.
- (132) Monerie, M.; Allain, J.-Y.; Poignant, H.; Auzel, F. In *Fluorescence, Up-conversion, and lasing in Er-doped quasi-single mode fluorozirconate fibres*, Proceedings of ECOC'89, Gothenburg, Sweden, Sept 1989; paper TuB12–6.
- (133) Pollnau, M.; Ghisler, C.; Bunea, G.; Lüthy, W.; Weber, H. P. *Appl. Phys. Lett.* 1995, 66, 3564.

- (134) Golding, P. S.; Jackson, S. D.; King, T. A.; Pollnau, M. *Phys. Rev.* 2000, B62, 856.
- (135) Silversmith, A. J. *Lumin.* 1994, 60/61, 636.
- (136) Chen, X.; Nguyen, T.; Qui, L.; DiBartolo, B. J. *Lumin.* 1999, 83/84, 471.
- (137) Pollnau, M.; Heumann, E.; Huber, G. *Appl. Phys.* 1992, A54, 404.
- (138) Lüthi, S. R.; Pollnau, M.; Güdel, H.; Hehlen, M. P. *Phys. Rev.* 1999, 60, 162.
- (139) Hehlen, M. P.; Krämer, K.; Güdel, H.; McFarlane, R. A.; Schartz, R. N. *Phys. Rev.* 1994, B49, 12475.
- (140) Wenger, O.; Gamelin, D. R.; Güdel, H. U.; Butashin, A. V.; Kaminskii, A. *Phys. Rev.* 1999, B60, 5312.
- (141) Riedener, T.; Egger, P.; Hulliger, J.; Güdel, H. *Phys. Rev.* 1997, B56, 18000.
- (142) Riedener, T.; Güdel, H. *J. Chem. Phys.* 1997, 107, 2169.
- (143) Pollnau, M.; Lüthy, W.; Weber, H. P.; Krämer, K.; Güdel, H.; McFarlane, R. A. *OSA Topics on Advanced Solid State Lasers*; Payne, A., Pollock, C., Eds.; OSA: Washington, DC, 1996; Vol. 1, p 493.
- (144) Hehlen, M. P.; Frei, G.; Güdel, H. *Phys. Rev.* 1994, B50, 16264.
- (145) Zhang, X.; Jouart, J. P.; Mary, G.; Liu, X.; Yuan, J. J. *Lumin.* 1997, 72/74, 983.
- (146) Spinger, B.; Danilov, V. P.; Prokhorov, A. M.; Schwan, L. O.; Schmid, D. *SPIE* 2001, 4766, 191.
- (147) Felix, S. F.; Gouveia, E. A.; de Araujo, M. T.; Sombra, A. S. B.; Gouveia-Neto, A. S. J. *Lumin.* 2000, 87/89, 1020.
- (148) Tkachuk, A. M.; Razumova, I. K.; Malyshev, A. V.; Gapontsev, V. P. *J. Lumin.* 2001, 94/95, 317.
- (149) Dierolf, V.; Kutsenko, A. B.; von der Hosten, W. J. *Lumin.* 1999, 83/84, 487.
- (150) Nunez, L.; Herreros, B.; Duchowicz, R.; Lifante, G.; Tocho, J. O.; Cusso, F. J. *Lumin.* 1994, 60/61, 81.
- (151) Herreros, B.; Lifante, G.; Cusso, F.; Towsend, P. D.; Chandler, P. J. *J. Lumin.* 1997, 72/74, 198.
- (152) Cokcroft, N. J.; Murdoch, K. M. J. *Lumin.* 1994, 60/61, 891.
- (153) Chen, X. B.; Zhang, G. Y.; Mao, Y. H.; Hou, Y. B.; Feng, Y.; Hao, Z. *J. Lumin.* 1996, 69, 151.
- (154) Wyss, C. P.; Kehrl, M.; Huber, T.; Morris, P. J.; Lüthy, W.; Weber, H. P.; Zagumennyi, A. I.; Zavartsev, Y. D.; Studenikin, P. A.; Shcherbakov, I. A.; Zerrouk, A. F. *J. Lumin.* 1999, 82, 137.
- (155) Riedener, T.; Güdel, H.; Valley, G. C.; McFarlane, R. A. *J. Lumin.* 1995, 63, 327.
- (156) Gomes, A. S. L.; de Araujo, C. B. J. *Lumin.* 1991, 48/49, 876.
- (157) Wu, X.; Denis, J. P.; Özen, G.; Pellé, F. J. *Lumin.* 1994, 60/61, 212.
- (158) Auzel, F.; Pecile, D. *J. Lumin.* 1976, 11, 321. Pecile, D. De l'influence de la matrice sur l'addition de photons par transferts d'énergie (APTE) dans les couples  $\text{Yb}^{3+}\text{-Er}^{3+}$  et  $\text{Yb}^{3+}\text{-Tm}^{3+}$ ; Thèse, Université P. et M. Curie, Paris, 1976.
- (159) Jacquier, J. *Lumin.* 1994, 60/61, 175.
- (160) Wenger, O. S.; Wickleder, C.; Krämer, K.; Güdel, H. *J. Lumin.* 2001, 94/95, 101.
- (161) Hubert, S.; Song, C. L.; Genet, M.; Auzel, F. *J. Solid State Chem.* 1986, 61, 252.
- (162) Auzel, F.; Hubert, S.; Delamoye, P. *J. Lumin.* 1982, 26, 251.
- (163) Deren, P. J.; Karbowiak, M.; Krupa, J. C.; Drozdowski, J. *J. Alloys Compd.* 1998, 275/277, 393.
- (164) Stump, N. A.; Murray, G. M.; Del Cul, G. D.; Haire, R. G.; Peterson, J. R. *Radiochim. Acta* 1993, 61, 129.
- (165) Deren, P. J.; Krupa, J. C.; Streck, W. *J. Lumin.* 1997, 72/74, 655.
- (166) Deren, P. J.; Feries, J.; Krupa, J. C.; Streck, W. *Chem. Phys. Lett.* 1997, 264, 614.
- (167) Deren, P. J.; Krupa, J. C.; Yin, M.; Joubert, M. F.; Streck, W. *Spectrochim. Acta (A)* 1998, A54, 2105.
- (168) Deren, P. J.; Joubert, M. F.; Krupa, J. C.; Mahiou, R.; Yin, M. *J. Alloys Compd.* 2002, 341, 134.
- (169) Deren, P. J.; Streck, W.; Zych, E.; Drozdowski, J. *Chem. Phys. Lett.* 2000, 332, 308.
- (170) Cresswell, P. J.; Robbins, D. J.; Thomson, A. J. *J. Lumin.* 1978, 17, 311.
- (171) Moncorgé, R.; Breteau, J. M.; Auzel, F. *Philos. Mag.* 1985, B51, 489.
- (172) Wenger, O. S.; Güdel, H. U. *Inorg. Chem.* 2001, 40, 5747. Jacobsen, S. M.; Güdel, H. U. *J. Lumin.* 1989, 43, 125.
- (173) Heer, S.; Wermuth, M.; Krämer, K.; Ehrentraut, D.; Güdel, H. U. *J. Lumin.* 2001, 94/95, 337.
- (174) Heer, S.; Wermuth, M.; Krämer, K.; Güdel, H. U. *Phys. Rev.* 2002, 65, 125112.
- (175) Heer, S.; Wermuth, M.; Krämer, K.; Güdel, H. U. *Chem. Phys. Lett.* 2001, 334, 293.
- (176) Lim, K. S.; Lee, C. W.; Kim, S. T.; Seo, H. J.; Kim, C. D. *J. Lumin.* 2000, 85/89, 1008.
- (177) Wenger, O. S.; Valiente, R.; Güdel, H. U. *High-Press. Res.* 2002, 22, 57.
- (178) Wenger, O. S.; Güdel, H. U. *Inorg. Chem.* 2001, 40, 157.
- (179) Wenger, O. S.; Valiente, R.; Güdel, H. U. *Phys. Rev.* 2001, B64, 235116.
- (180) Wenger, O. S.; Gamelin, D. R.; Güdel, H. U. *J. Am. Chem. Soc.* 2000, 122, 7408.
- (181) Gamelin, D. R.; Güdel, H. U. *J. Am. Chem. Soc.* 1998, 120, 12143.
- (182) Gamelin, D. R.; Güdel, H. U. *J. Phys. Chem.* 2000, B104, 10222.
- (183) Sugano, S.; Tanabe, Y.; Kamimura, H. *Multiplets of Transition-Metal Ions in Crystals*; Academic Press: New York, 1970; p 109.
- (184) Gamelin, D. R.; Güdel, H. U. *Inorg. Chem.* 1999, 38, 5154.
- (185) Wermuth, M.; Güdel, H. U. *J. Phys.: Condens. Matter* 2001, 13, 9583.
- (186) Wermuth, M.; Güdel, H. U. *Chem. Phys. Lett.* 1997, 281, 81.
- (187) Wermuth, M.; Güdel, H. U. *J. Lumin.* 2000, 87, 1014.
- (188) Wermuth, M.; Güdel, H. U. *J. Am. Chem. Soc.* 1999, 121, 10102.
- (189) Wermuth, M.; Güdel, H. U. *J. Chem. Phys.* 2001, 114, 1393.
- (190) Wermuth, M.; Güdel, H. U. *Phys. Rev.* 2001, B63, 245118.
- (191) Page, R. H.; Schaffers, K. I.; Waide, P. A.; Tassano, J. B.; Payne, S. A.; Krupke, W. F.; Bischel, W. K. *J. Opt. Soc. Am.* 1998, B15, 996.
- (192) Mita, Y.; Yamamoto, H.; Katayanagi, K.; Shionoya, S. *J. Appl. Phys.* 1995, 78, 1219.
- (193) Chamaro, M. A.; Cases, R. *J. Lumin.* 1990, 46, 59.
- (194) Yeh, D. C.; Sibley, W. A.; Suscavage, M. J. *J. Appl. Phys.* 1988, 63, 4644.
- (195) Kermaoui, A.; Özen, G.; Goldner, P.; Denis, J. P.; Pellé, F. *J. Phys. Chem. Solids* 1994, 55, 677.
- (196) Auzel, F. French Patent No. 1.532.609, 1968.
- (197) Tokin IR Catcher; Tokin America (155 Nicholson Lane, San Jose, CA, 95134), 1987.
- (198) Photo-Turkey-1; Sumita Optical Glass Inc. (4-7-25 Harigaya, Urawa-City, Saitama, Japan), 1994.
- (199) Breteau, J. M.; Ayrat, J. L.; Micheron, F.; Auzel, F. *J. Appl. Phys.* 1990, 67, 1102.
- (200) Downing, E.; Hesselink, L.; Ralston, J.; Macfarlane, R. *Science* 1996, 273, 1185.
- (201) Auzel, F.; Pecile, D. *J. Lumin.* 1973, 8, 32.
- (202) Bril, A.; Sommerdijk, J. L.; de Jager, A. W. *J. Electrochem. Soc.* 1974, 121, 660.
- (203) Quimby, R. S.; Drexhage, M. G.; Suscavage, M. J. *Electron. Lett.* 1987, 23, 32.
- (204) Malta, O. L.; Santa-Cruz, P. A.; de Sa, G. F.; Auzel, F. *J. Solid State Chem.* 1987, 68, 314.
- (205) Malta, O. L.; Santa-Cruz, P. A.; de Sa, G. F.; Auzel, F. *J. Lumin.* 1985, 33, 261.
- (206) Wang, Y.; Ohwaki, J. *Appl. Phys. Lett.* 1993, 63, 3268.
- (207) Wang, Y.; Ohwaki, J. *J. Appl. Phys.* 1993, 74, 1272. Ohwaki, J.; Wang, Y. *Jpn. J. Appl. Phys.* 1994, 33, L334.
- (208) Ohwaki, J.; Wang, Y. *Appl. Phys. Lett.* 1994, 65, 129.
- (209) Auzel, F.; Santa-Cruz, P. A.; de Sa, G. F. *Rev. Phys. Appl. (France)* 1985, 20, 273.
- (210) Kurochkin, A. V.; Mailibaeva, L. M.; Manashirov, O. Y.; Sattarov, D. K.; Smirnov, V. B. Part 1. *Opt. Spectrosc.* 1992, 73, 442. Kurochkin, A. V.; Mailibaeva, L. M.; Manashirov, O. Y.; Sattarov, D. K.; Smirnov, V. B. Part 2. *Opt. Spectrosc.* 1992, 73, 447.
- (211) Kurochkin, A. V.; Manshistrov, O. Ya.; Sattarov, D. K.; Smirnov, V. B.; Tsyurupa, O. V. *Svetotekhnika* 1992, 5, 4 (Translated by Allerton Press Inc., 1993).
- (212) Danielmeyer, H. G.; Blätte, M. *Appl. Phys. (Germany)* 1973, 1, 269.
- (213) Deutschbein, O.; Auzel, F. In *Quantum Electronics*; Grivet, P., Bloembergen, N., Eds.; Dunod and Columbia University Press: Paris and New York, 1963; p 851.
- (214) Bagdasarov, K. S.; Zhekov, V. I.; Lobachev, V. A. J.; Murina, M.; Prokhorov, A. M. *Sov. J. Quantum Electron.* 1983, 13, 262.
- (215) Van der Weg, W. F.; Van Tol, M. W. *Appl. Phys. Lett.* 1981, 38, 705.
- (216) de Leeuw, D. M.; Hooft, G. W. t. *J. Lumin.* 1983, 28, 275.
- (217) Smith, D. J. *Lumin.* 1981, 23, 209.
- (218) Johnson, L. F.; Guggenheim, H. J. *Appl. Phys. Lett.* 1971, 19, 44.
- (219) Pollack, S. A.; Chang, D. B. *J. Appl. Phys.* 1988, 64, 2885.
- (220) Tong, F.; Risk, W. P.; Macfarlane, R. M.; Lenth, W. *Electron. Lett.* 1989, 25, 1389.
- (221) Lenth, W.; MacFarlane, R. M. *J. Lumin.* 1990, 45, 346.
- (222) Hebert, T.; Wannemacher, R.; Lenth, W.; Macfarlane, R. M. *Appl. Phys. Lett.* 1990, 57, 1727.
- (223) Macfarlane, R. M.; Tong, F.; Silversmith, A. J.; Lenth, W. *Appl. Phys. Lett.* 1988, 52, 1300.
- (224) Brede, R.; Heumann, E.; Koltke, J.; Danger, T.; Huber, G. *Appl. Phys. Lett.* 1993, 63, 2030.
- (225) Heine, F.; Heumann, E.; Danger, T.; Schweizer, T.; Huber, G. *Appl. Phys. Lett.* 1994, 65, 383.
- (226) Möbert, P. E.-A.; Heumann, E.; Huber, G. *Opt. Lett.* 1997, 22, 1412.
- (227) Auzel, F. *Amplifiers and Lasers with Optical Fibers. In Defects in Insulating Materials*; Kanert, O., Spaeth, J.-M., Eds.; World Scientific: Singapore, 1993; p 43.
- (228) Mears, R. J.; Reekie, L.; Poole, S. B.; Payne, D. N. *Electron. Lett.* 1986, 22, 159.

- (229) Allain, J.-Y.; Monerie, M.; Poignant, H. *Electron. Lett.* 1990, 26, 166.
- (230) Allain, J.-Y.; Monerie, M.; Poignant, H. *Electron. Lett.* 1990, 26, 261.
- (231) Whitley, T. J.; Millar, C. A.; Wyatt, R.; Brierley, M. C.; Szebesta, D. *Electron. Lett.* 1991, 27, 1785.
- (232) Grubb, S. G.; Bennett, K. W.; Cannon, R. S.; Humer, W. F. *Electron. Lett.* 1992, 28, 1243.
- (233) Smart, R. G.; Hanna, D. C.; Tropper, A. C.; Davey, S. T.; Carter, S. F.; Szebesta, D. *Electron. Lett.* 1991, 27, 1308.
- (234) Selected papers on Upconversion Lasers; Gosnell, T. R., Ed.; SPIE Milestone Series MS 161; SPIE Optical Engineering Press: Bellingham, WA, 2000.
- (235) Komukai, T.; Yamamoto, T.; Sugawa, T.; Miyajima, Y. *Electron. Lett.* 1992, 28, 830.
- (236) Krasutsky, N. J. *J. Appl. Phys.* 1983, 54, 1261.
- (237) Lenth, W.; Macfarlane, R. M. *J. Lumin.* 1990, 45, 346.
- (238) Oetliker, U.; Riley, M. J.; May, P. S.; Güdel, H. U. *J. Lumin.* 1992, 53, 553.
- (239) Ni, H.; Rand, S. C. *Opt. Lett.* 1992, 17, 1222.
- (240) Auzel, F.; Chen, Y. H.; Meichenin, D., ICL'93, Storrs, CN, USA, 9–12 Aug 1993. Auzel, F.; Chen, Y. H.; Meichenin, D., *J. Lumin.* 1994, 60/61, 692.
- (241) Chen, Y. H.; Auzel, F. *Electron. Lett.* 1994, 30, 323.
- (242) Auzel, F.; Chen, Y. H. *J. Non-Cryst. Solids* 1995, 184, 57.
- (243) Chen, Y. H.; Auzel, F. *J. Phys. D: Appl. Phys.* 1995, 28, 207.
- (244) Auzel, F.; Chen, Y. H. *J. Lumin.* 1995, 65, 45.
- (245) Pelletier-Allard, N.; Pelletier, R. *Phys. Rev.* 1987, B26, 4425.
- (246) Joubert, M. F.; Guy, S.; Jacquier, B. *Phys. Rev.* 1993, B48, 10031.
- (247) Kueny, A. W.; Case, W. E.; Koch, M. E. *J. Opt. Soc. Am.* 1993, B10, 1834.
- (248) Goldner, P.; Pellé, F. *Opt. Mater.* 1995, 5, 239.
- (249) Brenier, A.; Boulon, G.; Madej, C.; Pédrini, C.; Lou, L. *J. Lumin.* 1993, 54, 271.
- (250) Auzel, F. *Acta Phys. Pol.* 1996, 90, 7.
- (251) Gomes, A. S. L.; Maciel, G. S.; de Araujo, R. E.; Acioli, L. H.; de Araujo, C. B. *Opt. Commun.* 1993, 103, 361.
- (252) Brenier, A.; Courrol, L. C.; Pédrini, C.; Madej, C.; Boulon, G. *J. Lumin.* 1994, 58, 285.
- (253) Dyson, J. M.; Jaffe, S. M.; Eilers, H.; Jones, M. L.; Dennis, W. M.; Yen, W. M. *J. Lumin.* 1994, 60/61, 668.
- (254) Brenier, A.; Jurdyc, A. M. *J. Lumin.* 1996, 69, 131.
- (255) Brenier, A.; Courrol, L. C.; Pedrini, C.; Madej, C.; Boulon, G. *Opt. Mater.* 1994, 3, 25.
- (256) Guy, S. L'avalanche de photons; application à l'ion  $Tm^{3+}$  dans différents matériaux. Thèse, Université Claude-Bernard-Lyon I, 1995. Guy, S. S.; Joubert, M. F.; Jacquier, B. *Phys. Rev.* 1997, B55, 8240.
- (257) Joubert, M. F.; Guy, B.; Linares, C.; Jacquier, B.; Adam, J. L. *J. Non-Cryst. Solids* 1995, 184, 98.
- (258) Jouart, J. P.; Bouffard, M.; Klein, G.; Mary, G. *J. Lumin.* 1994, 60/61, 93.
- (259) Bielejec, E.; Kisel, E.; Silversmith, A. *J. Lumin.* 1997, 72/74, 62.
- (260) Liu, G. K.; Chen, Y. H.; Beitz, J. V. *J. Lumin.* 1999, 81, 7.
- (261) Gamelin, D. R.; Wermuth, M.; Güdel, H. U. *J. Lumin.* 1994, 83/84, 405.
- (262) Hubert, S.; Meichenin, D.; Zhou, B.; Auzel, F. *J. Lumin.* 1991, 50, 7.
- (263) Guy, S.; Joubert, M. F.; Jacquier, B. *J. Lumin.* 1997, 72/74, 65.
- (264) Case, W. E.; Koch, M. E.; Kueny, A. W. *J. Lumin.* 1990, 45, 351.
- (265) Goldner, P.; Fesquet, M.; Auzel, F. *J. Opt. Soc. Am.* 1998, B15, 2688.
- (266) Kük, S.; Diening, A.; Heumann, E.; Mix, E.; Sandrock, T.; Sebald, K.; Huber, G. *J. Alloys Compd.* 2000, 300/301, 65.
- (267) Osiak, E.; Sokolska, I.; Kük, S. *J. Lumin.* 2001, 94/95, 289.
- (268) Pelletier-Allard, N.; Pelletier, R. *J. Lumin.* 1991, 48/49, 867.
- (269) Deren, P. J.; Krupa, J. C.; Strek, W. *J. Alloys Compd.* 2000, 300/301, 18.
- (270) Koch, M. E.; Kueny, A. W.; Case, W. E. *Appl. Phys. Lett.* 1990, 56, 1083.
- (271) Chen, Y. H.; Auzel, F. *Electron. Lett.* 1994, 30, 1602.
- (272) Scheps, R. *IEEE* 1994, QE30, 2914.
- (273) Scheps, R. *IEEE* 1995, QE31, 309.
- (274) Sandrock, T.; Scheife, H.; Heuman, E.; Huber, G. *Opt. Lett.* 1997, 22, 808.
- (275) McGonigle, A. J. S.; Girard, S.; Coutts, D. W.; Moncorgé, R. *Electron. Lett.* 1999, 35, 1640.
- (276) Nicolas, S.; Descroix, E.; Guyot, Y.; Joubert, M.-F.; Abdulsabirov, R. Yu.; Korableva, S. L.; Naumov, A. K.; and Semashko, V. V. *Opt. Mater.* 2001, 16, 233.
- (277) Tverjanovich, A.; Grioriev, Y. G.; Degtyarev, S. V.; Kurochkin, A. V.; Man'shina, A. A.; Tver'yanovich, Yu. S. *J. Non-Cryst. Solids* 2001, 286, 89.
- (278) Hehlen, M. P.; Güdel, H. U.; Shu, Q.; Rai, S.; Rand, S. C. *Phys. Rev. Lett.* 1994, 73, 1103.
- (279) Heber, J. Z. *Phys. B: Condens. Matter* 1987, 68, 115.
- (280) Heber, J. *J. Alloys Compd.* 2000, 300/301, 32.
- (281) Bonifacio, R.; Lugiato, L. A. In *Dissipative Systems in Quantum Optics*; Bonifacio, R., Ed.; Springer-Verlag: Berlin, 1982; p 2.
- (282) Auzel, F.; Hubert, S.; Meichenin, D. *Europhys. Lett.* 1988, 7, 459.
- (283) Auzel, F. Document de Travail PCM.171, Utilisation du transfert d'énergie entre ions de terres-rares pour leur application éventuelles aux compteurs quantiques; addition de deux et trois photons; CNET, Issy-les -Moulineaux (France), 1967; unpublished.
- (284) Hehlen, M. P.; Güdel, H. U.; Shu, Q.; Rand, S. C. *J. Chem. Phys.* 1996, 104, 1232.
- (285) Gamelin, J. *Chem. Phys.* 2000, B104, 11045.
- (286) Auzel, F. *J. Lumin.* 2001, 93, 129.
- (287) Bednarkiewicz, A.; Strek, W. *J. Phys. D: Appl. Phys.* 2002, 35, 2503.
- (288) Zijlmans, H. J. M. A. A.; Bonnet, J.; Burton, J.; Kardos, K.; Vail, T.; Niedbala, R. S.; Tanke, H. *J. Anal. Biochem.* 1999, 267, 30.
- (289) Heer, S.; Lehman, O.; Haase, M.; Güdel, H. U. *Angew. Chem., Int. Ed.* 2003, 42, 3179.

CR020357G

# Rare-earth-doped glasses for fiber amplifiers in broadband telecommunication

Setsuhisa Tanabe\*

Faculty of Integrated Studies, Kyoto University, Kyoto 606-8501, Japan

Received 30 April 2002; accepted 28 May 2002

**Abstract** – Rare-earth-doped optical amplifiers have a great potential for broadband Wavelength-Division-Multiplexed (WDM) telecommunication by tailoring host glass compositions. In order to design the emission spectra of doped rare-earth ions, it is important to understand the relationship between the local ligand field and various optical properties of specific 4f-levels, such as the radiative transition probability, the nonradiative decay probability, which dominate the spectral line width and quantum efficiency of amplification transitions. For the  $\text{Er}^{3+}$ :1.55  $\mu\text{m}$  transition, the role of the Judd–Ofelt  $\Omega_6$  parameters is presented, which is correlated to the Er–ligand bond covalency in glasses. The  $\text{Tm}^{3+}$ : 1.46- $\mu\text{m}$  transition shows quantum efficiency over 90% high enough for the S-band application, in heavy metal oxide glasses with moderate phonon energy and wider spectra than fluorides. A way to improve population inversion by selective energy transfer with codoped lanthanide ions is presented. Finally, the energy level structures and resultant spectral properties of  $\text{Pr}^{3+}$ ,  $\text{Nd}^{3+}$  and  $\text{Dy}^{3+}$  ions, 1.3- $\mu\text{m}$ -active ions, are compared. The hypersensitivity of  $\text{Dy}^{3+}$  transitions appears especially in chalcogenide glasses, where the nonradiative loss due to multiphonon decay is also minimized. In conclusion, glass materials have opportunities to vary the radiative cross section, quantum efficiency, and gain flatness, which are important for novel amplifiers in the future DWDM system. *To cite this article: S. Tanabe, C. R. Chimie 5 (2002) 815–824* © 2002 Académie des sciences / Éditions scientifiques et médicales Elsevier SAS

rare earths / glass / optical amplifier / telecommunication / Wavelength-Division Multiplexing / optical fiber

**Résumé** – Les télécommunications à large bande basées sur le multiplexage en division de longueur d'onde (WDM) font appel à des amplificateurs optiques dopés avec des terres rares. Le spectre d'émission de ces terres rares peut être ajusté en modifiant la composition du verre. Il faut pour cela connaître la relation entre le champ local et les caractéristiques optiques des niveaux concernés, en particulier les probabilités de transition radiative et de désexcitation non radiative, qui déterminent la largeur spectrale et le rendement quantique des transitions. Le rôle du paramètre de Judd–Ofeld  $\Omega_6$  dans la transition de l'erbium à 1,55  $\mu\text{m}$  est corrélé à la covalence de la liaison Er–ligande dans le verre. Les transitions du  $\text{Tm}^{3+}$  pour la bande S et celle des ions  $\text{Pr}^{3+}$ ,  $\text{Nd}^{3+}$  et  $\text{Dy}^{3+}$  à 1,3  $\mu\text{m}$  sont également abordées et discutées. Dans les matériaux vitreux, on peut ainsi faire varier la section efficace radiative, le rendement quantique et la constance du gain, ce qui peut se révéler important pour les nouveaux amplificateurs dans les futurs systèmes DWDM. *Pour citer cet article : S. Tanabe, C. R. Chimie 5 (2002) 815–824* © 2002 Académie des sciences / Éditions scientifiques et médicales Elsevier SAS

terres rares / verre / amplificateur optique / télécommunication / Wavelength-Division Multiplexing (WDM) / fibre optique

## 1. Introduction

The growing demand and future potentials of an advanced information society stimulate research for devices composing a network system with excellent flexibility and larger information capacities at much faster rates. Installation of broadband Wavelength-

Division-Multiplexing (WDM) optical network system is indispensable and novel amplifier materials, which would overcome the performance of the present silica-based erbium-doped fiber amplifier (EDFA), can be a key to enable more number of channels. Among several possible choices of devices, rare-earth-doped amplifiers have implied high-power conversion effi-

\* Correspondence and reprints.

E-mail address: stanabe@gl.s.mbox.media.kyoto-u.ac.jp (S. Tanabe).

ciency than Raman and scalability of gain spectra by tailoring the host-glass composition. In telecommunication systems, the invention of the EDFA [1] can be likened to that of the transistors in electronics in terms of its technological impact. The technology to amplify the light signal directly without the conversion of light/electricity/light has been achieved by stimulated emission of 4f optical transition in rare-earth-doped fibers [2], which realizes ideal amplification with high gain and low noise. The technological development of optical telecommunication is based on the growth of technologies of fiber fabrication and those of laser diodes (LD). In fact, the invention of efficient III-V LD has also enabled efficient pumping of  $\text{Er}^{3+}$  with its three-level system [3–5]. In addition, there exists the history of technological transition from passive fibers to active fibers [2], in which we can find a quite interesting relationship between active ions and the host glasses. Although the fiber amplifiers are already playing crucial roles in the optical networks both at 1.55  $\mu\text{m}$  and at 1.3  $\mu\text{m}$  bands, there exist further requirements to fully utilize the window of optical fibers with superior performance. The requirements are wide and flat gain spectrum around 1.53–1.65  $\mu\text{m}$  (C+L band) in a novel EDFA and around 1.45–1.51  $\mu\text{m}$  (S-band) in  $\text{Tm}^{3+}$  (TDFA) for the WDM systems [6], greater gain per pump-power at 1.31  $\mu\text{m}$  in  $\text{Pr}^{3+}$  [7, 8] or possibly  $\text{Dy}^{3+}$ -doped glasses [9–11].

According to the report of the Japanese Photonic Network Research Committee, the DWDM system will require 3000 channels in the year 2010 [12]. To enable 3000-channel WDM, we need more various amplifiers as well as a transmission fiber with a window from 1 to 1.65  $\mu\text{m}$ . Fig. 1 shows a typical loss

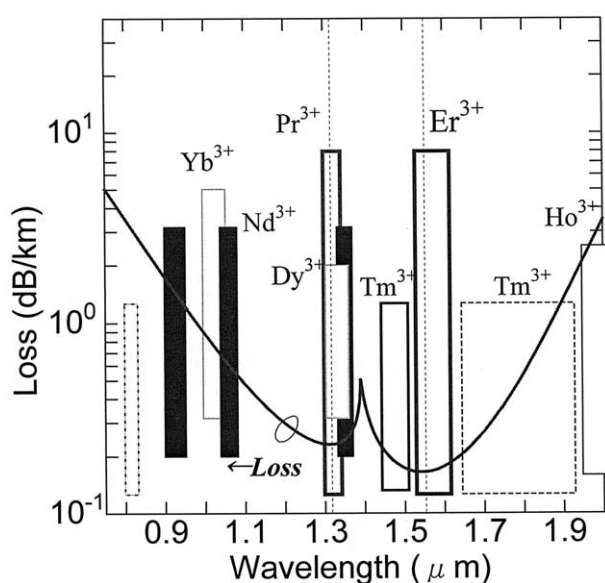


Fig. 1. Loss characteristics of silica fiber and emission bands of some rare-earth ions.

spectrum of the present silica fiber and emission bands of several rare-earth ions.

Not only in fiber forms, planar waveguide forms will also play a role in photonic devices, since integration of optical circuits improves functions with fewer components [13]. Because a shorter device length is usually expected for these waveguides, it might suffer from the problem of concentration quenching and new solutions of host materials would be required, due to the need of greater doping concentrations of rare-earth ions. In devices of either form, it is necessary to understand the 4f transitions of the ions, the structure of their sites in glass to design amplifier materials with better properties. This paper reviews some studies on the spectroscopic properties, radiative and nonradiative processes, and site structure of rare-earth ions in glasses at each wavelength.

## 2. Research scheme for rare-earth laser glasses

An optical amplifier works by the principle of light amplification by stimulated emission of radiation, nothing different from that of lasers. It requires a pump to create a population inversion in the amplifier medium. When an incoming signal photon stimulates an excited electron, the electron relaxes back into a lower energy state and emits a second signal photon with the same phase as the incoming photon. This process of stimulated emission amplifies the signal. The success of the first generation silica-based EDFA is that the energy level of  $\text{Er}^{3+}$  ions can cause amplification to emit a photon with precisely the wavelength at which the network operates, with high efficiency, even in silica hosts having high phonon energy and poor RE solubility. The erbium was really a lucky boy to be the first, with an ideal energy level structure workable in silica and several pumping LDs available. Anyway, it is not a surprising idea to apply a research scheme for various rare-earth laser glasses to the design of novel amplifiers. To quantitatively comprehend optical phenomena of rare-earth ions in glasses, it is important to evaluate radiative and non-radiative decay process of related 4f levels. The Judd-Ofelt theory is usually adopted to obtain the radiative transition probabilities including emission by utilizing the data of absorption cross-sections of several f-f electric-dipole lines, especially for four-level emissions. The physical and chemical implement of three  $\Omega_t$  parameters ( $t=2,4,6$ ) are becoming clearer by combining the information of the local ligand field of doped ions by other spectroscopic techniques such as the  $^{151}\text{Eu}$ -Mössbauer effect [14]. In some cases, the isomer shift and quadrupole splitting give us more discrete information about the rare-earth environment

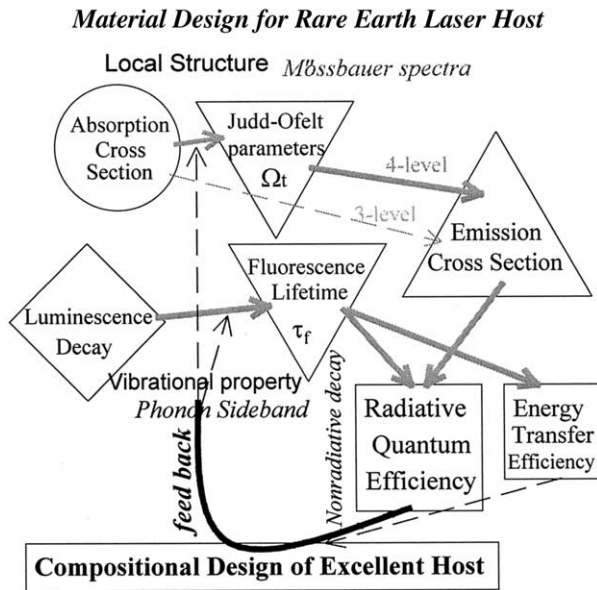


Fig. 2. Research scheme for efficient laser materials.

in glass; bond covalency and symmetry [15]. The nonradiative decay rate can be evaluated experimentally by combining the lifetime measurement, which include contributions of multiphonon decay, energy transfer such as cross relaxation, cooperative up-conversion, etc. In order to distinguish each contribution, systematic studies on concentration dependence of the rates are necessary. The phonon sideband spectra of  $\text{Eu}^{3+}$  ion can be supplementary to inclusive understanding of local structure in glass hosts, where the stretching vibrational mode of the network former bond often plays an important role [16] in the decay as well as in the phonon-assisted energy transfer [17]. The above-mentioned research scheme is shown in Fig. 2. In many cases, the site selectivity of doped RE ions cannot be predicted in multicomponent glasses. However, we can feed back the several characteristics obtained for selected glasses toward a better material design based on logical direction.

### 3. The 1.55- $\mu\text{m}$ band in $\text{Er}^{3+}$ -doped glasses for broadband amplifiers

There is now a worldwide consensus that the WDM networking has superior functions and applications for future telecommunication systems [18] to the single channel TDM only at 1.55  $\mu\text{m}$ . It offers not only large-scale information capacity, but also flexibility and transparency by utilizing the properties of light. Among various properties of EDFA, such as low-noise, broad bandwidth (not broad enough now!!) and efficient gain, the ability to amplify more than one

wavelength at a time has replaced the regenerator for each channel. Although the excellent performance of the present silica-based EDFA can be used for a WDM system, but with fewer channels, there exists requirement for a larger number of channels, which could be possible by using an EDFA with a wider gain spectrum [6]. From a practical standpoint, the flatness of the gain is also critically important because the light intensity for different channels would be varied by the multi-step amplifications if the gain of the amplifier were not independent of wavelengths. Therefore, the design of a host for  $\text{Er}^{3+}$  for wide and flat spectra of the  ${}^4I_{13/2}$ - ${}^4I_{15/2}$  transition at around 1.5–1.6  $\mu\text{m}$  is a target at present.

For the transitions between the states with the difference in the total angular momentum by  $\Delta J = 1$ , there exists the contribution of the magnetic-dipole transition [19] in the  ${}^4I_{13/2}$ - ${}^4I_{15/2}$ . The spontaneous emission probability of this transition is given by:

$$A_{J'J} = \frac{64 \pi^4 e^2}{3 h(2J'+1) \lambda^3} \left\{ \left[ \frac{n(n^2+2)^2}{9} \right] \times S^{\text{ed}} + n^3 \times S^{\text{md}} \right\} \quad (1)$$

where  $h$  is the Planck constant,  $m$  and  $e$  are the mass and charge of the electron,  $c$  is the velocity of light,  $n$  is the refractive index at the mean wavelength,  $\lambda$ ,  $S^{\text{ed}}$  and  $S^{\text{md}}$  are the line strengths of the electric-dipole and magnetic-dipole transitions, respectively. The  $S^{\text{md}}$  is characteristic of the transition and thus a constant. Thus the second term is not varied with ligand field and dominated only by the refractive index, which has usually about 30% contribution in silicate glasses. That is part of the reason why the  $\text{Er}^{3+}$  ions in silicate glasses have a narrow 1.55  $\mu\text{m}$  spectrum [20]. In order to get flat emission spectra, it can be effective to increase the relative contribution of the electric-dipole transition, the spectra of which can be varied due to the variations of width of the Stark splitting ( $J+1/2$ ), inhomogeneous broadening in amorphous structures and also to sensitivity to the local fields [21–23]. While the line strength of the magnetic-dipole transition is independent of ligand fields, whereas that of the electric-dipole transition is a function of them [20, 21]. According to the Judd–Ofelt theory [24, 25], the line strength of the electric dipole components of the 1.55- $\mu\text{m}$  transition is given by [26]:

$$\begin{aligned} S^{\text{ed}}[{}^4I_{13/2}; {}^4I_{15/2}] &= \sum_{t=2,4,6} \Omega_t \langle {}^4I_{13/2} \| U^{(t)} \| {}^4I_{15/2} \rangle^2 \\ &= 0.019 \Omega_2 + 0.118 \Omega_4 + 1.462 \Omega_6 \quad (2) \end{aligned}$$

where the three coefficients of  $\Omega_t$  are the reduced matrix elements of the unit tensor operators,  $U^{(t)}$ , calculated in the intermediate-coupling approximation, and  $\Omega_t$  ( $t=2,4,6$ ), are the intensity parameters. Since the  $\langle \text{SLJ} \| U^{(t)} \| \text{S'L'J} \rangle$  of other transitions are also a constant characteristic of each transition, three inten-

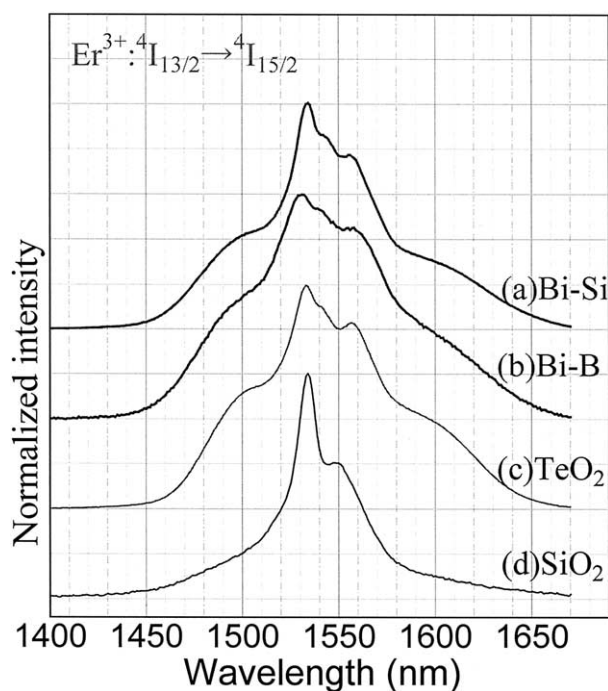


Fig. 3. Fluorescence spectra of  $\text{Er}^{3+}$ -doped glasses; (a) Bi-silicate, (b) Bi-borate, (c) Tellurite and (d) Al-silica.

sity parameters  $\Omega_t$  ( $t=2,4,6$ ) can be obtained from more than three measured absorption cross-sections by using the method of least squares fitting [27]. What varies depending on the host composition and structures is the electric-dipole transitions, where the  $\Omega_6$  parameter is dominant. Excellent spectra with larger cross-section are observed in tellurite [6] and bismuth-based oxide glasses [28] (Fig. 3), than aluminosilicates [20]. The higher bond-ionicity is confirmed for the glasses with a large  $\Omega_6$  of  $\text{Er}^{3+}$  by  $^{151}\text{Eu}$  Mössbauer spectroscopy, which can be explained by the largest contribution of the overlap integral of 4f and 5d orbitals [14, 21]. Also there may be another possible reason. The relative ratio of the field correction factors  $(n^2 + 2)^2/9n^2$  takes a minimum at  $n = 1.414$  and increases monotonically with increasing  $n$ ; i.e., under constant  $S^{\text{ed}}$  and  $S^{\text{md}}$ , the relative contribution of ED transition should increase with increasing  $n$  of the host glass, which is not practically the case, because these values are not independent. However, it is empirically true that many glass hosts with a large  $n$  show broad  $\text{Er}^{3+}$  emission spectra. There are few exceptions from the tendency that the  $\text{Er}^{3+}$  ions in those glasses take a large  $\Omega_6$  value, since the electron polarizability and bond covalency are strongly correlated.

## 4. Tm-doped glasses for S-band amplifier

### 4.1. Background of S-band requirement

Due to the rapid increase of information traffic, great research effort has been paid to development of

telecommunication devices for the WDM network system [29]. Because the silica-based transmission fiber has a wide and low-loss window from 1.4 to 1.65  $\mu\text{m}$ , there is an emergent demand for optical amplifiers, which can be used around 1.4 and 1.6  $\mu\text{m}$ , in addition to the present silica-based EDFA. Tellurite-based EDFA was reported to have 80-nm-wide gain up to 1.6  $\mu\text{m}$  (L-band), which also shows various excellent material properties [30, 31]. For the 1.45–1.49- $\mu\text{m}$  band (S<sup>+</sup>-band), the fluoride-based Tm-doped fiber (TDF) [32] can be used as an amplifier, although it still presents difficulties compared with the use of EDFA. One of the reasons for inferior performance of TDF is a longer lifetime of the terminal  $^3\text{F}_4$  level than that of the initial  $^3\text{H}_4$  level [33]. The performance of the TDF is improved by use of an up-conversion pumping scheme with a 1.06- $\mu\text{m}$  laser, which produces a population inversion. Codoping of other lanthanide ion, such as  $\text{Ho}^{3+}$ , was also found to improve the population inversion by means of the energy transfer from the  $^3\text{F}_4$  level [34]. In addition, a larger branching ratio,  $\beta$  of the  $^3\text{H}_4 \rightarrow ^3\text{H}_6$  band at 0.80  $\mu\text{m}$  than that of the 1.46  $\mu\text{m}$  make it difficult to realize amplification, because the fiber can easily lase at 0.80  $\mu\text{m}$ , resulting in the gain saturation [35]. According to the Judd–Ofelt calculation,  $\beta$  of 0.80  $\mu\text{m}$  is nearly 90%, which is 11 times larger than that of 1.46  $\mu\text{m}$  emission in most glasses [36, 37]. Therefore, the suppression of the 0.80  $\mu\text{m}$  amplified spontaneous emission (ASE) is desirable to avoid lasing at unexpected wavelength for improving the amplifier performance. In either case, in spite of difficulty as practical materials, nonoxide-fiber hosts with lower phonon energy have been used, because the  $^3\text{H}_4$  level is more easily quenched in high-phonon-energy environment, due to its small energy gap. However, the energy gap of the  $^3\text{H}_4$  level is not so small as that of the  $\text{Pr}^{3+} : ^1\text{G}_4$  for 1.3- $\mu\text{m}$  amplifiers and thus good performance can be expected in some oxide hosts with low phonon energy and better fiberizability.

Fig. 4 shows the relation between the multiphonon decay rate,  $W_p$  of the  $\text{Tm}^{3+} : ^3\text{H}_4$ ,  $\text{Pr}^{3+} : ^1\text{G}_4$  levels and the inverse phonon energy of various glass hosts. We can see the lower  $W_p$  of the  $\text{Tm}^{3+} : ^3\text{H}_4$  in tellurite than that of the  $\text{Pr}^{3+} : ^1\text{G}_4$  in ZBLAN, even with higher phonon energy.

In this chapter, the tellurite glass was chosen as a host because it has relatively low phonon energy, excellent properties for fiber fabrications [30, 38], and thus can be considered as a candidate material for TDF.

### 4.2. Spectroscopy of singly doped glass

#### 4.2.1. Fluorescence spectra

Fig. 5 shows the  $\text{Tm}^{3+}$  energy level and a fluorescence spectrum in the tellurite glass, excited at

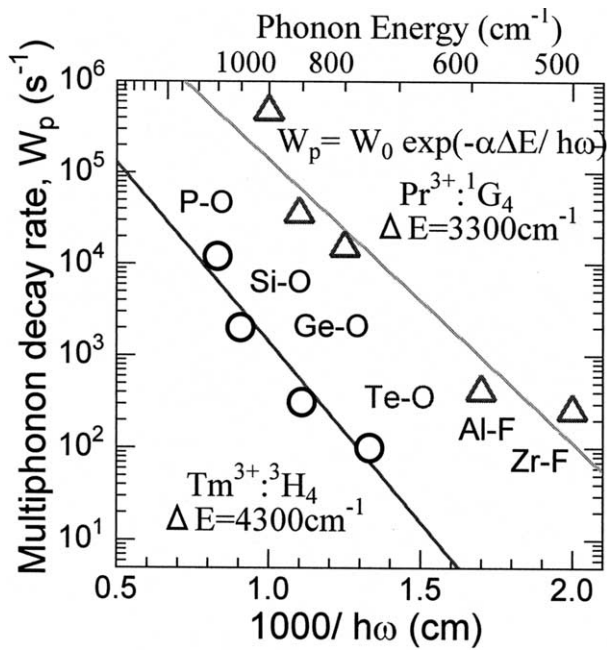


Fig. 4. Relationship between multiphonon decay rates of  $\text{Tm}^{3+}:\text{}^3\text{H}_4$ ,  $\text{Pr}^{3+}:\text{}^1\text{G}_4$  levels and inverse phonon energy.

790 nm. The emission bands at 0.80  $\mu\text{m}$ , 1.46  $\mu\text{m}$ , and 1.80  $\mu\text{m}$  are due to the  ${}^3\text{H}_4 \rightarrow {}^3\text{H}_6$ ,  ${}^3\text{H}_4 \rightarrow {}^3\text{F}_4$ , and  ${}^3\text{F}_4 \rightarrow {}^3\text{H}_6$  transitions, respectively. The wavelength region longer than 1.3  $\mu\text{m}$  is multiplied by 10 times. The area integration was carried out after converting the wavelength into wavenumber scale, which is directly proportional to the energy. The relative intensity ratio of 0.80 to 1.46  $\mu\text{m}$  was about 11, almost unchanged with glass compositions and Tm-concen-

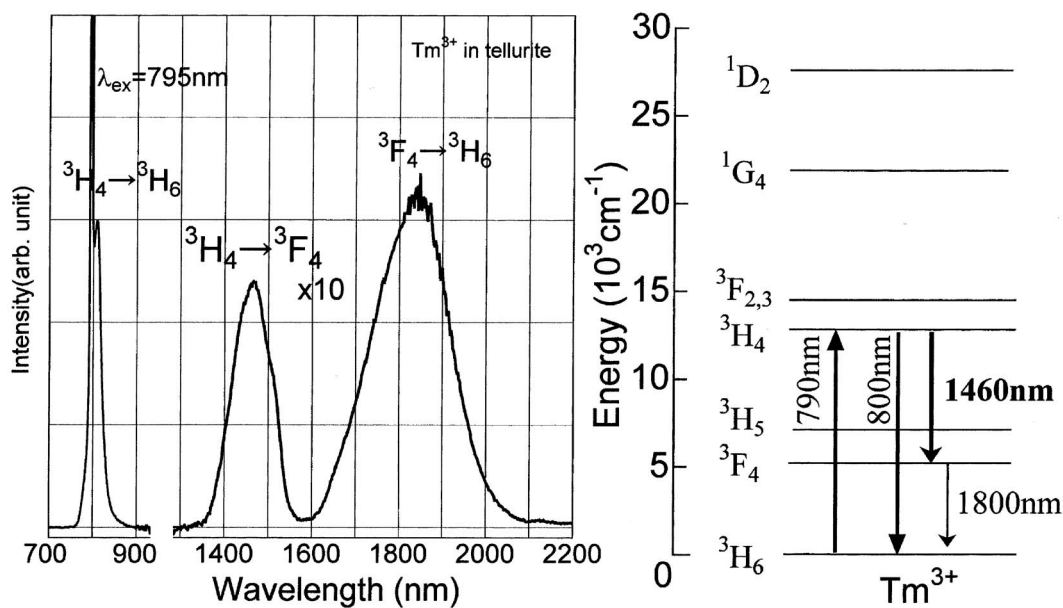


Fig. 5. Fluorescence spectra of  $\text{Tm}^{3+}$ -doped tellurite glass. Energy level of  $\text{Tm}^{3+}$  ion is also shown for assignment.

Table 1. Spontaneous emission probability and branching ratios of  $\text{Tm}^{3+}:\text{}^3\text{H}_4$  level in the tellurite glass.

| Transition   | $A^{\text{ed}}$ ( $\text{s}^{-1}$ ) | $A^{\text{md}}$ ( $\text{s}^{-1}$ ) | Calculated branch ratio $\beta$ (%) | Ratio of measured emission band |
|--|-------------------------------------|-------------------------------------|-------------------------------------|---------------------------------|
| ${}^3\text{H}_4 \rightarrow {}^3\text{H}_6$  | 2426                                | –                                   | 88.8                                | ~11                             |
| ${}^3\text{H}_4 \rightarrow {}^3\text{F}_4$  | 229                                 | –                                   | 8.4                                 | 1                               |
| ${}^3\text{H}_4 \rightarrow {}^3\text{H}_5$  | 54                                  | 23                                  | 2.8                                 | –                               |
| $A_{\text{total}} = 2732 \text{ s}^{-1}$ ,<br>$\tau_{\text{rad}} = A^{-1} = 366 \text{ s}$ |                                     |                                     |                                     |                                 |

tration. On the other hand, that of 1.46 to 1.80  $\mu\text{m}$  was largely changed with these factors, which is due to the effect of the nonradiative relaxations.

#### 4.2.2. Judd–Ofelt analysis and quantum efficiency in tellurite

The obtained Judd–Ofelt parameters of  $\text{Tm}^{3+}$  in the present glass were:  $\Omega_2 = 4.69 \text{ pm}^2$ ,  $\Omega_4 = 1.83 \text{ pm}^2$ ,  $\Omega_6 = 1.14 \text{ pm}^2$ . Table 1 shows spontaneous emission probabilities,  $A$  and  $\beta$  from the  ${}^3\text{H}_4$  level of  $\text{Tm}^{3+}$  ions in the tellurite glass. The  $\beta$  of 0.80- $\mu\text{m}$  emission is 11 times larger than that of 1.4- $\mu\text{m}$  emission, which is almost similar to the case in fluoride and other oxide glasses. The calculated  $\tau_{\text{R}}$  was 366  $\mu\text{s}$ , while the measured lifetime was 350  $\mu\text{s}$ . This indicates that the quantum efficiency of the  ${}^3\text{H}_4$  level is 96% in tellurite glass, which is comparable to that in  $\text{ZrF}_4$ -based fluoride glasses (~100%).

#### 4.2.3. Concentration dependence of emission

Fig. 6 shows the  $\text{Tm}_2\text{O}_3$ -concentration dependence of ratios of the  $\tau_{\text{f}}({}^3\text{F}_4)/\tau_{\text{f}}({}^3\text{H}_4)$  and the integrated intensity of (1.80  $\mu\text{m})/(1.46 \mu\text{m})$  of fluorescence spectra. Both

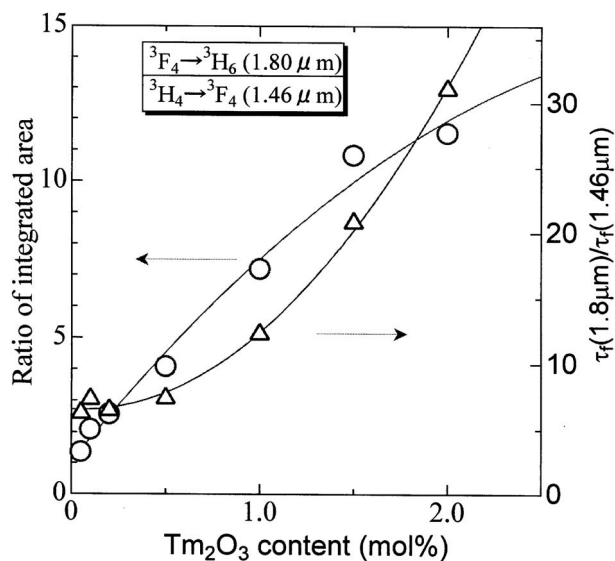


Fig. 6. Ratio of integrated area and lifetime of 1.4 μm/1.8 μm in 72 TeO<sub>2</sub>–20 ZnO–5 Na<sub>2</sub>O–(2.9–x) Y<sub>2</sub>O<sub>3</sub>–x Tm<sub>2</sub>O<sub>3</sub> glasses.

ratios increase drastically with increasing the Tm<sub>2</sub>O<sub>3</sub> content. These phenomena are well understood by the so-called ‘Two-for-One Process’ [31], which is a result of the cross relaxation between two Tm<sup>3+</sup> ions; [<sup>3</sup>H<sub>4</sub>,<sup>3</sup>H<sub>6</sub>] → [<sup>3</sup>F<sub>4</sub>,<sup>3</sup>F<sub>4</sub>] and unfavorable for population inversion between the <sup>3</sup>H<sub>4</sub> and <sup>3</sup>F<sub>4</sub> levels. Therefore, a low concentration is desirable to keep a high quantum efficiency of the <sup>3</sup>H<sub>4</sub> level for 1.4-μm application.

#### 4.2.4. Temperature dependence

Fig. 7 shows temperature variation of the fluorescence spectra. The peak intensity of the 1.46-μm band

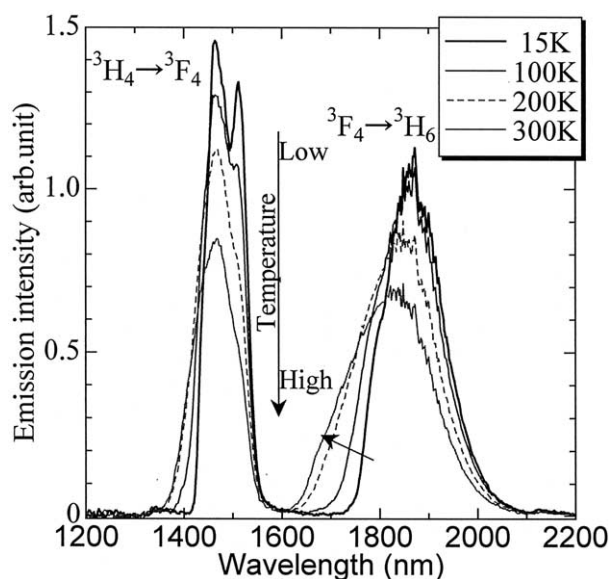


Fig. 7. Temperature dependence of fluorescence spectra of 72 TeO<sub>2</sub>–20 ZnO–5 Na<sub>2</sub>O–2.9 Y<sub>2</sub>O<sub>3</sub>–0.1 Tm<sub>2</sub>O<sub>3</sub> glass.

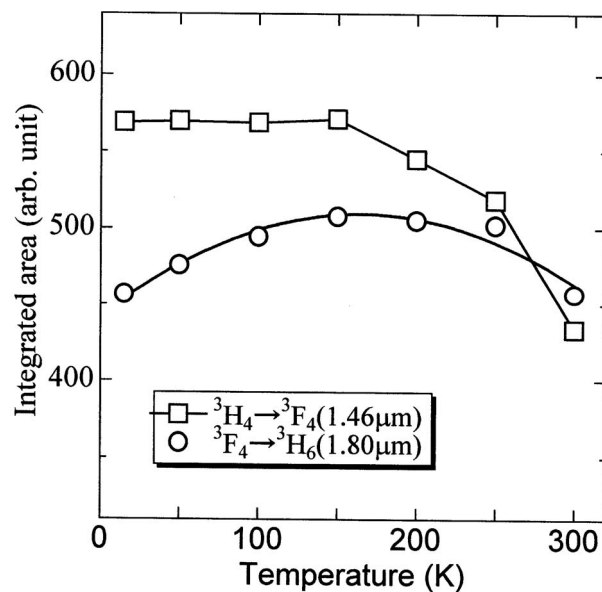


Fig. 8. Temperature dependence of the integrated area of the 1.4-μm and 1.8-μm band in the 0.1 Tm<sub>2</sub>O<sub>3</sub> glass.

increases with lowering temperature, while the line shape of the 1.8-μm band becomes sharp. It can be seen that the mean wavelength of both bands shift to the longer side. The temperature dependence of integrated intensities of both bands is plotted in Fig. 8. The integrated area of the 1.46-μm band is almost unchanged at lower temperature and drops with temperature above 150 K. On the other hand, that of the 1.8-μm band increases slightly and decreases above 250 K. The tendency of the 1.46-μm emission can be explained by considering the temperature dependence of the nonradiative decay from the <sup>3</sup>H<sub>4</sub> level, which has smaller energy gap to the next lower level. The increasing tendency of the 1.8-μm band is ascribed to the improved population from the upper level by non-radiative processes. Therefore, the lower the temperature is, the better the population inversion becomes. Another advantage of the lower temperature can be the much-improved intensity at 1.50–1.52 μm, which is hardly obtained by conventional EDFA, though not impossible by TDFA [39].

#### 4.3. Effect of codoping of Ho, Tb, Eu

One of the possibilities to improve the population inversion can be a selective quenching of the terminal level by codoping of other lanthanide [34, 40], because nothing is better than to pump directly the <sup>3</sup>H<sub>4</sub> with 0.79-μm LD of AlGaAs rather than upconversion scheme [35, 41]. The role expected for a codopant is to quench the <sup>3</sup>F<sub>4</sub> level selectively without quenching the <sup>3</sup>H<sub>4</sub> level. From this viewpoint, the Eu<sup>3+</sup>, Tb<sup>3+</sup> and Ho<sup>3+</sup> can be a candidate among 13 4f-active lanthanide

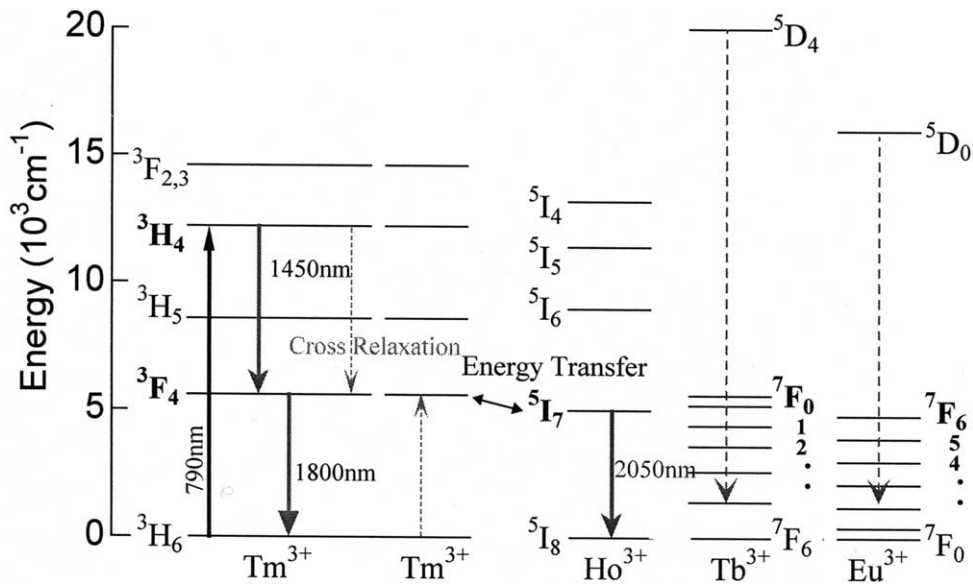


Fig. 9. Energy level of  $Tm^{3+}$ ,  $Ho^{3+}$ ,  $Tb^{3+}$  and  $Eu^{3+}$  ion.

ions. The energy level diagrams of these ions are shown in Fig. 9. The  $Ln$ -concentration dependence of the lifetimes of the  $Tm^{3+}:^3H_4$  and  $^3F_4$  levels is plotted in Fig. 10. Among three codopants, the  $Eu^{3+}$  ion quenches both levels most significantly and the  $Ho^{3+}$  ion shows the best selectivity; i.e., the least effect on the  $^3H_4$  lifetime with a large quenching effect on the  $^3F_4$ . The variation of the fluorescence spectra of  $Tm$ - $Ho$  codoped tellurite glasses are shown in Fig. 11. The spectra are normalized by the intensity of 1.46- $\mu m$  band, because it showed the least change. We see a drastic decrease of the 1.8- $\mu m$  band and a rapid increase of the  $Ho^{3+}:^5I_7 \rightarrow ^5I_8$  emission intensity at 2  $\mu m$ . This result is an evidence of the  $Tm^{3+}:^3F_4 \rightarrow Ho^{3+}:^5I_7$  energy transfer.

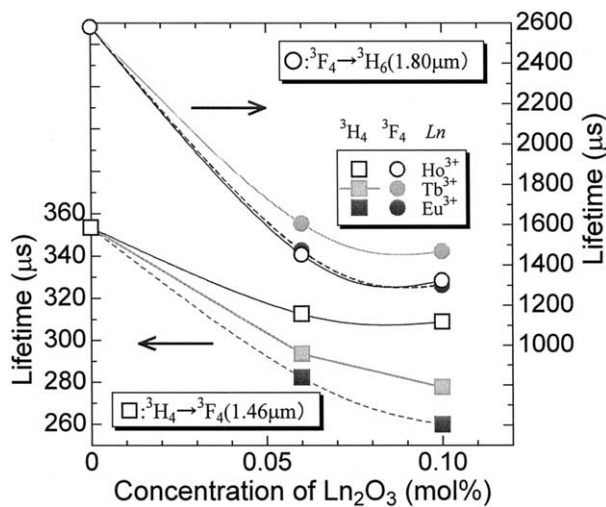


Fig. 10. Effect of codopant on the lifetime of  $Tm^{3+}$  levels.

## 5. Active ions at 1.3 $\mu m$

### 5.1. Comparison of candidates

The world land-based optical networks installed are composed of 1.3  $\mu m$  zero-dispersion silica fiber. However, no practical amplifiers have sufficient performance at 1.3- $\mu m$  like EDFAs at 1.55- $\mu m$  band. Fig. 12 shows the energy levels of  $Pr^{3+}$ ,  $Nd^{3+}$ , and  $Dy^{3+}$  ions, which are active ions at 1.3  $\mu m$ . Based on the huge amount of data on laser glasses for 1.06- $\mu m$  applications [42], the  $Nd^{3+}$  ion was extensively studied as a candidate at first

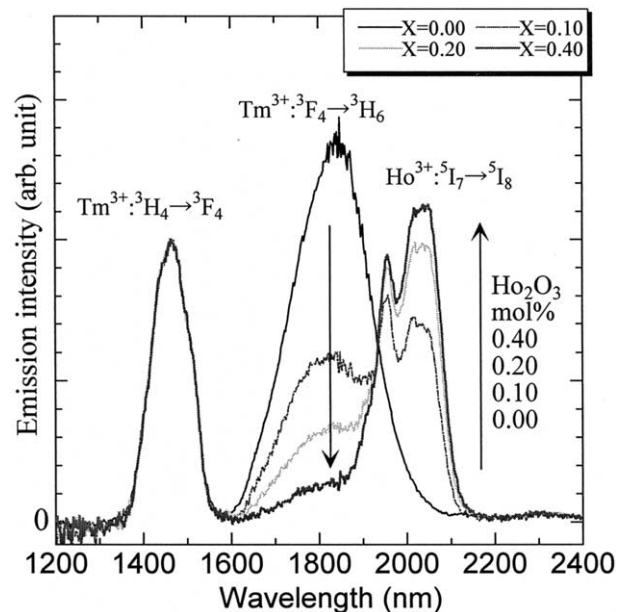
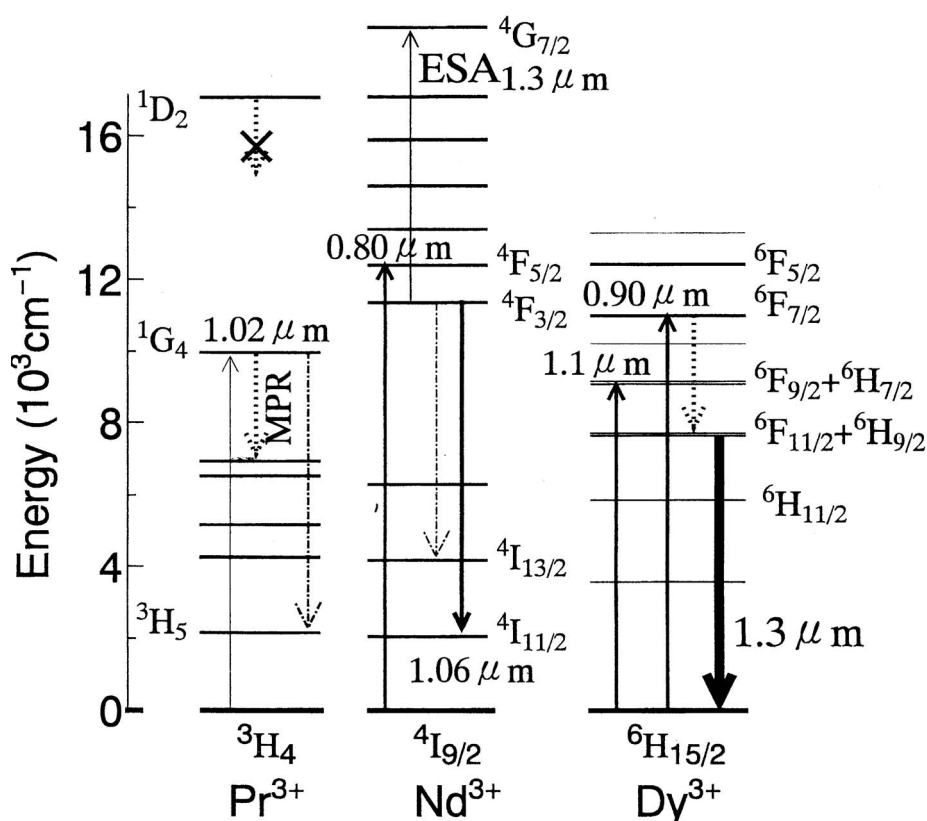


Fig. 11. Fluorescence spectra of 72  $TeO_2$ -20  $ZnO$ -5  $Na_2O$ -(2.9-x)  $Y_2O_3$ -x  $Ho_2O_3$ -0.1  $Tm_2O_3$  glasses.

Fig. 12. Energy level of  $\text{Pr}^{3+}$ ,  $\text{Nd}^{3+}$  and  $\text{Dy}^{3+}$  ion.

in many glasses. However, the excited state absorption from the  ${}^4\text{F}_{3/2}$  and the resulting gain shift to  $1.35 \mu\text{m}$  were found to be a problem as well as a small branching ratio compared with that of  $1.06 \mu\text{m}$ , which is a cause of intense amplified spontaneous emission (ASE) [43]. The  $\text{Pr}^{3+}$  ion is probably most often studied in fluoride [7] and chalcogenide glasses [8] and practical devices have already been produced [44]. The branching ratio from the  ${}^1\text{G}_4$  level is usually more than 60% in most glasses [45]. The nonradiative loss due to the small energy gap limits the choice of host to nonoxide glasses. In addition, the small absorption cross-section of the only pumpable level ( ${}^1\text{G}_4$ ) at  $1.02 \mu\text{m}$  must be overcome by high-power pumping laser. Nonradiative population from the upper  ${}^1\text{D}_2$  level cannot be expected due to its larger energy gap. Since it is difficult to get high-quality lasers at  $1.02 \mu\text{m}$  with semiconductor lasers, an  $0.8 \mu\text{m}$ -LD- pumped Nd:YLiF<sub>4</sub> solid-state laser ( $\lambda = 1047 \text{ nm}$ ) is often used as a pumping source

[45]. Among various glasses, the Ga–Na–S system has the highest quantum efficiency of 62% and the largest gain per pumping power at  $1.34 \mu\text{m}$  [8]. However, the gain at  $1.31 \mu\text{m}$  is still low partly due to the peak shift to longer wavelength in sulfides [8].

Compared with these two ions, the  $\text{Dy}^{3+}$  has unique properties, though it is also affected by multiphonon loss. The  $\text{Dy}^{3+}$  ion can be pumped by  $0.8 \mu\text{m}$ ,  $0.9 \mu\text{m}$ ,  $1.1 \mu\text{m}$  or  $1.28 \mu\text{m}$  with large cross sections, for which the high-power LD's can be used. Table 2 shows the reduced matrix elements of  $1.3\text{-}\mu\text{m}$  emission transitions for  $\text{Pr}^{3+}$ ,  $\text{Nd}^{3+}$  and  $\text{Dy}^{3+}$  ions [11]. While the transition probabilities in  $\text{Pr}^{3+}$  and  $\text{Nd}^{3+}$  ions depend most largely on  $\Omega_6$ , that in  $\text{Dy}^{3+}$  is dominated by the  $\Omega_2$  parameter, which is most sensitive to the local symmetry and thus to the glass composition. The transition, the cross section of which is very sensitive to the local structure, is called 'hypersensi-

Table 2. Reduced matrix elements of  $1.3\text{-}\mu\text{m}$  emission transitions for  $\text{Pr}^{3+}$ ,  $\text{Nd}^{3+}$  and  $\text{Dy}^{3+}$  ions [11].

| $\text{Ln}^{3+}$ | $4\text{F}^{\text{N}}$ | aJ   | bJ'                   | $\langle U^{(2)} \rangle^2$ | $\langle U^{(4)} \rangle^2$ | $\langle U^{(6)} \rangle^2$ | $\lambda$ ( $\mu\text{m}$ ) |
|------------------|------------------------|--|-----------------------|-----------------------------|-----------------------------|-----------------------------|-----------------------------|
| $\text{Pr}^{3+}$ | 2                      | ${}^1\text{G}_4$                           | ${}^3\text{H}_5$      | 0.0307                      | 0.0715                      | 0.3344                      | 1.32                        |
| $\text{Nd}^{3+}$ | 3                      | ${}^4\text{F}_{3/2}$                       | ${}^4\text{I}_{13/2}$ | 0                           | 0                           | 0.2117                      | 1.35                        |
| $\text{Dy}^{3+}$ | 9                      | ${}^6\text{H}_{9/2} + {}^6\text{F}_{11/2}$ | ${}^6\text{H}_{15/2}$ | 0.9394                      | 0.8465                      | 0.4078                      | 1.32                        |

itive transition' [46]. The 615-nm emission of the  $\text{Eu}^{3+}$  ion, used for red-phosphor, is a typical example, where the  $\langle |U^{(2)}| \rangle^2$  is the largest among the three  $\langle |U^{(t)}| \rangle^2$  [47].

## 5.2. Spectroscopy of dysprosium in glasses

### 5.2.1. Judd–Ofelt parameters and optical transitions

Absorption spectra of  $\text{Dy}^{3+}$  in the fluoride and tellurite glasses are shown in Fig. 13, where the assignment of transitions is also indicated [11]. We can see that the absorption coefficients of transition peaks in this near-infrared region are not so distinct from each other for the fluoride glass. On the other hand, in the tellurite glass the intensity of  ${}^6\text{F}_{11/2}+{}^6\text{H}_{9/2}$  band is the largest among all transitions. The  $\Omega_t$  parameters obtained for the glasses are shown in Fig. 14. The  $\Omega_2$  value is the largest in the sulfide and tellurite glasses and decreases in the order  $\text{Ga}_2\text{S}_3 > \text{TeO}_2 > \text{ZrF}_4 > \text{InF}_3$ , whereas  $\Omega_6$  increases in this order. The change in the absorption cross-section of the  ${}^6\text{F}_{11/2}+{}^6\text{H}_{9/2}$  band due to glass compositions can be ascribed to the set of the reduced matrix elements [11]. The  $\langle {}^6\text{F}_{11/2} | U^{(2)} | {}^6\text{H}_{15/2} \rangle^2$  is the largest among three  $\langle |U^{(t)}| \rangle^2$  ( $t = 2, 4, 6$ ), thus the  $S_{JJ'}$  of this band is dependent on the  $\Omega_2$  of  $\text{Dy}^{3+}$  ion in the host. The  $\langle |U^{(2)}| \rangle^2$  of other transitions are small or zero and the  $S_{JJ'}$  of them is dependent mainly on  $\Omega_6$ . It is known that  $\Omega_2$  is affected by the local symmetry of ligand field and bond covalency [15]. The electronegativity of the anions is as follows;  $\text{S} < \text{O} < \text{F}$  [48]. Therefore, the chemical bond covalency between the

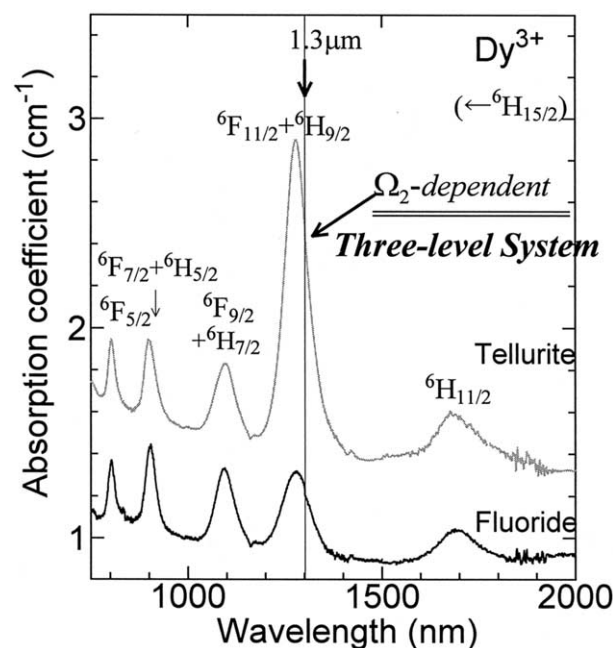


Fig. 13. Absorption spectra of  $\text{Dy}^{3+}$ -doped glasses.

Table 3. Lifetime and quantum efficiency of the  $\text{Dy}^{3+}$  level for 1.3- $\mu\text{m}$  emission in several glass systems.

| Host       | Lifetime ( $\mu\text{s}$ ) | Quantum efficiency |
|------------|----------------------------|--------------------|
| Pb–Bi–Ga–O | 5                          | 1.5% [53]          |
| Ge–Ga–S    | 38                         | 17% [12]           |
| Ga–La–S    | 59                         | 19% [13]           |
| Ge–As–Se   | 300                        | 90% [49]           |

$\text{Dy}^{3+}$  and the ligand varies with compositions:  $\text{Ga}_2\text{S}_3 > \text{TeO}_2 > \text{ZrF}_4 > \text{InF}_3$ . Therefore, the opposite tendency of  $\Omega_2$  and  $\Omega_6$  against glass compositions can be understood in terms of the differences in the bond covalency in the glasses [37].

### 5.2.2. Can dysprosium be a candidate?

Because of the large branching ratio and cross section of 1.3  $\mu\text{m}$ , an efficient amplifier can be expected if the nonradiative loss were reduced. Table 3 shows the lifetime and quantum efficiency of  $\text{Dy}^{3+}$  in several glasses. A selenide glass host can give 90% quantum efficiency [49], which is mainly due to the phonon energy being much smaller than even sulfides. This efficiency seems high enough for practical devices. Moreover, smaller electron-phonon coupling strength in chalcogenides [50] seems more promising for smaller multiphonon loss at levels with a small energy gap than in a host with comparable phonon energy, such as chlorides.

One more problem of  $\text{Dy}^{3+}$  is bottlenecking at lower levels with longer lifetimes resulting in depression of pumping efficiency and large emission intensities at longer-wavelength side [51], because the energy gap of the lower levels is larger than that of the 1.3- $\mu\text{m}$  level. If the quantum efficiency of the

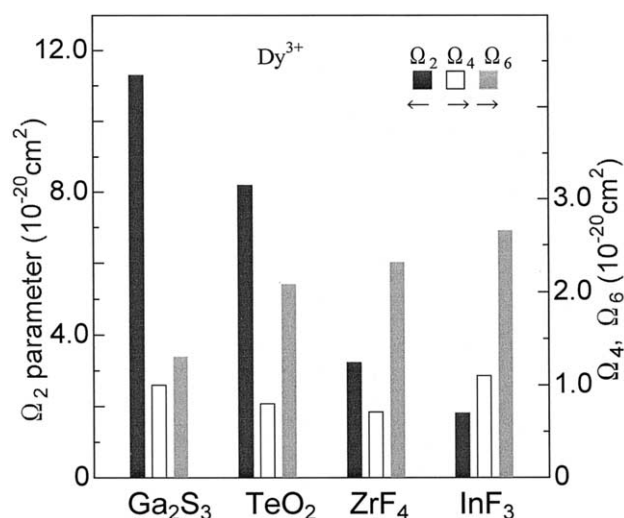


Fig. 14.  $\Omega_t$  parameters of  $\text{Dy}^{3+}$  ions in glasses.

1.3- $\mu\text{m}$  level is large enough, the effect of bottlenecking at lower levels would be negligible, since the excited initial state relaxes directly to the ground state due to the branching ratio of more than 90% [52]. There seems a great potential in Dy<sup>3+</sup>-doped chalcogenides. Further progress in the fabrication of low-loss single-mode fiber is expected.

## 6. Conclusions

The broad and flat spectral features of Er<sup>3+</sup>:1.55  $\mu\text{m}$  transition can be obtained in novel glass compositions

with a large  $\Omega_6$  parameter. The Er<sup>3+</sup> spectral change is accompanied by compositional evolution of Er–O bond ionicity and local structure.

The Tm<sup>3+</sup>:1.46  $\mu\text{m}$  transition shows high quantum efficiency in heavy metal oxide glasses due to the larger energy gap of the <sup>3</sup>H<sub>4</sub> level than the Pr<sup>3+</sup>:<sup>1</sup>G<sub>4</sub>. Selective quenching of the terminal level is possible in a Ho-codoped system.

New materials are expected for the optical amplifiers in the future WDM network system, to control the 4f transitions of RE ions, which show a variety of spectroscopy in glasses.

## References

- [1] R.J. Mears, L. Reekie, I.M. Jauncey, D.N. Payne, Tech. Digest OFC/IOOC'87, Reno, Nevada, 1987, p. 167.
- [2] C.J. Koestner, E. Snitzer, Appl. Opt. 3 (1964) 1182.
- [3] S.B. Poole, D.N. Payne, M.E. Fermann, Electron. Lett. 21 (1985) 737.
- [4] E. Snitzer, H. Po, F. Hakimi, R. Tumminelli, B.C. McCollum, Tech. Digest OFC'88, 1988, p. 447.
- [5] E. Snitzer, R. Woodcock, Appl. Phys. Lett. 6 (1965) 45.
- [6] A. Mori, Y. Ohishi, M. Yamada, H. Ono, Y. Nishida, K. Oikawa, S. Sudo, OFC'97, 1997, PD1.
- [7] Y. Ohishi, T. Kanamori, T. Kitagawa, S. Takahashi, E. Snitzer, G.H. Sigel Jr, Opt. Lett. 16 (1991) 1747.
- [8] E. Ishikawa, H. Tawarayama, K. Ito, H. Aoki, H. Yanagita, H. Toratani, Tech. Rep. IECIE, 1996 OPE96-111.
- [9] K. Wei, D.P. Machewirth, J. Wenzel, E. Snitzer, G.H. Sigel, Opt. Lett. 19 (1994) 904.
- [10] D.W. Hewak, B.N. Samson, J.A. Medeiros Neto, R.I. Laming, D.N. Payne, Electron. Lett. 30 (1994) 968.
- [11] S. Tanabe, T. Hanada, M. Watanabe, T. Hayashi, N. Soga, J. Am. Ceram. Soc. 78 (1995) 2917.
- [12] <http://www.joho.soumu.go.jp/pressrelease/japanese/tsusin/000615j502.html>.
- [13] J. Ballato, R. Riman, E. Snitzer, J. Non-Cryst. Solids 213–214 (1997) 126.
- [14] S. Tanabe, K. Hirao, N. Soga, J. Non-Cryst. Solids 113 (1989) 178.
- [15] S. Tanabe, K. Hirao, N. Soga, J. Non-Cryst. Solids 142 (1992) 148.
- [16] S. Tanabe, S. Todoroki, New Glass 7 (1992) 189.
- [17] S. Tanabe, K. Suzuki, N. Soga, T. Hanada, J. Lumin. 65 (1995) 247.
- [18] C.A. Brackett, J. Lightwave, Technol. 14 (1996) 936.
- [19] W.T. Carnal, P.R. Fields, K. Rajnak, J. Chem. Phys. 49 (1968) 4424.
- [20] S. Tanabe, T. Hanada, J. Non-Cryst. Solids 196 (1996) 101.
- [21] S. Tanabe, T. Ohyagi, S. Todoroki, T. Hanada, N. Soga, J. Appl. Phys. 73 (1993) 8451.
- [22] S. Tanabe, T. Hanada, T. Ohyagi, N. Soga, Phys. Rev. B 48 (1993) 10591.
- [23] S. Tanabe, S. Yoshii, K. Hirao, N. Soga, Phys. Rev. B 45 (1992) 4620.
- [24] B.R. Judd, Phys. Rev. 127 (3) (1962) 750.
- [25] G.S. Ofelt, J. Chem. Phys. 37 (3) (1962) 511.
- [26] M.J. Weber, Phys. Rev. 157 (1967) 262.
- [27] S. Tanabe, T. Ohyagi, N. Soga, T. Hanada, Phys. Rev. B 46 (1992) 3305.
- [28] N. Sugimoto, S. Tanabe, S. Ito, T. Hanada, Proc. 10th Meeting Glasses for Photonics, Tokyo, January 1999, p. 32.
- [29] H. Taga, Tech. Digest 10th Optical Amplifiers and their Applications, OSA, Washington, DC, June 1999, WC1, 1999, p. 22.
- [30] A. Mori, Y. Ohishi, S. Sudo, Electron. Lett. 33 (10) (1997) 863.
- [31] J.S. Wang, E.M. Vogel, E. Snitzer, Opt. Mater. 3 (1994) 187.
- [32] T. Sakamoto, A. Aozasa, T. Konamori, K. Hoshino, M. Yamada, M. Shimizu, Tech. Digest 10th Optical Amplifiers and their Applications, OSA, Washington DC, June, 1999, WD2-1, p. 50.
- [33] R.M. Percival, D. Szebesta, J.R. Williams, Electron. Lett. 30 (13) (1994) 1057.
- [34] T. Sakamoto, M. Shimizu, T. Kanamori, Y. Terunuma, Y. Ohishi, M. Yamada, S. Sudo, IEEE Photonics Tech. Lett. 7 (9) (1995) 983.
- [35] T. Komukai, T. Yamamoto, T. Sugawa, Y. Miyajima, IEEE J. Quantum Electron. 31 (11) (1995) 1880.
- [36] S. Tanabe, K. Suzuki, N. Soga, T. Hanada, J. Opt. Soc. Am. B 11 (5) (1994) 933.
- [37] S. Tanabe, K. Tamai, K. Hirao, N. Soga, Phys. Rev. B 53 (13) (1996) 8358.
- [38] S. Tanabe, T. Kouda, T. Hanada, Opt. Mater. 12 (1999) 35.
- [39] T. Kasamatsu, Y. Yano, H. Sekita, Opt. Lett. 24 (23) (1999) 1684.
- [40] P.M. Percival, D. Szebesta, S.T. Davey, Electron. Lett. 29 (12) (1993) 1054.
- [41] S. Tanabe, K. Tamai, K. Hirao, N. Soga, Phys. Rev. B 47 (5) (1993) 2507.
- [42] S.E. Stokowsky, R.A. Saroyan, M.J. Weber, Nd-doped laser glass spectroscopic and physical properties, Lawrence Livermore National Laboratories, University of California, CA, 1981.
- [43] S.G. Grubb, W.L. Barnes, E.R. Taylor, D.N. Payne, Electron. Lett. 26 (1990) 121.
- [44] T. Whitley, R. Wyatt, D. Szebesta, S. Davey, J.R. Williams, Tech. Digests OAA'92, Washington, DC, 1992, PD4.
- [45] Y. Ohishi, J. Temmyo, Bull. Ceram. Soc. Jpn 28 (1993) 110.
- [46] C.K. Jørgensen, B.R. Judd, Mol. Phys. 8 (1964) 281.
- [47] M.J. Weber, in: H.M. Crosswhite, H.M. Moos (Eds.), Optical Properties of Ions in Crystals, Wiley-Interscience, New York, USA, 1966, p. 467.
- [48] L. Pauling, The Nature of Chemical Bond, 3rd ed., Cornell University Press, Ithaca, New York, 1960, p. 93.
- [49] L.B. Shaw, B.J. Cole, J.S. Sanghera, I.D. Aggarwal, D.T. Schaafsma, OFC'98 Tech. Digest, WG8, 1998, p. 141.
- [50] S. Tanabe, in: G. Adachi (Ed.), Science of Rare Earths, Kagaku-Dojin Kyoto, 1999, p. 780 (in Japanese).
- [51] B.N. Samson, T. Schweitzer, D.W. Hewak, R.I. Laming, Opt. Lett. 22 (1997) 703.
- [52] J. Heo, Y.B. Shin, H.-S. Kim, Tech. Digest OFC'99, San Diego, CA, USA, February 1999 #WG7, p. 120.
- [53] Y.-G. Choi, J. Heo, J. Non-Cryst. Solids 217 (1997) 199.



ELSEVIER

Optical Materials 16 (2001) 93–103



www.elsevier.nl/locate/optmat

# Towards rare-earth clustering control in doped glasses

F. Auzel \*, P. Goldner

*Groupe Optique des Terres Rares, CNRS, UPR 211, 1 Pl. A.Briand, 92190 Meudon, France*

## Abstract

In this paper, the basic limitation for optical amplifiers linked with the existence of the so-called clustering of rare-earth (RE) ions is addressed. Clusters of RE dopant are related both to what could be called “interaction clusters” and to “chemical clusters”. Such interaction clusters do not depend on the chemical processes of the glass preparation and cannot be reduced through it. However, the existence of chemical clusters of spatial extension of a few Å can tremendously increase ion–ion interactions of all kinds. The physical process of co-operative luminescence is closely related to chemical clustering. Using this effect with  $\text{Yb}^{3+}$  as a probing ion, clear signatures of RE clusters can be obtained for different glass compositions and RE concentrations. Developing this approach, a new doping principle is proposed. It is based on the recognition that introducing the doping RE into the glass composition through given precursor crystals with large RE–RE distances, allows some control of the clustering of RE ions and of their self-quenching. So even after complete melting of the precursor and independently of the final glass composition the glass is shown to keep some memory of the doping procedure. © 2001 Elsevier Science B.V. All rights reserved.

*Keywords:* Rare-earth clusters; Co-operative luminescence; Doping process; Er-doped glasses

## 1. Introduction

Though one of the recent major application breakthroughs in the rare-earth (RE) field is the general use of erbium-doped fibre amplifiers (EDFA) for optical communications, such amplifiers are still bulky and expensive which limit them to terrestrial long trunk and under-sea cable applications. In order to obtain compact amplifiers for the distribution network, doping concentration has to be increased up to the chemical and physical limits.

It has been recently proposed that the physical process of co-operative luminescence be closely related to chemical clustering and that using this

effect with  $\text{Yb}^{3+}$  as a probing ion, clear signatures of RE clusters could be obtained for different glass compositions and RE concentrations [1–3]. In addition, a systematic study has been performed on silica and boro-silica glasses, confirming the clear influence of the composition on co-operative emission intensity [4].

Along these lines, a new doping principle has also been proposed [2,3]. It is based on the simple recognition that during crystal growing, the various atomic forces at the atomic scale are able to define the atomic positions of atoms with the crystal cells’ regularity. In particular, in the case of a crystal with RE as constituents, the RE–RE distances are automatically fixed by the crystal nature. It is shown that introducing the doping RE into the glass composition through such precursor crystals allows some control of the clustering of RE ions even after complete melting of the

\* Corresponding author.

*E-mail address:* auzel@cnrs-bellevue.fr (F. Auzel).

precursor. This is found to be independent of the final glass composition which keeps some memory of the doping process. It is also found that mastering the clustering process allows some reduction of the self-quenching process for the useful transition at 1.5  $\mu\text{m}$  of  $\text{Er}^{3+}$ .

In this paper, the basic limitation linked with the existence of the so-called clustering of RE ions is addressed. It is first shown that the “clusters” of RE dopant, as found in the literature from fibre amplification experiments [5–10], are related to what could be called “interaction clusters” with size much larger than for “chemical clusters”. Such interaction clusters could have spatial extension of more than 20–100  $\text{\AA}$  for non-radiative interaction clusters and up to millimetres for radiative ones. Clearly such clusters have nothing to do with chemical clusters which are the only ones depending on the chemical processes of the glass preparation. The existence of chemical clusters of spatial extension of a few  $\text{\AA}$  would increase tremendously ion–ion interactions of all kinds. One needs to obtain signature of such clusters which are the only ones that chemistry could eventually modify.

In glasses, we have shown [1] that co-operative luminescence [11–13] is a phenomenon which, requesting very close proximity of interacting RE ions in order to be experimentally observable, is a very good signature of clusters constituted by ions at practical distances of less than about 5  $\text{\AA}$ . Such distances, or shorter, between interacting ions are also the order of magnitude of chemical clusters. Then if we are able to observe, even on bulk samples, a signature for clustering, it is worthwhile to propose new ways to introduce the doping ions inside the considered vitreous materials. In the following, using lattice cells as spacers fixed by nature, we show that the clustering of ions can be controlled to some extent.

## 2. The concentration of active ions in the vitreous medium and their limitations

### 2.1. The chemical limitation

As for the concentration increase, the limitations are first at the chemical level; either because

one-constituent glass leaves too little space to the large RE ions (1  $\text{\AA}$ ), which are rejected by the glass; this is the case for pure silica glass, where concentration is chemically limited to about 100 ppm ( $0.7 \times 10^{18} \text{ cm}^{-3}$ ) and this directs us towards multicomponent glasses; or because the RE elements behaving usually as glass modifiers and not as glass formers tend to devitrify glasses when they are incorporated at too high concentrations. We believe that it is this chemical limitation which for silica glasses has led to the useful introduction of Al in the glass composition [9,14] making more easier the homogeneous introduction of the RE even at low level concentration. On the other hand, multicomponent glasses, such as phosphate, allow high RE content before devitrification may occur; the highest chemical concentration we know for such a glass reaches  $3 \times 10^5$  ppm ( $2.2 \times 10^{21} \text{ cm}^{-3}$ ).

However, a high amount of active ions in the glass does not mean that it could be used usefully because then the physical limitation takes place.

### 2.2. The physical limitation

The concentration limitation takes place also at the physical level usually before the maximum chemical concentration is reached. This is due to the ion–ion interactions giving rise to “concentration quenching” which is excitation independent. The ion–ion transfer helps the excitation energy to be then diffused through the sample until some energy sink is encountered such as  $(\text{OH})^-$  radicals which are very effective. There is also the clustering of ions as revealed by energy transfers towards one of the both considered ions being already in an excited state; this effect giving rise to APTE up-conversion [12] is excitation dependent. Energy transfers by dipole–dipole interactions can take place at distance reaching 30  $\text{\AA}$ , whereas the chemical cluster effect, by definition, exists for nearby ions separated by distances less than a few  $\text{\AA}$  and for such a reason is very effective. There is also the radiative energy transfer when ions are in resonance; they can exchange real photons and this process can take place of course at macroscopic distances as revealed by the role of the

sample geometry on the lifetime measurement [15]. It means that millimeter or centimeter distances can be involved in diffusion between ions. This may also help in concentration quenching and up-conversion by energy transfers.

### 3. Clusters of active ions in doped glasses

#### 3.1. “Physical” or interaction clusters

Most of the information on clusters of RE in glass fibre for amplifying systems comes from amplifier studies and as such are macroscopic descriptions based on microscopic hypothesis about interactions between RE ions [5–10]. Besides self-quenching, the fact that there exists non-saturable absorption in Er-doped fibre below an excitation level of 1 W, together with a relative gain reduction when concentration is increased, leads to the consideration of the so-called pair-induced quenching or PIQ. It is in fact caused by a pair of ions connected by up-conversion energy transfers (APTE effect [12]). When both ions are in their intermediate excited state, they relax rapidly; one ion stays in its ground state (the origin of the non-saturable absorption), the other one in its doubly excited state relaxes losing useful energy.

In such a model nothing limits the clusters to a chemical cluster of limited size. In fact such description may involve clusters of size reaching even millimeter in the case of radiative diffusion or at least of several tens of Å size, far from what can be viewed as a chemical cluster. We would like to term such clusters observed by macroscopic measurements in fibre experiments: interaction clusters.

#### 3.2. Chemical clusters and their physical signature by a co-operative luminescence probe

APTE up-conversion (up-conversion by sequential energy transfers) does not correspond to the same order of perturbation as co-operative processes [12]. These last have to be considered only when the first cannot take place. Such is the case when energy levels do not exist to allow energy transfers, for example in Yb<sup>3+</sup> doped systems

[11]. Then co-operative up-conversion is likely within chemical clusters with distances between ions in the 5 Å range or less [1–3].

Fig. 1 presents the energy scheme and the typical up-conversion efficiencies for APTE effect and co-operative luminescence. Assuming that the ion–ion interaction between the two considered RE ions be of the same nature in both processes (e.g., dipole–dipole), APTE and co-operative luminescence could be observed at the same detectivity level only when the two involved ions are at very different distances of one from the other. On the average we shall have for the ratio of the critical distances  $R_0$  of both processes

$$\frac{R_{0(\text{coop})}}{R_{0(\text{APTE})}} \approx \left( \frac{\eta_{\text{APTE}}}{\eta_{\text{coop}}} \right)^{1/6} \approx (10^5)^{1/6} \approx 6.8,$$

where it is assumed that the ion–ion interaction is of the dipole–dipole type with an  $R^{-6}$  distance dependence. As typical  $R_0$  for such interaction ranges from 6 [15] to 30 Å [16],  $R_{0(\text{coop})}$  should be:  $30/6.8 \leq 4.5$  Å. In case of shorter range interaction, for instance of the dipole–quadrupole type which varies as  $R^{-8}$ , even shorter distances could be probed [13]. From this consideration, we had proposed that the co-operative luminescence of Yb<sup>3+</sup> ions be used as a probe for the chemical clustering of RE ions, assuming an analogous chemical behaviour for all ions in the RE series [1,2].

### 4. Proposition for a new doping principle: consideration of the crystalline doping precursor

From the literature, one finds that doping oxide glasses with RE ions is usually performed by chemically introducing RE in the form of its oxide RE<sub>2</sub>O<sub>3</sub> or for fluoride with the RE fluoride RE F<sub>3</sub> or by one of both for fluorophosphate glasses. A good sample of such a general principle is found for instance in the review book “Nd-doped laser glass, spectroscopic and physical properties” [17], where for 250 various compositions of glasses from 11 different industrial origins, all presented glass examples make use of the above way in introducing the doping RE ion. For concentrations

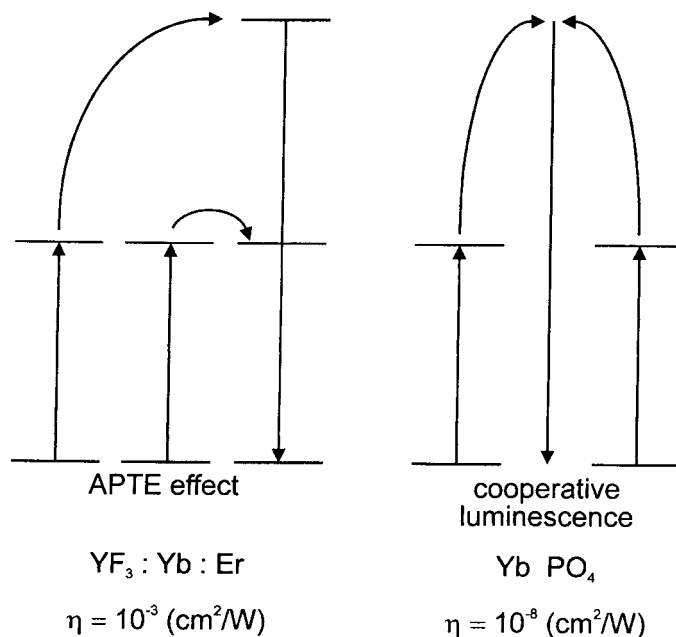


Fig. 1. Energy scheme for APTE and cooperative up-conversion for Yb–Er and Yb ion system and their respective efficiencies [3].

below  $10^{20} \text{ cm}^{-3}$ , such a usual method does not show its drawback which we believe is that, during the dissolution process of the glass melting, some ions stay aggregated at the initial minimum inter-ionic distances. For  $\text{RE}_2\text{O}_3$  and for  $\text{REF}_3$  these distances are, respectively, 3.5 and 3.6 Å. These distances are evidently much shorter than the average distance given by statistics for an homogeneous distribution

$$R_{\text{A}} = 6.17 \times 10^7 (c_{\text{cm}^{-3}})^{-1/3}$$

from which at  $10^{20} \text{ cm}^{-3}$ , one obtains  $R_{\text{A}} = 13.4 \text{ Å}$ , much larger than the minimum distance of the doping species. It is quite likely then that in the melted glass some oxide or fluoride-rich zones still exist where the RE–RE minimum distance is the one of the doping RE oxide or fluoride, that is much shorter than 13.4 Å. From such hypothesis we have proposed [2,3] that the doping ion be introduced from precursor crystallites with already large minimum RE–RE distances. During the crystallite synthesis the very existence of well-defined crystal cells ensures that even in case the dissolution of the RE doping is not homogenised

by the melting process, the large initial minimum distance between the RE ions is somewhat kept. From such hypothesis crystalline precursors with large RE–RE shortest distances have to be looked for.

One can make a choice from among the following list (Table 1), for which the minimum RE–RE distances are all larger than 4.5 Å.

Modifying only the RE doping precursor does not change the linear absorption spectra of the Yb-doping ion, as revealed by Fig. 2. It shows the classical  ${}^2\text{F}_{7/2} \rightarrow {}^2\text{F}_{5/2}$  absorption transition of an  $\text{Yb}^{3+}$ -doped phosphate glass (P) of fixed overall

Table 1  
Doping precursors with large RE–RE minimum distances<sup>a</sup>

| Doping crystalline precursors                                  | RE–RE minimum distances (Å) |
|--|-----------------------------|
| $\text{LnK}_5\text{Li}_2\text{F}_{10}$                         | 6.7                         |
| $\text{Na}_5\text{Ln}(\text{WO}_4)_4$                          | 6.45                        |
| $\text{LnAl}_3\text{B}_4\text{O}_{12}$                         | 5.9                         |
| $\text{LnLiP}_4\text{O}_{12}$ and $\text{LnKP}_4\text{O}_{12}$ | 5.6                         |
| $\text{LnP}_3\text{O}_9$                                       | 5.2                         |
| $\text{LnP}_5\text{O}_{14}$                                    | 5.2                         |

<sup>a</sup> Ln stands for the considered RE ion.

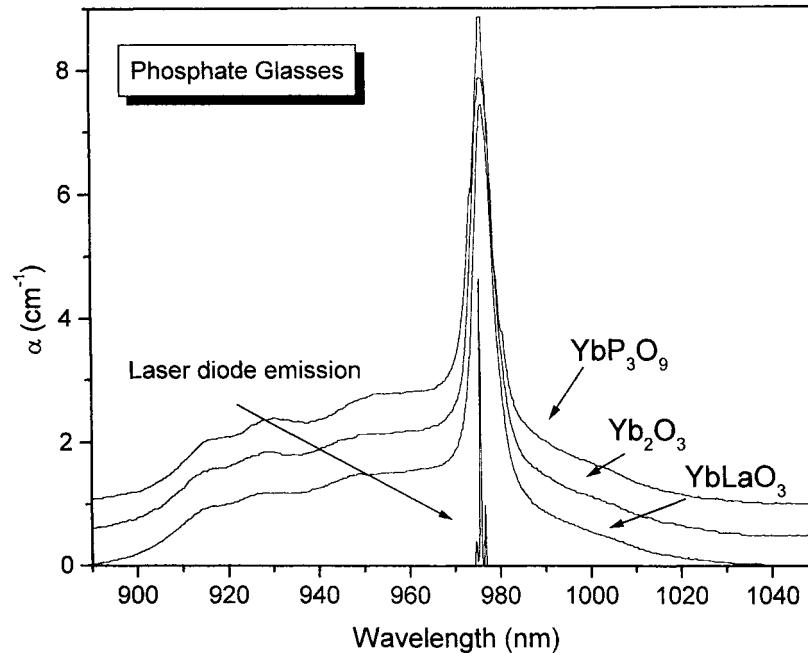


Fig. 2. Absorption spectra of the phosphate glass (P) doped at the same  $\text{Yb}^{3+}$  concentration with various doping precursors. Spectra have been arbitrarily shifted by  $0.5 \text{ cm}^{-1}$  in order to distinguish them more easily. The narrow lines show the laser diode emission.

composition ( $\text{P}_2\text{O}_5 = 80.99\%$ ;  $\text{MgO} = 7.65\%$ ;  $\text{Li}_2\text{O} = 11.36\%$ ) (percentage in weight) doped with various precursors in such a way that all glasses are  $\text{Yb}^{3+}$ -doped at the same level of  $5.2 \times 10^{20} \text{ cm}^{-3}$ . However, it should be noted that when the doping precursor contains ions which are not already in the glass composition is such as  $\text{YbLaO}_3$ ,  $\text{YbOF}$ , or  $\text{YbF}_3$  in the phosphate glass, the final doped-glass composition is slightly modified. The emission spectrum of the laser diode used for the co-operative luminescence excitation is also shown for information. It can be remarked that neither the shape nor the intensity of the absorption spectra are really modified by the doping procedure; the IR emission spectra are not modified either.

On the contrary, Fig. 3 reveals that the corresponding co-operative luminescence is largely modified in intensity by the doping precursor types. The co-operative signal is normalised by the coefficient:  $[\alpha(\lambda)\tau P(\lambda)]^2$  to take care of any eventual changes in the  ${}^2\text{F}_{5/2}$  lifetime, or absorption,  $\alpha(\lambda)$ , at the excitation wavelength of the laser di-

ode giving an excitation power density  $P(\lambda)$ . The variations of this coefficient are usually small because neither  $\tau$  nor  $\alpha(\lambda)$  are much modified by the nature of the precursor.

The less intense normalised co-operative signal is given by the precursor with the largest Yb–Yb shortest distance ( $\text{YbP}_3\text{O}_9$ :  $5.2 \text{ \AA}$ ), and the more intense by the precursors with the smallest shortest distances ( $\text{Yb}_2\text{O}_3$ :  $3.5 \text{ \AA}$ ). The fact that the glass doped with  $\text{YbLaO}_3$ , which has a slightly larger Yb–Yb distance ( $4.2 \text{ \AA}$ ), is found too near the one doped with  $\text{Yb}_2\text{O}_3$ , is attributed to the change in the overall composition due to the large amount of La introduced by the precursor and not present in the base glass. Its effect is not seen on the linear absorption spectrum. This again shows the higher sensitivity of the non-linear spectra to the doping process.

As an indication, the self-convolution shape of the IR emission spectrum is also plotted in Fig. 3 revealing the spectral zone where the co-operative signal is to be expected. Some emissions coming from the APTE emission of  $\text{Er}^{3+}$  and  $\text{Tm}^{3+}$

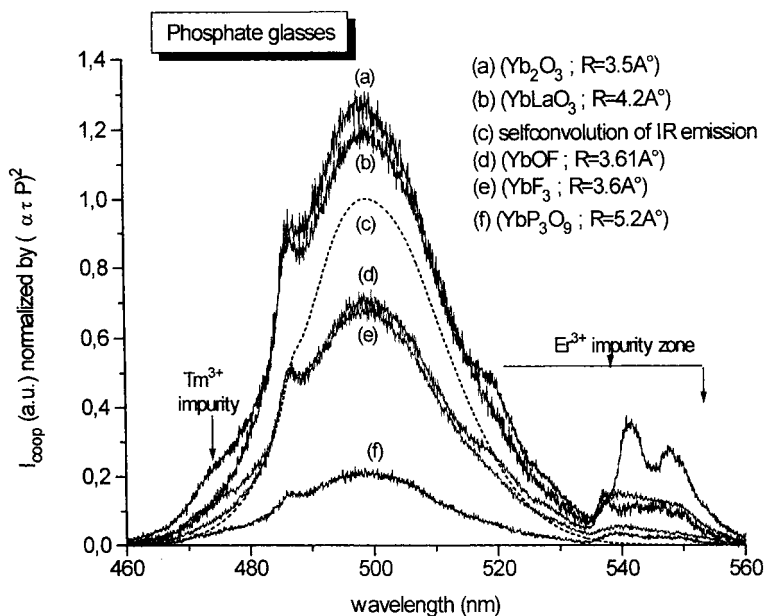


Fig. 3. Normalised blue co-operative emission from  $\text{Yb}^{3+}$  in the phosphate glass (P) doped with various doping precursors and  $\text{Yb}^{3+}$  IR emission self-convolution showing the spectral range for the clusters' emission against  $\text{Er}^{3+}$  and  $\text{Tm}^{3+}$  impurities up-conversion regions.

impurities can be observed, though their concentration (about 3 ppm) is a factor  $10^{-4}$  less than the  $\text{Yb}^{3+}$  one. This reflects the much larger efficiency of the APTE effect with respect to the co-operative one.

The influence of the  $\text{Yb}^{3+}$ -doping precursor on the co-operative signal has also been studied for a fluorophosphate glass (VF) of the following base composition before the dopant introduction:  $\text{MgF}_2 = 21.9\%$ ;  $\text{CaF}_2 = 14.8\%$ ;  $\text{BaF}_2 = 33.41\%$ ;  $\text{AlF}_3 = 21.9\%$ ;  $\text{P}_2\text{O}_5 = 11.8\%$ ;  $\text{La}_2\text{O}_3 = 0.85\%$ ;  $\text{Na}_2\text{O}_3 = 4.66\%$  (weight percentages).

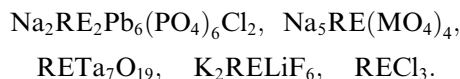
The various doping precursors are introduced in such a way that the total composition of the glass is kept identical with an  $\text{Yb}^{3+}$  concentration of  $8.8 \times 10^{20} \text{ cm}^{-3}$  (equivalent to 8% weight of  $\text{Yb}_2\text{O}_3$ ).

Fig. 4 presents the co-operative emission spectra for three precursors. Again the less intense emission is for the precursor with largest RE–RE shortest distances. The intense APTE parasitic spectra from Tm and Er impurities are linked to the fact that the APTE effect is more sensitive to non-radiative multiphonon transition within the

emitting impurity than the co-operative effect linked only with Yb and its two IR levels separated by a large gap.

Besides the precursor list given in Table 1, the range of new precursors can still be extended by the following remark.

When minimum RE–RE distances are not available for encompassed doping crystalline species, we propose to look for weak crystal field materials as defined by their scalar crystal field parameter  $N_v$  [18], because it has been shown that weak crystal field materials are generally those with large RE–RE distances [18]. They correspond to materials with  $N_v \leq 1800 \text{ cm}^{-1}$ . From such a consideration, the above list of doping precursors can with reasonable certainty be extended to



When pure fluoride and fluorooxide glasses are considered, fluoride precursors shall be used for fluoride glasses and/or oxide precursors for oxide and fluorooxide glasses.

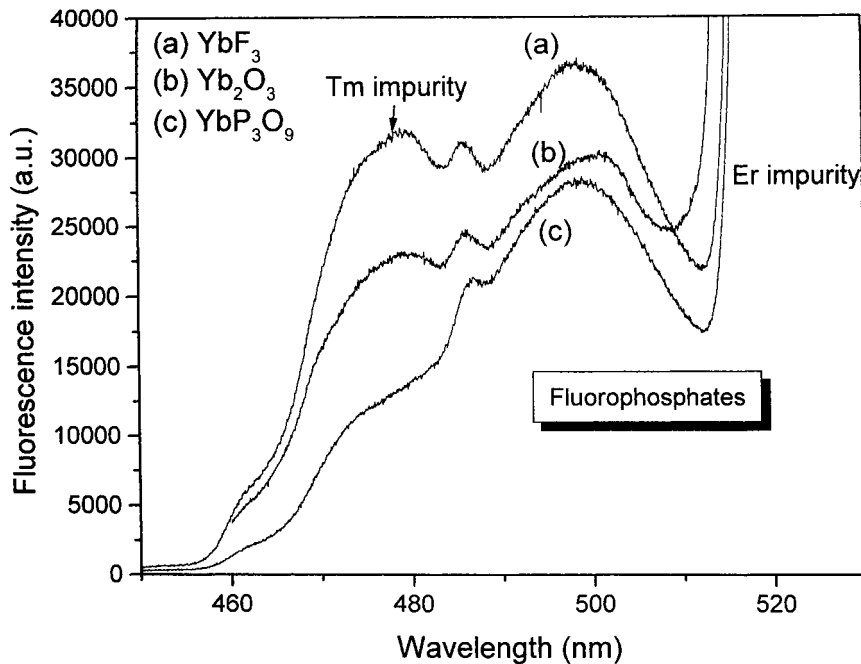


Fig. 4. Blue co-operative emission for the  $\text{Yb}^{3+}$ -doped fluorophosphate glass (VF) for different doping precursors.

It is worthwhile to recall here a particular result which could be a special case of the above doping procedure though different in its approach. In order to obtain low quenching Nd phosphate glasses, it has been proposed in [19] to look for glasses with chemical formulas in the neighbourhood of the ultraphosphate region that is near the pentaphosphate crystal composition which is known for its low Nd concentration quenching. However, the doping precursor is still here  $\text{Nd}_2\text{O}_3$  [20]. Because of the weak concentration quenching found for such glasses, we believe that during the glass making procedure of these phosphate glasses, at some initial step, the quasi-pentaphosphate Nd-microcrystal structures exist in the melt providing the large minimum RE-RE distance. It so provides a low Nd self-quenching through the lower ligand field at the Nd sites [18]. As shown below, concentration quenching can still be reduced by starting, even for such glasses, from  $\text{RE}_5\text{O}_{14}$  or  $\text{RE}_3\text{O}_9$  precursors instead of  $\text{RE}_2\text{O}_3$  ones as in [19]. A systematic study of the co-operative signal, the signature for our ion-clustering definition, has shown it to be reduced by a factor 1.4 near the

ultraphosphate region and 2.4 in the metaphosphate-orthophosphate one by using the  $\text{YbP}_3\text{O}_9$  precursor instead of  $\text{Yb}_2\text{O}_3$  [21]. This shows that even when the composition is favourable to a reduced ion-clustering, the proposed precursor approach can still reduce it further.

### 5. Co-operative emission and self-quenching of $\text{Er}^{3+}$ for different doping precursors

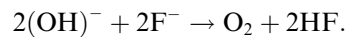
Though as stated in Section 2.2, the whole of concentration quenching is not due to the existence of clusters but also due to the diffusion to sinks (OH or other impurities) or due to other RE ions even far away from each other. We can however try to see what amount of such self-quenching may be linked to the existence of chemical clusters. We shall consider the phosphate glass (P), the fluorophosphate glass (VF) described above, and a tellurotungstate glass (TT), of the following composition: (molar percentages:  $\text{TeO}_2 = 58.73\%$ ;  $\text{Li}_2\text{O} = 14.67\%$ ;  $\text{Na}_2\text{O} = 10.24\%$ ;  $\text{WO}_3 = 16.36\%$ ).

The  $\text{Er}^{3+}$  self-quenching properties are characterised by the reduction of the emission lifetime of the  $\text{Er}^{3+} \ ^4\text{I}_{13/2}$  level with the doping  $\text{Er}^{3+}$  concentration. The various types of glasses described above have been studied for a each glass composition with an increasing Er concentration introduced either by  $\text{Er}_2\text{O}_3$  or by a large nearest distance precursor, here  $\text{ErP}_5\text{O}_{14}$  or  $\text{NaEr}(\text{WO}_4)_4$  (see Table 1).

Fig. 5 shows the lifetime behaviour of VF. The improvement brought about by the largest nearest RE–RE distance precursor is clearly observed. It is also the case for the TT glass (Fig. 6). However, for the phosphate glass, Fig. 7, no strong improvement can be found for the large nearest RE–RE distance precursor.

Comparing Figs. 5 and 7, one can see that for the P glass, there does not exist any plateau for the lifetime decay, contrary to the VF case; here, even at a weak concentration of  $10^{19} \text{ cm}^{-3}$ , already a strong self-quenching is revealed by the much lower lifetime value at weaker concentrations: 5 ms against 9 ms for VF.

Comparing the P and VF glasses, near-IR absorption spectra in the hydroxyl absorption spectral range reveal that VF glasses contain much less  $(\text{OH})^{-1}$  ions than P ones (see Fig. 8). From this, it can be understood that in P glasses most of the self-quenching process is mainly due to diffusion to  $(\text{OH})$  sinks through long distance Er–Er energy transfer more than to shorter Er–Er intra-cluster steps. The advantage of fluorophosphate over phosphate glasses has been known for a long time [22]: the Er lifetime is usually higher though using the same type of preparation because some destruction of  $(\text{OH})^{-}$  takes place through the following reaction:



Whatever the involved self-quenching process, it is interesting to quantify self-quenching by its rate,  $R_Q$ , for the various glasses and doping precursors of Figs. 5–7

$$R_Q = \frac{1}{\tau_{\text{large}}} - \frac{1}{\tau_{\text{weak}}},$$

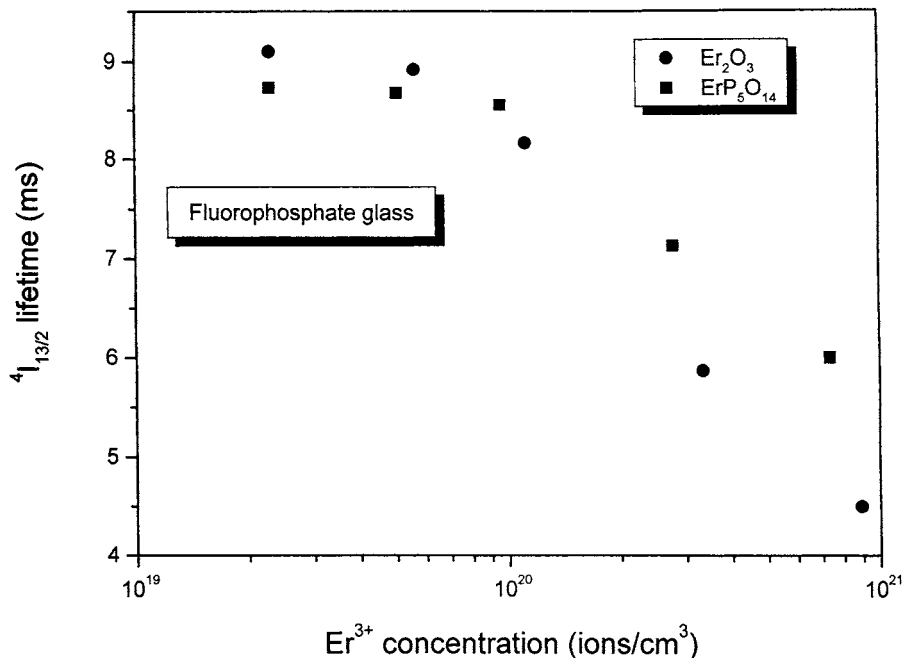


Fig. 5.  $\text{Er}^{3+}$  ( $^4\text{I}_{13/2}$ ) lifetime variation versus  $\text{Er}^{3+}$  concentration for two doping precursors in the fluorophosphate glass (VF).

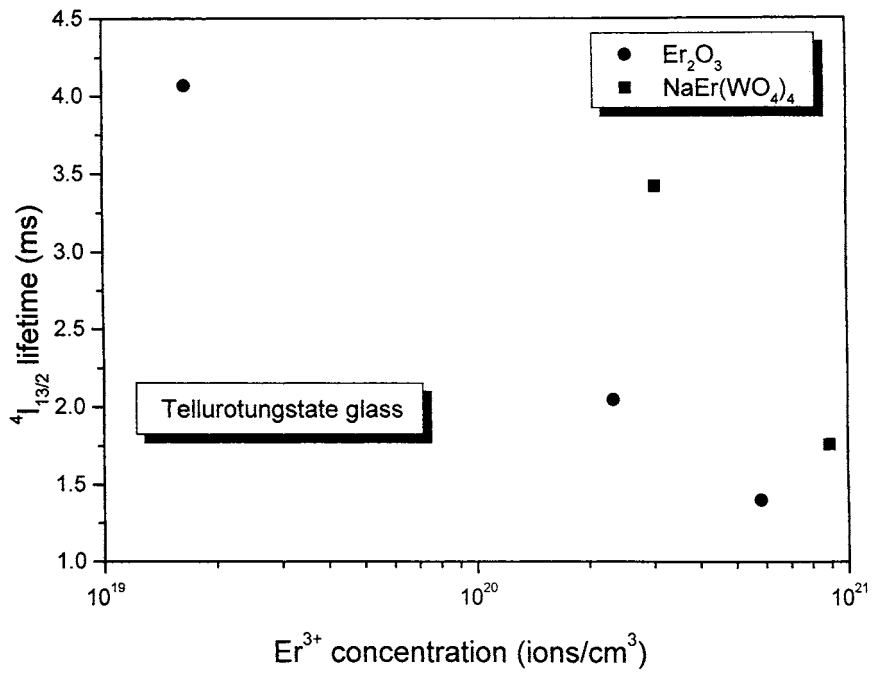


Fig. 6.  $Er^{3+}$  ( ${}^4I_{13/2}$ ) lifetime variation versus  $Er^{3+}$  concentration for two doping precursors in the tellurotungstate glass (TT).

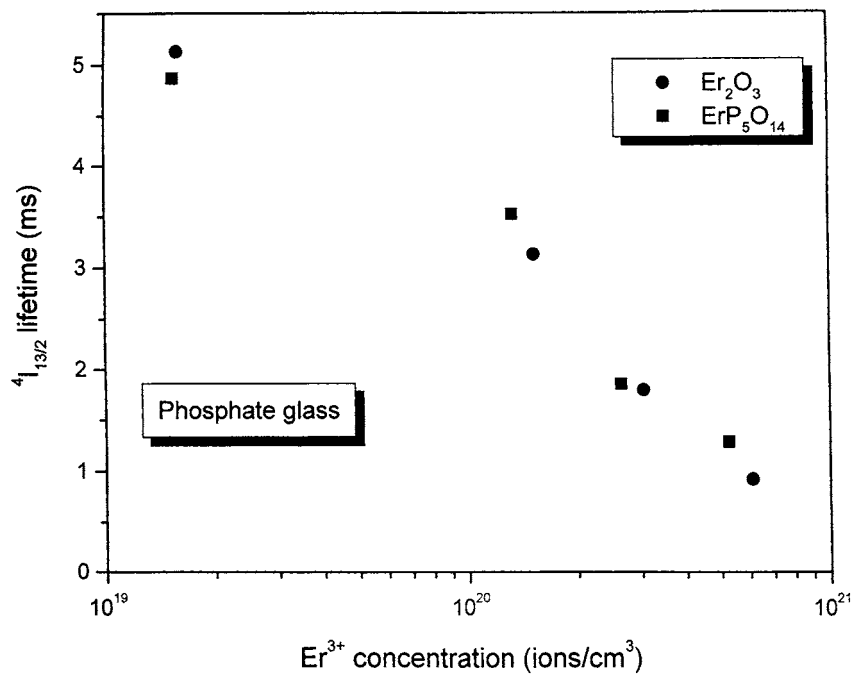


Fig. 7.  $Er^{3+}$  ( ${}^4I_{13/2}$ ) lifetime variation versus  $Er^{3+}$  concentration for two doping precursors in the phosphate glass (P).

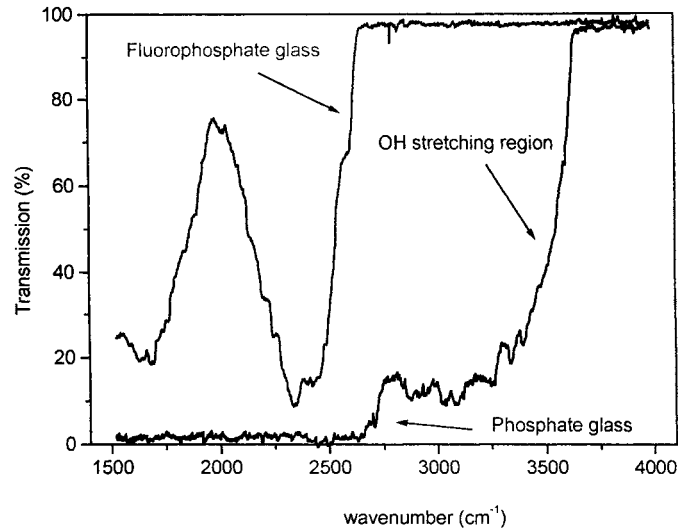


Fig. 8. Near IR transmission spectra of the phosphate (P) and of the fluorophosphate glass (VF) for same thicknesses; note for (P) the strong  $(\text{OH})^-$  absorption below  $3500 \text{ cm}^{-1}$ .

where  $\tau_{\text{weak}}$  is the measured lifetime ( ${}^4\text{I}_{13/2} \rightarrow {}^4\text{I}_{15/2}$  at  $1.54 \text{ m}$  in  $\text{Er}^{3+}$ ) at a concentration of  $1.5 \times 10^{19} \text{ cm}^{-3}$  of Er, and  $\tau_{\text{large}}$  is the same at  $6 \times 10^{20} \text{ cm}^{-3}$ .

Doping the above compositions by the usual  $\text{Er}_2\text{O}_3$  precursor provides the above weak and large concentrations of Er in glasses P, VF and TT, respectively, called samples A, C, E. The same concentrations are obtained by introducing crystallised  $\text{ErP}_5\text{O}_{14}$  giving samples B and D and by introducing Er in glass TT by the crystallised precursor  $\text{Na}_5\text{Er}(\text{WO}_4)_4$ , giving sample F. The self-quenching rates obtained for these various samples are given below in Table 2.

Table 2  
Self-quenching rate ( $R_q$ ) of  $\text{Er } {}^4\text{I}_{13/2}$  according to precursor type for different glasses

| Phosphate glass (P)                        | $R_q(\text{s}^{-1})$ |
|--|----------------------|
| A( $\text{Er}_2\text{O}_3$ )               | 918                  |
| B( $\text{ErP}_5\text{O}_{14}$ )           | 596                  |
| Fluorophosphate glass (VF)                 |                      |
| C( $\text{Er}_2\text{O}_3$ )               | 88                   |
| D( $\text{ErP}_5\text{O}_{14}$ )           | 41                   |
| Tellurotungstate glass (TT)                |                      |
| E( $\text{Er}_2\text{O}_3$ )               | 470                  |
| F( $\text{Na}_5\text{Er}(\text{WO}_4)_4$ ) | 172                  |

By the new doping process, self-quenching is shown to be still reduced by a factor of 1.5, in the phosphate glass P, though both types A and B are already of the ultraphosphate type according to Van Wazer definition [23].

Defining a ratio  $R$  as  $\text{M}_2\text{O}/\text{P}_2\text{O}_5$ , where “M is an equivalent of any cation or organic radical in a phosphate”, for  $0 \leq R \leq 1$ , one has the ultraphosphate class, for  $R = 1$  the metaphosphate one, for  $2 \leq R \leq 3$ , the pyro-orthophosphate class and for  $R = 3-4$ , the orthophosphate one. In Table 2 both glasses A and B having  $R = 0.9$  are in the orthophosphate class which by Denker et al. [19] should be of the weak quenching type; yet doping by our precursor principle still improves the self-quenching reduction obtained by the ultraphosphate composition choice. This behaviour is confirmed by the co-operative luminescence signature [21].

Other glasses have reduced self-quenching by factors from 2.1 for the fluorophosphate to 2.7 for the tellurotungstate. The differences between the average self-quenching rates of the phosphate glass and the two others come from the larger water content of the former, which tends to reduce the contrast of the doping precursors' role. Present results confirm the self-quenching improvement due to the use of the new doping precursors:

factors of: 1.6, 3.2 and 1.8 had been, respectively, found for phosphate, fluorophosphate and phosphotungstate glasses [3]. The observed systematic in the self-quenching behaviour for the various precursors is a good proof of their role.

## 6. Conclusion

We have introduced a new doping principle, based on crystallised precursors with large minimum RE–RE distances or with low scalar crystal field values. This principle allows to reduce the chemical clustering effect as analysed from co-operative luminescence, independently of the glass compositions. It is also shown that this doping principle allows a reduction in the self-quenching processes for the part which can be attributed to clustering. We have presented here the effect of inorganic precursors. In organic molecules, still larger RE–RE minimum distances are available, of the order of 10 Å. This has induced us to consider organic doping precursors under crystalline powder form. Along this line, an RE-bipyridine precursor [24], has brought about a reduction of both the co-operative signature of Yb<sup>3+</sup> and the self-quenching of Er<sup>3+</sup> in a fluorophosphate glass, so bringing further support to our new doping principle.

## Acknowledgements

It is a pleasure to thank D. Meichenin and D. Morin formerly in our Laboratory at CNET, for their help in, respectively, setting up the first co-operative luminescence system and in preparing the first glass samples of this study. We thank also M. Genotelle for some of the fluorophosphate glass preparation.

## References

- [1] F. Auzel, D. Meichenin, F. Pellé, P. Goldner, *Opt. Mater.* 4 (1994) 35.
- [2] F. Auzel, D. Morin, Patent BF No. 96 13327, 1996.
- [3] F. Auzel, P. Goldner, *Mater. Sci. Forum* 315/317 (1999) 34.
- [4] B. Schaudel, P. Goldner, M. Prassas, F. Auzel, *J. Alloys Compd.* 300/301 (2000) 443.
- [5] P. Blixt, J. Nilsson, T. Carlén, B. Jaskorzynska, *IEEE Trans. Photon. Tech. Lett.* 3 (1991) 996.
- [6] G. Nykolak, P.C. Becker, J. Shmulovich, Y.H. Wong, D.J. DiGiovanni, A.J. Bruce, *IEEE Photon. Tech. Lett.* 5 (1993) 1014.
- [7] E. Delevaque, T. Geoges, M. Monerie, P. Lamouler, J.F. Bayon, *IEEE Photon. Tech. Lett.* 5 (1993) 73.
- [8] J. Nilsson, B. Jaskorzynska, P. Blixt, *IEEE Photon. Tech. Lett.* 5 (1993) 1427.
- [9] R.S. Quimby, W.J. Miniscalco, B. Thomson, *J. Appl. Phys.* 76 (1994) 4472.
- [10] E. Maurice, G. Monnom, B. Dussardier, D.B. Ostrowsky, *Opt. Lett.* 20 (1995) 2487.
- [11] E. Nakazawa, S. Shionoya, *Phys. Rev. Lett.* 25 (1970) 1710.
- [12] F. Auzel, *J. Lumin.* 45 (1990) 341.
- [13] P. Goldner, F. Pellé, D. Meichenin, F. Auzel, *J. Lumin.* 71 (1997) 137.
- [14] B.J. Ainslie, *J. Lightwave Tech.* 9 (1991) 220.
- [15] F. Auzel, *Ann. Telecom. (Paris)* 24 (1969) 363.
- [16] G. Blasse, in: K.A. Gschneider, L. Eyring (Eds.), *Handbook on the Physics and Chemistry of Rare-Earth*, vol. 4, North-Holland, Amsterdam, 1979, p. 253.
- [17] S.E. Stokowski, R.A. Saroyan, M.J. Weber, vols. 1 and 2, Lawrence Livermore National Laboratory, University of California, Livermore, 94550 California, 1988.
- [18] F. Auzel, *Mat. Res. Bull.* 14 (1979) 223.
- [19] B.I. Denker, V.V. Osiko, P.P. Pashinin, A.M. Prokhorov, *Sov. J. Quantum Electron.* 11 (1981) 289.
- [20] Y. Voronko, B.I. Denker, A.A. Zlenko, A.Y. Karasik, Y.S. Kuzminov, G.V. Maksimova, V.V. Osiko, A.M. Prokhorov, V.A. Sychugov, G.P. Shipulo, I.A. Shcherbakov, *Sov. Phys. Dokl.* 21 (1976) 146.
- [21] P. Goldner, B. Schaudel, F. Auzel, *J. Lumin.* (2000) (to be published).
- [22] F. Auzel, D. Morin, French patent No. 1.527.101, 1967.
- [23] J.R. Van Wazer, *Phosphorus and its Compounds*, vol. 1, Interscience, New York, 1958, p. 421.
- [24] F. Auzel, P. Goldner, G.F. de Sa, *J. Non-Cryst. Solids* 265 (2000) 185.

## INTENSITIES OF 4f-4f TRANSITIONS IN GLASS MATERIALS

Oscar L. Malta\*

Departamento de Química Fundamental, Centro de Ciências Exatas e da Natureza, Universidade Federal de Pernambuco, 50670-901 Recife - PE

Luís D. Carlos

Departamento de Física, Centro de Investigação em Materiais Cerâmicos e Compósitos, Universidade de Aveiro, 3810-193 Aveiro, Portugal

Recebido em 2/12/02; aceito em 10/4/03

In this article we review some of the basic aspects of rare earth spectroscopy applied to vitreous materials. The characteristics of the intra-atomic free ion and ligand field interactions, as well as the formalisms of the forced electric dipole and dynamic coupling mechanisms of 4f-4f intensities, are outlined. The contribution of the later mechanism to the 4f-4f intensities is critically discussed, a point that has been commonly overlooked in the literature of rare earth doped glasses. The observed correlation between the empirical intensity parameter  $\Omega_2$  and the covalence of the ion first coordination shell is discussed accordingly to the theoretical predictions.

Keywords: rare earth ions; photoluminescence spectroscopy; 4f-4f intensities.

### INTRODUCTION

Glass materials containing trivalent rare earth ions have been widely studied due to their potential applications as optical devices (lasers and fibers for optical amplifiers, among others) or as the active component in photonics<sup>1-3</sup>. For instance, high-power terawatt lasers ( $10^{12}$  W is equivalent to 1000 joules released in a nanosecond pulse) incorporating Nd<sup>3+</sup> ions are currently used for thermonuclear fusion<sup>1</sup>. Recently there has been also a great deal of interest in the conversion of infrared into visible light by energy up-conversion, due to the potential application in photonics, including optical data storage, lasers, sensors, and optical displays<sup>5,6</sup>. The rare-earth doped glasses have indeed a great advantage over crystalline systems since generally they can be easily prepared with high optical quality and in a large variety of chemical compositions. They can be used either in large bulk devices or in optical fiber waveguides to confine the pumping light with a high density over a long interaction length.

The optical properties of these materials are directly related to the 4f-4f transitions in a 4f<sup>N</sup> electronic configuration. In our days, the theoretical background for the rationalization of these intraconfigurational transitions, both radiative and non-radiative, is well established<sup>7-17</sup>. The standard Judd-Ofelt theory<sup>7,8</sup> has been used to evaluate absorption and emission cross-sections in the great majority of the works on these rare earth doped glasses. The so-called intensity parameters  $\Omega_\lambda$  ( $\lambda = 2, 4$  and  $6$ ) have been used to give information on covalency, quality and mechanical properties of the medium<sup>1</sup>. Nevertheless, a certain number of problems still exist, related to the application of the theory and to the interpretation of results obtained from it, particularly in the case of glasses, as one may note from the literature. Among these problems we may emphasize the systematic neglect of the dynamic coupling mechanism contributing to the 4f-4f intensities<sup>10-14,16</sup>.

We wish here to outline the main aspects of the aforementioned theoretical background and to discuss briefly some rather problematic

points concerning the use of the theory and the interpretation of results.

### SOME CHARACTERISTICS OF THE RARE EARTH IONS

#### The Hamiltonian for the free ion

The Hamiltonian,  $H_{FI}$ , for the rare earth free ion is composed by one part due to the central field,  $H_0$ , and by several other interactions, which are generally treated as perturbations. Among these interactions the interelectronic repulsion,  $H_c$ , and the spin-orbit interaction,  $H_{so}$ , are the most relevant.

$$H_{FI} = H_0 + H_c + H_{so} \quad (1)$$

The magnitudes of these interactions follow the order  $H_0 > H_c > H_{so}$ .

In the diagonalization procedure of the Hamiltonian  $H_{FI}$  the spin-spin, spin-other-orbit and orbit-orbit interactions are in general of much less importance. Thus, in a first step, the eigenfunctions of  $H_{FI}$  may be constructed from the eigenfunctions of the angular momentum operators  $L^2$ ,  $S^2$ ,  $J^2$  and  $J_z$ .  $L$  is the total orbital angular momentum,  $S$  the total spin angular momentum,  $J$  the total angular momentum,  $J = L+S$ ,  $J_z$  the z component of  $J$ , with  $L = \sum \ell_i$  and  $S = \sum s_i$ ,  $\ell$  and  $s$  being mono-electronic orbital and spin angular momentum, respectively. The quantum number  $J$  ( $MJ = -J, -J+1, \dots, +J$ ) must satisfy the condition  $|L - S| \leq J \leq L+S$ . For rare earth ions, an adequate scheme to represent a basis of eigenfunctions is the well-known L-S coupling scheme  $|4f^N \alpha SLJM_J\rangle$ . This notation implies that these eigenstates are pure 4f<sup>N</sup> states, or, in other words, no configuration interaction (CI) via  $H_{FI}$  is taken into account. CI effects, for each given case, have been considered without increasing the dimension of the matrix  $[H_{FI}]$  through the use of effective operators acting within the 4f<sup>N</sup> configuration.

In the construction of the eigenstates  $|4f^N \alpha SLJM_J\rangle$  one frequently finds that they are not unambiguously defined by the quantum numbers  $S, L, J$  and  $M_J$ . This problem can be solved by the

\*e-mail: omlm@npd.ufpe.br

use of group theory. Racah<sup>18</sup> has demonstrated that the irreducible representations of certain sub-groups of the  $GL(4\ell + 2)$  continuous group may be used as quantum numbers to classify these eigenstates. This is due to the fact that they form bases for these irreducible representations. Thus, in the above scheme  $\alpha$  represents the set of additional quantum numbers necessary to specify the eigenstate. A common procedure in the literature has been to diagonalize the Hamiltonian  $H_{FI}$  on a basis formed by the above eigenstates. The usual form of  $H_{FI}$  is<sup>19,20</sup>:

$$H_{FI} = E_b(4f^N) + \sum_{k=0,1,2,3} E_k e_k + \zeta_{4f} \sum_i \bar{\ell}_i \cdot \bar{s}_i + CI \quad (2)$$

where  $E_b$  is the energy of the baricenter of the  $4f^N$  configuration (eigenvalue of the central field Hamiltonian). The second and third terms in the right-hand-side of this expression correspond to the interelectronic repulsion and spin-orbit interaction, respectively. The last term contains configuration interaction effects. Matrix elements of the components in equation (2) are evaluated by irreducible tensor operator techniques<sup>19-22</sup>. The radial quantities in equation (2),  $E_k$  and  $\zeta_{4f}$ , the Racah and spin-orbit parameters, respectively, may in principle be calculated from *ab initio* methods (the  $E^0$  parameter can be absorbed by  $E_b$ ). However they are commonly treated as adjustable parameters, for which the input data are the experimentally observed energies of the baricenters of the J manifolds. The great advantage of this latter procedure is that, after diagonalization, one gets usually much more reliable free ion wavefunctions, what is essential to the evaluation of properties of rare earth ion doped materials.

### The eigenfunctions in the intermediate coupling

Taking into account the fact that the interelectronic repulsion is not diagonal in the quantum number  $\alpha$  and that the spin-orbit interaction is not diagonal in the quantum numbers  $\alpha$ , S and L, these latter are no longer good quantum numbers. As a consequence, after diagonalization of  $H_{FI}$ , the eigenstates will be given by a linear combination of the states  $|(4f^N)\alpha SLJM_J\rangle$ , that is,

$$|(4f^N)\psi JM_J\rangle = \sum_{\alpha SL} C(\alpha SL) |(4f^N)\alpha SLJM_J\rangle \quad (3)$$

in which the  $C(\alpha SL)$  coefficients of the linear combination satisfies the condition

$$\sum_{\alpha SL} |C(\alpha SL)|^2 = 1 \quad (4)$$

Equation (3) expresses the so-called intermediate coupling scheme. The eigenstates given in this scheme, as mentioned before, are essential to describe the behavior of rare earth ions. A good example is the case of transitions between multiplets of different multiplicities, which otherwise cannot be described. A typical case is illustrated by the transitions between the  ${}^5D_J$  and  ${}^7F_J$  multiplets of the  $\text{Eu}^{3+}$  ion. Labeling a multiplet by the usual notation  ${}^{2S+1}L_J$  is a mere indication of the dominant component in the summation in equation (3). An interesting and useful aspect is that, since a rather weakly chemical environment affects the 4f orbitals, for each rare earth ion the eigenstates in the intermediate coupling scheme are essentially the same for different environments.

## THE LIGAND FIELD

### The usual form of the ligand field Hamiltonian

Although weak, the interaction between 4f electrons and the

chemical environment is responsible for the most interesting spectroscopic features of rare earth ions. The non-spherical even parity part of this interaction, responsible for the Stark splitting of 4f levels, is commonly written as:

$$H_{LF} = \sum_{k,q,i} B_q^k C_q^{(k)}(i) \quad (5)$$

where the  $B_q^k$ 's ( $k = 2, 4$  and  $6$ ) are the so-called ligand field parameters of even rank and  $C^{(k)}$  is a Racah tensor operator of rank  $k$ <sup>19-22</sup>. The values of  $k$  are restricted by parity and triangularity rules for f orbitals<sup>19,20</sup>. The allowed values of  $q$  depend on the symmetry of the ligand field around the rare earth ion, and in this expression the index  $i$  runs over the 4f electrons.

The Hamiltonian  $H_{LF}$  as given by equation (5) is a one-particle operator. A relevant point here is that the form of equation (5) has a more general character than it might be supposed, in the sense that all one particle ligand field models lead to this form of  $H_{LF}$ . Despite the fact that the  $B_q^k$ 's, for a given point symmetry, can be calculated from theoretical models, it has been a common practice to treat them also as adjustable parameters called phenomenological or experimental  $B_q^k$ 's. As for the case of the free ion radial parameters in equation (2), the input data are the observed energies of the 4f levels under the action of the ligand field. The total Hamiltonian to be diagonalized is now

$$H = H_{FI} + H_{LF} \quad (6)$$

The ligand field interaction is also of fundamental importance for the case of 4f-4f transition intensities. These transitions are in principle electric dipole forbidden by Laporte's rule. However, provided that the site occupied by the rare earth ion does not present a center of inversion, Laporte's rule is relaxed due to odd parity terms in the ligand field Hamiltonian. The more general form of  $H_{LF}$  is actually

$$H_{LF} = H_{LF}(\text{even}) + H_{LF}(\text{odd}) \quad (7)$$

It is important to note that if the diagonalization of the total Hamiltonian  $H$  in equation (6) is restricted to a basis formed by the states  $|(4f^N)\alpha SLJM_J\rangle$ , due to parity selection rules, the component  $H_{LF}(\text{odd})$  will have no effect on the final results. This odd component is generally expressed as:

$$H_{LF}(\text{odd}) = \sum_{t,p,i} \gamma_p^t r_i^t C_p^{(t)}(i) \quad (8)$$

where  $r_i$  is the radial coordinate of the  $i$ -th electron,  $\gamma_p^t$ 's ( $t = 1, 3, 5$  and  $7$ ) are the so-called odd rank ligand field parameters, and  $C^{(t)}$  is a Racah tensor operator of rank  $t$ . The values of  $t$  are restricted by parity and triangularity rules involving f, d and g orbitals<sup>7,8</sup>. Now the index  $i$  runs, in principle, over all electrons of the rare earth ion. As for the values of  $q$  in equation (5), the allowed values of  $p$  depend on the symmetry around the rare earth ion. In the case of intensities the role of  $H_{LF}(\text{odd})$  is to connect (mix) states belonging to electronic configurations of opposite parity. It follows that transitions between 4f levels become partially electric dipole allowed.

### The ligand field and symmetry

As previously mentioned, the values of  $q$  and  $p$  in equations (5) and (8), respectively, are restricted by the symmetry of the site occupied by the rare earth ion. Thus, for example, in a  $C_{4v}$  symmetry the allowed values are:  $k = 2, q = 0$ ;  $k = 4, q = 0, \pm 4$ ;  $k = 6, q = 0, \pm 4$ ;  $t = 1, p = 0$ ;  $t = 3, p = 0$ ;  $t = 5, p = 0, \pm 4$ ;  $t = 7, p = 0, \pm 4$ . This is

a consequence of the fact that the ligand field parameters are actually a summation over the individual contributions from the surrounding atoms. Each individual contribution behaves as the spherical harmonics and the summation vanishes in a given symmetry for certain values of  $q$  and  $p$ . A detailed work on this subject may be found elsewhere<sup>23,24</sup>.

One of the consequences of the action of  $H_{LF}$  (even) is that  $J$  is no longer a good quantum number. This produces the so-called  $J$ -mixing effect (a rather small effect due to the weak interaction between the 4f orbitals and the chemical environment), and as a result of the diagonalization of the total Hamiltonian  $H$  in equation (6) the final eigenstates have the general form:

$$|(4f^N)\Gamma\rangle = \sum_{\alpha,S,L,J,M_J} A(\alpha,S,L,J,M_J;\Gamma) |(4f^N)\alpha SLJM_J\rangle \quad (9)$$

with the condition

$$\sum_{\alpha,S,L,J,M_J} |A(\alpha,S,L,J,M_J;\Gamma)|^2 = 1 \quad (10)$$

Each eigenstate given by equation (9) is now labeled by an irreducible representation,  $\Gamma$ , of the symmetry point group.

In the case of glasses, since there is a variety of different sites that can be occupied by the rare earth ion, we cannot talk about a well-defined set of ligand field parameters. The Stark splitting is in general not well determined in this case, what makes it difficult to define even an average set of ligand field parameters.

In Figure 1 a schematic representation of the intra-atomic and ligand field interactions previously discussed is presented.

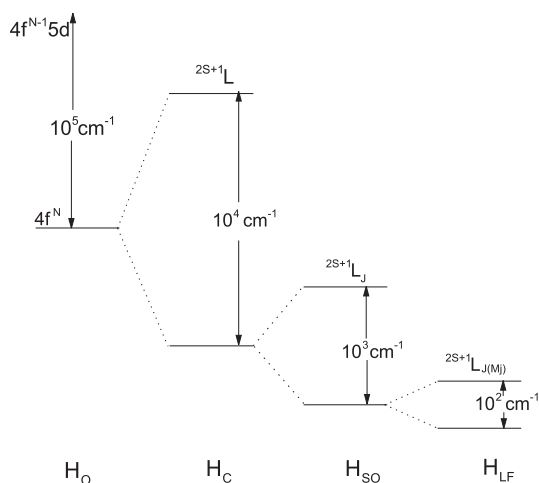


**Figure 1.** Schematic representation and order of magnitude of the effects of the intra-atomic and ligand field interactions acting on a  $4f^N$  configuration

## 4F-4F INTENSITIES

### Mechanisms of 4f-4f intensities

The characteristic absorption and emission spectra of rare earth compounds in the visible, near ultraviolet and near infrared is attributed to transitions between 4f levels, as they present sharp lines, mainly at low temperature, with oscillator strengths typically in the order of  $10^{-6}$ . These transitions are forbidden to first order by electric dipoles, but are allowed by the electric quadrupole, vibronic, magnetic dipole and forced electric dipole mechanisms. It has been noticed, since more

than fifty years ago, that among these only the magnetic dipole and forced electric dipole mechanisms could account for the observed intensities<sup>25</sup>. The magnetic dipole character of the  ${}^5D_0 \rightarrow {}^7F_1$  transition of the  $\text{Eu}^{3+}$  ion was demonstrated in 1939 by Deutschbein<sup>26</sup>. The coefficient of spontaneous emission between two manifolds  $J$  and  $J'$ , due to the magnetic dipole mechanism, is given by:

$$A_{J,J'} = \frac{4 e^2 \omega^3}{3 \hbar c^3} n^3 S_{\text{md}} \quad (11)$$

where the magnetic dipole line strength  $S_{\text{md}}$  (in units of  $e^2$ , where  $e$  is the electronic charge,  $e = -4.8 \times 10^{-10} \text{e.s.u.}$ ), is

$$S_{\text{md}} = \frac{\hbar^2}{4m_e c^2} \left\langle \left\langle (4f^N)\psi'J' \parallel L + 2S \parallel (4f^N)\psi J \right\rangle \right\rangle^2 \frac{1}{2J+1} \quad (12)$$

In the previous equations,  $\omega$  is the angular frequency of the  $J \rightarrow J'$  transition ( $\omega = 2\pi c\sigma$ ,  $\sigma$  being the transition energy in  $\text{cm}^{-1}$ ),  $n$  is the refraction index of the medium and the angular momentum operators  $L$  and  $S$  are in units of  $\hbar$ . The eigenstates in equation (12) are calculated using the intermediate coupling scheme. The magnetic dipole mechanism cannot account for most of the 4f-4f transitions in the rare earth series, not only because the predicted oscillator strengths are in general smaller than  $10^{-6}$  but also due to the restrictive selection rules on the  $J$  quantum number ( $\Delta J = 0, \pm 1$ ), as far as  $J$  is considered a good quantum number.

Judd<sup>7</sup> and Ofelt<sup>8</sup> treated the forced electric dipole mechanism in detail for the first time in 1962 through the powerful technique of irreducible tensor operators<sup>19-22</sup>. Two years later Jorgensen and Judd<sup>27</sup> studied the influence of an additional 4f-4f mechanism. It was originally referred to as the pseudoquadrupolar mechanism, due to inhomogeneities of the dielectric constant. The authors proposed that it could be as operative as, or, for some transitions, even more relevant than the forced electric dipole mechanism. These two processes will be briefly described in the next two sub-sections.

### The Judd-Ofelt theory

The electric dipole strength,  $S_{\text{ed}}$  (in units of  $e^2$ ), of a transition between two states  $\phi$  and  $\phi'$  is given by

$$S_{\text{ed}} = \left| \langle \phi' | \sum_i \bar{r}_i | \phi \rangle \right|^2 \quad (13)$$

If the states  $\phi$  and  $\phi'$  are pure  $4f^N$  states, as those given by equations (3) and (9), then by the parity selection rule (Laporte's rule) the dipole strength  $S_{\text{ed}}$  is identically null. However, provided that there is no center of inversion in the site occupied by the rare earth ion, this selection rule is relaxed by the odd component of the ligand field Hamiltonian,  $H_{LF}$  (odd), which mixes states of electronic configurations with opposite parity. Thus, since  $H_{LF}$  (odd) is a one particle operator, the configurations that can be mixed with the ground  $4f^N$  configuration are those of the type  $4f^{N-1}nd$ ,  $4f^{N-1}ng$  ( $n \geq 5$ ) and  $n'd^{4d+1}4f^{N+1}$  ( $d = 2, n' = 3$  and  $4$ , corresponding to core excitations). In the standard Judd-Ofelt theory the initial step is to consider this mixing by means of perturbation theory up to first order in the wavefunctions. If we take the perturbation on the eigenstates given by equation (9), then we may write:

$$|\phi\rangle = |(4f^N)\Gamma\rangle + \sum_{B\beta} \frac{\langle B\beta | H_{LF}(\text{odd}) | (4f^N)\Gamma \rangle}{E(\Gamma) - E(B\beta)} |B\beta\rangle \quad (14)$$

where  $B$  designates an excited configuration of opposite parity and  $\beta$  its states. The state  $|\phi'\rangle$  has a similar expression. The matrix element in equation (13), abbreviated as  $\bar{\mu}_{\text{ed}}$ , is consequently given by:

$$\bar{\mu}_{ed} = \sum_{\beta\beta'} \left[ \frac{\langle (4f^N)\Gamma' | \sum_i \bar{r}_i | B\beta \rangle \langle B\beta | H_{LF}(\text{odd}) | (4f^N)\Gamma \rangle}{E(\Gamma) - E(B\beta)} + \frac{\langle (4f^N)\Gamma' | H_{LF}(\text{odd}) | B\beta \rangle \langle B\beta | \sum_i \bar{r}_i | (4f^N)\Gamma \rangle}{E(\Gamma') - E(B\beta)} \right] \quad (15)$$

An interesting estimation of the 4f–4f oscillator strengths can be made from equation (15). For an electric dipole allowed transition the oscillator strength can be as high as 1. For rare earth ions the ligand field interaction is typically of the order of 100 cm<sup>-1</sup> and the interconfigurational energy differences for the lowest excited configuration of opposite parity (4f<sup>N-1</sup> 5d) is typically of the order of 10<sup>5</sup> cm<sup>-1</sup>. This gives a factor of 10<sup>-3</sup> in equation (15), which squared leads to the typical order of magnitude of 4f–4f oscillator strengths (10<sup>-6</sup>).

The summation over B and β in equation (15) reminds the possibility of using a closure procedure, and indeed this is the next step in the Judd-Ofelt treatment. This summation becomes much more treatable if one assumes that the intraconfigurational energy differences are much smaller than the energy differences between the baricenters of the ground and excited configurations. Or, in other words, if one assumes that E(Γ) - E(Bβ) ≅ E(Γ') - E(Bβ) ≅ E<sub>b</sub>(4f<sup>N</sup>) - E<sub>b</sub>(B) = ΔE(B). The main point now is to use the following relation involving two irreducible tensor operators x<sub>q</sub><sup>(k)</sup> = ∑<sub>i</sub> x<sub>q</sub><sup>(k)</sup>(i) and z<sub>q</sub><sup>(k')</sup> = ∑<sub>i</sub> z<sub>q</sub><sup>(k')</sup>(i)<sup>7,8</sup>.

$$\sum_{\beta} \langle (4f^N)\Gamma' | X_q^{(k)} | B\beta \rangle \langle B\beta | Z_q^{(k')} | (4f^N)\Gamma \rangle = \sum_{\lambda, Q} (-1)^Q (2\lambda + 1) \langle 4f | x^{(k)} | n\ell \rangle \langle n\ell | z^{(k')} | 4f \rangle \begin{pmatrix} k' & k & \lambda \\ q' & q & -Q \end{pmatrix} \begin{Bmatrix} f & k & \ell \\ k' & f & \lambda \end{Bmatrix} \langle (4f^N)\Gamma' | U_Q^{(\lambda)} | (4f^N)\Gamma \rangle \quad (16)$$

In this equation the quantities in ( ) and { } are 3-j and 6-j symbols, respectively<sup>19-22</sup>. The mono-electronic reduced matrix elements involving x<sup>(k)</sup> and z<sup>(k')</sup> contain the radial part corresponding to these operators, and U<sup>(λ)</sup> is an irreducible unit tensor operator<sup>19-22</sup>. In the case of core excitations (ℓ = d, n = 3 and 4) a minus sign appears in the right-hand-side of equation (16). In our case, the ranks k and k' are equal to 1 (from the dipole operator) and t (from H<sub>LF</sub>(odd)), respectively. Thus, it may be shown that the only difference between the two terms in the right-hand-side of equation (15) is in the 3-j symbols, which are related by

$$\begin{pmatrix} 1 & t & \lambda \\ q & p & -Q \end{pmatrix} = (-1)^{1+t+\lambda} \begin{pmatrix} t & 1 & \lambda \\ p & q & -Q \end{pmatrix}$$

Since t is odd only even values of λ will lead to nonvanishing values of μ<sub>ed</sub>. From the triangularity rules for the 6-j symbol in equation (16), it follows that λ ≤ 2t, i.e. λ ≤ 6. The unit tensor operator U<sup>(0)</sup> is a scalar and cannot contribute to transition probabilities. Therefore, the operative values of λ are 2, 4 and 6.

The matrix element μ<sub>ed</sub> may then be put in the form:

$$\bar{\mu}_{ed} = \sum_{\lambda, t, Q, p, q} (-1)^Q (2\lambda + 1) \begin{pmatrix} 1 & t & \lambda \\ q & p & -Q \end{pmatrix} B_{\lambda t p}^{ed} \langle (4f^N)\Gamma' | U_Q^{(\lambda)} | (4f^N)\Gamma \rangle \bar{e}_q^* \quad (17)$$

where the spherical unit vectors satisfy the condition  $\bar{e}_q^* \cdot \bar{e}_{q'} = \delta_{qq'}$ , and the quantities B<sub>λ t p</sub><sup>ed</sup> are given by:

$$B_{\lambda t p}^{ed} = \Xi(t, \lambda) \gamma_p^t \quad (18)$$

where

$$\Xi(t, \lambda) = 2 \sum_{n, \ell} \begin{Bmatrix} f & 1 & \ell \\ t & f & \lambda \end{Bmatrix} \langle f | C^{(0)} | \ell \rangle \langle \ell | C^{(0)} | f \rangle \langle 4f | r | n\ell \rangle \langle n\ell | r' | 4f \rangle \frac{1}{\Delta E(n\ell)} \quad (19)$$

If one is not interested in the transition intensities between Stark levels (Γ, Γ') but rather in the integrated intensities between J and J' manifolds, to a first approximation the J–mixing effects may be neglected and the 4f<sup>N</sup> eigenstates in equation (17) may be replaced by the eigenstates in the intermediate coupling scheme defined in equation (3). Thus, the total electric dipole strength is a sum over M<sub>J</sub> and M<sub>J'</sub> divided by 2J+1, assuming that the components of the initial J manifold are equally thermally populated. Using the Wigner-Eckart theorem and the orthogonality relation between 3–j symbols, it may be easily shown that the total electric dipole strength in equation (13) is then given by:

$$S_{ed} = \frac{1}{2J+1} \sum_{\lambda=2,4,6} \Omega_{\lambda}^{ed} \langle (4f^N)\Psi'J' | U^{(\lambda)} | (4f^N)\Psi J \rangle^2 \quad (20)$$

where

$$\Omega_{\lambda}^{ed} = (2\lambda + 1) \sum_{t, p} \frac{|B_{\lambda t p}^{ed}|^2}{2t + 1} \quad (21)$$

An alternative way of performing the summation in equation (15) has been the use of the average energy denominator method, introduced by Bebb and Gold<sup>28</sup>. The advantage is that one has to deal with a single average energy difference in equation (15). It has been shown that the predicted values of the so-called intensity parameters B<sub>λ t p</sub><sup>ed</sup> and Ω<sub>λ</sub><sup>ed</sup> are very similar to those given by the standard Judd-Ofelt treatment<sup>14</sup>. The coefficient of spontaneous emission taking into account both the forced electric dipole and the magnetic dipole mechanisms, is then given by:

$$A_{JJ'} = \frac{4e^2\omega^3}{3\hbar c^3} \left[ \frac{n(n^2+2)^2}{9} S_{ed} + n^3 S_{md} \right] \quad (22)$$

It should be noted, however, that the previous equation is valid as far as the J–mixing is neglected. Otherwise a cross term between the electric dipole and magnetic dipole transition moments may appear. The corresponding expression for the oscillator strength may be obtained from the relation:

$$P_{JJ'} = \frac{2J+1}{2J'+1} \frac{m_e c^3}{2\omega^2 e^2 n^2} A_{JJ'} \quad (23)$$

### The dynamic coupling

This mechanism was originally proposed by Jørgensen and Judd<sup>27</sup> in an attempt to explain the uncommon intensity variation of certain 4f–4f transitions denominated hypersensitive transitions. A simplified visualization of this mechanism is shown in Figure 2.

The incident radiation field induces oscillating dipoles in the surrounding atoms and, as a consequence, an additional oscillating electric field is produced. This electric field, being produced close to the rare earth ion, has large local gradients and may induce 4f–4f transitions with oscillator strengths in the order of, or even greater than 10<sup>-6</sup>. To a first approximation the induced oscillating dipoles depend on the isotropic dipolar polarizabilities of the surrounding atoms, α, as indicated in Figure 2. The interaction energy with the 4f electrons, H<sub>DC</sub>, is given by:

$$H_{DC} = e \sum_{i,j} \bar{\mu}_j \cdot \frac{(\bar{r}_i - \bar{R}_j)}{|\bar{r}_i - \bar{R}_j|^3} \quad (24)$$

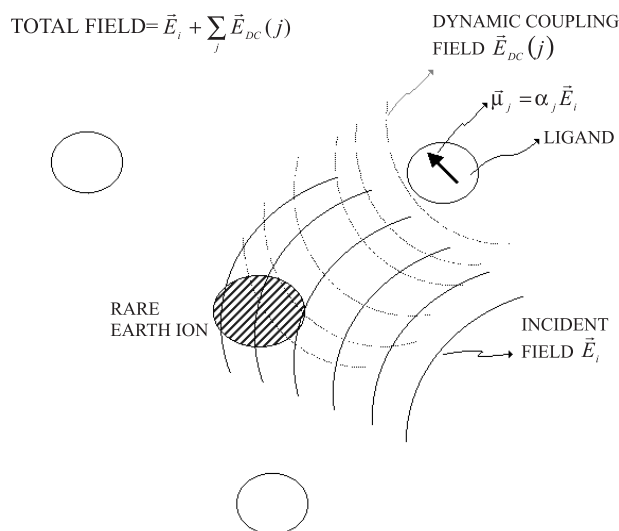


Figure 2. A pictorial representation of the dynamic coupling

$H_{DC}$  must be added to the interaction, with the incident field, that leads to the forced electric dipole mechanism. When expanded in terms of irreducible tensor operators<sup>19,20</sup>, the even rank components of  $H_{DC}$  lead to a transition moment (in units of  $e$ ) that has exactly the same form as the transition moment given in equation (17), that is:

$$\bar{\mu}_{DC} = \sum_{\lambda, t, Q, p, q} (-1)^Q (2\lambda + 1) \begin{pmatrix} 1 & t & \lambda \\ q & p & -Q \end{pmatrix} B_{\lambda t p}^{DC} \langle (4f^N) \Gamma' | U_Q^{(\lambda)} | (4f^N) \Gamma \rangle \bar{e}_q^* \quad (25)$$

where

$$B_{\lambda t p}^{DC} = - \left[ \frac{(\lambda + 1)(2\lambda + 3)}{(2\lambda + 1)} \right]^{1/2} \langle 4f | r^\lambda | 4f \rangle (1 - \sigma_\lambda) \langle f || C^{(\lambda)} || f \rangle \Gamma_p \delta_{t, \lambda+1} \quad (26)$$

and

$$\Gamma_p^t = \left( \frac{4\pi}{2t+1} \right)^{1/2} \sum_j \frac{\alpha_j}{R_j^{t+1}} Y_p^{t*}(\Omega_j) \quad (27)$$

$Y_p^t$  is a spherical harmonic and  $(1 - \sigma_\lambda)$  in equation (26) is a shielding factor, due to the filled 5s and 5p sub-shells of the rare earth ion<sup>14</sup>. The total intensity parameter is now  $B_{\lambda t p} = B_{\lambda t p}^{ed} + B_{\lambda t p}^{DC}$ , which is the quantity to be used in equation (21) to obtain the total  $\Omega_\lambda$  parameters.

Several interesting aspects may be discussed about the forced electric dipole and dynamic coupling mechanisms. An analysis from typical values of the quantities that appear in equations (18) and (26) indicate that these two mechanisms contribute to the total transition moment with opposite signs<sup>16</sup>. Both the odd rank ligand field parameters,  $\gamma_p^t$ , and the polarizability dependent quantities  $\Gamma_p^t$  contain generally the same type of sum over the surrounding atoms. Therefore, they carry out the same symmetry information. The only difference is that  $\Gamma_p^t$  does not depend on the spherical harmonic of rank 1 ( $Y_p^1$ ) as it may be noted from the Kronecker's delta in equations (26).

As the site occupied by the rare earth ion becomes more symmetric, the lower rank  $\gamma_p^t$  and  $\Gamma_p^t$  tend to vanish more rapidly than the higher rank ones, or in a more general way, the former quantities are more sensitive to changes in symmetry than the latter, though the higher rank  $\gamma_p^t$  and  $\Gamma_p^t$  are more sensitive to changes in distances. This goes in the correct sense towards the rationalization of the so-called hypersensitive transitions, which are normally dominated by the effective operator  $\Omega_2 U^{(2)}$ . On the other hand, this also seems to agree with the empirical suggestion that the effects involving slight changes in the positions of the ligands belonging to the second coordination

shell could be reflected in the  $\Omega_4 U^{(4)}$  and  $\Omega_6 U^{(6)}$  effective operators<sup>29,30,31</sup>. However, it has been observed that the symmetry alone cannot account for the enormous variation sometimes observed in the intensities of those hypersensitive transitions for different chemical environments. Theoretical estimates have shown that the dynamic coupling contribution is able to account for this enormous intensity variation through the polarizabilities of the surrounding atoms, or groups of atoms.

Thus, for example, in going from the gaseous compound  $NdF_3$  to gaseous  $NdI_3$  there is a change in polarizability, from the ion  $F^-$  to the ion  $I^-$ , of almost one order of magnitude. This might produce a change of almost two orders of magnitude in the intensities dominated by  $\Omega_2 U^{(2)}$ . Abnormal changes in the intensities dominated by  $\Omega_4 U^{(4)}$  and  $\Omega_6 U^{(6)}$  may not occur, since for these cases the remarkable increase in the distance Nd-X ( $X = F$  and  $I$ ) may compensate for the increase in the polarizability values. This can explain the fact that nearly all glass materials containing trivalent rare earth ions (and also the aqua ions and other complexes in solution) show a moderate variation of both  $\Omega_4$  and  $\Omega_6$  parameters, between 1 and  $5 \times 10^{-20} \text{ cm}^2$ <sup>1,32</sup>, contrarily to the changes in the  $\Omega_2$  values, which vary from less than 1 to  $40 \times 10^{-20} \text{ cm}^2$  in condensed matter (table 1 of Ref. 1) and even up to  $275 \times 10^{-20} \text{ cm}^2$  for  $NdI_3$  vapor.

A point that should be stressed here is that, in contrast with a common procedure found in the literature in the case of rare earth-doped glasses, the dynamic coupling mechanism cannot, in any circumstances, be neglected. When the  $\Omega_\lambda$  intensity parameters are phenomenologically determined from experimental intensities, the forced electric dipole and dynamic coupling mechanisms are absorbed simultaneously and cannot be distinguished. Therefore, when treating energy transfer processes between rare earth ions, one should bear in mind that in the dipole-dipole or dipole-quadrupole expressions for the transfer rates the  $\Omega_\lambda$ 's which appear refer only to the forced electric dipole contribution, that is,  $\Omega_\lambda^{ed}$ . This is one of the reasons that motivate the theoretical calculations of the individual  $B_{\lambda t p}^{ed}$  and  $B_{\lambda t p}^{DC}$  contributions. These theoretical calculations in vitreous materials turn out to be an enormous problem, due to the large variety of different site symmetries occupied by the rare earth ion, unless a model system with a well defined statistical distribution of site symmetry types is available. In this case the  $\Omega_\lambda$  parameters represent average values over all types of sites.

## INTENSITY PARAMETERS IN VITREOUS MATERIALS

One of the effects of a distribution of different symmetry sites occupied by the rare earth ion is to produce the inhomogeneous line broadening. The Stark levels overlap in such a way that, in most cases, even the fluorescence line-narrowing technique cannot help to identify a particular site occupied by the rare earth ion. Figure 3 shows the emission spectrum of the  $Eu^{3+}$  ion in fluoroborate glasses<sup>33</sup>, where this effect can be clearly noted, particularly in the  ${}^5D_0 \rightarrow {}^7F_2$  hypersensitive transition at  $\sim 612 \text{ nm}$ .

As already mentioned, the  $\Omega_\lambda$  intensity parameters in vitreous materials correspond to statistical average values over all sites, and these values, determined experimentally, incorporate both the forced electric dipole and the dynamic coupling contributions. The dependence on the polarizabilities of the neighboring ions confers to the latter mechanism a stronger dependence on the nature of the chemical environment. For the sake of comparison, in a 100% ionic model of the ligand field interaction, the charge of the fluorine and chlorine ions, for example, is  $-1$ , in units of the electronic charge, while their dipolar isotropic polarizabilities are, respectively,  $1 \text{ \AA}^3$  and  $\sim 3 \text{ \AA}^3$ . This may account for the hypersensitive behavior of certain 4f-4f transitions, which are generally dominated by  $\Omega_2 U^{(2)}$ .

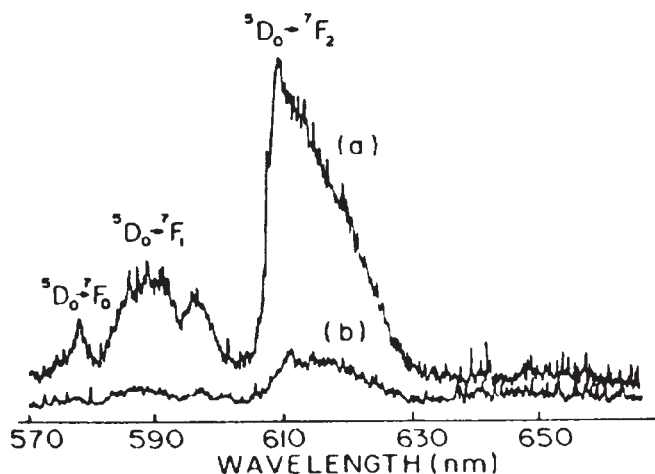


Figure 3. Luminescence spectrum of the  $\text{Eu}^{3+}$  ion, in the presence (a) and in the absence (b) of silver particles, in a fluoroborate glass

A correlation has been noticed in the sense that compounds expected to have a higher degree of covalency tend to present higher values of  $\Omega_2$ , suggesting that in these cases the dynamic coupling mechanism dominates. This correlation can be clearly seen from the  $\Omega_2$  values collected in table 1 of Ref. 1 and in Ref. 32, where the oxides and chalcogenides present higher values for this intensity parameter than the fluorides, which are known to have the least covalent bonding with the rare earths.

The case of the fluoride phosphate  $\text{Eu}^{3+}$  and  $\text{Tb}^{3+}$  glasses, for instance, is another example that nicely illustrates this correlation. In these glasses,  $\Omega_2$  increases linearly with the increase of the phosphate content, due to the replacement of fluoride ions presenting lower electron polarizability by the oxygen atoms having higher polarizability<sup>34</sup>. Another correlation has also been noted between the  $\Omega_4$  and  $\Omega_6$  parameters and the amplitudes of localized vibrational modes involving the rare earth ion<sup>1</sup>, giving an indication of the rigidity of the material. It is, however, rather difficult to rationalize this correlation in terms of the quantities that appear in equations (18) and (26).

An interesting and controversial case of intensity parameters is the  $\text{Pr}^{3+}$  ion. In many compounds with  $\text{Pr}^{3+}$  it is found that the phenomenological  $\Omega_2$  parameter is negative, what, from the definition of the  $\Omega_\lambda$  [equation (21)], is not acceptable. It has been argued<sup>9</sup> that for this ion the lowest excited configuration of opposite parity,  $4f\ 5d$ , is too close ( $\sim 50000\ \text{cm}^{-1}$ ) to the ground configuration ( $4f^2$ ), invalidating the approximation made on the energy denominators in equation (15).

There are different ways in which corrections could be introduced. One is to take into account the  $4f^N$  wavefunctions up to higher than first order in perturbation theory<sup>12</sup>. Another one is, for example, to make appropriate expansions on the inverse of the energy differences in equation (15), as it has been done in Ref. 35. In either way one finds that the odd rank effective operators  $\Omega_\lambda^{\text{ed}} U^{(\lambda)}$  ( $\lambda = 1, 3$  and  $5$ ) may be of significance when  $\text{DE}(5d)$  is small, as in the case of the  $\text{Pr}^{3+}$  ion. However, one should bear in mind that even in this case, depending on the chemical environment, the dynamic coupling mechanism may dominate, what would make more difficult to evaluate precisely the effect of the odd rank effective operators. There are evidences in the case of the isoelectronic ion  $\text{U}^{4+}(5f^2)$ , found by Auzel<sup>36</sup>, indicating a rather independent behavior of the  $5f-5f$  transition intensities with the position of the  $5f\ 6d$  excited levels of opposite parity, suggesting a dominance of the dynamic coupling mechanism.

Another aspect about  $\text{Pr}^{3+}$  compounds concerns the statistical procedure, which is usually adopted for extracting the  $\Omega_\lambda$  intensity parameters from experimental oscillator strengths (least-squares method). It is possible that in this case the set of linear equations is particularly sensitive to very small variations, within experimental errors, in the oscillator strengths. A method in which branching ratios are included in the least-squares procedure was proposed by Quimby and Miniscalco<sup>37</sup>, and a method in which the standard deviation for each individual oscillator strength is introduced in the minimization procedure has been used by Goldner and Auzel<sup>38</sup>, both leading to reliable intensity parameters.

## CONCLUDING REMARKS

Some very basic aspects of the theory of  $4f-4f$  transition intensities applied to vitreous materials have been discussed above. The characteristics of the intra-atomic rare earth free ion and ligand field interactions, as well as the formalisms of the forced electric dipole and dynamic coupling mechanisms of  $4f-4f$  intensities, have been outlined. One of the main points was to call attention to the contribution from the dynamic coupling mechanism to the intensities, a point that has been commonly overlooked in the literature of rare earth doped glass materials. Not taking into account this mechanism is equivalent to assume that the phenomenological  $\Omega_\lambda$  intensity parameters coincide with  $\Omega_\lambda^{\text{ed}}$ , corresponding to the forced electric dipole contribution alone. This would be a clear misinterpretation of the theory. From the theoretical expressions given in equations (18) and (26) it is possible to rationalize the correlation between  $\Omega_2$  and covalence, as discussed in Ref. 1. However, the same is not evident concerning the correlation between  $\Omega_4$  and  $\Omega_6$  and the rigidity of the medium. The case of the  $\text{Pr}^{3+}$  ion has been briefly discussed under the light of the forced electric dipole and dynamic coupling mechanisms, and attention has been called to the fact that for this ion statistical problems may arise when determining phenomenological intensity parameters from experimental oscillator strengths.

## ACKNOWLEDGMENTS

Financial support from the CNPq (Brazilian agency), RENAMI and IMMC (Brazilian projects), and the FCT (Portuguese agency, POCTI CTM/33653/00 program) is acknowledged.

## REFERENCES

1. Reisfeld, R.; Jørgensen, C. K. In *Handbook on the Physics and Chemistry of Rare Earths*; Gschneidner Jr., K. A.; Eyring, L., eds.; North-Holland: Amsterdam, 1987, vol. 9, ch. 58, p. 1.
2. *Rare Earth Doped Fiber Lasers and Amplifiers*; Digonnet, M. J. F., ed.; Marcel Dekker: New York, 1993.
3. Fuxi, G.; *Optical and Spectroscopic Properties of Glasses*, Springer-Verlag: Berlin, 1992.
4. Weber, M. J. In ref. 1, vol. 4, ch. 35, p. 275.
5. Collins, S. F.; Baxter, G. W.; Wade, S. A.; Sun, T.; Grattan, K. T. V.; Zhang, Z. Y.; Palmer, A. M.; *J. Appl. Phys.* **1998**, *84*, 4649.
6. Downing, E.; Hesselink, L.; Ralston, J.; MacFarlane, R.; *Science* **1996**, *273*, 1185.
7. Judd, B. R.; *Phys. Rev.* **1962**, *127*, 750.
8. Ofelt, G. S.; *J. Chem. Phys.* **1962**, *37*, 511.
9. Peacock, R. D.; *Structure and Bonding* **1975**, *22*, 83.
10. Judd, B. R.; *J. Chem. Phys.* **1979**, *70*, 4830.
11. Reid, M. F.; Dallara, J. J.; Richardson, F. S.; *J. Chem. Phys.* **1983**, *79*, 5743.
12. Smentek-Mielczarek, L.; Hess Jr., B. A.; *J. Chem. Phys.* **1987**, *87*, 3509.
13. Reid, M. F.; Betty, N. G.; *Mol. Phys.* **1989**, *67*, 407.
14. Malta, O. L.; Ribeiro, S. J. L.; Faucher, M.; Porcher, P.; *J. Phys. Chem. Solids* **1991**, *52*, 587.
15. Orlovskii, Y. V.; Pukhov, K. K.; Basiev, T. T.; Tsuboi, T.; *Optical Materials* **1995**, *4*, 583.

16. Malta, O. L.; Couto dos Santos, M. A.; Thompson, L. C.; Ito, N. K.; *J. Lumin.* **1996**, *69*, 77.
17. Basiev, T. T.; Orlovskii, Y. V.; Pukhov, K. K.; Sigachev, V. B.; Doroshenko, M. E.; Vorob'ev, I. N.; *J. Lumin.* **1996**, *68*, 241.
18. Racah, G.; *Phys. Rev.* **1949**, *76*, 1352.
19. Judd, B. R.; *Operator Techniques in Atomic Spectroscopy*, McGraw-Hill Book Company: New York, 1963.
20. Wybourne, B. G.; *Spectroscopic Properties of Rare Earths*, Wiley-Intersciences: New York, 1965.
21. Silver, B. L.; *Irreducible Tensor Methods: An Introduction for Chemists*, Academic Press: London, 1976.
22. Condon, E. U.; Odabasi, H.; *Atomic Structure*, Cambridge University Press, 1980.
23. Prather, J. L.; *Atomic Energy Levels in Crystals*, National Bureau of Standards Monograph 19, NBS: Washington, 1961.
24. Görrler-Walrand, C.; Binnemans, K. In ref. 1, vol. 23, ch. 155, p. 121.
25. Broer, L. J. F.; Gorter, C. J.; Hoogschagen, J.; *Physica* **1945**, *11*, 231.
26. Deutschbein, O.; *Ann. Physik* **1939**, *36*, 183.
27. Jörgensen, C. K.; Judd, B. R.; *Mol. Phys.* **1964**, *8*, 281.
28. Bebb, H. B.; Gold, A.; *Phys. Rev.* **1966**, *143*, 1.
29. Brito, H. F.; Malta, O. L.; Souza, L. R.; Meneses, J. F. S.; Carvalho, C. A. A.; *J. Non-Cryst. Solids* **1999**, *247*, 129.
30. Bizeto, M. A.; Constantino, V. R. L.; Brito, H. F.; *J. Alloys Compd.* **2000**, *311*, 159.
31. Carlos, L. D.; Messaddeq, Y.; Brito, H. F.; Sá Ferreira, R. A.; de Zea Bermudez, V.; Ribeiro, S. J. L.; *Adv. Mater.* **2000**, *12*, 594.
32. Görrler-Walrand, C.; Binnemans, K. In ref. 1, vol. 25, ch. 167, p. 101.
33. Malta, O. L.; Santa-Cruz, P. A.; de Sá, G. F.; Auzel, F.; *J. Lumin.* **1985**, *33*, 261.
34. Ebendorff-Heidepriem, H.; Ehrhart, D.; *J. Non-Cryst. Solids* **1996**, *208*, 205.
35. Flórez, A.; Malta, O. L.; Messaddeq, Y.; Aegerter, M.; *J. Non-Cryst. Solids* **1997**, *213/214*, 315.
36. Auzel, F.; personal communication.
37. Quimby, R. S.; Miniscalco, W. J.; *J. Appl. Phys.* **1994**, *75*, 613.
38. Goldner, P.; Auzel, F.; *J. Appl. Phys.* **1996**, *79*, 7972.

# Temperature Sensor Based on Frequency Upconversion in $\text{Er}^{3+}$ -Doped Fluoroindate Glass

G. S. Maciel, L. de S. Menezes, A. S. L. Gomes, Cid B. de Araújo,  
Y. Messaddeq, A. Florez, and M. A. Aegerter

**Abstract**—We describe the characterization of a temperature sensor based on the infrared-to-visible frequency upconversion process excited in a sample of  $\text{Er}^{3+}$ -doped fluoroindate glass. The present results demonstrate the feasibility of constructing a compact practical device using a low-power CW 1.48- $\mu\text{m}$  diode laser as the excitation source.

## I. INTRODUCTION

RARE-earth (RE) doped materials are of interest for temperature sensors because their absorption and emission properties are temperature dependent. To date a number of such sensors has been presented and the most successful approach is based on the study of RE fluorescence whose decay-time is a function of the sample temperature. For this kind of application the fluorescent material is excited by a pulsed light source of an appropriate wavelength and the fluorescence signal decay-time is determined by a time-resolved processing circuit. This method was introduced about ten years ago [1] and has been employed by several authors [1]–[5].

More recently a new approach also based on the temperature dependence of the RE fluorescence was proposed in [6]. The authors used a fluoride glass codoped with  $\text{Er}^{3+}$  and  $\text{Yb}^{3+}$  and measured the sample's temperature by determining the signal ratio of two fluorescence lines of a Boltzmannian population associated to excited states. The signal processing was simplified since the temperature was determined from the ratio of two line intensities, instead of time-resolved measurements. However, an important requirement for practical application of the new method is the selection of an appropriate material that must present a large upconversion signal while

excited with low-power laser diodes. The use of oxide glasses, for example, is not practical because the large nonradiative relaxation suffered by the RE ions when incorporated in this class of host makes them poor upconverters. On the other hand, fluorozirconate glasses are not appropriate either because of their sensitivity to humidity.

In the present paper we report the use of a new class of fluoroindate glasses doped with  $\text{Er}^{3+}$  as a temperature sensor based on the method introduced in [6]. Accordingly, the efficient infrared-to-visible upconversion process is achieved using a 1.48- $\mu\text{m}$  CW low-power (5 mW) laser diode that excites a significant population to the thermally coupled excited levels  $^2\text{H}_{11/2}$  and  $^4\text{S}_{3/2}$ , which generate the double frequency fluorescence signal required.

The samples used were prepared following the procedure given in [7] and have the compositions (mol %):  $39 - x \text{InF}_3 - 20\text{ZrF}_2 - 16\text{BaF}_2 - 20\text{SrF}_2 - 2\text{GdF}_3 - 2\text{NaF} - 1\text{GaF}_3 - x\text{ErF}_3$  ( $x = 2, 3$ ). These fluoroindate glasses present high transparency from the ultraviolet to the middle-infrared and large resistance to atmospheric moisture. Moreover, our recent studies [8]–[11] have shown their large potential for photonic applications because their phonons have small energies ( $\leq 507 \text{ cm}^{-1}$ ), they present large frequency upconversion efficiency and it is possible to incorporate large concentrations of RE ions to the matrix.

Fig. 1 shows schematically the excitation and decay channels related to the states  $^2\text{H}_{11/2}$  and  $^4\text{S}_{3/2}$ , whose fluorescence intensity ratio is the basis of our sensor. As indicated by the solid arrows, the pump diode laser resonant with  $^4\text{I}_{15/2} \rightarrow ^4\text{I}_{13/2}$  transition initiates the upconversion process. The upconverted fluorescences at  $\approx 522 \text{ nm}$  and  $\approx 543 \text{ nm}$  are quite strong and readily visible by the naked eye. The spectra obtained for  $23^\circ\text{C}$  and  $175^\circ\text{C}$  are presented in Fig. 2. We have observed that when the glass temperature is raised, the intensities of both fluorescence lines at  $\approx 522 \text{ nm}$  and  $\approx 543 \text{ nm}$  decrease as well as their ratio. On the other hand, their peak positions did not change in the temperature range of our measurements ( $23$ – $175^\circ\text{C}$ ). The behavior of the fluorescence signal,  $I_s$ , with the laser intensity,  $I_p$ , was also determined and the dependence,  $I_s \propto I_p^N$ , with  $N \approx 3$  was verified. This result indicates that three laser photons participate in the upconversion process. For the  $\text{Er}^{3+}$  concentrations and laser wavelength used, frequency upconversion is mainly due to energy transfer processes and the contribution of excited state absorption is negligible [11]. Accordingly, after excitation to the  $^4\text{I}_{13/2}$  state, energy transfer between three

Manuscript received July 27, 1995; revised August 22, 1995. This work was supported in part by the Brazilian Agencies Conselho Nacional de Desenvolvimento Científico e Tecnológico (CNPq), Financiadora de Estudos e Projetos (FINEP), and Fundação de Amparo à Ciência e Tecnologia de Pernambuco (FACEPE).

G. S. Maciel, L. de S. Menezes, A. S. L. Gomes, and Cid B. de Araújo are with the Departamento de Física, Universidade Federal de Pernambuco, 50670-901 Recife, PE, Brasil.

Y. Messaddeq was with the Instituto de Física de São Carlos, Universidade de São Paulo, 13560-970 São Carlos, SP, Brasil. He is now with the Departamento de Química, Universidade do Estado de São Paulo, 14800-900 Araraquara, SP, Brasil.

A. Florez is with the Instituto de Física de São Carlos, Universidade de São Paulo, 13560-970 São Carlos, SP, Brasil, on leave from the Departamento de Física, Universidade Industrial de Santander, A.A. 678 Bucaramanga, Colombia.

M. A. Aegerter is with the Instituto de Física de São Carlos, Universidade de São Paulo, 13560-970 São Carlos, SP, Brasil.

IEEE Log Number 9415355.

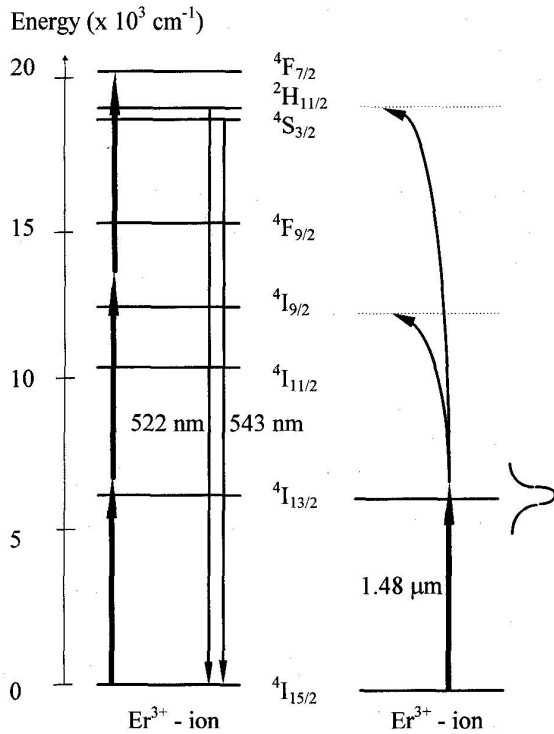


Fig. 1. Simplified energy levels scheme of  $\text{Er}^{3+}$ . The downwards arrows indicate the upconverted fluorescence and the curved arrows on the right side stand for energy transfer.

excited  $\text{Er}^{3+}$  ions at that level will take one ion to the states  $^2\text{H}_{11/2}$  or  $^4\text{S}_{3/2}$ . The energy transfer can be resonant or nonresonant with phonon emission or absorption compensating the energy mismatch. Afterwards, radiative transitions to the ground state give rise to the observed green fluorescence at  $\approx 522$  nm ( $^2\text{H}_{11/2} \rightarrow ^4\text{I}_{15/2}$ ) and  $\approx 543$  nm ( $^4\text{S}_{3/2} \rightarrow ^4\text{I}_{15/2}$ ). The temperature behavior observed is consistent with previous reports for fluorozirconate glasses [12]. Because of the small energy gap ( $\approx 750$   $\text{cm}^{-1}$ ) between the levels  $^2\text{H}_{11/2}$  and  $^4\text{S}_{3/2}$ , the state  $^2\text{H}_{11/2}$  may also be populated from  $^4\text{S}_{3/2}$  by thermal excitation and a quasithermal equilibrium occurs between the two levels. As a consequence of the quasithermal equilibrium, the ratio of the two fluorescence intensities may be written as  $R = I_{522}/I_{543} = C \exp\{-\Delta E/kT\}$ , where  $\Delta E$  is the energy gap between the levels  $^2\text{H}_{11/2}$  and  $^4\text{S}_{3/2}$ ,  $k$  is the Boltzmann constant, and  $C$  is a parameter that depends on the levels lifetime and their electronic weight.

To determine the temperature behavior of the  $R$ -ratio under conditions similar to the ones required for a practical temperature sensor, the laser light was delivered to the glass sample through a single-mode-fiber. The fluorescence intensity was measured using an optical spectrum analyzer and for the signal capture the sample was butted to a two-meter-long multimode fiber. Thus, the temperature transducer was very compact. The behavior of the  $R$ -ratio is shown in Fig. 3 for the sample with  $x = 3$ . The exponential dependence of the  $R$ -ratio with temperature was asserted from the best fit presented in Fig. 3(a), which gives  $C = 11.2$  and  $\Delta E = 769$   $\text{cm}^{-1}$ .

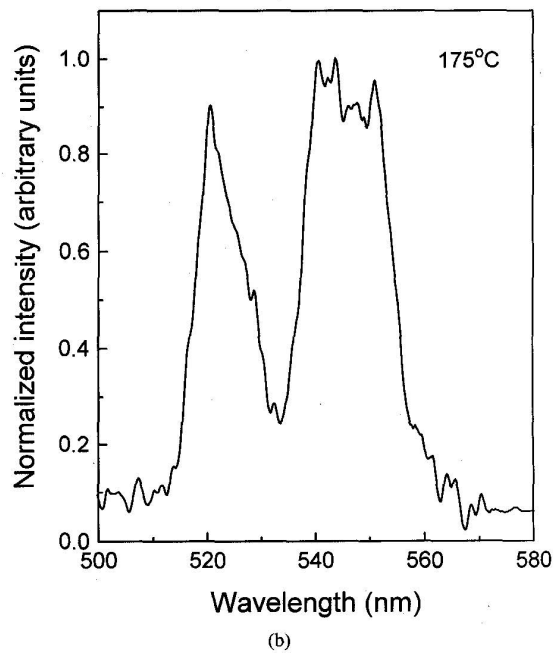
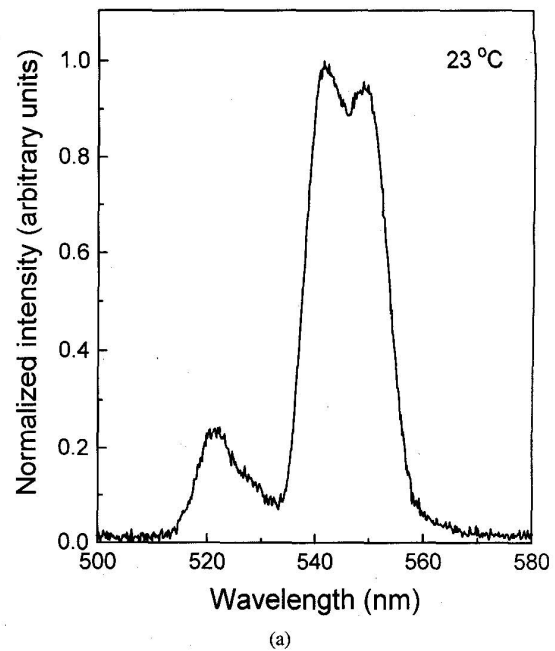
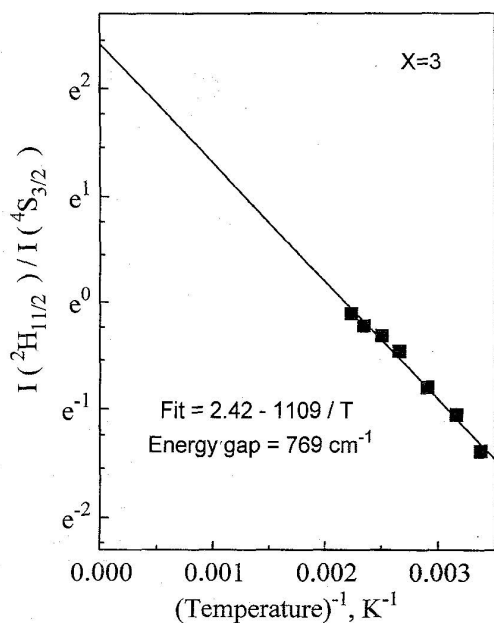
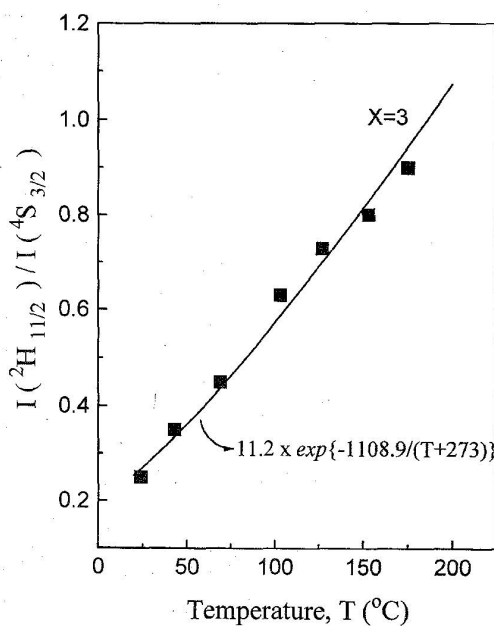


Fig. 2. Green upconverted fluorescence (normalized to the stronger line) corresponding to the transitions  $^2\text{H}_{11/2} \rightarrow ^4\text{I}_{15/2}$  ( $\approx 522$  nm) and  $^4\text{S}_{3/2} \rightarrow ^4\text{I}_{15/2}$  ( $\approx 543$  nm): (a) 23 °C; (b) 175 °C. Sample concentration:  $x = 3$ .

For the sample with  $x = 2$  we have obtained  $C = 7.39$  and  $\Delta E = 742$   $\text{cm}^{-1}$ . From the  $C$  values we obtain the ratio between the levels lifetimes  $\tau(^2\text{H}_{11/2})/\tau(^4\text{S}_{3/2}) = 2.36$ , and 3.59 for  $x = 2$ , and  $x = 3$ , respectively. The different values obtained are due to the dependence of the levels lifetime with the  $\text{Er}^{3+}$  concentration [9]. From Fig. 3(b) we calculated the sensor sensitivity as 0.004/°C.



(a)



(b)

Fig. 3. (a) Logarithmic plot of the relative intensities of the transitions at 522 nm and 543 nm ( $I_{522}/I_{543}$ ) versus the inverse temperature; (b) Relative intensities versus the sample temperature. Sample concentration:  $x = 3$ .

The present results for the upconversion efficiency can be favorably improved if  $\text{Yb}^{3+}/\text{Er}^{3+}$  codoped samples are used.

Another important aspect to consider is the suitability of the fluoroindate glass to be fibered, and the possibility to use the doped fiber as the active sensing element.

Finally, we mention that a practical device will require a simple and inexpensive electronic circuit to process the ratio between the two signals instead of the elaborate circuitry used in the devices based on the analysis of decay-time temperature dependence. From the calculated sensor sensitivity, a precision  $\geq \pm 1$  °C can be obtained if the electronic circuitry allows division with four digits or more. Moreover, the temperature sensor is insensitive to light intensity variations of the pumping source as well as possible fluctuations and losses of the optical signal during propagation through the addressing fiber coupled to the sensor.

#### ACKNOWLEDGMENT

The authors thank B. J. P. da Silva for polishing the samples.

#### REFERENCES

- [1] K. T. V. Grattan and A. W. Palmer, "Infrared fluorescence decay-time temperature sensor," *Rev. Sci. Instrum.*, vol. 56, pp. 1764-1787, 1985.
- [2] M. C. Farries, M. E. Fermann, R. I. Laming, S. B. Poole, D. N. Payne, and A. P. Leach, "Distributed temperature sensor using  $\text{Nd}^{3+}$ -doped optical fiber," *Electron. Lett.*, vol. 22, pp. 418-419, 1986.
- [3] L. Scrivener, P. D. Maton, A. P. Appleyard, and E. J. Tarbox, "Fabrication and properties of large core, high NA, high  $\text{Nd}^{3+}$  content multimode optical fibers for temperature sensor applications," *Electron. Lett.*, vol. 26, pp. 872-873, 1990.
- [4] W. Quoi, R. A. Lieberman, L. G. Cohen, D. J. Shenk, and J. R. Simpson, "Rare-earth doped optical fibers for temperature sensing," *J. Lightwave Technol.*, vol. 10, pp. 847-852, 1992.
- [5] F. Wysocki, M. J. F. Dignonnet, B. Y. Kim, and H. J. Shaw, "Characteristic of erbium-doped superfluorescent fiber sources for interferometric sensor applications," *J. Lightwave Technol.*, vol. 12, pp. 550-558, 1994.
- [6] H. Berthou and C. K. Jorgensen, "Optical fiber temperature sensor based on upconversion-excited fluorescence," *Opt. Lett.*, vol. 15, pp. 1100-1102, 1990.
- [7] Y. Messaddeq, A. Delben, M. Boscolo, M. A. Aegerter, A. Soufiane, and M. Poulain, "New fluoroindate glass compositions," *J. Non-Crystall. Solids*, vol. 161, pp. 210-212, 1993.
- [8] R. M. Almeida, J. C. Pereira, Y. Messaddeq, and M. A. Aegerter, "Vibration spectra and structure of fluoroindate glass," *J. Non-Crystall. Solids*, vol. 161, pp. 105-108, 1993.
- [9] R. Reiche, L. A. O. Nunes, C. C. Carvalho, Y. Messaddeq, and M. A. Aegerter, "Blue and green upconversion in  $\text{Er}^{3+}$ -doped fluoroindate glasses," *Solid State Commun.*, vol. 85, pp. 773-777, 1993.
- [10] L. E. E. de Araújo, A. S. L. Gomes, Cid B. de Araújo, Y. Messaddeq, A. Florez, and M. A. Aegerter, "Frequency upconversion of orange light into blue light in  $\text{Pr}^{3+}$ -doped fluoroindate glasses," *Phys. Rev. B*, vol. 50, pp. 16219-16223, 1994.
- [11] Cid B. de Araújo, L. de S. Menezes, L. H. Acioli, A. S. L. Gomes, Y. Messaddeq, A. Florez, and M. A. Aegerter, "Infrared-to-visible CW frequency upconversion in  $\text{Er}^{3+}$ -doped fluoroindate glasses," to be published.
- [12] D. Shinn, W. A. Sibley, M. G. Drexhage, and R. N. Brown, "Optical transitions of  $\text{Er}^{3+}$  ions in fluorozirconate glass," *Phys. Rev. B*, vol. 27, pp. 6635-6648, 1983.

# Rare-earth-doped transparent glass ceramics

M. Clara Gonçalves, Luís F. Santos, Rui M. Almeida\*

*Departamento de Engenharia de Materiais / ICEMS, Instituto Superior Técnico, av. Rovisco Pais, 1049-001 Lisboa, Portugal*

Received 15 April 2002; accepted 16 October 2002

**Abstract** – Glass ceramics are a known class of polycrystalline ceramic materials, where, depending on the glass matrix and the particular crystalline phases, one can obtain materials with improved mechanical, thermal, electrical or optical properties. The characteristics and applications of optical glass ceramics are reviewed, with particular emphasis on rare-earth-doped transparent glass ceramics for photonics, including the search for new transparent glass ceramic compositions and the development of suitable methods to process such materials into functional devices. *To cite this article: M. Clara Gonçalves et al., C. R. Chimie 5 (2002) 845–854* © 2002 Académie des sciences / Éditions scientifiques et médicales Elsevier SAS

rare earth / glass ceramics / photonics

**Résumé** – Les vitrocéramiques constituent une classe bien connue de matériaux céramiques polycristallins qui, selon la matrice vitreuse et les phases cristallines, possèdent des propriétés mécaniques, thermiques, électriques ou optiques améliorées. Les caractéristiques et les applications optiques des vitrocéramiques sont passées en revue, avec une insistance particulière sur les vitrocéramiques transparentes et dopées en terres rares pour application photonique, incluant les recherches effectuées sur les compositions de nouvelles vitrocéramiques transparentes et le développement des méthodes appropriées pour inclure de tels matériaux dans des dispositifs possédant une fonction particulière. *Pour citer cet article : M. Clara Gonçalves et al., C. R. Chimie 5 (2002) 845–854* © 2002 Académie des sciences / Éditions scientifiques et médicales Elsevier SAS

terres rares / vitrocéramiques / photonique

## 1. Glass ceramics – historical view

Glass ceramics, discovered by S.D. Stookey (Corning Glass Works, USA) in the mid-1950s [1–4], are polycrystalline ceramic materials, formed through the controlled nucleation and crystallisation of glass, where the amount of residual glassy phase is usually less than 50%. The precursor glass is melted, quenched and shape-processed and is then thermally converted into a composite material formed by a crystalline phase dispersed within a glass matrix. The basis of controlled internal crystallisation lies in efficient nucleation, often enabled by a small amount of a nucleating agent, that allows the development of fine, randomly oriented grains, in a ceramic generally without voids, microcracks, or other porosity [5].

The development of practically useful glass ceramics is relatively recent, but the first attempts in this direction may be referenced to Réaumur [6], as long ago as 1739, who produced polycrystalline materials from soda–lime–silica glass; yet the control of the crystallisation process was not achieved. Further, the crystallisation was initiated at the surface, resulting in weak and brittle articles. Only some 200 years after Réaumur's work, a directed research program started at Corning Glass Works, leading to the discovery of photosensitive glasses [1–4] and to the first glass ceramics patents, PYROFLAM® [7] and VISIONS® [8]. These contain small amounts of copper, silver or gold, which can be precipitated in the form of very small crystals during heat treatment of the precursor glasses. Stookey [1–4] successfully made use of colloidal particles precipitated within the glass, as nucle-

\* Correspondence and reprints.

E-mail address: rui.almeida@ist.utl.pt (R.M. Almeida).

ation sites for its controlled crystallisation. Stookey developed a wide range of glass compositions that contained titanium dioxide as the nucleating agent, which promoted phase separation. Since then, many different types of nucleating agents for glass-ceramic production have been reported [5].

From the early times of glass fabrication, the emphasis has been on preventing devitrification from occurring. Devitrification implies the growth of crystalline material and, if this occurs during the later stages of melting or during the shaping of glass, it has a very harmful effect. Therefore, many studies of devitrification have been carried out, in order to develop an understanding of the phenomenon and to enable it to be suppressed or controlled. Although some glass compositions are self-nucleating and volume nucleation occurs, crystallisation or devitrification in vitreous systems occurs most readily from the surface, where crystals are nucleated by flaws or other defect sites. Two kinetic processes are well known to precede devitrification: phase separation by nucleation and growth, the latter is generally or by spinodal decomposition. So far, only nucleation–growth has been shown to lead to optically transparent glass-ceramic material. Spinodal decomposition is generally viewed as a negative effect, since there is loss of glass transparency [9].

Depending on the glass host and the crystal phase compositions, one can obtain materials with improved mechanical, thermal, electrical or optical properties. The applications of glass ceramics have covered six major categories up to now – cook-top panels, dinnerware, electronics, medicine and dentistry, tough glass ceramics and optical materials. Low thermal expansion cook-top panels, woodstove windows and fire doors, represent today the commercially most attractive glass-ceramic product. In electronics, glass ceramics have found major application in microelectronic packaging and products like Fotoform® [10], Fotoeram® [10] and Foturan® [11] have been registered. In dentistry and medicine, where bioglass ceramics found wide use as implants for dental and bone prostheses, a series of new products have been developed and patented under the trademarks Bioglass® [12], Fluoride Bioglass® [13], Ceravital® [14], and Cerabone® [15]. Natural bones and teeth are multiphase materials with specific properties very difficult to simulate, where glass devitrification appears to be a very effective way to achieve improved properties, including machinability. Tough glass ceramics have been developed since the first well-known Macor® product [16], in which the easily cleaved crystalline mica decreased the sensitivity to flaw propagation to such an extent that it could be machined with normal metallic tools. At Corning Glass Works, a variety called Dicor® [17]

was developed for use in dental restoration and, at the Otto Schott Institute in Jena [18], similar products have been developed. Special optical materials, where the dimensional stability, luminescence, or photosensitivity characteristics of glass ceramics can be exploited in a variety of new applications, including photorefractivity, non-linear optical behaviour or optical amplification, have also been fabricated. The best-known commercial optical glass-ceramic is Zerodur®, produced by Schott [19], first designed for large telescope mirror blanks, but now routinely used for laser gyroscopes in airplanes. The key property requirement in all these glass-ceramic applications is an extremely low coefficient of thermal expansion in the temperature interval of work.

The state-of-the-art in a new class of transparent glass-ceramic (TGC) materials will be discussed in the present paper, in connection with photonics. Two main aspects are related to the development of a new optical technology, the first being the search of novel material properties and the second, of equal importance, being the development of suitable methods to process these materials into functional devices. Both aspects are reviewed in the sections below, with emphasis on the first one.

## 2. Transparent glass ceramics

TGC can be obtained under several conditions, where the achievement of low optical absorption and scattering is essential. According to the Rayleigh–Gans theory, crystal sizes well below the wavelength of the incident light present negligible attenuation due to scattering, which, for visible light, represents particle radii lower than ~15 nm [20]. A refractive index difference between the amorphous and crystalline phases of less than 0.1 is also required [20]. However, according to Beall and Pinckney [20], based on Hopper's model [21], crystal sizes of 30 nm and differences in refractive index of 0.3 may be acceptable, provided the crystal spacing is not more than six times the average crystal size. TGC can also be obtained for even larger crystal sizes, if optical isotropy is achieved within the glass ceramic. In fact,  $\beta$ -quartz crystals up to 10  $\mu\text{m}$ , in the  $\text{SiO}_2\text{--Al}_2\text{O}_3\text{--MgO--ZnO--ZrO}_2$  system, still provide good transparency in the glass ceramic [20].

Some of the most promising applications of TGC are: large telescope mirror blanks, liquid crystal displays, solar cells and photonic devices. Precision optical equipment, such as telescope mirrors, requires extremely low expansion coefficient and high transmission. Glass ceramics such as Zerodur® – an aluminosilicate glass with 50-nm  $\beta$ -quartz crystals and with 70% of crystalline phase – has almost zero thermal

expansion ( $0 \pm 0.02 \times 10^{-6} \text{ K}^{-1}$ ) in the temperature range of 0–100 °C and ~90% transmittance between 0.6 and 2.0  $\mu\text{m}$  [5, 9].

Liquid crystal displays for laptop computers are based on TGC of lithium aluminosilicate compositions, with  $\beta$ -quartz solid solution as the crystal phase, as developed by Nippon Electric Glass Co. (Japan), under the name of Neoceram® N-0 [22].

Solar cells and photonic devices require high transmission and efficient luminescence, respectively. TGC containing Cr-doped mullite can be used both in laser applications and solar concentrators [5].

## 2.1. Photonics applications

Photonics may be defined as the technology of information transfer by means of light [23]. Optical non-linearity of materials forms the basis of this ultimate technological revolution, which follows the electronics era.

### 2.1.1. Laser emission

A laser is a source of monochromatic radiation of high intensity, coherence and directionality, in the ultraviolet, visible or infrared optical regions. The laser mechanism is based on the radiative process of stimulated emission. A requirement of laser action is the existence of a metastable excited state with a long lifetime, as the starting level of stimulated emission. Another requirement is the existence of a larger population in this initial metastable state than in the final state, corresponding to the phenomenon of population inversion [24].

Three or four energy-level schemes are used to reach these emission processes, responsible for laser action. The energy levels involved belong to rare-earth (RE) or transition-metal ions. Of special concern for laser action are the non-radiative transitions that lead to undesirable energy dissipation. In glass, the non-radiative transitions of RE ions are accomplished by a series of different mechanisms – multiphonon relaxation, cross-relaxation and co-operative up-conversion. Multiphonon relaxation occurs by a simultaneous creation of several phonons, which suffice to equal the energy of the transition between the excited level and the next lower level; when this is larger than the highest vibrational energy of the solid matrix, several phonons may have to be created in order to bridge the energy gap. Since the probability for multiphonon decay decreases exponentially with the number of required phonons [25], it is desirable to surround the active ion by a matrix that possesses low vibrational energies. In glasses, the highest energy vibrations are stretchings of the anions against the glass forming cations, whose frequency varies with the glass compo-

Table 1. Highest vibrational energies,  $h\nu$  ( $\text{cm}^{-1}$ ), in inorganic glasses [26].

| Glasses           | $h\nu$ ( $\text{cm}^{-1}$ ) |
|-------------------|-----------------------------|
| Silicate          | 1000–1100                   |
| Germanate         | 800–975                     |
| Tellurite         | 600–850                     |
| Fluoride          | 500–600                     |
| Chalcogenide      | 200–300                     |
| LaBr <sub>3</sub> | 175                         |

sition. The highest vibrational energies in various types of glasses are listed in Table 1 [26].

The presence of residual OH species in the glass host increases the non-radiative decay rates, because of coupling between the RE states and the high energy stretching vibrations of the OH groups ( $\sim 3200 \text{ cm}^{-1}$ ). This contribution to non-radiative decay is very important in the case of the  $\text{Er}^{3+}$  ion, since two OH phonons are sufficient to bridge the energy gap between the  $^4\text{I}_{13/2}$  and  $^4\text{I}_{15/2}$  levels. Therefore, the residual OH content of the glass must be controlled to be as low as possible [24].

The other two dissipative processes – cross-relaxation and co-operative up-conversion – both involve RE ion–ion interactions, wherein the intensity of fluorescence decreases as the concentration of the active ions increases. Cross-relaxation may take place between any two closed spaced RE ions that happen to have two pairs of energy levels separated by the same amount. One of the ions, in an excited state, gives half of its energy to a ground state ion, so that both ions end up in the intermediate level. From this level, they both relax quickly to the ground state, via multiphonon relaxation. The cross-relaxation process is believed to be the dominant factor in the concentration quenching of  $\text{Nd}^{3+}$  in glass matrices [24]. The spontaneous co-operative up-conversion process may occur when two neighbouring ions are in an excited state: one of them, A, gives its energy to the other, B, thus promoting B to a higher level, while A relaxes to the ground state. From this higher energy level, the B ion relaxes rapidly, radiatively or non-radiatively. This co-operative up-conversion process is believed to be the major cause of concentration quenching in  $\text{Er}^{3+}$ -doped glasses.  $\text{Er}^{3+}$  has no intermediate states between the  $^4\text{I}_{13/2}$  metastable level and the ground state, thus cross-relaxation between an excited ion and one in the ground state cannot occur [24].

RE ions of the lanthanide series have been the most extensively used active ions for laser operation, because there are a large number of fluorescing states and wavelengths to choose among the 4f electron configurations, as illustrated in Fig. 1, for some of the more commonly used RE ions. Nevertheless, one of

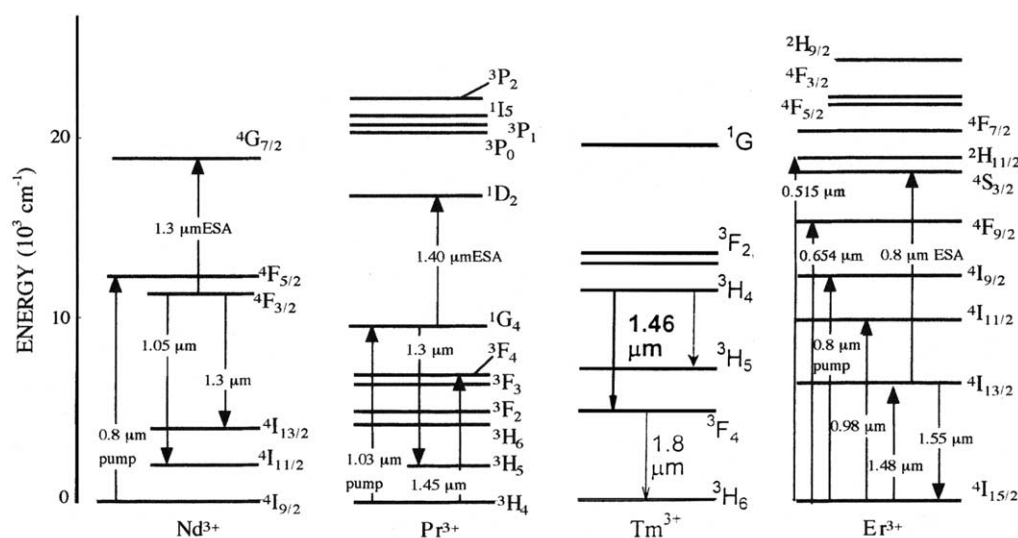


Fig. 1. Simplified electronic energy level diagrams of three different RE ions and relevant transitions for pumping and emission. (Adapted from ref. [24].)

the obstacles to the use of RE ions can be a short lifetime of the excited states and non-radiative decay paths, which depend on the local environment of the ion and on the matrix vibrational energies. Thus, the efficiency of the radiative decay in oxide glasses is generally low, compared with halide and sulphide glasses (cf. Table 1). Of the many RE ions,  $\text{Er}^{3+}$  is well known for its favourable characteristics for laser transition.  $\text{Er}^{3+}$  ions operate as a three-level system, through the  ${}^4\text{I}_{13/2}$ – ${}^4\text{I}_{15/2}$  transition [27–30]. They can be pumped directly into the metastable upper lasing level  ${}^4\text{I}_{13/2}$  (1.49  $\mu\text{m}$ ), or into higher levels, from which non-radiative decay occurs to the metastable  ${}^4\text{I}_{13/2}$  level. The lower lasing level, in this case, is the ground state ( ${}^4\text{I}_{15/2}$ ). Absorption of lasing photons from the ground state directly to the upper lasing level may take place, causing competition with the emission of lasing photons, a phenomenon known as self-absorption, typical of three-level systems [24].

### 2.1.2. Frequency up-conversion

At present, there is great interest in luminescent materials for efficient frequency conversion from infrared to visible radiation, mainly because a visible source pumped by a near infrared laser is useful for high-capacity data storage optical devices. This stimulated excitation process is designated by up-conversion and is a particular type of laser action. Therefore, both the fluorescence lifetime and the stimulated emission cross-section of the RE excited level should be maximised, whereas the non-radiative decay mechanisms should be minimised. The glassy host is required to possess a minimal absorption coefficient within the wavelength region of interest, plus

the capability of incorporating large RE concentrations, low vibrational energies and a high refractive index.  $\text{Er}^{3+}$  is the most commonly used RE dopant that can provide up-converted visible fluorescence, both in fluoride crystals and glasses. In conventional oxide glasses, there is no report of the up-conversion phenomenon, because of large non-radiative losses, due to high-energy vibrations, e.g. Si–O ( $\sim 1100\text{ cm}^{-1}$ ) and B–O ( $\sim 1400\text{ cm}^{-1}$ ), which couple to the  $\text{Er}^{3+}$  ions. Up-conversion pumped fluorescence expectation has therefore been placed on non-traditional oxide glass systems, with lower vibrational energies. In the stimulated up-conversion processes, excited state absorption (ESA) and energy transfer (ET) involving RE ions in the solid matrix are important mechanisms. Much work has been devoted to up-conversion lasers involving  $\text{Er}^{3+}$  ions, to produce green and red up-conversion output, respectively. The sensitisation of  $\text{Er}^{3+}$  with  $\text{Yb}^{3+}$  may also be favourable for infrared up-conversion [31–33].

### 2.1.3. Amplification at 1.3 and 1.5 $\mu\text{m}$

A driving force for research in RE doped fibres and integrated optics waveguides has been their use for amplifying weak signals in optical communications systems at 1.3 and 1.5  $\mu\text{m}$ . This may be achieved by simply splicing a section of RE-doped fibre into the transmission one and injecting pump light through a fibre coupler. The signal generated within the RE emission band stimulates emission of radiation at the same frequency, amplifying the optical communication signal with high gain, high efficiency and low noise, which is highly advantageous for optical communications [24].

There are five main RE candidates for use as dopants in fibre or waveguide amplifiers for optical communications systems:  $\text{Er}^{3+}$ ,  $\text{Tm}^{3+}$ ,  $\text{Nd}^{3+}$ ,  $\text{Pr}^{3+}$  and  $\text{Dy}^{3+}$ .  $\text{Er}^{3+}$  and  $\text{Tm}^{3+}$  are the choice for the 1.4–1.6- $\mu\text{m}$  window centred at 1.5  $\mu\text{m}$ , based on the  $^4\text{I}_{13/2}$ – $^4\text{I}_{15/2}$  transition of  $\text{Er}^{3+}$  and the  $^3\text{H}_4$ – $^3\text{F}_4$  transition of  $\text{Tm}^{3+}$ . The  $^4\text{F}_{3/2}$ – $^4\text{I}_{13/2}$  emission of  $\text{Nd}^{3+}$ , the  $^1\text{G}_4$ – $^3\text{H}_5$  transition of  $\text{Pr}^{3+}$  and the  $^6\text{F}_{11/2}$  ( $^6\text{H}_{9/2}$ )– $^6\text{H}_{15/2}$  transition of  $\text{Dy}^{3+}$  are all potentially useful for the 1.3- $\mu\text{m}$  telecommunication window.

As with the laser mechanism, the major problems concerning amplification efficiency are related to dissipative processes. In addition to all the non-radiative relaxation processes already mentioned – multiphonon relaxation, cross-relaxation and co-operative up-conversion – other dissipative processes may decrease the amplification efficiency. The phenomena of excited-state absorption (ESA) and amplified spontaneous emission (ASE) are two of the most compromising processes, which can be partially eliminated by changing the glass composition.

## 2.2. Glass ceramics for photonics

### 2.2.1. Silicate oxyfluoride glass ceramics

Glass can play many varied roles in RE laser systems, namely as the laser host medium. Fluoride glasses and crystals are highly transparent materials, from the near-UV to the middle IR, with excellent RE ion solubility and low vibrational energies, making them excellent candidates as laser host materials [34], when compared to oxide glasses such as the silicates, which have limited transparency (from ~300–3000 nm) and RE solubility. The combination of high optical transparency, large stimulated emission cross-section and low non-radiative relaxation rates enhances the probabilities of observing fluorescent emissions that are normally quenched in oxide glasses. Nevertheless, fluoride glasses have less favourable chemical, thermal and mechanical properties, compared to oxide glasses and, as a result, are difficult to prepare and to handle [34]. In fact, most oxide glasses are much more attractive from the point of view of chemical and mechanical stabilities and are easier to melt and to fabricated as rods, optical fibres, or planar waveguides than fluoride glasses.

Early in 1975, Auzel et al. [35] reported a class of partially crystalline infrared up-conversion materials which were prepared from classical glass forming oxides such as  $\text{SiO}_2$ ,  $\text{GeO}_2$  and  $\text{P}_2\text{O}_5$ , mixed with  $\text{PbF}_2$  and a RE oxide, which showed a luminescence efficiency nearly twice as high as the  $\text{LaF}_3:\text{Yb:Er}$  phosphor. Since these materials were formed by a glass matrix and a crystal phase as large as 10  $\mu\text{m}$ , they were not transparent.

More recently, in 1993, Wang and Ohwaki [36] reported for the first time a transparent and optically isotropic oxyfluoride glass-ceramic, based on a cubic fluoride crystal phase, containing  $\text{Er}^{3+}$  and  $\text{Yb}^{3+}$  ions, dispersed throughout a continuous aluminosilicate base glass. This TGC was shown to combine the optical advantages of RE-doped fluoride crystals with the ease of forming and handling of conventional oxide glasses. From the X-ray diffraction peak widths and the Scherrer formula, 20-nm nanocrystals, tentatively identified as cadmium lead fluoride,  $\text{Pb}_x\text{Cd}_{1-x}\text{F}_2$ , were found to precipitate from the precursor aluminosilicate glasses through a suitable heat treatment. The resonant energy transfer between ytterbium and erbium was used to produce up-conversion and fluorescence in the red–green region. With an excitation wavelength of 0.97  $\mu\text{m}$ , the measured up-conversion emission intensity from the glass-ceramic was 100 times that of the precursor oxyfluoride glass and 2–10 times that of a fluoroaluminosilicate glass [36], indicating excellent up-conversion efficiency and strongly suggesting the segregation of  $\text{Yb}^{3+}$  and  $\text{Er}^{3+}$  ions within  $\text{Pb}_x\text{Cd}_{1-x}\text{F}_2$  nanocrystals. The authors attributed this enhanced up-converted (anti-Stokes) fluorescence to a more efficient energy transfer from  $\text{Yb}^{3+}$  to the  $^4\text{F}_{9/2}$  and  $^4\text{S}_{3/2}$  states of  $\text{Er}^{3+}$ . These oxyfluoride glass ceramics have potential application in blue–green laser devices and also as hosts for  $\text{Pr}^{3+}$ , in amplifiers for the 1.3- $\mu\text{m}$  telecommunication window. However, the crystals have a cubic lattice structure and this limits the concentration of some of the trivalent RE elements, which can be incorporated into the crystal phase. Another problem with these materials is that they require cadmium in the formulation; so this type of glass might not be desirable for a large-scale manufacturing operation.

Tick et al. [37] fabricated ytterbium-free oxyfluoride glass ceramics containing yttrium and zinc fluorides and praseodymium-doped nanocrystals of cadmium lead fluorides. The crystallite sizes were estimated from the X-ray line width of the strongest two peaks and the volume fraction of crystalline phase was estimated by integrating the area of the peaks and comparing it to the total area of the glassy halo, indicating that these glass ceramics contained 15–30% by volume of crystals, with sizes between 9–18 nm. Since these nanocrystals were believed to correspond to a Cd–Pb-rich fluoride composition, with a refractive index as large as 1.8, and the residual host glass had to be an aluminosilicate, with a refractive index as low as 1.5, the scattering Hopper model [21] indicated that the essential condition for high transparency was a structure comprised of uniformly dispersed nanoparticles, with interparticle spacing of dimensions comparable to the particle size. As long as both the

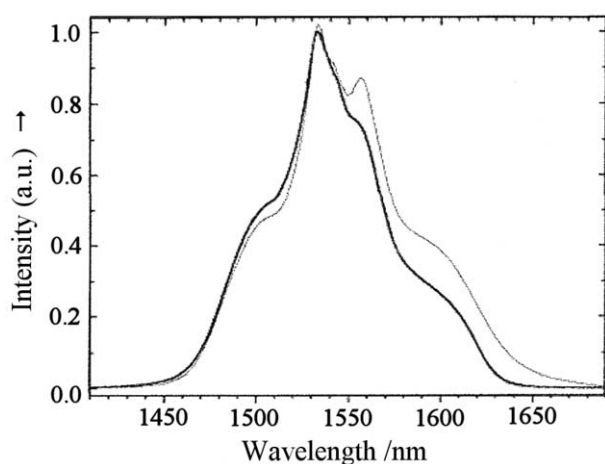


Fig. 2. Normalised photoluminescence spectra of  $\text{Er}^{3+}$  ( ${}^4\text{I}_{13/2} \rightarrow {}^4\text{I}_{15/2}$  transition) in the precursor oxyfluoride glass (thick solid line) and in a developed glass ceramic heat treated at  $440\text{ }^\circ\text{C}$  for 5 h (dashed line). (Adapted from ref. [38].)

particle size and interparticle spacing remained of the order of a few tens of nanometers or less, refractive index matching was not essential in achieving high transparency, within this quasi-continuous solid approach.

Kukkonen et al. [38], based on high resolution transmission electron microscopy, have discussed the crystallisation mechanism of the above oxyfluoride glasses upon heat treatment and have proposed that the oxyfluoride phase separates to a mainly  $\text{PbF}_2$  crystalline phase, hosting the  $\text{Er}^{3+}$  dopant and not to a more complex solid solution of  $\text{CdF}_2$  with  $\text{PbF}_2$ , i.e.,  $\text{Pb}_x\text{Cd}_{1-x}\text{F}_2$ . The broadest and flattest emission spectrum of  $\text{Er}^{3+}$  for the  ${}^4\text{I}_{13/2} \rightarrow {}^4\text{I}_{5/2}$  transition was recently reported for a cerammed  $\text{SiO}_2\text{-Al}_2\text{O}_3\text{-CdF}_2\text{-PbF}_2\text{-ZnF}_2$  glass precursor composition, where 2–12-nm  $\beta\text{-PbF}_2$  crystals, hosting  $\text{Er}^{3+}$  dopant ions, had developed [39], whose photoluminescence spectra are shown in Fig. 2. This glass ceramic may be important for the reduction of self-absorption and the respective noise in EDFA's. These authors reported

also a new glass-ceramic type, denominated *quasi-crystal*, with a typical size of nanocrystals (or embryos) of 2–3 nm. The emission intensity of  $\text{Er}^{3+}$ -doped quasi-glass ceramic was flat across the 1530–1560 nm range, which falls in the most often employed C-band of Dense Wavelength Division Multiplexing (DWDM) systems [39].

Méndez-Ramos et al. [40] reported the optical properties of  $\text{Eu}^{3+}$  ions in oxyfluoride glass ceramics with the precursor glass composition  $30\text{ SiO}_2\text{-15 Al}_2\text{O}_3\text{-29 CdF}_2\text{-22 PbF}_2\text{-1.5 YF}_3$  (in mol%). The ceramming process in these oxyfluoride glasses produced a glass ceramic where  $\text{EuF}_3$  crystals were initially produced and then acted as a nucleating agent for  $\text{Pb}_x\text{Cd}_{1-x}\text{F}_2$  crystal formation. A lifetime of 5.4 ms, obtained for the  ${}^5\text{D}_0$  level of the  $\text{Eu}^{3+}$  ions in  $\text{EuF}_3$  crystals, was close to the value of 4.5 ms, measured in the glass ceramic.

Fibres can be drawn from these TGC materials, for amplifiers operating at  $1.3\text{ }\mu\text{m}$ . A  $\text{Pr}^{3+}$  fluorescence band wider than in fluorozirconate glasses has been found [41]. Tick et al. [42] measured the passive scattering losses in near single mode fibres, with TGC composition cores [37]. Using difference spectra, those authors showed that the incremental intrinsic losses in these glass-ceramic structures were in the neighbourhood of  $100\text{ dB km}^{-1}$  [42].

It is not necessary to have all the RE ions inside the crystalline phase. For certain applications, such as gain-flattened amplifiers for DWDM systems, for example, a combination of  $\text{Er}^{3+}$  ions in the glass matrix and in the crystalline phase may be optimal. The quantum efficiencies, obtained from the ratio of the measured lifetime to the radiative lifetime calculated using the Judd–Ofelt theory [43, 44], have been given by Quimby et al. [45] and later by Méndez-Ramos et al. [46], for the two glass ceramics reported by Tick et al. [37], with values between 8–9%, as shown in Table 2.

Another family of oxyfluoride TGC, based on 15-nm crystals of  $\text{LaF}_3$  in a sodium aluminosilicate

Table 2. Composition and properties of some glasses and corresponding transparent oxyfluoride glass ceramics (adapted from refs [20, 37]).

|   | Y. Wang and J. Ohwaki [36]   | P.A. Tick et al. [37]  | M.J. Dejneka [48]  | Y. Kawamoto et al. [51]  |
|---|--|--|--|--|
| Base glass composition (mol%)                       | 30 $\text{SiO}_2\text{-15 AlO}_{1.5}\text{-24 PbF}_2\text{-20 CdF}_2\text{-10 YbF}_3\text{-1 ErF}_3$ | 30 $\text{SiO}_2\text{-15 AlO}_{1.5}\text{-17 PbF}_2\text{-29 CdF}_2\text{-4 YF}_3\text{-5 ZnF}_2$ | 48.5 $\text{SiO}_2\text{-25.1 AlO}_{1.5}\text{-13.1 LaF}_3\text{-2.5 AlF}_3\text{-10.7 Na}_2\text{O}\text{-0.1 ErF}_3$ | 50 $\text{SiO}_2\text{-50 PbF}_{2-x}\text{ErF}_3$<br>( $x = 4$ and $5$ ) |
| Glass host  | $\text{SiO}_2\text{-Al}_2\text{O}_3$   | $\text{SiO}_2\text{-Al}_2\text{O}_3$   | $\text{SiO}_2\text{-Al}_2\text{O}_3\text{-Na}_2\text{O}$   | $\text{SiO}_2$   |
| Crystal phase                                       | $\text{Pb}_x\text{Cd}_{1-x}\text{F}_2$   | (Cd, Pb, Zn, Y) $\text{F}_{2.3}$   | $\text{LaF}_3\text{-0.1 ErF}_3$  | $\beta\text{-PbF}_2\text{:Er}^{3+}$                                      |
| Cubic lattice parameter (nm)                        | 0.572  | 0.575  | —  | 0.582  |
| Crystal dimension (nm)                              | 20   | 9–18   | 15   | 13   |
| Volume fraction (vol%)                              | —  | 20–30  | —  | —  |
| Refractive index                                    | —  | 1.75   | 1.55   | —  |
| CTE ( $\times 10^{-7}\text{ }^\circ\text{C}^{-1}$ ) | —  | 110  | —  | —  |
| $T_g$ ( $^\circ\text{C}$ )                          | 400  | 395  | 570  | —  |

glass, has been proposed by Dejneka [47, 48].  $\text{LaF}_3$  is an ideal low-phonon host for RE cations [49], due to its ability to form extensive solid solutions with all the RE ions [50]. Emission spectroscopy showed a partition of the  $\text{Eu}^{3+}$  ions between the low-phonon-energy  $\text{LaF}_3$  crystal and the glass host material. In fact,  $\text{Eu}^{3+}$ -doped glasses emit only red luminescence from the  $^5\text{D}_0$  level, but, after a suitable heat treatment, they emit blue and green luminescence as well, indicative of a low phonon energy RE environment.  $\text{Er}^{3+}$  fluorescence and lifetime measurements in this material showed a large width and flatness for the 1530 nm emission, suggesting a good amplifier performance.

Kawamoto et al. [51] found that oxyfluoride glasses can be obtained in the  $\text{SiO}_2\text{-PbF}_2\text{-ErF}_3$  system and heat treatment of these glasses yielded TGC in which  $\beta\text{-PbF}_2\text{:Er}^{3+}$  crystallites were dispersed in the glass matrix. The Scherrer equation yielded an average crystallite diameter near 13 nm. The diffraction peaks of the crystalline precipitate could be indexed in terms of the fluorite structure (space group:  $Fm\bar{3}m$ ), with a lattice constant  $a = 0.582$  nm. The lattice constant of the  $\beta\text{-PbF}_2$  crystal, with the fluorite structure, is  $a = 0.594$  nm [52]. The slightly smaller lattice constant of the present crystalline precipitate indicated that it was a solid solution of the type  $\beta\text{-PbF}_2\text{:Er}^{3+}$ , in which the  $\text{Pb}^{2+}$  ions, with an ionic radius of 0.129 nm, were partially substituted by  $\text{Er}^{3+}$  ions, with an ionic radius of 0.100 nm. These glass ceramics had highly efficient up-conversion luminescence, under 800 nm laser excitation.

The composition and properties of the oxyfluoride glass ceramics are summarised in Table 2. Clearly, three main types of optically transparent, silica-based glass ceramics have been achieved: (i) those prepared by Wang and Ohwaki [36] and Tick et al. [37], based upon the formation of a (Pb, Cd) $\text{F}_2$  cubic phase, incorporating  $\text{Er}^{3+}/\text{Yb}^{3+}$  or  $\text{Pr}^{3+}$ , in an aluminosilicate base glass; (ii) a second type, formed by  $\text{LaF}_3$  crystals in a sodium aluminosilicate base glass, reported by Dejneka [47]; finally, (iii) a third type, where  $\beta\text{-PbF}_2\text{:Er}^{3+}$  crystallites are dispersed in a silica glass matrix, as reported by Kawamoto et al. [51].

All the above transparent silica-based glass ceramics are not only very stable, but also all melting and processing can be done in platinum crucibles in air, at temperatures between 1000 and 1200 °C. Afterwards, the precursor glass is thermally treated at a temperature that is usually that of a crystallisation peak that lies just above  $T_g$ . The optimum ceramming temperature normally lies between the onset and the peak maximum of the crystallisation exotherm.

It has been found that the presence of the RE elements is needed in order to obtain a low temperature

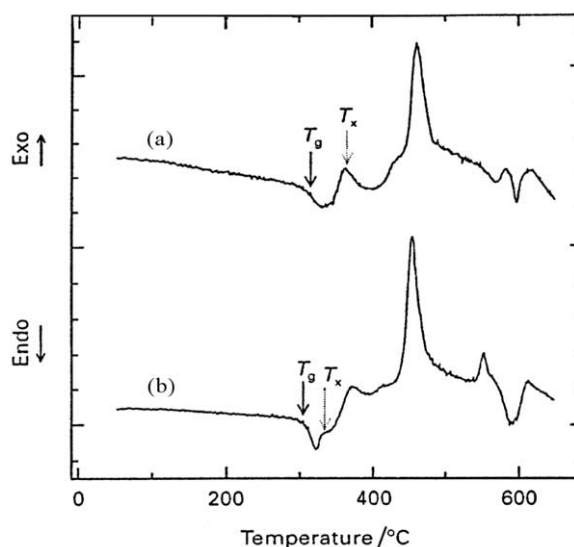


Fig. 3. DTA curves of the glass compositions  $50 \text{SiO}_2\text{-}50 \text{PbF}_2\text{-}x \text{ErF}_3$ , (a)  $x = 3$  and (b)  $x = 5$  (in mol%). (Adapted from ref. [51].)

crystallisation peak in these silicate-based systems, as illustrated in Fig. 3. The corresponding XRD patterns for the composition with 5% Er are shown in Fig. 4. Braglia et al. [41] pointed out that primary crystallisation is of paramount relevance in these oxyfluoride systems, since the photoluminescence intensity increased as the transformation to the nanocrystalline phase progressed. This finding was an indication that the surroundings of the RE ions were changed by the formation of crystallites, because of the ion migration either into these crystals, or toward the nano-crystal/glass boundaries.

The high-temperature properties of all these oxyfluoride glass ceramics, in which the optically active

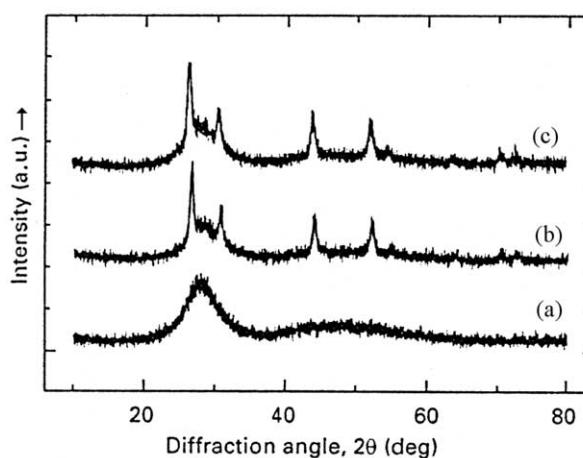


Fig. 4. XRD patterns of  $50 \text{SiO}_2\text{-}50 \text{PbF}_2\text{-}5 \text{ErF}_3$  (mol%) glass, heat treated at the first crystallisation temperature,  $T_x$ , for (a) 0 h, (b) 0.5 h and (c) 6 h. (Adapted from ref. [51].)

RE ions partition into a fluoride crystal phase, are more like those of an oxide than a fluoride glass. Oxyfluoride glass ceramics offer an economic alternative, with substantial performance improvements, over purely fluoride glasses. They combine the attributes of the fluoride crystal phase with those of a conventional silica-based glass matrix. A patent has already been registered with some of these glass compositions [53].

### 2.2.2. Germanate-oxyfluoride glass ceramics

Lead germanate oxyfluoride TGC were obtained in 1995 by Hirao et al. [54], in the  $\text{GeO}_2\text{-PbO-PbF}_2\text{-TmF}_3$  system, containing  $\sim 16$  nm  $\beta\text{-PbF}_2\text{:Tm}^{3+}$  crystals. Bueno et al. [55] and Mortier and Auzel [56] studied the  $\text{GeO}_2\text{-PbO-PbF}_2\text{-CdF}_2$  and  $\text{GeO}_2\text{-PbO-PbF}_2\text{-Er}^{3+}$ -doped systems, respectively. Both groups obtained cubic  $\beta\text{-PbF}_2\text{:Er}^{3+}$  nanocrystallites  $\sim 5\text{-}10$  nm and  $\sim 8\text{-}20$  nm in size, respectively, in TGC materials. Mortier et al. [56] measured the lifetime of the  ${}^4\text{I}_{11/2} \rightarrow {}^4\text{I}_{13/2}$  transition of  $\text{Er}^{3+}$  around  $2.7$   $\mu\text{m}$ , in germanate glasses of composition  $50\text{ GeO}_2\text{-}40\text{ PbO-}10\text{ PbF}_2$  (mol%) doped with  $1\text{-}4$  mol%  $\text{ErF}_3$ , before and after heat treatment, and found an increase from  $360$   $\mu\text{s}$  to  $3$  ms with the nanocrystallisation, for  $3$  mol%  $\text{Er}^{3+}$ , which was still less than the  $7$  ms of crystalline  $\text{PbF}_2$  doped with  $1$  mol%  $\text{ErF}_3$  [56, 57], suggesting that only some of the  $\text{Er}^{3+}$  ions were incorporated into  $\beta\text{-PbF}_2$  crystals.

Germanate oxyfluoride TGC were also obtained for higher concentrations of  $\text{PbF}_2$  and infrared up-conversion to the visible and near UV regions was observed in Yb-doped  $\text{PbF}_2\text{-GeO}_2\text{-Al}_2\text{O}_3\text{-Tm}_2\text{O}_3$  glasses and glass ceramics [58], as shown in Fig. 5. Improved fluorescence was also obtained for  $\text{Tm}^{3+}$  precipitated in  $\text{PbF}_2$  nanocrystals, upon ceramisation of germano-silicate oxyfluoride glass [59]. When compared with the glasses, the lifetime of the TGC compositions increased from  $\sim 400$  to  $\sim 500$   $\mu\text{s}$  at  $1.4$   $\mu\text{m}$  and remained unchanged at  $\sim 5.0$  ms at  $1.8$   $\mu\text{m}$ .

### 2.2.3. Tellurite oxyhalide glass ceramics

The search for other glass precursors for TGC has been motivated by the limited RE solubility and small non-linear behaviour of silica-based compositions, as well as the low chemical durability of purely fluoride compositions. Tellurite glasses have the lowest vibrational energies ( $\sim 700$   $\text{cm}^{-1}$ ) among oxide glasses (cf. Table 1), large refractive indices ( $n \sim 2$ ), large RE solubility and low melting points [60], thus suggesting their high potential as new optical functional materials, for optical amplifiers, frequency up-converters and lasers.

Although RE doped  $\text{TeO}_2$ -based glasses have been extensively studied by several authors [61], there is very little information on  $\text{TeO}_2$ -based TGC. Devel-

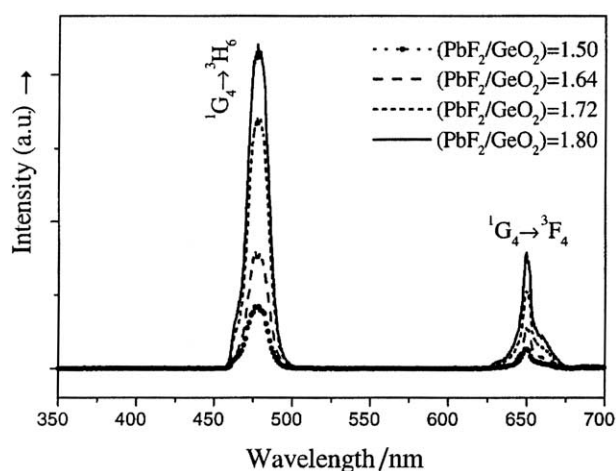


Fig. 5. Up-conversion emission spectra of  $\text{Tm}^{3+}/\text{Yb}^{3+}$ -co-doped  $\text{PbF}_2\text{-GeO}_2\text{-Al}_2\text{O}_3$  glass ceramics, containing  $3$  mol%  $\text{Al}_2\text{O}_3$ , as a function of the  $\text{PbF}_2/\text{GeO}_2$  ratio. (Adapted from ref. [58].)

oped by Shioya et al. [62], the first  $\text{TeO}_2$ -based TGC consisted of an unknown cubic crystalline phase with an average diameter of  $\sim 20\text{-}40$  nm, crystallised from a  $70\text{ TeO}_2\text{-}15\text{ Nb}_2\text{O}_5\text{-}15\text{ K}_2\text{O}$  glass composition (mol%). This glass ceramic presented better optical and dielectric properties than those of the parent glass and second-harmonic generation (SHG) was achieved [62, 63]. Oishi et al. [64] doped this composition (modified with  $\text{MgO}$ ), with  $1.2$  mol%  $\text{Er}^{3+}$  and  $\text{Eu}^{3+}$  and optically TGC could be obtained, presenting higher up-conversion fluorescence intensity around  $550$  nm than the corresponding  $\text{TeO}_2$ -based glass precursors. It was also shown [65] that ceramisation of these glasses raised their Vickers hardness values, improving their mechanical properties. Hirano et al. [66] introduced several RE ions in the same system and obtained up-conversion fluorescence intensities about  $20$  times higher than in the corresponding  $70\text{ TeO}_2\text{-}15\text{ Nb}_2\text{O}_5\text{-}15\text{ K}_2\text{O}$  glass composition, with  $1$  mol%  $\text{Er}_2\text{O}_3$ .

Recently, tellurium oxyfluoride TGC have also been obtained [67] with the composition  $80\text{ TeO}_2\text{-}10\text{ PbF}_2\text{-}10\text{ CdF}_2$  (mol%), whose crystalline phase was identified to be  $\text{PbTe}_3\text{O}_7$ , by XRD and EXAFS, but no information was given concerning their luminescence properties. Erbium-doped tellurium oxyhalide TGC have also recently been obtained in the  $\text{TeO}_2\text{-ZnO-ZnCl}_2$  system, for the  $60\text{ TeO}_2\text{-}20\text{ ZnO-}20\text{ ZnCl}_2$  and  $40\text{ TeO}_2\text{-}20\text{ ZnO-}40\text{ ZnCl}_2$  (mol%) compositions doped with  $1\text{-}10$  mol%  $\text{ErCl}_3$  [68]. The precursor tellurite glasses, modified by zinc or lead oxide plus the corresponding halides, have been investigated [69] and the corresponding glass-forming regions were determined. Compositions in the  $\text{TeO}_2\text{-ZnO-ZnX}_2$  and  $\text{TeO}_2\text{-PbO-PbX}_2$  glass systems, in particular with  $\text{X} = \text{Cl}$ , yielded stable glasses of

good optical quality.  $\text{TeO}_2\text{-ZnO-ZnCl}_2$  glasses with 20 mol% ZnO were selected as hosts for  $\text{ErCl}_3$ , up to 10 mol%. The 1.5- $\mu\text{m}$  photoluminescence spectra and metastable level lifetimes of  $\text{Er}^{3+}$  in these glasses, especially with  $\sim 3\text{--}5$  mol%  $\text{ErCl}_3$ , suggest that they may be suitable for optical amplifier applications [69]. A measured lifetime of  $\sim 7$  ms, was obtained for the  ${}^4\text{I}_{13/2} \rightarrow {}^4\text{I}_{15/2}$  transition of  $\text{Er}^{3+}$ , in these tellurite glass ceramic [68].

#### 2.2.4. Other glass ceramic compositions

Purely fluoride TGC have been prepared by Jewell et al. [70] in a  $\text{ZrF}_4$ -doped CLAP ( $\text{CdF}_2\text{-LiF-AlF}_3\text{-PbF}_2$ ) glass. According to the authors, more than 80% transmission in the visible was achieved, even for 95% crystallisation. Mortier et al. [71] also prepared TGC in a fluoride system ( $\text{ZrF}_4\text{-LaF}_3\text{-ErF}_3\text{-GaF}_3\text{-AlF}_3$ ), by liquid–liquid phase separation, resulting in spinodal decomposition. Good transparency was obtained for a high crystallisation level (90%), due to a good refractive index matching between the glass and crystal phases.

Fluorescence was observed in europium-doped fluorobromozirconate TGC [72], where  $\text{Eu}^{2+}$  ions were believed to precipitate in  $\text{BaBr}_2$  crystals.

Recently, lithium–borate–oxide–based TGC have been synthesised in the  $\text{Li}_2\text{B}_4\text{O}_7\text{-Bi}_2\text{WO}_6$  [73] and  $\text{Li}_2\text{B}_4\text{O}_7\text{-SrO-Bi}_2\text{O}_3\text{-Nb}_2\text{O}_5$  systems [74], comprising spherical ferroelectric nanocrystalline phases:  $\text{Bi}_2\text{WO}_6$ ,

with  $\sim 2\text{--}33$  nm and  $\text{SrBi}_2\text{Nb}_2\text{O}_9$ , with  $\sim 20$  nm, respectively, embedded in a  $\text{Li}_2\text{B}_4\text{O}_7$  glass matrix. These glass ceramics have increased dielectric constants and low dielectric losses, when compared with the parent glasses, as well as high second-harmonic generation efficiencies.

TGC can also be efficient hosts for transition metal ions, as demonstrated by Beall [75] for  $\text{Cr}^{4+}$ -doped forsterite ( $\text{Mg}_2\text{SiO}_4$ ) and Pinckney et al. [76], with  $\text{Ni}^{2+}$ -doped gallate spinel. Beall isolated a forsterite-rich glass composition via nanoscale phase separation in the  $\text{SiO}_2\text{-Al}_2\text{O}_3\text{-MgO-K}_2\text{O}$  system. When doped with chromium oxide, both  $\text{Cr}^{4+}$  luminescence and absorption became similar to those of single crystals. However, transparency was only achieved with the addition of  $\text{TiO}_2$  as a nucleating agent.

### 3. Conclusions

TGC have a number of useful properties, especially for photonics applications. Here, the precipitation of a fluoride or other halide crystalline phase with low maximum vibrational energy, containing a RE ion such as  $\text{Er}^{3+}$ , within an oxide or oxyhalide glass matrix of high stability, achieves improved luminescence properties for the RE ion, without sacrificing good glass-forming ability, glass stability and ease of glass fabrication. Therefore, TGC is a very promising new type of photonic material.

### References

- [1] S.D. Stookey, *Ind. Eng. Chem.* 45 (1953) 115.
- [2] S.D. Stookey, Photosensitively Opacifiable Glass, US Patent No. 2 684 911, 1954.
- [3] S.D. Stookey, *Ind. Eng. Chem.* 51 (1959) 805.
- [4] S.D. Stookey, Ceramic Body and Method of Making It, US Patent No. 2 971 853, 1961.
- [5] W. Höland, G. Beall, *Glass Ceramic Technology*, The American Ceramic Society, 2002.
- [6] M. Réaumur, *Mém. Acad. R. Sci. Paris* (1739) 370.
- [7] Pyroflam®, Registered Newell SA Trademark.
- [8] Visions®, Registered Corning Glass Works Trademark.
- [9] Z. Strnad, *Glass Ceramic Materials*, Elsevier, Amsterdam, The Netherlands, 1986.
- [10] (a) Fotoform®, Fotoceram®, Registered Corning Glass Works Trademarks; (b) G.H. Beall, *Annu. Rev. Mater. Sci.* 22 (1992) 91.
- [11] Foturan®, Registered Schott Glaswerke and mtg Mikroglas Technik AG, Mainz, Germany Trademark.
- [12] Bioglass®, Registered US Trademark, University of Florida, Gainesville, FL, USA, 32611.
- [13] R. Li, A.E. Clark, L.L. Hench, *J. Appl. Biomater.* 2 (1991) 231.
- [14] H. Brömer, E. Pfeil, H.H. Käs, German Patent No. 2 326 100, 1973.
- [15] T. Kokubo, *Glastech. Ber.* 67C (1994) 105.
- [16] D.G. Grossmann, *Am. Machinist* (May 1978) 139.
- [17] K.A. Malament, D.G. Grossman, *J. Prosthetic Dent.* 57 (1987) 674.
- [18] W. Vogel, W. Höland, *Angew. Chem. Int. Ed. Engl.* 26 (1987) 527.
- [19] Schott Glaswerke Mainz, Brochure No. 10041, 1991.
- [20] G.H. Beall, L.R. Pinckney, *J. Am. Ceram. Soc.* 82 (1999) 5.
- [21] R.W. Hopper, *J. Non-Cryst. Solids* 70 (1985) 111.
- [22] Neoceram®, Registered Nippon Electric Glass Trademark.
- [23] P.A. Tick, Extended Abstracts of the International Symposium on Non-Oxide Glasses, Sheffield, UK, 1998, p. 14.
- [24] M. Yamane, Y. Asahara, *Glasses for Photonics*, Cambridge University Press, Cambridge, UK, 2002.
- [25] T. Miyakawa, D.L. Dexter, *Phys. Rev. B* 1 (1970) 2961.
- [26] R. Reisfeld, C.K. Jorgensen, Excited State Phenomena in Vitreous Materials, in: K.A. Gschneidner Jr, L. Eyring (Eds.), *Handbook on the Physics and Chemistry of Rare Earths*, Vol. 9, North Holland, Amsterdam, 1987, p. 1.
- [27] M.J. Weber, Non-Metallic Compound II, in: K.A. Gschneidner Jr, L.R. Eyring (Eds.), *Handbook on the Physics and Chemistry of Rare Earths*, Vol. 4, Chap. 35, North-Holland Physics Publishing, Amsterdam, 1979, p. 275.
- [28] D.W. Hall, M.J. Weber, in: M.J. Weber (Ed.), *CRC Handbook of Laser Science and Technology, Supplement 1: Lasers*, CRC Press, Boca Raton, 1991, p. 137.
- [29] M.J. Weber, *J. Non-Crystalline Solids* 123 (1990) 208.
- [30] J.A. Caird, S.A. Payne, M.J. Weber (Eds.), *CRC Handbook of Laser Science and Technology, Supplement 1, Lasers*, CRC Press, Boca Raton, 1991, p. 3.
- [31] F. Auzel, *J. Lumin.* 45 (1990) 341.

- [32] Y. Mita, K. Hiram, N. Ando, H. Yamamoto, S. Shionoya, *J. Appl. Phys.* 74 (1993) 4703.
- [33] Y. Mita, *J. Appl. Phys.* 43 (1972) 1772.
- [34] R.M. Almeida, Fluoride Glasses, in: K.A. Gschneidner Jr, L. Eyring (Eds.), *Handbook on the Physics and Chemistry of Rare Earths*, Vol. 15, Elsevier Science Publishers, 1991, p. 287.
- [35] F. Auzel, D. Pecile, D. Morin, *J. Electrochem. Soc.* 122 (1975) 101.
- [36] Y. Wang, J. Ohwaki, *Appl. Phys. Lett.* 63 (1993) 3268.
- [37] P.A. Tick, N.F. Borrelli, L.K. Cornelius, M.A. Newhouse, *J. Appl. Phys.* 78 (1995) 93.
- [38] L.L. Kukkonen, I.M. Reaney, D. Furniss, M.G. Pellat, A.B. Seddon, *J. Non-Cryst. Solids* 290 (2001) 25.
- [39] V.K. Tikhomirov, D. Furniss, A.B. Seddon, M. Ferrari, R. Rolli, *J. Mater. Sci. Lett.* 21 (2002) 293.
- [40] J. Méndez-Ramos, V. Lavín, I.R. Martín, U.R. Rodríguez-Mendoza, V.D. Rodríguez, D. Lozano-Gorrín, P. Núñez, *J. Appl. Phys.* 89 (2001) 5307.
- [41] M. Braglia, C. Bruschi, G. Dai, J. Kraus, S. Mosso, M. Baricco, L. Battezzati, F. Rossi, *J. Non-Cryst. Solids* 256–257 (1999) 170.
- [42] P.A. Tick, N.F. Borrelli, I.M. Reaney, *Opt. Mater.* 15 (2000) 81.
- [43] B.R. Judd, *Phys. Rev.* 127 (1962) 750.
- [44] G.S. Ofelt, *J. Chem. Phys.* 37 (1962) 511.
- [45] R.S. Quimby, P.A. Tick, N.F. Borrelli, L.K. Cornelius, *J. Appl. Phys.* 83 (1998) 1649.
- [46] J. Méndez-Ramos, V. Lavín, I.R. Martín, U.R. Rodríguez-Mendoza, J. González-Almeida, V.D. Rodríguez, D. Lozano-Gorrín, P. Núñez, *J. Alloys Compds* 323–324 (2001) 753.
- [47] M.J. Dejneka, *Proc. SPIE* 3280 (1998) 132.
- [48] M.J. Dejneka, *J. Non-Cryst. Solids* 239 (1998) 149.
- [49] M.J. Weber, *J. Chem. Phys.* 48 (1968) 4774.
- [50] O.V. Kudryavtseva, L.S. Garashina, K.K. Rivkina, B.P. Sobolev, *Sov. Phys. Crystallogr.* 18 (1974) 531.
- [51] Y. Kawamoto, R. Kanno, J. Qiu, *J. Mater. Sci.* 33 (1998) 63.
- [52] JCPDS International Centre for Diffraction Data Card No. 6-0251.
- [53] P. Tick, United States Patent, No. US 6 281 151 B1, 28 August 2001.
- [54] K. Hirao, K. Tanaka, M. Makita, N. Soga, *J. Appl. Phys.* 78 (1995) 3445.
- [55] L.A. Bueno, P. Melnikov, Y. Messaddeq, S.L.J. Ribeiro, *J. Non-Cryst. Solids* 247 (1999) 87.
- [56] M. Mortier, F. Auzel, *J. Non-Cryst. Solids* 256–257 (1999) 361.
- [57] M. Mortier, P. Goldner, C. Château, M. Genotelle, *J. Alloys Compds* 323–324 (2001) 245.
- [58] F.C. Guinhos, P.C. Nóbrega, P.A. Santa-Cruz, *J. Alloys Compds* 323–324 (2001) 358.
- [59] H. Hayashi, S. Tanabe, T. Hanada, *J. Appl. Phys.* 89 (2001) 1041.
- [60] J.S. Wang, E.M. Vogel, E. Snitzer, *Opt. Mater.* 3 (1994) 187.
- [61] R.A.H. El-Mallawany, *Tellurite Glasses Handbook – Physical Properties and Data*, CRC Press, Boca Raton, 2001.
- [62] K. Shioya, T. Komatsu, H.G. Kim, R. Sato, K. Matusita, *J. Non-Cryst. Solids* 189 (1995) 16.
- [63] H.G. Kim, T. Komatsu, K. Shioya, K. Matusita, K. Tanaka, K. Hirao, *J. Non-Cryst. Solids* 208 (1996) 303.
- [64] H. Oishi, Y. Benino, T. Komatsu, *Phys. Chem. Glasses* 40 (1999) 212.
- [65] T. Watanabe, Y. Benino, K. Ishizaki, T. Komatsu, *J. Ceram. Soc. Jpn* 107 (1999) 1140.
- [66] K. Hirano, Y. Benino, T. Komatsu, *J. Phys. Chem. Solids* 62 (2001) 2075.
- [67] M.A.P. Silva, Y. Messaddeq, V. Briois, M. Poulain, F. Villain, S.J.L. Ribeiro, *J. Phys. Chem. Solids* 63 (2002) 605.
- [68] Luís M. Fortes, Luís F. Santos, M. Clara Gonçalves, Rui M. Almeida, unpublished work.
- [69] L.M. Fortes, L.F. Santos, M. Clara Gonçalves, Rui M. Almeida (submitted for publication).
- [70] J.M. Jewell, E. Joseph Friebele, Ishwar D. Aggarwal, *J. Non-Cryst. Solids* 188 (1995) 285.
- [71] M. Mortier, A. Monteville, G. Patriarche, G. Mazé, F. Auzel, *Opt. Mater.* 16 (2001) 255.
- [72] A. Edgar, S. Schweizer, S. Assmann, J.M. Spaeth, P.J. Newman, D.R. MacFarlane, *J. Non-Cryst. Solids* 284 (2001) 237.
- [73] G.S. Murugan, K.B.R. Varma, *J. Non-Cryst. Solids* 279 (2001) 1.
- [74] N. Syam Prasad, K.B.R. Varma, *Mater. Sci. Eng. B90* (2002) 246.
- [75] G.H. Beall, *Proc. Int. Congr. Glass*, Vol. 2, Edinburgh, Scotland, 2001, p. 170.
- [76] L.R. Pinckney, B.N. Samson, G.H. Beall, J. Wang, *Proc. 104th Annual Meeting & Exhibition, The American Ceramic Society, St. Louis, Missouri, USA, 2002*, p. 120.

**Rare earth-doped glass microbarcodes**

Matthew J. Dejneka, Alexander Streltsov, Santona Pal, Anthony G. Frutos, Christy L. Powell, Kevin Yost, Po Ki Yuen, Uwe Müller, and Joydeep Lahiri

*PNAS* 2003;100;389-393; originally published online Jan 6, 2003;  
doi:10.1073/pnas.0236044100

**This information is current as of December 2006.**

**Online Information & Services**

High-resolution figures, a citation map, links to PubMed and Google Scholar, etc., can be found at:

[www.pnas.org/cgi/content/full/100/2/389](http://www.pnas.org/cgi/content/full/100/2/389)

**References**

This article cites 13 articles, 3 of which you can access for free at:

[www.pnas.org/cgi/content/full/100/2/389#BIBL](http://www.pnas.org/cgi/content/full/100/2/389#BIBL)

This article has been cited by other articles:

[www.pnas.org/cgi/content/full/100/2/389#otherarticles](http://www.pnas.org/cgi/content/full/100/2/389#otherarticles)

**E-mail Alerts**

Receive free email alerts when new articles cite this article - sign up in the box at the top right corner of the article or [click here](#).

**Rights & Permissions**

To reproduce this article in part (figures, tables) or in entirety, see:

[www.pnas.org/misc/rightperm.shtml](http://www.pnas.org/misc/rightperm.shtml)

**Reprints**

To order reprints, see:

[www.pnas.org/misc/reprints.shtml](http://www.pnas.org/misc/reprints.shtml)

Notes:

# Rare earth-doped glass microbarcodes

Matthew J. Dejneka\*, Alexander Streltsov, Santona Pal, Anthony G. Frutos, Christy L. Powell, Kevin Yost, Po Ki Yuen, Uwe Müller, and Joydeep Lahiri\*

Science and Technology Division, Corning Incorporated, Corning, NY 14831

Edited by George M. Whitesides, Harvard University, Cambridge, MA, and approved November 25, 2002 (received for review October 7, 2002)

**The development of ultraminiaturized identification tags has applications in fields ranging from advanced biotechnology to security. This paper describes micrometer-sized glass barcodes containing a pattern of different fluorescent materials that are easily identified by using a UV lamp and an optical microscope. A model DNA hybridization assay using these "microbarcodes" is described. Rare earth-doped glasses were chosen because of their narrow emission bands, high quantum efficiencies, noninterference with common fluorescent labels, and inertness to most organic and aqueous solvents. These properties and the large number (>1 million) of possible combinations of these microbarcodes make them attractive for use in multiplexed bioassays and general encoding.**

Encoded bead bioassays are emerging as an attractive alternative to traditional slide-based microarrays because bead-based bioassays offer multiplexing of both probes and samples (the "analyte"), and they have significantly fewer drawbacks related to mass transport-limited binding of analytes to the immobilized probes. Several approaches have been described for the fabrication of encoded beads: those in which the coding material is randomly distributed in the bead (1, 2) and those in which the coding material is present in a defined pattern on the bead (3). Because different patterns of the same coding materials (e.g., position and thickness of metal stripes on cylindrical particles) result in distinguishable beads (3), a larger number of uniquely encoded beads can be obtained relative to beads with randomly distributed coding materials (e.g., polymer beads infused with mixtures of quantum dots) (2).

Current methods for fabricating encoded beads are limited in terms of either the number of possible codes or the compatibility of the beads with bioassays and fluorescence detection. The most widely used method for making encoded beads, infusing polymer microspheres with mixtures of fluorescent dyes in predefined ratios, is not well suited for the fabrication of large ( $>10^5$ ) numbers of uniquely distinguishable beads. Trau and coworkers have used silica microspheres containing fluorescent dyes for encoding polymer beads by using split-pool methods, and have also described the formation of dye-doped concentric silica layers around core silica particles (4). There are only a limited number of spectrally well-resolved dyes that do not also interfere with commonly used biological labels. Moreover, measurements of intensities and their ratios are inherently difficult, which limits the number of levels at which a dye can be incorporated to give distinguishable beads. Mixtures of quantum dots embedded in polymer microspheres offer significant advantages over conventional fluorescent dyes because they are relatively more photostable and have narrow emission linewidths (2). However, quantum dots are made of toxic materials (e.g., CdS, CdSe, CdTe) (5), and difficulties distinguishing between codes based on different amounts of the same quantum dots are similar to those for organic dyes. For both organic dyes and quantum dots, the use of polymer beads as a host matrix raises issues related to background fluorescence and poor compatibility with organic solvents (1). The use of cylindrical beads with metal stripes as codes described by Natan and coworkers (3) overcomes many of the limitations described above. Nevertheless, there are significant limitations. Decoding of beads based on differences in

reflectivity can be challenging (6). The use of particles consisting of several different surfaces (e.g., Au, Ag, Pt) and lateral widths (for each stripe) requires careful consideration of the surface chemistry and results in different surface areas for immobilization of the probe and binding of the analyte. Although the use of chemistries based on monolayers of alkanethiolates on gold is well established, gold-based surfaces significantly compromise the sensitivity of detection by fluorescence because of quenching by the gold (7).

Rare earth (RE) ions in a silicate glass matrix are an ideal material for the fabrication of encoded beads. REs are a spectroscopically rich (8) species (Fig. 1), a property that facilitates their use as optical codes in a spectral window distinct from fluorescent dyes used for labeling biological samples. The lanthanide  $4f$  orbitals are buried beneath the  $6s$ ,  $5p$ , and  $5d$  orbitals; hence, spectra arising from  $f-f$  transitions are narrow and insensitive to their environment, unlike transition metal ( $3d$ ) spectra (9, 10). Triply ionized RE ions in glassy hosts typically have emission line widths of  $\approx 10$ – $20$  nm (FWHM, full width at half maximum) in the visible portion of the spectrum, which is about half that observed for quantum dots (25–40 nm) and much narrower than that observed for organic dyes (30–50 nm) or transition metal ions ( $\approx 100$  nm) (2, 11, 12). This feature allows more resolvable bands to be packed into the same spectral bandwidth, which enables a larger number of distinct combinations. Because RE emissions involve only atomic transitions, they are extremely resistant to photobleaching. The energy level structure in RE ions also creates the possibility for large shifts between the excitation and emission bands. This shift can be several hundred nanometers containing discrete gaps with zero absorption. By comparison, the HOMO–LUMO (highest occupied molecular orbital–lowest unoccupied molecular orbital) transition in organic dyes typically results in overlapping excitation and emission bands and a Stokes shift of only 10–30 nm between the absorption and emission maxima. Thus, multiple RE ions can be simultaneously excited in the UV and conveniently decoded by observing their emission in the visible, without interfering with organic tags that have excitations in the visible. The silica-based glass matrix itself offers significant advantages relative to polymer-based materials: lower phonon energies that alleviate issues with nonradiative decay, readily available silane chemistries that facilitate the immobilization of biomolecules, compatibility with organic solvents that enable procedures requiring nonaqueous solvents, and low background fluorescence that provides lower limits of detection. In addition, glass preforms can be efficiently drawn down into miles of very thin fiber or ribbons whose structure is an exact miniature of the parent preform, allowing large complex structures to be replicated down to the desired size.

## Materials and Methods

**Glass Fabrication.** RE-doped alkaline earth aluminosilicate glass compositions for a particular "color" were mixed, melted in a

This paper was submitted directly (Track II) to the PNAS office.

Abbreviation: RE, rare earth.

\*To whom correspondence may be addressed. E-mail: dejnekamj@corning.com or lahrij@corning.com.

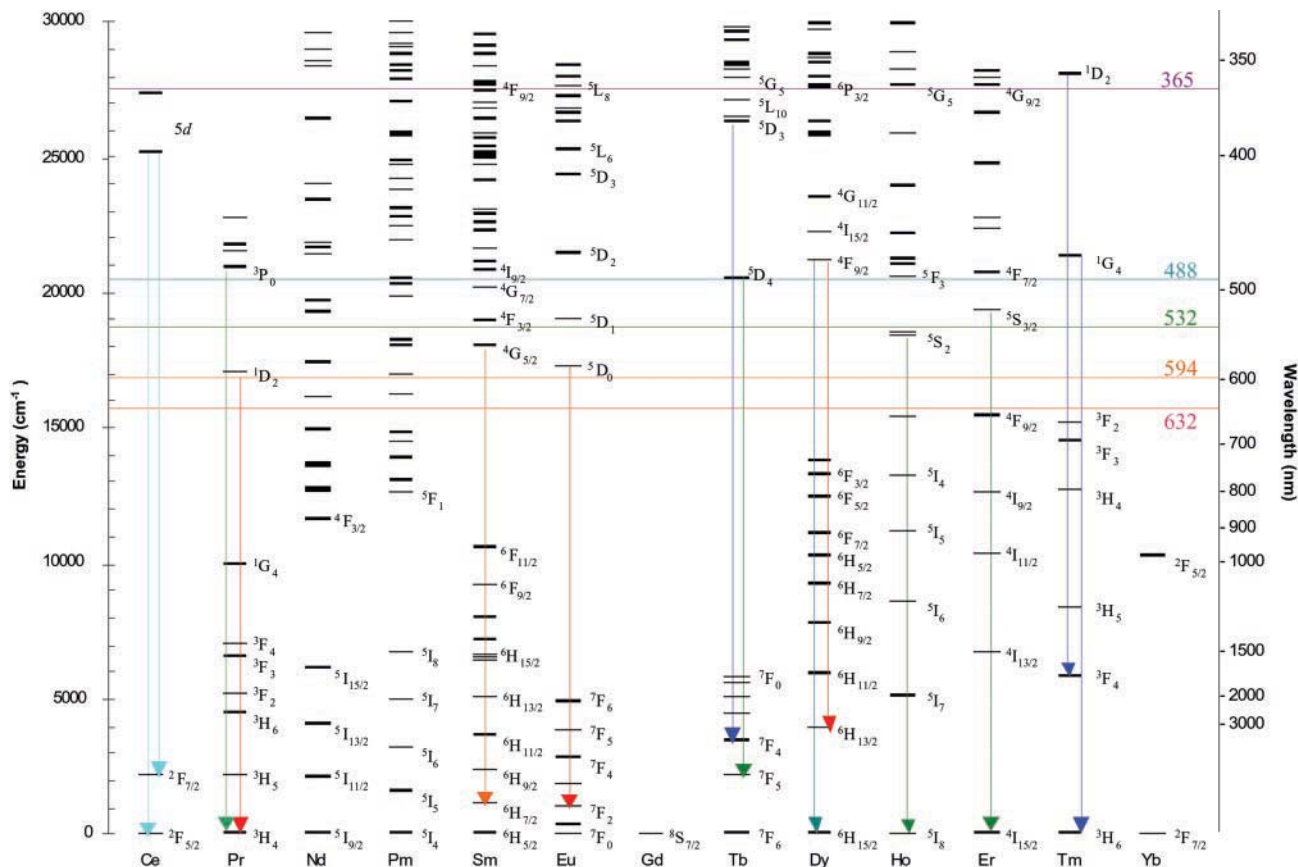


**Fig. 1.** Energy level diagram of trivalent RE ions with dominant visible emission transitions observed in silicate glasses designated by arrows representing the approximate color of the fluorescence. Horizontal lines extending across the diagram designate the location of common organic label excitation sources labeled by wavelength in nm. The 365-nm line was used to excite the RE ions.

platinum crucible at 1,650°C, cast into 10-mm-thick patties, and annealed for 1 h at 750°C. The optimal doping levels were obtained by maximizing the relative fluorescence intensity as a function of RE (RE<sub>2</sub>O<sub>3</sub>) concentration. Ce, Dy, and Tm exhibited optimal brightness between 0.25 and 0.5 mol % RE<sub>2</sub>O<sub>3</sub>, which corresponds to  $\approx 10^{20}$  RE ions per cm<sup>3</sup> and an average RE ion separation of 2 nm. Because emission intensity from the <sup>5</sup>D<sub>4</sub> level in Tb<sup>3+</sup> is free of concentration quenching and continues to increase above 1 mol % RE<sub>2</sub>O<sub>3</sub>, a level of  $\approx 0.2$  mol % was chosen as optimal to match the intensities of the other dopants and to avoid overwhelming them with the strong fluorescence from Tb<sup>3+</sup>.

**Fabrication of Barcodes.** Conventional optical fiber draw methods were used to fabricate the encoded fiber ribbons. First, the optimized glasses were melted and cast into 25 × 25 mm square bars and annealed for 1 h at 750°C. These bars were drawn into lengths of square (3.5-mm sides) canes and stacked in a predetermined order to define a barcode pattern. The assembly was then fused in a graphite press in a furnace at 900°C under N<sub>2</sub>. The fused preform was drawn at 1,200°C into a ribbon fiber (20 μm thick, 100 μm wide). The ribbon fiber was scribed every 20 μm at a rate of 5 mm/s with 800-nm femtosecond laser pulses (100 mW average power) by using a computer-controlled stage. The scribed ribbon fiber was then sonicated for 60 s in water to break the ribbon along the scribes into individual barcodes.

**Hybridization Assay.** The *HSPCB* gene (human heat shock 90-kDa protein, β1) and the *ybc* gene (from *Bacillus subtilis*) were obtained by PCR amplification. The cDNAs were immobilized

on γ-aminopropylsilane (GAPS)-coated beads by incubating the beads with the DNA suspended in 50% DMSO/≈5 mM sodium citrate buffer (pH 5.5) for 30 min, at a concentration of 0.25 mg/ml. Excess DNA was removed by washing the beads with water. Hybridization with complex human lung probe (Cy3 labeled) was carried out in buffer (pH 7.2) containing 50% formamide, 2× SSC (1× SSC = 0.15 M sodium chloride/0.015 M sodium citrate), and 0.1% SDS at 42°C for 40 min, with shaking. After hybridization, the beads were sequentially washed with 2× SSC, 0.1% SDS (10 min), 0.1× SSC/0.1% SDS (5 min), and 0.1× SSC (twice, 2 min each), and 0.1× SSC.

**Barcode Decoding and Fluorescence Reading.** The barcodes were decoded and imaged by using a spectral imager (SpectraCube, Applied Spectral Imaging, Migdal Haemek, Israel) mounted on a fluorescence microscope (Olympus AX 70) equipped with a mercury lamp (100 W). A dichroic filter was used to select the excitation wavelength, a 420-nm long-pass filter was used for observing the RE fluorescence, and a 570-nm bandpass filter was used to collect the Cy3 fluorescence.

## Results and Discussion

**Considerations for Choosing REs.** The ideal RE ions for microbarcodes should have nonoverlapping, bright visible luminescence for ease of detection, a common excitation source for simultaneous interrogation of all barcode elements, and no overlap of excitation (and/or emission) with commonly used fluorescent labels (e.g., FITC, Cy3, Cy5, and Texas red) to enable their use in quantitative bioassays. Our choice of candidate REs and

excitation and emission wavelengths was based on a consideration of these desired properties.

**Energy Levels.** For a RE ion to emit in the visible, there must be an energy gap between an upper excited state and a lower excited state (or the ground state) that is between 14,000 and 25,000  $\text{cm}^{-1}$  (corresponding to visible emission wavelengths  $\approx 700\text{--}400$  nm). The parasitic nonradiative relaxation rate is exponentially dependent on the integer number of phonons required to bridge the gap between the upper excited state and the next lower level. In practical terms, this gap must be at least 4 phonons wide to prevent quenching by nonradiative multiphonon decay (13). Silicate glasses have a maximum vibrational or phonon energy of  $\approx 1,100$   $\text{cm}^{-1}$  (14); therefore, any candidate emitting levels in a silica-based glass must be  $>4,400$   $\text{cm}^{-1}$  above the next lower lying level. For example, upon excitation at 365 nm,  $\text{Eu}^{3+}$  ions in a silicate glass nonradiatively relax from the  $^5\text{L}_8$  absorbing level to the metastable  $^5\text{D}_0$  level, because all of the intermediate levels are separated by fewer than 3 phonons, which is why emission from these levels is absent from silicate-based materials (15). The gap between the  $^5\text{D}_0$  and next lower lying level, the  $^7\text{F}_6$ , is  $>10$  phonons, so relaxation from the  $^5\text{D}_0$  is nearly 100% radiative to the  $^7\text{F}_j$  levels, resulting in fluorescent emission centered at 610 nm.

Examination of Fig. 1 suggests that the following seven transitions should emit in the visible and be reasonably efficient:  $\text{Pr}^{3+}$ ,  $^1\text{D}_2 \rightarrow ^3\text{H}_5$ ,  $^3\text{H}_4$ ;  $\text{Sm}^{3+}$ ,  $^4\text{G}_{5/2} \rightarrow ^6\text{H}_j$ ;  $\text{Eu}^{3+}$ ,  $^5\text{D}_0 \rightarrow ^7\text{F}_j$ ;  $\text{Tb}^{3+}$ ,  $^5\text{D}_4 \rightarrow ^7\text{F}_j$ ;  $\text{Dy}^{3+}$ ,  $^4\text{F}_{9/2} \rightarrow ^6\text{F}_{15/2}$ ,  $^6\text{F}_{13/2}$ ;  $\text{Tm}^{3+}$ ,  $^1\text{D}_2 \rightarrow ^3\text{F}_4$ ; and  $\text{Tm}^{3+}$ ,  $^1\text{G}_4 \rightarrow ^3\text{F}_4$ ,  $^3\text{H}_6$ . While  $\text{Nd}^{3+}$ ,  $\text{Ho}^{3+}$ , and  $\text{Er}^{3+}$  have visible transitions, they are all quenched in silicate glasses because of multiphonon decay. Even though  $\text{Ce}^{3+}$  does not have any intra- $f$  transitions in the visible, the lowest lying  $5d$  orbitals are  $\approx 24,000$   $\text{cm}^{-1}$  above the ground state; therefore, the  $\text{Ce}^{3+}$   $5d \rightarrow ^2\text{F}_{5/2}$ ,  $^2\text{F}_{7/2}$  transitions provide an eighth possibility for encoding, although these transitions are much broader than intra- $f$  transitions.

To enable multiplexed excitation of the barcodes, we used a UV source. Mercury lamps are cheap, efficient, and powerful UV sources that emit at 254 and 365 nm. We chose the 365-nm line because  $\text{Ce}^{3+}$ ,  $\text{Sm}^{3+}$ ,  $\text{Eu}^{3+}$ ,  $\text{Tb}^{3+}$ ,  $\text{Dy}^{3+}$ , and  $\text{Tm}^{3+}$  all have absorption bands that overlap with the 365-nm Hg emission line and because damage to biological samples would be minimized relative to illumination at 254 nm.

**Determination of Spectral Interference.** As mentioned earlier, a key requirement for a good RE marker is low spectral interference with fluorescent dyes commonly used in bioassays. Relative to fluorescent dyes, lanthanide ions are typically more efficient emitters and also have significantly longer fluorescent lifetimes. If there were overlap, these properties would make deconvolution of the fluorescence emission from the organic label and the RE difficult and would compromise the sensitivity of fluorescence assays. The background contribution of the RE ions was evaluated by fabricating microscope slides from RE-doped glasses and comparing their fluorescence to that of a regular glass slide (Fig. 2). Laser-based microarray scanners optimized to be maximally sensitive to FITC, Cy3, Texas red, and Cy5 were used for detection. The experiment showed that  $\text{Eu}^{3+}$ ,  $\text{Sm}^{3+}$ , and  $\text{Pr}^{3+}$ -doped glasses exhibit higher background counts than the bare glass slide, whereas the  $\text{Dy}^{3+}$ ,  $\text{Tm}^{3+}$ ,  $\text{Ce}^{3+}$ , and  $\text{Tb}^{3+}$ -doped slides have backgrounds that are equal to or lower than that of a conventional glass slide. The high  $\text{Pr}^{3+}$  background is due to excitation overlap of the 488-nm (FITC) and 594-nm (Texas red) pumps with the  $^3\text{P}_0$  and  $^1\text{D}_2$  levels that radiatively relax to the  $^3\text{H}_4$  and  $^3\text{H}_5$  levels, respectively. The unexpected excitations of  $\text{Eu}^{3+}$  on the Cy3 (532 nm) and Cy5 (632 nm) excitation channels are due to absorption tails arising from the feebly thermally populated  $^7\text{F}_1$  and  $^7\text{F}_2$  states to the  $^5\text{D}_1$  and  $^5\text{D}_0$  excited states,

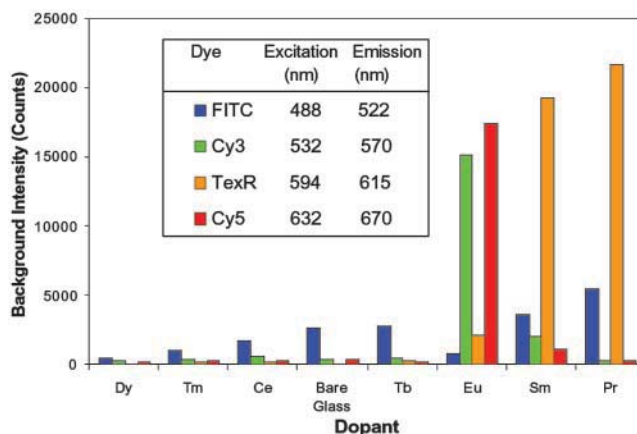


Fig. 2. Background fluorescence of RE-doped glasses relative to a bare microscope slide.

respectively.  $\text{Sm}^{3+}$  is similar to  $\text{Eu}^{3+}$  in that it is absorption from the thermally excited  $^6\text{H}_{7/2}$  (not the ground state) to the  $^4\text{G}_{5/2}$  that creates absorption overlap with the 594-nm pump and a high background in the Texas red band. While the  $^4\text{I}_{9/2}$  and  $^4\text{F}_{3/2}$  energy levels in  $\text{Sm}^{3+}$  exhibit excitation overlap with the 488- and 532-nm pumps, these absorptions are weak, and its emission bands do not strongly overlap with the FITC and Cy3 emission filters, although they are extremely close and could change dramatically with different filter sets.  $\text{Pr}^{3+}$ ,  $\text{Eu}^{3+}$ , and  $\text{Sm}^{3+}$  were therefore eliminated as potential RE markers for fluorescence-based bioassays, but they are potential candidates for other applications.

**Spectral Properties of Candidate REs.** Because of their low background fluorescence, we investigated the use of  $\text{Dy}^{3+}$ ,  $\text{Tm}^{3+}$ ,  $\text{Ce}^{3+}$ , and  $\text{Tb}^{3+}$ -doped glasses as candidate microbarcodes. Fig. 3 shows fluorescence spectra of glasses doped with  $\text{Ce}^{3+}$ ,  $\text{Tm}^{3+}$ ,  $\text{Tb}^{3+}$ , and  $\text{Dy}^{3+}$ ; the spectra are well resolved and easily distinguished with the naked eye. UV excitation makes the  $\text{Ce}^{3+}$ ,  $\text{Tm}^{3+}$ ,  $\text{Tb}^{3+}$ , and  $\text{Dy}^{3+}$ -doped glasses glow cyan, blue, green, and pale orange/yellow, respectively. The electronic transitions corresponding to these emissions can be deduced from Fig. 1. Excitation at 365 nm pumps the  $\text{Ce}^{3+}$  ion into an upper  $5d$  level, which nonradiatively relaxes to the lowest  $5d$  level. Thereafter,

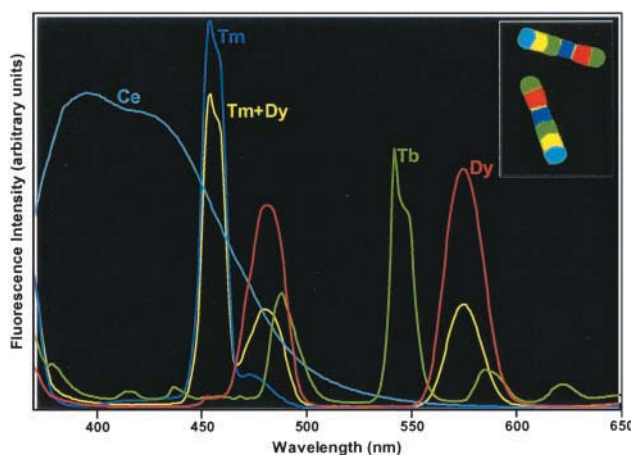
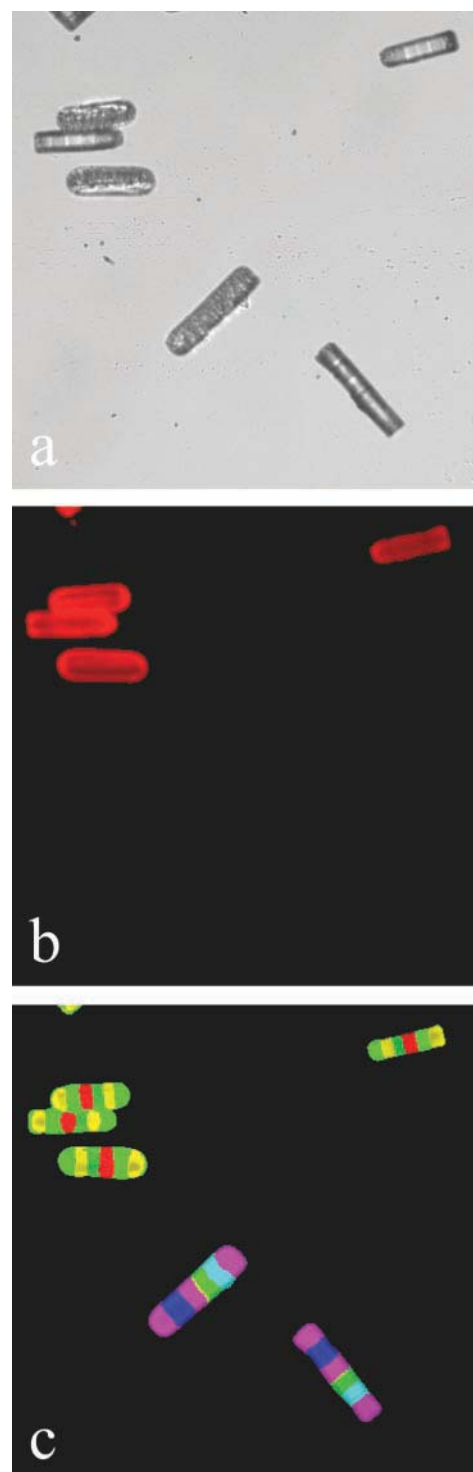


Fig. 3. False-color image of two  $100 \times 20$   $\mu\text{m}$  barcodes (Inset) and corresponding fluorescence spectrum barcode elements. The same color scheme is used for the spectra and the image [e.g., the yellow band in the barcode corresponds to the yellow (combination Tm+Dy) line spectrum].

the ions radiatively relax to the  $^2F_{5/2}$  and  $^2F_{7/2}$  levels, creating broad  $5d \rightarrow 4f$  peaks at about 390 and 430 nm, respectively. The  $Tb^{3+}$  transitions are the most complex. Excitation at 365 nm populates the  $^5G_5$  and  $^5L_{10}$  levels resonant with the Hg emission. The excited ions quickly cascade down to the metastable  $^5D_3$  state. Some light is emitted from the  $^5D_3$  to the  $^7F_J$  manifold as evident in the weak peaks at 380, 415, 435, and 450–470 nm. However, most of the energy is transferred to the  $^3D_4$  state by pairwise cross-relaxation, which leads to emissions at 490, 540, 585, and 620 nm, caused by transitions to the  $^7F_6$ ,  $^7F_5$ ,  $^7F_4$ , and  $^7F_3$  levels, respectively.  $Tm^{3+}$  emits directly from the pumped  $^1D_2$  excited state at 455 nm ( $^1D_2 \rightarrow ^3F_4$ ) with a small shoulder at 475 nm ( $^1G_4 \rightarrow ^3H_6$ ).  $Dy^{3+}$  is excited to the  $^6P_{3/2}$  level, which nonradiatively cascades down to the  $^4F_{9/2}$  level, resulting in  $^4F_{9/2} \rightarrow ^6H_{15/2}$  and  $^4F_{9/2} \rightarrow ^6H_{13/2}$  transitions at 480 and 575 nm, respectively. All of the ions have emissions near 480 nm; therefore, this region of the spectrum is impractical for readout as barcodes. Diagnostic peaks at 400, 455, 540, and 575 nm for  $Ce^{3+}$ ,  $Tm^{3+}$ ,  $Tb^{3+}$ , and  $Dy^{3+}$ , respectively, offer the best spectral separation and quantum yield, and are therefore optimal wavelengths for readout.

**Increasing Microbarcode Combinations.** The maximum number of possible bar code combinations in a ribbon-shaped fiber with  $N$  members and  $C$  colors is given by  $C^N$ . The actual number of nondegenerate barcodes is  $\approx C^N/2$  (when  $N$  is even, number of codes =  $[C^N + C^{N/2}]/2$ ; when  $N$  is odd, number of codes =  $[C^N + C^{(N+1)/2}]/2$ ). For example, a six-member ribbon with a palette of four colors will yield a maximum of  $4^6$  or 4,096 combinations and 2,080 nondegenerate combinations. Although it is possible to increase the number of barcodes by varying the scribe-length of the ribbon, the number of bands in a ribbon, and the concentration of the candidate lanthanide, the most convenient option for decoding involves a simple yes/no determination of color and sequence within a ribbon. With this objective in mind, we created five “combination colors”: binary combinations of  $Ce^{3+}$ – $Tb^{3+}$ ,  $Ce^{3+}$ – $Dy^{3+}$ ,  $Tm^{3+}$ – $Tb^{3+}$ ,  $Tm^{3+}$ – $Dy^{3+}$ , and  $Tb^{3+}$ – $Dy^{3+}$ . These doped glasses were observed to have clearly resolvable fluorescence and negligible quenching. The emission spectrum of the  $Tm^{3+}$ – $Dy^{3+}$  combination is illustrated in Fig. 3; the spectrum is a sum of the spectra of the individual ions. The expanded nine-color palette brings the number of barcode combinations to  $9^6$  or  $\approx 530,000$  (or  $\approx 265,000$  nondegenerate). The  $Ce^{3+}$ – $Tm^{3+}$  combination was not used because the  $Ce^{3+}$  emission tail overlaps with the  $Tm^{3+}$  emission at 454 nm, which could complicate the readout. Triplet combinations of  $Ce^{3+}$ – $Tb^{3+}$ – $Dy^{3+}$ , and  $Tm^{3+}$ – $Tb^{3+}$ – $Dy^{3+}$  are also possible. Given these encoding options, fabricating  $>10^6$  uniquely distinguishable barcodes by using RE-doped glass fibers is theoretically achievable.

**Microbarcode Assay.** The use of the barcodes in a fluorescence assay was demonstrated by using a DNA hybridization experiment. After silanization of the barcodes with  $\gamma$ -aminopropylsilane (GAPS), one set of barcodes (Tb-DyTm-Tb-Dy-Tb-DyTm; set A) was treated with DNA corresponding to the human *HSPCB* gene; the second set of barcodes (TbTm-Tm-TbTm-Tb-Ce-TbTm; set B) was treated with DNA corresponding to the *Bacillus subtilis* gene *ybac*. The immobilization of DNA on GAPS (and other amine-presenting surfaces such as polylysine) is primarily attributed to polyvalent electrostatic interactions between the negatively charged DNA backbone and positively charged amino groups on the surface (16). We chose to fabricate barcode B because it represents a particularly difficult scenario for decoding. TbTm (shown as purple in Fig. 4C) is present in three positions of the six-member bead, sandwiched between Tb (green) and Tm (blue), and next to Ce (cyan), which has a similar light-blue emission. The barcodes were pooled and hybridized



**Fig. 4.** Fluorescence false-color images of barcode particles A and B used in a DNA hybridization assay using Cy3-labeled DNA. (a) “White light” image. (b) Cy3 channel image. (c) RE images obtained by using a 420-nm long-pass filter.

for 40 min with a sample consisting of Cy3-labeled cDNA obtained by reverse transcription from human lung poly(A)<sup>+</sup> RNA (1 pmol of Cy3 per  $\mu$ l). This sample, which represents the expression of all of the genes found in the human lung, was used because it simulates a real hybridization experiment and provides a higher stringency test for nonspecific binding relative to hybridization with only the PCR-amplified DNA corresponding to the *HSPCB* gene. After the assay, the barcodes were dispensed

onto a microscope slide for observation. Fig. 4a shows images of the barcodes illuminated with white light; the barcodes are indistinguishable. When illuminated at 530 nm and monitored at 570 nm (conditions corresponding to the detection of Cy3), only some of the beads fluoresced (Fig. 4b). Fig. 4c shows the same beads illuminated with 365-nm light and viewed through a 420-nm long-pass filter. Two sets of beads are clearly revealed. Matching Fig. 4 b and c shows that there is an exact correspondence between beads comprising set A and beads that exhibit positive Cy3 signals (from Fig. 4b). These data demonstrate the expected specific hybridization of the labeled probe to beads presenting the *HSPCB* gene and the lack of nonspecific binding under the conditions of the assay.

We have also carried out experiments in which biotin (derivatized with a terminal NH<sub>2</sub> group) was covalently attached to epoxide-functionalized barcodes and demonstrated specific binding of Cy3-labeled anti-biotin to these beads (data not

shown). As mentioned earlier, the entire repertoire of silane chemistries for immobilization of biological molecules should be feasible on these barcodes.

## Conclusion

Although encoded bead assays offer the possibility of significantly improved assay performance relative to conventional microarrays, the development of this technology has been hampered by the limited attributes of materials used to fabricate the beads. RE-doped glass beads have properties that overcome most of these identified limitations and are therefore ideally suited for use in encoded-bead bioassays. While the number of uniquely distinguishable beads ( $>10^6$ ) is more than sufficient for highly multiplexed bioassays, removing the constraints imposed by spectral compatibility with fluorescent biological tags expands the palette of combinations even further. The fabrication of RE-doped barcodes is not limited to fiber draw techniques, and alternative approaches are possible.

1. Michael, K. L., Taylor, L. C., Schultz, S. L. & Walt, D. R. (1998) *Anal. Chem.* **70**, 1242–1248.
2. Han, M., Gao, X., Su, J. Z. & Nie, S. (2001) *Nat. Biotechnol.* **19**, 631–635.
3. Nicewarner-Peña, S. R., Freeman, R. G., Reiss, B. D., He, L., Walton, I. D., Cromer, R., Keating, C. D. & Natan, M. J. (2001) *Science* **294**, 137–141.
4. Trau, M. & Battersby, B. J. (2001) *Adv. Mater.* **13**, 975–979.
5. Michalet, X., Pinaud, F., Lacoste, T. D., Dahan, M., Bruchez, M. P., Alivisatos, A. P. & Weiss, S. (2001) *Single Mol.* **2**, 261–276.
6. Walton, I. D., Norton, S. M., Balasingham, A., He, L., Oviso, D. F., Gupta, D., Raju, P. A., Natan, M. J. & Freeman, R. G. (2002) *Anal. Chem.* **74**, 2240–2247.
7. Li, L., Ruzgas, T. & Gaigalas, A. K. (1999) *Langmuir* **15**, 6358–6363.
8. Carnall, W. T., Goodman, G. L., Rajnak, K. & Rana, R. S. (1989) *J. Chem. Phys.* **90**, 3443–3457.
9. Boikess, R. & Edelson, E. (1985) *Chemical Principles* (Harper & Row, New York).
10. Resifeld, R. & Jørgensen, C. (1977) *Lasers and Excited States of Rare Earths* (Springer, New York).
11. Bruchez, M., Jr., Moronne, M., Gin, P., Weiss, S. & Alivisatos, A. P. (1998) *Science* **281**, 2013–2016.
12. Chan, W. C. W. & Nie, S. (1998) *Science* **281**, 2016.
13. Dejneka, M. J. (1998) *MRS Bull.* **23**, 57–62.
14. Sigel, G. H. J. (1978) in *Glass I: Interaction with Electromagnetic Radiation*, eds. Tomozawa, M. & Doremus, R. H. (Academic, New York), Vol. 12, pp. 5–89.
15. Dejneka, M., Snitzer, E. & Riman, R. E. (1995) *J. Lumin.* **65**, 227–245.
16. Hegde, P., Qi, R., Abernathy, K., Gay, C., Dharap, S., Gaspard, R., Hughes, J. E., Snesrud, E., Lee, N. & Quackenbush, J. (2000) *BioTechniques* **29**, 548–562.



# Photon management with lanthanides

Andries Meijerink \*, René Wegh, Peter Vergeer, Thijs Vlugt

*Debye Institute, Department of Chemistry, Utrecht University, Princetonplein 5, 3584 CC Utrecht, The Netherlands*

Available online 8 November 2005

## Abstract

Efficient conversion of photons from high energy radiation (e.g. ultraviolet or X-rays) to lower energies (visible) has been optimized by using luminescent materials based on the optical properties of lanthanide ions. Presently, luminescent materials with efficiencies close to the theoretical maximum are applied in e.g. fluorescent tubes, X-ray imaging and color television. Contrary to the mature status of luminescent materials in these fields, areas requiring new luminescent materials are emerging. There is great challenge in research on up- and downconversion materials and lanthanide ions are the prime candidates to achieve efficient materials. Here downconversion processes will be discussed for VUV phosphors with  $\text{Pr}^{3+}$ . The efficiency of resonant energy transfer of the  $^1\text{S}_0$ – $^1\text{I}_6$  energy from  $\text{Pr}^{3+}$  to  $\text{Eu}^{3+}$  and  $\text{Mn}^{2+}$  is investigated. The aim is to convert the 405 nm photon of the first step of the well-known cascade emission of  $\text{Pr}^{3+}$  into a more useful visible photon. For co-doping with  $\text{Eu}^{3+}$  it is observed that the  $\text{Pr}^{3+}$  emission is quenched, most probably through a metal-to-metal charge-transfer state. The energy transfer from  $\text{Pr}^{3+}$  to  $\text{Mn}^{2+}$  is found to be inefficient.

An alternative for downconversion through resonant energy transfer is the non-resonant process of cooperative sensitization. For the Tb–Yb couple efficient cooperative energy transfer from the  $^3\text{D}_4$  level of  $\text{Tb}^{3+}$  to two  $\text{Yb}^{3+}$  neighbors is observed with a transfer rate of  $0.26 \text{ ms}^{-1}$ . This corresponds to an upper limit of 188% for the conversion efficiency of visible (490 nm) photons to infrared ( $\sim 1000 \text{ nm}$ ) photons.

© 2005 Elsevier B.V. All rights reserved.

## 1. Introduction

The lanthanides occupy a special place in the periodic table of elements. They are situated at the bottom of the periodic table, one row above the actinides. The word lanthanide has a Greek origin (“ $\lambda\nu\theta\alpha\nu\epsilon\iota\nu$ ”) which means “to lie hidden”. This may seem appropriate in view of the position of the lanthanides in the periodic table and the fact that it took more than a century to separate and discover all the lanthanides. Nevertheless, at present lanthanides are prominently present in a wide range of products related to e.g. the catalytic, magnetic and optical properties of the lanthanide ions. Especially in optical applications the lanthanides have become (literally) visible in the past decades. The applications of lanthanide ions in the field of optical materials is related to the unique energy level diagrams of

the lanthanides which are known as the Dieke diagram. The rich energy level structure make that lanthanide ions are perfect “photon managers” that can be used to efficiently convert radiation into light of any desired wavelength [1]. In the past four decades the use of lanthanide ions as photon managers has rapidly increased.

The first commercial luminescent material based on lanthanide luminescence was  $\text{YVO}_4:\text{Eu}^{3+}$ . This material was discovered in the early 1960s and found to efficiently convert the energy of high energy electrons into visible (red) light in a color television. The high luminescence efficiency triggered the application of lanthanide luminescence in other areas, for example in luminescent materials for fluorescent tubes and X-ray imaging. The fluorescence tube is based on a mercury discharge and research has resulted in luminescent materials (phosphors) for the conversion of 254 nm ultraviolet (UV) radiation into visible light. With the introduction of lanthanide-based luminescent materials, the quantum efficiency for the conversion of 254 nm UV radiation into red, green or blue light has reached

\* Corresponding author. Tel.: +31 30 253 2202; fax: +31 30 253 2403.  
E-mail address: [a.meijerink@phys.uu.nl](mailto:a.meijerink@phys.uu.nl) (A. Meijerink).

the limit of close to 100%. Further research on lamp phosphors is mainly aimed at cost price reduction and marginal improvements of the efficiency or stability. Due to the mature status of the product, research on luminescent materials for mercury discharge fluorescent tubes has strongly decreased in the past decades. The same is true for luminescent materials used in cathode ray tubes and X-ray imaging. The efficiency of these materials is close to the theoretical maximum and research on new luminescent materials for these applications has decreased due to the ideal photon management qualities of lanthanides.

On the other hand, new areas of research have emerged in the past decades. Extensive research is conducted for e.g. (upconversion) lasers based on lanthanides, lanthanide doped fiber amplifiers for telecommunication, 3-D television with lanthanide doped crystals or glasses, scintillators and optical switches [1,2]. Lanthanide doped photonic materials research has become a prominent area of research. Two specific areas in the field that have recently emerged are the search for more efficient and stable luminescent materials for the conversion of high energy UV (vacuum ultraviolet, VUV) radiation into visible light (for xenon-based fluorescent tubes and plasma display panels) and the conversion of low energy UV or blue light (for white light GaN diodes). The search for new luminescent materials for the conversion of vacuum ultraviolet radiation from a xenon discharge (around 172 nm) into visible light involves research on finding ways for the generation of two visible photons for a single VUV photon [3,4]. This so-called quantum cutting process is possible using the energy level structure of lanthanide ions. After an introduction into the VUV spectroscopy of lanthanides, this paper will discuss recent developments in the field of quantum cutting. Subsequently, efficient quantum cutting by cooperative energy transfer is demonstrated for the Tb–Yb couple converting one visible photon into two infrared photons. The visible to infrared downconversion with quantum yields close to 200% may be used to increase the efficiency of solar cells.

## 2. Experimental

### 2.1. Sample preparation

In all experiments measurements are performed on microcrystalline powders synthesized by common solid state synthesis. Fluorides were prepared by mixing starting fluorides in stoichiometric ratios, adding ~2 g of ammonium fluoride and firing the intimate mixture in a nitrogen atmosphere at typically 600 °C. Powder samples of  $\text{Yb}_x\text{Y}_{0.99-x}\text{Tb}_{0.01}\text{PO}_4$  were prepared from stock solutions of  $\text{Yb}^{3+}$  and  $\text{Y}^{3+}$ , both containing 1% of  $\text{Tb}^{3+}$ , prepared by dissolving rare earth (RE) oxides in concentrated hydrochloric acid. The rare earth ions in the mixed solution were precipitated by adding a solution with an excess of oxalic acid. The precipitate was washed thoroughly to eliminate chloride ions. Heating the compound to 1050 °C under an

oxygen atmosphere converted the oxalates to oxides. The powder obtained was mixed with diammonium phosphate (10 mol% excess) and fired again at 1350 °C under a 1:3  $\text{H}_2:\text{N}_2$  atmosphere. All samples were checked for phase purity using powder-XRD and found to be single-phase.

### 2.2. Optical measurements

Emission and excitation measurements were performed using a SPEX DM3000F spectrofluorometer with a 450 W Xe-lamp as excitation source. The excitation light was dispersed by a double-grating 0.220 m SPEX 1680-monochromator (1200 l/mm) blazed at 300 nm. The light emitted by the sample was focussed on a fiber guiding the light to a monochromator where the emission light was dispersed by a 150 l/mm grating (Scientific Spectra Pro) blazed at 500 nm with 0.300 m focal length and detected using a Princeton Instruments 300i CCD camera. VUV spectroscopy was done at a SPEX DM3000F spectrofluorometer adapted for the VUV and at the HIGITI beamline of the DESY synchrotron in Hamburg. Time-resolved measurements were performed using a Lambda Physik LPD3000 tunable dye laser filled with a Coumarine 307 dye solution. It is pumped by a Lambda Physik LPX100 excimer (XeCl) laser. The typical pulse width of this setup is ~20 ns. The emission was detected using a Hamamatsu R928 PMT and monitored as a function of time using a Tektronix 2440 digital oscilloscope.

## 3. Vacuum ultraviolet spectroscopy and quantum cutting

The vacuum ultraviolet region of the electromagnetic spectrum covers the region between 50 and 200 nm ( $200\,000\text{--}50\,000\text{ cm}^{-1}$ ). Research on the VUV energy levels of lanthanides has been very limited until recently. Extensive research in this area was triggered by the need of new phosphors for VUV excitation for mercury free fluorescent tubes and plasma display panels. In these devices the VUV radiation generated in a Xe discharge (around 172 nm) needs to be converted into visible light. For the intraconfigurational  $4f^n$  levels the VUV research has resulted in the extension of the Dieke diagrams into the VUV [5]. For the  $4f^{n-1}5d$  levels high resolution excitation VUV spectra were measured and a model was developed explaining the  $4f^{n-1}5d$  energy level structure [6]. In addition to the increased fundamental understanding of the VUV energy levels of lanthanides, an efficient process for the conversion of one VUV photon into two visible photons was found in gadolinium fluorides doped with  $\text{Eu}^{3+}$ . A two-step resonant energy-transfer process starting from the  $^6\text{G}$  level of  $\text{Gd}^{3+}$  results in the emission of two visible (red) photons emitted by two  $\text{Eu}^{3+}$  ions [3]. An alternative quantum cutting process involves a cascade emission from the  $^1\text{S}_0$  level of  $\text{Pr}^{3+}$  [7,8]. Albeit efficient, the photon emitted in the first step has a wavelength around 405 nm which is not favorable for lighting applications. In order to convert this 405 nm photon into a more useful wavelength,

two couples of luminescent ions were investigated, viz. Pr–Eu and Pr–Mn.

For the Pr–Eu couple efficient energy transfer through the cross-relaxation process  $\text{Pr}^{3+}({}^1\text{S}_0 \rightarrow {}^1\text{I}_6)$  and  $\text{Eu}^{3+}({}^7\text{F}_{0,1} \rightarrow {}^5\text{D}_3, {}^5\text{L}_6)$  is expected. Zachau and coworkers tried to transfer the energy of the  $\text{Pr}^{3+}{}^1\text{S}_0 \rightarrow {}^1\text{I}_6$  transition to the  $\text{Eu}^{3+}$  ion [9]. Despite the presence of good spectral overlap between the  $\text{Pr}^{3+}$  emission and  $\text{Eu}^{3+}$  absorption lines no  $\text{Eu}^{3+}$  emission was observed upon excitation of  $\text{Pr}^{3+}$ . Based on these observations it was concluded that the expected energy transfer does not occur. This is remarkable, since an important condition for energy transfer, the presence of resonance between the  $\text{Pr}^{3+}{}^1\text{S}_0 \rightarrow {}^1\text{I}_6$  transition and absorptions of the  $\text{Eu}^{3+}$  ion is fulfilled. In this case energy transfer can occur through exchange interaction or multipole–multipole interaction.

Calculations of the energy-transfer rate assuming dipole–dipole interaction show that energy transfer between nearest-neighbor  $\text{Pr}^{3+}{}^1\text{S}_0 \rightarrow {}^1\text{I}_6$  and  $\text{Eu}^{3+}{}^7\text{F}_{0,1} \rightarrow {}^5\text{D}_3, {}^5\text{L}_6$  has a similar probability as radiative decay from the  $\text{Pr}^{3+}{}^1\text{S}_0$  level. As a result, energy transfer and subsequent  $\text{Eu}^{3+}$  emission should occur. To investigate the observed absence of  $\text{Eu}^{3+}$  emission upon excitation in the  ${}^1\text{S}_0$  level of  $\text{Pr}^{3+}$  luminescence spectra and time-resolved luminescence signals were measured for  $\text{YF}_3:\text{Pr}^{3+}$  1%,  $\text{Eu}^{3+}$   $x\%$  ( $x = 0, 5$  and  $10$ ) as shown in Fig. 1. The experiments show a strong quenching of the  $\text{Pr}^{3+}{}^1\text{S}_0$  emission in the presence of  $\text{Eu}^{3+}$  ions. This quenching process is attributed to non-radiative relaxation via a  $\text{Eu}^{2+}\text{–Pr}^{4+}$  metal-to-metal charge-transfer state. Quenching of the  $\text{Pr}^{3+}{}^1\text{S}_0$  emission by  $\text{Yb}^{3+}$  confirms this quenching mechanism.

An alternative to transferring the  ${}^1\text{S}_0\text{–}{}^1\text{I}_6, {}^3\text{P}_J$  energy to a lanthanide ion (like  $\text{Eu}^{3+}$ ) is to include a 3d transition

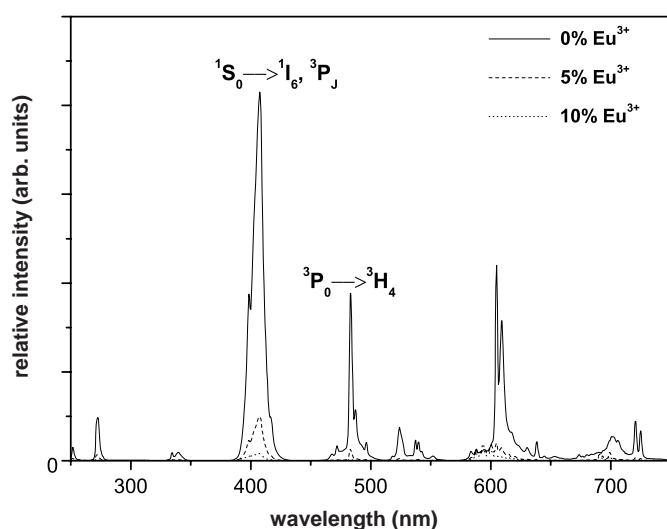


Fig. 1. Emission spectra (RT) of  $\text{YF}_3$  doped with 1%  $\text{Pr}^{3+}$  and co-doped with  $\text{Eu}^{3+}$  plotted on a relative intensity scale. The concentrations of  $\text{Eu}^{3+}$  are indicated in the figure. Excitation is into the  $\text{Pr}^{3+} 4f^2 \rightarrow 4f5d$  band at 190 nm. The  $\text{Pr}^{3+}{}^1\text{S}_0 \rightarrow {}^1\text{I}_6, {}^3\text{P}_J$  and  ${}^3\text{P}_0 \rightarrow {}^3\text{H}_4$  transitions are indicated in the figure. Note the quenching of the  $\text{Pr}^{3+}$  emissions when  $\text{Eu}^{3+}$  is co-doped.

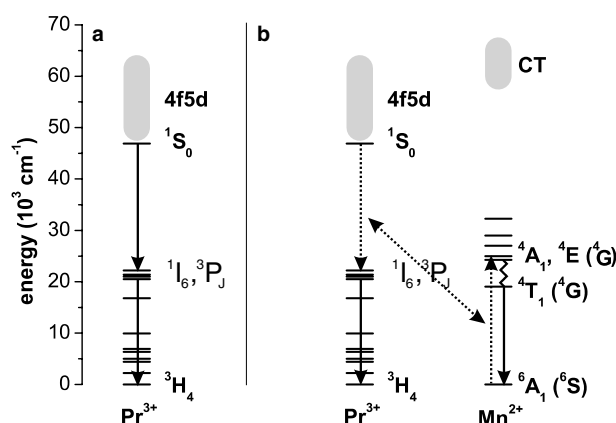


Fig. 2. Schematic of the  $\text{Pr}^{3+}$  cascade emission (left hand side) and the desired energy-transfer process between  $\text{Pr}^{3+}({}^1\text{S}_0)$  and  $\text{Mn}^{2+}$  (right hand side). Solid lines denote radiative transitions. CT stands for charge transfer. The energy-transfer process is depicted by dotted lines. The zig-zag line denotes non-radiative relaxation. After the energy-transfer process both  $\text{Pr}^{3+}$  and  $\text{Mn}^{2+}$  each emit one photon.

metal ion as an acceptor. In particular, energy transfer to  $\text{Mn}^{2+}$  ( $3d^5$ ) is promising. The  $\text{Mn}^{2+}$  ion has narrow absorption bands around 400 nm due to transitions from the  ${}^6\text{A}_1$  ground state to  ${}^4\text{A}_1$  and  ${}^4\text{E}$  excited states. The cross-relaxation scheme is shown in Fig. 2. In view of the spectral overlap between the  ${}^1\text{S}_0 \rightarrow {}^1\text{I}_6, {}^3\text{P}_J$  emission and the  $\text{Mn}^{2+}$  excitation lines around 400 nm, energy transfer is expected to occur. To investigate if energy transfer from  $\text{Pr}^{3+}$  to  $\text{Mn}^{2+}$  does occur, a number of fluoride host lattices in which  $\text{Pr}^{3+}$  shows cascade emission (high energy fd state) have been co-doped with  $\text{Pr}^{3+}$  and various concentrations of  $\text{Mn}^{2+}$ . To determine whether or not the desired spectral conversion of the 405 nm emission occurs by energy transfer to  $\text{Mn}^{2+}$ , luminescence spectra are recorded and analyzed.

For the downconversion of one VUV photon into two visible photons using  $\text{Pr}^{3+}$  and  $\text{Mn}^{2+}$  several conditions have to be met: (1) there should be a cascade emission originating from the  ${}^1\text{S}_0$  level of the  $\text{Pr}^{3+}$  ion (i.e. the lowest-energy fd state has to be higher in energy than the  ${}^1\text{S}_0$  state), (2) there should be spectral overlap between the  $\text{Pr}^{3+}{}^1\text{S}_0 \rightarrow {}^1\text{I}_6$  emission lines and absorption lines of the  $\text{Mn}^{2+}$  ion in the fluoride host lattice and (3) the distance between the Pr and Mn ions needs to be small to allow for interaction between ions.

Optical spectroscopy experiments on singly doped (Pr or Mn) systems provide information to show whether or not the first two conditions are met. If this is the case, measurements on doubly doped systems (Pr and Mn) can be done to investigate if the interaction between neighboring ions is strong enough to give rise to efficient energy transfer. For all fluoride host lattices investigated in this section, the first two conditions are met. As a typical example, only the results for  $\text{SrY}_2\text{F}_8$  are discussed in detail.

In Fig. 3 luminescence spectra are shown for  $\text{SrY}_2\text{F}_8$  samples doped with a single type of ion (Pr or Mn) and

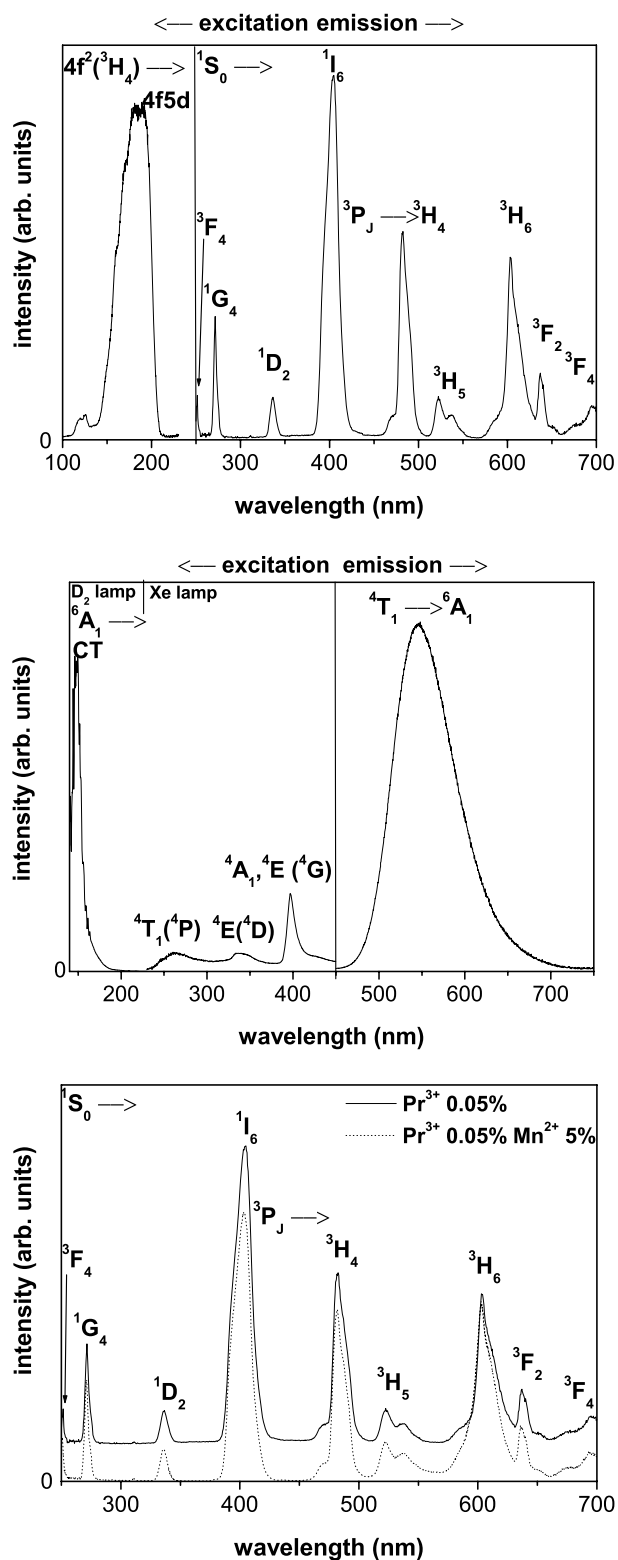


Fig. 3. (top) Excitation (10 K,  $\lambda_m = 401$  nm) and emission (RT,  $\lambda_x = 186$  nm) spectra for  $\text{SrY}_2\text{F}_8:\text{Pr}^{3+}$  0.05%, (middle) Excitation (RT,  $\lambda_m = 555$  nm) and emission (RT,  $\lambda_x = 161$  nm) spectra for  $\text{SrY}_2\text{F}_8:\text{Mn}^{2+}$  1%, (bottom) emission spectra (RT,  $\lambda_x = 185$  nm) for  $\text{SrY}_2\text{F}_8$  doped with 0.05%  $\text{Pr}^{3+}$  (drawn line) or with 0.05%  $\text{Pr}^{3+}$  and 5%  $\text{Mn}^{2+}$ .

for a doubly doped sample. The emission spectrum of  $\text{SrY}_2\text{F}_8:\text{Pr}^{3+}$  (Fig. 3(top)) upon excitation in the 4f5d band

(190 nm) shows a number of sharp lines in the UV and visible part of the spectrum. The spectrum is dominated by the strong  $^1S_0 \rightarrow ^1I_6$  emission line around 405 nm. In the higher energy region weaker lines corresponding to other  $^1S_0$  emissions are observed and in the visible range there are  $^3P_0$  emission lines. The observation of  $^1S_0$  emission from  $\text{Pr}^{3+}$  shows that the 4f5d state is situated above the  $^1S_0$  level. The excitation spectrum of the  $\text{Mn}^{2+}$  emission (Fig. 3(middle)) shows a sharp line around 400 nm and some weaker lines at shorter wavelengths. The 400 nm line is assigned to the  $^6A_{1g} \rightarrow ^4A_{1g}, ^4E_g$  transitions within the  $3d^5$  configuration of  $\text{Mn}^{2+}$ . The emission spectrum of the  $\text{Mn}^{2+}$  ion in  $\text{SrY}_2\text{F}_8$  consists of a broad band around 560 nm. The luminescence spectra of  $\text{SrY}_2\text{F}_8:\text{Pr}^{3+}$  and  $\text{SrY}_2\text{F}_8:\text{Mn}^{2+}$  show that the first two conditions for energy transfer are met: the 4f5d state is at higher energy than the  $^1S_0$  and the  $^1S_0 \rightarrow ^1I_6$  emission line of  $\text{Pr}^{3+}$  has a good spectral overlap with the  $^6A_{1g} \rightarrow ^4A_{1g}, ^4E_g$  absorption lines of  $\text{Mn}^{2+}$ .

To investigate if the energy-transfer process (cross-relaxation) shown in Fig. 2 can occur, the luminescence properties of doubly doped (Pr and Mn)  $\text{SrY}_2\text{F}_8$  were investigated. In Fig. 3 (bottom) the emission spectra of  $\text{SrY}_2\text{F}_8:\text{Pr}^{3+}$  are shown for samples with the same  $\text{Pr}^{3+}$  concentration (0.05 mol%) and two different  $\text{Mn}^{2+}$  concentration (0% or 5%). The emission in the visible spectral range shows that the spectra do not change upon adding  $\text{Mn}^{2+}$ . If the energy-transfer  $\text{Pr}^{3+}(^1S_0 \rightarrow ^1I_6)$  to  $\text{Mn}^{2+}(^6A_{1g} \rightarrow ^4A_{1g}, ^4E_g)$  occurs, one would expect to observe a  $\text{Mn}^{2+}$  emission band around 560 nm that increases in intensity upon raising the Mn concentration. The absence of a  $\text{Mn}^{2+}$  emission band indicates that energy transfer does not occur. The observation that the Pr emission spectrum does not change is further evidence for the absence of cross-relaxation. Clearly, there is no energy transfer from Pr and Mn in spite of the favorable spectral overlap and a considerable number of nearest-neighbor pairs of Pr–Mn. From this observation one can conclude that even in the nearest-neighbor pairs the energy transfer cannot compete with radiative decay from the  $^1S_0$  state. Similar research on Pr and/or Mn doped  $\text{YF}_3$ ,  $\text{CaF}_2$  and  $\text{LiBaF}_3$  provided similar results: no evidence for energy transfer from Pr to Mn is obtained.

The absence of energy transfer is not well-understood. Calculations of the energy-transfer rate for dipole–dipole interaction show that the critical distance for energy transfer is approximately 3.5 Å, which is slightly smaller than the nearest-neighbor distance but small enough that some energy transfer and thus  $\text{Mn}^{2+}$  emission should be observed.

#### 4. Cooperative sensitization

The idea for the two quantum cutting systems discussed in Section 3 is based on resonant energy transfer. Splitting of the energy is achieved by population of an intermediate energy level of the donor. If overlap between donor emis-

sion and acceptor absorption is absent, second-order downconversion may become the dominant relaxation process (competing with spontaneous emission). In this process a donor excites two acceptors simultaneously. The resonance condition is fulfilled if the sum of the energy of the absorption transitions of the two acceptor centres equals the energy of the emission of the donor.

This cooperative sensitisation process was predicted in 1957 by Dexter [10] but it was only recently that a paper has been published in which the occurrence of cooperative sensitisation (or second-order downconversion) was presented [11]. A promising system to study second-order energy-transfer processes is the combination of one  $\text{Tb}^{3+}$  and two  $\text{Yb}^{3+}$  ions: the  $\text{Tb}^{3+}{}^5\text{D}_4 \rightarrow {}^7\text{F}_6$  transition is located at approximately twice the energy of the  $\text{Yb}^{3+}{}^2\text{F}_{5/2} \rightarrow {}^2\text{F}_{7/2}$  transition and  $\text{Yb}^{3+}$  has no other levels up to the UV region (see Fig. 4).

The purpose of this section is to study second-order downconversion in Tb–Yb compounds and to elucidate its efficiency and energy-transfer mechanism. Energy transfer in powders of  $\text{Yb}_x\text{Y}_{(1-x)}\text{PO}_4$  doped with 1%  $\text{Tb}^{3+}$  is studied by emission, excitation and time-resolved luminescence measurements. The time-resolved luminescence measurements are compared with theories for phonon-assisted energy transfer [12] and second-order downconversion through a cooperative or an accretive energy-transfer mechanism [13] by exact calculations and simulations using Monte Carlo methods.

To investigate whether energy transfer from  $\text{Tb}^{3+}$  to  $\text{Yb}^{3+}$  occurs, an emission spectrum upon excitation in the

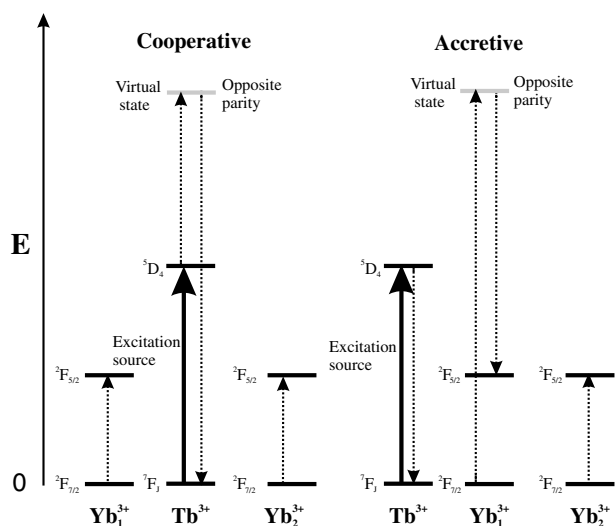


Fig. 4. Schematic representation of the cooperative and accretive pathways for energy transfer from  $\text{Tb}^{3+}$  to  $\text{Yb}^{3+}$ . The bold arrows indicate excitation of  $\text{Tb}^{3+}$  into the  ${}^5\text{D}_4$  state, after which energy transfer may occur. The energy-transfer processes are depicted by the dotted lines. In both mechanisms a virtual state is involved. For the cooperative mechanism, the virtual state is located on  $\text{Tb}^{3+}$ . For the accretive mechanism, the virtual state is located on  $\text{Yb}^{3+}$ . Since the total amount of energy is unchanged after the energy transfer, the resonance condition implies that the transition energy of  $\text{Tb}^{3+}$  balances the sum of the transition energies of the  $\text{Yb}^{3+}$  ions.

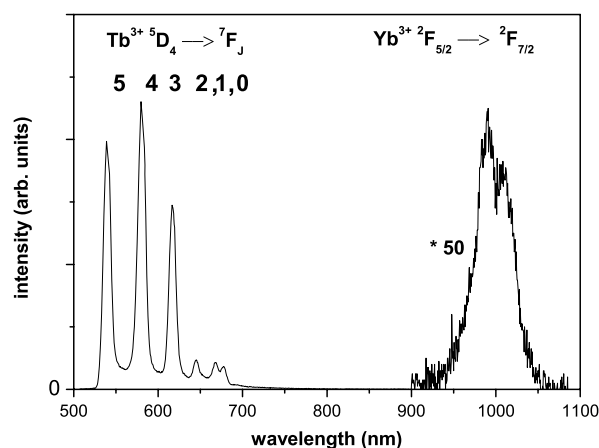


Fig. 5. Visible/near infrared emission spectrum of  $\text{Y}_{0.74}\text{Yb}_{0.25}\text{Tb}_{0.01}\text{PO}_4$  upon  $\text{Tb}^{3+}{}^7\text{F}_6 \rightarrow {}^5\text{D}_4$  excitation (489 nm). The spectral region between 900 and 1100 nm is amplified by a factor of 50.

$\text{Tb}^{3+}{}^5\text{D}_4$  level was recorded. Fig. 5 shows the emission spectrum of  $\text{Yb}_{0.25}\text{Y}_{0.74}\text{Tb}_{0.01}\text{PO}_4$  at room temperature upon  $\text{Tb}^{3+}{}^7\text{F}_6 \rightarrow {}^5\text{D}_4$  excitation. In the region of 500–700 nm a series of lines is observed while in the 900–1100 nm region an emission band of much lower intensity appears (multiplied 50 times in Fig. 5). The lines in the visible part of the spectrum are due to  $\text{Tb}^{3+}{}^5\text{D}_4 \rightarrow {}^7\text{F}_J$  multiplet emissions. They are similar to previous measurements on  $\text{YPO}_4$  doped with  $\text{Tb}^{3+}$  [14]. Transitions to different ground state terms with  $J$  ranging from 5 to 0 are clearly resolved in the spectrum. The  $\text{Tb}^{3+}{}^5\text{D}_4 \rightarrow {}^7\text{F}_6$  emission line is absent because of the use of a 540 nm cut-off filter. This filter was used to prevent second-order  $\text{Tb}^{3+}$  emissions in the wavelength region of 900–1100 nm, since these emissions would obscure the detection of  $\text{Yb}^{3+}$  emission lines. The features in this part of the spectrum are attributed to the  $\text{Yb}^{3+}{}^2\text{F}_{5/2} \rightarrow {}^2\text{F}_{7/2}$  transitions. Compared to the  $\text{Tb}^{3+}$  emission, the intensity of the  $\text{Yb}^{3+}$  luminescence is weak. This is due to the low response of the grating and the  $\sim 15$ . In addition concentration quenching (the migration of excitation energy over  $\text{Yb}^{3+}$  ions to quenching sites) reduces the luminescence quantum yield.

Excitation spectra of  $\text{Tb}^{3+}$  and  $\text{Yb}^{3+}$  emission in  $\text{Yb}_{0.25}\text{Y}_{0.74}\text{Tb}_{0.01}\text{PO}_4$  were recorded to give convincing evidence for the presence of  $\text{Tb}^{3+} \rightarrow \text{Yb}^{3+}$  energy transfer. Fig. 6 shows the wavelength region where the  $\text{Tb}^{3+}{}^7\text{F}_6 \rightarrow {}^5\text{D}_4$  transition is located. The solid line depicts the excitation spectrum of the  $\text{Tb}^{3+}{}^5\text{D}_4 \rightarrow {}^7\text{F}_3$  emission. The dotted line shows the excitation spectrum of the  $\text{Yb}^{3+}{}^2\text{F}_{5/2} \rightarrow {}^2\text{F}_{7/2}$  emission. In both spectra lines are located around 485–495 nm. For the spectrum monitoring the  $\text{Tb}^{3+}{}^5\text{D}_4 \rightarrow {}^7\text{F}_3$  emission, the excitation lines are ascribed to the well-known  ${}^7\text{F}_6 \rightarrow {}^5\text{D}_4$  transitions. The excitation spectrum of the  $\text{Yb}^{3+}$  emission is very similar to the  $\text{Tb}^{3+}{}^5\text{D}_4 \rightarrow {}^7\text{F}_3$  excitation spectrum. The observation of the  $\text{Tb}^{3+}{}^7\text{F}_6 \rightarrow {}^5\text{D}_4$  lines in the excitation spectrum of  $\text{Yb}^{3+}$  shows that energy transfer from  $\text{Tb}^{3+}$  to  $\text{Yb}^{3+}$  is present.

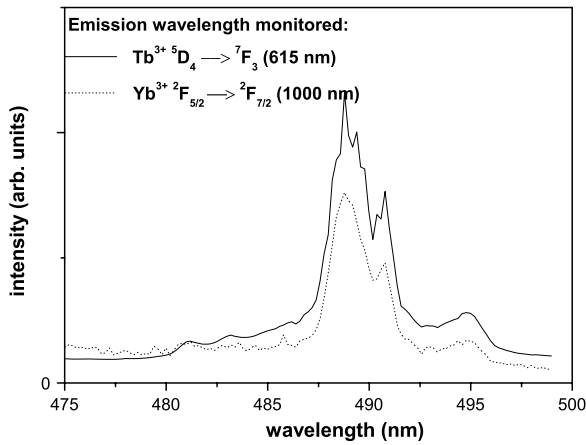


Fig. 6. Excitation spectra of the  $\text{Tb}^{3+}{}^5\text{D}_4 \rightarrow {}^7\text{F}_3$  emission (615 nm, solid line) and the  $\text{Yb}^{3+}{}^2\text{F}_{5/2} \rightarrow {}^2\text{F}_{7/2}$  emission (1000 nm, dotted line) in  $\text{Y}_{0.74}\text{Yb}_{0.25}\text{Tb}_{0.01}\text{PO}_4$ .

The results discussed above provide evidence for the presence of  $\text{Tb}^{3+} \rightarrow \text{Yb}^{3+}$  energy transfer. It is interesting to investigate the mechanism and efficiency of the energy-transfer process. An alternative for an energy-transfer process involving two  $\text{Yb}^{3+}$  ions is mentioned in the literature as phonon-assisted energy transfer [15,16]. On the basis of emission and excitation spectra this competing process cannot be excluded. Analysis of the transient luminescence curves provides insight in the energy-transfer mechanism.

In Fig. 7 the decay curves of the  $\text{Tb}^{3+}{}^5\text{D}_4 \rightarrow {}^7\text{F}_4$  luminescence (544.0 nm) are plotted for  $\text{Yb}^{3+}$  concentrations of 0%, 5%, 15%, 25%, 50%, 75% and 99%. The  $\text{Tb}^{3+}$  emission in  $\text{YPO}_4:\text{Tb}^{3+}$  1% shows a nearly single exponential decay as expected (only radiative decay). A mono-exponential fit yields a decay time of 2.3 ms. A decay time between 2 and 3 ms is a typical value compared to  $\text{Tb}^{3+}{}^5\text{D}_4$  emission in oxides where the site of  $\text{Tb}^{3+}$  lacks inversion symmetry [16]. When the  $\text{Yb}^{3+}$  concentration is increased, the decay curve decreases more rapidly and it becomes non-exponential. For  $\text{YbPO}_4:\text{Tb}^{3+}$  1% the fastest decay is observed and the curve is again nearly single exponential. The faster decline as a function of  $\text{Yb}^{3+}$  concentration may be explained by the introduction of extra decay pathways due to the  $\text{Yb}^{3+}$ -doping: energy transfer from  $\text{Tb}^{3+}{}^5\text{D}_4$  to  $\text{Yb}^{3+}$  enhances the  $\text{Tb}^{3+}{}^5\text{D}_4$  decay rate.

The presence of  $\text{Yb}^{3+}$  ions also explains the non-exponential behaviour at intermediate doping concentrations and the single exponential behaviour for 99%  $\text{Yb}^{3+}$ . At intermediate doping concentrations the  $\text{Yb}^{3+}$  and the  $\text{Y}^{3+}$  ions are randomly distributed over the  $\text{RE}^{3+}$  lattice sites. Thus, the environment of every  $\text{Tb}^{3+}$  ion is different, leading to a variety of transfer rates. At an  $\text{Yb}^{3+}$  fraction of 99% the  $\text{Tb}^{3+}$  ions are surrounded by  $\text{Yb}^{3+}$  ions only, leading to a single decay component. Therefore, the 99%  $\text{Yb}^{3+}$  decay curve in Fig. 7 is again nearly single exponential. Fitting this curve with a single exponential function yields a decay time of 0.25 ms.

Assuming that the radiative rate of the  $\text{Tb}^{3+}{}^5\text{D}_4$  emission does not change when  $\text{Y}^{3+}$  is substituted for  $\text{Yb}^{3+}$ ,

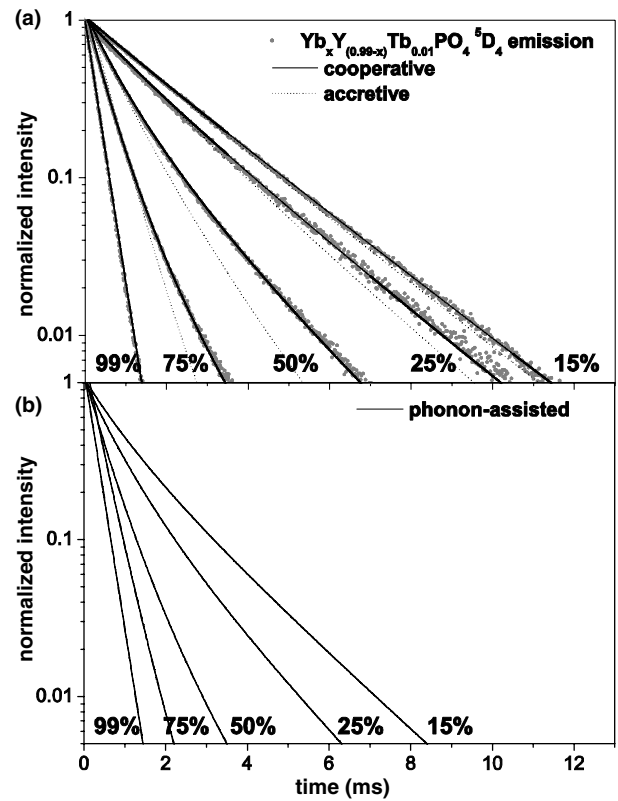


Fig. 7. (a) Luminescence decay curves of the  $\text{Tb}^{3+}{}^5\text{D}_4$  emission for various concentrations of  $\text{Yb}^{3+}$  plotted with simulation results. The dots are the experimental results. The solid lines are simulated curves using a cooperative dipole-dipole model. Dashed lines are simulated curves using an accretive dipole-dipole model (see Fig. 4). (b) Simulated decay curves for the phonon-assisted dipole-dipole model. For both figures the  $\text{Yb}^{3+}$  concentrations are indicated in the figure.

the energy-transfer rate in  $\text{YbPO}_4$  can be calculated by subtracting the  $\text{Tb}^{3+}{}^5\text{D}_4$  radiative decay rate from the decay rate in  $\text{YbPO}_4$ . This results in an energy-transfer rate of  $35 \times 10^2 \text{ s}^{-1}$  in  $\text{YbPO}_4:\text{Tb}^{3+}$  1%. This is roughly an order of magnitude faster than the radiative decay rate of  $\text{Tb}^{3+}$  and indicates that the energy-transfer process is efficient.

To distinguish between the three energy-transfer mechanisms the decay curves were compared to the decay behaviour predicted by Monte Carlo simulations. Experiments and simulated results for the cooperative, the accretive and the phonon-assisted dipole-dipole models are shown in Fig. 7 (see Ref. [4] for further details). To obtain the computed curves, the radiative decay rate and the energy-transfer rate in  $\text{YbPO}_4$  (as determined from single exponential fits to the decay curves of  $\text{YPO}_4$  and  $\text{YbPO}_4$  in Fig. 7) were used as input parameters. Therefore, at 99%  $\text{Yb}^{3+}$  concentration, the three simulated curves all match the experimental curve. However, the cooperative model matches the experiments for all  $\text{Yb}^{3+}$  concentrations while the accretive and phonon-assisted energy-transfer model deviate substantially. At all intermediate  $\text{Yb}^{3+}$  concentrations, the decay profiles of the phonon-assisted model and the accretive model fall off faster than the cooperative model. The excellent agreement between the experimentally

measured luminescence decay curves and the calculated curves for cooperative energy transfer via dipole–dipole interaction provides strong evidence that this mechanism is operative in the (Y, Yb)PO<sub>4</sub>:Tb<sup>3+</sup> system.

The energy-transfer efficiency is shown to be 88% for YbPO<sub>4</sub>:Tb<sup>3+</sup> 1%. This means that 88 out of 100 Tb<sup>3+</sup> ions each transfer their energy to two Yb<sup>3+</sup> ions. This makes a quantum efficiency of 188% possible. Materials exploiting Tb–Yb cooperative quantum cutting may be useful to increase the efficiency of silicon-based solar cells by down-converting the green-to-UV part of the solar spectrum to ~1000 nm photons, with almost complete doubling of the number of photons. The weak IR emission of the presently studied materials (see Fig. 5) shows that, although the physics of the energy-transfer process allow for efficient quantum cutting, the actual quantum efficiency in the IR is still low. In order to obtain a material with an actual quantum efficiency close to 200%, two drawbacks should be overcome. First, due to the high Yb<sup>3+</sup> concentration needed for efficient downconversion, concentration quenching of the Yb<sup>3+</sup> emission is a major issue. To overcome this problem, incorporation of ions with an excited state at slightly lower energy than the <sup>2</sup>F<sub>5/2</sub> state of Yb<sup>3+</sup> ion (but still higher than the bandgap of silicon) may be used. These ions will function as traps for the energy in the <sup>2</sup>F<sub>5/2</sub> state so that migration of excitation energy to quenching sites is suppressed. Another possibility is the use of one-dimensional systems in order to localize the energy migration. The second obstacle is the low absorption cross section for green-to-UV light of Yb/YPO<sub>4</sub> doped with Tb<sup>3+</sup>. The absorption cross section may be enhanced in two ways. First, a bulk material with a lower bandgap may be used so that the host itself would absorb part of the solar spectrum, after which energy transfer to a Tb<sup>3+</sup> ion should occur. Second, sensitizer ions could be used to absorb the desired part of the solar spectrum and transfer the excitation energy to the <sup>5</sup>D<sub>4</sub> state of Tb<sup>3+</sup> for the Tb–Yb downconversion process.

## 5. Conclusion

The possibility of efficient visible quantum cutting has been investigated for materials in which Pr<sup>3+</sup> shows a cascade emission from the <sup>1</sup>S<sub>0</sub> level. In order to convert the 405 nm photon emitted by Pr<sup>3+</sup> in the first step into a more useful visible wavelength, two types of co-activators were added, viz. Eu<sup>3+</sup> or Mn<sup>2+</sup>. In the case of Eu<sup>3+</sup> a quenching of the <sup>1</sup>S<sub>0</sub> emission from Pr<sup>3+</sup> is observed. The quenching is ascribed to relaxation through a metal-to-metal charge-transfer state. Upon adding Mn<sup>2+</sup> as a co-activator, no

energy transfer is observed even at concentrations as high as 5%. The origin of the absence of energy transfer is unclear. In the second part of the paper second-order downconversion in Yb<sub>x</sub>Y<sub>(1-x)</sub>PO<sub>4</sub>:Tb<sup>3+</sup> 1% is studied. Emission, excitation, and time-resolved luminescence measurements reveal the occurrence of energy transfer from the <sup>5</sup>D<sub>4</sub> level of Tb<sup>3+</sup> to two Yb<sup>3+</sup> ions. Monte Carlo simulations of the luminescence decay curves are shown to be a useful tool for the determination of the energy-transfer mechanism. When a cooperative dipole–dipole model is assumed, the simulated and the experimental curves show an excellent agreement for all Yb<sup>3+</sup> concentrations. Based on the poor agreement between simulated and measured luminescence decay curves, it is possible to exclude an accretive dipole–dipole mechanism and a phonon-assisted energy-transfer process. The efficiency of the quantum cutting process is 88% in YbPO<sub>4</sub>:Tb<sup>3+</sup> 1%. This allows for an overall quantum efficiency (VIS + IR) of 188%, which is close to the limit of 200%.

## Acknowledgements

The authors are grateful to H.W. de Wijn and M. Gieselbach for helpful discussions. The work described here was supported by the Council for Chemical Sciences (CW), with financial aid from the Netherlands Foundation for Technical Research (STW).

## References

- [1] G. Blasse, B.C. Grabmaier, *Luminescent Materials*, Springer Verlag, Berlin, 1994.
- [2] C. Ronda, *J. Alloys, Compounds* 225 (1995) 534.
- [3] R.T. Wegh, H. Donker, K.D. Oskam, A. Meijerink, *Science* 283 (1999) 663.
- [4] P. Vergeer, T.J.H. Vlugt, M.H.F. Kox, M.I. den Hertog, J.P.J.M. van der Eerden, A. Meijerink, *Phys. Rev. B* 71 (2005) 014119.
- [5] P.S. Peijzel, A. Meijerink, R.T. Wegh, M.F. Reid, G.W. Burdick, *J. Solid State Chem.* 178 (2) (2005) 448.
- [6] L. van Pieterse, M.F. Reid, R.T. Wegh, S. Soverna, A. Meijerink, *Phys. Rev. B* 65 (2002) 045113.
- [7] W.W. Piper, J.A. DeLuca, F.S. Ham, *J. Lumin.* 8 (1974) 344.
- [8] J.L. Sommerdijk, A. Bril, A.W. de Jager, *J. Lumin.* 9 (1974) 288.
- [9] M. Zachau, F. Zwaschka, F. Kummer, *Proc. Electrochem. Soc.* 97 (29) (1998) 314.
- [10] D.L. Dexter, *Phys. Rev.* 108 (1957) 630.
- [11] T.T. Basiev, M.E. Doroshenko, V.V. Osiko, *JETP Lett.* 71 (2000) 8.
- [12] T. Miyakawa, D.L. Dexter, *Phys. Rev. B* 1 (1970) 2961.
- [13] D.L. Andrews, R.D. Jenkins, *J. Chem. Phys.* 114 (2001) 1089.
- [14] R.C. Ropp, *J. Electrochem. Soc.* 115 (1968) 841.
- [15] W. Streck, P. Deren, A. Bednarkiewicz, *J. Lumin.* 87 (9) (2000) 999.
- [16] I.R. Martin, A.C. Yanes, J. Mendez-Ramos, M.E. Torres, V.D. Rodriguez, *J. Appl. Phys.* 89 (2001) 2520.

## Photoluminescence of rare-earth-doped glasses

G. C. RIGHINI<sup>(1)</sup>(\*) and M. FERRARI<sup>(2)</sup>(\*\*)

<sup>(1)</sup> *Istituto di Fisica Applicata “Nello Carrara” and Dipartimento Materiali e Dispositivi  
CNR - Via Madonna del Piano 10, 50019 Sesto Fiorentino (Firenze), Italy*

<sup>(2)</sup> *CSMFO Group, Istituto di Fotonica e Nanotecnologie, CNR, Sezione di Trento  
Via Sommarive 14, 38050 Povo (Trento), Italy*

(ricevuto il 13 Marzo 2006)

**Summary.** — Rare-earth elements are of interest in several high-tech and environmental application areas, the two major ones concerning magnetic and optical devices. In the latter field, one can exploit the unique photoluminescence properties of rare-earth ions to develop novel or advanced lasers and optical amplifiers. Glasses have been known for a long time as a convenient host for rare earths and have been widely used for the fabrication of solid-state lasers. Recently, guided-wave format has added several advantages, namely the small size, the high pump power density, and the larger flexibility in design and fabrication. Thus, in the last few years, due to the great development of optical communications, an increasing research and development activity has been focused on the design and manufacture of fibre optic and integrated optic lasers and amplifiers, especially of those based on  $\text{Er}^{3+}$ -doped glasses. The aim of the present paper is to highlight the application of the spectroscopic techniques to the characterization of rare-earth-doped glasses and to present a brief overview of the efforts and progresses made in the area of micro-optic and integrated-optic lasers and amplifiers. A brief summary of the fundamentals of the photoluminescence properties and of the measurements techniques is also provided.

PACS 78.55.-m – Photoluminescence, properties and materials.

PACS 42.62.Fi – Laser spectroscopy.

PACS 42.70.-a – Optical materials.

PACS 42.82.-m – Integrated optics.

---

(\*) E-mail: giancarlo.righini@cnr.it

(\*\*) E-mail: mferrari@science.unitn.it

---

|    |        |  |
|----|--------|--|
| 2  | 1.     | Introduction   |
| 5  | 2.     | Rare-earth-doped glasses   |
| 7  | 3.     | Spectroscopic techniques for optical materials assessment                  |
| 7  | 3.1.   | Absorption measurements  |
| 9  | 3.1.1. | Absorption spectroscopy for OH <sup>-</sup> content assessment             |
| 11 | 3.2.   | Luminescence measurements  |
| 13 | 3.3.   | Raman and Brillouin scattering for optical-glasses characterization        |
| 20 | 4.     | Absorption and emission cross-section measurement                          |
| 25 | 5.     | Quantum efficiency evaluation  |
| 28 | 6.     | Radiation trapping, self-absorption and concentration-quenching phenomena  |
| 31 | 7.     | Photonic band gap structures with glassy materials                         |
| 33 | 8.     | Rare-earth-doped glasses for lasers and amplifiers                         |
| 33 | 8.1.   | Integrated optical amplifiers  |
| 36 | 8.2.   | Optical and spectroscopic properties of Er <sup>3+</sup> -doped waveguides |
| 38 | 8.2.1. | Sol-gel silica-hafnia films  |
| 39 | 8.2.2. | Soda-lime-alumino-silicate (SLAS) glasses                                  |
| 41 | 8.2.3. | Tellurite glass waveguides   |
| 42 | 9.     | Microspherical lasers  |
| 45 | 10.    | Conclusions and perspectives   |

---

## 1. – Introduction

Photoluminescence (PL) is the emission of light from a material under optical excitation. It is one of the kinds of the more general phenomenon of luminescence, namely the emission of optical radiation resulting from various types of excitation: chemical or biochemical changes, electrical energy, subatomic motions, reactions in crystals, or stimulation of an atomic system. Accordingly, one can speak about bio-, chemi-, electro-, thermo-, radio-luminescence, and so on.

When light of sufficient energy is incident on a material, photons are absorbed and electronic excitations are created. Eventually, the electrons return to the ground state: if this relaxation is radiative, the emitted light is the photoluminescence signal. The intensity of this signal gives a measure of the relative rates of radiative and nonradiative recombinations.

Often one can also refer to fluorescence or phosphorescence: the latter is a type of luminescence that occurs naturally in many minerals and metallic compounds, in some organic compounds, and in some living organisms such as marine fauna and insects (the most familiar one being the firefly, whose light flashes are produced by bioluminescence). Phosphorescence is distinguished from fluorescence for two main reasons: a) in phosphorescence there is a longer time period between the excitation and the emission of light; b) phosphorescence may continue for some time (even hours) after the exciting source has been removed, while fluorescence ceases when excitation is off.

Photoluminescence effects have been observed for thousands of years; the oldest known written observations on bioluminescent phenomena in nature were made in China, dating roughly from 1500 to 1000 B.C. regarding fireflies and glow-worms. Only during the 16th and 17th centuries, in Europe, the first efforts were made to understand and apply such phenomena. Indeed, the first object of scientific study of luminescent phenomena was a natural stone, subsequently referred to as the “Bolognian Phosphorus” or “Bolognian Stone” or “Litheophosphorus”, which had been discovered in 1602 on Monte Paderno,

| Rare Earth Elements |    |    |    |    |    |    |    |    |    |    |    |    |    |    |  |  |  | Y<br>39 |
|---------------------|----|----|----|----|----|----|----|----|----|----|----|----|----|----|--|--|--|---------|
| La                  | Ce | Pr | Nd | Pm | Sm | Eu | Gd | Tb | Dy | Ho | Er | Tm | Yb | Lu |  |  |  |         |
| 57                  | 58 | 59 | 60 | 61 | 62 | 63 | 64 | 65 | 66 | 67 | 68 | 69 | 70 | 71 |  |  |  |         |
| Lanthanides         |    |    |    |    |    |    |    |    |    |    |    |    |    |    |  |  |  |         |

|    |    |    |    |    |    |    |    |    |    |    |    |    |    |    |    |    |    |
|----|----|----|----|----|----|----|----|----|----|----|----|----|----|----|----|----|----|
| H  |    |    |    |    |    |    |    |    |    |    |    |    |    |    |    |    | He |
| Li | Be |    |    |    |    |    |    |    |    |    |    | B  | C  | N  | O  | F  | Ne |
| Na | Mg |    |    |    |    |    |    |    |    |    |    | Al | Si | P  | S  | Cl | Ar |
| K  | Ca | Sc | Ti | V  | Cr | Mn | Fe | Co | Ni | Cu | Zn | Ga | Ge | As | Se | Br | Kr |
| Rb | Sr | Y  | Zr | Nb | Mo | Tc | Ru | Rh | Pd | Ag | Cd | In | Sn | Sb | Te | I  | Xe |
| Cs | Ba | Lu | Hf | Ta | W  | Re | Os | Ir | Pt | Au | Hg | Tl | Pb | Bi | Po | At | Rn |
| Fr | Ra | Ac | Lr |    |    |    |    |    |    |    |    |    |    |    |    |    |    |

Fig. 1. – Position of the rare-earth elements in the periodic table of elements.

just outside of Bologna, Italy, by Vincenzo Casciarolo, an amateur alchemist [1]. The beginning of luminescence science, however, can be dated to 1852, when George Stokes interpreted the light-emitting phenomenon and formulated the law (the Stokes Law or the Stokes Shift) that the fluorescent light is of longer wavelength than the exciting light [2]. It was Stokes who coined, in 1853, the term “fluorescence” from *fluorspar* (calcium fluoride), the name of the mineral where he first noticed the phenomenon, and the ending *-escence* analogous to opalescence, phosphorescence, etc.

Nowadays, photoluminescence is mostly exploited for materials’ characterization: from the analysis of the PL signal one can derive much information on the emitting material, and PL may be particularly useful in surface diagnostic, because the phenomenon often originates from the surface layers of the material. A noticeable advantage of PL analysis is that it is a simple, versatile, and non-destructive technique. Obviously, PL depends much on the nature of the optical excitation, as the excitation energy selects the initial photoexcited state and governs the penetration depth of the incident light.

Among the materials that can be usefully investigated by using PL techniques, an important class is that of rare-earth-doped glasses. Their impact is mostly related to the development of optical communications and to the recent request of increasing the bandwidth capacity of optical fibre systems.

The rare-earth elements (REEs) form the largest chemically coherent group in the periodic table (fig. 1); though generally not so well known, because of their specificity, REEs have many high-tech and environmental applications. Europium, for instance, is used as the red phosphor in colour cathode-ray tubes and liquid-crystal displays. Alloys containing one REE (such as Nd, Sm, Gd, Dy, Pr) have revolutionized the permanent magnet technology. Forefront research is now looking at the properties of the unique magnetic-martensitic phase transformation in  $R_5T_4$  materials (where R is Gd and other rare earths and T, for instance, is Si, Ge, or Sn) in order to understand the underlying electronic structure and the microscopic interactions bringing extremely strong coupling of the magnetic moments with the lattice [3]. A better understanding of this phase trans-

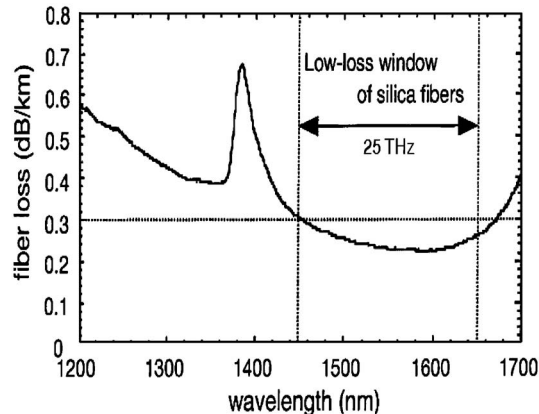


Fig. 2. – Transmission curve in the near-infrared region of a typical single-mode fibre for optical communication systems.

formation and other basic phenomena may lead to the development of novel material systems exhibiting extremely large magnetocaloric, magnetostrictive, and magnetoresistance responses to small changes of magnetic field, temperature, and pressure. Even environmental applications of REEs have grown significantly over the past decades. REEs, for instance, are essential constituents of automotive catalytic converters. Widespread use of new energy-efficient fluorescent lamps (using Y, La, Ce, Eu, Gd, and Tb) may alleviate energy consumption. Large-scale application of magnetic-refrigeration technology, based on a “giant magnetocaloric effect” near room temperature exhibited by the  $\text{Gd}_5(\text{Si}_2\text{Ge}_2)$  alloy, also could significantly reduce energy consumption and  $\text{CO}_2$  emissions.

Coming to the field of optics, cerium, the most abundant and least expensive element in the group, is very much appreciated as polishing agent for glass. Neodymium is very well known as the active dopant of glass or YAG (yttrium aluminium garnet) for solid-state lasers. The most popular application of REEs over the last decades, however, has been that of the development of fibre and integrated-optics lasers and amplifiers [4, 5].

Erbium (alone or together with ytterbium) in glass or other dielectric materials (such as lithium niobate) has become one of the key materials in photonic systems. Its relevance is due to two factors: i) the optical amplifier (OA) is a key enabling technology to achieve the high-speed and high-volume transmission required in current optical transmission systems [4-6]; and ii) the photoluminescence peak of Er is at a wavelength around  $1.5 \mu\text{m}$ , just inside the so-called third window of fibre communication systems. The broadness of the amplification band is of particular concern nowadays; let us refer to fig. 2, which shows the typical transmission curve of a single-mode commercial silica fibre for optical communications. The low-loss window (if we choose the  $0.3 \text{ dB/km}$  threshold) is over  $200 \text{ nm}$  wide ( $\approx 25 \text{ THz}$ ); by exploiting this entire band it would be easy to achieve multi-Tb/s transmission. In fact, by using a  $0.4 \text{ nm}$  (or  $\approx 50 \text{ GHz}$ ) channel spacing—as is done currently in DWDM (dense wavelength division multiplexing) systems—one could allocate 500 communication channels, each one with a transmission speed over  $10 \text{ Gb/s}$ , thus making system bit rates over  $5 \text{ Tb/s}$  possible. Not only erbium, however, is important for communication systems; for instance, the first  $10 \text{ Tb/s}$  WDM transmission in single fibre was demonstrated in 2001 by using a gain-shifted thulium-doped fibre amplifier in a system using  $273 \text{ 50-GHz}$ -spaced channels, each with  $40 \text{ Gb/s}$  capacity [7].

This paper is intended to serve both as an introduction to the field of photoluminescence techniques applied to rare-earth-doped glasses and as a review of recent works aiming, on the one hand, at the characterization of novel glasses and, on another hand, at the development of integrated optical devices exploiting such properties. By necessity, this review is not exhaustive, and we have only attempted to offer the non-specialized reader a brief overview of the ongoing activities and of the problems to be faced in this field.

## 2. – Rare-earth-doped glasses

Oxide glasses are well known as excellent hosts for rare-earth ions: one of the first solid-state lasers was demonstrated in 1961 in Nd<sup>3+</sup>-doped glass [8]. Lasing in a Nd<sup>3+</sup>-doped multi-component glass fibre was reported three years later [9]. The same material structure was exploited to demonstrate the first thin-film waveguide glass amplifier, in 1972 [10], and the first integrated optical glass laser, in 1974 [11]. The interest for Er<sup>3+</sup>-doped glasses arose quite later, in the late 1980s, when the main operational wavelength for optical-fibre communication systems shifted towards the 1.5  $\mu\text{m}$  band [12]. Since then, many remarkable results in the development of more efficient glass matrices and in the actual fabrication of rare-earth-doped (RED) glass integrated optical amplifiers have been achieved.

RE (lanthanide) ions are characterized by [Xe].4*f*<sup>12</sup>.6*s*<sup>2</sup> electronic configuration; all of them have the same outer-shell configuration, namely 5*s*<sup>2</sup>5*p*<sup>6</sup>6*s*<sup>2</sup>. The most stable ionisation state is the trivalent one, with the 5*s* and 5*p* electrons remaining untouched and acting to screen the energy levels of the 4*f* electrons from the effect of the surrounding environment. The transition probabilities between 4*f* states, however, are sensitive to the ions surrounding the rare earth, and the design of a proper RED glass involves the study of a number of spectroscopic parameters. The Judd-Ofelt theory [13,14] is usually adopted to calculate, by assuming certain approximations, transition probabilities from the data of absorption cross-sections of several *f-f* transitions. According to this theory, the strength of an *f-f* transition may be expressed by the sum of the products of three intensity parameters  $\Omega_i$  ( $i = 2, 4, 6$ ) times the squared matrix elements  $U(i)$  between the initial *J*-states and the terminal *J'* state. Once the phenomenological parameters  $\Omega_i$  have been calculated, it is possible to derive the strength of any absorption or emission transition, as well as the stimulated emission cross-section, the fluorescence branching ratio from level *J* to *J'*, and the radiative lifetime of an excited level. Radiative lifetime, however, may be calculated even in a simpler way, by using Einstein relation for the transition probability between absorption and emission coefficients; this issue will be treated in more detail in the following section. The energy levels of the RE ions are shown in fig. 3.

One of the major limits to the quantum efficiency  $\eta$  of a given transition in a RE ion in a glass, defined as the ratio between the measured fluorescence lifetime  $\tau_{\text{meas}}$  and the radiative lifetime  $\tau_{\text{rad}}$  of the excited state, is constituted by nonradiative relaxations, that in turn may be classified as a) multiphonon relaxations; b) cross relaxations; and c) cooperative upconversion processes. Phonon relaxations correspond to the collisional decay of an excited energy level, due to the crystalline lattice vibrations or, in other words, to the rapid short-range movement of the closely spaced atoms. Multiphonon relaxations between two energy states occur by the simultaneous emission of several phonons that are sufficient to conserve the energy of the transition. Table I reports typical phonon energies of different glass matrices; the probability of multiphonon relaxation may be assessed by

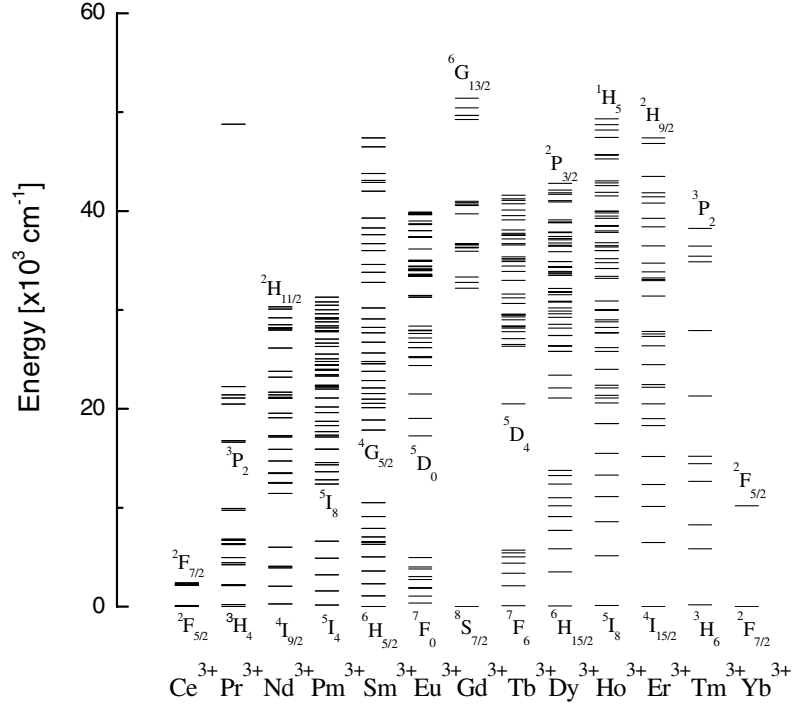


Fig. 3. – Energy levels of trivalent rare-earth ions. Electronic energies were determined on the basis of published data [100].

using a simple energy gap model [15]. The multiphonon decay rates as a function of energy gap to the next lower level have been measured experimentally for silicate glasses doped with  $\text{Nd}^{3+}$ ,  $\text{Er}^{3+}$ ,  $\text{Pr}^{3+}$  and  $\text{Tm}^{3+}$ ; it was found that an approximately exponential dependence holds, independently of the RE ion or electronic level [16].

Cross relaxations and cooperative upconversion processes, on the other hand, lead to fluorescence quenching, *i.e.* to the decrease of fluorescence intensity when the RE concentration is increased. One has to consider, in fact, that, with increasing concentration of RE ions, the ion spacing decreases and may be small enough to allow them

TABLE I. – Maximum phonon energy of various glass matrices.

| Glass            | Phonon energy<br>( $\text{cm}^{-1}$ ) |
|------------------|---------------------------------------|
| Borate           | $\sim 1400$                           |
| Phosphate        | 1100–1200                             |
| Silicate         | $\sim 1100$                           |
| Germanate        | $\sim 900$                            |
| Tellurite        | $\sim 700$                            |
| Fluorozirconate  | $\sim 500$                            |
| Sulfide (Ga, La) | $\sim 450$                            |

to interact and transfer energy. Cross relaxation may occur between RE ions of the same type if they have two pairs of energy levels characterized by the same energy gap  $\Delta E$ . An excited ion A (donor) transfers half of its energy to a ground-state ion B (acceptor), so that both ions move to a same intermediate level, from which they decay non-radiatively to the ground level. It appears that this kind of dissipative phenomenon is the major responsible of concentration quenching of  $\text{Nd}^{3+}$  through the energy transfers  $\text{Nd}^{3+}(^4F_{3/2} \downarrow ^4I_{15/2}) \Rightarrow \text{Nd}^{3+}(^4F_{9/2} \uparrow ^4I_{15/2})$ ; subsequent relaxation from  $^4I_{15/2}$  to  $^4F_{9/2}$  occurs via phonons. Co-operative up-conversion process occurs between two excited ions A and B: A gives its energy to B, so that A relaxes to ground state, while B goes to a higher energy level. From this higher level B can relax either emitting a photon with higher energy (*i.e.* higher frequency and lower wavelength) than the exciting photon—it is this case which gave the “up-conversion” label to the process—or via phonons and a lower-energy photon. In any case, at least one exciting photon is lost for the amplifying process, and fluorescence quenching in  $\text{Er}^{3+}$  may be primarily attributed to this process.

The interested reader is referred for further details to the many precious books published on the physics of glass lasers [5, 17-21].

### 3. – Spectroscopic techniques for optical materials assessment

The aim of this section is to recollect some basics concerning the use of spectroscopic techniques such as absorption, luminescence, Raman and Brillouin spectroscopy for the study of optical materials. Particular attention is being paid to their application to thin films and planar waveguides activated by various optically active elements, in particular rare-earth ions; some interesting aspects related to massive systems will be discussed as well. The interest of absorption and luminescence spectroscopy is obvious in photonics. These two techniques, in particular, allow one to determine the spectroscopic properties of the optical species imbedded in a matrix [22-24]. The spectroscopic and optical techniques are currently used for optimization and pre-competitive fabrication of innovative devices. The fundamentals of optical spectroscopy, both theoretical and experimental, can be found in several textbooks and scientific papers, *e.g.*, in [22-27] and references therein. The spectroscopic properties, namely emission quantum efficiency, lifetime of the excited electronic states, dynamical processes, etc., of systems activated by luminescent ions are investigated by luminescence spectroscopy. The typical experimental configuration used to study the spectroscopic properties of a planar waveguide is shown in fig. 4. This set-up is practically the same one used in *m*-line spectroscopy, where the light is injected into the film by prism coupling [28, 29]. This configuration allows an appreciable increase of contrast, as well as selectivity of both mode and polarization. Detailed discussions about the waveguiding geometry are reported in several books and review articles [30-32].

**3.1. Absorption measurements.** – Absorption spectra are fundamental to determine the factors governing several properties of optical materials, such as losses, absorption cross-sections and refractive index. The simplest schema is to measure the decrease of the optical intensity of the beam travelling the material as a function of the wavelength  $\lambda$ . In the linear behaviour, the absorption coefficient  $\alpha$  for a sample of thickness  $L$  is given by the Lambert-Beers law:

$$(3.1.1) \quad I(\lambda) = I_0(\lambda) \exp[-\alpha(\lambda)L],$$

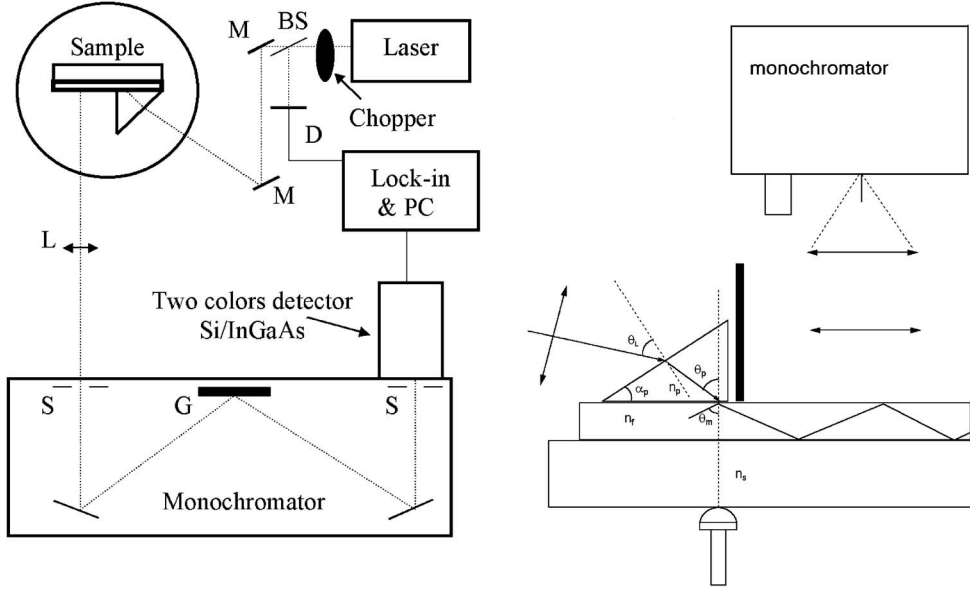


Fig. 4. – Experimental set-up used for luminescence measurements in waveguide configuration. The laser light is injected into the guide by prism coupling, as in the typical arrangement used for  $m$ -line spectroscopy: slits (S); grating (G); lens (L); mirror (M); beam splitter (BS); reference diode (D). Adapted from [77].

where  $I$  is the intensity measured after an optical path length  $L$ , and  $I_0$  is the intensity incident on the sample. Because  $L$  has the dimension of a length ( $L$ ), the absorption coefficient  $\alpha$  has dimension  $L^{-1}$  and it is usually measured in  $\text{cm}^{-1}$ . The absorption coefficient is related to the imaginary part of the refractive index  $n_i(\lambda)$  by

$$(3.1.2) \quad \alpha(\lambda) = \frac{4\pi}{\lambda} n_i(\lambda).$$

In the discussion of the absorption spectra, other quantities are currently used:

*Transmission:*

$$(3.1.3) \quad T(\lambda) = \frac{I(\lambda)}{I_0(\lambda)}.$$

*Optical density or absorbance:*

$$(3.1.4) \quad OD(\lambda) = -\log(T(\lambda)) \quad \text{or} \quad T(\lambda) = 10^{-OD(\lambda)}.$$

*Extinction coefficient:*

$$(3.1.5) \quad \varepsilon(\lambda) = \frac{\alpha(\lambda)}{C} = -\frac{\log(T(\lambda))}{C \cdot L},$$

where  $C$  is the concentration measured in  $\text{mol l}^{-1}$ . The units of the extinction coefficient or molar absorptivity are  $\text{mol}^{-1} \text{l cm}^{-1}$ .

*Absorption cross-section:*

$$(3.1.6) \quad \sigma(\lambda) = \frac{\alpha(\lambda)}{N},$$

where  $N$  is the density of the absorbing centres given in  $\text{cm}^{-3}$  unit. The absorption cross-section quantifies the ability of an ion to absorb light and is one of the most common values used in photonics for sample characterization. The amount of power absorbed by an ion when light is incident upon it at wavelength  $\lambda$  is given by

$$(3.1.7) \quad P(\lambda) = \sigma(\lambda)I(\lambda),$$

where  $I$  is the intensity of the light incident upon the ion, given in  $\text{Watt cm}^{-2}$ . The dimension of  $\sigma$  is that of an area. The cross-section can be thought of as a sort of target area that can intercept a light flux by catching the photons that flow through it.

The extinction coefficient and the cross-section are related by

$$(3.1.8) \quad \varepsilon(\lambda) = \sigma(\lambda) \frac{N_A}{\ln 10} \cong l \cdot \sigma(\lambda) \cdot 2.6154 \cdot 10^{20},$$

where  $N_A = 6.0221367 \cdot 10^{23} \text{ mol}^{-1}$  is Avogadro's number.

The absorption coefficient can be measured in  $\text{dB cm}^{-1}$  by the equation

$$(3.1.9) \quad I(\lambda) = I_0(\lambda)10^{-\frac{\gamma}{10}L},$$

where  $\gamma$  is the attenuation coefficient expressed in  $\text{dB cm}^{-1}$ . Comparing the expressions used for  $\gamma$  ( $\text{dB cm}^{-1}$ ) and  $\alpha$  ( $\text{cm}^{-1}$ ), it results that the two values are related by

$$(3.1.10) \quad \gamma = 4.343 \alpha.$$

An exhaustive presentation of the optical theory applied to infrared absorption spectroscopy is reported in [33].

**3.1.1. Absorption spectroscopy for  $\text{OH}^-$  content assessment.** Let us now refer to some applications where absorption, transmission and reflectance spectra play an important role in characterization of materials. Absorption spectroscopy is largely employed in chemical sensing, often in conjunction with optical fibres or planar waveguides [34-37]. An important example, where infrared absorption measurements can give useful information on optical materials, concerns the estimation of  $\text{OH}^-$  content in rare-earth-activated glasses. The O-H stretching vibration affects the fluorescence decay of  $\text{Er}^{3+}$  ions at  $1.5 \mu\text{m}$  because two O-H vibrations are enough to bridge the gap of about  $6500 \text{ cm}^{-1}$  between the ground state,  $^4I_{15/2}$ , and the first excited state,  $^4I_{13/2}$ , of the  $\text{Er}^{3+}$  ion [22, 38-41]. The consequence of the presence of residual  $\text{OH}^-$  species in the material is a strong reduction of the quantum efficiency of the  $^4I_{13/2}$  level. Although the presence of  $\text{OH}^-$  group is the main determinant of the performance of sol-gel-based devices, because it is intrinsic to the sol-gel processing, the detrimental non-radiative relaxation channel due to vibrations of  $\text{OH}^-$  groups is effective also in melt-derived glasses.

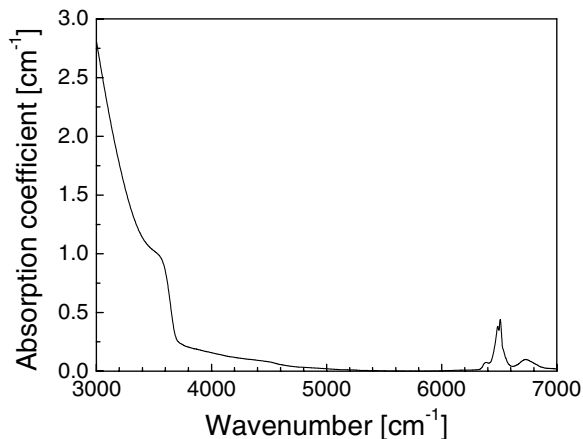


Fig. 5. – Room temperature FTIR absorption spectrum of a  $\text{Er}^{3+}$ -activated silicate glass (77.29  $\text{SiO}_2$ : 11.86  $\text{K}_2\text{O}$ : 10.37  $\text{PbO}$ : 0.48  $\text{Sb}_2\text{O}_3$ ) in the IR region [42].

Figure 5 shows the absorption spectrum of a glass produced at Cristallerie Baccarat by a conventional melt-quenching technique with the following molar composition: 77.29  $\text{SiO}_2$ : 11.86  $\text{K}_2\text{O}$ : 10.37  $\text{PbO}$ : 0.48  $\text{Sb}_2\text{O}_3$  and activated by  $\text{Er}^{3+}$  ions [42]. The spectrum shows the multiphonon tail of the absorption edge, which partially overlaps the wide band (3000–3700  $\text{cm}^{-1}$ ) assigned to the presence of hydroxyl groups in the glass matrix, centred at about 3570  $\text{cm}^{-1}$  [43, 44]. The amplitude of this fundamental  $\text{OH}^-$  stretching band allows the estimation of the  $\text{OH}^-$  concentration by the Beer-Lambert law  $C = (\alpha \times 0.434)(1/\varepsilon)$ , where  $C$  is the concentration of the bonded species whose vibrations induce the IR light absorption,  $\alpha$  is the absorption coefficient and  $\varepsilon$  is the extinction coefficient. A rough estimation of water content is obtained assuming that the value of the extinction coefficient is comparable to what it is found for aluminosilicate glasses ( $\varepsilon_{3520 \text{ nm}} = 40 \text{ l}_{\text{glass}}/\text{mol}_{\text{OH}} \text{ cm}_{\text{glass}}$ ) [43] and andesitic glasses ( $\varepsilon_{3570 \text{ nm}} = 70 \pm 0.7 \text{ l}_{\text{glass}}/\text{mol}_{\text{OH}} \text{ cm}_{\text{glass}}$ ) [44, 45]. Taking a value of the extinction coefficient  $\varepsilon_{3570 \text{ nm}} \sim 70 \text{ l}_{\text{glass}}/\text{mol}_{\text{OH}} \text{ cm}_{\text{glass}}$  and  $\alpha \sim 1 \text{ cm}^{-1}$ , the resulting  $C_{\text{OH}}$  concentration is as low as  $6 \times 10^{-6} \text{ mol cm}^{-3}$ , which corresponds to an  $\text{OH}^-$  content of about  $3.6 \times 10^{18} \text{ cm}^{-3}$ .

Another well-established procedure to determine the hydroxyl content is the so-called “baseline absorbance method”, developed by Heigl *et al.* at Esso Laboratories in 1947 for the analysis of hydrocarbon mixtures [46]. The intensity of absorption of the individual peaks associated with the specific chemical species, which are chosen in order to minimize the interference between two or more compounds, is expressed as “base-line” optical density. This is calculated from the equation  $OD_{\text{Base}} = -\log \frac{I}{I_{\text{Base}}}$ , where  $OD_{\text{Base}}$  is the base line optical density,  $I$  is the absorption intensity measured as the distance from the zero line to the selected absorption peak, and  $I_{\text{Base}}$  is the distance from zero line to a straight line, the base line, joining two spectral points located on either side of the absorption peak. This equation is a modification of eq. (3.1.4), by the substitution of  $I_{\text{Base}}$ , the zero to base-line distance, for  $I_0$ , the incident light intensity. The base-line points are selected after the most favourable analytical peaks have been determined, and in the standard absorption spectra the base line is drawn parallel to the background. The method was applied first by Pope and Mackenzie to determine the hydroxyl content

of densified  $\text{Nd}^{3+}$ -activated silica glass prepared by the sol-gel route [47]. Taking into account the  $\text{OH}^-$  transmission at  $2.6 \mu\text{m}$  ( $T_a$ ) and  $2.7 \mu\text{m}$  ( $T_b$ ), respectively, the relation  $[\text{OH}](\text{ppm}) = (1000/d) \log(T_a/T_b)$  allowed the estimation of the  $\text{OH}^-$  content in a sample with a thickness  $d$  [46, 47].

Both the two methods described above are based on the proportionality between concentration and absorption peak; they can be applied to a wide variety of samples, and permit a satisfactory accuracy. A detailed discussion concerning the infrared spectroscopy study of water-related species in silica glasses can be found in [48, 49], and a phenomenological model for the  $\text{OH}^-$  absorption effect to the attenuation coefficient in telecommunication fibres is reported in [50].

**3.2. Luminescence measurements.** – In material systems activated by chromophores ions, the spectroscopic properties, such as emission quantum efficiency, lifetime of the excited electronic states, and dynamical processes such as non-radiative relaxation mechanism, upconversion and cooperative processes [51], may be well investigated by luminescence spectroscopy.

Rare-earth-doped glasses are used in a large number of optical devices because of the large number of absorption and emission bands available using the various rare-earth elements [52, 53]. As an example, the variation in the green intensity ratio between the  ${}^2H_{11/2}$  and  ${}^4S_{3/2}$  energy levels to the ground state of  $\text{Er}^{3+}$  ions has been used as the measure parameter in temperature sensors [54, 55].

Many papers reporting the enhancement of luminescence properties as a function of physical and chemical properties of rare-earth-activated glasses and crystals, or presenting some potential application as optical sensors, describe the luminescence spectroscopy as a suitable tool for quantitative characterization. In general, it is correct to state that the luminescence intensity of an indicator is dependent on the concentration of the respective chemical species or on the variation of the physical and chemical properties of the system [52, 56–58]. The disadvantage of intensity-based luminescence techniques, however, is that they suffer from variations in the intensity of the light sources, in the sensitivity of the detector, and in variation of the intensity of refractivity. A possibility of overcoming these problems is to use complementary results obtained by measuring the luminescence decay time of indicator chromophores and by the time-resolved fluorescence spectroscopy [23, 24, 59]. In the usual description of the photoluminescence process the intensity,  $I_{ij}$ , of an emission transition  $i \rightarrow j$  is proportional to the spontaneous emission probability,  $A_{ij}$ , of the transition and the population density of the excited state,  $N_i$ :  $I_{ij} \approx A_{ij}N_i$ . The normalization to the total concentration  $N_T$  of optically active ions, gives  $I_{ij}/N_T \approx A_{ij}n_i$ , where  $n_i = N_i/N_T$ . The relative population,  $n_i$ , can be determined from rate equations of the specific investigated system. This requires the consideration of the processes involved in the population and relaxation of the energy levels of the luminescent ions [23, 24]. In practical situations, the fluorescence experiments are performed under continuous or pulsed excitation. In the first case the system is considered in equilibrium, *i.e.*  $dn_i/dt = 0$ . By recording the fluorescence signal at a certain frequency, while varying the frequency of the exciting radiation, the so-called excitation spectrum is obtained. Such a spectrum can be correlated to the absorption spectrum of the system. The excitation spectrum is identical to the absorption spectrum if the ion decays rapidly from any higher excited state to the emitting state, which is known as Kasha's rule [60]. If the excitation spectrum shows deviation from the absorption spectrum, the measure is an indication of inhomogeneity of the spectral behaviour.

Measurements of the excitation spectrum are important in multisite systems, and can uncover the bands responsible for the energy storage and subsequent emission of the radiative energy. Important information has been obtained from excitation spectra in nanocomposite materials [58] and multicomponent glasses [61]. Under pulsed excitation, interesting information about the relaxation mechanisms can be obtained. In particular, the fluorescence decay time or lifetime of the emitting state can be determined. The intensity  $I(t)$  of luminescence, resulting from exciting light whose intensity  $K(t)$  varies with time  $t$  in an arbitrary way can be expressed by a Duhamel integral

$$(3.2.1) \quad I(t) = \int_0^\infty K(t-t')\phi(t')dt',$$

where  $\phi(t)$  is the decay function for pulsed excitation. This is generally valid under the condition that the number of excited molecules is small enough compared with the total number of molecules in the system and that the system does not undergo a permanent change such as photochemical reaction. For the particular case of a steady-state excitation turned off at  $t = 0$ ,  $K(t) = 1$  for  $t < 0$  and  $K(t) = 0$  for  $t > 0$  in eq. (3.2.1), and the intensity of luminescence at a later time  $t$  is given by:  $I(t) = \int_t^\infty \phi(t')dt'$ .

Two kinds of decay times can be considered. One is the mean duration of luminescence defined by  $\tau_m = \frac{\int_0^\infty t\phi(t)dt}{\int_0^\infty \phi(t)dt}$ . The other is the  $1/e$  decay time  $\tau_e$ , or the time interval after which the intensity of luminescence has decreased by a factor of  $e$  from its value at  $t = 0$ . Thus,  $\tau_e$  is defined as the root of the equation  $\phi(\tau_e) = \phi(0)/e$ . Of course, if the decay function is purely exponential,  $\phi(t) = \phi(0)\exp[-\frac{t}{\tau}]$  and  $\tau = \tau_m = \tau_e$ . Integration of eq. (3.2.1) with respect to  $t$  gives  $\int_{-\infty}^\infty I(t)dt = \int_0^\infty \phi(t)dt \int_{-\infty}^\infty K(t)dt$ . The physical meaning of this relation is that the total luminescence energy emitted in a sufficiently long time interval is proportional to the total energy of the exciting light in the same interval, and the proportional constant  $\int_0^\infty \phi(t)dt$  corresponds to the luminescence yield of the observed state.

The correct definition for the quantum yield  $\Phi$  of a luminescent system is the ratio of the spontaneous emitted photons per unit time  $N_{em}$  divided by the total number of absorbed photons  $N_{abs}$  per unit time,  $\Phi = N_{em}/N_{abs}$ . The absolute measurement of the quantum yield is very difficult because of the geometry of the emission and the presence of re-absorption. It is usually measured in comparison with samples with known quantum yields or by using an integrating sphere. From eq. (3.1.7) the number  $N_{abs}$  of absorbed photons of energy  $\eta\omega$  is given by  $N_{abs} = N_T \frac{P_{abs}}{\eta\omega} = N_T \sigma_{abs}(\omega) \frac{I}{\eta\omega}$ . By considering negligible the temperature dependence of the absorption cross-section [26,27]  $N_{em} = N_{abs} \frac{\tau_{meas}}{\tau_r}$ . Therefore, the quantum efficiency of a luminescent state characterized by a radiative lifetime  $\tau_r$  and an experimentally measured lifetime  $\tau_{meas}$  is given by  $\Phi = \tau_{meas}/\tau_r$ .

In general, the fluorescence decay function  $\phi(t)$  is not exponential, as discussed before, due to local environment inhomogeneities. In the most general case, when the relaxation refers to a number of locally active channels varying throughout the system, the stretched exponential or Kohlrausch model [62,63] is used:  $\phi(t) = \phi(0)[\exp[-\frac{t}{\tau}]]^\beta$ , where  $0 < \beta < 1$ . In the simplest case, where the distance between the fluorophore and the interaction sites is homogeneously distributed, the total decay function is calculated by the integration of the differential equation that describes the time evolution of the excited state and the

summing-up over all sites,

$$(3.2.2) \quad \phi(t) = \phi(0) \exp \left[ -\frac{(1+c)t}{\tau} - a \left( \frac{t}{\tau} \right)^{1/2} \right],$$

where  $a$  is the interaction parameter between chromophore and matrix, and  $c$  is the quenching parameter, which depends on the concentration of the chemical species to detect. If two different components of  $\phi(t)$  can be observed, then it is possible to write the relation  $\phi(t) = A\phi_A(t) + B\phi_B(t)$ , where  $A$  and  $B$  describe the relative amounts of the two chemical species or local environments present in the system. It has to be noted that the difference between the decay times corresponding to the forms  $A$  and  $B$  must be significant, a factor 100 being a good value of reference. The non-exponential decay function reported above has been used by Kitamura *et al.* [64] to describe the energy migration among organic molecules, which were dispersed in amorphous silica glass, and the energy trapping by the organic molecules aggregated in the glass. As mentioned before, in particular cases where the decay curves exhibit two well-separated components  $\phi(t)$ , with lifetimes  $\tau_1$  and  $\tau_2$ , it is possible to determine the amounts of the two kinds of ions involved in the process. This is of particular interest in  $\text{Er}^{3+}$ -activated glasses, in order to have an assessment of the fraction of ions in the  ${}^4I_{13/2}$  state that are available for optical amplification [65]. The fluorescence decay function  $\phi(t)$  is then described by a sum of two exponentials,  $\phi(t) = A_1 \exp[-\frac{t}{\tau_1}] + A_2 \exp[-\frac{t}{\tau_2}]$ . The number  $N_i$  ( $i = 1, 2$ ) of ions which will decay with the lifetime  $\tau_i$  is obtained by integration of the previous equation, so that  $N = N_1 + N_2 = A_1\tau_1 + A_2\tau_2$ . Using this approximation, Zampedri *et al.* have shown that in  $(100-x)\text{SiO}_2-(x)\text{TiO}_2-1\text{ErO}_{3/2}$  planar waveguides prepared by the sol-gel route, for  $x \leq 12$ , about 65% of the  $\text{Er}^{3+}$  ions in the  ${}^4I_{13/2}$  metastable state decay exponentially with a lifetime of about 8 ms [65].

**3.3. Raman and Brillouin scattering for optical-glasses characterization.** – Raman and Brillouin spectroscopies are powerful non-destructive tools for the structural characterization of materials, in particular of multicomponent glass systems. These techniques, however, are widely used for the study of inorganic, organic and hybrid materials, both in massive, fibre and planar waveguide format. In the case of optically guiding structures, the exciting laser light is usually coupled to the system by butt coupling or through a grating, or by prism coupling, as shown in fig. 4. The theoretical and experimental background of Raman spectroscopy has been illustrated in several articles and scientific books. A clear and exhaustive presentation, corroborated by a rich bibliography, was given by Demtröder [25]. A recent review, concerning Raman and Brillouin spectroscopy for study of sol-gel-derived glasses, was given by Montagna [66]. The Raman effect is an inelastic scattering event in which a photon of energy  $\eta\omega_i$  is destroyed and a scattered photon of energy  $\eta\omega_{s/as} = \eta\omega_i \pm E$  is created.  $E = |E_f - E_i|$  is the energy of the phonon created or destroyed in the processes necessary to move the system from the initial state  $E_i$  to the final state  $E_f$ . When the energy of the scattered photon is lower than the energy of the incident photon, we have a normal Stokes process; if the contrary occurs, we have an anti-Stokes process. The basic schema and the energy relations for Raman scattering are shown in fig. 6. The application of Raman spectroscopy as both qualitative and quantitative analytical detector is only limited by its inherent lack of sensitivity: approximately 1 in  $10^7$  photons is scattered at an optical frequency different from that of source excitation [67].

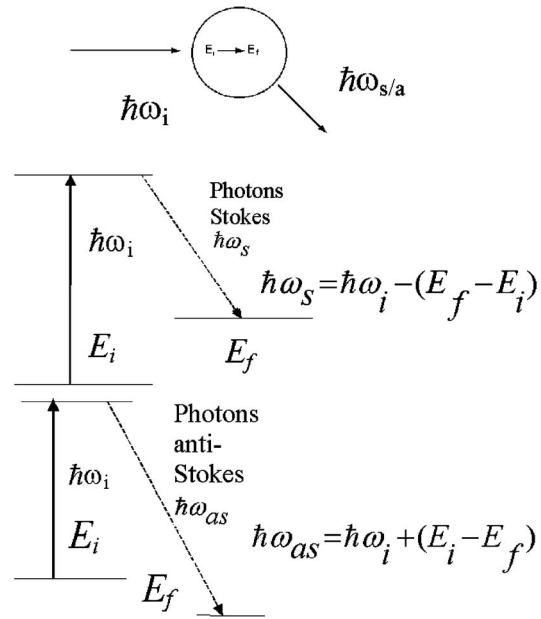


Fig. 6. – Basic schema and energy relations for Raman scattering.

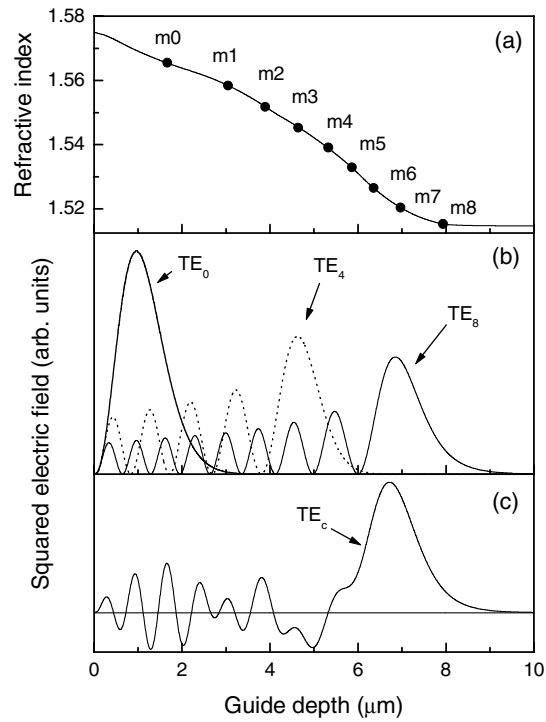


Fig. 7. – (a) Refractive index profile at 543.5 nm; (b) squared electric-field profiles for  $m = 0, 4, 8$ , respectively; (c) linear combination  $\text{TE}_c$  of the squared electric fields.

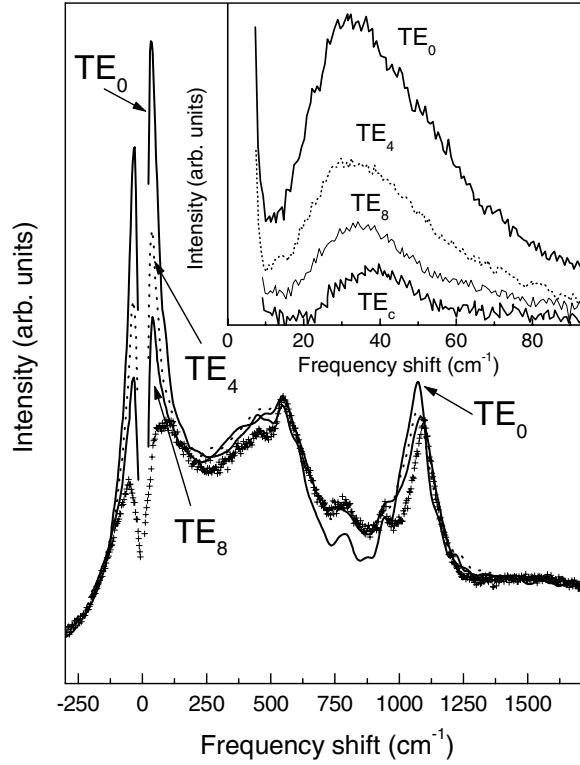


Fig. 8. – Raman spectra of the substrate (+) and of the  $m = 0$  (solid line), 4 (dot line), and 8 (solid line) TE modes. In the inset, the low-frequency part of the spectra.  $TE_c$  labels the spectrum obtained by the linear combination used to produce the squared electric profile of fig. 7(c).

The combination of dielectric waveguides and Raman spectroscopy, however, leads to a useful and sensitive method to analyse thin active layers present on top of the waveguides. In the case of a graded-index waveguide, it is also possible to perform Raman and luminescence depth-selective measurements [68]. Referring to this case, fig. 7 shows (a) the refractive index profile, together with (b) the profile of the squared electric field for some transverse electric (TE) modes, in a graded-index waveguide obtained by silver exchange on a soda-lime glass substrate. The  $TE_0$  mode is confined in a layer of about  $2\ \mu\text{m}$  thickness, but the depth reached by the light increases with the mode number  $m$ . The  $TE_m$  selectivity is evident in fig. 8, where the optical modes of the Raman spectrum show a dependence on composition, and in particular on the concentration of the diffused silver. In fact, the peak at about  $1000\ \text{cm}^{-1}$  shifts to lower frequencies and increases in intensity when  $m$  decreases, *i.e.* when the Ag content increases. Moreover, the low-frequency peak, which is better visible in the low-frequency region of the Raman spectrum shown in the inset of fig. 8, shifts towards higher frequencies as  $m$  increases. This observation is confirmed by the particular linear combination of the Raman spectra indicated by  $TE_c$ , which is drawn in fig. 7(c). It shows how the linear combination  $TE_c$  of the nine modes results in a squared electric field that is maximum in the region around  $7\ \mu\text{m}$ . The corresponding Raman spectrum (in the inset of fig. 8) shows that the

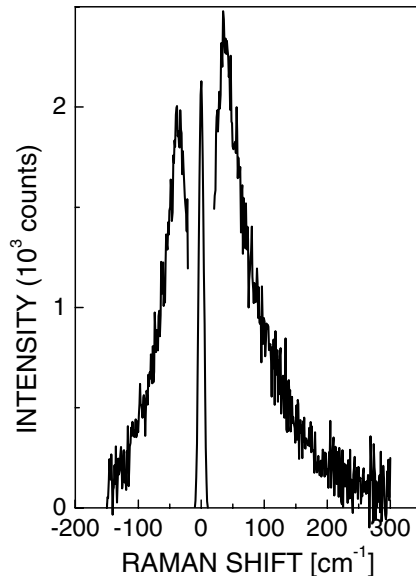


Fig. 9. – Room temperature VV spectrum of a silver exchanged silica waveguide, obtained by waveguide excitation of the  $TE_0$ , mode at  $\lambda = 514.5$  nm. Adapted from [30].

maximum of the peak is shifted towards higher frequencies. This indicates that in the selected region around  $7 \mu\text{m}$ , where the Ag concentration is quite low, small metal clusters are present. This has been confirmed by transmission electron microscopy measurements on similar samples: the mean-size dimension and the size dispersion decrease as the Ag concentration decreases. The only assumption made in this analysis was that the spectra measured for excitation in one of the TE modes were the sums of contributions from different depths, with weights given by the local value of the squared electric field. This should be a good assumption for the luminescence and also for Raman, which is a coherent scattering effect, but with a coherence length in the glass on the nanometer scale, namely, much shorter than the film thickness [68].

Waveguide Raman spectroscopy is also a powerful tool for determining the particle size in a nanocomposite system [30]. After the first works of E. Duval *et al.* on spinel nanocrystals in cordierite glasses [70], low-frequency Raman scattering from symmetric and quadrupolar acoustic vibrations of the spherical clusters has become a reliable method to determine the size of nanoparticles. In fact, the frequency of all acoustic modes scales as the inverse of the linear dimension of the particle, which can indeed be deduced from the peak energy in the Raman spectra. For spherical particles, the only Raman active modes are the symmetric and quadrupolar spheroidal modes [71, 72]. The two modes give polarized and depolarized Raman spectra, respectively. The surface mode, namely the lowest frequency mode in the sequence with a given angular symmetry, has much higher Raman activity than the inner modes.

The Raman spectrum of a free spherical particle is expected to involve the contribution of only one discrete vibration. For silver particles, for example, the quadrupolar surface vibration is expected to dominate the Raman spectrum, all other modes having intensity

of few percent [72]. For a free sphere, the frequency of this mode is given by

$$(3.3.1) \quad \omega_2 = \frac{2\pi Av_t}{d},$$

where  $v_t$  is the mean transverse sound velocity ( $\sim 1660$  m/s for Ag),  $d$  is the diameter of the particle,  $A$  is a constant of the order of unity ( $A = 0.85$  for Ag). This equation can be used to obtain the size distribution of the nanoparticles from the shape of the Raman peak. To do this, two important effects must be considered. First, a free sphere has a discrete set of vibrational modes, but when the sphere is embedded in an elastic medium, the discrete set broadens into a continuum (homogeneous broadening). Second, the Raman activity is strongly dependent on the size of the particles  $I(\omega, R) \approx R^3 \approx \omega^{-3}$ . In the presence of an important size distribution (inhomogeneous broadening), the maximum of the experimental peak does not correspond to the maximum of the distribution, but to particles with size bigger than the mean size. Both these effects produce a shift of the peak towards lower frequencies. This gives rise to an overestimation of the particle size if equation  $\omega_2 = 2\pi Av_t/d$  is applied taking exactly the value of  $\omega_2$  corresponding to the peak. The correct mean size and the size distribution are obtained by deconvoluting the homogeneous line shape and by considering the frequency (size) dependence of the Raman coupling coefficient. Figure 9 shows the excited spectrum of an Ag-containing film waveguide obtained by  $\text{Ag}^+$ - $\text{Na}^+$  ion-exchange in soda-lime glass [69]. The spectrum was taken in VV polarization by exciting the  $\text{TE}_0$  mode of the guide with about 10 mW of the 514.5 nm line of the  $\text{Ar}^+$  laser. By using eq. (3.3.1) with  $\omega_2 = 36 \text{ cm}^{-1}$  (the value of the peak energy), one would obtain  $d = 1.3$  nm. By considering the low-frequency shift of the peak, produced by the homogeneous and inhomogeneous broadening, a mean size of about 1 nm is estimated, with an upper limit of the broad size distribution of about 1.5 nm, in good agreement with the TEM data.

The low-frequency Raman scattering technique was successfully employed in a number of material cases, such as the study of nucleation of  $\text{Ga}_2\text{O}_3$  nanocrystals in the  $\text{K}_2\text{O}$ - $\text{Ga}_2\text{O}_3$ - $\text{SiO}_2$  glass system [73], oxy-fluoride ultra-transparent glass ceramics [74], silicantania waveguides [75], and silicon quantum dots in glass matrix [76].

Raman spectroscopy is also very useful in structural characterization of glassy systems, because it allows one to get detailed information about the network intermingling and densification degree. As an example, Raman spectra of xerogels show the presence of  $\text{OH}^-$  groups, which strongly influence the matrix stability and are detrimental for the quantum yield of rare-earth-activated glasses; several studies and detailed discussions can be found in refs. [66, 77]. Let us discuss here the analysis of the densification process of an  $\text{Er}_2\text{O}_3$ - $\text{SiO}_2$  monolithic xerogel [78]. Curves (a) to (g) in fig. 10 show the VV polarized Raman spectra of the silica xerogels containing 0, 1000, 2000, 5000, 10000, 20000 and 40000 Er/Si ppm, respectively. In order to achieve densification, all the samples were annealed with a thermal treatment in air at 950 °C for 120 hours with a heating rate of 0.1 °C/min. Raman spectra allowed us to put in evidence that not all the xerogels exhibited the same degree of densification. Three spectral regions are shown in fig. 10: (I) anti-Stokes and Stokes low-frequency region, (II) the region between 250 and 1500  $\text{cm}^{-1}$  and (III) the region between 3500 and 3800  $\text{cm}^{-1}$ . Figure 10(I) clearly shows the so-called Boson peak, which is a characteristic of the glassy state and is a strong indication of complete densification of the sample. In the sample containing 2000 Er/Si ppm (curve (c) in fig. 10(I)), for instance, the Boson peak is not present. The Raman spectra of fig. 10(II) show bands at 430, 800, 1100 and 1190  $\text{cm}^{-1}$ , assigned to the silica network. The band

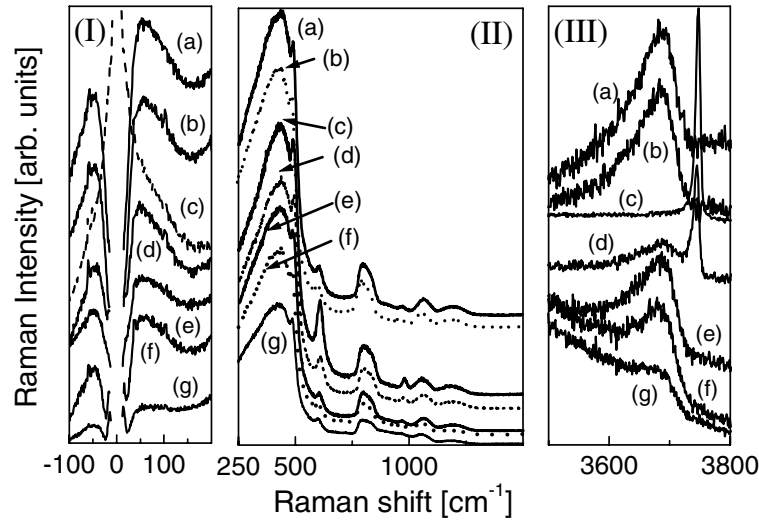


Fig. 10. – Room temperature Raman spectra of the 0 (a), 1000 (b), 2000 (c), 5000 (d), 10000 (e), 20000 (f) and 40000 (g) Er/Si ppm doped  $\text{Er}_2\text{O}_3\text{-SiO}_2$  xerogel annealed at  $950^\circ\text{C}$  for 120 h. (I) and (III) excitation at 488 nm; (II) excitation at 458 nm [78].

at  $960\text{ cm}^{-1}$  is due to the Si-OH vibration. The defects bands D1 and D2, located at  $490$  and  $610\text{ cm}^{-1}$ , respectively, are more intense for the samples doped with 2000 and 5000 Er/Si ppm than for the others samples. Finally, the Raman spectra in fig. 10(III) show two bands centred at about  $3670$  and  $3750\text{ cm}^{-1}$ : the latter one is present only for the 2000 and 5000 Er/Si ppm doped samples. This band is assigned to the O-H stretching vibration of free silanol groups on the surface of a porous structure [79]. It is much sharper than the bands of physical and chemical water, because the SiOH groups at the pore surface are only weakly perturbed by site-sensitive interactions. The broad band centred at  $3670\text{ cm}^{-1}$  is the fingerprint of OH groups in the densified silica structure [80]. In conclusion, the Raman spectra undoubtedly indicate that complete densification is achieved after annealing at  $950^\circ\text{C}$  in all samples, except in those activated by 2000 and 5000 Er/Si ppm.

As to another important diagnostic tool, namely Brillouin scattering in solids, an exhaustive discussion is reported in ref. [81]. The Brillouin scattering results from the interaction between incident light beam and thermally generated acoustic waves, and can be successfully employed in determining the elastic and photo-elastic constants of glasses.

In this application area, Shen *et al.* recently showed that rare-earth modifier ions play a very important role in the structure of glasses, due to their higher coordination number and large atomic size [82]. Looking at Brillouin scattering spectra of  $\text{Eu}^{3+}$ - and  $\text{Pr}^{3+}$ -doped soda alumina silicate glasses, their photo-elastic constants were determined by comparing the relative Brillouin scattering intensity and frequencies of these glasses with those of fused quartz. The results indicated that the glass structure becomes more rigid, and the bonding structure becomes more ionic, when the rare-earth concentration is increased. The authors showed that the elastic constants, Young's modulus and bulk modulus of  $\text{Eu}^{3+}$ -activated glasses were higher than those of  $\text{Pr}^{3+}$ -activated glasses.

In order to perform and analyse Brillouin scattering experiments in planar waveguide

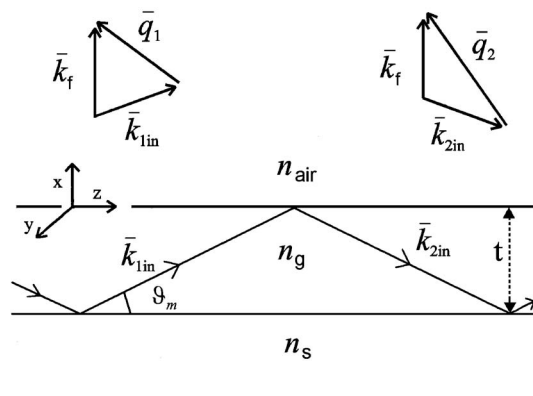


Fig. 11. – Wave propagation in the planar waveguide:  $\bar{q}_1$  and  $\bar{q}_2$  are the exchanged wave vectors of the scattered light in the zigzag paths. In TE modes, the electric field is along the  $y$ -direction, the light propagates along the  $z$ -direction, and  $x$  is perpendicular to the plane of the waveguide in the direction of the scattered wave.  $n_s$  and  $n_g$  stand for the refractive indices of the substrate and waveguide, respectively [66].

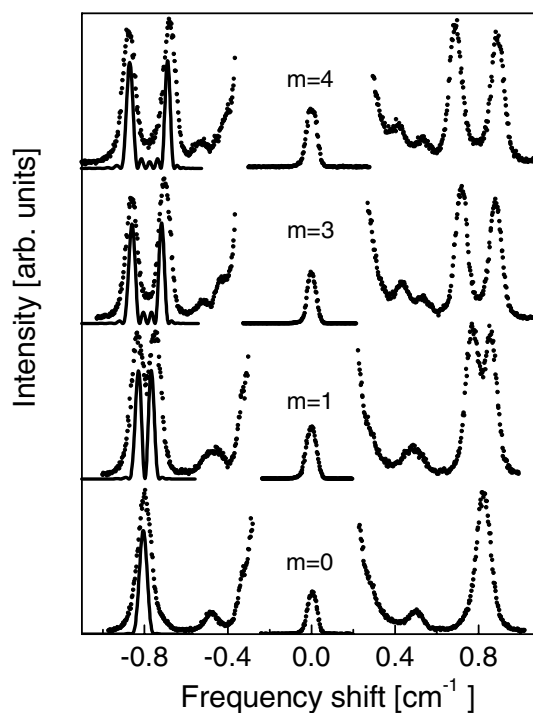


Fig. 12. – Brillouin spectra (dotted line) of a silica-titania thick planar waveguide obtained by excitation in different  $TE_m$  modes and detection perpendicular to the plane of the guide. The continuous curves (solid line) in the anti-Stokes part are the spectra calculated by using a numerical model, which considers the spatial distribution of the modal exciting field [83].

configuration, an *ad hoc* model has to be adopted [66, 83-85]. The wave propagation in a guiding film is shown in fig. 11; Brillouin scattering from acoustic vibration depends on the exchanged  $q$  vector of the scattered photon, and is a coherent process, which involves the whole illuminated region. In a homogeneous waveguide the light propagates along a zigzag path so that at a fixed angle of detection two values of  $q$  are sampled. Since the two  $q$  values change with the mode index, Brillouin spectra present doublets at different frequencies for different excitation modes. Under these conditions the Brillouin scattering intensity  $I_{BS}$  is given by

$$(3.3.2) \quad I(\vec{q}_1, \vec{q}_2, \omega) \propto \frac{T}{\omega^2} \left| \int q_1 e^{i(\vec{k}_p - \vec{q}_1)\vec{r}} + e^{i\gamma} q_2 e^{i(\vec{k}_p - \vec{q}_2)\vec{r}} d\vec{r} \right|^2,$$

where  $T$  is the temperature,  $\omega = v_{L,T} k_p$ ,  $v_{L,T}$  is the longitudinal, transverse sound velocity,  $\vec{k}_p$  the wave vector of the phonons which scatter the light, and  $\gamma$  is the relative phase of the zigzag fields in the  $m$  mode of the guide. The linear dependence of  $I_{BS}$  on  $T$  is always present in  $I_{BS}$  equation. The Brillouin spectrum of a glass waveguide, however, shows four peaks in the Stokes and four in the anti-Stokes spectrum, two peaks being due to longitudinal phonons and the other two to transverse phonons. The energy separation between the couple of peaks increases with the mode index.

This model neglects the contribution to the scattering coming from the evanescent field in the substrate, and considers the waveguide as a homogeneous film with constant refractive index. A single fit parameter, *i.e.* the longitudinal sound velocity, is used to calculate the  $m+1$  spectra obtained by exciting the different modes of the waveguide. As an example, fig. 12 shows the Brillouin spectrum of a silica-titania waveguide obtained by exciting different TE modes with an argon laser at 514.5 nm and collecting the diffused light in a direction nearly perpendicular to the waveguide plane. Two longitudinal and two transverse peaks are observed, whose splitting increases with the mode index  $m$  (except for the  $m=0$  excitation, where no splitting is observed). The spectra calculated by using a numerical model, which considers the spatial distribution of the exciting field in the mode, are reported on the anti-Stokes spectrum of the longitudinal phonons. Using this approach, the longitudinal sound velocity in planar waveguides was determined with high accuracy, and it was demonstrated that waveguide Brillouin spectroscopy, coupled with waveguide Raman spectroscopy, is a powerful tool for structural characterization of guiding structures [83, 85].

#### 4. – Absorption and emission cross-section measurement

A widely used method for relating the absorption and emission spectra of rare-earth-activated glasses and crystals, and in particular for  $\text{Er}^{3+}$  ions, is the McCumber theory [86], with the procedure developed by Miniscalco and Quimby [87]. An attractive aspect of McCumber's theory is that its validity is based on general assumptions. One of these, which is accepted by the scientific community, is that there is a thermal distribution of population among the individual Stark level components of each Stark manifold. Another assumption is that the energy width of each individual Stark level is small compared with  $k_B T$ , where  $k_B$  is the Boltzmann constant and  $T$  is the absolute temperature. Detailed discussion about the validity of the McCumber model is reported in [88-90]. Anyway, the McCumber model has been successfully applied to the modelling of the performance of traditional and innovative bulk glasses as well as of a wide variety of fibre- and waveguide-based lasers and amplifiers.

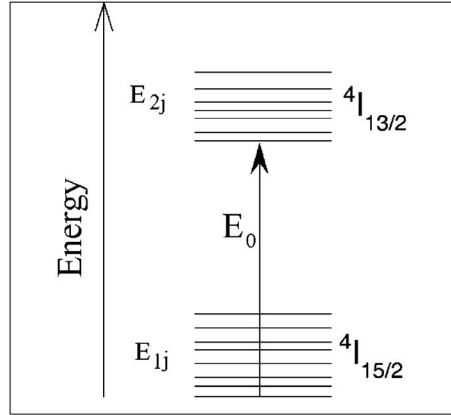


Fig. 13. – Diagram of the Stark manifold of the two lowest-energy levels of  $\text{Er}^{3+}$  ion.

In this section the basics of the model will be presented, and the  $\text{Er}^{3+}$ -activated glasses will be used as examples of absorption and emission cross-section measurements [42,91]. Figure 13 shows a representative energy level diagram for the two Stark manifolds in an  $\text{Er}^{3+}$ -activated glass. The ground state  ${}^4I_{15/2}$  is a manifold of eight sublevels of energy  $E_{1j}$ , and the  ${}^4I_{13/2}$  excited state is a manifold of seven sublevels of energy  $E_{2j}$ . The McCumber relation states that the absorption cross-section  $\sigma_a(\nu)$  and the emission cross-section  $\sigma_e(\nu)$  between these manifolds are related by

$$(4.1) \quad \sigma_e(\nu) = \sigma_a(\nu) \exp[(\varepsilon - h\nu)/k_B T],$$

where  $\nu$  is the frequency of the photon of energy  $h\nu$  involved in the process, and  $\varepsilon$  is the temperature-dependent excitation energy. The physical interpretation of  $\varepsilon$  is as the

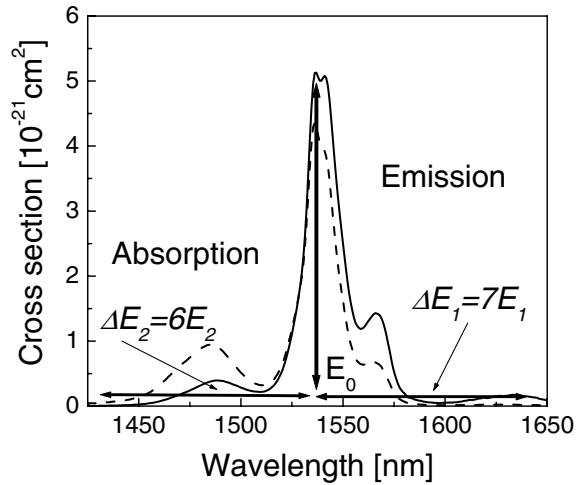


Fig. 14. – Absorption and emission cross-section spectra of  $\text{Er}^{3+}$  ion at  $1.5 \mu\text{m}$  of a silicate glass, which illustrate the McCumber-Miniscalco-Quimby procedure. Adapted from [42].

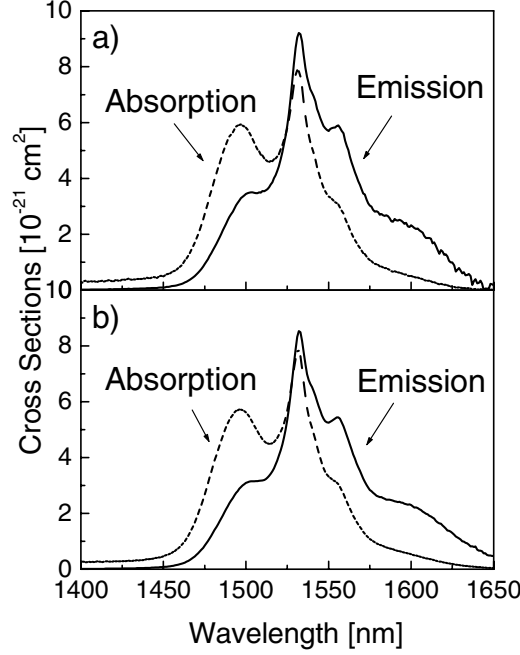


Fig. 15. – Absorption and emission cross-sections of  $\text{Er}^{3+}$  ion at  $1.5 \mu\text{m}$  in the tellurite glasses of molar composition (a)  $75 \text{ TeO}_2$ :  $12 \text{ ZnO}$ :  $10 \text{ Na}_2\text{O}$ :  $2 \text{ PbO}$ :  $1 \text{ Er}_2\text{O}_3$  and (b)  $75 \text{ TeO}_2$ :  $12 \text{ ZnO}$ :  $10 \text{ Na}_2\text{O}$ :  $2 \text{ GeO}_2$ :  $1 \text{ Er}_2\text{O}_3$  [91].

net free energy required to excite one  $\text{Er}^{3+}$  ion from the  ${}^4I_{15/2}$  to the  ${}^4I_{13/2}$  state at temperature  $T$ :

$$(4.2) \quad \exp \left[ \frac{\varepsilon}{k_B T} \right] = \frac{\sum_{j=1}^8 \exp \left[ -\frac{E_{1j}}{k_B T} \right]}{\sum_{j=1}^7 \exp \left[ -\frac{E_{2j}}{k_B T} \right]} \exp \left[ \frac{E_0}{k_B T} \right] = C \exp \left[ \frac{E_0}{k_B T} \right],$$

where  $E_0 = E_{21} - E_{11}$  is the difference in energy between the lowest energy levels of the two Stark manifolds as shown in fig. 13. Since the manifold widths exceed  $k_B T$ , the absorption and emission spectra are offset from each other, the absorption to higher frequency and the emission to lower frequency, as shown in fig. 14. Equation (4.1) states that absorption and emission cross-sections are equal only at the crossing frequency  $\nu_c = \varepsilon/h$  when  $C = 1$  and  $\varepsilon = E_0$  (see eq. (4.2)).

Another parameter often used in the literature is the ratio  $R$  of peak emission to peak absorption cross-sections. The relation between  $R$  and  $C$  strongly depends on the spectral shape and it is not simple. In fact, as it may be observed in fig. 14, in general  $C$  and  $R$  differ, so that crossing is not perfect. Figure 14 and eq. (4.1) indicate that at frequencies higher than  $\nu_c$ , the emission cross-section is smaller than the absorption cross-section, and vice versa for  $\nu < \nu_c$ .

The inherent difficulty of the strict application of the McCumber method is that the

sublevel energies of  $\text{Er}^{3+}$  are difficult to be accurately known and, in principle, they must be measured for every host [92,93]. The procedure developed by several authors [87-90] does not require the knowledge of these energies. The McCumber-Miniscalco-Quimby model first assumes a simplified electronic structure in which the Stark levels for a given manifold are equally spaced:  $E_{1j} = (j-1)E_1$  and  $E_{2j} = (j-1)E_2$  for the  ${}^4I_{15/2}$  and for the  ${}^4I_{13/2}$  manifolds, respectively. This reduces the number of parameters in eq. (4.2) from 14 to 3: i) the energy  $E_1$  separating the Stark components of the ground state; ii) the energy  $E_2$  separating the Stark components of the first excited state; iii) the energy  $E_0$  which determines the separation between the two states. In this framework, the energy  $E_0$  is chosen as the average of the absorption and emission peaks (see fig. 14). The second approximation consists in putting the energy spread of the  ${}^4I_{15/2}$  state,  $\Delta({}^4I_{15/2}) = 7E_1$ , at the 95% low-energy half-width of the room temperature emission spectrum, since the peak has already been identified with the transition between the lowest component of the two manifolds. This procedure provides an approximate value of  $E_1$ . In a similar way, the 95% high-energy half-width of the absorption spectrum is adopted for the width of the excited state manifold,  $\Delta({}^4I_{13/2}) = 6E_2$ , thus providing an approximate value for  $E_2$ . Figure 14 well describes the approximation introduced by the McCumber-Miniscalco-Quimby model. By using these values of  $E_1$  and  $E_2$  in eq. (4.2), one can get an approximate expression for the constant  $C$ :

$$(4.3) \quad C = \frac{\sum_{j=1}^8 \exp \left[ -(j-1) \frac{E_1}{k_B T} \right]}{\sum_{j=1}^7 \exp \left[ -(j-1) \frac{E_2}{k_B T} \right]}.$$

Figure 15 shows the calculated absorption and emission cross-sections for two tellurite glasses [91]: the resulting values are very similar to those calculated for other tellurite systems. Their very high values are due to the high values of the refractive index, since the stimulated emission cross-section of rare-earth ions increases with the refractive index as  $(n^2+2)^2/n$  for electric-dipole transitions, and as  $n$  for magnetic-dipole transitions [94].

The effective bandwidth  $\Delta\lambda$ , related to the emission cross-section, is defined by  $\Delta\lambda = \int \sigma_e(\lambda) d\lambda / \sigma_P(\lambda)$ , where  $\sigma_P(\lambda)$  is the peak value of the emission cross-section [94, 95]. This value, together with those of absorption and emission cross-sections, is especially important for the amplifiers in the wavelength-division-multiplexing (WDM) network systems [4,5]. Table II lists the cross-sections and the bandwidth concerning the  ${}^4I_{13/2} \leftrightarrow {}^4I_{15/2}$  transition of  $\text{Er}^{3+}$  ion in some glass hosts. It is evident from table II that the parameters  $\Delta\lambda$ ,  $\sigma_a$ , and  $\sigma_e$  strongly depend on the glass composition, which play a crucial role on the whole spectroscopic properties through the modification of the local environment of the rare-earth ions [96].

Finally, the internal gain coefficient  $g$  at wavelength  $\lambda$  can be estimated by means of the formula  $g(\lambda) = \sigma_e(\lambda)N_2 - \sigma_a(\lambda)N_1$ , where  $\sigma_a(\lambda)$  and  $\sigma_e(\lambda)$  are the absorption and stimulated emission cross-sections at wavelength  $\lambda$ , and  $N_1$  and  $N_2$  are the density of ions in the ground and excited state, respectively ( $N_1+N_2 = N$ ,  $N$  being the density of erbium ions) [4]. Referring to the values reported in fig. 15, in the case of total inversion ( $N_2 = N$ ) at 1532 nm, Rolli *et al.* obtain a gain coefficient of 4.06 and 3.78  $\text{cm}^{-1}$ , respectively, for two tellurite samples activated by different  $\text{Er}^{3+}$  content, namely  $N = 4.405 \times 10^{20} \text{ cm}^{-3}$  and  $N = 4.426 \times 10^{20} \text{ cm}^{-3}$  [91]. Benoit *et al.* in silicate glasses estimated to obtain

TABLE II. – *Effective bandwidth ( $\Delta\lambda$ ), absorption ( $\sigma_a$ ) and emission ( $\sigma_e$ ) cross-sections for the  ${}^4I_{13/2} \leftrightarrow {}^4I_{15/2}$  transition of  $\text{Er}^{3+}$  at the indicated wavelength for some glass hosts.*

| Host matrix                                       | $\lambda$<br>(nm) | $\sigma_a$<br>( $10^{-21} \text{ cm}^2$ ) | $\sigma_e$<br>( $10^{-21} \text{ cm}^2$ ) | $\Delta\lambda$<br>(nm) | Ref. |
|---|-------------------|---|---|-------------------------|------|
| Al-P silica                                       | 1531              | 6.6                                       | 5.7                                       | 43                      | [87] |
| Silicate L22                                      | 1536              | 5.8                                       | 7.3                                       | 20                      | [87] |
| Silicate (Baccarat)                               | 1537              | 4.3                                       | 5.1                                       | 18                      | [42] |
| Fluorophosphate<br>L11                            | 1533              | 7   | 7   | 27–43                   | [87] |
| Fluorophosphate<br>L14                            | 1531              | 5   | 5   | 63                      | [87] |
| $\text{GeO}_2\text{-SiO}_2$                       | 1530              | 7.9                                       | 6.7                                       | 25                      | [69] |
| $\text{Al}_2\text{O}_3\text{-SiO}_2$              | 1530              | 5.1                                       | 4.4                                       | 55                      | [69] |
| $\text{GeO}_2\text{-Al}_2\text{O}_3\text{-SiO}_2$ | 1530              | 4.7                                       | 4.4                                       |                         | [69] |
| Tellurite   | 1532              | 7.9                                       | 8.2                                       | 66                      | [91] |

an internal gain coefficient of about 2.0 dB at 1537 nm. Figure 16 shows the internal gain curves *vs.* the wavelength for a silicate glass, at different values of the fractional upper-state population  $N_2/N$  [42]. The change in the upper-state population strongly modifies the internal gain coefficient of the glass in the full 1460–1580 nm spectral range. Indeed, for low values of the population inversion, the glass is like an absorber of the light for the shorter wavelengths, while it amplifies the longer wavelengths.

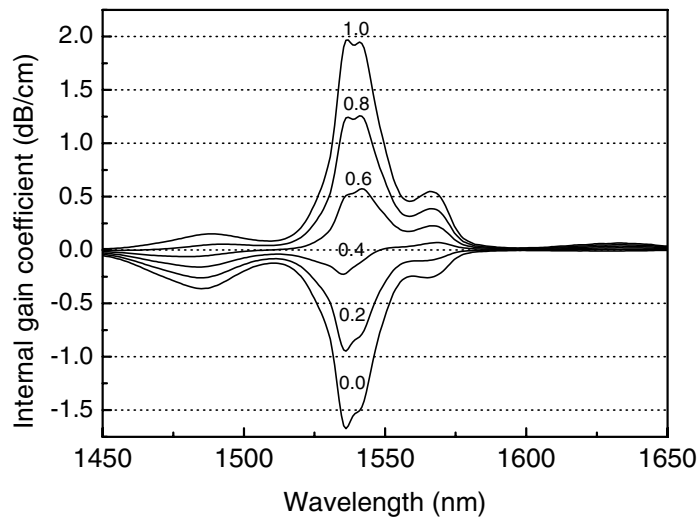


Fig. 16. – Calculated internal gain coefficient *vs.* wavelength in a silicate glass for different values of the fractional upper-state population  $N_2/N$  indicated on the graph for each curve [42].

## 5. – Quantum efficiency evaluation

As mentioned in the previous section, the measured lifetime ( $\tau_{\text{meas}}$ ) must be compared with the radiative lifetime,  $\tau_{\text{rad}}$ , to obtain the quantum efficiency  $\eta$  defined by their ratio:  $\eta = \tau_{\text{meas}}/\tau_{\text{rad}}$ . The value of  $\tau_{\text{rad}}$  can be calculated via different theoretical approaches and numerical analysis. First, if the emission cross-section is known, on the basis of McCumber-Miniscalco-Quimby model the radiative lifetime can be calculated from the following equation:  $1/\tau_{\text{rad}} = \frac{8\pi n^2}{c^2} \int \nu^2 \sigma_{\text{em}}(\nu) d\nu$ . The second approach consists in a model based on Einstein's relation for the emission probability of a two-levels system for which  $g_1$  and  $g_2$  are the degeneracy of the lower state 1 and the upper state 2, respectively [97]. For such a degenerate system one condition has to be satisfied: either the sublevels making up each level are all equally populated, or the transition strengths between the sublevels are all equal. Taking into account only the decay pathway via the spontaneous emission for the  $2 \rightarrow 1$  transition, and denoting  $A_{21}$  as the corresponding transition rate (Einstein  $A$  coefficient), the radiative lifetime of the upper state 2 is given by

$$(5.1) \quad \frac{1}{\tau_{21}} = A_{21} = \frac{8\pi}{\lambda^2} \frac{g_1}{g_2} \int \sigma_{12}(\nu) d\nu,$$

where  $\lambda = \lambda_0/n$  is the wavelength of the transition in the medium ( $\lambda_0$  is the wavelength in vacuum, and  $n$  the refractive index), and  $\sigma_{12}(\nu)$  is the absorption cross-section at the frequency  $\nu$  [21, 91].

The two above-mentioned methods are of particular interest for the estimation of  ${}^4I_{13/2}$  radiative quantum yield. A more general approach in determining the radiative lifetime is based on the so-called Judd-Ofelt theory, which yields an assessment of the oscillator strength characterizing the intensity of a transition between two  ${}^{2S+1}L_J$  multiplets within the  $4f^n$  configuration of a rare-earth ion [13, 14]. In the framework of the Judd-Ofelt theory, the theoretical oscillator strengths  $P_{\text{cal}}^{\text{ed}}$  are expressed as a sum of transition matrix elements, involving intensity parameters  $\Omega_q$ , with  $q = 2, 4, 6$ , which depend on the host matrix:

$$(5.2) \quad P_{\text{cal}}^{\text{ed}}(J, J') = \frac{8\pi^2 mc}{3h\lambda(2J+1)} \frac{(n^2+2)^2}{9n} \sum_{q=2,4,6} \Omega_q \left\langle aSL, J \left\| U^{(q)} \right\| a'S'L', J' \right\rangle^2,$$

where  $\lambda$  is the mean wavelength of the transition and  $n$  is the refractive index. Because the transition matrix elements  $\langle \|U^{(q)}\| \rangle$  are essentially the same from host to host, the values calculated by Morrison are widely employed [98, 99]. Using the set of free-ion parameters obtained by Carnall in aqueous solution [100], Morrison computed the reduced matrix elements between all of the intermediate-coupled wave functions representing the multiplets of the electronic configuration  $4f^n$  of the free ion. The intensity parameters, called Judd-Ofelt parameters, are then obtained by the chi-square method [101]. This method minimises the relative differences between the theoretical oscillator strength and the experimental one,  $P_{\text{exp}}^{\text{ed}}$ , measured in the absorption spectrum:

$$(5.3) \quad P_{\text{exp}}^{\text{ed}} + P_{\text{cal}}^{\text{md}} = \frac{mc^2}{\pi e^2} \frac{2303}{N_A} \int_{\text{band}} \varepsilon(\nu) d\nu,$$

TABLE III. – Intensity parameters  $\Omega_q$  (in units of  $10^{-20} \text{ cm}^2$ ) in the 77.29 SiO<sub>2</sub>: 11.86 K<sub>2</sub>O: 10.37 PbO: 0.48 Sb<sub>2</sub>O<sub>3</sub> glass activated by 0.2 mol% Er<sup>3+</sup> and 0.5 mol% Er<sup>3+</sup>. The calculated radiative lifetime and the estimated quantum efficiency of the Er<sup>3+</sup> <sup>4</sup>I<sub>13/2</sub> metastable level, obtained using the three different methods described in sect. 5, are also reported [42].

| Er <sup>3+</sup><br>content<br>(mol%) | $\Omega_2$ | $\Omega_4$ | $\Omega_6$ | r.m.s.                | $\tau_{\text{rad}}$ (ms) |          |          |
|---------------------------------------|------------|------------|------------|-----------------------|--------------------------|----------|----------|
|                                       |            |            |            |                       | Quantum efficiency       |          |          |
|                                       |            |            |            |                       | Judd-Ofelt               | Einstein | McCumber |
| 0.2                                   | 3.36       | 0.75       | 0.17       | $1.38 \times 10^{-7}$ | 17.8 ms                  | 18.9 ms  | 20.1 ms  |
|                                       |            |            |            |                       | 79.8%                    | 75.1%    | 70.6%    |
| 0.5                                   | 3.19       | 0.56       | 0.16       | $6.5 \times 10^{-8}$  | 18.4 ms                  | 17.9 ms  | 19.3 ms  |
|                                       |            |            |            |                       | 62.5%                    | 64.2%    | 59.6%    |

where  $\varepsilon(\nu)$  is the molar absorptivity,  $\nu$  is the wave number and  $N_A$  is Avogadro's number. Each value of the oscillator strength is weighed by its own uncertainty. These uncertainties have been evaluated by considering the reliability of the absorption bands integration including the baseline subtraction. As an indicative example, table III reports the obtained Judd-Ofelt (J-O) parameters in the case of a silicate glass [42], together with the root mean square (r.m.s.) deviations of the oscillator strengths, calculated as

$$(5.4) \quad \text{r.m.s.} = \left[ \frac{1}{N-3} \sum_{i=1}^N \left( P_{\text{exp}}^{\text{ed}}(i) - P_{\text{cal}}^{\text{ed}}(i) \right)^2 \right]^{1/2},$$

where  $N$  is the number of fitted bands. After obtaining the J-O parameters, the total spontaneous emission probabilities and the radiative lifetimes  $\tau_r$  of the most important excited states of the rare-earth ions can be estimated. The electric-dipole contributions have been computed as follows [102]:

$$(5.5) \quad A_{\text{ed}}(\Psi J; \Psi' J') = \frac{64\pi^4 e^2}{3h\lambda^3(2J+1)} \chi_{\text{ed}} \sum_{q=2,4,6} \Omega_q \left\langle aSL, J \left\| U^{(q)} \right\| a'S'L', J' \right\rangle^2,$$

where  $\Omega_q$  is the set of J-O parameters determined from the chi-square minimisation,  $\lambda$  is the mean wavelength of the transition,  $\chi_{\text{ed}} = \frac{n(n^2+2)^2}{9}$  is the local field correction, and  $\langle \|U^{(q)}\| \rangle$  are the reduced matrix elements tabulated by Morrison [98,99]. The magnetic-dipole contributions only depend on the magnetic-dipole operator and are given by

$$(5.6) \quad A_{\text{md}}(\Psi J; \Psi' J') = \frac{4\pi^2 e^2 h}{3\lambda^3 m^2 c^2 (2J+1)} \chi_{\text{md}} \left\langle aSL, J \left\| (L+2S)^{(1)} \right\| a'S'L', J' \right\rangle^2,$$

where  $\chi_{\text{md}} = n^3$  is the local field correction and  $\langle \|(L+2S)^{(1)}\| \rangle$  are the magnetic dipole matrix elements also tabulated by Morrison in the intermediate-coupled wave functions set. The radiative lifetime of an excited state  $i$  is then governed by  $\tau_{\text{rad}}(i) = (\sum_j A(i, j))^{-1}$ , where  $A(i, j) = A_{\text{ed}}(i, j) + A_{\text{md}}(i, j)$  and the summation is over all the terminal states  $j$ . Finally, the emission branching ratios are given by  $\beta_{ij} = A(i, j)\tau_{\text{rad}}(i)$ .

When two emitting states are separated by a small energy gap, the thermalization phenomenon must be taken into account. For instance,  ${}^2H_{11/2}$ ,  ${}^4S_{3/2}$  and  ${}^4F_{5/2}$ ,  ${}^4F_{3/2}$  pairs of emitting levels of the  $\text{Er}^{3+}$  ion are in thermal equilibrium and are commonly treated by considering the Boltzmann distribution.

All these methods allowing one to estimate the radiative lifetime lead to an indirect measure of the quantum efficiency. In a recent paper, the  $\text{Er}^{3+} {}^4I_{13/2}$  radiative lifetime was calculated applying the three methods described above for a same silicate sample; the resulting values were in good agreement between them, despite the different procedures employed from one method to the other, but the McCumber method provided the longest lifetimes and therefore the lowest quantum efficiencies [42]. It is obvious that the different results are related to the approximation used in each method. Both in Einstein relationships between absorption and emissions processes and in Judd-Ofelt model the approximation holds that all Stark levels of the ground  $J$  state are equally populated. It is the so-called “natural excitation” of Condon and Shortley [103]. Both in Judd-Ofelt and two-levels models the generally used value for the degeneracy factor  $g_2/g_1$  is  $(2J_2 + 1)/(2J_1 + 1)$ . This issue has been exhaustively discussed by Auzel in a recent paper [104], where it is underlined that the results for quantum efficiency calculations of the  ${}^4I_{13/2}$  to  ${}^4I_{15/2}$  transition of several  $\text{Er}^{3+}$ -doped glasses show errors up to 50% for a maximum Stark splitting of about  $260 \text{ cm}^{-1}$  at 300 K, when the value of the degeneracy factor  $g_2/g_1 = (2J_2 + 1)/(2J_1 + 1) = 14/16 = 0.87$  is used. It turns out that the Einstein and Judd-Ofelt approach overestimate the quantum efficiency. The correction proposed by Auzel started from the assumption that the  ${}^4I_{13/2}$  to  ${}^4I_{15/2}$  transition of  $\text{Er}^{3+}$  could be experimentally described by four transitions between two unresolved levels separated by their maximum Stark splittings: 180 and  $260 \text{ cm}^{-1}$ . Taking into account their respective Boltzmann population distribution at 300 K and the experimental intensities for the four groups of their relative matrix elements, the effective degeneracy factor  $g_2/g_1$  was determined to be  $\cong 1.36$  instead of 0.87, for  $\Delta E/k_B T \cong 1.25$ . Very recently, such source of error has been considered for the Yb case as well, where quantum efficiencies much larger than one had been obtained. Instead of  $g_2/g_1 = 6/8 = 0.75$ , it was found that, at 300 K, the effective degeneracy factor was 1.18 [105]. This corresponds to an error of about 40% when the “natural excitation” approximation was used [104].

Finally, we mention an interesting method for the direct measurement of the quantum yield described by Auzel *et al.* [106]. They used a photoacoustic cell, with a piezoelectric transducer in mechanical contact with the  $\text{Er}^{3+}$ -activated glass. The 980 nm line of a continuous wave Ti:Sapphire laser, resonant with the  ${}^4I_{15/2} \rightarrow {}^4I_{11/2}$  transition of the  $\text{Er}^{3+}$  ion, was used as excitation source. The absorption and the photoacoustic excitation spectra were simultaneously recorded. When the exciting beam is modulated at low frequency, typically few dozens of Hz, the quantum efficiency is proportional to the ratio of the photoacoustic signal  $P$  to the absorbed excitation intensity  $A$ . In the case of  $\text{Er}^{3+}$  silicate glasses, the relation assumes the straightforward form  $\frac{P}{A} = a + b\eta(1/\eta\omega)$ , which is the equation for a straight line, where  $a$  and  $b$  are phenomenological constants. The slope of the line, normalized to its intercept *vs.*  $1/\eta\omega$ , gives directly the quantum efficiency.

More generally, photoacoustic spectroscopy is well suited for the study of materials which are opaque or exhibit important scattering. An interesting discussion about this technique is reported in [107] and references therein.

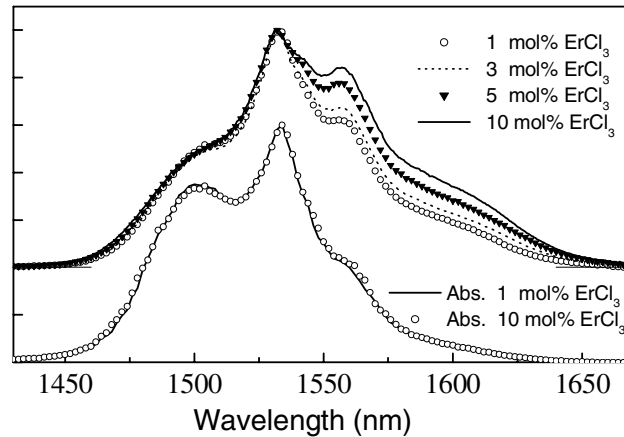


Fig. 17. – Normalized photoluminescence spectra of the  ${}^4I_{13/2} \rightarrow {}^4I_{15/2}$  transition for tellurite glasses activated by different  $\text{Er}^{3+}$  content collected upon excitation at 980 nm in identical experimental conditions. Normalized absorption spectra of the  ${}^4I_{13/2} \leftarrow {}^4I_{15/2}$  transition for 1 and 10 mol%  $\text{Er}^{3+}$ -activated glasses, are also reported. Adapted from [109].

## 6. – Radiation trapping, self-absorption and concentration-quenching phenomena

The previous discussion on the radiative lifetime measurements and the quantum efficiency, being connected to the goal of maximizing the fluorescence signal from an active optical glass, has been preliminary to the analysis of some important effects related to the rare-earth concentration in the glass itself.

As already noted in sects. 4 and 5, the design of an erbium-doped broad-band amplifier first of all requires the measurement of the  ${}^4I_{13/2} \rightarrow {}^4I_{15/2}$  effective transition bandwidth and lifetime. One of the phenomena affecting the accuracy of these measurements is self-absorption, which is defined as the reabsorption of luminescence by the analyte and interfering impurities in the excitation volume [108]. In a recent paper, Mattarelli *et al.* discussed the measurement of bandwidth and lifetime in the presence of self-absorption and indicated an experimental procedure to obtain their actual value [109]. A series of tellurite glasses, with nominal molar composition  $60\text{TeO}_2\text{-}20\text{ZnO-}20\text{ZnCl}_2\text{-}x\text{ErCl}_3$ , where  $x = 1, 3, 5, 10$ , were prepared. It was shown that, while the normalized absorption spectra in the region of the  ${}^4I_{13/2} \rightarrow {}^4I_{15/2}$  transition of the  $\text{Er}^{3+}$  ion overlap one with the other, the normalized PL spectra exhibit a shape dependent on the  $\text{Er}^{3+}$  content (see fig. 17). It is noteworthy that the PL bandwidth  $\Delta\lambda$ , if calculated using the emission intensity  $I(\lambda)$  instead of the emission cross-section as defined in sect. 4, passes from 77 nm for the least doped sample ( $x = 1$ ) up to 84 nm for the most doped one ( $x = 10$ ) [109]. These results could lead to think that the growth of the  $\text{Er}^{3+}$  concentration is associated with the occupation by the active ions of more and more different microscopic environments, giving rise to a greater inhomogeneous broadening. This explanation, however, contrasts with the evidence of the absorption spectra, where the shape of the electronic transition does not change with the doping level (fig. 17). The observed broadening of the emission must, on the contrary, be ascribed to the self-absorption effect, that leads to overestimate the real emission bandwidth [110]. In fact, because of the overlap of the absorption and

emission spectra around the  $1.53\ \mu\text{m}$  peak, reabsorption around the peak wavelength is much more effective than that at other wavelengths. As a consequence, the measured emission intensity around the peak wavelength will be lower than its intrinsic value.

The influence of self-absorption on the luminescence shape can be described in first approximation, *i.e.* neglecting contributions from photons reflected or re-emitted after a first absorption, by the relationship

$$(6.1) \quad I_d(\lambda) = I_0(\lambda) \exp[-\alpha(\lambda)d],$$

where  $I_d(\lambda)$  is the collected PL intensity for a penetration depth  $d$ ,  $I_0(\lambda)$  is the initially generated luminescence, and  $\alpha(\lambda)$  is the absorption coefficient. Equation (6.1) means that it is also possible to reconstruct  $I_0(\lambda)$  by multiplying the collected PL spectra by the correction factor  $\exp[\alpha(\lambda)d]$ . Mattarelli *et al.* have applied this procedure to PL measurements performed at different depths on the same sample, showing a remarkable agreement of the initially generated spectra  $I_0(\lambda)$  [109]. In order to check the effectiveness of the procedure, PL spectra were collected from finely ground powders of each sample, with an average size of about  $300\text{--}400\ \mu\text{m}$ , where the deforming effect of self-absorption was strongly reduced. The PL spectra of the powders showed a shape independent of the  $\text{Er}^{3+}$  concentration, and they closely overlapped with the reconstructed spectra  $I_0(\lambda)$ . When the McCumber-Miniscalco-Quimby model is applied, the shape of the emission spectrum thus calculated reflects perfectly the spectra obtained with the above-shown method, giving the true value of the effective bandwidth, *i.e.* about  $66\ \text{nm}$ . These results confirm the goodness of the approximation in determining the self-absorption contribution from the absorption spectra.

Radiation trapping can also induce a misleading evaluation of the luminescence quantum efficiency, defined as the ratio of observed to radiative lifetime. Auzel *et al.* discussed the radiation trapping effect on the measured lifetime of several rare-earth ions in a single crystal [111]. When population inversion can be neglected, the measured lifetime in the trapping condition ( $\tau_{\text{tr}}$ ) is related to the intrinsic lifetime without trapping ( $\tau_{\text{intr}}$ ) by:  $\tau_{\text{tr}} = \tau_{\text{intr}}(1 + \sigma Nd)$ , where  $\sigma$  is the transition cross-section,  $N$  is the ion doping concentration, and  $d$  is the average absorption length in the lifetime measurement experiment. It is evident that reabsorption can lead to a strong increase of the luminescence decay time and to a proportionally overestimated quantum efficiency. As an example, much higher  $\tau_{\text{tr}}$  values (between 20 and 140% higher) were measured in tellurite massive glasses than in the corresponding powders, the latter being surely related to the intrinsic lifetime  $\tau_{\text{intr}}$  [109].

The principle of radiation trapping can be demonstrated simply by coating a glass or crystal with a highly reflecting film and leaving apertures open for the entrance of excitation light and for observation of the luminescence decay. Noginov [112] experimentally demonstrated a sixfold increase for the  $\text{Yb}^{3+}$  lifetime in  $\text{Yb}^{3+}:\text{BaY}_2\text{F}_8$  gold-coated crystal; in the uncoated sample the  $\text{Yb}^{3+}$  lifetime was  $2.9\ \text{ms}$ , to be compared with the lifetime of  $18\ \text{ms}$  measured in the gold-coated sample. Analogously, for the  $^4I_{13/2}$  transition in  $\text{Er}^{3+}:\text{BaY}_2\text{F}_8$ , he measured  $13\ \text{ms}$  for the uncoated crystal and  $31\ \text{ms}$  for the gold-coated one. It is clear that radiation trapping enhances energy storage, energy transfer, and up conversion in rare-earth-activated materials. However, if the reabsorption effect is appropriately tailored, it can potentially decrease the threshold for compact continuous-wave pumped lasers.

Another effect that strongly decreases the efficiency of luminescent materials is the so-called concentration quenching. In the case of high rare-earth concentrations, the ions

are closer together, so that deleterious non-radiative energy exchanges between neighbouring ions can take place. The dissipative processes related to ion-ion interactions leading to concentration quenching in glasses have been the object of several studies, both theoretical and experimental, as shown by the number of publications dealing with the argument [87, 89, 113-118]. In the following we will refer only to the  $\text{Er}^{3+}$  ion, which is the most widely used in guided-wave amplifiers and lasers. When the erbium concentration increases, the average distance between neighbouring  $\text{Er}^{3+}$  ions simultaneously decreases and electric dipole-dipole interactions between the different  $\text{Er}^{3+}$  ions become more significant. Under this condition, processes which include energy migration and up-conversion can take place, lowering the fraction of excited  $\text{Er}^{3+}$  ions at a given pump power. As a consequence, a decrease of the luminescence lifetime of the metastable  $^4I_{13/2}$  state as a function of increasing  $\text{Er}^{3+}$  concentration occurs, as described by the following empirical formula [87, 113]:

$$(6.2) \quad \tau_{\text{meas}} = \frac{\tau_0}{1 + \left(\frac{\rho_{\text{Er}}}{Q}\right)^p},$$

where  $\tau_{\text{meas}}$  is the observed luminescence lifetime,  $\tau_0$  the ideal luminescence lifetime in the limit of zero rare-earth concentration,  $\rho_{\text{Er}}$  the  $\text{Er}^{3+}$  ion concentration,  $Q$  the quenching concentration and  $p$  a phenomenological parameter characterizing the steepness of the corresponding quenching curve. It could be considered that  $p$  is determined by the mechanism of the energy transfer between the rare-earth ions [110]. In this framework,  $p$  is close to 2 when the electric dipole-dipole transition is the dominant energy-transfer mechanism between neighbouring  $\text{Er}^{3+}$  ions. When the effect of electric dipole- and quadrupole-quadrupole transitions cannot be neglected,  $p$  should be larger than 2. However, in order to avoid difficulties with the physical meaning of  $p$ , usually only  $Q$  is estimated from the fitting curve, as the concentration at which the lifetime becomes half of  $\tau_0$  (in fact,  $\tau_{\text{meas}}$  is equal to  $\tau_0/2$  when  $\rho_{\text{Er}}$  is equal to  $Q$ ). The phenomenological equation (6.2) deserves some comments and, as a general rule, the  $Q$  parameter has to be considered in the light of complementary measurements, which may put in evidence other relaxation mechanisms. By definition,  $\tau_0$  is the value of the PL lifetime of the rare-earth ion in the material, in the limit of zero ion concentration, *i.e.* in the absence of any concentration quenching phenomena. Therefore, if the material has no multiphonon relaxation due to the matrix, which is approximately true for heavy-metal silicates, and if there are no residual  $\text{OH}^-$  species, then  $\tau_0$  should approximately coincide with the radiative lifetime  $\tau_{\text{rad}}$ . But, if there a residual  $\text{OH}^-$  exists, even in the limit of zero rare-earth concentration, the  $\tau_0$  value should be less than the radiative lifetime. A detailed discussion with a numerical analysis about the validity of the concentration quenching relation is reported in [77].

Several researchers have noted that codoping with  $\text{Al}^{3+}$  is effective at dispersing rare-earth ions in silica gel and silicate glass matrices [96, 119-121]. A detailed interpretation of why and when rare-earth ion isolation occurs is still not well established [122]. A general point of view, however, is that rare-earth ions will be preferably partitioned by  $\text{Al}^{3+}$ , forming Al-O-RE bonds, rather than sitting together to form RE-O-RE bonds. Subsequently, the spacing among RE elements is larger in the alumina-doped silica host rather than in the non-alumina-containing host.

## 7. – Photonic band gap structures with glassy materials

Photonic crystals are structures characterized by a refractive index periodicity in space on a length scale comparable to the wavelength of interest, and, consequently, by a certain frequency range where light cannot propagate in any direction; this frequency range is known as the photonic band gap (PBG) [123-125]. It was predicted by Purcell [126] that an atom in a wavelength-size cavity can radiate much faster than in the free space. This effect was measured in a cavity formed by two parallel mirrors by Haroche *et al.* [127]. On the other hand, if its transition frequency falls within the photonic band gap, the atom cannot radiate away energy, and thus spontaneous emission can be completely inhibited [128]. Several configurations have been proposed to exploit the physical property that spontaneous-emission rate of rare-earth ions can be modified by the influence of the local optical environment. This effect has been demonstrated in one-dimensional systems such as  $\text{Eu}^{3+}$ -doped dielectric slab [129],  $\text{Er}^{3+}$ -activated Si/SiO<sub>2</sub> microcavity [130],  $\text{Er}^{3+}$  and dye-doped SiO<sub>2</sub> colloidal photonic crystals [131], and  $\text{Pr}^{3+}$ -doped Ta<sub>2</sub>O<sub>5</sub>/SiO<sub>2</sub> micro-resonators [132].

Photonic crystals are nowadays the key for the future technological development of planar optical circuits. To exploit the unique properties of photonic crystals it is important to develop new ways of making optically functional photonic crystals that integrate the self-assembly chemistry methods and the microfabrication techniques, with the aim of creating new photonic crystal devices and chips that are suitable for high-volume manufacturing processes.

Recently, it has been proved that the sol-gel technique represents a viable approach to the fabrication of PBG structures and, in particular, of rare earth-activated 1-D photonic crystals and microcavities [133-135]. A recent review of the origin and development of PBG materials and structures made by sol-gel processing since 1987, with emphasis on recent developments, can be found in [136]. Thin films of SiO<sub>2</sub> and TiO<sub>2</sub> were used to fabricate one-dimensional photonic crystal devices using the sol-gel method [137]. The microcavity resonator consisted of a TiO<sub>2</sub> Fabry-Perot cavity sandwiched between two SiO<sub>2</sub>/TiO<sub>2</sub> mirrors of three bi-layers each. The resonance wavelength was at 1500 nm and the quality factor  $Q$  of the microcavity was 35.

As another example, Zampedri *et al.* reported a sol-gel-derived 1D cavity realized by an  $\text{Eu}^{3+}$ -activated dielectric layer placed between two distributed Bragg reflectors (DBR) [135]. These DBRs consisted of 7 alternated quarter-wave layers of TiO<sub>2</sub> and SiO<sub>2</sub>. The active layer between the two DBRs consisted of a TiO<sub>2</sub> half-wave layer doped with 2 mol% of  $\text{Eu}^{3+}$ . The sample was deposited on vitreous silica substrate. The starting solution was  $\text{Ti}(\text{O}-n\text{-C}_3\text{H}_7)_4$  and  $\text{Si}(\text{OC}_2\text{H}_5)_4$ , with molar ratio  $\text{H}_2\text{O}/\text{TiO}_2 = 1$  and  $\text{H}_2\text{O}/\text{SiO}_2 = 2$ , employed for titania and silica layer preparation, respectively. The spinning deposition technique was used. After each spinning, the sample was dried at 200 °C for 1 minute on a hot-plate and then annealed at 1000 °C for about 90 s. Angle-dependent reflectance spectra and luminescence measurements were performed as described in [77]. For luminescence measurements with 1D microcavities, two angles must be controlled: the angle of excitation and the angle of collection of the luminescence. In fact, the excitation angle must be chosen so that the laser beam is not reflected by the DBRs, but good part of the excitation light could reach the active layer. The angle of collection of the luminescence is chosen in order to superimpose the cavity resonance to the rare-earth emission. For normal incidence, a stop band from about 510 nm to 800 nm, with maximum reflectance of 98%, was obtained, which is shown in fig. 18. The cavity resonance corresponded to the peak at 618 nm with a full width at half maximum

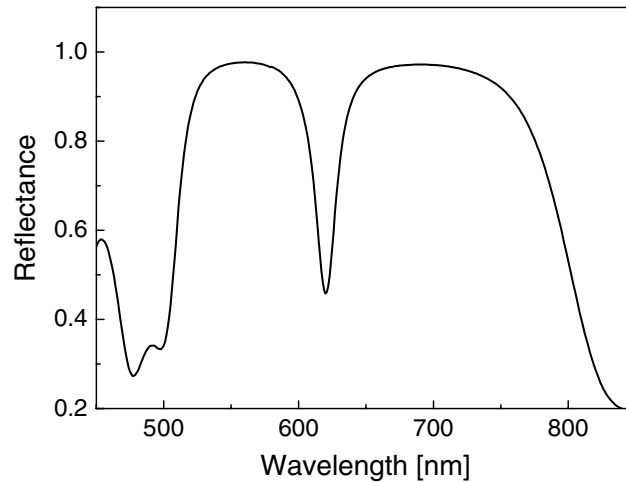


Fig. 18. – Normal incidence reflectance spectra of a sol-gel-fabricated Fabry-Perot microcavity, consisting of two mirrors of 7 alternated quarter wave layers of  $\text{TiO}_2$  and  $\text{SiO}_2$ , plus a 2 mol%  $\text{Eu}^{3+}$ -activated  $\text{TiO}_2$  half-wave defect layer [135].

(FWHM) of 12 nm. The cavity resonance depends on the detection angle; a quality factor  $Q \cong 54$  was obtained in this case, with the reflectance measured for an incidence angle of  $0^\circ$ . The fabrication technique must be precisely controlled on the nanometric scale for fabrication of higher- $Q$  microcavities; it is crucial, in particular, to avoid variations in the index and thickness of the different stacked layers.

Photoluminescence spectra of the microcavities show the interesting effect of luminescence enhancement. In the system described above [135], the luminescence, corresponding to the emission from  ${}^5D_0$  state to the  ${}^7F_J$  ( $J = 2, 1$ ) levels of the  $\text{Eu}^{3+}$  ion, could be tuned by the PBG system in a wide frequency range, practically corresponding to the whole stop band. The maximum of the luminescence was detected at angles less than  $10^\circ$ . The luminescence line was modified both in intensity and bandwidth by the cavity. The FWHM value of about 12 nm for the  ${}^5D_0 \rightarrow {}^7F_2$  emission had to be compared to the typical FWHM of about 25 nm observed in sol-gel-derived bulk glasses. When the doped layer, with a thickness of about 140 nm, was inserted into the cavity, an intense emission was detected. Oppositely, when the same layer was deposited on a silica substrate, a very low intensity, comparable to the noise, was observed. This enhancement of the luminescence was already demonstrated for instance by Vredenberg *et al.* [130] for a  $\text{Si}/\text{SiO}_2$  cavity activated by  $\text{Er}^{3+}$  ions. The intensity enhancement occurs because at any particular wavelength the emission rate into a resonant cavity mode, which is highly directional, is increased, while in almost all other directions is reduced. This redistribution of emitted intensity is a well-known cavity effect and has been numerically analysed in detail for a complete set of cavity modes in planar dielectric microcavities [128]. It is evident that the possibility of controlling spontaneous emission makes these planar structures of great interest for fabrication of high emissive devices such as directive light-emitting diodes or low threshold microlasers.

It is evident that three-dimensional (3D) cavities would provide a really significant improvement in the light extraction; since, however, there exist serious difficulties in fabricating 3D PBG structures, in particular with deterministic defects, much effort is

being devoted to the less demanding 2D photonic crystal structures. Even these 2D structures, if associated with waveguide control in the third dimension, may actually provide an excellent overall 3D confinement. Rare-earth-doped glasses, however, do not lend themselves as very convenient materials for 2D or 3D PBG structures, due to the relatively low refractive index and consequent low index contrast. Despite of this limitation, some 2D fibre and waveguide devices have been proposed, by using microstructured glass technology [138].

## 8. – Rare-earth-doped glasses for lasers and amplifiers

Optical glasses are the corner stone in a huge number of technological applications. This is definitely true for laser systems. At the top of the scale, one can mention the National Ignition Facility (NIF) at the Lawrence Livermore National Laboratory, which has the goal to achieve controlled thermonuclear burn in the laboratory using laser light. The entire NIF project is expected to be completed in mid-2009, with ignition experiments beginning a year later [139]. NIF represents both the largest laser and the largest optical instrument ever built, requiring 7500 large optics and more than 30000 small optics. Optical materials, and in particular optical glasses, play a crucial role in NIF fabrication, where the neodymium-activated glass laser slab, operating at 1053 nm, is the hearth of the laser system.

Over almost 40 years there has been extensive research covering a large number of active ions in every known glass system. Neodymium, however, remains the primary RE element of interest for most commercial applications of glass lasers, and, more generally, of solid-state lasers. Only recently, a growing interest has been focused on erbium and ytterbium: the former ion is fundamental for applications in the optical telecommunications (but also has interest for eye-safe laser applications, such as in rangefinders), while the latter is useful as co-dopant of erbium (because of the energy-transfer effect that increases pumping efficiency at 980 nm) but is assuming larger and larger importance for the development of medium-to-high power fibre lasers. Ytterbium-doped silica fibres exhibit a broad-gain bandwidth, high optical conversion efficiency, and large saturation fluence. A cladding-pumped Yb-doped fibre laser with continuous-wave optical power of 1.36 kW at 1.1  $\mu\text{m}$ , with 83% slope efficiency and near diffraction-limited beam quality, has been demonstrated [140]. By combining an assembly of highly reliable diode-pumped single Yb-fibre lasers, industrial systems with output up to 50 kW are also available [141].

Other rare-earth ions under investigation include samarium and holmium for visible emission, praseodymium for the 1.3  $\mu\text{m}$  window, thulium and again holmium for longer near-infrared wavelengths. A summary of the main emission wavelengths of the most important RE ions is presented in table IV, where possible sensitising ions are indicated as well. Here we refer to a sensitising ion as the additional dopant that absorbs the pump radiation and transfers it to the lasing ion, thus increasing the overall pumping efficiency [142].

At the bottom of the scale of rare-earth-doped glass devices, at least for their miniaturised size, there are the integrated optical (IO) lasers and amplifiers: the following sub-section is devoted to an overview of IO amplifiers, which have gained much interest in the last years for their application in optical communication systems.

**8.1. Integrated optical amplifiers.** – There are three major applications for optical amplifiers in modern optical networks; they can be used as power amplifier/boosters (placed

TABLE IV. – *Emission wavelengths of the main RE ions in glass.*

| Dopant<br>RE ion | Approximate emission<br>wavelength(s) ( $\mu\text{m}$ ) | Sensitising ion  |
|------------------|---|--|
| $\text{Pr}^{3+}$ | 0.89 1.04 1.34  |  |
| $\text{Nd}^{3+}$ | 0.93 1.06 1.35  | $\text{Cr}^{3+}$ , $\text{Mn}^{2+}$ , $\text{Ce}^{3+}$ |
| $\text{Sm}^{3+}$ | 0.65  |  |
| $\text{Eu}^{3+}$ | 0.62  |  |
| $\text{Tb}^{3+}$ | 0.54  |  |
| $\text{Ho}^{3+}$ | 0.55 1.38 2.05  |  |
| $\text{Er}^{3+}$ | 1.30 1.54 1.72 2.75                                     | $\text{Cr}^{3+}$ , $\text{Yb}^{3+}$                    |
| $\text{Tm}^{3+}$ | 0.80 1.47 1.95 2.25                                     | $\text{Er}^{3+}$ , $\text{Yb}^{3+}$                    |
| $\text{Yb}^{3+}$ | 1.03  | $\text{Nd}^{3+}$                                       |

directly after the laser diode transmitter), in-line amplifiers (repeaters), or preamplifiers (placed in front of the detector to enhance its sensitivity). The corresponding requirements may be different, especially in terms of input signal power handling, maximum optical gain, and signal-to-noise ratio (SNR). There are a few possible technological routes for implementing optical amplifiers: they include semiconductor optical amplifiers (SOAs) [143], erbium-doped fibre amplifiers (EDFAs) [144-146], and Raman optical amplifiers [147]. Hybrid configurations, such as Raman-assisted EDFAs, have also been extensively studied, because they show low noise figure [148].

EDFAs represent a mature technology, and they are routinely used in current telecommunication systems. Another application of optical amplifiers, especially in local access networks, has to do with the loss compensation of passive components (such as interleavers and  $1 \times N$  splitters). In such a case, the final aim would be that of integrating active and passive devices on a single chip: for this reason, the integrated-optics (IO) format [149] is more appealing. IO amplifiers are being extensively investigated, and a few types of erbium-doped waveguide amplifiers (EDWAs) are already commercially available [150].

The goal of developing fibre systems operating over an ultra-wide band, covering the wavelengths between 1.3 and  $2 \mu\text{m}$ , would require the use of different rare-earth (RE) elements and different glass matrices. The potential amplification bands in that wavelength region of some combinations of glasses and rare earths are indicated in table V. The energy levels are labelled according to the well-known Russel-Saunders multiplet notation  $^{2S+1}L_J$ , where  $S$  is the total spin quantum number,  $L$  is the total orbital angular-momentum quantum number, and  $J$  is the quantum number of the total momentum of that particular level or state ( $J = L + S$ ) [151]. The choice of the glass matrix largely affects the amplifier's performance, and oxide glasses are not suitable hosts for exploiting the radiative transitions of  $\text{Pr}^{3+}$  in the 1260–1350 nm region, of  $\text{Tm}^{3+}$  in the 1460–1510 nm region, and of  $\text{Ho}^{3+}$  over 2000 nm.

So far, however, most of the research efforts have been focused on the use of  $\text{Er}^{3+} \ ^4I_{13/2} \rightarrow \ ^4I_{15/2}$  transition in the 1500–1600 nm band, and for that purpose oxide glasses, and

TABLE V. – *Potential amplification bands in the near-infrared region of some RE ions in glass.*

| Operating range<br>(nm) | Dopant<br>RE ion | Transition                          | Oxide<br>host | Fluoride<br>host |
|-------------------------|------------------|-------------------------------------|---------------|------------------|
| 1260–1350               | Pr <sup>3+</sup> | $^1G_4 \rightarrow ^3H_5$           | –             | +                |
| 1320–1400               | Nd <sup>3+</sup> | $^4F_{3/2} \rightarrow ^4I_{13/2}$  | +             | +                |
| 1460–1510               | Tm <sup>3+</sup> | $^3F_4 \rightarrow ^3H_4$           | –             | +                |
| 1500–1600               | Er <sup>3+</sup> | $^4I_{13/2} \rightarrow ^4I_{15/2}$ | +             | +                |
| 1700–2015               | Tm <sup>3+</sup> | $^3H_4 \rightarrow ^3H_6$           | +             | +                |
| 2040–2080               | Ho <sup>3+</sup> | $^5I_7 \rightarrow ^5I_8$           | –             | +                |

especially silicates and phosphates, proved to be much more convenient than non-oxide glasses, due to their easier fabrication and processing, and to the higher chemical resistance. Thus, EDFAs and EDWAs based on oxide glasses remain at the moment the most viable solution to cover the *C*-band and its short side (*S*<sup>+</sup>-band: 1450–1530 nm; or *S*-band: 1480–1520 nm) and long side (*L*-band: 1560–1610 nm).

Bulk rare-earth-doped glasses may be fabricated by conventional melt-quenching, sol-gel or CVD processes [20]. For integrated optics, several fabrication processes have been developed; material requirements are much more stringent than for optical fibres, due to the different manufacture technologies and to the much higher rare-earth concentration required in short-length planar devices. Even if in principle non-oxide glasses, such as fluorides and other halides, may possess better properties (*e.g.*, much lower phonon energy), so far the largest part of the experimental results—and all the available commercial amplifiers—have been obtained using silicates and phosphates glasses, mostly because of their greater chemical robustness and environmental stability.

The development of erbium-doped integrated optical amplifiers may follow three main manufacturing routes:

- local doping of a bulk glass or of a glass thin film with rare-earth ions by diffusion or ion-implantation; the process leads to a local increase of the refractive index, and therefore also produces a waveguide [152-155];
- fabrication of a rare-earth-doped bulk glass by conventional melting process or by sol-gel, and subsequent fabrication of the waveguide by diffusion processes (by ion-exchange, in particular) [156-163];
- deposition of a glass thin-film waveguide containing rare-earth ions by RF magnetron sputtering, chemical vapour deposition (CVD), electron-beam vapour deposition, flame hydrolysis deposition (FHD), or sol-gel processes [164-169].

A combination of two different technologies has also been demonstrated, such as sol-gel to deposit the Er-doped thin film and ion-exchange to define the channel waveguide [170], or flame hydrolysis deposition of the guiding layer and aerosol Er-doping [171], or ion-exchange in a glass to fabricate the waveguide and ion implantation to dope it with erbium [172]. Moreover, advances are being made in laser-based fabrication and patterning processes of glass structures, which include pulsed-laser-deposition [173-175], laser machining [176, 177], UV-laser and femtosecond-laser writing of channel waveguides in bulk glasses or in glassy thin-film [178-181].

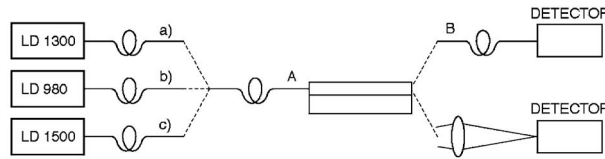


Fig. 19. – Experimental set-up used to measure the optical properties of an  $\text{Er}^{3+}$ -doped waveguide, pumped at 980 nm. Pigtailed laser diodes and output coupling configurations may be combined in different ways to perform specific measurements.

**8.2. Optical and spectroscopic properties of  $\text{Er}^{3+}$ -doped waveguides.** – The goal of achieving a high optical gain in an  $\text{Er}^{3+}$ -doped glass can be reached only if the proper spectroscopic properties of the glass are combined with a low propagation loss waveguide. Thus, it is very important to optimize the RE doping level. Generally, at low  $\text{Er}^{3+}$  concentration, the lifetime of the metastable level is longer and quantum efficiency is higher, but obviously the total intensity of stimulated emission is lower, while at higher concentrations, fluorescence quenching may occur, due to ion clustering or ion-to-ion interaction. It is also important that absorption and emission spectra be wavelength-shifted one with respect to the other, so that the peaks of absorption and emission cross-sections are located at different wavelengths, in order to reduce re-absorption phenomena in the waveguide. This is possible because the  $^4I_{13/2}$  Stark levels are non-uniformly populated, and the  $^4I_{13/2} \rightarrow ^4I_{15/2}$  transition may be shifted to a longer wavelength with respect to absorption.

For most of the amplifiers in the  $1.53 \mu\text{m}$  band, the active doping includes ytterbium ions: ytterbium co-doping allows to transfer energy from excited  $\text{Yb}^{3+}$  ions to close  $\text{Er}^{3+}$  ions through a cooperative cross-relaxation process, thus significantly enhancing system absorption at 980 nm and making the pumping mechanism more efficient. The presence of  $\text{Yb}^{3+}$  ions may also be effective in reducing unwanted  $\text{Er}^{3+}$ - $\text{Er}^{3+}$  ion energy transfer interactions by increasing the mean inter-atomic distance.

As to the waveguide itself, it is necessary to achieve minimal propagation losses, because they would affect, among other factors, the pump threshold, *i.e.* the power at which the material becomes transparent, the signal amplification being able to compensate for propagation and absorption losses.

The pumping scheme is also important, in order to actually excite the maximum number of erbium ions; in most cases the pump is a laser diode emitting at  $\sim 980 \text{ nm}$  wavelength, which corresponds to the peak of the absorption band due to the  $^4I_{15/2} \rightarrow ^4I_{11/2}$  transition. In order to achieve high pumping power, laser diode arrays are used, or a contradirectional scheme is employed, with two laser diodes injecting their power at the two ends of the fibre-EDWA-fibre system. Proper modelling is necessary, in order to select the optimal doping concentration and operational parameters [181-183].

The most important characteristic to indicate the performance of an EDWA is the net gain. Since it is not always clear, when reading some of the published papers, what kind of gain was actually measured, let us recall the definitions of gain and refer to fig. 19 to explain how a full characterization of an active waveguide may be performed, by using, in different configurations, the same basic devices, namely laser diodes, fibres, detectors, and the waveguide to be tested.

The *net optical gain*, also called *external gain*, can be measured as the ratio between the maximum intensity of the signal measured at the end of the output fibre (B) and

the signal intensity at the end of the input fibre (A), for a given value of the pump laser intensity. The intensity of the amplified spontaneous emission (ASE) should be subtracted from the output signal.

If, however, one wants to understand how that value of gain is obtained, it would be useful to perform a more detailed analysis, by measuring:

- a) The insertion loss of the waveguide at a wavelength outside the absorption band of  $\text{Er}^{3+}$  ions, *e.g.*, at 1300 nm. This measurement can be done by comparing the intensity at the output of the delivery fibre (A) with that at the end of the collecting fibre (B). It gives an assessment of scattering losses; moreover, a correction due to the wavelength difference between 1.3 and 1.5  $\mu\text{m}$ , according to Raleigh law  $I_s = a\lambda^{-4}$ , is possible.
- b) The spontaneous emission intensity. This is measured by detecting the signal at the output of the collecting fibre (B) when the waveguide is pumped, *i.e.* when the delivery fibre (A) is carrying only the beam at 980 nm.
- c) The coupling loss between the fibre and the channel waveguide may be evaluated by comparing the intensities detected when the light coming out from the channel is collected by a fibre or by a lens (usually, a microscope objective). Then, one can assume that the coupling loss is not significantly different for the input and the output coupling.
- d) The absorption of erbium ions. This value is derived from the measure of the insertion loss at 1.5  $\mu\text{m}$ , in the absence of the pump, by subtracting the coupling losses.

A preliminary and quick measure of the amplifier performance can be given by the *signal enhancement* (sometimes also referred to as *relative gain* or ON/OFF ratio), *i.e.* the ratio of output signals when the laser pump is on and off. This is not, however, a true optical gain, due to the effect of absorption of erbium ions, which is significant when the pump is off and becomes negligible when the ground state is depleted of electrons by the pump light. The *internal gain* may be obtained by subtracting from the signal enhancement the absorption due to erbium ions at 1.5  $\mu\text{m}$ ; by further subtracting the coupling losses, the value of the net optical gain  $G$  is finally obtained.

Table VI gives an idea of the state of the art in EDWAs, by presenting a few out of the many results published in the literature, with particular reference to devices fabricated in silicate and phosphate glasses. It has to be underlined that comparison of these results should be considered only qualitative, because it cannot be stated that measurement methods and units are used everywhere in a consistent way. For instance, in some cases the intensity of the pump signal is given as the optical power actually injected into the waveguide, while in other cases only the power available at the end of the input fibre is given.

Besides the gain, the other most important specification for an EDWA is its amplifier bandwidth, since the broad-band operation is critical for the use in DWDM systems. In fact, an EDWA has to simultaneously amplify many channels, with the best possible uniformity; as the gain is generally dependent on wavelength, each signal will experience different optical gain, with bad effect on the transmission bit-error rate (BER) and on the signal-to-noise ratio (SNR) differential among channels. Thus, not only the width of the emission band is important, but its shape as well, because it affects the uniformity of gain

TABLE VI. – *Characteristics and performance of a few Er<sup>3+</sup>-doped integrated optical amplifiers, as reported in the literature.*

| Material               | Doping ion(s)                  |                                | Fabrication technology | Max. Net Gain (dB/cm) | Pump power (mW) <sup>(a)</sup> | Ref.  |
|------------------------|--------------------------------|--------------------------------|------------------------|-----------------------|--------------------------------|-------|
|                        | Er                             | Yb                             |                        |                       |                                |       |
| Aluminophosphosilicate | 0.25 mol%                      | 0.25 mol%                      | sol-gel                | 1.1                   | 175                            | [168] |
| Borosilicate           | 3 wt%                          | 5 wt%                          | ion                    | 2.3                   | 130                            | [157] |
|                        | Er <sub>2</sub> O <sub>3</sub> | Yb <sub>2</sub> O <sub>3</sub> | exchange               |                       |                                |       |
| Doped BK7              | 1 wt%                          | 5 wt%                          | ion                    | 1.0                   | 110                            | [186] |
|                        | Er <sub>2</sub> O <sub>3</sub> | Yb <sub>2</sub> O <sub>3</sub> | exchange               |                       |                                |       |
| P-doped silica         | 0.55 wt%                       |                                | FHD <sup>(c)</sup>     | 0.7                   | 640                            | [164] |
| Phosphate              | ◆ <sup>(b)</sup>               | ◆ <sup>(b)</sup>               | ion exchange           | 2.5                   | 120                            | [159] |
| Phosphate              | 2 wt%                          | 2 wt%                          | ion exchange           | 2.9                   | 120                            | [186] |
| Soda-lime silicate     | $2.3 \times 10^{20}$           | $3.8 \times 10^{20}$           | ion                    | 1.5                   | 250                            | [160] |
|                        | ions/cm <sup>3</sup>           | ions/cm <sup>3</sup>           | exchange               |                       |                                |       |
| Soda-lime silicate     | $0.7 \times 10^{20}$           |                                | sputtering             | 0.8                   | 80                             | [165] |
|                        | ions/cm <sup>3</sup>           |                                |                        |                       |                                |       |

<sup>(a)</sup>If not indicated, pump wavelength is 980 nm. <sup>(b)</sup>Doping percentage not available. <sup>(c)</sup>FHD: flame hydrolysis deposition.

over the transmission channels. This fact has stimulated further research towards glass hosts providing wider photoluminescence bands and, more generally, a good compromise between the different operational characteristics, namely high gain, broad band and flat amplification.

A few examples of novel glass compositions are presented in the following subsections, which refer to recent activities carried out by the authors and collaborators, and concern silica-hafnia sol-gel films, aluminosilicate ion-exchangeable glasses and tellurite glasses.

**8.2.1. Sol-gel silica-hafnia films.** Silica-based glasses offer solubility for rare-earth ions of about  $6 \times 10^{20} \text{ cm}^{-3}$ , are transparent in the visible to near-infrared region, and are easily compatible with IO technology. Silica-hafnia thin films are known as stable optical coatings with high damage resistance at 1054 nm, and have been proposed for mirrors and polarizers for the National Ignition Facility. Thus, it was decided to test the structural and optical properties of Er<sup>3+</sup>-doped optical waveguides made by silica-hafnia; for that purpose, by using the sol-gel process, several films of composition  $(100 - x)\text{SiO}_2 - x\text{HfO}_2$  ( $x = 10, 20, 30, 40$ ) were produced and tested. For each composition, two films were grown, containing 0.01 and 0.3 mol% Er<sup>3+</sup> ions, respectively [184].

All the films were deposited on cleaned pure-silica substrates by dip coating. After each layer's deposition, the sample was annealed in air for 50 s at 900 °C. After a 10-dip

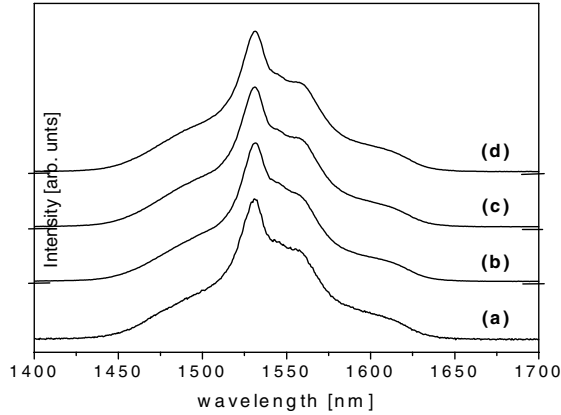


Fig. 20. – Photoluminescence spectra relative to the  ${}^4I_{13/2} \rightarrow {}^4I_{15/2}$  transition of the  $\text{Er}^{3+}$  ions for the (a) SH40, (b) SH30, (c) SH20, and (d) SH10 waveguides, obtained upon excitation at 514.5 nm.

cycle, the film was heated for 2 min at 900 °C. Finally, the waveguides were subject to a further annealing at 900 °C, whose duration was different for each waveguide; for instance, for the samples containing 0.3 mol%  $\text{Er}^{3+}$ , the annealing time was varying from 30 hours ( $x = 10$ ) down to 5 minutes ( $x = 40$ ). As the refractive index was changing with each composition, the thickness of each film was chosen so to have a single mode of propagation (one TE and one TM mode) supported at 633 nm. More details on the fabrication process are available in previous papers [184,185]. Measurements of propagation losses were done in various samples, giving an average value of about 0.9 dB/cm at 632.8 nm.

Photoluminescence (PL) measurements in the region of the  ${}^4I_{13/2} \rightarrow {}^4I_{15/2}$  transition and decay curves from the  ${}^4I_{13/2}$  level were made in guided-wave configuration, using prism coupling and either the 980 nm line of a Ti:sapphire laser or the 514.5 nm line of an argon laser as excitation source. The PL spectra relative to the  ${}^4I_{13/2} \rightarrow {}^4I_{15/2}$  transition of the  $\text{Er}^{3+}$  ions for all the waveguides exhibited a main emission peak at 1.53  $\mu\text{m}$  and a broad spectral width of about  $50 \pm 2$  nm. Figure 20 shows the emission spectra of the samples doped with 0.3 mol%  $\text{Er}^{3+}$  for excitation at 514.5 nm; the shape and the bandwidth of these spectra, however, did not change with the excitation wavelength, indicating that site selection was negligible. The similarity of PL spectra for all waveguides seems to indicate that a small inhomogeneous broadening is present, independently of  $\text{HfO}_2$  content.

The measured lifetime of the  ${}^4I_{13/2}$  metastable state decreases with the increasing of the  $\text{HfO}_2$  molar concentration, from a maximum of 8.5 ms when the ratio  $\text{SiO}_2/\text{HfO}_2$  is 90:10 and  $\text{Er}^{3+}$  concentration 0.01 mol%, to a minimum of 5.8 ms when the ratio increases to 60:40 and erbium concentration is 0.3% mol. By considering that in completely densified silicate glasses the multiphonon decay does not significantly affect the  ${}^4I_{13/2}$  level lifetime, we can assume that the lifetimes measured at 0.01 mol%  $\text{Er}^{3+}$  doping level are very close to the radiative ones. Under this hypothesis, we can estimate that quantum efficiency even in the samples doped with 0.3 mol% of erbium is always higher than 84%.

**8.2.2. Soda-lime-alumino-silicate (SLAS) glasses.** Soda-lime-silicate glasses are quite widely used in optics, and in integrated optics as well. As an example, a net optical gain of 1.5 dB/cm was demonstrated in a glass of this type, co-doped with  $\text{Er}^{3+}$  and

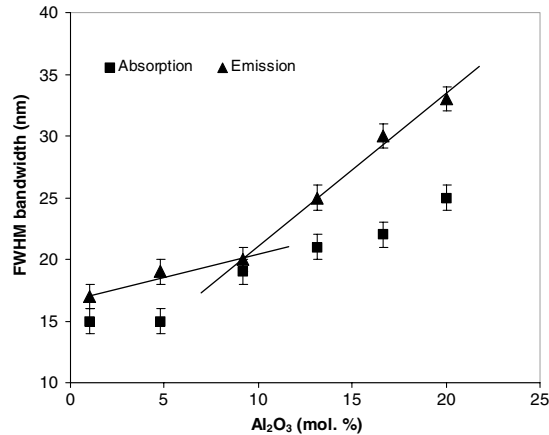


Fig. 21. – Absorption and emission bandwidths of SLAS samples as a function of  $\text{Al}_2\text{O}_3$  concentration. The lines are traced only as a guide to the eye.

$\text{Yb}^{3+}$  [160]. One disadvantage of this kind of glass, however, was represented by the narrow fluorescence bandwidth, the full-width half-maximum (FWHM) value being around 17 nm. On the other hand, it was known that the introduction of aluminium in a silicate glass may lead to increase the emission bandwidth [187]. Thus, it was decided to try to improve the characteristics of the original glass by adding different quantities of aluminium oxide (up to about 20 mol%) and by investigating their effect on glass optical properties, in particular on the emission bandwidth around  $1.5 \mu\text{m}$ .

The new glasses were prepared by conventional melting process and had a basic composition of the type  $\text{Na}_2\text{O}-\text{CaO}-\text{Al}_2\text{O}_3-\text{SiO}_2$ , with small percentages of  $\text{P}_2\text{O}_5$  and  $\text{K}_2\text{O}$ . Melting occurred in an electrically heated furnace within Pt crucibles, following the same heating cycle: from 20 to  $1000^\circ\text{C}$  at  $10^\circ\text{C}/\text{min}$ , with a 24 h soaking time at  $1000^\circ\text{C}$ , from 1000 to  $1550^\circ\text{C}$  at  $20^\circ\text{C}/\text{min}$  and finally 1 hour of soaking time at the maximum temperature of  $1550^\circ\text{C}$ . Eventually, the melt was quenched in a graphite mould to obtain small pieces of glass having a bar form; each bar was then cut to 1 mm thickness and optically polished on both faces.

Planar optical waveguides were produced by using the  $\text{Ag}^+ \leftrightarrow \text{Na}^+$  exchange process in a dilute  $\text{AgNO}_3$  solution ( $\text{AgNO}_3 : \text{NaNO}_3 = 0.5 : 99.5 \text{ mol}\%$ ) at  $325^\circ\text{C}$ . Both the fluorescence spectra of  $\text{Er}^{3+}$  and the lifetime  $\tau$  of the  $^4I_{13/2}$  level were detected using a 976 nm laser diode as excitation source. Further details on fabrication and characterization of these glasses are available elsewhere [188]. An interesting result was that the bandwidth almost doubled when passing from 1 to 20 mol% of alumina. The broadening of both the absorption and the fluorescence spectrum is also shown in fig. 21, where one can notice that the slope of increase of the emission bandwidth changes significantly from the region where the alumina content is lower than 9 mol% to the region where the content is equal or higher than 13 mol%. Correspondingly, an abrupt change in the physical (density) and optical (bulk refractive index) properties of the glass was observed as well (fig. 22) [188]. These facts suggest that the behaviour of this class of glasses has a drastic change when the concentration of aluminium ions becomes larger than that of sodium ions. A possible explanation refers to the different effect that the aluminium oxide has on the silica network, as glass modifier and as glass former, respectively. In

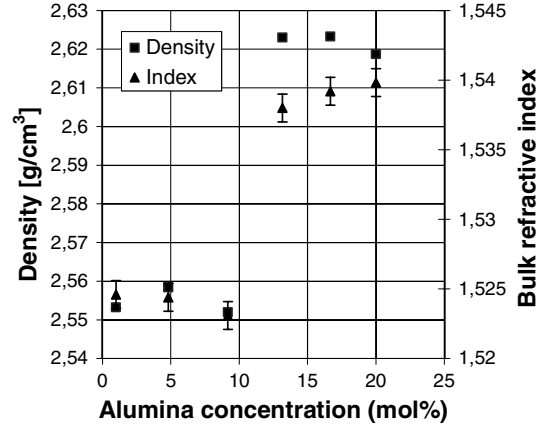


Fig. 22. – Density and bulk refractive index of the six glass samples as a function of alumina content. The error on the measurement of density is lower than  $0.0004 \text{ g/cm}^3$  and therefore in the plot the error bar would be smaller than the symbol used.

particular, in the network modifier case (samples with  $\text{Al}_2\text{O}_3$  concentration lower than 10 mol%), the aluminium ions contribute to disrupting the silica structure and producing non-bridging Al-O groups, which can coordinate the  $\text{Er}^{3+}$  ions, so reducing the Er-Er interaction and increasing the lifetime of the metastable  $^4I_{13/2}$  level. A further increase of aluminium oxide, on the contrary, reduces the non-bridging oxygen ions to form the Al-O-Si bridging oxygen.

The radiative lifetimes were calculated using Judd-Ofelt analysis; for all the samples, the quantum efficiency  $\eta = \tau_{\text{meas}}/\tau_{\text{rad}}$  is larger than 55%. Quantum efficiency near 75% is estimated for the sample having high  $\text{Al}_2\text{O}_3$  concentration (16.67 mol%): this sample, therefore, exhibiting high  $\eta$  and broad emission bandwidth, can represent a glass with high potential for an EDWA.

**8.2.3. Tellurite glass waveguides.** In the recent years, a growing attention has been paid to  $\text{TeO}_2$ -based  $\text{Er}^{3+}$ -doped glasses, which exhibit large stimulated emission cross-sections, broad emission bandwidth, wide infrared transmittance (up to  $6 \mu\text{m}$ ), and low phonon energy. Modelling has shown that the tellurite-glass host material can offer two kinds of advantage for the fabrication of high-gain integrated optical amplifiers: i)  $\text{Er}^{3+}$ -doped tellurite waveguides exhibit higher signal gains than  $\text{Er}^{3+}$ -doped silica waveguides, and ii) the broader bandwidth that  $\text{Er}^{3+}$  exhibits in tellurites, coupled to its higher emission cross-section coefficient, reduces the deleterious gain peaking effect and therefore makes it easier to reach the goal of a gain-flattened optical amplifier [182].

We studied two families of tellurite glasses, one including tungsten and the other one including zinc [189]. The composition of the samples we synthesized and characterized is summarized in table VII. Samples S1 and S2, which pertain to the zinc-tellurite set, also contain 2 mol% of Pb and Ge, respectively. Their respective bandwidths were 63 nm and 66 nm, and their lifetimes resulted to be  $3.3 \pm 0.2$  and  $2.9 \pm 0.2$  ms. The corresponding calculated quantum efficiencies resulted to be 94% and 83%. Similar values of lifetimes and quantum efficiencies were found for the other samples.

Near-infrared to visible upconversion upon CW excitation at 976 nm has been observed in all the zinc tellurite samples, even at low excitation powers ( $\approx 1 \text{ mW}$ ) indicating

TABLE VII. – *Molar composition of investigated erbium-doped tellurite glasses* [91, 162].

| Sample | TeO <sub>2</sub> | Na <sub>2</sub> O | ZnO | WO <sub>3</sub> | PbO | GeO <sub>2</sub> | Er <sub>2</sub> O <sub>3</sub> |
|--------|------------------|-------------------|-----|-----------------|-----|------------------|--------------------------------|
| V1     | 60               | 15                |     | 25              |     |                  | 0.05                           |
| V2     | 60               | 15                |     | 25              |     |                  | 0.5                            |
| V3     | 60               | 15                |     | 25              |     |                  | 1                              |
| V4     | 60               | 15                |     | 25              |     |                  | 1.5                            |
| V5     | 60               | 15                |     | 25              |     |                  | 2                              |
| S1     | 75               | 10                | 12  |                 | 2   |                  | 1                              |
| S2     | 75               | 10                | 12  |                 |     | 2                | 1                              |
| N1     | 80               | 10                | 9   |                 |     |                  | 1                              |
| N2     | 80               | 9                 | 9   |                 |     |                  | 2                              |

that these glasses also have potential as efficient hosts for upconversion generation.

Planar waveguides were successfully obtained in both types of glass, by using Ag<sup>+</sup>-Na<sup>+</sup> ion-exchange; eutectic mixtures of AgNO<sub>3</sub>, KNO<sub>3</sub> and NaNO<sub>3</sub> salts were used to keep the process temperature lower than the transition temperature of the glasses. Characterization of the diffusion process shows that the diffusion depth clearly decreases with increasing Er<sup>3+</sup> concentration. Tungsten-tellurite glasses appear to be more convenient for IO device fabrication because of the shorter exchange times necessary to produce a single-mode waveguide at 1.5 μm [162]. This is due to the higher exchange temperature (330 °C instead of 280 °C), made possible by the higher transition temperature of this glass ( $T_g = 356$  °C) with respect to zinc-tellurite glass ( $T_g = 290$  °C). Both types of glasses, on the whole, exhibit modal and spectroscopic characteristics that, even with their pros and cons, make them quite promising for the development of broad-band integrated optical amplifiers.

## 9. – Microspherical lasers

In dielectric spheres light can be guided through high- $Q$  whispering-gallery-modes (WGMs) with a unique combination of strong temporal and spatial confinement of light. Glass microspheres are therefore of interest for a large number of applications as cavity quantum electrodynamics, nonlinear optics, photonics, and chemical or biological sensing [190]. After the early works of Garret *et al.* [191] and the works on Morphology Dependent Resonances (MDRs) and lasing effects in droplets during the 1980's [192], rare-earth-doped glass microsphere lasers recently became a subject of numerous studies and have been demonstrated as potentially compact laser sources [193, 194]. Figure 23 shows the up-converted green light propagating at the surface of an erbium-doped glass microsphere, upon excitation by a laser diode emitting at 980 nm through a half-taper fibre (not visible in the photo) for evanescent-field coupling. The microsphere is glued to the end of an optical fibre for easy handling.

A microspherical laser based on Er<sup>3+</sup>/Yb<sup>3+</sup> co-doped phosphate glass, optically pumped at 1480 nm, with emission at around 1550 nm, was demonstrated [195]. Interesting effects on the laser emission were noticed, due to the interaction between the WGM modes of the glass sphere and an external metal mirror. Johnson [196] presented a theoretical treatment of the MDRs of a dielectric sphere in close proximity to a surface of infinite conductivity and calculated the changes of the locations and widths of the

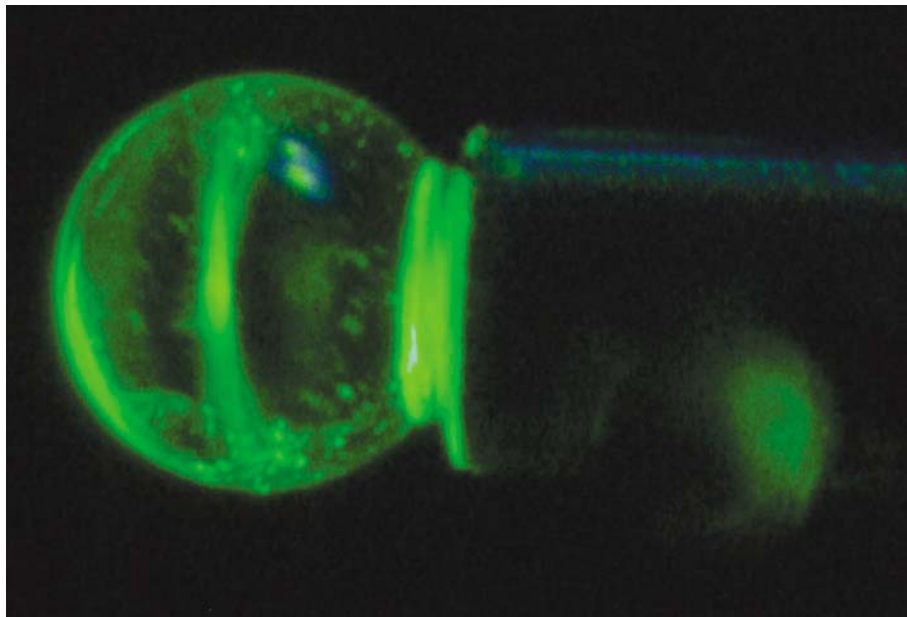


Fig. 23. – Magnified image of a microspherical resonator ( $2R \cong 150 \mu\text{m}$ ) in  $\text{Er}^{3+}$ -doped glass, where the up-converted light propagating in whispering gallery modes is clearly visible.

resonances as the sphere approaches the surface. We decided to further investigate this phenomenon and we analysed both the wavelength and the intensity of the emitted signal of a microspherical laser as a function of the distance from a silver or a gold mirror.

The phosphate glass used was an  $\text{Er}^{3+}/\text{Yb}^{3+}$  co-doped phosphate glass (Schott IOG-2) doped with 2% weight of  $\text{Er}_2\text{O}_3$  and co-doped with 3% weight of  $\text{Yb}_2\text{O}_3$ . Though the use of ytterbium co-doping is traditionally associated to 980 nm pumping wavelength, we chose instead 1480 nm as the pumping wavelength, in order to obtain a good overlap between the pump and the laser mode volumes in the microsphere. Ytterbium ions were used only to reduce some of the possible drawbacks of a very high erbium concentration ( $1.7 \cdot 10^{20}$  ions/cm<sup>3</sup>), like self-pulsing or concentration quenching [197].

Spheres were produced by fusion of glass powders with a microwave plasma torch. Powders were injected axially and melt when passing through the flame, superficial tension forces giving them their spherical form. Free spheres with diameters in the range 10 to 200  $\mu\text{m}$  were collected a few centimetres below. They were then glued to a stretched tip of an optical fibre ( $\sim 20 \mu\text{m}$  in diameter), which in turn was mounted on a submicrometer translational stage.

To excite high- $Q$  WGMs, light has to be launched from a phase-matched evanescent wave of an adjacent waveguide such as an angle polished or a tapered fibre or a prism under total internal reflection [198]. We used a single half-fibre-taper, which couples the pump light in the microsphere and—at the same time—allows coupling the fluorescence or laser light out of the microsphere. This half-taper was obtained by heating and stretching a standard telecommunication fibre until breaking. The drawn length was typically 850  $\mu\text{m}$ , and the taper end was reduced down to 1.5  $\mu\text{m}$  in diameter. The experimental set-up is sketched in fig. 24(a). The pump is a laser diode (maximum power

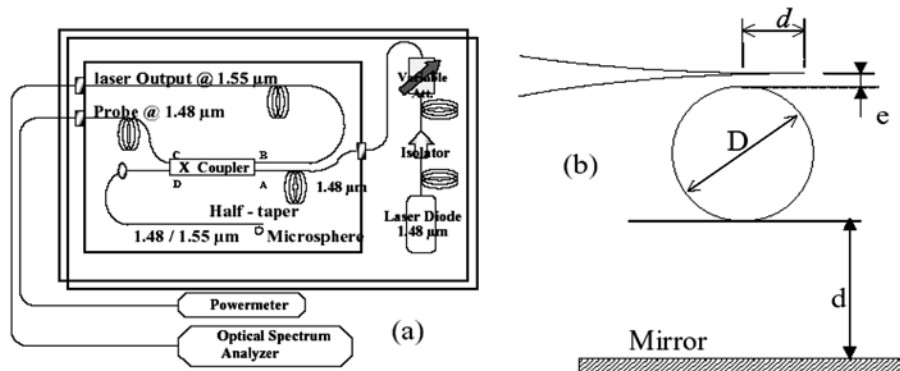


Fig. 24. – (a) Experimental set-up and (b) geometry of the coupling between the microsphere resonator and a metallic mirror.

1 W) operating around  $1.48 \mu\text{m}$ . A WDM X-coupler at  $1.48\text{--}1.55 \mu\text{m}$  allowed us to use the same fibre to pump and to collect the fluorescence or the laser signal. This latter was analyzed with a  $70 \text{ pm}$  resolution Optical Spectrum Analyzer (OSA). For the experiment with an external cavity, the metallic flat mirror was mounted on a microtranslational stage below the micro-sphere (fig. 24(b)).

For any sphere diameter, the optical spectrum of the laser below the threshold showed an enhancement of the fluorescence intensity and a higher peak density than those obtained coupling light with a prism, as demonstrated in a previous paper [199]. More modes can thus be excited in the sphere even above threshold. The inset of fig. 25 shows WGMs laser spectra for an isolated microsphere ( $d \gg D$ ) with a diameter  $D \sim 70 \mu\text{m}$ . Peak laser emission is obtained around  $1601 \text{ nm}$ , corresponding to a rather large gap  $e$

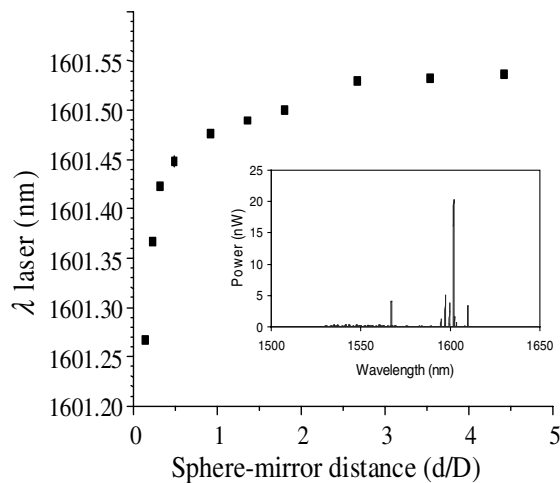


Fig. 25. – Lasing wavelength *vs.* relative sphere-to-mirror distance ( $d$  is the distance;  $D$  is the diameter of the sphere) around  $1601 \text{ nm}$ . Inset shows the multimode laser effect with the peak at  $1601 \text{ nm}$  for the isolated sphere ( $D \sim 70 \mu\text{m}$ ).

and a low pumping ratio. For a lower gap value, associated to a higher pumping ratio, we obtained laser effects at lower wavelengths [200].

Several papers have been written on WGMs or MDRs, but most of the research has focused on cases in which the sphere can be considered to be isolated, *i.e.* there are no strong perturbing effects from other nearby particles or surfaces. The WGMs of a sphere resting on a surface or with close neighbouring particles are also of theoretical and practical interest [199]. Johnson's theoretical treatment [196] of the MDRs of a dielectric sphere near a plane of infinite conductivity examines how the locations and widths of the resonances change as the sphere approaches the surface. If a sphere of diameter  $D$  is initially located at a distance  $d$  that is more than approximately  $2D/3$  away from the point of contact with the conducting plane, the resonances will have the same locations and widths as they do in an isolated sphere. Then, as the sphere is brought closer to and eventually in contact with the surface, the locations and widths of the resonances change. Most of the change in location and width occurs when the sphere is quite close to the conducting plane. Approximately 90% of the total resonance shift occurs when the distance from the point of contact is less than 0.05 of the diameter of the sphere.

In our experiments we used a silver or gold mirror with no dielectric coating over the reflective surface. This seems to be the closest approximation to the idealized case of the perfect mirror of infinite conductivity for which the method of images is strictly valid [199]. At this point, it is important to say that with our experimental set-up, we cannot go closer to the mirror than  $d = 3.5 \mu\text{m}$ . This means that, since our typical size of sphere is  $D \sim 70 \mu\text{m}$ ,  $d_{\text{min}}/D = 0.05$  and therefore we could not explore the zone where Johnson predicted 90% of the effect. We noticed, however, an influence of the mirror on both fluorescence and laser lines for distances up to  $2.5 \times D$ . Under the coupling conditions producing laser emission around 1600 nm, we moved the mirror from  $d = 175 \mu\text{m}$  to  $d = 7 \mu\text{m}$ . Correspondingly, we observed a line shift of almost 0.3 nm towards the lower wavelength, as shown in fig. 25, associated to an enhancement of the intensity [14]. For a lower wavelength, moving the mirror closer to the microsphere induced the same "blue shift", but also caused the laser extinction while increasing the threshold [200].

## 10. – Conclusions and perspectives

Photoluminescence properties of rare-earth-doped (RED) glasses are a key factor for the development of some optical components, like integrated optical amplifiers, whose characteristics are critical for achieving the flat and broad-band optical gain that seems needed in future communication systems. RED glasses are also fundamental for the development of several kinds of lasers, both in massive and integrated optics format. Erbium-doped waveguide amplifiers (EDWAs), based on  $\text{Er}^{3+}$ - or  $\text{Er}^{3+}/\text{Yb}^{3+}$ -doped glasses are already exhibiting high performances: net gains higher than 4 dB/cm and 0.15 dB/mW have been demonstrated in different oxide glasses, and commercially available devices include  $1 \times 4$  and  $1 \times 8$  amplified splitters/combiners, where the gain produced by the amplifier compensates the losses intrinsic to the splitting function. The search for more and more efficient compositions and guiding structures, however, is still going on. In fact, while the silica-based  $\text{Er}^{3+}$ -doped fibre amplifiers have driven the revolution in the transmission capacity of optical communication systems, further bandwidth growth will require the exploitation of new materials.

The investigation of photoluminescence properties of the RED glasses by absorption, emission, Raman and Brillouin spectroscopic techniques allowed us to increase more and

more our knowledge of their basic properties and to address the research of new materials. A few examples have been reported here, concerning glass families of great potential interest for optical communications systems. A first class is represented by SiO<sub>2</sub>-HfO<sub>2</sub> binary systems: Er<sup>3+</sup>-doped sol-gel planar waveguides have shown high quantum efficiency and  $\approx 50$  nm FWHM bandwidth around 1.53  $\mu$ m. A second class is constituted by soda-lime-alumino-silicate glasses, that combine the very good chemical durability of silicates and the easy waveguide fabrication process by ion exchange with the better spectroscopic properties induced by the presence of a relatively high percentage of aluminium. An increase up to 60% of the effective fluorescence bandwidth was achieved, and a high value of quantum efficiency was calculated for these glasses. Finally, Er<sup>3+</sup>-doped tellurite glasses turned out to be worth of more attention, due to the broad-band emission and high emission cross-section, which can allow one to achieve higher and flatter gain than in other oxide glasses. A major problem, however, remain to be solved in tellurite glasses, namely how to efficiently manufacture channel waveguides.

We can conclude that, besides their other significant properties, rare-earth elements are of great importance in the field of optics and that there is a continuous attempt of exploiting their photoluminescence properties for the development of novel glasses, in particular aiming at the production of higher-performance broad-band integrated optical amplifiers.

\* \* \*

We would like to thank a number of colleagues who have been collaborating with us since many years: S. BERNESCHI, M. BRENCI, R. CALZOLAI, F. COSI, G. NUNZI CONTI, S. PELLI (IFAC CNR, Firenze), P. BASSI (University of Bologna), C. ARMELLINI, A. CHIAPPINI, A. CHIASERA, Y. JESTIN (IFN CNR, Trento), M. MATTARELLI, M. MONTAGNA, E. MOSER, C. TOSELLO (University of Trento), M. BETTINELLI, A. SPEGHINI (University of Verona), P. FÉRON (ENSSAT - Laboratoire d'Optronique, Lannion), R. R. GONÇALVES (Universidade de São Paulo, Brasil), C. DUVERGER (Université du Maine, Le Mans), A. MONTEIL (Université d'Angers), E. DUVAL (Université Claude Bernard, Lyon).

## REFERENCES

- [1] NEWTON HARVEY N., *A History of Luminescence: From the Earliest Times Until 1900* (Dover Phoenix Editions) 2005.
- [2] JAMES F. A. J. L., *Notes and Records R. Soc. London*, **38** (1983) 79-107.
- [3] [http://www.metcer.ameslab.gov/research/Complex\\_Materials/Complex\\_Materials.html](http://www.metcer.ameslab.gov/research/Complex_Materials/Complex_Materials.html).
- [4] DESURVIRE E., *Erbium-Doped Fiber Amplifiers, Principles and Applications* (John Wiley, New York) 1994.
- [5] DIGONNET M. J. F., *Rare-Earth-Doped Fiber Lasers and Amplifiers* (Marcel Dekker, Inc.) 2001.
- [6] LI T., *IEEE Proc.*, **81** (1993) 1568-1579.
- [7] FUKUCHI K., KASAMATSU T., MORIE M., OHHIRA R., ITO T., SEKIYA K., OGASAHARA D. and ONO T., *Proceedings of the Optical Fiber Communication Conference, OFC-2001*, Vol. 4 (2001) PD24-1 - PD24-3.
- [8] SNITZER E., *Phys. Rev. Lett.*, **7** (1961) 444.
- [9] KOESTER C. J. and SNITZER E., *Appl. Opt.*, **3** (1964) 1182-1186.
- [10] YAJIMA H., KAWASE S. and SEKIMOTO Y., *Appl. Phys. Lett.*, **21** (1972) 407-409.
- [11] SARUWATARI M. and IZAWA T., *Appl. Phys. Lett.*, **24** (1974) 603-605.

- [12] See for instance: DIGONNET M. J. F. (Editor), *Selected Papers on Rare-Earth-Doped Fiber Laser Sources and Amplifiers*, Vol. MS **37** (SPIE Press, SPIE, Bellingham) 1992.
- [13] JUDD B. R., *Phys. Rev.*, **127** (1962) 750-761.
- [14] OFELT G. S., *J. Chem. Phys.*, **37** (1962) 511-520.
- [15] VAN DIJK J. M. F. and SCHUURMANS M. F. H., *J. Chem. Phys.*, **78** (1983) 5317-5323.
- [16] LAYNE C. B., LOWDERMILK W. H. and WEBER M. J., *Phys. Rev. B*, **16** (1977) 10-21.
- [17] PATEK K., *Glass lasers* (Ilife Books, London) 1970.
- [18] REISFELD R. and JORGENSEN C. K., *Lasers and Excited States of Rare Earths* (Springer, Berlin) 1977.
- [19] WEBER M., *Handbook of Laser Science and Technology* (CRC, Boca Raton) 1986-1987.
- [20] GAN F., *Laser Materials* (World Scientific, Singapore) 1995.
- [21] BECKER P. C., OLSSON, N. A. and SIMPSON J. R., *Erbium Doped Fibre Amplifiers: Fundamentals and Technology* (Academic Press, San Diego) 1999.
- [22] EBENDORFF-HEIDPRIEM H. and EHRT D., *Glastech. Ber. Glass. Technol.*, **71** (1998) 289-299.
- [23] YEN M. W. and SELZER P. M. (Editors), *Laser Spectroscopy of Solids* (Springer, Berlin) 1981.
- [24] ZSCHOKKE J. (Editor), *Optical Spectroscopy of Glasses* (Reidel, Dordrecht) 1986.
- [25] DEMTRÖDER W., *Laser Spectroscopy, Basic Concepts and Instrumentation* (Springer, Berlin) 1996.
- [26] DI BARTOLO B., *Optical Interaction in Solids* (John Wiley & Sons Inc., New York) 1967.
- [27] MENZEL R., *Photonics Linear and Nonlinear Interactions of Laser Light and Matter* (Springer, Berlin) 2001.
- [28] PELLI S. and RIGHINI G. C., in *Advances in Integrated Optics*, edited by MARTELUCCI S., CHESTER A. N. and BERTELOTTI M. (Plenum Press, New York) 1994, pp. 1-20.
- [29] TIEN P. K., *Rev. Mod. Phys.*, **49** (1997) 361.
- [30] FERRARI M., GONELLA F., MONTAGNA M. and TOSELLO C., *J. Raman Spectrosc.*, **27** (1996) 793-797.
- [31] DUVERGER C., TURRELL S., BOUZAOUI M., TONELLI F., MONTAGNA M. and FERRARI M., *Philos. Mag. B*, **77** (1998) 363-372.
- [32] MENDES S. B. and SAAVEDRA S. S., *Opt. Express*, **4** (1999) 449-456.
- [33] YAMAMOTO K. and ISHIDA H., *Vibrational Spectroscopy*, **8** (1994) 1-36.
- [34] GRATAN K. T. V. and MEGGIT B. T., *Optical Fiber Sensors Technology* (Chapman & Hall, London) 1995.
- [35] LAVERS C. R., ITOH K., WU S. C., MURABAYASHI M., MAUCLINE I., STEWART G. and STOUT T., *Sensors and Actuators B*, **69** (2000) 85-95.
- [36] LIN J., *Trends Anal. Chem.*, **19** (2000) 541-552.
- [37] HOCDE S., BOUSSARD-PLEDEL C., FONTENEAU G., LECOQ D., MA H. L. and LUCAS J., *J. Non-Cryst. Solids*, **274** (2000) 17-22.
- [38] STONE B. T. and BRAY K. L., *J. Non-Cryst. Solids*, **197** (1996) 136-144.
- [39] DUVERGER C., MONTAGNA M., ROLLI R., RONCHIN S., ZAMPEDRI L., FOSSI M., PELLI S., RIGHINI G. C., MONTEIL A., ARMELLINI C. and FERRARI M., *J. Non-Cryst. Solids*, **280** (2001) 261-268.
- [40] SLOOFF L. H., DE DOOD M. J. A., VAN BLAADEREN A. and POLMAN A., *J. Non-Cryst. Solids*, **296** (2001) 158-164.
- [41] MARQUES A. C., ALMEIDA R. M., CHIASERA A. and FERRARI M., *J. Non-Cryst. Solids*, **322** (2003) 272-277.
- [42] BENOIT V., BHAKTHA S. N., BOULARD B., CHAUSSEMENT S., CHIAPPINI A., CHIASERA A., DUVAL E., ETIENNE S., FERRARI M., GAILLARD-ALLEMAND B., JESTIN Y., MATTARELLI M., MONTAGNA M., MONTEIL A., MOSER E., NUNZI CONTI G., PELLI S., PORTALES H., RAO D. N., RIGHINI G. C. and VISHUNUBHATLA K. C., *Proc. SPIE*, **5723** (2005) 79-88.
- [43] HOUDE-WALTER S. N., PETERS P. M., STEBBINS J. F. and ZENG Q., *J. Non-Cryst. Solids*, **286** (2001) 118-131.

- [44] MANDEVILLE C. W., WEBSTER J. D., RUTHERFORD M. J., TAYLOR B. E., TIMBAL A. and FAURE K., *Am. Mineral.*, **87** (2002) 813-821.
- [45] KING P. L., VENNEMANN T. W., HOLLOWAY J. R., HERVIG R. L., LOWENSTERN J. B. and FORNERIES J. F., *Am. Mineral.*, **87** (2002) 1077-1089.
- [46] HEIGL J. J., BELL M. F. and WHITE J. U., *Anal. Chem.*, **19** (1947) 293-298.
- [47] POPE E. J. A. and MACKENZIE J. D., *J. Non-Cryst. Solids*, **106** (1988) pp. 236-241.
- [48] DAVIS K. M. and TOMOZAWA M., *J. Non-Cryst. Solids*, **201** (1996) 177-198.
- [49] INNOCENZI P., *J. Non-Cryst. Solids*, **316** (2003) 309-319.
- [50] BREDOL M., LEERS D., BOSSELAAR L. and HUTJENS M., *J. Lightwave Technol.*, **8** (1990) 1536-1540.
- [51] AUZEL F., *Chem. Rev.*, **104** (2004) 139-173.
- [52] POTTER B. G. jr. and SINCLAIR M. B., *J. Electroceramics*, **2-4** (1998) 295-308.
- [53] KENYON A. J., *Prog. Quantum Electron.*, **26** (2002) 225-284.
- [54] MAURICE E., MONNOM G., DUSSARDIER B., SAÏSSY A., OSTROWSKY D. B. and BAXTER G. W., *Appl. Opt.*, **34** (1995) 8019-8025.
- [55] DOS SANTOS P. V., DE ARAUJO M. T., GIUVEIA-NETO A. S., MEDEIROS NETO J. A. and SOMBRA A. S. B., *Appl. Phys. Lett.*, **73** (1998) 578-580.
- [56] TRUKHIN A. N., JANSON J. L. and TRUHINS K., *J. Non-Cryst. Solids*, **347** (2004) 80-86.
- [57] ALOMBERT-GOGET G., GAUMER N., OBRIOT J., RAMMAL A., CHAUSSÉDENT S., MONTEIL A., PORTALES H., CHIASERA A. and FERRARI M., *J. Non-Cryst. Solids*, **351** (2005) 1754-1758.
- [58] CHIASERA A., FERRARI M., MATTARELLI M., MONTAGNA M., PELLI S., PORTALES H., ZHENG J. and RIGHINI G. C., *Opt. Mater.*, **27** (2005) 1743-1747.
- [59] CAMPOSTRINI R., CARTURAN G., FERRARI M., MONTAGNA M. and PILLA O., *J. Mater. Res.*, **7** (1992) 745-753.
- [60] KASHA M., *Discuss. Faraday Soc.*, **9** (1950) 14-19.
- [61] PUCKER G., GATTERER K., FROTZER H. P., BETTINELLI M. and FERRARI M., *Phys. Rev. B*, **53** (1996) 6225-6234.
- [62] HUBER D. L., *Phys. Rev. B*, **31** (1985) 6070-6071.
- [63] HUBER D. L., *Mol. Cryst. Liq. Cryst.*, **291** (1996) 17-21.
- [64] KITAMURA T., TAKAHASHI Y., YAMANAKA T. and UCHIDA K., *J. Lumin.*, **48&49** (1991) 373-376.
- [65] ZAMPEDRI L., FERRARI M., ARMELLINI C., VISINTAINER F., TOSELLO C., RONCHIN S., ROLLI R., MONTAGNA M., CHIASERA A., PELLI S., RIGHINI G. C., MONTEIL A., DUVERGER C. and GONÇALVES R. R., *J. Sol-Gel Sci. Technol.*, **26** (2003) 1033-1036.
- [66] MONTAGNA M., in *Handbook of Sol Gel Science and Technology*, edited by SAKKA S., Vol. II (Kluwer Academic Publishers, Boston) 2005, pp. 91-117.
- [67] WOODWARD L. A., *Raman Spectroscopy* (Plenum Press, New York) 1967.
- [68] FERRARI M., MONTAGNA M., RONCHIN S., ROSSI F. and RIGHINI G. C., *Appl. Phys. Lett.*, **75** (1999) 1529-1531.
- [69] BARNES W. L., LAMING R. I., TARBOX E. J. and MORKEL P. R., *IEEE J. Quantum Electron.*, **27** (1991) 1004-1010.
- [70] DUVAL E., BOUKENTER A. and CHAMPAGNON B., *Phys. Rev. Lett.*, **56** (1986) 2052-2055.
- [71] DUVAL E., *Phys. Rev. B*, **46** (1992) 5795-5797.
- [72] MONTAGNA M. and DUSI R., *Phys. Rev. B*, **52** (1995) 10080-10089.
- [73] CECCATO R., DAL MASCHIO R., GIALANELLA S., MARIOTTO G., MONTAGNA M., ROSSI F., FERRARI M., LIPINSKA-KALITA K. E. and OHKI Y., *J. Appl. Phys.*, **90** (2001) 2522-2527.
- [74] TIKHOMIROV V. K., FURNISS D., SEDDON A. B., REANEY I. M., BEGGIORA M., FERRARI M., MONTAGNA M. and ROLLI R., *Appl. Phys. Lett.*, **8** (2002) 1937-1939.
- [75] MONTAGNA M., MOSER E., VISINTAINER F., FERRARI M., ZAMPEDRI L., MARTUCCI A., GUGLIELMI V. and IVANDA M., *J. Sol-Gel Sci. Technol.*, **26** (2003) 241-244.
- [76] IVANDA M., HOHL A., MONTAGNA M., MARIOTTO G., FERRARI M., CRNJAK OREL. Z., TURKOVIĆ A. and FURIĆ K., *J. Raman Spectrosc.*, **37** (2006) 161-165.

- [77] FERRARI M., in *Handbook of Sol Gel Science and Technology*, edited by SAKKA S., Vol. II (Kluwer Academic Publishers, Boston) 2005, pp. 359-388.
- [78] FERRARI M., ARMELLINI C., RONCHIN S., ROLLI R., DUVERGER C., MONTEIL A., BALU N. and INNOCENZI P., *J. Sol Gel Sci. Technol.*, **19** (2000) 569-572.
- [79] BRINKER C. J. and SCHERER G. W., *Sol-Gel Science: The Physics and Chemistry of Sol-Gel Processing* (Academic Press) 1990.
- [80] GOTTARDI V., GUGLIELMI M., BERTOLUZZA A., FAGNANO C. and MORELLI M. A., *J. Non-Cryst. Solids*, **63** (1984) 71-80.
- [81] DIL J. D., *Rep. Prog. Phys.*, **45** (1982) 285-334.
- [82] SHEN G.-Q., UTEGULOV Z. N., WICKSTED J. P. and MIAN S. M., *Phys.-Chem. Glasses*, **43** (2002) 73-79.
- [83] MONTAGNA M., FERRARI M., ROSSI F., TONELLI F. and TOSELLO C., *Phys. Rev. B*, **58** (1998) R547-R550.
- [84] CHIASERA A., MONTAGNA M., ROSSI F. and FERRARI M., *J. Appl. Phys.*, **94** (2003) 4876-4881.
- [85] CHIASERA A., MONTAGNA M., MOSER E., ROSSI F., TOSELLO C., FERRARI M., ZAMPEDRI L., CAPONI S., GONÇALVES R. R., CHAUSSEMENT S., MONTEIL A., FIORETTO D., BATTAGLIN G., GONELLA F., MAZZOLDI P. and RIGHINI G. C., *J. Appl. Phys.*, **94** (2003) 4882-4889.
- [86] MCCUMBER D. E., *Phys. Rev.*, **134** (1964) A229-A306.
- [87] MINISCALCO W. J. and QUIMBY R. S., *Opt. Lett.*, **16** (1991) 258-260.
- [88] PAYNE S. A., CHASE L. L., SMITH L. K., KWAY W. L. and KRUPKE W. F., *IEEE J. Quantum Electron.*, **28** (1992) 2619-2630.
- [89] QUIMBY R. S., *J. Appl. Phys.*, **92** (2002) 180-187.
- [90] DIGONNET M. J. F., MURPHY-CHUTORIAN E. and FALQUIER D. G., *IEEE J. Quantum Electron.*, **38** (2002) 1629-1637.
- [91] ROLLI R., MONTAGNA M., CHAUSSEMENT S., MONTEIL A., TIKHOMIROV V. K. and FERRARI M., *Opt. Mater.*, **21** (2003) 743-748.
- [92] DESURVIRE E. and SIMPSON J. R., *Opt. Lett.*, **15** (1990) 547-549.
- [93] GUY S., BIGOT L., VASILIEF I., JACQUIER B., BOULARD B. and GAO Y., *J. Non-Cryst. Solids*, **336** (2004) 165-172.
- [94] WEBER M. J., MYERS J. D. and BLACKBURN D. H., *J. Appl. Phys.*, **52** (1981) 2944-2949.
- [95] FENG X., TANABE S. and HANADA T., *J. Appl. Phys.*, **89** (2001) 3560-3567.
- [96] TANABE S., *J. Non-Cryst. Solids*, **259** (1999) 1-9.
- [97] CHEN B. J., RIGHINI G. C., BETTINELLI M. and SPEGHINI A., *J. Non-Cryst. Sol.*, **322** (2003) 319-323.
- [98] MORRISON C. A. and LEAVITT R. P., *J. Chem. Phys.*, **71** (1979) 2366-2374.
- [99] LEAVITT R. P. and MORRISON C. A., *J. Chem. Phys.*, **73** (1980) 749-757.
- [100] CARNALL W. T., FIELDS P. R. and RAJNAK K., *J. Chem. Phys.*, **49** (1968) 4424-4442.
- [101] GSCHNEIDNER K. A. and EYRING L., *Handbook on the Physics and Chemistry of Rare Earth*, Vol. **25** (Elsevier, Amsterdam) 1998.
- [102] WEBER M. J., *Phys. Rev.*, **157** (1967) 262.
- [103] CONDON E. U. and SHORTLEY G. H., *The Theory of Atomic Spectra* (University Press, Cambridge) 1963.
- [104] AUZEL F., *J. Alloys Compounds*, **380** (2004) 9-14.
- [105] DAI S. X., YANG J. H., WEN L., HU L. and JIANG Z., *J. Lumin.*, **104** (2003) 55-63.
- [106] AUZEL F., MEICHENIN D., MENDORIOZ A., BALDA R. and FERNANDEZ J., *J. Lumin.*, **72-74** (1997) 152-154.
- [107] REDDY K. T. R., SLIFKIN M. A. and WEISS A. M., *Opt. Mater.*, **16** (2001) 87-91.
- [108] IUPAC Compendium of Chemical Terminology, 2nd Edition (1997) <http://www.iupac.org/publications/compendium/>
- [109] MATTARELLI M., MONTAGNA M., CHIASERA A., FERRARI M., ZAMPEDRI L., RIGHINI G. C., FORTES L. M., GONÇALVES M. C., SANTOS L. F. and ALMEIDA R. M., *Europhys. Lett.*, **71** (2005) 394-399.
- [110] FENG X., TANABE S. and HANADA T., *J. Am. Ceram. Soc.*, **84** (2001) 165-171.

- [111] AUZEL F., BALDACCHINI G., LAVERSENNE L. and BOULON G., *Opt. Mater.*, **24** (2003) 103-109.
- [112] NOGINOV M. A., *Appl. Opt.*, **36** (1997) 4153-4158.
- [113] STOKOWSKI S. E., SAROYAN R. A. and WEBER M. J., Lawrence Livermore National Laboratory Report M-095 (1981) Rev. 2.
- [114] QUIMBY R. S., MINISCALCO W. J. and THOMPSON B., *J. Appl. Phys.*, **76** (1994) 4472-4478.
- [115] SNOEKS E., VAN DEN HOVEN G. N. and POLMAN A., *IEEE J. Quantum Electron.*, **32** (1996) 1680-1684.
- [116] MYSLINSKI P., NGUYEN D. and CHROSTOWSKI J., *J. Lightwave Technol.*, **15** (1997) 112-120.
- [117] AUZEL F. and GOLDNER P., *Opt. Mater.*, **16** (2001) 93-103.
- [118] VALLÉS J. A., LÁZARO J. A. and REBOLLEDO M. A., *IEEE J. Quantum Electron.*, **38** (2002) 318-323.
- [119] ZHOU Y., LAM Y. L., WANG S. S., LIU H. L., KAM C. H. and CHAN Y. C., *Appl. Phys. Lett.*, **71** (1997) 587-589.
- [120] ROCCA F., FERRARI M., KUZMIN A., DAL DOSSO N., DUVERGER C. and MONTI F., *J. Non-Cryst. Solids*, **293-295** (2001) 112-117.
- [121] CHIASERA A., MONTAGNA M., ROLLI R., RONCHIN S., PELLI S., RIGHINI G. C., GONÇALVES R. R., MESSADDEQ Y., RIBEIRO S. J. L., ARMELLINI C., FERRARI M. and ZAMPEDRI L., *J. Sol-Gel Sci. Technol.*, **26** (2003) 943-946.
- [122] MONTEIL A., CHAUSSEDENT S., ALOMBERT-GOGET G., GAUMER N., OBRIOT J., RIBEIRO S. J. L., MESSADDEQ Y., CHIASERA A. and FERRARI M., *J. Non-Cryst. Solids*, **348** (2004) 44-50.
- [123] YABLONOVITCH E., *Phys. Rev. Lett.*, **58** (1987) 2059-2062.
- [124] JOANNOPOULOS J. D., MEADE R. D. and WINN J. N., *Photonic Crystals, Molding the Flow of Light* (Princeton University Press) 1995.
- [125] SOUKOULIS C. M., *Photonic Crystals and Light Localization in the 21st Century* (Kluwer, Dordrecht) 2001.
- [126] PURCELL E. M., *Phys. Rev.*, **69** (1946) 681-681.
- [127] GOY P., RAIMOND J. M., GROSS M. and HAROCHE S., *Phys. Rev. Lett.*, **50** (1983) 1903-1906.
- [128] RIGNEAULT H. and MONNERET S., *Phys. Rev. A*, **54** (1996) 2356-2368.
- [129] URBACH H. P. and RIKKEN G. L. A., *Phys. Rev. A*, **57** (1998) 3913.
- [130] VREDENBERG A. M., HUNT N. E. J., SCHUBERT E. F., JACOBSON D. C., POATE J. M. and ZYDZIK G. J., *Phys. Rev. Lett.*, **71** (1993) 517-520.
- [131] VOS W. L. and POLMAN A., *MRS Bulletin*, **26** (2001) 642.
- [132] JACQUIER B., LEBRASSEUR E., GUY S., BELAROUCI A. and MENCHINI F., *J. Alloys Comp.*, **303-304** (2000) 207.
- [133] BELLESSA J., RABASTE S., PLENET J. C., DUMAS J., MUGNIER J. and MARTY O., *Appl. Phys. Lett.*, **79** (2001) 2142-2144.
- [134] RABASTE S., BELLESSA J., BRIOUDE A., BOVIER C., PLENET J. C., BRENIER R., MARTY O., MUGNIER J. and DUMAS J., *Thin Solid Films*, **416** (2002) 242-247.
- [135] ZAMPEDRI L., TOSELLO C., PORTALES H., MONTAGNA M., MATTARELLI M., CHIAPPINI A., RIGHINI G. C., PELLI S., NUNZI-CONTI G., MARTINO M., PORTAL S., MARQUES A. C., ALMEIDA R. M., JESTIN Y., FERRARI M. and CHIASERA A., *Appl. Surface Sci.*, **248** (2005) 3-7.
- [136] ALMEIDA R. M. and PORTAL S., *Curr. Opin. Solid State & Mater. Sci.*, **7** (2003) 151-157.
- [137] CHEN K. M., SPARKS A. W., LUAN H. C., LIM D. R., WADA K. and KIMERLING L. C., *Appl. Phys. Lett.*, **75** (1999) 3805.
- [138] BECKER E. V., ROMANOVA E. A., MELNIKOV L. A., SINICHKIN YU. P., SOROKIN V. YU., ELTERMAN I. V., SKIBINA N. B., BELOGLAZOV V. I., SHERBAKOV A. V., BATURIN V. V., BEMSON T. M. and SEWELL P., *IEEE Proc. LEOS 2001*, **2** (2001) 705-706.
- [139] MILLER G. H., MOSES E. I. and WUEST C. R., *Opt. Eng.*, **43** (2004) 2841-2853.

- [140] JEONG Y., SAHU J., PAYNE D. and NILSSON J., *Opt. Express*, **12** (2004) 6088-6092.
- [141] See, for instance, [http://www.ipgphotonics.com/html/90\\_1-20kw\\_mm\\_01070nm.cfm](http://www.ipgphotonics.com/html/90_1-20kw_mm_01070nm.cfm)
- [142] HAYDEN J. S. and NEUROTH N., in BACH H. and NEUROTH N. (Editors), *The Properties of Optical Glasses* (Springer Verlag, Berlin) 1998, pp. 308-324.
- [143] MORITO K. and TANAKA S., *Photon. Technol. Lett.*, **17** (2005) 1298-1300.
- [144] MEARS R. J., REEKIE L., JAUNCEY M. and PAYNE D. N., *Electron. Lett.*, **23** (1987) 1026-1028.
- [145] DESURVIRE E., SIMPSON J. R. and BECKER P. C., *Opt. Lett.*, **12** (1987) 888-890.
- [146] YEH C.-H., LEE C.-C. and CHI S., *Photon. Technol. Lett.*, **16** (2004) 1637-1639.
- [147] VORREAU P., KILPER D. C. and WHITE C. A., *Photon. Technol. Lett.*, **17** (2005) 1405-1407.
- [148] SEO H. S., CHUNG W. J. and AHN J. T., *Photon. Technol. Lett.*, **17** (2005) 1181-1183.
- [149] MENTZER M. A., *Principles of Optical Circuit Engineering* (Marcel Dekker, New York) 1990.
- [150] Look, for instance, at these web sites: [www.teemphotonics.com](http://www.teemphotonics.com), [www.inplane.com](http://www.inplane.com).
- [151] See for instance: SILFVAST W. T., *Laser Fundamentals* (Cambridge University Press, U.K.) 1998, Chapt. 3.
- [152] LUMHOLT O., BEMAS H., CHABLI A., CHAUMONT J., GRAND G. and VALETTE S., *Electron. Lett.*, **28** (1992) 2242-2243.
- [153] CHELNOKOV A. V., LOURTIOZ J.-M., BOUCAUD PH., BERNAS H., CHAUMONT J. and PLOWMAN T., *Electron. Lett.*, **31** (1995) 636-638.
- [154] CHRYSOU C. E., PITT C. W., CHANDLER P. J. and HOLE D. E., *IEE Proc.-Optoelectron.*, **145** (1998) 325-330.
- [155] KIK P. G. and POLMAN A., *J. Appl. Phys.*, **93** (2003) 5008-5012.
- [156] HONKANEN S., NAJAFI S. I., POYHONEN P., ORCEL G., WANG W. J. and CHROSTOWSKI J., *Electron. Lett.*, **27** (1991) 2167-2168.
- [157] CAMY P., ROMAN J. E., WILLEMS F. W., HEMPSTEAD M., VAN DER PLAATS J. C., PREL C., BEGUIN A., KOONEN A. M. J., WILKINSON J. S. and LERMINIAUX C., *Electron. Lett.*, **32** (1996) 321-323.
- [158] JIANG S., LUO T., HWANG B. C., NUNZI CONTI G., MYERS M., RHONEHOUSE D., HONKANEN S. and PEYGHAMBARIAN N., *Opt. Eng.*, **37** (1998) 3282-3286.
- [159] KEVORKIAN A., *Proc. SPIE*, **3289** (1998) 54-56.
- [160] RIGHINI G. C., BRENCI M., FORASTIERE M. A., PELLI S., RICCI G., NUNZI CONTI G., PEYGHAMBARIAN N., FERRARI M. and MONTAGNA M., *Philos. Mag. B*, **82** (2002) 721-734.
- [161] JOSE G., SORBELLO G., TACCHEO S., CIANCI E., FOGLIETTI V. and LAPORTA P., *J. Non-Cryst. Solids*, **322** (2003) 256-261.
- [162] NUNZI CONTI G., TIKHOMIROV V. K., BETTINELLI M., BERNESCHI S., BRENCI M., CHEN B., PELLI S., SPEGHINI A., SEDDON A. B. and RIGHINI G. C., *Opt. Eng.*, **42** (2003) 2805-2811.
- [163] PELLI S., BETTINELLI M., BRENCI M., CALZOLAI R., CHIASERA A., FERRARI M., NUNZI CONTI G., SPEGHINI A., ZAMPEDRI L., ZHENG J. and RIGHINI G. C., *J. Non-Cryst. Solids*, **345&346** (2004) 372-376.
- [164] KITAGAWA T., HATTORI K., SHUTO K., YASU M., KOBAYASHI M. and HORIGUCHI M., *Electron. Lett.*, **28** (1992) 1818-1819.
- [165] GHOSH R. N., SHMULOVICH J., KANE C. F., DE BARROS M. R. X., NYKOLAK G., BRUCE A. J. and BECKER P. C., *IEEE Photon. Technol. Lett.*, **8** (1996) 518-520.
- [166] ORIGNAC X., BARBIER D., DU X. M. and ALMEIDA R. M., *Appl. Phys. Lett.*, **69** (1996) 895-897.
- [167] MARTUCCI A., BRUSATIN G., GUGLIELMI M., STROHOFER C., FICK J., PELLI S. and RIGHINI G. C., *J. Sol-Gel Sci. Technol.*, **13** (1998) 535-539.
- [168] HUANG W., SYMS R. R. A., YEATMAN E. M., AHMAD M. M., CLAPP T. V. and OJHA S. M., *IEEE Photon. Technol. Lett.*, **14** (2002) 959-961.
- [169] ALMEIDA R. M., MORAIS P. J. and MARQUES A. C., *Philos. Mag. B*, **82** (2002) 707-719.
- [170] FICK J., MARTUCCI A. and GUGLIELMI M., *J. Sol-Gel Sci. Technol.*, **19** (2000) 573-576.

- [171] BEBBINGTON J., BARBAROSSA G., BONAR J. R. and AITCHINSON J. S., *Appl. Phys. Lett.*, **62** (1993) 337-339.
- [172] SNOEKS E., VAN DEN HOVEN G. N., POLMAN A., HENDRIKSEN B., DIEMEER M. B. J. and PRIOLO F., *J. Opt. Soc. Am. B*, **12** (1995) 1468-1474.
- [173] SERNA R., BALLESTEROS J. M., JIMÉNEZ DE CASTRO M., SOLIS J. and AFONSO C. N., *Appl. Phys.*, **84** (1998) 2352-2354.
- [174] CARICATO A. P., FERNANDEZ M., FERRARI M., LEGGIERI G., MARTINO M., MATTARELLI M., MONTAGNA M., RESTA V., ZAMPEDRI L., ALMEIDA R. M., CON M. C., FORTES L. and SANTOS L. F., *Mater. Sci. Eng. B*, **105** (2003) 65-69.
- [175] PÉREZ-CASERO R., GUTIÉRREZ-LLORENTE A., PONS-Y-MOLL O., SEILER W., DEFOURNEAU R. M., DEFOURNEAU D., MILLION E., PERRIÈRE E., GOLDNER P. and VIANA B., *J. Appl. Phys.*, **97** (2005) 054905.
- [176] OZKAN A. M. and MIGLIORE L., *Proc. SPIE*, **4978** (2003) 162-168.
- [177] KARNAKIS D. M., KNOWLES M. R. H., ALTY K. T., SCHLAF M. and SNELLING H. V., *Proc. SPIE*, **5718** (2005) 216-227.
- [178] OSELLAME R., TACCHEO S., CERULLO G., MARANGONI M., POLLI D., RAMPONI R., LAPORTA P. and DE SILVESTRI S., *Electron. Lett.*, **38** (2002) 964-965.
- [179] EBENDORFF-HEIEPRIEM H., *Opt. Mater.*, **25** (2004) 109-116.
- [180] SEBASTIANI S., NUNZI CONTI G., PELLI S., RIGHINI G. C., CHIASERA A., FERRARI M. and TOSELLO C., *Opt. Express*, **13** (2005) 1696-1701.
- [181] DI PASQUALE F. and ZOBOLI M., *J. Lightwave Technol.*, **11** (1993) 1565-1574.
- [182] CHRYSOSU, C. E., DI PASQUALE, F. and PITT, C. W., *IEEE J. Select. Topics Quantum Electron.*, **6** (2000) 114-121.
- [183] D'ORAZIO A., DE SARIO M., MESCIA L., PETRUZZELLI V., PRUDENZANO F., CHIASERA A., MONTAGNA M., TOSELLO C. and FERRARI M., *J. Non-Cryst. Solids*, **322** (2003) 278-283.
- [184] ZAMPEDRI L., RIGHINI G. C., PORTALES H., PELLI S., NUNZI CONTI G., MONTAGNA M., MATTARELLI M., GONCALVES R. R., FERRARI M., CHIASERA A., BOUZAOU M. and ARMELLINI C., *J. Non-Cryst. Solids*, **345&346** (2004) 580-584.
- [185] GONCALVES R. R., CARTURAN G., FERRARI M., ZAMPEDRI L., MONTAGNA M., PELLI S., RIGHINI G. C., RIBEIRO S. J. L. and MESSADDEQ Y., *Opt. Mater.*, **25** (2004) 131-140.
- [186] WONG S. F., PUN E. Y. B. and CHUNG P. S., *IEEE Photon. Technol. Lett.*, **14** (2002) 80-82.
- [187] HEHLEN M. P., COCKROFT N. J., GOSNELL T. R. and BRUCE A. J., *Phys. Rev. B*, **56** (1997) 9302-9318.
- [188] BERNESCHI S., BETTINELLI M., BRENCI M., NUNZI CONTI G., PELLI S., SEBASTIANI S., SILIGARDI C., SPEGHINI A. and RIGHINI G. C., *J. Non-Cryst. Solids*, **351** (2005) 1747-1753.
- [189] NUNZI CONTI G., TIKHOMIROV V. K., BETTINELLI M., BERNESCHI S., BRENCI M., CHEN B., PELLI S., SPEGHINI A., SEDDON A. B. and RIGHINI G. C., *Opt. Eng.*, **42** (2003) 2805-2811.
- [190] VAHALA K. J., *Nature*, **424** (2003) 839-846.
- [191] GARRET C. G. B., KAISER W. and LONG W. L., *Phys. Rev.*, **124** (1961) 1807.
- [192] BARBER P. W. and CHANG R. K., *Optical Effects Associated with Small Particles* (World Scientific, Singapore) 1988.
- [193] SANDOGHDAR V. S., TREUSSART F., HARE J., LEFÈVRE-SEGUIN V., RAIMOND J. M. and HAROCHE S., *Phys. Rev. A*, **54** (1996) 1777.
- [194] LISSILLOUR F., FERON P., DUBREUIL N., DUPRIEZ P., POULAIN M. and STEPHAN G., *Electron. Lett.*, **36** (2000) 1382.
- [195] RIGHINI G. C., ARNAUD C., BERNESCHI S., BETTINELLI M., BRENCI M., CHIASERA A., FERON P., FERRARI M., MONTAGNA M., NUNZI CONTI G., PELLI S., PORTALES H., SILIGARDI C., SPEGHINI A. and ZAMPEDRI L., *Opt. Mater.*, **27** (2005) 1711-1717.
- [196] JOHNSON B. R., *J. Opt. Soc. Am. A*, **11** (1994) 2055.
- [197] OHTSUKI T., HONKANEN S., NAJAFI S. I. and PEYGHAMBARIAN N., *J. Opt. Soc. Am. B*, **14** (1997) 1838.

- [198] ILCHENKO V. S., YAO X. S. and MALEKI L., *Opt. Lett.*, **24** (1999) 723.
- [199] LISSILLOUR F., MESSEGER D., STÉPHAN G. M. and FÉRON P., *Opt. Lett.*, **26** (2001) 1051.
- [200] ARNOUD C., BOUSTIMI M., FÉRON P., NUNZI CONTI G. and RIGHINI G., *SPIE Proc.*, **5333** (2004) 140.

# All-optical switching in rare-earth doped channel waveguide

Cid B. de Araújo and A. S. L. Gomes

*Departamento de Física, Universidade Federal de Pernambuco, 50670-901 Recife, PE, Brazil*

R. Srivastava

*Photonics Research Laboratory, University of Florida, Gainesville, Florida 32611*

(Received 26 August 1994; accepted for publication 11 November 1994)

The operation of an all-optical switch in a rare-earth doped channel waveguide is described. The switching mechanism is based on an optically induced intramodal energy exchange, driven by a resonantly enhanced nonlinearity of a  $\text{Nd}^{3+}$  ion. Switching times around  $410 \mu\text{s}$  at a repetition rate of 1 kHz was demonstrated. © 1995 American Institute of Physics.

A number of potentially useful all-optical switches and modulators have been demonstrated using channel or planar glass waveguides.<sup>1-5</sup> These devices are based on different optical processes, and the search for alternative components for photonic systems generally leads to the discovery of alternative switching mechanisms. Recently, optical-optical switching in  $\text{Er}^{3+}$  (Ref. 6) and in  $\text{Nd}^{3+}$  (Ref. 7) doped fibers with a length longer than 1 m have been described, exploiting the same effect: energy exchange between two lobes of a high order propagating mode. In both cases the switching was driven by a resonantly enhanced nonlinearity.

Here, we describe the application of the same all-optical switching process in an 8 mm long  $\text{Nd}^{3+}$  doped glass channel waveguide. As the process has been observed in erbium doped fibers pumped by a diode laser,<sup>6</sup> our results open up the possibility of very compact integrated devices, which we demonstrate here for the neodymium ion, but can be extended to other potentially useful rare-earth ions such as erbium or praseodymium doped in glass based waveguides.

The experimental scheme used is shown in Fig. 1. The second harmonic of a  $Q$ -switched and mode-locked Nd:YAG laser (100 ps pulses contained in a 30 pulses envelope separated by 10 ns and operating at repetition rates up to 1 kHz) has been employed as the pump beam, whereas the signal beam was derived from a 1 mW cw He-Ne laser. The  $\text{Nd}^{3+}$  doped channel waveguide used in this work has been used before as an amplifier to achieve a 15 dB gain at 1064 nm.<sup>8</sup> As described in Ref. 8, the waveguide was made from a silicate glass, especially prepared for ion exchange, containing 16%  $\text{Na}_2\text{O}$  and 2%  $\text{Nd}_2\text{O}_3$  by weight. The  $\text{K}^+ \leftrightarrow \text{Na}^+$  exchange was performed at 370 °C. Several channels 8 mm long and width varying from 2 to 10  $\mu\text{m}$  were buried in the glass creating a surface-index change  $\Delta n = 8.7 \times 10^{-3}$  for the TE mode. The glass absorption coefficient at 532 nm is 0.08/mm, which results in a  $\sim 50\%$  absorption for the 8 mm long channels used in this experiment. The pump beam at 532 nm is resonant with the  $^4I_{9/2} \rightarrow ^4G_{7/2}$  transition in the neodymium ion, whereas the signal beam at 632.8 nm is in a transparent window. The two beams were copropagated through the waveguide with the same polarization. The transmitted signal beam was detected by a fast (ns) photodiode and conveniently processed using either a digital oscilloscope or a lock-in amplifier.

The signal beam was preferentially launched equally in the  $\text{TE}_{00}$  and  $\text{TE}_{01}$  modes of a chosen 5  $\mu\text{m}$  wide channel,

whereas the pump beam (532 nm) was launched in the  $\text{TE}_{00}$  mode. Typical overall coupling efficiencies of 5% for the signal beam and 2% for the pump beam were achieved. The signal intensity distribution at the waveguide output appears as two lobes, as indicated in Fig. 1. The pump beam induces a differential phase shift in the two components of the signal beam because of the  $\text{TE}_{00}$  and  $\text{TE}_{01}$  spatial distribution and, as a consequence, a change in intensity occurs from one lobe to the other. An aperture placed in front of the detector was used to discriminate the two lobes of the signal beam. Maximum switching between the lobes was achieved for the maximum input average pump power of 7 mW (corresponding to peak intensities of  $\sim 9 \text{ GW/cm}^2$ ), limited by the waveguide front damage.

The nature of the optical nonlinearity exploited here is entirely electronic. The nonlinear refractive index of the waveguide medium depends on the electronic population distribution among the  $\text{Nd}^{3+}$  energy levels and transitions parameters such as levels lifetime, linewidths, and oscillators strength.<sup>9</sup> Thus, the switching process is controlled by the pump laser which induces intensity dependent changes in the waveguide refractive index.

Several features of the intramode energy transfer were analyzed. The power dependence of the switched signal (from one lobe to the other) as a function of pump power gave rise to a linear dependence, as expected for a single pump photon absorbed in the transition  $^4I_{9/2} \rightarrow ^4G_{7/2}$  of the neodymium ion. Sizable signals, corresponding to the refractive index changes have been observed in the 8 mm long channel waveguide. On the other hand, if an unpolarized

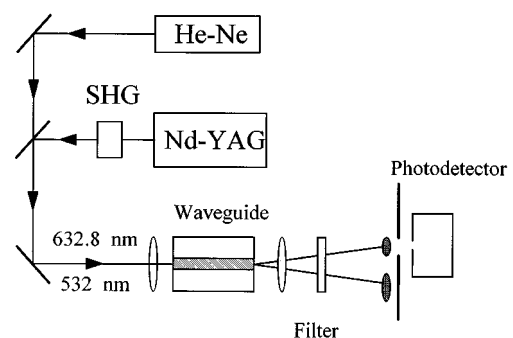


FIG. 1. Experimental scheme for intramode switching in  $\text{Nd}^{3+}$  doped channel glass waveguide. SHG is a second harmonic generator.

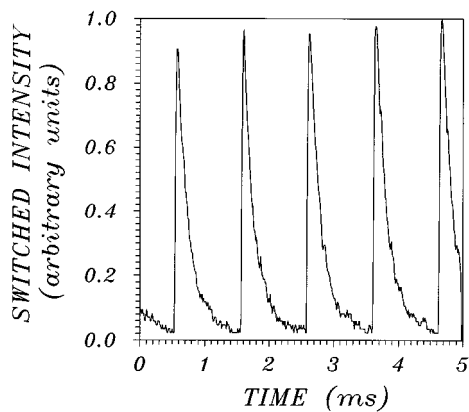


FIG. 2. Measured power in one port of the switch. The repetition rate was 1 kHz.

probe beam is used instead of a polarized one, the switched out pulse at the output port follows the polarization of the pump beam. The other polarization component is not affected. From the power dependence of the switched signal as a function of the laser intensity we estimated the nonlinear refractive index at the probe frequency ( $\approx 10^{-13} \text{ cm}^2/\text{W}$ ). This value is in agreement with the previous report for rare-earth doped fibers.<sup>10</sup>

Figure 2 shows the measured power in one lobe at a repetition rate of 1 kHz. A fitting to the experimental curve shows an exponential decay, which is governed by the lifetime of the  $^4G_{7/2}$  level ( $\sim 410 \mu\text{s}$ ). This decay time of the switched signal limits the maximum repetition rate of the switching process to about 2.5 kHz. We did not detect any evidence of the ion clusters, as described for the fiber work in Ref. 6, such as to reduce the fluorescence decay time and increase the maximum switchable repetition rate. It is worthwhile to point out that clustering of the active ions is a detrimental effect for applications like in optical amplifiers, and the waveguides used here has proved to be an excellent amplifying medium at  $1064 \text{ nm}^8$  and the absence of clusters, which enhances ion-ion interaction, is certainly an important aspect of this application. On the other hand, the modulator can be operated at large repetition rates using beam frequencies off-resonance with the  $\text{Nd}^{3+}$  transitions, but close to them. In such a condition, the dynamical behavior of the switching process will not be affected by the levels lifetime, and the relevant material parameters which will contribute to the signal decay are the dephasing time rates. For this case, the frequency denominator of the nonlinear refractive index changes with  $(\omega_0 - \omega_s)(\omega_0 - \omega_d)^2$ , where  $\omega_0$  is the  $\text{Nd}^{3+}$  transition frequency and  $\omega_s(\omega_d)$  is the signal (driving) frequency. Moreover, when  $\omega_d$  is much closer to the resonance than  $\omega_s$ , the driving beam intensity can be much less than that of the signal beam, and it will be possible for a weak driving beam to control a stronger signal beam. This kind of optical transistor action was recently demonstrated using an all-optical beam deflector<sup>11</sup> and is expected to be observed in the present modulator, provided tunable frequency lasers are available. Another interesting feature of the switching process is shown in Figs. 3(a) and 3(b) which were obtained

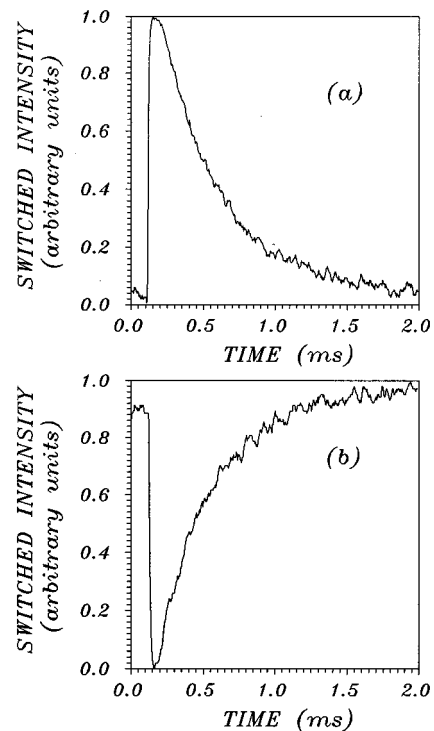


FIG. 3. (a) Measured power in one lobe and (b) measured power in the other lobe (obtained by displacing the aperture and detector). The  $180^\circ$  phase shift shows the energy exchange process. The repetition rate was 500 Hz. Both curves can be fitted by a single exponential with decay of  $410 \mu\text{s}$ .

with 500 Hz repetition rate and 7 mW of pump power. The observed decay time is the same obtained with a 1 kHz repetition rate, showing that thermal effects are not contributing to the results. By analyzing the output lobes we verify that a  $180^\circ$  phase difference exists between the switched signals as measured in the two lobes. This behavior manifests directly in the phase sensitive lock-in amplifier, but also looking directly at the energy of each lobe. This result is another clear indication that the energy transfer between the two lobes is induced by the driving beam.

In summary, we have demonstrated optically induced switching of a probe beam by exploiting a nonlinearity resonantly enhanced in a  $\text{Nd}^{3+}$  doped glass waveguide. This initial study used  $\text{Nd}^{3+}$  ions but other rare-earth ions will also perform well. The selection of appropriate dopants and laser frequencies may provide an important step towards a new type of compact modulators.

This work was partially supported by the Brazilian Agencies Financiadora de Estudos e Projetos (FINEP/PADCT) and Conselho Nacional de Desenvolvimento Científico e Tecnológico (CNPq).

<sup>1</sup>N. Finlayson, W. C. Banyai, E. M. Wright, C. T. Seaton, G. I. Stegeman, T. J. Cullen, and C. N. Ironside, *Appl. Phys. Lett.* **53**, 1144 (1988).

<sup>2</sup>S. R. Friberg, Y. Silberberg, M. K. Oliver, M. J. Andrejco, M. A. Saifi, and P. W. Smith, *Appl. Phys. Lett.* **51**, 1135 (1987).

<sup>3</sup>Y. Liu, E. Liu, G. Li, S. Zhang, J. Luo, F. Zhou, M. Cheng, B. Li, and H. Ge, *Appl. Phys. Lett.* **64**, 2079 (1994).

- <sup>4</sup>S. Nakamura, K. Tajima, N. Hamao, and Y. Sugimoto, *Appl. Phys. Lett.* **62**, 925 (1993).
- <sup>5</sup>A. S. L. Gomes, C. B. de Araújo, A. Miliou, and R. Srivastava, *Electron. Lett.* **29**, 1246 (1993).
- <sup>6</sup>R. H. Pantell, R. W. Sadowski, M. J. F. Digonnet, and H. J. Shaw, *Opt. Lett.* **17**, 1026 (1992).
- <sup>7</sup>R. W. Sadowski, M. J. F. Digonnet, R. H. Pantell, and H. J. Shaw, *Opt. Lett.* **18**, 927 (1993).
- <sup>8</sup>A. N. Miliou, X. F. Cao, R. Srivastava, and R. V. Ramaswamy, *IEEE Photonics Technol. Lett.* **PTL-4**, 416 (1993).
- <sup>9</sup>R. H. Pantell, M. J. F. Digonnet, R. W. Sadowski, and H. J. Shaw, *J. Lightwave Technol.* **11**, 1416 (1993); Y. L. Xue, P. L. Chu, and W. Zhang, *J. Opt. Soc. Am. B* **10**, 1840 (1993).
- <sup>10</sup>S. C. Fleming and T. J. Whitley, *Electron. Lett.* **27**, 1959 (1991).
- <sup>11</sup>H. Ma and C. B. de Araújo, *Appl. Phys. Lett.* **63**, 3553 (1993).



ELSEVIER

Available online at [www.sciencedirect.com](http://www.sciencedirect.com)

SCIENCE @ DIRECT®

Journal of Luminescence 102–103 (2003) 391–394

JOURNAL OF  
LUMINESCENCE

[www.elsevier.com/locate/jlumin](http://www.elsevier.com/locate/jlumin)

# Nanomaterials containing rare-earth ions Tb, Eu, Er and Yb: preparation, optical properties and application potential

T. Kim Anh<sup>a,b,\*</sup>, L. Quoc Minh<sup>a</sup>, N. Vu<sup>a</sup>, T. Thu Huong<sup>a</sup>, N. Thanh Huong<sup>a</sup>,  
C. Barthou<sup>c</sup>, W. Streck<sup>d</sup>

<sup>a</sup>*Institute of Materials Science, NCST of Vietnam, 18 Hoang Quoc Viet Road, Cau Giay, Hanoi, Viet Nam*

<sup>b</sup>*International Training Institute for Materials Science, Dai hoc Bach Khoa, 1 Dai Co Viet, Hanoi, Viet Nam*

<sup>c</sup>*Lab. d Optique des Solides UMR7601, Univ. P. & M. Curie, 4 Place Jussieu, F 75252 Paris Cedex 05, France*

<sup>d</sup>*Institute of Low Temperature and Structure Research, PAS, 2 Okolna, Wroclaw, Poland*

## Abstract

This paper focuses on preparation, optical properties and application potential of some nanomaterials based on  $Y_2O_3:Eu,Tb,Er,Yb$  and  $SiO_2-TiO_2$  and  $SiO_2-ZiO_2$  doped with Er and Yb.  $Y_2O_3$  nanophosphors are prepared by the combustion method with different doped concentrations. The nanocrystal size of  $Y_2O_3:Eu$  is from 4.4 to 72.2 nm depending on the technology condition. The luminescent spectra, up-conversion and lifetimes were measured and compared. The influence of the technological conditions on the luminescent properties was investigated in detail. The energy transfer effect was studied by the luminescent spectra and the lifetimes in the temperature dependence for the samples with rare-earth concentrations of 5 mol%. The relative concentration between Eu and Tb is 8/2 for energy transfer from Tb to Eu. The  $SiO_2-TiO_2$  and  $SiO_2-ZiO_2$  thin films containing Er rare-earth ion were prepared by the sol-gel technique. Optical properties were investigated and the influence of the Er concentration on the luminescent spectra as well as the influence of the Ti concentration on the refractive index of thin films was presented.

© 2003 Elsevier Science B.V. All rights reserved.

**Keywords:** Nanophosphors; Sol-gel; Rare earths; Waveguide

## 1. Introduction

Materials with nanostructure are increasingly interesting for optoelectronics and also for photonics. Nanomaterials display novel, often enhanced, properties compared to traditional materials, nanophosphors: synthesis, properties and applica-

tions were presented [1,2]. Luminescence properties of nanocrystalline  $Y_2O_3:Eu^{3+}$  in different host materials were studied [3]. High-definition displays call for sub-micron particle sizes to maximize screen resolution and screen efficiency. Nanophosphors codoped with Tb, Eu for high intensity of red region by energy transfer between Tb and Eu as well as  $Y_2O_3:Er,Yb$  for infrared region and up-conversion effect are interesting.  $SiO_2-TiO_2$  system offers the possibility of producing a material with a controllable refractive index from 1.46 (the refractive index of pure silica) to 2.2 (pure

\*Corresponding author. Institute of Materials Science, NCST of Vietnam, 18 Hoang Quoc Viet Road, Cau Giay, Hanoi, Viet Nam. Tel.: +84-4-7560371; fax: +84-4-7562039.

E-mail address: [kimanh@ims.ncst.ac.vn](mailto:kimanh@ims.ncst.ac.vn) (T.K. Anh).

amorphous  $\text{TiO}_2$ ).  $\text{SiO}_2$ – $\text{ZrO}_2$  thin films doped with rare earth are currently of much interest in planar waveguides application, because they are homogeneous and have the ability to tune the refractive index and wavelength [4]. Sol–gel chemistry, where all chemicals mix in the matrices in a molecular scale combined with the spin-coating or dip-coating technique, is a good method for producing rare-earth-doped planar waveguides [5]. We report the preparation, structure and optical properties of  $\text{SiO}_2$ – $\text{TiO}_2$ :Er or  $\text{SiO}_2$ – $\text{ZrO}_2$ :Er thin films and discuss briefly the possibility of the development of nanomaterials for active waveguides.

## 2. Experiment

The  $\text{Y}_2\text{O}_3$ :Eu,  $\text{Y}_2\text{O}_3$ :Tb,Eu and  $\text{Y}_2\text{O}_3$ :Er,Yb nanophosphors with different concentrations of RE were obtained from the calcination of the basic carbonate.  $\text{Eu}^{3+}$ ,  $\text{Tb}^{3+}$  or  $\text{Er}^{3+}$  and  $\text{Yb}^{3+}$  (RE) ions are easily hydrolyzed and then the precipitation of basic carbonate in an aqueous solution of urea or glycine.  $\text{SiO}_2$ – $\text{TiO}_2$ :Er and  $\text{SiO}_2$ – $\text{ZrO}_2$ :Er thin films were prepared via the hydrolysis and condensation of tetraethoxysilane  $\text{Si}(\text{OC}_2\text{H}_5)_4$  (TEOS) 98% Merck with Tetraisopropylorthotitanate  $\text{Ti}(\text{OC}_3\text{H}_7)_4$  Fluka [6] or  $\text{Zr}(\text{OC}_3\text{H}_7)_4$  Aldrich. The spin coating method on Si substrates in the clean room of the class 100, dip coating method and rapid thermal annealing were used.

The photoluminescence spectra were studied by the monochromator Jobin-Yvon HR 460, and a multichannel CCD detection from Instruments SA model Spectraview-2D and Triax 320 for infrared range measurements. The decay were analyzed by a PM Hamamatsu R928 and Nicolet 490 scope with a time constant of the order of 7 ns.  $\text{N}_2$ , diode, Ti-Sapphire or argon lasers were used as excitation sources for the different wavelengths. The morphology and particle sizes of  $\text{Y}_2\text{O}_3$ :RE was observed by using a high-resolution transmission electron microscope (TEM) Philips CM 200. The  $\text{Y}_2\text{O}_3$ :RE powder,  $\text{SiO}_2$ – $\text{TiO}_2$ :Er and  $\text{SiO}_2$ – $\text{ZrO}_2$ :Er were checked by the X-ray diffractometer D 5000 (Siemens) and Atom Force Microscope E<sup>+</sup> Digital (AFM).

## 3. Results and discussion

The value for crystallite size can be extracted according to the Warren–Averbach theory. The particle sizes are 4.4, 5.6, 15.2, 46.1 and 72.2 nm for  $\text{Y}_2\text{O}_3$ :Eu nanophosphors with various annealing times and temperatures 550°C, 60 min, 600°C, 30 min, 700°C, 30 min, 900°C, 30 min and 900°C, 60 min, respectively. The high-resolution TEM images of  $\text{Y}_2\text{O}_3$ :Er 5 mol% nanophosphors, 600°C, 30 min annealing was presented in Fig. 1. The development of efficient nanophosphors has been one of the key issues in commercializing the new type of flat panel display with respect to potentially higher display resolution. The optical efficiency of prepared spherical  $\text{Y}_2\text{O}_3$ :Eu as red phosphor was twice as much as that of commercial products in cathode luminescent according to Cho et al [7]. In order to increase efficient luminescence in the red phosphor, Eu is codoped with Tb for energy transfer effect. The luminescent spectra of  $\text{Y}_2\text{O}_3$ :Tb,Eu 5 mol% for three ratios 9/1, 8/2 and 7/3 are shown in Fig. 2 and relative ratio 8/2 has the strongest energy transfer. The full-width at half-maximum (FWHM) is also greater for the nanoparticles. Under 337.1 nm excitation,

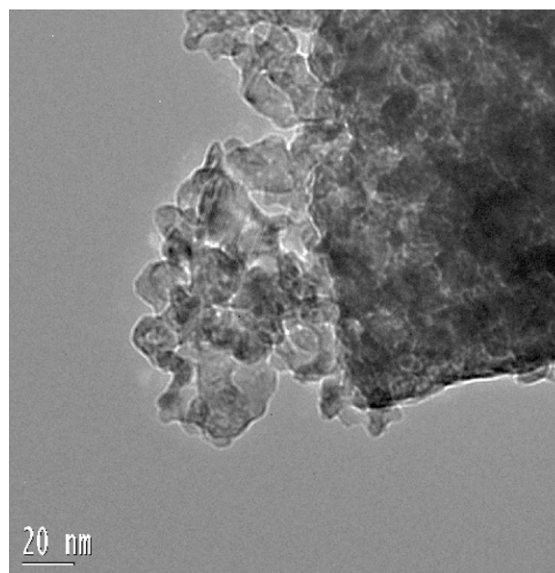


Fig. 1. High-resolution TEM image of  $\text{Y}_2\text{O}_3$ :Er (5 mol%) 600°C, 30 min.

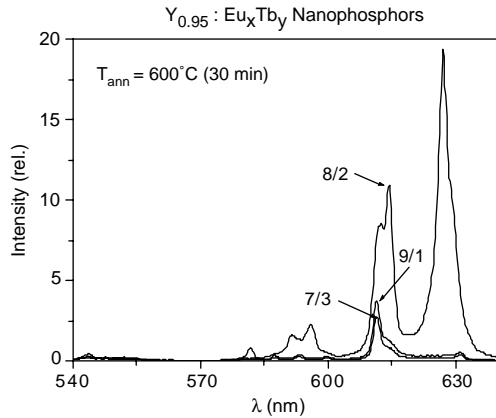


Fig. 2. Luminescent spectra of  $Y_{0.95}:Eu_xTb_y$  with the mole ratio of Eu/Tb: 7/3, 8/2, 9/1.  $\lambda_{exc} = 337.1$  nm.

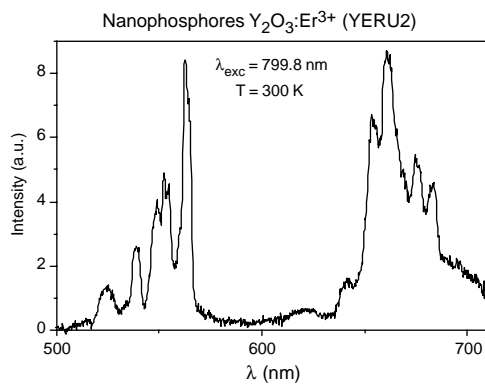


Fig. 3. Emission spectra of  $Y_2O_3:Er^{3+}$  (10%) nanophosphor.  $\lambda_{exc} = 799.8$  nm. Power laser: 550 mW.

$Y_2O_3:Tb, Eu$  presents for the  $^5D_0$  excited level of  $Eu^{3+}$  lifetimes of 360, 640 and 940  $\mu s$  for the ratio of Eu/Tb 8/2, 7/3 and 9/1, respectively. The up-conversion effect is observed for both  $Y_2O_3:Er$  and  $Y_2O_3:Er, Yb$ . Fig. 3 presents the up-conversion spectra of  $Y_2O_3:Er$  10 mol% at 799.8 nm excitation. The infrared luminescent spectra of  $Y_2O_3:Er$  10 mol% is presented in Fig. 4 for two annealing temperatures: 600°C and 700°C. To compare the green and the red up-conversion, we can propose two mechanisms. First mechanism for dominant green luminescence: the laser light brings the ion  $Er^{3+}$  into  $^4I_{9/2}$  level, which then non-radiatively decays to the  $^4I_{11/2}$  and  $^4I_{13/2}$  levels. Energy transfer processes bring the ion into  $^4F_{3/2}$  and  $^2H_{11/2}$ , non-radiative decay to the lower levels and

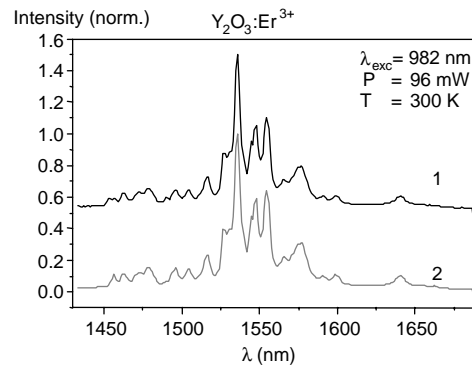


Fig. 4. Luminescent spectra in the infrared region of  $Y_2O_3:Er^{3+}$  (10 mol%) nanophosphors.  $\lambda_{exc} = 982$  nm. (1) 600°C, 30 min and (2) 700°C, 30 min.

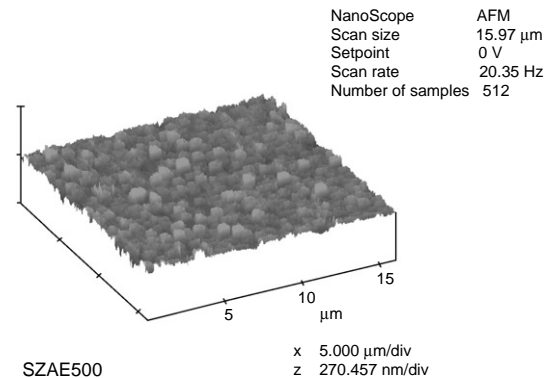


Fig. 5. AFM of the  $Er^{3+}$ -doped 83Silica/17Zirconia/Alumina (15%) sample was annealed at 880°C.

the  $^2H_{11/2}$ ,  $^4S_{3/2}$  transitions to  $^4I_{15/2}$ , and  $^4F_{9/2}$  transitions to  $^4I_{15/2}$  occur. The second mechanism is red luminescence stronger than green one. Laser beam brings the ion to the excited  $^4I_{9/2}$  level. One ion non-radiatively decays to the  $^4I_{13/2}$  level, and second one decays to the  $^4I_{11/2}$  level. Energy transfer processes bring the ion to the  $^4F_{9/2}$  and a red emission can be observed.

For codoped samples with Yb, an energy transfer from the  $^2F_{5/2}$  excited state of  $Yb^{3+}$  to  $Er^{3+}$  can occur.

For thin films prepared by dip coating, the AFM of the  $Er^{3+}$ -doped 83 Silica/17 Zirconia/Alumina (15%) sample annealed at 880°C is shown in Fig. 5. One can notice that the roughness is about 51 nm compared to the value of 24 nm for

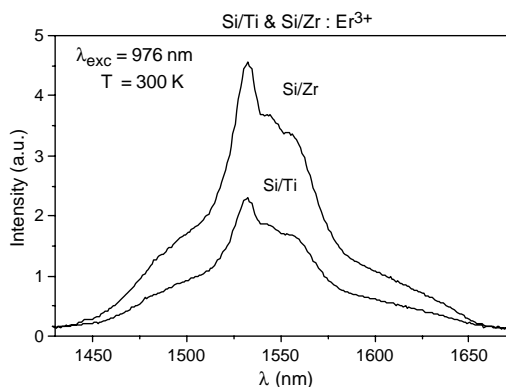


Fig. 6. Luminescent spectra of the  $\text{Er}^{3+}$  (5%) in Silica/Titania codoped with  $\text{Yb}^{3+}$  (12.5%) and Al (10%) annealed at  $950^\circ\text{C}$  and Silica/Zirconia samples codoped with  $\text{Yb}^{3+}$  (15%) and Al (6%) annealed at  $850^\circ\text{C}$ .

the case without Alumina. This value is convenient for planar waveguide application. Fig. 6 represents the luminescent spectra of the  $\text{Er}^{3+}$  (5%) in Silica/Titania codoped with  $\text{Yb}^{3+}$  (12.5%) and Al (10%) annealed at  $950^\circ\text{C}$  and the  $\text{Er}^{3+}$  (5%) in Silica/Zirconia samples codoped with  $\text{Yb}^{3+}$  (15%) and Al (6%) annealed at  $850^\circ\text{C}$ . The FWHM of the corresponding band from the  $^4\text{I}_{13/2}$ – $^4\text{I}_{15/2}$  transition is above 50 nm. The adding of alumina increases the process of densification of the silica–zirconia and silica–titania system. The refractive index varied from 1.49 to 1.60 with respect to the Ti concentration. Refractive index and thickness of  $90\text{SiO}_2$ – $10\text{TiO}_2$ ,  $85\text{SiO}_2$ – $15\text{TiO}_2$  and  $80\text{SiO}_2$ – $20\text{TiO}_2$  thin films at different annealing temperatures are presented in Ref. [8]. For example, for  $900^\circ\text{C}$  annealing temperature, the measured refractive indexes are 1.53, 1.56 and 1.60, respectively. The  $\text{SiO}_2$ – $\text{TiO}_2$ :Er thin films and  $\text{SiO}_2$ – $\text{ZrO}_2$ :Er thin films show the transitions from  $^4\text{I}_{13/2}$  to  $^4\text{I}_{15/2}$  of  $\text{Er}^{3+}$  in the infrared region (1530 nm) and  $^4\text{S}_{3/2}$  level to  $^4\text{I}_{15/2}$  in the visible region (550 nm).

#### 4. Conclusion

Nanophosphor  $\text{Y}_2\text{O}_3$ :RE (Tb, Eu, Er, Yb) 5–10 mol% samples were prepared by combustion method and the crystal size can be monitored in the range of 10–80 nm depending on technology

conditions.  $\text{SiO}_2$ – $\text{TiO}_2$ :Er and  $\text{SiO}_2$ – $\text{ZrO}_2$ :Er thin films were deposited by the spin coating and dip coating methods in order to study the optical properties as well as the possible application for planar waveguide. The typical transitions of trivalent Er and Eu were observed and discussed. Energy transfer and up-conversion mechanisms were studied. Refractive index for  $\text{SiO}_2$ – $\text{TiO}_2$  thin films can be tailored in a wide range by controlling the relative quantity of the two precursors. The emission depends on the temperature of the thermal processing and on the Er, Yb concentrations. This material will be promising for active waveguides in telecommunication application.

#### Acknowledgements

We would like to thank Prof. Nguyen Van Hieu, Prof. Clement Sanchez, and Dr. Paul Simons for their help. Our work was financially supported by the project Franco-Vietnamese 2001, the Institute of Materials Science, NCNST of Vietnam, the International Training Institute for Materials Science, the National Basic Research Programs of Vietnam 2001–2002.

#### References

- [1] G.Y. Hong, S.H. Kwon, J.S. Yoo, C.J. Summers, Extended Abstracts of the Fifth International Conference on the Science and Technology of Display Phosphors, San Diego, CA, November, 1999, pp.187–190
- [2] B.R. Ratna, A.D. Dinsmore, Y. Tian, S.B. Qadri, D.S. Hsu, H.F.Gray, Extended Abstracts of the Fifth International Conference on the Science and Technology of Display Phosphors, San Diego, CA, November 1999, pp. 295–296
- [3] R. Schmechel, M. Kennedy, H. von Seggern, H. Winkler, M. Kolbe, A. Fischer, L. Xiaomao, A. Benker, M. Winterer, H. Hahn, J. Appl. Phys. 89 (3) (2001) 1679.
- [4] C. Sanchez, B. Lebeau, MRS Bull. 26 (2001) 377.
- [5] X. Orignac, D. Barbier, X.M. Du, R.M. Almeida, Appl. Phys. Lett. 69 (7) (1996) 895.
- [6] L.Q. Minh, T.K. Anh, P. Benalloul, C. Barthou, in: E. Giacobino, et al. (Eds.), Advances in Optics and Spectroscopy, National University Press, Hanoi, 2001, pp. 505–509.
- [7] S.H. Cho, L.S. Yoo, J.D. Lee, J. Electrochem. Soc. 145 (3) (1998) 1017.
- [8] L.Q. Minh, N.T. Huong, C. Barthou, P. Benaloul, W. Strek, T.K. Anh, Mater. Sci. 20 (2) (2002) 63.

## Er<sup>3+</sup>-doped BaTiO<sub>3</sub> nanocrystals for thermometry: Influence of nanoenvironment on the sensitivity of a fluorescence based temperature sensor

Márcio A. R. C. Alencar, Glauco S. Maciel,<sup>a)</sup> and Cid B. de Araújo  
*Departamento de Física, Universidade Federal de Pernambuco, 50670-901 Recife, PE, Brazil*

Amitava Patra  
*Sol-Gel Division, Central Glass and Ceramic Research Institute Jadavpur, Kolkata 700 032, India*

(Received 15 December 2003; accepted 20 April 2004; published online 20 May 2004)

Frequency upconverted emissions centered at 526 and 547 nm from two thermodynamically coupled excited states of Er<sup>3+</sup> doped in BaTiO<sub>3</sub> nanocrystals were recorded in the temperature range from 322 to 466 K using a diode laser emitting at 980 nm as the excitation source. The ensemble measurements of the fluorescence intensity ratio (FIR) of the signals at 526 and 547 nm as a function of the temperature showed that the sensitivity (the rate in which the FIR changes with the temperature) of such sensor depends on the size of the nanocrystal. This is explained taking into consideration modifications of nonradiative relaxation mechanisms with the size of the nanocrystals.

© 2004 American Institute of Physics. [DOI: 10.1063/1.1760882]

Enormous interest in nanostructured materials for photonic applications has emerged in recent years. One class of such materials is represented by rare-earth doped nanocrystals (REDONs) that have been investigated for use as phosphors in amplifiers, lasers, and imaging of biological systems.<sup>1–3</sup> The promising optical properties of REDONs for photonic applications led, also, to investigations of frequency upconversion (UC).<sup>4,5</sup> Presently it is recognized that the UC efficiency depends on the nanoparticle shape, the site symmetry, and the statistical distribution of active ions. Also, the process of “miniaturization” of materials to the nanometer scale revealed that the radiative electronic relaxation probabilities of rare-earth ions doped in dielectric nanoparticles may be significantly different from their bulk counterparts.<sup>6–8</sup>

As we move towards nanotechnology, it is worthwhile to investigate the potential of REDONs as nanosensors. The application of rare-earth-doped bulk materials for temperature measurements has been considered by many authors using different techniques. In particular, temperature sensors based on the fluorescence intensity ratio (FIR) among different emission lines is an important method.<sup>9–12</sup> Generally, the FIR method involves measurements of the fluorescence intensities from two closely spaced electronic energy levels which are thermally coupled and which are assumed to be in a thermodynamical quasiequilibrium state.

In this letter we report the exploitation of REDONs for temperature measurements using the FIR method. We present ensemble measurements on frequency UC of erbium ions (Er<sup>3+</sup>) doped in BaTiO<sub>3</sub> nanocrystals to evaluate this material as a potential candidate for use as FIR based temperature nanosensors. The fluorescence properties of the Er<sup>3+</sup>-doped BaTiO<sub>3</sub> nanocrystals were analyzed by changing the temperature of samples made of nanocrystallites of different sizes and Er<sup>3+</sup> concentrations.

The sol-emulsion-gel method has been used for the preparation of Er<sup>3+</sup>-doped BaTiO<sub>3</sub> nanoparticles.<sup>13</sup> Barium acetate [Ba(CH<sub>3</sub>COO)<sub>2</sub>·H<sub>2</sub>O], titanium isopropoxide [Ti(OiPr)<sub>4</sub>] and erbium acetate were used as the starting materials for BaTiO<sub>3</sub> sol preparation. First, Ba(Ac)<sub>2</sub> was dissolved in water and acetic acid by stirring. Second, the required amount of titania sol was slowly added to this solution under vigorous stirring at room temperature. A clear transparent sol was thus obtained. Then, the required amount of erbium acetate was added to this sol. Afterward, the aqueous sol containing the desired constituents is added to a water-immiscible organic liquid under agitation. The gel particles were separated by centrifugation, followed by washing with acetone and methanol. The dried materials were calcined at different temperatures up to 1000 °C. Transmission electron microscopy was employed to determine the morphology and the particle size of the resulting powders. The crystalline phases of calcined powders were identified by x-ray diffraction. Diffraction patterns of the samples indicated the cubic phase of BaTiO<sub>3</sub> nanoparticles.<sup>13</sup> The crystallite size increases with an increase in the sintering temperature. The particle sizes were estimated using the Scherrer equation and transmission electronic microscopy, yielding average crystal sizes of ~26±4 and ~58±9 nm at 700 and 1000 °C, respectively, for 0.5 mol % Er<sub>2</sub>O<sub>3</sub> and ~60±10 nm for 2.0 mol % Er<sub>2</sub>O<sub>3</sub> at 1000 °C. The powders were pressed into thin disks and then cut into small pieces for optical measurements. Characteristics of the samples with different sizes and Er<sup>3+</sup> concentrations, labeled A, B, and C, are given in Table I.

For the fluorescence measurements the samples were placed on a hot plate and the temperature was monitored with thermocouples located close to the samples. The small size of the samples (typical diameter of ~3 mm; thickness ~0.2 mm) favors temperature homogeneity of the samples.

<sup>a)</sup>Corresponding author; electronic mail: glauco@df.ufpe.br

TABLE I. Samples characteristics and parameters used to fit the experimental data of the fluorescence intensity ratio for emission bands centered at 526 and 547 nm using a linear function  $\ln(\text{FIR}) = -(\alpha/T) + \beta$ .

| Sample | Er <sup>3+</sup> concentration (mol %) | Size of BaTiO <sub>3</sub> nanocrystals (nm) | $\alpha$ (K) | $\beta$   |
|--------|--|--|--------------|-----------|
| A      | 0.5                                    | 58   | 1140 ± 50    | 2.8 ± 0.1 |
| B      | 2.0                                    | 60   | 1200 ± 100   | 2.3 ± 0.3 |
| C      | 0.5                                    | 26   | 940 ± 50     | 1.8 ± 0.1 |

The samples were excited with a low power continuous-wave diode laser (wavelength: 980 nm; intensity:  $2.0 \times 10^3 \text{ W/cm}^2$ ) and the upconverted fluorescence (easily visible by the naked eye) was collected with a multimode fiber connected to a monochromator attached to a photomultiplier. The UC signal was sent to a personal computer for processing.

Figure 1 shows a simplified energy level scheme of Er<sup>3+</sup> and the frequency UC pathway investigated. The Er<sup>3+</sup> ions are excited through two-step one-photon absorption from the ground state  $^4I_{15/2}$  to the excited state  $^4F_{7/2}$  that relax nonradiatively to the emitting levels  $^2H_{11/2}$ ,  $^4S_{3/2}$  and  $^4F_{9/2}$ .

Figure 2 shows fluorescence bands centered at 526, 547, and 660 nm corresponding to  $^2H_{11/2} \rightarrow ^4I_{15/2}$ ,  $^4S_{3/2} \rightarrow ^4I_{15/2}$ , and  $^4F_{9/2} \rightarrow ^4I_{15/2}$  transitions, respectively. Note that the relative intensity between the emissions centered at 526 and 547 nm changes with the temperature for the three samples studied.

Figure 3 summarizes the behavior of the FIR for the emission lines centered at 526 and 547 nm as a function of the temperature, where the intensities were determined by integrating the area below the fluorescence curves. Note that the monolog plot of the experimental data yielded linear dependence of the FIR with inverse of the temperature. The data are fitted with a linear curve  $\ln(\text{FIR}) = -(\alpha/T) + \beta$  and Table I displays the average values for adjustable parameters  $\alpha$  and  $\beta$  taken from many sets of measurements. The slope of the linear curve (parameter  $\alpha$ ) is related to the sensitivity of the sensor defined as the rate in which the FIR changes with the temperature. The sensitivity found for our samples is  $\leq 0.0052 \text{ K}^{-1}$ . Note that  $\alpha$  does not change, within experimental error, for the samples with different Er<sup>3+</sup> concentrations and the same size but it changes when the nanoparticle

size is reduced. To explain this behavior we discuss the physical origin of  $\alpha$ . It has been established that the FIR from two thermally coupled energy levels separated in energy by  $\Delta E$  can be written as<sup>14</sup>

$$\text{FIR} = \frac{I_2}{I_1} = \frac{c_2(\nu_2)p_2^r\nu_2N_2}{c_1(\nu_1)p_1^r\nu_1N_1} = \frac{c_2(\nu_2)P_2^r\nu_2g_2}{c_1(\nu_1)P_1^r\nu_1g_1} \exp\left(\frac{-\Delta E}{kT}\right), \tag{1}$$

where the fluorescence intensities for the upper and lower thermally coupled levels are  $I_2$  and  $I_1$ , respectively (the fluorescence intensity is defined as  $I_i \sim N_i\nu_i p_i^r$  with  $i=1, 2$ ). The preexponential factor is a function of the fluorescence collection efficiencies,  $c_i(\nu_i)$ , the emission frequencies,  $\nu_i$ , and the spontaneous (radiative) emission rates,  $p_i^r$ , of the two thermally coupled levels with density of populations  $N_i$ . The Boltzmann constant is represented by  $k$ . Fitting parameter  $\alpha$  is related in a monolog plot to  $\Delta E/k$  and therefore the results shown in Table I could suggest that the energy spacing between states  $^4S_{3/2}$  and  $^2H_{11/2}$  would change with the size of the nanoparticles. This hypothesis is discarded because the wavelengths of the baricenter corresponding to transitions  $^4S_{3/2} \rightarrow ^4I_{15/2}$  and  $^2H_{11/2} \rightarrow ^4I_{15/2}$  do not change with the size and temperature of the samples.

Note that considering  $I_i \sim N_i\nu_i p_i^r$  does not take into account the changes of intensities with the temperature. This disagrees with our experimental results which show that the fluorescence bands decrease when the temperature increases

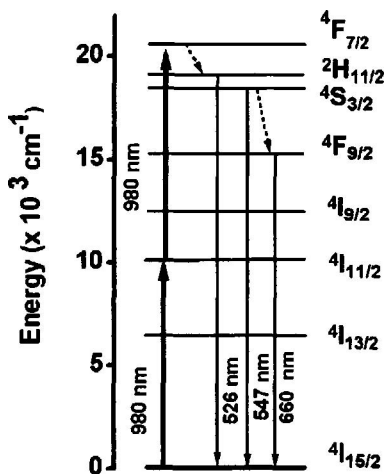


FIG. 1. Simplified Er<sup>3+</sup> energy levels scheme and frequency upconversion pathway.

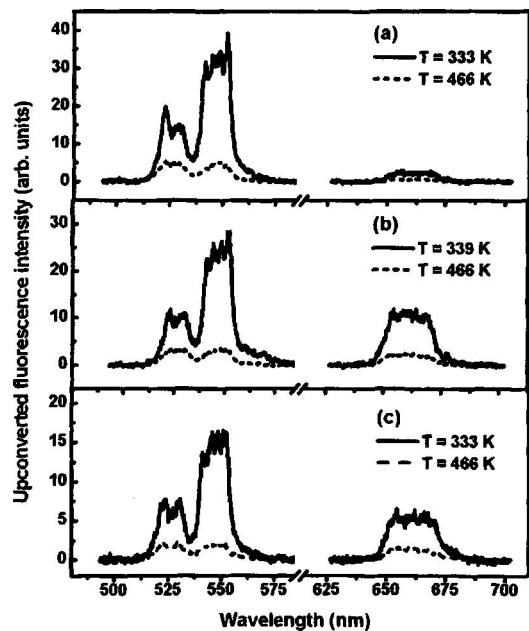


FIG. 2. Upconversion fluorescence from (a) sample A, (b) sample B, and (c) sample C, under diode laser irradiation (wavelength: 980 nm, intensity:  $2.0 \times 10^3 \text{ W/cm}^2$ ).

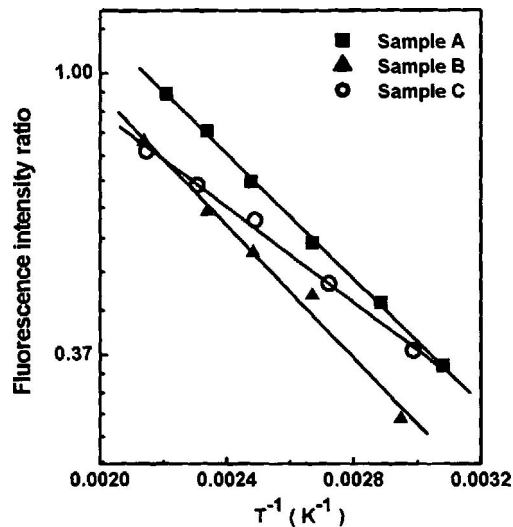


FIG. 3. Plot of the fluorescence intensity ratio for emission bands centered at 526 and 547 nm as a function of inverse temperature on a monolog scale. The fitting curves are linear functions,  $\ln(\text{FIR}) = -(\alpha/T) + \beta$ .

as shown in Fig. 2. To correct Eq. (1) we recall that temporal evolution of an excited state density of population can be described as  $N(t) = N(0)\exp(-t/\tau)$ , where  $\tau$  is the lifetime. The inverse of  $\tau$  is equal to the sum of the radiative emission rate and the nonradiative relaxation rate (NRR). The NRR changes with the temperature<sup>14</sup> and as a consequence  $\tau = \tau(T)$ . In the steady-state regime of excitation and fluorescence detection, it is the average intensity  $\langle I_i \rangle$  that matters and therefore one should consider  $\langle I_i \rangle \sim N_i(0)\tau_i(T)\nu_i p_i^r$ . This expression shows that when the temperature rises, the fluorescence intensity decreases because the lifetime is shortened due to the increase of the NRR. Therefore, Eq. (1) for the FIR from the two thermally coupled energy levels,  ${}^4S_{3/2}$  and  ${}^2H_{11/2}$ , is rewritten as

$$\text{FIR} = \frac{I_2}{I_1} = \frac{c_2(\nu_2)p_2^r\nu_2g_2\tau_2(T)}{c_1(\nu_1)p_1^r\nu_1g_1\tau_1(T)} \exp\left(\frac{-\Delta E}{kT}\right), \quad (2)$$

where we considered that the lifetime of levels  ${}^2H_{11/2}$  and  ${}^4S_{3/2}$  are temperature dependent.

In bulk materials, the temperature dependence of the NRR is determined by the “effective phonon mode” of the host.<sup>15,16</sup> However, as the size of the crystal decreases, the contribution of fluorescent ions located at surface sites becomes increasingly important. The fluorescence from these ions is influenced by nonradiative relaxation channels that are not only related to lattice vibrational modes but also to high-energy modes of residual carbonates ( $\sim 1500 \text{ cm}^{-1}$ ) and hydroxyl ions ( $\sim 3350 \text{ cm}^{-1}$ ) adsorbed in the crystallite surfaces.<sup>13</sup> By increasing the calcination temperature the hydroxyl and carbonate contents of the samples are reduced. Thus, sample C, calcined at  $700^\circ\text{C}$ , is expected to have a higher NRR than samples A and B calcined at  $1000^\circ\text{C}$ . The extra high-energy modes modify the NRR of levels  ${}^2H_{11/2}$  and  ${}^4S_{3/2}$ , therefore it is expected that sample C presents different sensitivity, as shown in Fig. 3.

It is worthwhile to compare the herein proposed nanosensor with a recently reported device based on oxidation of a gallium film inside a carbon nanotube.<sup>17</sup> The major

drawback of that kind of sensor is that it is a one-time-use nanothermometer. Once the gallium film is oxidized another measurement of the temperature requires a fresh nanotube. Another limitation is that the nanothermometer of Ref. 17 only measures temperatures in an oxygen-containing environment (for oxidation of the gallium film). A temperature nanosensor based on the FIR from a single REDON would be a permanent device, which could be illuminated with a low cost diode laser, and would not require specific environmental conditions. The fluorescence detection scheme allows real-time reading of the temperature. One possible use of this nanosensor is for biological applications. In this case, it is thought that the sensitivity changes when the nanocrystal is immersed in an aqueous medium because the luminescence lifetime of a REDON also changes with the surrounding medium.<sup>18</sup> We are currently investigating this.

In conclusion, we have demonstrated that  $\text{Er}^{3+}$ -doped  $\text{BaTiO}_3$  nanocrystals are suitable for use as FIR based temperature nanosensors. Our results showed that the sensitivity of the nanothermometer is influenced by nonradiative relaxation channels which depend on the size of the nanocrystal.

The authors acknowledge financial support by Brazilian agencies Conselho Nacional de Desenvolvimento Científico e Tecnológico (CNPq) and Fundação de Apoio à Ciência e Tecnologia do Estado de Pernambuco (FACEPE). One of the authors A.P. thanks Dr. H. S. Maiti, Director of the Central Glass and Ceramic Research Institute, for his constant encouragement and active cooperation in carrying out this work. The Department of Science and Technology (NSTI Grant No. SR/S5/NM-05/2003) is acknowledged for financial support.

- <sup>1</sup>J. W. Stouwdam and F. C. J. M. van Veggel, *Nano Lett.* **2**, 733 (2002).
- <sup>2</sup>B. Li, G. Williams, S. C. Rand, T. Hinklin, and R. M. Laine, *Opt. Lett.* **27**, 394 (2002).
- <sup>3</sup>M. J. Dejneka, A. Streltsov, S. Pal, A. G. Frutos, C. L. Powell, K. Yost, P. K. Yuen, U. Müller, and J. Lahiri, *Proc. Natl. Acad. Sci. U.S.A.* **100**, 389 (2003).
- <sup>4</sup>D. Matsuura, *Appl. Phys. Lett.* **81**, 4526 (2002).
- <sup>5</sup>A. Patra, C. S. Friend, R. Kapoor, and P. N. Prasad, *Appl. Phys. Lett.* **83**, 284 (2003).
- <sup>6</sup>H.-S. Yang, K. S. Hong, S. P. Feofilov, B. M. Tissue, R. S. Meltzer, and W. D. Dennis, *J. Lumin.* **83–84**, 139 (1999).
- <sup>7</sup>H. Schniepp and V. Sandoghdar, *Phys. Rev. Lett.* **89**, 257403 (2002).
- <sup>8</sup>A. Mehta, T. Thundat, M. D. Barnes, V. Chhabra, R. Bhargava, A. P. Bartko, and R. M. Dickson, *Appl. Opt.* **42**, 2132 (2003).
- <sup>9</sup>H. Berthou and C. K. Jørgensen, *Opt. Lett.* **15**, 1100 (1990).
- <sup>10</sup>G. S. Maciel, L. de S. Menezes, A. S. L. Gomes, C. B. de Araújo, Y. Messaddeq, A. Florez, and M. A. Aegerter, *IEEE Photonics Technol. Lett.* **7**, 1474 (1995).
- <sup>11</sup>P. V. dos Santos, M. T. de Araújo, A. S. Gouveia-Neto, J. A. Medeiros-Neto, and A. S. B. Sombra, *IEEE J. Quantum Electron.* **35**, 395 (1999).
- <sup>12</sup>S. A. Wade, S. F. Collins, and W. G. Baxter, *J. Appl. Phys.* **94**, 4743 (2003).
- <sup>13</sup>A. Patra, C. S. Friend, R. Kapoor, and P. N. Prasad, *Chem. Mater.* **15**, 3650 (2003).
- <sup>14</sup>M. D. Shinn, W. A. Sibley, M. G. Drexhage, and R. N. Brown, *Phys. Rev. B* **27**, 6635 (1983).
- <sup>15</sup>F. Auzel and F. Pellé, *Phys. Rev. B* **55**, 11006 (1997).
- <sup>16</sup>L. de S. Menezes, G. S. Maciel, C. B. de Araújo, and Y. Messaddeq, *J. Appl. Phys.* **94**, 863 (2003).
- <sup>17</sup>Y. Gao, Y. Bando, Z. Liu, D. Golberg, and H. Nakanishi, *Appl. Phys. Lett.* **83**, 2913 (2003).
- <sup>18</sup>R. S. Meltzer, S. P. Feofilov, B. Tissue, and H. B. Yuan, *Phys. Rev. B* **60**, R14012 (1999).